Springer Proceedings in Mathematics & Statistics

Jan Awrejcewicz *Editor*

Dynamical Systems in Theoretical Perspective

Łódź, Poland December 11–14, 2017

Springer

Springer Proceedings in Mathematics & Statistics

Volume 248

Springer Proceedings in Mathematics & Statistics

This book series features volumes composed of selected contributions from workshops and conferences in all areas of current research in mathematics and statistics, including operation research and optimization. In addition to an overall evaluation of the interest, scientific quality, and timeliness of each proposal at the hands of the publisher, individual contributions are all refereed to the high quality standards of leading journals in the field. Thus, this series provides the research community with well-edited, authoritative reports on developments in the most exciting areas of mathematical and statistical research today.

More information about this series at http://www.springer.com/series/10533

Jan Awrejcewicz
Editor

Dynamical Systems in Theoretical Perspective

Łódź, Poland December 11–14, 2017

Springer

Editor
Jan Awrejcewicz
Department of Automation,
Biomechanics and Mechatronics
Łódź University of Technology
Łódź, Poland

ISSN 2194-1009 ISSN 2194-1017 (electronic)
Springer Proceedings in Mathematics & Statistics
ISBN 978-3-319-96597-0 ISBN 978-3-319-96598-7 (eBook)
https://doi.org/10.1007/978-3-319-96598-7

Library of Congress Control Number: 2018948717

Mathematics Subject Classification (2010): 28D-XX, 34Ccc, 37-XX, 46L-xx, 65-XX, 70-XX, 74-XX, 76-XX

This Springer imprint is published by the registered company Springer Nature Switzerland AG
The registered company address is: Gewerbestrasse 11, 6330 Cham, Switzerland

Preface

The present volume is devoted to the 14th edition of a cyclic scientific event—the International Conference "Dynamical Systems: Theory and Applications" (DSTA)—organised by the Department of Automation, Biomechanics and Mechatronics of the Lodz University of Technology every two years. DSTA belong to important events gathering a great number of researchers and engineers from different fields of science where modelling and analysis of dynamical systems play an important role. The volume is a result of a selection of the representative, theory-oriented chapters written by the participants of the 14th edition of the DSTA Conference.

The book not only provides the readers with an overview of the recent developments in the field of dynamical systems but also helps finding answers to readers' own problems and aims to inspire further research.

Argáez et al. (Chapter "Computational Approach for Complete Lyapunov Functions") presented results of the research aimed to improve the complete algorithm for Lyapunov function computation that resulted in better approximation to the chain-recurrent set in the system.

In Chapter "Non-conservative Instability of Cantilevered Nanotube Via Cell Discretization Method", Auciello et al. employed the cell discretization method to analyse the dynamic instability of the cantilevered single-walled carbon nanotube with concentrated mass and subjected to a follower force at the end. Application of the discrete system model obtained by reduction of the nanotube to a set of rigid bars linked by elastic constraints allowed the authors to take into account non-local effects, added mass and the direction of the follower force.

Bełdowski et al. (Chapter "Fractional Calculus Evaluation of Hyaluronic Acid Crosslinking in a Nanoscopic Part of Articular Cartilage Model System") studied mechanics of physical crosslinking of hyaluronic acid in the presence of common phospholipids in the synovial joint organ systems. Applying fractional calculus, they obtained results suggesting sub-diffusion characteristics in the investigated system.

Biś and Namiecińska (Chapter "Topological and Measure-Theoretical Entropies of a Solenoid") applied the topological and measure-theoretical approach to dynamical properties of a solenoid and discussed homogeneous measures.

Björnsson and Hafstein (Chapter "Lyapunov Functions for Almost Sure Exponential Stability") focused on proving Mao's theorems on the Lyapunov functions for a wider class of functions aiming to make them much more applicable.

In Chapter "Numerical Analysis of Dynamic Stability of an Isotropic Plate by Applying Tools Used in Dynamics", Borkowski presented the results of an analysis of an isotropic plate in terms of its dynamic stability (or instability). For this purpose, he applied tools that are usually used in the vibrations theory of dynamical systems.

Byrtus and Dyk (Chapter "Rigid Jeffcott Rotor Bifurcation Behaviour Using Different Models of Hydrodynamic Bearings") focused on dynamics of a modified version of the Jeffcott rotor. They applied different models of hydrodynamic bearings. The research allowed them to detect non-linear phenomena such as bifurcations.

In Chapter "The Burden of the Coinfection of HIV and TB in the Presence of Multi-drug Resistant Strains", Carvalho and Pinto introduced fractional-order modelling of infection with HIV and multi-drug resistant tuberculosis strains. It yielded biologically reliable results for analysis of the burden of the coinfection and treatment for both diseases.

In Chapter "Value Distribution and Growth of Solutions of Certain Painlevé Equations", Ciechanowicz and Filipuk estimated new results for four chosen Painlevé equations for value distribution and the growth theory, with such values as defect, deviation or multiplicity index.

Based on the singular perturbation method, Danik et al. (Chapter "Numerical-Analytical Algorithms for Nonlinear Optimal Control Problems on a Large Time Interval") obtained algorithms that can be applied for numerical-analytical investigations of the non-linear continuous and discrete optimal control on a large finite time interval.

In Chapter "The Dynamic Behavior of the Vehicle Wheels Under Impact Loads—FEM and Experimental Researches", Demiyanushko et al. applied experimental and finite element methods for studies of the dynamic behaviour of the vehicle wheels subjected to the impact load.

Goncalves Luz Junior et al. (Chapter "Optimal Control for Robot Manipulators with Three-Degrees-of-Freedom") focused on the modelling and simulation of optimal control of robot manipulators for a planar robot with three-degrees-of-freedom.

In Chapter "Optimal Control of Automotive Multivariable Dynamical Systems", Jackiewicz discussed adaptive systems for automotive applications based on the direct or self-tuning optimal controller strategies fixed by means of memetic algorithms.

Jackowska-Zduniak and Foryś (Chapter "Mathematical Model of Two Types of Atrioventricular Nodal Reentrant Tachycardia: Slow/Fast and Slow/Slow") proposed application of a model consisting of two coupled van der Pol equations to describe heart's pathological behaviour in heart's conducting system such as slow/fast and slow/slow type of atrioventricular nodal reentrant tachycardia.

Motion of a small-scale Darrieus counter-rotating vertical axis wind turbine was the subject of the study described by Klimina et al. in Chapter "Two-Frequency Averaging in the Problem of Motion of a Counter-Rotating Vertical Axis Wind

Turbine". The authors focused on two-frequency averaging over two angular coordinates of the designed dynamical model.

Knap et al. (Chapter "Process-Oriented Approach to the Design of Cyber-Physical Systems") described a simple way of projecting the cyber-physical systems projects, which is comprehensible for engineers working in different fields. The proposed task-oriented approach to designing CPS draws attention to identification of the connection between resources and allows for identification of threats to the components, connections between them or to the working system.

A dynamic model of a hypothetical missile-artillery system mounted on a moving object was presented by Koruba et al. in Chapter "An Inverse Dynamics Analysis of the Remote Controlled Artillery-Missile System Under the Influence of Disturbances", taking into account driving torques for the azimuth, the elevation angle and the angular and linear displacements of the set base relative to the given stationary coordinate system.

In Chapter "Approximate Identification of Dynamical Systems", Kozánek et al. dealt with an approximate identification of linear dynamical systems by time response on unknown initial displacement (or velocity) with the help of the Fourier transform.

Makowski (Chapter "Algorithm for Damping Control in Vehicle Suspension Equipped with Magneto-Rheological Dampers") devoted his study to the control algorithms of semi-active systems for suspension of a vehicle equipped with controlled magneto-rheological dampers.

In Chapter "Shadowing, Entropy and Minimal Sets", Oprocha described consequences of the shadowing property for global and local aspects of dynamics, taking into account, for instance, approximation of invariant measures by ergodic measures.

Ozga (Chapter "Analysis of Vibrations of an Oscillator Using Statistical Series") applied the statistical series method to solve problems of determination of an approximate distribution of the strength of stochastic impulses forcing vibrations of an oscillator with damping in systems subjected to random series of impulses.

Pawlak and Korczak-Kubiak (Chapter "On Local Aspects of Entropy") introduced the notion of a full entropy point and an unbalanced point. Also, they used graphical approximation by functions having either the full entropy point or the unbalanced point.

In Chapter "Optimal Control of Hybrid Systems with Sliding Modes", Pytlak et al. focused on the numerical procedure for solving hybrid optimal control problems with sliding modes. The proposed approach was coped with differential–algebraic equations and guaranteed accurate tracking of the sliding motion surface.

Rysak et al. (Chapter "Study of the High-Amplitude Solutions in the System of Magnetic Sliding Oscillator with Many Degrees of Freedom") investigated phenomena of the high-amplitude solutions in the system of magnetic sliding oscillator with many degrees of freedom.

In Chapter "Theoretical Investigations on the Behavior of Artificial Sensors for Surface Texture Detection", Scharff et al. analysed the influence of different magnitudes of velocities and friction coefficients on the proposed quasi-static model of the artificial tactile sensor.

Sumi et al. (Chapter "Dynamic Analysis of a Compliant Tensegrity Structure for the Use in a Gripper Application") focused on investigations of the dynamic behaviour of a planar tensegrity structure with multiple static equilibrium configurations with respect to its further use in a two-finger-gripper application.

A study of a synchronisation phenomenon as observed in a rotating structure consisting of three composite beams and a hub was described by Szmit et al. in Chapter "Synchronisation Analysis of a De-tuned Three-Bladed Rotor".

Szulim and Radkowski (Chapter "The Analytical Approach for Identification of Magnetically Induced Vibrations of Working in Faulty State BLDC Motor") presented a comparison of numerical and experimental results for identification of magnetically induced vibrations of a BLDC motor working in a faulty state.

In Chapter "Micro-Dynamics of Thin Tolerance-Periodic Cylindrical Shells", Tomczyk and Szczerba focused on thin linearly elastic Kirchhoff–Love-type open circular cylindrical shells of a functionally graded macrostructure and on the tolerance-periodic microstructure in circumferential direction.

Bielski and Wojnar (Chapter "Stokes Flow Through a Tube with Wavy Wall") investigated the propagation of long gravity waves past an incompressible fluid in a channel and in a tank with an uneven bottom by means of an asymptotic homogenisation theory.

In Chapter "Implementation of the Adaptive Control Algorithm for the KUKA LWR 4+ Robot", Woliński investigated a dynamical model of the adaptive controller for the KUKA lightweight redundant robotic manipulator robot.

In Chapter "Vibrations of a Multi-span Beam Subjected to a Moving Stochastic Load", Zakęś and Śniady presented a study of the dynamic behaviour of a multi-span uniform continuous beam excited by a moving stochastic load.

I greatly appreciate the help of the Springer Editor, Elizabeth Leow, in publishing the chapters recommended by the Scientific Committee of the DSTA 2017 Conference after a standard peer review procedure. Also, I would like to express my gratitude to reviewers for their voluntary help and support.

Łódź, Poland
June 2018

Jan Awrejcewicz

Contents

Computational Approach for Complete Lyapunov Functions 1
Carlos Argáez, Peter Giesl and Sigurdur Freyr Hafstein

Non-conservative Instability of Cantilevered Nanotube Via Cell Discretization Method 13
Nicola Maria Auciello, Maria Anna De Rosa, Maria Lippiello and Stefania Tomasiello

Fractional Calculus Evaluation of Hyaluronic Acid Crosslinking in a Nanoscopic Part of Articular Cartilage Model System 25
Piotr Bełdowski, Piotr Weber, Tristan De Leon, Wayne K. Auge II and Adam Gadomski

Topological and Measure-Theoretical Entropies of a Solenoid 37
Andrzej Biś and Agnieszka Namiecińska

Lyapunov Functions for Almost Sure Exponential Stability 51
Hjortur Björnsson and Sigurdur Freyr Hafstein

Numerical Analysis of Dynamic Stability of an Isotropic Plate by Applying Tools Used in Dynamics 63
Lukasz Borkowski

Rigid Jeffcott Rotor Bifurcation Behaviour Using Different Models of Hydrodynamic Bearings 75
Miroslav Byrtus and Štěpán Dyk

The Burden of the Coinfection of HIV and TB in the Presence of Multi-drug Resistant Strains 87
Ana Carvalho and Carla M. A. Pinto

Value Distribution and Growth of Solutions of Certain Painlevé Equations 99
Ewa Ciechanowicz and Galina Filipuk

Numerical-Analytical Algorithms for Nonlinear Optimal Control Problems on a Large Time Interval 113
Yulia Danik, Mikhail Dmitriev, Dmitry Makarov and Tatiana Zarodnyuk

The Dynamic Behavior of the Vehicle Wheels Under Impact Loads—FEM and Experimental Researches 125
Irina Demiyanushko, Aleksandr Vakhromeev, Evgeny Loginov and Violetta Mironova

Optimal Control for Robot Manipulators with Three-Degress-of-Freedom 135
Jose Adenilson Gonalves Luz Junior, Angelo Marcelo Tusset, Frederic Conrad Janzen, Rodrigo Tumolin Rocha, Jose Manoel Balthazar and Airton Nabarrete

Optimal Control of Automotive Multivariable Dynamical Systems 151
Jacek Jackiewicz

Mathematical Model of Two Types of Atrioventricular Nodal Reentrant Tachycardia: Slow/Fast and Slow/Slow 169
Beata Jackowska-Zduniak and Urszula Foryś

Two-Frequency Averaging in the Problem of Motion of a Counter-Rotating Vertical Axis Wind Turbine 183
Liubov Klimina, Ekaterina Shalimova, Marat Dosaev, Boris Lokshin and Vitaly Samsonov

Process-Oriented Approach to the Design of Cyber-Physical Systems 193
Lech Knap, Jędrzej Mączak and Michał Trojgo

An Inverse Dynamics Analysis of the Remote Controlled Artillery-Missile System Under the Influence of Disturbances 205
Zbigniew Koruba, Daniel Gapiński and Piotr Szmidt

Approximate Identification of Dynamical Systems 217
Jan Kozánek, Štěpán Chládek, Jaroslav Zapoměl and Lucie Švamberová

Algorithm for Damping Control in Vehicle Suspension Equipped with Magneto-Rheological Dampers 235
Michal Makowski

Shadowing, Entropy and Minimal Sets 249
Piotr Oprocha

Analysis of Vibrations of an Oscillator Using Statistical Series 261
Ozga Agnieszka

On Local Aspects of Entropy 271
Ryszard J. Pawlak and Ewa Korczak-Kubiak

Optimal Control of Hybrid Systems with Sliding Modes 283
Radosław Pytlak, Damian Suski and Tomasz Tarnawski

Study of the High-Amplitude Solutions in the System of Magnetic Sliding Oscillator with Many Degrees of Freedom 295
Andrzej Rysak, Magdalena Gregorczyk, Konrad Chwełatiuk and Daniel Gąska

Theoretical Investigations on the Behavior of Artificial Sensors for Surface Texture Detection 311
Moritz Scharff, Maximilian Darnieder, Joachim Steigenberger, Jorge H. Alencastre and Carsten Behn

Dynamic Analysis of a Compliant Tensegrity Structure for the Use in a Gripper Application 323
Susanne Sumi, Philipp Schorr, Valter Böhm and Klaus Zimmermann

Synchronisation Analysis of a De-Tuned Three-Bladed Rotor 335
Zofia Szmit, Jerzy Warmiński and Jarosław Latalski

The Analytical Approach for Identification of Magnetically Induced Vibrations of Working in Faulty State BLDC Motor 349
Przemysław Szulim and Stanisław Radkowski

Micro-dynamics of Thin Tolerance-Periodic Cylindrical Shells 363
Barbara Tomczyk and Paweł Szczerba

Stokes Flow Through a Tube with Wavy Wall 379
Włodzimierz Bielski and Ryszard Wojnar

Implementation of the Adaptive Control Algorithm for the KUKA LWR 4+ Robot 391
Łukasz Woliński

Vibrations of a Multi-span Beam Subjected to a Moving Stochastic Load 403
Filip Zakęś and Paweł Śniady

Computational Approach for Complete Lyapunov Functions

Carlos Argáez, Peter Giesl and Sigurdur Freyr Hafstein

Abstract Ordinary differential equations arise in a variety of applications, including climate modeling, electronics, predator-prey modeling, etc., and they can exhibit highly complicated dynamical behaviour. Complete Lyapunov functions capture this behaviour by dividing the phase space into two disjoint sets: the chain-recurrent part and the transient part. If a complete Lyapunov function is known for a dynamical system the qualitative behaviour of the system's solutions is transparent to a large degree. The computation of a complete Lyapunov function for a given system is, however, a very hard task. We present significant improvements of an algorithm recently suggested by the authors to compute complete Lyapunov functions. Previously this methodology was incapable to fully detect chain-recurrent sets in dynamical systems with high differences in speed. In the new approach we replace the system under consideration with another one having the same solution trajectories but such that they are traversed at a more uniform speed. The qualitative properties of the new system such as attractors and repellers are the same as for the original one. This approach gives a better approximation to the chain-recurrent set of the system under study.

Keywords Complete Lyapunov Function · Dynamical Systems
Lyapunov theory · Meshless collocation · Radial Basis Functions

C. Argáez (✉) · S. F. Hafstein
Science Institute, University of Iceland, Dunhagi 5, 107,
Reykjavík, Iceland
e-mail: carlos@hi.is

S. F. Hafstein
e-mail: shafstein@hi.is

P. Giesl
Department of Mathematics, University of Sussex,
Falmer BN1 9QH, UK
e-mail: P.A.Giesl@sussex.ac.uk

J. Awrejcewicz (ed.), *Dynamical Systems in Theoretical Perspective*,
Springer Proceedings in Mathematics & Statistics 248,
https://doi.org/10.1007/978-3-319-96598-7_1

1 Introduction

Let us consider a general autonomous ordinary differential equation (ODE) $\dot{\mathbf{x}} = \mathbf{f}(\mathbf{x})$, where $\mathbf{x} \in \mathbb{R}^n$. A (classical) Lyapunov function [1] is a scalar-valued function defined in a neighborhood of an invariant set. It is built to show the stability of such a set and can be used to analyse its basin of attraction. Hence, it is linked to one attractor, e.g. an equilibrium or a periodic orbit. In particular, a (strict) Lyapunov function attains its minimum on the attractor and is strictly decreasing along solutions of the ODE.

This idea is generalized to a complete Lyapunov function [2–5], which completely characterizes the behaviour of the dynamical system in the whole phase space.

> A complete Lyapunov function is a scalar-valued function $V : \mathbb{R}^n \to \mathbb{R}$ which is defined not only on a neighbourhood of one attractor but in the whole phase space under the condition of being non-increasing along solutions of the ODE.

The phase space can be divided into the area where the complete Lyapunov function strictly decreases along solution trajectories and the area where it is constant along solution trajectories. If the complete Lyapunov function is sufficiently smooth, these properties can be expressed by the orbital derivative $V'(\mathbf{x}) = \nabla V(\mathbf{x}) \cdot \mathbf{f}(\mathbf{x})$, i.e. the derivative along solutions of the ODE. The first area, where $V'(\mathbf{x}) < 0$, characterizes the region where solutions pass through and the larger this area is, the more information is obtained from the complete Lyapunov function. The second area, where $V'(\mathbf{x}) = 0$, includes the chain-recurrent set; the complete Lyapunov function is constant on each transitive component of the chain-recurrent set. In short, the first one determines where solutions pass through while the second accounts for determining the long-time behaviour.

Dynamical systems model real-world systems and describe their often complicated behaviour, e.g. the double [6] and triple pendulum with periodic forcing [7] and dry friction [8], leading to time-periodic and non-smooth systems, or the dynamics of the wobblestone [9]. There are many methods to analyse the qualitative behaviour of a given dynamical systems: one of them directly simulates solutions with many different initial conditions. This becomes very expensive and unable to provide general information on the behaviour of a given system, unless estimates are available, e.g. when shadowing solutions. More sophisticated methods include invariant manifolds and their computation, which form boundaries of basins of attraction for the attractors [10]. The cell mapping approach [11] or set oriented methods [12] divide the phase space into cells and compute the dynamics between them, see e.g. [13]. These ideas have been used for a computational approach to construct complete Lyapunov functions [14], where the authors consider the discrete system given by the time-T map, divide the phase space into cells and compute the dynamics between them through an induced multivalued map. This is done with the computer package GAIO [15]. Then, using graphs algorithms, an approximate complete Lyapunov function is computed [16]. However, even for low dimensions, a high number of

cells is required to compute the Lyapunov function under this approach. We will use a different methodology, significantly improving the method described in [17].

Our new approach follows from a method to compute classical Lyapunov functions for a given equilibrium by approximating the solution to $V'(\mathbf{x}) = -1$, i.e. the orbital derivative. We approximate the solution of this partial differential equation (PDE) by means of mesh-free collocation with Radial Basis Functions: over a finite set of collocation points X, we compute an approximation v to V that solves the PDE in all collocation points.

At points of the chain-recurrent set, such as an equilibrium or periodic orbit, the PDE does not have a solution; the numerical method, however, always has one. The idea is to use the area F, where the approximation is poor, to approximate the chain-recurrent set. Following the fact that a complete Lyapunov function should be constant in the chain-recurrent set, in the next step, we solve the PDE $V'(\mathbf{x}) = 0$ for $\mathbf{x} \in F$ and $V'(\mathbf{x}) = -1$ elsewhere.

For the numerical method we thus split the collocation points X into a set $X^0 = X \cap F$, where the approximation is poor, and $X^- = X \setminus X^0$, where it works correctly. Then we solve the PDE $V'(\mathbf{x}) = 0$ for all $\mathbf{x} \in X^0$ and $V'(\mathbf{x}) = -1$ for all $\mathbf{x} \in X^-$.

As a result, the approximated function v gives us information about the solution to the ODE under consideration. On the one hand, the set X^0 where $v'(\mathbf{x}) \approx 0$ approximates the chain-recurrent set, including equilibria, periodic orbits and homoclinic orbits, and on the other hand, the set X^- in which $v'(\mathbf{x}) \approx -1$ approximates the part where the flow is gradient-like. Information about the stability and attraction properties is obtained through the level sets of the function v: minima of v correspond to attractors while maxima represent repellers. For more details of the method see [17].

In this paper we significantly improve the method from [17], described above. Firstly, the method in [17] was not able to accurately identify the chain-recurrent set in more complicated examples, in particular examples where the speed $\|\mathbf{f}(\mathbf{x})\|$ with which solutions of the ODE are passed through varies considerably. Hence, in this paper we replace the original system $\dot{\mathbf{x}} = \mathbf{f}(\mathbf{x})$ with the system

$$\dot{\mathbf{x}} = \hat{\mathbf{f}}(\mathbf{x}), \quad \text{where} \quad \hat{\mathbf{f}}(\mathbf{x}) = \frac{\mathbf{f}(\mathbf{x})}{\sqrt{\delta^2 + \|\mathbf{f}(\mathbf{x})\|^2}} \tag{1}$$

with parameter $\delta > 0$.

The new system has the same solution trajectories as the original system, but these are traversed at a more uniform speed, namely $\|\hat{\mathbf{f}}(\mathbf{x})\| = \frac{\|\mathbf{f}(\mathbf{x})\|}{\sqrt{\delta^2+\|\mathbf{f}(\mathbf{x})\|^2}} \approx 1$. The smaller δ is, the closer the speed is to 1.

This modification improves the ability of the method to find the chain-recurrent set significantly, as we will show in the paper.

Secondly, the function V satisfying $V'(\mathbf{x}) = 0$ for $\mathbf{x} \in F$ and $V'(\mathbf{x}) = -1$ elsewhere is not smooth due to the jump in the orbital derivative, while the error estimates

in mesh-free collocation require the solution of the PDE to be smooth. To overcome this problem, we propose to replace the discontinuous right-hand side function by a smooth function.

Let us give an overview of the paper: In Sect. 2 we present the method with the modified system (1) and show the improvements over the previous method from [17] in three examples. Section 3 studies the dependence on the parameter δ. Section 4 discusses replacing the discontinuous right-hand side by a smooth function and applies the improved method to the same three examples before ending with conclusions in Sect. 5.

2 Normalized Speed

As discussed above, we fix a parameter $\delta > 0$ and consider the modified system (1) with normalized speed. We fix a finite set of collocation points X, none of which is an equilibrium point for the system. For our examples we used a subset of the hexagonal grid

$$\alpha_{\text{Hexa-basis}} \left\{ k \begin{pmatrix} 1 \\ 0 \end{pmatrix} + l/2 \begin{pmatrix} 1 \\ \sqrt{3} \end{pmatrix} \,:\, k, l \in \mathbb{Z} \right\}$$

with parameter $\alpha_{\text{Hexa-basis}} > 0$. We approximate the solution of the PDE $V'(\mathbf{x}) = \nabla V(\mathbf{x}) \cdot \hat{\mathbf{f}}(\mathbf{x}) = -1$ using mesh-free collocation with the kernel $\Phi(\mathbf{x}) := \psi_{l,k}(c\|\mathbf{x}\|)$ given by the Wendland function $\psi_{l,k}$ and parameter $c > 0$, for details see [17, 18]. We denote the approximation by v.

To identify the collocation points where the approximation is poor, indicating the chain-recurrent set, we evaluate $v'(\mathbf{x})$ near each collocation point – note that in the collocation point the orbital derivative is -1 by construction. In particular, in $\mathbb{R}^2$, for a given collocation point $\mathbf{x}_j$, we build a set of points $Y_{\mathbf{x}_j}$ placed in two spheres with center $\mathbf{x}_j$, namely:

$$Y_{\mathbf{x}_j} = \{\mathbf{x}_j + r\alpha_{\text{Hexa-basis}}(\cos(\theta), \sin(\theta)) \,:\, \theta \in \{0, 2\pi/32, 4\pi/32, 6\pi/32, \ldots, 2\pi\}\} \tag{2}$$

$$\cup\{\mathbf{x}_j + \frac{r}{2}\alpha_{\text{Hexa-basis}}(\cos(\theta), \sin(\theta)) \,:\, \theta \in \{0, 2\pi/32, 4\pi/32, 6\pi/32, \ldots, 2\pi\}\} \tag{3}$$

where $r > 0$ is a parameter and $\alpha_{\text{Hexa-basis}}$ is the parameter used to build the hexagonal grid defined above. We define a tolerance parameter $\gamma > -1$ and mark a collocation point $\mathbf{x}_j$ as being in the chain-recurrent set ($\mathbf{x}_j \in X^0$) if there is at least one point $\mathbf{y} \in Y_{\mathbf{x}_j}$ such that $v'(\mathbf{y}) > \gamma$.

We will now present the method applied to three systems with different properties; these are the same systems as in [17] so that we can compare the two methods.

2.1 Attractive and Repelling Periodic Orbits

The dynamical system given by

$$\begin{pmatrix}\dot{x}\\ \dot{y}\end{pmatrix} = \mathbf{f}(x, y) = \begin{cases} -x(x^2 + y^2 - 1/4)(x^2 + y^2 - 1) - y \\ -y(x^2 + y^2 - 1/4)(x^2 + y^2 - 1) + x \end{cases} \tag{4}$$

has two periodic orbits and an equilibrium. The equilibrium at the origin is asymptotically stable, and so is the periodic orbit with radius 1, while the periodic orbit with radius $1/2$ is unstable.

We used a hexagonal grid with $\alpha_{\text{Hexa-basis}} = 0.02$ in the set $[-1.5, 1.5]^2 \subset \mathbb{R}^2$ which gives a total of 29,440 collocation points, the Wendland function with parameters $(l, k, c) = (5, 3, 1)$, the critical value $\gamma = -0.5$, and $\delta^2 = 10^{-8}$. Furthermore, for the evaluation grid we set $r = 0.5$. We have compared the new method (normalized, right-hand side) with the non-normalized method of [17] (left-hand side), see Fig. 1.

In the lower right figure in Fig. 1, we can see that the equilibrium at the origin is found with less error than in the lower left figure where there are more points around $(0, 0)$. The chain-recurrent set actually looks very well-defined in both cases because of the relatively simple dynamics.

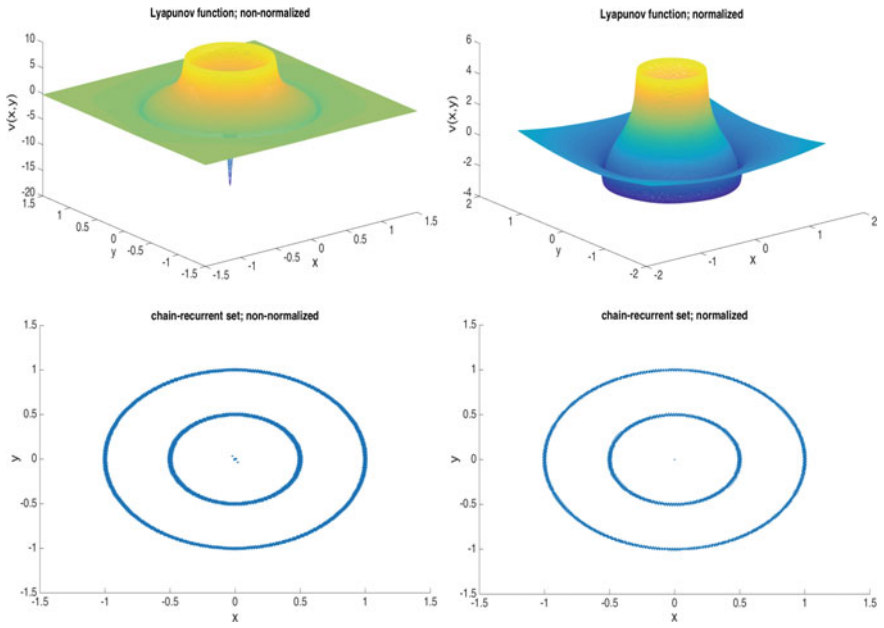

Fig. 1 Lyapunov functions for system (4) under both non-normalized (upper left) and for the normalized approach (upper right). Chain-recurrent set for both systems non-normalized (lower left) and normalized (lower right)

2.2 Van der Pol Oscillator

System (5) is the two-dimensional form of the Van der Pol oscillator. The system has an asymptotically stable periodic orbit and an unstable equilibrium at the origin.

$$\begin{pmatrix} \dot{x} \\ \dot{y} \end{pmatrix} = \mathbf{f}(x, y) = \begin{cases} y \\ (1 - x^2)y - x \end{cases} \tag{5}$$

We have a hexagonal grid with $\alpha_{\text{Hexa-basis}} = 0.1$ in the set $[-4.0, 4.0]^2 \subset \mathbb{R}^2$ which gives a total of 7708 collocation points, the Wendland function with parameters $(l, k, c) = (4, 2, 1)$, the critical value $\gamma = -0.5$, and $\delta^2 = 10^{-8}$. As before we set $r = 0.5$ in the evaluation grid. We have compared the new method (normalized) with the non-normalized method of [17], see Fig. 2.

The improvement of the proposed method can be seen clearly in the lower figures in Fig. 2: the chain-recurrent set is much better detected in the normalized system.

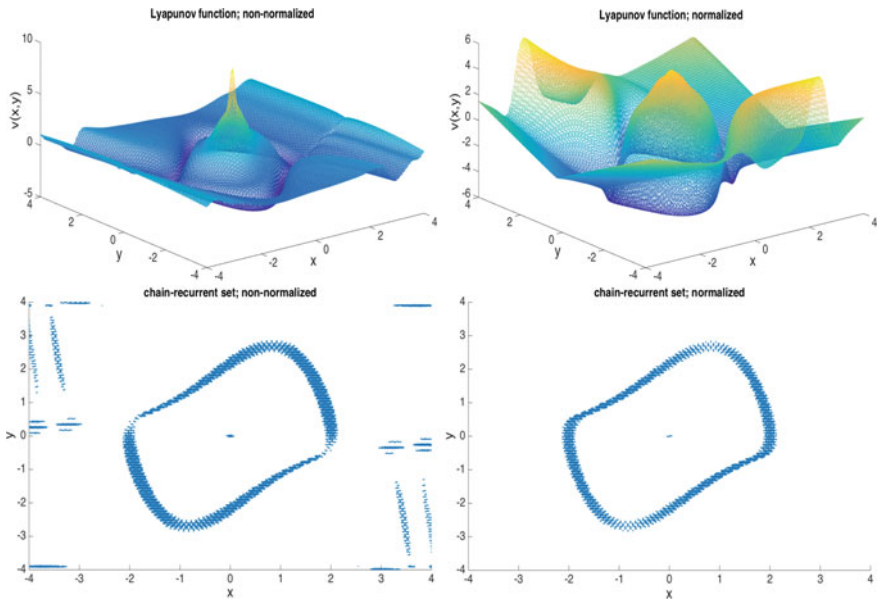

Fig. 2 Lyapunov functions for system (5) under both non-normalized (upper left) and for the normalized approach (upper right). Chain-recurrent set for both systems non-normalized (lower left) and normalized (lower right)

2.3 Homoclinic Orbit

The system (6) has an asymptotically stable homoclinic orbit and an unstable equilibrium at the origin.

$$\begin{pmatrix}\dot{x}\\ \dot{y}\end{pmatrix} = \mathbf{f}(x,y) = \begin{cases} x(1-x^2-y^2) - y((x-1)^2 + (x^2+y^2-1)^2) \\ y(1-x^2-y^2) + x((x-1)^2 + (x^2+y^2-1)^2) \end{cases} \tag{6}$$

We used a hexagonal grid with $\alpha_{\text{Hexa-basis}} = 0.02$ in the set $[-1.5, 1.5]^2 \subset \mathbb{R}^2$ which gives a total of 29,440 collocation points, the Wendland function with parameters $(l, k, c) = (4, 2, 1)$, the critical value $\gamma = -0.75$, and $\delta^2 = 10^{-8}$. Again we used $r = 0.5$ in the evaluation grid. The new method (normalized) is compared with the non-normalized method of [17] in Fig. 3.

In this case, we can see a clear enhancement on the detection of the chain-recurrent set. In Fig. 3 (lower left) the failing set over-estimates the chain-recurrent set, while in Fig. 3 (lower right) the normalized method detects the chain-recurrent set much better.

Summarizing, the new method is able to better detect chain-recurrent sets.

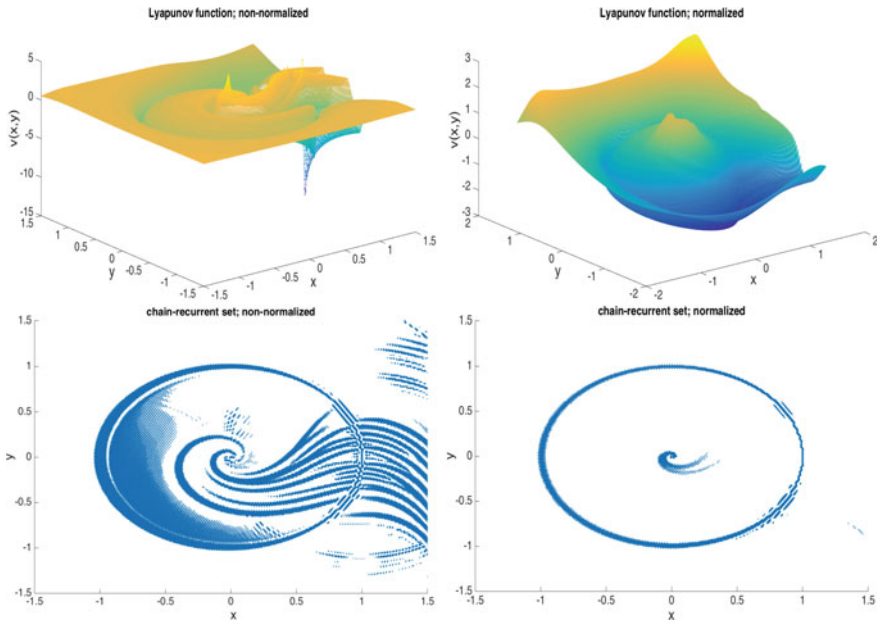

Fig. 3 Lyapunov functions for system (6) under both non-normalized (upper left) and for the normalized approach (upper right). Chain-recurrent set for both systems non-normalized (lower left) and normalized (lower right)

3 Behaviour of the Lyapunov Functions Depending on the Values of δ

Using the system defined in Sect. 2.1 by Eq. (4), we show the dependence of the behaviour of the Lyapunov function for a normalized system with different parameters δ. We have chosen to show examples for $\delta^2 = 10^{-10}$ and $\delta^2 = 1$. Figure 4 shows how the Lyapunov function changes with different values of δ^2: for small δ^2 (black) the function has a derivative close to 0 around the equilibrium point, while for large δ^2 (red) the function has a steep slope. Since Eq. (1) leads to the PDE

$$\nabla V(\mathbf{x}) \cdot \mathbf{f}(\mathbf{x}) = -\sqrt{\delta^2 + \|\mathbf{f}(\mathbf{x})\|^2},$$

near the equilibrium the right-hand side is $\approx -\delta$. Hence, the gradient of V must become large because $\mathbf{f}(\mathbf{x})$ is small close to the equilibrium.

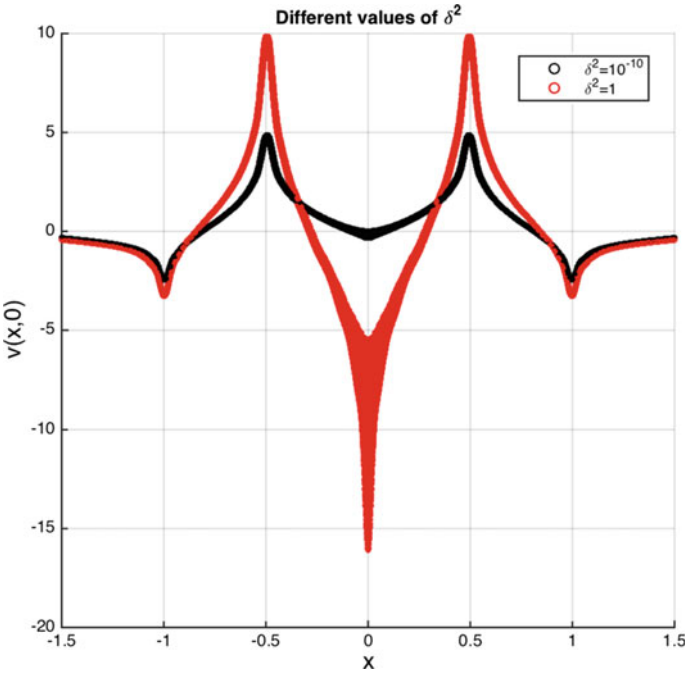

Fig. 4 Lyapunov function for system (4) around the equilibrium point. With $\delta^2 = 1$ the gradient of V is much larger close to the equilibrium at zero than with $\delta^2 = 10^{-10}$

4 Smooth Function

Our second main objective is in the next step to find a PDE which has a smooth solution and, subsequently, approximate its solution numerically.

The method from [17] starts with the PDE $V'(\mathbf{x}) = -1$, which does not have a solution on chain-recurrent sets; for an equilibrium $\mathbf{x}_0$, e.g. we clearly have $V'(\mathbf{x}_0) = 0$. By using mesh-free collocation to approximate a solution of $V'(\mathbf{x}) = -1$ we obtain an approximation v which satisfies $v'(\mathbf{x}) \approx -1$ in areas which are not chain-recurrent and results in a poor approximation in the chain-recurrent set. Let us denote the area where the approximation is poor by F.

In the method described in [17] we then study the PDE

$$V'(\mathbf{x}) = \begin{cases} 0 & \text{if } \mathbf{x} \in F, \\ -1 & \text{if } \mathbf{x} \notin F. \end{cases}$$

As the right-hand side is discontinuous, the solution V will not be a smooth function.

We assume that F is a compact set and improve the method by considering the following PDE with smooth right-hand side

$$V'(\mathbf{x}) = r(\mathbf{x}) := \begin{cases} 0 & \text{if } \mathbf{x} \in F, \\ -\exp\left(-\frac{1}{\xi \cdot \mathfrak{d}^2(\mathbf{x})}\right) & \text{if } \mathbf{x} \notin F, \end{cases} \tag{7}$$

where $\mathfrak{d}(\mathbf{x}) = \min_{\mathbf{y} \in F} \|\mathbf{x} - \mathbf{y}\|$ is the distance between the point $\mathbf{x}$ and the set F and $\xi > 0$ is a parameter.

To implement the method numerically, we construct the approximation to the complete Lyapunov function with our new approach. We first normalize our system $\dot{\mathbf{x}} = \mathbf{f}(\mathbf{x})$ by replacing it with the system (1). Note that we only need to evaluate the right-hand side $r(\mathbf{x})$ at the collocation points. Recall that we identify a collocation point $\mathbf{x}_j$ to be in an area of poor approximation F, as described above, if there exists at least one $\mathbf{y} \in Y_{\mathbf{x}_j}$ with $v'(\mathbf{y}) > \gamma$. Then we split the set of collocation points X into the subset X^0 consisting of points in an area of poor approximation and the remaining points $X^- = X \setminus X^0$.

For all collocation points $\mathbf{x}_j \in X$ we then approximate the distance of $\mathbf{x}$ to the set F, represented by X^0, by

$$\mathfrak{d}(\mathbf{x}_j) \approx \min_{\mathbf{y} \in X^0} \|\mathbf{x}_j - \mathbf{y}\|;$$

note that $\mathfrak{d}(\mathbf{x}_j) = 0$ for all $\mathbf{x}_j \in X^0$.

Now, the right-hand side $r(\mathbf{x})$ of the Eq. (7) at a collocation point $\mathbf{x}_j \in X$ is set to be $r(\mathbf{x}_j) = 0$ if $\mathbf{x}_j \in X^0$, and $r(\mathbf{x}_j) = \exp\left(-\frac{1}{\xi \cdot \mathfrak{d}^2(\mathbf{x}_j)}\right)$ if $\mathbf{x}_j \in X^-$.

For our test systems (4), (5) and (6) we have already shown the normalized Lyapunov functions in Figs. 1, 2 and 3, respectively, so now we show the solution of

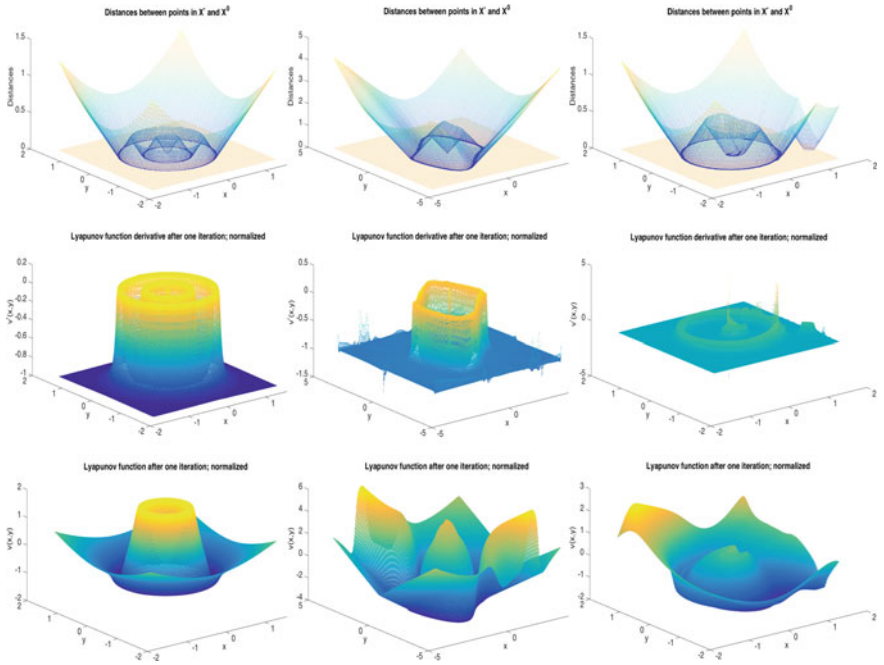

Fig. 5 First row: values of $\mathfrak{d}$ as a function of the collocation points for systems (4) in column 1, (5) in column 2 and (6) in column 3, respectively. Second and third row: Lyapunov functions (third row) and their derivatives (second row) for systems (4) in column 1, (5) in column 2 and (6) in column 3 respectively, with the modified, smooth right-hand side

(7) as described above in Fig. 5. In this case, for all computations in Fig. 5, the normalization factor used is $\delta = 10^{-8}$ with $\xi = 300$. The second row shows that the orbital derivatives of the approximated functions are smooth functions.

5 Conclusions

In this paper we have significantly improved a method to construct complete Lyapunov functions and determine the chain-recurrent set. The two main improvements were firstly to consider a system with normalized speed, which enabled us to detect the chain-recurrent set more accurately. Secondly, we have replaced the discontinuous right-hand side of the PDE under consideration by a smooth function so that the PDE has a smooth solution, which is well approximated by the proposed method.

Acknowledgements The first author in this paper is supported by the Icelandic Research Fund (Rannís) grant number 163074-052, Complete Lyapunov functions: Efficient numerical computation. Special thanks to Dr. Jean-Claude Berthet for all his good comments and advice on C++.

References

1. Lyapunov, A.M.: The general problem of the stability of motion. Int. J. Control **3**(55), 521–790 (1992)
2. Conley, C.: Isolated Invariant Sets and the Morse Index. In: American Mathematical Society, CBMS Regional Conference Series, vol. 38 (1978)
3. Conley, C.: The gradient structure of a flow I. Ergodic Theory Dynam. Syst. **8**, 11–26 (1988)
4. Hurley, M.: Chain recurrence, semiflows, and gradients. J. Dyn. Diff. Equat. **3**(7), 437–456 (1995)
5. Hurley, M.: Lyapunov functions and attractors in arbitrary metric spaces. Proc. Amer. Math. Soc. **126**, 245–256 (1998)
6. Awrejcewicza, J., Wasilewskia, G., Kudra, G., Reshminb, S.: An experiment with swinging up a double pendulum using feedback control. J. Comput. Syst. Sci. Int. **51**(2), 176–182 (2012)
7. Awrejcewicz, J., Kudra, G., Wasilewski, G.: Experimental and numerical investigation of chaotic regions in the triple physical pendulum. Nonlinear Dyn **50**, 755–766 (2007)
8. Awrejcewicz, J., Kudra, G., Wasilewski, G.: Chaotic zones in triple pendulum dynamics observed experimentally and numerically. Appl. Mech. Mater. **9**, 1–17 (2008)
9. Awrejcewicz, J., Kudra, G.: Mathematical modelling and simulation of the bifurcational wobblestone dynamics. Discontinuity, Nonlinearity, Complexity **3**(2), 123–132 (2014)
10. Krauskopf, B., Osinga, H., Doedel, E.J., Henderson, M., Guckenheimer, J., Vladimirsky, A., Dellnitz, M., Junge, O.: A survey of methods for computing (un)stable manifolds of vector fields. Internat. J. Bifur. Chaos Appl. Sci. Engrg., **3**(15), 763–791
11. Hsu, C. S.: Cell-to-cell mapping. In: Applied Mathematical Sciences. vol. 64. Springer-Verlag, New York (1987). https://doi.org/10.1007/978-1-4757-3892-6
12. Dellnitz, M., Junge, O.: Set oriented numerical methods for dynamical systems. In: Handbook of Dynamical Systems, vol. 2, pp. 221–264. North-Holland, Amsterdam (2002). https://doi.org/10.1016/S1874-575X(02)80026-1
13. Osipenko, G.: Dynamical systems, graphs, and algorithms. In: Lecture Notes in Mathematics. vol. 1889. Springer-Verlag, Berlin (2007)
14. Kalies, W., Mischaikow, K., VanderVorst, R.: An algorithmic approach to chain recurrence. Found. Comput. Math. **4**, 409–449 (2005)
15. Dellnitz, M., Froyland, G., Junge, O.: The algorithms behind GAIO - set oriented numerical methods for dynamical systems. Ergodic Theory. Analysis, and Efficient Simulation of Dynamical Systems, pp. 145–174. Springer, Berlin (2001)
16. Ban, H., Kalies, W.: A computational approach to Conley's decomposition theorem. J. Comput. Nonlinear Dynam. **1**(4), 312–319 (2006)
17. Argáez, C., Giesl, P., Hafstein, S.: Analysing dynamical systems – towards computing complete lyapunov functions. In: Proceedings of the 7th International Conference on Simulation and Modeling Methodologies, Technologies and Applications – Volume 1: SIMULTECH, pp. 134–144 (2017)
18. Giesl, P.: Construction of Global Lyapunov Functions Using Radial Basis Functions. In: Lecture Notes in Math., vol. 1904. Springer (2007)

Non-conservative Instability of Cantilevered Nanotube Via Cell Discretization Method

Nicola Maria Auciello, Maria Anna De Rosa, Maria Lippiello and Stefania Tomasiello

Abstract Based on the nonloocal elasticity theory, this paper deals with the dynamic instability analysis of cantilevered single-walled carbon nanotube with concentrated mass, located at a generic position, and subject to a follower force at the free end. Accounting for the small scale effect, the governing equations of motion are derived using an alternative Hamilton's variational principle and the governing equations are solved numerically employing the Cell-Discretization Method (CDM) in which the nanotube is reduced to a set of rigid bars linked together by means of elastic constraints. The resulting discrete system takes into account nonlocal effects, added mass, and position of added mass, and follower force direction. A comparative analysis is performed in order to verify the accuracy and validity of the proposed numerical method. The effects of the nonlocal parameter and dimensionless mass on the dynamic instability of single-walled carbon nanotube are shown and discussed in details. The effect of a sub-tangential follower force on the stability of cantilever single-walled carbon nanotube is studied. Finally, the validity of the proposed analysis is confirmed by comparing the present results with those obtained from the litertaure and listed in bibliography.

Keywords Dynamic instability · Follower force · Variational principle · CDM

N. M. Auciello · M. A. De Rosa (✉)
School of Engineering, University of Basilicata,
Viale dell'Ateneo Lucano 10, 85100 Potenza, Italy
e-mail: maria.derosa@unibas.it

N. M. Auciello
e-mail: nicola.auciello@unibas.it

M. Lippiello
University of Naples Federico II, DiSt, Via Forno Vecchio 36, 80134 Naples, Italy
e-mail: maria.lippiello@unina.it

S. Tomasiello
University of Salerno, CORISA, 84084 Fisciano (SA), Italy
e-mail: stomasiello@unisa.it

J. Awrejcewicz (ed.), *Dynamical Systems in Theoretical Perspective*,
Springer Proceedings in Mathematics & Statistics 248,
https://doi.org/10.1007/978-3-319-96598-7_2

1 Introduction

Outstanding mechanical, physical and electronic properties of carbon nanotubes (CNTs) have stimulated intensive studies in a variety of fields of science and engineering since their first discovery in 1991 thanks to Iijima's paper [1].

The literature regarding the material properties and mechanical behaviour of CNTs is very rich and two main theoretical approaches, based on the molecular dynamics and continuum mechanics, have been developed. Although the classical continuum theories are able to predict the mechanical behavior of nanostructures, it turned up to be unsuitable, because the small size effects are neglected. Thus adopting the nonlocal elasticity theory, as developed by Eringen in [2, 3], is usual. Applying the Erigen's theory, many papers investigating the mechanical properties of CNTs have been appearing. In particular, elastic models of beams have been implemented to study static and dynamic problems, such as bending, buckling and free vibration of carbon nanotubes, using Euler- Bernoulli [4, 5] and Timoshenko [6–8] beam models.

In recent years, due to the remarkable properties of CNTs, a growing interest, in the analysis of the vibrations of nanotubes under a nonconservative field, such as a follower forces, and their influence on free-vibration of CNTs, has attracted the attention of many reseachers, although few papers regarding the structural stability of the CNTs can be found in literature (see [9–11]).

The present paper deals with the nonlocal dynamic instability of a cantilevered single-walled carbon nanotube with an attached concentrated mass, located at a generic position, and its position of added mass and subject to a follower force, at the free-end. The governing equations of motion are derived using an alternative Hamilton's variational principle and are solved numerically employing the Cell-Discretization Method (CDM), which reduces the nanotube to a set of rigid bars linked together by means of elastic constraints. The resulting discrete system takes into account nonlocal effects, added mass, and its position, and follower force direction. A comparative analysis is performed in order to verify accuracy and validity of the proposed numerical method. The effects of nonlocal parameter and dimensionless mass on the dynamic instability of SWCNT are shown and discussed in details. The effect of a sub-tangential follower force on the stability of cantilever single-walled carbon nanotube is studied.

2 Formulation and Solution of the Problem

2.1 Governing Equations of Motion for Dynamic Instability of Nonlocal Single-Walled Nanotube

Consider a single-walled carbon nanotube (SWCNT), clamped at the left end and free at the right one, of length L. The nanotube is subject to a subtangential force p, at the free end, and carrying a concentrated mass M_γ, located at a generic position, as

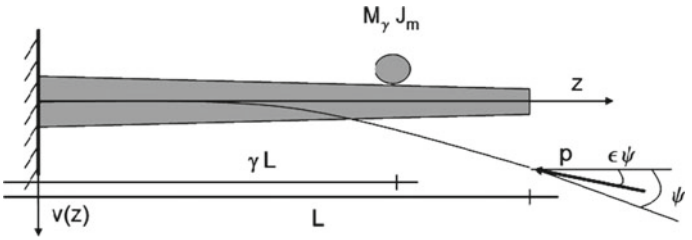

Fig. 1 Geometry of single-walled carbon nanotube (SWCNT)

shown in Fig. 1. The direction of the force p is specified by $\epsilon\ \psi$, where $\epsilon\ \psi$ denotes the angle between the z-axis and the direction of the compressive subtangential force.

According to the Hamilton's Principle, the motion equations of the system are derived as follows:

$$\int_{t_1}^{t_2} (\delta \mathrm{T} - \delta \mathrm{E_t})\, \mathrm{d}t + \int_{t_1}^{t_2} \delta \mathrm{W_{nc}} \mathrm{d}t = 0 \tag{1}$$

where δ denotes the variation, t is time, T and E are the kinetic and total potential energy of the nanotube, respectively, while $\mathrm{W_{nc}}$ represents the nonconservative virtual work of the applied load.

The kinetic energy of the nanostructure under consideration can be expressed as:

$$\mathrm{T} = \frac{1}{2}\int_0^{\mathrm{L}} \left[\rho \mathrm{A}\left(\frac{\partial v(z,t)}{\partial t}\right)^2\right] \mathrm{d}z + \frac{1}{2}\mathrm{M}_\gamma \left(\frac{\partial v(\gamma \mathrm{L},t)}{\partial t}\right)^2 + \frac{1}{2}\mathrm{J_m}\left(\frac{\partial}{\partial z}\frac{\partial v(\gamma \mathrm{L},t)}{\partial t}\right)^2, \tag{2}$$

where $v(z)$ is the transverse displacement of the nanotube, with z being the spatial coordinate along the nanotube, A is the cross-sectional area, ρ the mass density of SWCNT, M_γ denotes the concentrated mass, at the abscissa $z = \gamma \mathrm{L}$, and $\mathrm{J_m}$ is rotary inertia of the added mass.

The total potential energy $\mathrm{E_t}$ assumes the following form:

$$\begin{aligned}\mathrm{E_t} &= \mathrm{L_e} - \mathrm{P} - \mathrm{V} \\ &= \frac{1}{2}\int_0^{\mathrm{L}} \mathrm{EI}\left(\frac{\partial^2 v(z,t)}{\partial z^2}\right)^2 \mathrm{d}z - \int_0^{\mathrm{L}} \left((e_0 a)^2 \rho \mathrm{A}\frac{\partial^2 v(z,t)}{\partial t^2}\right)\left(\frac{\partial^2 v(z,t)}{\partial z^2}\right) \mathrm{d}z \\ &\quad - \int_0^{\mathrm{L}} \left((e_0 a)^2 \mathrm{p}\frac{\partial^2 v(z,t)}{\partial z^2}\right)\left(\frac{\partial^2 v(z,t)}{\partial z^2}\right) \mathrm{d}z - \frac{1}{2}\int_0^{\mathrm{L}} \mathrm{p}\left(\frac{\partial v}{\partial z}\right)^2 \mathrm{d}z\end{aligned} \tag{3}$$

i.e. $\mathrm{E_t}$ is sum of three different contributions: the strain energy $\mathrm{L_e}$ of the nanotube, the potential energy P of the inertial force $\left(\rho \mathrm{A}\frac{\partial^2 v(z,t)}{\partial t^2}\right)$ due to additional displacement $\left((e_0 a)^2 \frac{\partial^2 v(z,t)}{\partial z^2}\right)$ and finally the potential energy V of axial component of the follower

force p. In Eq. (3), E is Young's modulus, I the second moment of the cross-sectional area A, e_0 is a nonlocal scaling parameter, which has to be experimentally determined for each material, and a is an internal characteristic length.
Taking into account the expressions of kinetic and potential energy, one gets:

$$\begin{aligned}
&\mathrm{T} - \mathrm{E_t} = \\
&\frac{1}{2}\int_0^{\mathrm{L}} \left[\rho \mathrm{A}\left(\frac{\partial v(z,t)}{\partial t}\right)^2\right] \mathrm{d}z + \frac{1}{2}\mathrm{M}_\gamma \left(\frac{\partial v(\gamma \mathrm{L},t)}{\partial t}\right)^2 + \frac{1}{2}\mathrm{J_m}\left(\frac{\partial}{\partial z}\frac{\partial v(\gamma \mathrm{L},t)}{\partial t}\right)^2 - \\
&\frac{1}{2}\int_0^{\mathrm{L}} \mathrm{EI}\left(\frac{\partial^2 v(z,t)}{\partial z^2}\right)^2 \mathrm{d}z - \int_0^{\mathrm{L}} \left((e_0 a)^2 \rho \mathrm{A}\frac{\partial^2 v(z,t)}{\partial t^2}\right)\left(\frac{\partial^2 v(z,t)}{\partial z^2}\right) \mathrm{d}z + \\
&\int_0^{\mathrm{L}} \left((e_0 a)^2 \mathrm{p}\frac{\partial^2 v(z,t)}{\partial z^2}\right)\left(\frac{\partial^2 v(z,t)}{\partial z^2}\right) \mathrm{d}z + \frac{1}{2}\int_0^{\mathrm{L}} \mathrm{p}\left(\frac{\partial v}{\partial z}\right)^2 \mathrm{d}z
\end{aligned} \tag{4}$$

Finally, the nonconservative virtual work of these transverse components can be expressed as:

$$\delta W_{\mathrm{nc}} = -\mathrm{p}\epsilon \frac{\partial v(\mathrm{L},t)}{\partial z}\delta v(\mathrm{L},t) \tag{5}$$

The parameter ϵ completely defines the dynamic behaviour of the system: for $\epsilon = 0$ the classical conservative Euler case is recovered, whereas for $\epsilon = 1$ the nanobeam is subject to purely tangential forces (Beck problem). As ϵ varies in the range [0,1] critical loads are reached by means of divergence or flutter instability.

Since obtaining an exact analytical solution to Eq. (1) is not that easy, the present study relies on the approximation solution. For linear free vibration of a nanotube, the vibration modes are harmonic in time. Hence, the temporal and spatial terms for transverse deformation can be separeted as:

$$v(z,t) = \mathrm{v}(z)e^{i\omega t} \tag{6}$$

where $\mathrm{v}(z)$ represents the vibration amplitude shape function, $\mathrm{i} = \sqrt{-1}$ and ω is the natural frequency. To find the solution of the Eq. (1), the Cell-Discretization Method (CDM) is applied to solve the eigenvalue problem.

2.2 *Method of Solution: Cell-Discretization Method (CDM)*

The Cell Discretization Method (CDM) is an efficient numerical method for the solution of linear partial differential equations. The method has already been used by the authors [12, 13] and by Raithel and Franciosi [14] for different structural problems. Recently, De Rosa and Lippiello [15] have employed the CDM to investigate the free vibration frequencies problem of coaxial double-walled carbon nanotubes (DWCNTs) and in [16] for analyzing the free vibration analysis of single-walled

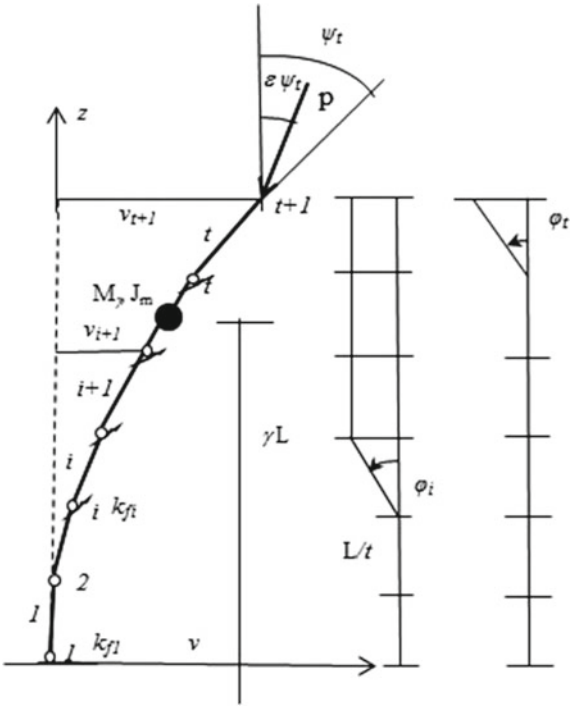

Fig. 2 Structural system discretization CD method

carbon nanotube (SWCNT) bounded at the ends, with translational and elastic constraints, and attached mass. In the present paper the CD method has been properly modified for the considered problem. The nanotube is reduced to a set of t rigid bars, linked together by $t + 1$ elastic cells, where masses and stiffnesses are supposed to be concentrated, (see Fig. 2). In this way, the structure is reduced to a system with finite number of degrees of freedom (MDOF). The Lagragian parameters can be assumed to be the φ_i rotations of the rigid bars, i.e. the generalized coordinates of the rigid-elastic system. All the possible configurations are functions of the following vector:

$$\mathbf{c} = [\varphi_1, \varphi_2, \ldots, \varphi_i, \ldots \varphi_t]^{\mathrm{T}} \tag{7}$$

and the vertical components of the nodal displacements and the relative rotations between the two faces of the elastic cells are given by the following expressions:

$$v_1 = 0, \qquad v_i = -\sum_{j=1}^{i-1} \varphi_j \frac{\mathrm{L}}{t}, \qquad i = 1, \ldots, t+1 \tag{8}$$

$$\psi_1 = \varphi_1, \qquad \psi_i = \varphi_i - \varphi_{i-1}, \qquad \psi_{t+1} = 0, \tag{9}$$

In matrix form, being **A** the displacements matrix and **B** the rotations matrix, it is possible to write:

$$\boldsymbol{v} = \mathbf{Ac}, \qquad \boldsymbol{\psi} = \mathbf{Bc}. \tag{10}$$

The rectangular matrices **A** and **B** have t + 1 rows and t columns, and each entry can be calculated according to Fig. 2. The form of matrix **A** is:

$$A_{ij} = \sum_{i=2}^{t+1} \sum_{j=2}^{i-1} i \frac{\mathrm{L}}{t} \tag{11}$$

with A_{1j} = 0, for j = 1, …,t; while the matrix **B**has B_{ii} = 1 and $B_{(i+1)i} = -1$, for $\mathrm{i} = 1, \ldots, \mathrm{t} - 1$. According to the present discretization, the axial components of the nodal displacements assume the following form:

$$w_1 = 0, \qquad w_i = -\frac{1}{2} \sum_{j=1}^{i-1} \varphi_j^2 \frac{\mathrm{L}}{t}, i = 1, \ldots, t + 1 \tag{12}$$

In the matrix form, the axial displacements of cell t+1 becomes:

$$w_{n+1} = -\frac{1}{2} \sum_{j=1}^{t} \varphi_j^2 \frac{\mathrm{L}}{t} = -\frac{1}{2} \mathbf{c}^{\mathrm{T}} \mathbf{D}_{\boldsymbol{l}} \mathbf{c}. \tag{13}$$

where $\mathbf{D}_{\boldsymbol{l}}$ is diagonal matrix of the terms $\frac{\mathrm{L}}{t}$.

Substituting the Eqs. (8–9) and (12–13) into Eq. (4), the kinetic energy should be expressed as functions of the Lagrangian coordinates as follows:

$$\mathrm{T} = \frac{1}{2} \int_0^{\mathrm{L}} \rho \mathrm{A} \dot{\boldsymbol{v}}^2 \mathrm{d}z + \frac{1}{2} \mathrm{M}_\gamma \left(\dot{\boldsymbol{v}}^2 \right)_{\gamma \mathrm{L}} + \frac{1}{2} \mathrm{J_m} \left(\dot{\boldsymbol{v}}' \right)_{\gamma \mathrm{L}}^2 \tag{14}$$

or, in discretized form:

$$\mathrm{T} = \frac{1}{2} \sum_{i=1}^{t+1} m_i \dot{v}_i^2 + \frac{1}{2} \mathrm{M}_\gamma \left(\dot{v}^2 \right)_{\gamma \mathrm{L}} + \frac{1}{2} \mathrm{J_m} \left(\dot{\varphi}^2 \right)_{\gamma \mathrm{L}}. \tag{15}$$

The mass is concentrated at the elastic cells and it is represented by the following terms of the diagonal matrix:

$$\mathrm{mt}_1 = \rho \mathrm{A}_1 \frac{\mathrm{L}}{2t}, \quad \mathrm{mt}_i = \rho \frac{\mathrm{A}_i + \mathrm{A}_{i-1}}{2} \frac{\mathrm{L}}{t}, \quad \mathrm{mt}_{t+1} = \rho \mathrm{A}_t \frac{\mathrm{L}}{2t}, \quad i = 2 \ldots .t, \tag{16}$$

and the Eq. (15) becomes:

$$\mathrm{T} = \frac{1}{2} \dot{\mathbf{c}}^{\mathrm{T}} \left[\mathbf{A}^{\mathrm{T}} \left(\boldsymbol{m}_t + \delta_{\mathrm{i}\gamma} \mathbf{M}_\gamma \mathbf{A} + \delta_{\mathrm{i}\gamma} \mathbf{J} \right) \right] \dot{\mathbf{c}} \tag{17}$$

where $\delta_{\mathrm{i}}\gamma$ denotes the Kronecker index, relative to the concentrated mass at the generic abscissa $\gamma \mathrm{L}$, and the matrix $\mathbf{J}$ represents the rotational inertia of the added mass.

The virtual work L_f' of the inertial forces due to nonlocal additional displacement can be expressed as:

$$\mathrm{L}_f' = \int_0^{\mathrm{L}} \left((e_0 a)^2 \rho \mathrm{A}(z) \ddot{\boldsymbol{v}}^2 \boldsymbol{v}''\right) \mathrm{d}z = t \frac{(e_0 a)^2}{\mathrm{L}} \left[\boldsymbol{A}\dot{\boldsymbol{c}}\right]^{\mathrm{T}} \boldsymbol{m}_t \mathbf{B}\dot{\mathbf{c}} = \dot{\mathbf{c}}^{\mathrm{T}} \mathbf{b}_{\mathbf{fl}} \dot{\mathbf{c}} \tag{18}$$

where

$$\mathbf{b}_{\mathbf{fl}} = t \frac{(e_0 a)^2}{\mathrm{L}} \mathbf{A}^{\mathrm{T}} \boldsymbol{m}_t \mathbf{B}. \tag{19}$$

The strain energy is concentrated at the elastic cell of the nanotube and it should be expressed as functions of the Lagragian coordinates as follows:

$$\begin{aligned} \mathrm{L}_{\mathrm{e}} &= -\frac{1}{2} \int_0^{\mathrm{L}} \mathrm{EI}(z) \boldsymbol{v}''^2 \mathrm{d}z = -\frac{1}{2} \sum_{i=1}^{\mathrm{t}} \mathrm{M}_i \psi_i = \\ &-\frac{1}{2} \left[\boldsymbol{k_f} \mathbf{B}\mathbf{c}\right]^{\mathrm{T}} \mathbf{B}\mathbf{c} = -\frac{1}{2} \mathbf{c}^{\mathrm{T}} \mathbf{B}^{\mathrm{T}} \boldsymbol{k_f} \mathbf{B}\mathbf{c} = \frac{1}{2} \mathbf{c}^{\mathrm{T}} \boldsymbol{k_t} \mathbf{c} \end{aligned} \tag{20}$$

where $\mathrm{M}_i = \mathrm{t} \frac{\mathrm{E}(\mathrm{I}_i + \mathrm{I}_{i-1})}{2\mathrm{L}} \psi_i = k_{\mathrm{fi}} \psi_i$, and $\boldsymbol{k_f}$ denotes the diagonal stiffness matrix, and

$$\boldsymbol{k_t} = \mathbf{B}^{\mathrm{T}} \boldsymbol{k_f} \mathbf{B} \tag{21}$$

The potential energy L_f'' of follower force due to nonlocal effect is given by:

$$\begin{aligned} \mathrm{L}_f'' &= \int_0^{\mathrm{L}} (e_0 a)^2 \, \mathrm{p} \, \boldsymbol{v}'' \boldsymbol{v}'' \mathrm{d}z = \\ &\mathrm{p} \, (e_0 a)^2 \, [\mathbf{B}\mathbf{c}]^{\mathrm{T}} \mathbf{B}\mathbf{c} = \mathrm{p} \, (e_0 a)^2 \, \mathbf{c}^{\mathrm{T}} \mathbf{B}^{\mathrm{T}} \mathbf{B}\mathbf{c} = \mathrm{p} \, \mathbf{c}^{\mathrm{T}} \boldsymbol{k}_{\mathbf{fL}} \mathbf{c} \end{aligned} \tag{22}$$

with

$$\boldsymbol{k}_{\mathbf{fl}} = \mathbf{B}^{\mathrm{T}} \mathbf{B} \tag{23}$$

The virtual work $\mathrm{L_N}$ of the conservative axial load is expressed as

$$\mathrm{L_N} = \frac{1}{2} \int_0^{\mathrm{L}} \mathrm{p} \left(\boldsymbol{v}'\right)^2 \mathrm{d}z = \frac{1}{2} \mathrm{p} \, \mathbf{c}^{\mathrm{T}} \mathbf{D}_{\boldsymbol{l}} \mathbf{c} \tag{24}$$

and the energy of the nonconservative axial load is given by:

$$\delta \mathrm{W_{nc}} = -\epsilon \, \mathrm{p} \frac{\partial \boldsymbol{v}(\mathrm{L}, t)}{\partial z} \delta \boldsymbol{v}(\mathrm{L}, t) = -\epsilon \, \mathrm{p} \, \varphi_t \, \delta \mathrm{v}_{t+1} = -\epsilon \, \mathrm{p} \, \mathbf{c}^{\mathrm{T}} \boldsymbol{k}_{\mathbf{nc}} \delta \mathbf{c} \tag{25}$$

where $\boldsymbol{k_{nc}}$ is a matrix with t rows and t columns, with $\boldsymbol{k_{nc}}_{t,j} = -1$ for j = 1, . . . , t. The global stiffness matrix is:

$$\boldsymbol{K} = \boldsymbol{k_t} + \mathrm{p}\,\boldsymbol{k_{fL}} + \epsilon\,\mathrm{p}\,\boldsymbol{k_{nc}} - \mathrm{p}\,\mathbf{D_l}, \tag{26}$$

and the global masses matrix is given by:

$$\mathbf{M} = \mathbf{m} - \mathbf{b_{fl}}. \tag{27}$$

with $\mathbf{m} = \left[\mathbf{A}^{\mathrm{T}}\left(\mathbf{m}_t + \delta_{\mathrm{i}}\gamma\mathbf{M}_\gamma\right)\mathbf{A} + \delta_{\mathrm{i}}\gamma\mathbf{J}\right]$.
The Lagrange equation for discrete systems is expressed as follows:

$$\frac{\mathrm{d}}{\mathrm{dt}}\left(\frac{\partial \mathrm{T}}{\partial \dot{\phi}_i}\right) - \frac{\partial \mathrm{T}}{\partial \phi_i} + \frac{\partial \mathrm{L}_e}{\partial \phi_i} = Q_i \tag{28}$$

and one gets:

$$\left(\mathbf{K} - \omega^2\mathbf{M}\right)\mathbf{c} = 0, \tag{29}$$

where ω is the circular frequency and $\boldsymbol{c}$ denotes the mode shape or eigenvector. A solution to this homogeneous system of equations exists only if the determinant of the coefficient's matrix is setted equal to zero:

$$\det\left(\mathbf{K} - \omega^2\mathbf{M}\right) = 0, \tag{30}$$

where ω^2 are the frequencies of natural vibration, or eigenvalues.

3 Numerical Comparisons and Discussion

In order to show the potentialities of the proposed approach (CDM), several numerical examples have been performed, using a general code developed in *Mathematica* [17]. Numerical results are illustrated and compared against the ones available in literature. In the numerical analyses, the influence of the nonlocal parameter, mass and position of the added mass, and the follower force on the natural frequency value is evaluated.
For convenience of analysis, the following nondimensional parameters are also introduced:

$$\Omega_1 = \sqrt[4]{\frac{\omega_1^2 \rho \mathrm{A}_0 \mathrm{L}^4}{\mathrm{EI}_0}} \tag{31}$$

where Ω_1 denotes the first nondimensional frequency value, A_0 and I_0 are the cross-sectional area and moment of inertia, respectively, of an uniform nanotube;

$$M_s = \frac{M_\gamma}{\rho A_0 L}; \qquad \eta = \frac{e_0 a}{L}, \qquad P = \frac{pL^2}{EI_0} \tag{32}$$

where M_s is the nondimensional added mass, η is the non local parameter and finally, P is the nondimensional coefficient of the axial load.

3.1 Model Validation

A prelimary numerical example aims at comparing the present results with the exact ones proposed in [16] and we refer to the parameters listed in Table 1 of [18]. A cantilevered single-walled carbon nanotube with attached mass and follower force p = 0 is considered. For two different values of nonlocal parameter η = [0, 1] and for nondimensional added mass M_s, which varies in the range [0, 1], in Table 1 the values of the first nondimensional frequency Ω_1 are tabled. As one can see, the numerical results by the CDM, obtained using a lower number of cells, i.e. $t = 100$, are in perfect agreement with the exact ones obtained in [16]. Moreover, from Table 1, one can see that the first non dimensional natural frequency value decreases with increases in concentrated mass M_s value. It is also observed that Ω_1 increases if the nonlocal effect η increases.

Table 1 Comparison of the first nondimensional frequency Ω_1 obtained from exact solution in [16] and CDM, for P = 0

M_s	$\eta = 0$ [16]	CDM	$\eta = 0.1$ [16]	CDM
0	1.8751	1.8751	1.8792	1.8792
0.1	1.7227	1.7227	1.7258	1.7258
0.2	1.6164	1.6164	1.6187	1.6187
0.3	1.6164	1.5361	1.53808	1.5380
0.4	1.4724	1.4724	1.4740	1.4740
0.5	1.4200	1.4200	1.4213	1.4213
0.6	1.3757	1.3757	1.3768	1.3768
0.7	1.3375	1.3375	1.3385	1.3385
0.8	1.3041	1.3041	1.3050	1.3050
0.9	1.2745	1.2745	1.2753	1.2753
1	1.2479	1.2479	1.2486	1.2486

3.2 Effect of Nondimensional Added Mass M_s and Taper Ratio Coefficient c on the First Nondimensional Frequency Ω_1 of a Non-uniform Nanotube

In this numerical example, the influence of nondimensional added mass M_s and the nondimensional taper ratio coefficient c on the first nondimensional frequency value of non-uniform nanotube is investigated. For this purpose, a clamped non-uniform nanotube with circular hallow cross-section and carrying a concentrated mass M_s, placed on the right-end of the nanotube, i.e. $M_s = 0.5$, is considered. In order to solve this problem, the geometrical and physical properties of nanotube of [19] are used and the following variations of cross-sectional area A and moment of inertia I are assumed:

$$A(z) = A_0 \left(1 + c\frac{z}{L}\right)^q; \qquad I(z) = I_0 \left(1 + c\frac{z}{L}\right)^{q+2} \tag{33}$$

where A_0 and I_0 represent the cross-sectional area and moment of inertia of the SWCNT at the left end, for $z = 0$, respectively, and c that must satisfy the inequality $c > -1$, in order to avoid the nanotube tapers to zero between its ends.

Assuming $P = 0$ and $q = 1$, in Table 2, the first nondimensional natural frequency Ω_1 is reported, as obtained using CDM, for different values of nonlocal effect coefficient η and taper ratio coefficient c, namely -0.5 and 0.5. As it can be noticed, the nondimensional natural frequency Ω_1 increases by increasing c and η. Moreover, from Table 2, it can be easily observed that the present results are in excellent agreement with the results given by De Rosa et al. in [19].

3.3 Effect of Nondimensional Nonconservative Force p and Nonlocal Coefficient η on the First Nondimensional Frequency Ω_1

In the following numerical example, the effect of nonlocal effect coefficient η and nonconservative force P on the first nondimensional frequency value Ω_1 is evaluated.

Table 2 First nondimensional natural frequency Ω_1 value for varying nonlocal effect η and taper ratio coefficient c, with $M_s = 0.5$ and $q = 1$

η	DQM	CDM	DQM	CDM	DQM	CDM
	$c = -0.5$	$c = -0.5$	$c = 0$	$c = 0$	$c = 0.5$	$c = 0.5$
0	1.31181	1.31173	1.41996	1.41995	1.47881	1.47873
0.04	1.31208	1.31199	1.42017	1.42016	1.47898	1.47891
0.08	1.31287	1.31279	1.42081	1.42079	1.47950	1.47942
0.12	1.31412	1.31412	1.42187	1.42185	1.48036	1.48028
0.16	1.31611	1.31602	1.42337	1.42335	1.48157	1.48150
0.2	1.31858	1.31850	1.42532	1.42530	1.48315	1.48307

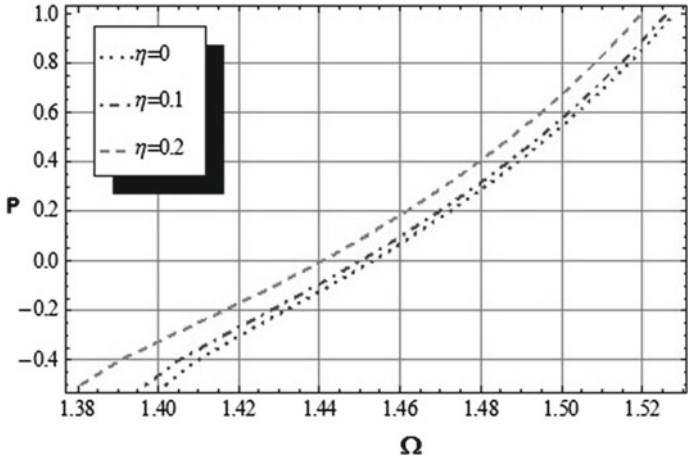

Fig. 3 The influence of nonconservative force P on the first nondimensional frequency Ω_1, for varying of nonlocal effect $\eta = 0, 0.1, 0.2$

In Fig. 3, the load-frequency curves are plotted for three values of nonlocal effect parameter η [0, 0.1, 0.2] and by fixing q = 1, P = 1 and $M_s = 0.5$. The three curves of Fig. 3 refer to different values of taper ratio coefficient c. As shown, by increasing c the first frequency increases, whereas if the nonlocal effect increases the first frequency value decreases. Moreover, it is interesting to note that if the nonlocal effect increases the first nondimensional natural frequency decreases when the nonconservative force is considered. More particularly, comparing the results quoted in Table 2, obtained for P = 0, with those plotted in Fig. 3, it can be easily observed that the nonconservative force P, at the free-end, influences the behavior of the nanotube significantly. In fact, for P = 0 if the nonlocal effect increases, Ω_1 increases; whereas for P = 1, Ω_1 decreases if the nonlocal coefficient η increases.

4 Conclusions

In the present paper, the nonlocal dynamic instability of a cantilevered single-walled carbon nanotube carrying a concentrated mass, at a generic position, and subject to a follower force, at the right end, is studied. According to the Eringen's and Euler-Bernoulli beam theories, the equation of motion are derived using the variational approach and are subsequently solved using Cell-Discretization Method. Some numerical examples show the effectiveness of the proposed approach, even through a comparison against the results in literature. The influence of nonlocal parameter, added mass and taper ratio coefficient on the dynamic instability of SWCNT is discussed.

References

1. Iijima, S.: Helical microtubules of graphitic carbon. Nature **354**, 56–58 (1991)
2. Eringen, A.C.: On differential equations of non local elasticity and solutions of screw dislocation and surface-waves. J. Appl. Phys. **54**, 4703–4710 (1983)
3. Eringen, A.C.: Nonlocal Continuum Fields Theories. Springer-Verlag, New York (2002)
4. Ghannadpour, S.A.M., Mohammadi, B., Fazilati, J.: Bending buckling and vibration problems of nonlocal Euler beams using Ritz method. Comp. Struct. **96**, 5843–589 (2013)
5. Grzelczyk, D., Stanczyk, B., Awrejcewicz, J.: Kinematics, dynamics and power consumption analysis of the hexapod robot during walking with tripod gait. Int. J. of Struct. Stability and Dynam. **17**(9), 1740010–17 (2017)
6. De Rosa, M.A., Lippiello, M.: Nonlocal Timoshenko frequency analysis of single-walled carbon nanotube with attached mass: an alternative hamiltonian approach. Comp. Part B **111**, 409–418 (2017)
7. Krysko, A.V., Awrejcewicz, J., Pavlov, S.P., Zhigalov, M.V., Krysko, V.A.: Chaotic dynamics of the size-dependent non-linear micro-beam model. Commun. Nonlinear Sci. Numer. Simula. **50**, 16–28 (2017)
8. Awrejcewicz, J., Krysko, A.V., Pavlov, S.P., Zhigalov, M.V., Krysko, V.A.: Stability of the size-dependent and functionally graded curvilinear timoshenko beams. J. Comp. Nonlinear Dynam. **12**(4), 041018–8 (2017)
9. Xiang, Y., Wang, C.M., Kitipornchai, S., Wang, Q.: Dynamic instability of nanorods/nanotubes subjected to an end follower force. J. Eng. Mech. ASCE **136**(8), 1054–1058 (2010)
10. Kazemi-Lari, M.A., Fazelzadeh, S.A., Ghavanloo, E.: Non-conservative instability of cantilever carbon nanotubes resting on viscoelastic foundation. Phys. E **44**, 1623–1630 (2012)
11. Bahaadini, R., Hosseini, M.: Effects of nonlocal elasticity and slip condition on vibration and stability analysis of viscoelastic cantilever carbon nanotubes conveying fluid. Comp. Mat. Scie. **114**, 151–159 (2016)
12. Auciello, N.M., Lippiello, M.: Vibration analysis of rotating non-uniform Rayleigh beams using "CDM" method. News in Engineering, **1**(1), ISSN: 1339–4886 (2013)
13. De Rosa, M.A., Lippiello, M.: Natural vibration frequencies of tapered beams. Eng. Trans. **57**(1), 44–66 (2009)
14. Raithel, A., Franciosi, C.: Dynamic analysis of arches using Lagrangian approach. J. Struct. Eng. **110**(4), 847–858 (1984)
15. De Rosa, M.A., Lippiello, M.: Free vibration analysis of DWCNTs using CDM and Rayleigh-Schmidt based on nonlocal Euler-Bernoulli beam theory. Sci. World J **2014**, 194529 (2014)
16. De Rosa, M.A., Lippiello, M.: Free vibration analysis of SWCNT using CDM in the presence of nonlocal effect. Int. J. of Eng. and Inn. Tech. (IJEIT), **4**(4) (2014)
17. Wolfram, S.: The Mathematica 8. Cambridge University Press (2010)
18. Mehdipour, I., Erfani-Moghadam, A., Mehdipour, C.: Application of an electrostatically actuated cantilevered carbon nanotube with an attached mass as a bio-mass sensor. Curr. Appl. Phys **13**, 1463–1469 (2013)
19. De Rosa, M.A., Lippiello M., Babilio, E., Ceraldi, C.: Nonlocal vibration analysis of a non-uniform carbon nanotube with elastic constraints and an attached mass. submitted to Composites Part B

Fractional Calculus Evaluation of Hyaluronic Acid Crosslinking in a Nanoscopic Part of Articular Cartilage Model System

Piotr Bełdowski, Piotr Weber, Tristan De Leon, Wayne K. Auge II and Adam Gadomski

Abstract This work presents a study of the mechanism of physical crosslinking of hyaluronic acid in the presence of common phospholipids in synovial joint organ systems. Molecular dynamic simulations have been executed to understand the formation of hyaluronan networks at various phospholipid concentrations. The results of the simulations suggest that the mechanisms exhibit subdiffusion characteristics. Transportation quantities derive as a function of time during numerical calculations of mean square displacement, and observations of sublinear growth were noted. Coarse-grained models are deployed to obtain a mathematical description where a random walker and several subdiffusion schemes of its motion describe the models. The findings of this study may establish mechanisms of biopolymer network formations in normal and pathologic synovial fluid and help elucidate the mechanism of facilitated AC biolubrication.

Keywords Hyaluronic acid · Molecular dynamics · Lubrication · Fractional calculas

P. Bełdowski (✉) · A. Gadomski
University of Science and Technology, Bydgoszcz, Poland
e-mail: piobel000@utp.edu.pl

A. Gadomski
e-mail: agad@utp.edu.pl

P. Weber
Gdańsk University of Technology, Gdańsk, Poland
e-mail: pioweber@pg.edu.pl

T. De Leon
Delaware State University, Dover, Delaware, USA
e-mail: tdeleon15@students.desu.edu

W. K. Auge II
NuOrtho, Boston, Massachussetts, USA
e-mail: nnmoc@aol.com

J. Awrejcewicz (ed.), *Dynamical Systems in Theoretical Perspective*,
Springer Proceedings in Mathematics & Statistics 248,
https://doi.org/10.1007/978-3-319-96598-7_3

1 Introduction

Hyaluronic acid is a major component in many systems in the body, and serves an important role in each of those systems. This study focuses on hyaluronic acid and its role in the complex synovial joint system and how it is influenced by common phospholipids [4, 9, 11, 19, 20]. In a healthy AC synovial joint system, hyaluronic acid contributes to viscoelasticity, lubrication, and overall joint support [1]. Hyaluronic acid is beneficial to the system when it is allowed to crosslink into a supramolecular structure needed for facilitated lubrication [5]. As changes in physiology occur, the properties of the hyaluronic acid in the system change [8]. In pathogenesis, a number of changes in the system occur, which ultimately alters the efficacy of HA. When common phospholipids interact with the HA, physical crosslinking is inhibited and the viscoelasticity of the synovial fluid decreases [17]. Using in silica experiments on the YASARA software program [21], models were designed to imitate a nanoscopic section of the fluid filled synovial joint. This occurence is examined by the findings of this study and indicate that the traditional treatment for osteoathritic joints of intra-articular HA injections is ineffective for lubrication, and other options should be explored.

Hyaluronic acid and phospholipids are both very important in the biolubrication mechanism of synovial joint organ systems. Both molecules are consider in non-surgical treatment of osteoarthritis via intra-articular injections in the clinical field and provide short term relief, but are not permanent solutions. As depicted in Fig. 1, the top image presents a healthy system with crosslinked HA while the bottom image depicts a system in which the green hyaluronic acid chains are not able to crosslink due to the increased levels of phospholipids.

2 Methods

The molecular dynamics simulation method has been used to look at the interactions between two components of synovial fluid. The system is composed of 16 chains of hyaluronic acid with a length of 25 nm (10 kDa) in the extended form and parallel to each other. The simulation box is filled with saline solution 0.9% NaCl to obtain 5% solution of HA, and then the different numbers of lipids (DPPC) are added to obtain concentration of HA and lipids at ratios between components denoted as $k_{PL:HA} = \frac{c_{PL}}{c_{HA}}$, where c_{PL} and c_{HA} represent concentration of PL and HA respectively. The modeled lipid DPPC (dipalmityphophatidocholine) has been chosed because of its highest concentration among other lipids in synovial fluid [7]. The simulation that ran for 10 ns was performed at constant temperature of 310 K at constant $pH = 7$. Figure 2 presents the initial structure of a system without water and lipids visualisation.

Assisted Model Building with Energy Refinement (AMBER) force field has been employed to mimic interactions between molecules, due to its universality and good description of interaction. YASARA structure package was used for molecular

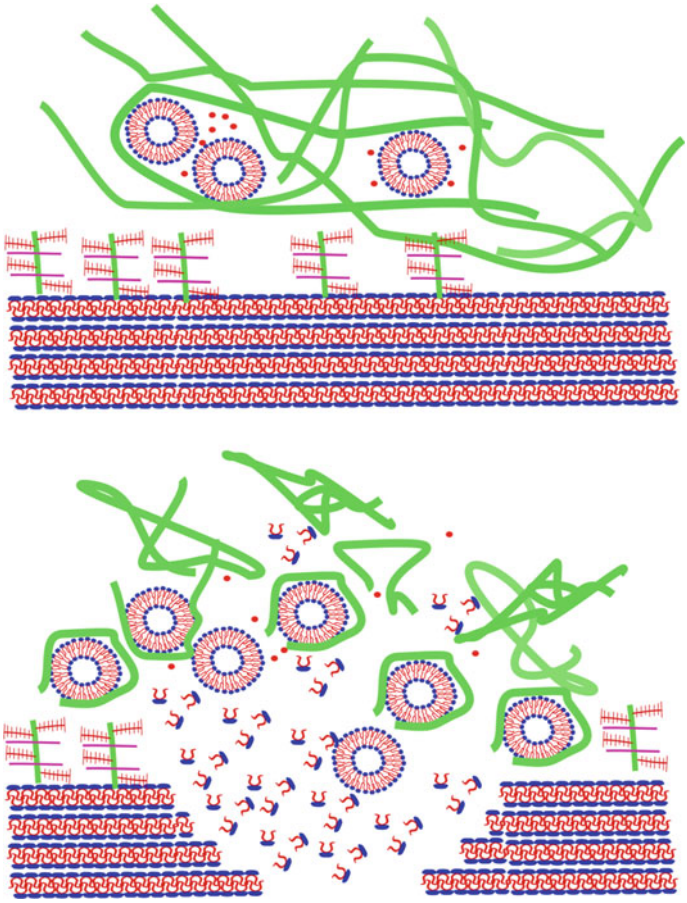

Fig. 1 The artistic depiction of articular cartilage at different stages of functionality. The top part present the healthy (normal) physiological conditions. Lower part present the abnormal (pathological conditions). Degeneration of AC surface leads to increase of phospholipids and lowers crosslinking mechanism

dynamics simulations. To describle a process of crosslinking of HA this work focused on two main phenomena when physical crosslinking occurs, namely hydrophobicity of the network and number of contacts reflecting how close chains are to each other.

The number of hydrophobic interactions between hydrophobic atoms is calculated by number of carbon atoms of groups close to other carbon based goroups with a distance less than 0.5 nm. Radius of gyration R_g is a measure:

$$\mathbf{R_g} = \sqrt{\frac{1}{N}\sum_{i=1}^{N}(\mathbf{R_i} - \mathbf{C})^2} \tag{1}$$

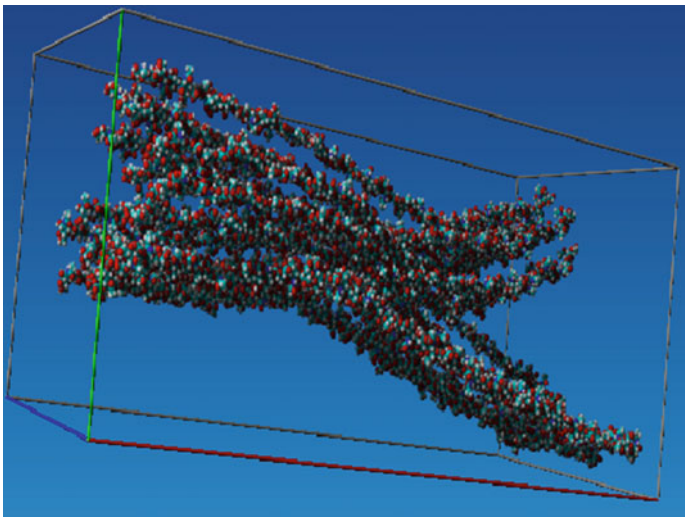

Fig. 2 The initial structures of systems of interest. Water molecules as well as lipids are not presented. Red dots represent oxygen atoms, blue - carbon and white hydrogen

Here $\mathbf{R_i}$ stand for position of each atom in the system and $\mathbf{C}$ is a center of a mass. Solvent accessible surface, a measure describing penetration of water molecules into molecule, consists of all the points that the center of the water probe (i.e. the nucleus of the oxygen atom in the water molecule) can reach while rolling over the solute. The shortest possible distance between the water oxygen nucleus and a solute atom is simply the sum of the Van der Waals radii of the solute atom and the water probe was calculated with method descibed by [14]. The number of contacts between atom lists those pairs of selected units that are closer than the specified cutoff parameter which in our case is 0.5 nm.

3 Results

Figure 3 presents the final structures of system at different PL concentrations with increasing number of phospholipids from top to bottom. Evolution of R_g (Fig. 4) shows that there is no significant difference between all three cases. The reason behind these is low cmc (critical micelle concentration) of DPPC lipids, where they tend to create micelles rather than interact with HA. Hence the penetration of HA network is low. The result is different that one obtained previously [17], however this is a result of initial conditions that imitates well established network. As presented in Fig. 5 water molecules penetration is increased with PLs concentration. Figure 6 shows an apparent mechanism of repelling water from network in absence of lipids. This means

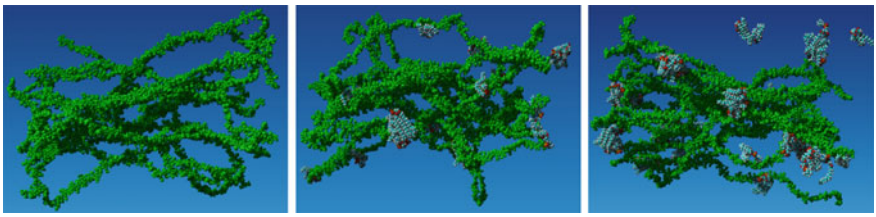

Fig. 3 The final structures of systems of interest. The HA has been colored green for better visualisation, color of atoms building lipids are colored in the same fashion as in the Fig. 2. From left to right the concentration of lipids increases

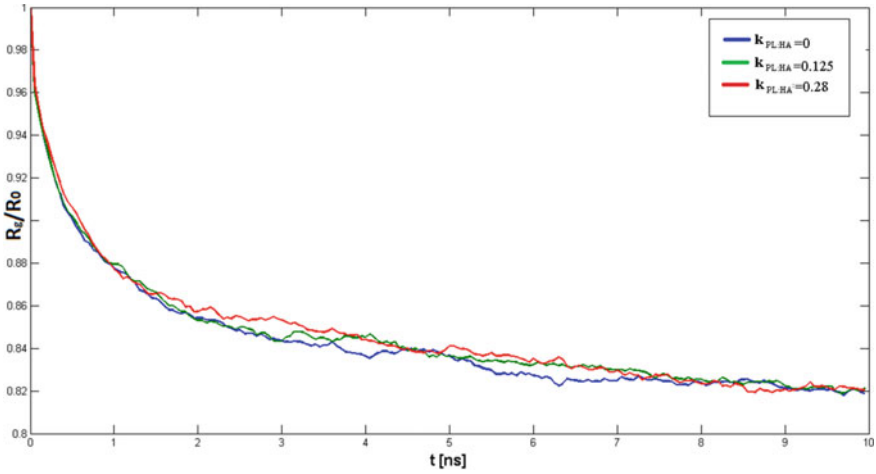

Fig. 4 Relative radius of gyration in function of time. All the cases are described in legend of a plot

that the presence of lipids help water molecules to better penetrate system. This means that the denser, stronger network is created in absence or low concentration of lipids. Figure 7 shows that mechanism from perspective of overall number of intramolecular contacts inside network.

4 Fractional Model of Phenomenon

Polymeric system usually exhibit anomalous dynamics, where the mean-square displacement of a single monomer increases as t^{α}, $0 < \alpha < 1$ until to a certain time limit τ. It means that until time τ the dynamics has subdiffusive character. After τ the process becomes diffusive, where mean-square displacement of a single monomer is proportional to time [10].

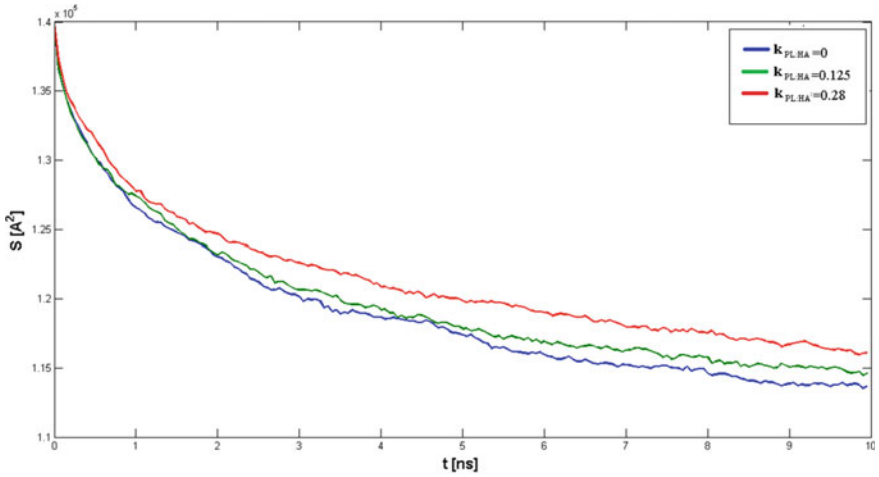

Fig. 5 Solvent accessible surface in function of time. All the cases are sescribed in legend of a plot

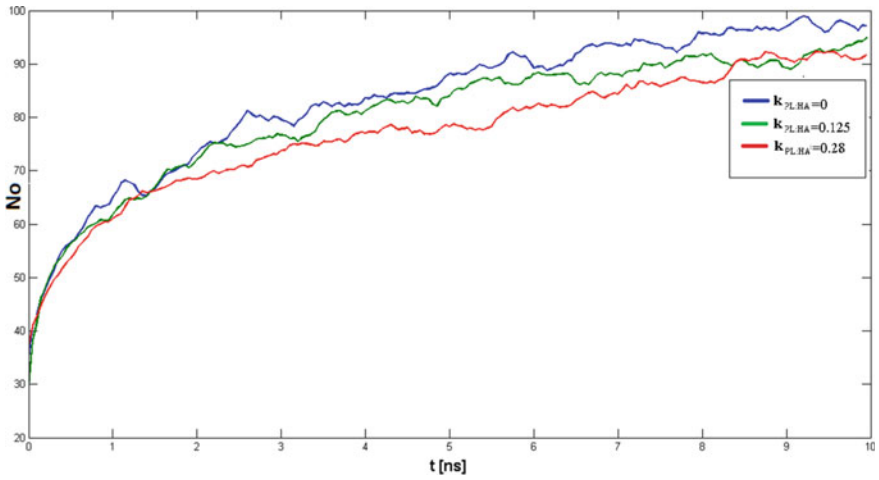

Fig. 6 Number of hydrophobic interactions between atoms in function of time. All the cases are described in legend of a plot

There is many models, that explain such observations [2]. This work uses various ideas coming from several of them. Example of such a model is the self-avoiding Rouse model [10], that gives an incomplete explanation about the observations. This model is based on assumptions of both: Rouse model [15] and self-avoiding walk model. The polymeric macromolecule is divided into smaller parts called submolecules. Submolecules can be treated as a rigid bead. In the most simple formulation of the Rouse model there is assumption that in polymeric dynamics neglect interactions between the submolecules that perform gaussian motion. Motions of

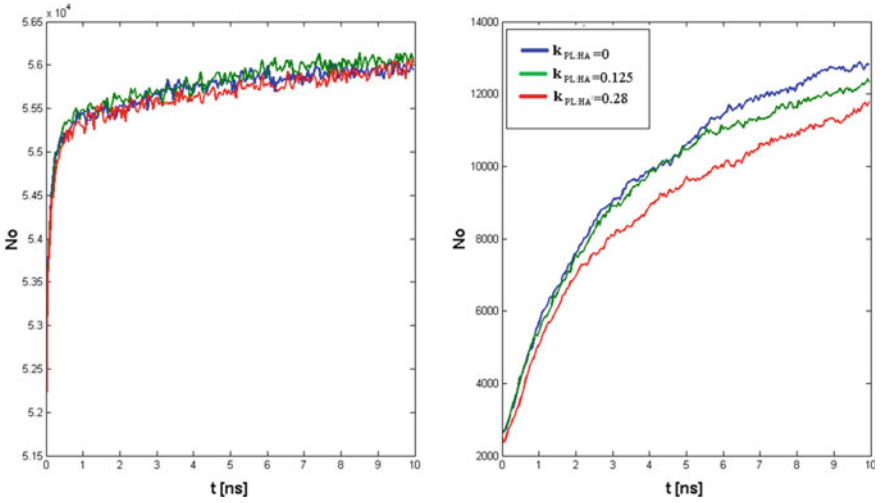

Fig. 7 Contacts between atoms in function of time. All the cases are described in legend of a plot. On the left hand side one can see the results for intra-molecular, on the right hand side inter-molceular contacts between HA chains

submolecules are independent between each other. This is a drawback of this theory. Self avoiding walk completes the Rouse theory, but not fully. There is introduced the fact, that submolecules (bead) of polymer can't occupy the same point in space. More advance models assume that between submolecules there are interactions (for example: the Zimm model). But our results suggest to use another model to describe them. We propose to use ideas presented in [3].

Polymeric systems are large macromolecules that have several lenght - scale dependent relaxation times. The longest one of them is called the terminal relaxation time τ. Time τ manifested in the decay of the polymer's end-to-end vector correlation function. Using idea of Rouse model one can divide HA molecule on submolecules and we follow their dynamics. Mean square displacement of a single submolecule of a polymer, for $t < \tau$, behave as t^{α}. For $t > \tau$ process is proportional to time. So one can conclude that the dynamics of a tagged submolecule in a polymer chain must be anomalous till the terminal relaxation time τ.

To compare simulations results with theoretical predictions we have plotted mean-square displacement of a single submolecule in the function of time in logarithmic - logarithmic scale. This results are presented on the Fig. 8. One can see that dependency of mean-square displacement of a single submolecule from time as power function, untill time τ is well fulfilled. Goodness of fit of a model to data from simulation is measured by using coefficient of determination R^2. In the table one can see that R^2 has very high values. It means that assumption about power dependency mean-square displacement of a single submolecule from time is well fulfilled.

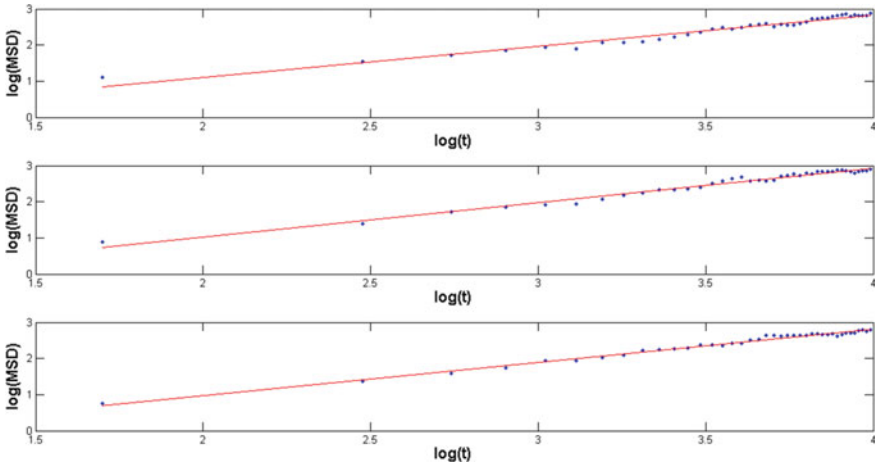

Fig. 8 MSD in loglog scale top row represent organised structure while lower row show random structure. Top to bottom one can see a system with growing concentration of lipids. Parameters of the fit are presented in Table 1

Table 1 Parameters of fitting with a linear function to MSD

Case	HA	HA+24	HA+56
R^2	0.9640	0.9801	0.9884
α	0.8621	0.9537	0.9192

Taking into account values of α parameter and its dependency from concentration we propose to describe process in the framework of a model presented in [3]. In the article there is explanation of behaviour of fully hydrated dipalmitoylphosphatidylcholine membrane during the gel-to-subgel phase transformation process. Author argumented that description of it is a problem of time scale. This work uses this idea to presented here results of simulations.

In dynamics of HA molecule one can distinguish two phases. First when one observes anomalous dynamics and the second when the system achieved its final structure and motion of its part is random. There is of course not only one system but statistical ensemble of such molecular systems. Properties of single polymeric molecule generally is determined by hydrophobic and hydrophilic forces. So the properties of statistical ensemble of molecule is also determined by them. To proposed model that describe the ensemble one can assume that there are some number of hydrophobic forces N_f and some number of hydrophilic forces N_h, both depend on time. One assumes that numbers of all forces acting on a molecule is constant:

$$N = N_f(t) + N_h(t). \tag{2}$$

Taking into account results of simulations of hydrophobic contacts we propose to use in description of $N_f(t)$ after time τ equation in the form:

$$M\frac{d}{dt}N_f(t) = (N - N_f(t)) \tag{3}$$

This equation has solution in the form:

$$N_f(t) = N_f(0)e^{-At} + N\left(1 - e^{-At}\right) \tag{4}$$

where $N_f(0)$ represents initial number of contacts. But before time τ one can observe processes, that causes unnormal kinetic. This part of the process can be described by formula:

$$ {}^{RL}_{0}D^{\alpha}_{t}\left[N_f(t)\right] = A_{\alpha}(N - N_f(t)), \tag{5}$$

where ${}_0D^{\alpha}_{t}[\cdot]$ is a Riemann-Liouville derivative defined, for $0 < \alpha < 1$, by formula [12, 16]

$$ {}^{RL}_{0}D^{\alpha}_{t}\left[f(t)\right] = \frac{1}{\Gamma(1-\alpha)}\frac{d}{dt}\int_0^t \frac{f(\tau)}{(t-\tau)^{\alpha}}d\tau. \tag{6}$$

To solve this equation one can use Caputo derivative defined, for $0 < \alpha < 1$, by:

$$ {}^{C}_{0}D^{\alpha}_{t}\left[f(t)\right] = \frac{1}{\Gamma(1-\alpha)}\int_0^t \frac{1}{(t-\tau)^{\alpha}}\frac{df(\tau)}{d\tau}d\tau \tag{7}$$

and relatonship between both kind of derivatives [12, 13]

$$ {}^{RL}_{a}D^{\alpha}_{t}\left[f(t)\right] = {}^{C}_{a}D^{\alpha}_{t}\left[f(t)\right] + \frac{t^{-\alpha}}{\Gamma(1-\alpha)}f(0). \tag{8}$$

Using the last relation one can write proposed equation in the following way:

$$ {}^{C}_{0}D^{\alpha}_{t}\left[N_f(t)\right] + \frac{t^{-\alpha}}{\Gamma(1-\alpha)}N_f(0) = A_{\alpha}(N - N_f(t)). \tag{9}$$

Using the Laplace transform method to solve differential equation one can obtain following solution for proposed equation and initial condition $N_f(0) = 0$:

$$N_f(t) = A_{\alpha}N\left[1 - \left(E_{\alpha,1}\left(-A_{\alpha}t^{\alpha}\right) + \left(A_{\alpha} - 1\right)t^{\alpha}E_{\alpha,1+\alpha}\left(-A_{\alpha}t^{\alpha}\right)\right)\right]. \tag{10}$$

Here, for $x > 0$, $\alpha > 0$ and $\beta > 0$, :

$$E_{\alpha,\beta}(x) = \sum_{k=0}^{\infty}\frac{x^k}{\Gamma(\beta + \alpha k)} \tag{11}$$

is a Mittag-Leffler function [6]. Transition from anomalous to normal kinetics is equivalent to replace fractional derivative to normal derivative.

5 Conclusions

There is well established connection between AC tribology and mechanisms of synovial joint organ system lubrication as governed in partial by HA:PL interaction [1, 18]. Presented results continues the description of system of interest as an interplay between HA network creation in various physiological conditions [8, 17]. This study further demonstrates that the increased concentration of PL connected to various physiological conditions have an influence on HA network creation.

Results show a mechanism of HA network creation/mentainance in a presence of phospholipids. Unlike in previous work on HA:PL interaction [17] there is no difference in geometrical parameters of a system, namely radius of gyration R_g (see Fig. 4). This is caused by initial conditions of the systems which meant to mimick the well established network of HA. Due to its hydrophilic nature HA interact rather within network than with lipids. There is however changed in interaction inside network. As presented in Fig. 1 increase in PL concentration results in lower number of intermolecular contacts between HA chains. Final strucures of simulations (Fig. 3) show that PL can penetrate HA network and can create complexes of HA network micelle like structures. This can also be seen when looking at the behavior of water molecules. Figure 5 shows that HA without phospholipids create denser network repelling water molecules from the interior. This can also be seen in Fig. 6, PL concentration cause in higher number of hydrophobic interactions between HA chains. This result is in good agreement with experimental results which show that PLs increase hydrophobicity of HA. Presented model of HA gel formation rationalize the obtained results in terms of fractional calculus. Process is governed by hydrophobic interactions therefore it is useful to describe HA gel formation in presented fashion. Due to the nature of HA:PL interactions polymer dynamics desciption approaches such as Rouse model are not useful.

Acknowledgements This work was supported by the internal grant No. BS39/14 of the Institute of Mathematics and Physics of the UTP University of Science and Technology in Bydgoszcz. This work was supported by the internal grant from Department of Atomic, Molecular and Optical Physics of Gdańsk University of Technology. P.W. wish to thank Organisers of Dynamical Systems in Theory and Applications, Łódź, Poland 2017 for financial support.

References

1. Dédinaté, A.: Biomimetic lubrication. Soft Matter **8**, 273–284 (2012)
2. Doi, M., Edwards, S.F.: The Theory of Polymer Dynamics. Oxford University Press, Oxford (1994)

3. Gadomski, A.: Nucleation-and-growth problem in model lipid membranes undergoing subgel phase transitions is a problem of time scale. Eur. Phys. J. B **9**, 569–571 (1999)
4. Goudoulas, T.B., Kastrinakis, E.G., Nychas, S.G., Papazoglou, L.G., Kazakos, G.M., Kosmas, P.V.: Rheological study of synovial fluid obtained from dogs: healthy, pathological, and post-surgery, after spontaneous rupture of cranial cruciate ligament. Ann. Biomed. Eng. **38**, 57–65 (2010)
5. Hari, G.G., Hales, C.A.: Chemistry and Biology of Hyaluronan. Elsevier Science, Amsterdam (2008)
6. Haubol, H.J., Matha, A.M., Saxena, R.K.: Mittag-Leffler functions and their applications. J. Appl. Math. **2011** (2011)
7. Hills, B.A.: Boundary lubrication in vivo. Proc. Inst. Mech. Eng. H **214**, 83–94 (2000)
8. Jung, S., Petelska, A., Bełdowski, P., Augé, W., Casey, T., Walczak, D., Lemke, K., Gadomski, A.: Hyaluronic acid and phospholipid interactions useful for repaired articular cartilage surfaces - a mini review toward tribological surgical adjuvants. Colloid Polym. Sci. **295**, 403–412 (2017)
9. Nitzan, D.W., Nitzan, U., Dan, P., Yedgar, S.: The role of hyaluronic acid in protecting surface-active phospholipids from lysis by exogenous phospholipase A2. Rheumatology **40**, 335–340 (2001)
10. Panja, D.: Anomalous Polymer Dynamics Is Non-Markovian: Memory Effects and The Generalized Langevin Equation Formulation. J. Stat. Mech. **6**, P06011 (2010)
11. Pasquali-Ronchetti, I., Quaglino, D., Mori, G., Bacchelli, B., Ghosh, P.: Hyaluronan-phospholipid interactions. J. Struct. Biol. **120**, 1–10 (1997)
12. Podlubny, I.: Fractional Differential Equations. Academic Press, San Diego (1999)
13. Podlubny, I.: Matrix approach to discrete fractional calculus. Fractional Calculus Appl. Anal. **3**, 359–386 (2000)
14. Richmond, T.J.: Solvent accessible surface area and excluded volume in proteins. Analytical equations for overlapping spheres and implications for the hydrophobic effect. J. Mol. Biol., **178**, 63–89 (1984)
15. Rouse, P.E.: A theory of the linear viscoelastic properties of dilute solutions of coiling polymers. J. Chem. Phys. **21**, 1272–1280 (1953)
16. Samko, S.G., Kilbas, A.A., Marichev, O.I.: Fractional integrals and derivatives - theory and applications. Gordon and Breach, Amsterdam (1993)
17. Siódmiak, J., Bełdowski, P., Augé, W., Ledziński, D., Śmigiel, S., Gadomski, A.: Molecular dynamic analysis of hyaluronic acid and phospholipid interaction in tribological surgical adjuvant design for osteoarthritis. Molecules **22**, 1436–1456 (2017)
18. Sorkin, R., Kampf, N., Zhu, L., Klein, J.: Hydration lubrication and shear-induced self-healing of lipid bilayer boundary lubricants in phosphatidylcholine dispersions. Soft Matter **12**, 2773–2784 (2016)
19. Wang, M., Liu, C., Thormann, E., Dédinaité, A.: Hyaluronan and phospholipid association in biolubrication. Biomacromolecules **14**, 4198–4206 (2013)
20. Wieland, D.C.F., Degen, P., Zander, T., Gayer, S., Raj, A., An, J., Dédinaité, A., Claesson, P., Willumeit-Rmer, R.: Structure of DPPC-hyaluronan interfacial layers?effects of molecular weight and ion composition. Rheumatology **412**, 729–740 (2016)
21. yasara, http://yasara.org/

Topological and Measure-Theoretical Entropies of a Solenoid

Andrzej Biś and Agnieszka Namiecińska

Abstract A mathematical solenoid is a geometric object which can be presented either in an abstract way as an inverse limit or in a geometric way as nested intersections of solid tori. In dynamical systems solenoids were introduced by Smale as hyperbolic attractors of a diffeomorphism of a three-dimensional manifold. The topological complexity of a solenoid can be expressed by a topological entropy which is equal to an upper capacity of some Carathéodory structure, in the sense of Pesin. We consider topological and measure-theoretical approach to dynamical properties of a solenoid and discuss homogeneous measures. In general case there is no invariant measure for a solenoid, therefore one can not say neither about measure-theoretical entropy nor about a measure of maximal entropy of a solenoid. We define $\delta-$measure-theoretical entropy of a solenoid, in sense of Katok, which is related to the topological entropy.

Keywords Charatheodory structure · Entropy · Homogeneous measure · Solenoid

1 Introduction

Nowadays, the notion of a solenoid appears in different areas of science, it is well-known in physics, biology and mathematics. In the paper we focus on its mathematical meaning. In the late 1920s a solenoid as a mathematical object was introduced by Vietoris [19] as inverse limit space over circle maps. A solenoid can be presented either in an abstract way as an inverse limit or in a geometric way as nested intersections of solid tori. For a given sequence of positive integers $\{k_n\}_{n\in\mathbb{N}}$, a solenoid can be described as the intersection of a sequence of tori $\{T_n\}_{n\in\mathbb{N}}$ such that T_{n+1} is

A. Biś (✉) · A. Namiecińska
Faculty of Mathematics and Computer Science,
University of Lodz, Banacha 22, 90-238 Lodz, Poland
e-mail: andbis@math.uni.lodz.pl

A. Namiecińska
e-mail: a.namiecinska@wp.pl

J. Awrejcewicz (ed.), *Dynamical Systems in Theoretical Perspective*,
Springer Proceedings in Mathematics & Statistics 248,
https://doi.org/10.1007/978-3-319-96598-7_4

wrapped around inside T_n longitudinally k_n times. Topological properties of inverse limits on intervals are relatively good understood (see [13]).

The standard construction of a solenoid, presented by Vietoris [19], was generalized and modified by McCord [16], Williams [22] and many other authors in different contexts. In dynamical systems a solenoid was introduced by S. Smale [18] as hyperbolic attractor of a diffeomorphism of a three-dimensional manifold. Solenoids appeared in many branches of mathematics: in geometry, dynamical systems, theory of groups, continuum theory, foliations and so on.

In the paper we study a sequence $f_\infty = (f_n : X_n \to X_{n-1})_{n=1}^\infty$ of continuous epimorphisms of compact metric spaces X_n, called bonding maps. We assume that all spaces X_n coincide with a compact metrizable space X. By *solenoid* determined by f_∞, we mean the inverse limit

$$X_\infty = \varprojlim X_k = \{(x_k)_{k=0}^\infty : x_{k-1} = f_k(x_k), k \in \mathbb{N} \cup \{0\}\}.$$

Clearly, X_∞ is a compact subset of the Hilbert cube ΠX_k. A distance function d_∞ on X_∞ is given by usual formula

$$d_\infty((x_k), (u_k)) = \sum_{k=0}^{\infty} \frac{1}{2^k} d_k(x_k, u_k).$$

Since X_∞ is uniquely determined by f_∞, we will often identify these two objects. A solenoid is both a metric space and a dynamical object of a complicated structure. Its complexity yields from the dynamics of bonding maps and can be investigated from topological or ergodic point of view.

Let X be a compact metric space and $f : X \to X$ be a continuous map or a homeomorphism. The pair (X, f) is called a topological dynamical system. Topological entropy is a main concept in topological dynamics, it is a nonnegative number which measures disorder and complexity of the system (X, f). Positive entropy of the dynamical system reflects its chaotic behaviour. The classical topological entropy of a single map was a very fruitful notion, therefore the concept of entropy was generalized to an action of algebraic structures (such as semigroups, groups and pseudogroups) on topological spaces, and to geometric objects such as distributions, laminations and foliations (see [20]).

In the paper we focus on dynamics of a solenoid. In general case there is no invariant measure for a solenoid, therefore it is not clear how to define its measure-theoretical entropy. Bowen [4] defined a notion of homogeneous measure for a classical dynamical system determined by a continuous map $f : X \to X$ of a compact metric space X. We discuss homogeneous measures for a solenoid. On the other hand a local measure entropy, which was originally introduced by Brin and Katok [6] for a dynamics of a single map, is also a powerful tool for investigations of dynamics of solenoids.

In Theorem 2 we show that if a solenoid admits a homogeneous measure then its local measure entropy does not depend on a point of the solenoid. Theorem 3 states

that the topological entropy of a solenoid, with a homogeneous measure, coincides with the local measure entropy.

Dimension theory is a very useful tool to analyze the complicated structure of invariant sets of dynamical systems. Bowen [5] pointed out that the topological entropy of a continuous map can be defined in a way similar to construction of Hausdorff dimension. Twenty five years later, Pesin in [17] discussed the interrelation between dimension theory and the theory of classical dynamical systems, he noticed that the construction of Hausdorff dimension and well-known Carathéodory construction in general measure theory can be generalized. To this aim, Pesin introduced in axiomatic way so called Carathéodory structure, which gives a new insight into thermodynamical formalism and allows to extend the classical notion of the topological pressure to non-compact or non-invariant sets. Also, a Carathéodory structure generates the Carathéodory dimension, lower and upper capacities of a set. Carathéodory structures applied to dynamical systems are a very powerful tool.

In general case, there is no invariant measure for a solenoid, therefore it is not clear how to define its measure-theoretical entropy, but we define $\delta-$measure-theoretical entropy of a solenoid, in the sense of A. Katok, which is related to its topological entropy. In Theorem 7 we prove that $\delta-$measure-theoretical entropy of a solenoid is upper estimated by its topological entropy.

2 A Classical Dynamical System

In mathematics, the study of a disrete dynamical system, determined by a continuous map $f : X \to X$ of a compact metric space X, as a whole is primarily concerned with the asymptotic behavior of such systems, that is how the system evolves after repeated applications of f. Its complexity can be described by its topological entropy $h_{top}(f)$ and measure-theoretical entropy $h_\mu(f)$ calculated with respect to an f-invariant Borel probability measure μ. For convenience of the reader, we recall briefly the basic definitions related to measure-theoretical entropy and topological entropy. For more detailed introduction to dynamical systems we recommend [21].

2.1 Measure-Theoretical Entropy of a Map

Let (X_1, B_1, μ_1) and (X_2, B_2, μ_2) be measure spaces. A map $T : X_1 \to X_2$ is called measurable if the preimage of any measurable set is measurable. A measurable transformation $T : X_1 \to X_2$ is measure preserving if $\mu_1(T^{-1}(A_2)) = \mu_2(A_2)$ for every $A_2 \in B_2$. Let $f : X \to X$ be a continuous map defined on a compact metric space (X, d). Assume that (X, B, μ) is a measure space and the map f is measure preserving. The measure μ is called $f-$invariant if $\mu(f^{-1}(A)) = \mu(A)$, for any $A \in B$. The Krylov-Bogoliubov Theorem (see [21]) guarantees the existence of a probability f-invariant measure μ defined on Borel σ-algebra generated by the collection of open

subsets of X. A partition of X is a finite family $A = \{A_1, A_2, \ldots, A_n\}$ of pairwise disjoint measurable subsets of X such that $A_1 \cup A_2 \cup \cdots \cup A_n = X$. For partitions A and B of X we define the following partitions:

$$A \vee B = \{A_i \cap B_j : A_i \in A \text{ and } B_j \in B\},$$

$$f^{-1}(A) = \{f^{-1}(A_i) : A_i \in A\},$$

$$A^{(n)} = A \vee f^{-1}(A) \vee \cdots \vee f^{-(n-1)}(A).$$

A measure entropy of a partition A of X with respect to the measure μ is defined by

$$H_\mu(A) = -\sum_{A_i \in A} \mu(A_i) \log(\mu(A_i)).$$

It is known (for details see [21]) that for any partition A of X there exists a limit

$$H_\mu(f, A) = \lim_{n\to\infty} \frac{1}{n} H_\mu(A^{(n)}).$$

Definition 1 Kolmogorov-Sinai or measure-theoretical entropy of a measurable map $f : X \to X$ with respect to an f-invariant measure μ is the quantity defined by

$$h_\mu(f) := \sup\{H_\mu(f, A) : A \text{ is a partition of } X\}.$$

2.2 Topological Entropy of a Map

Topological entropy of a continuous map was first introduced in 1965 by Adler et al. [1]. In metric spaces a different definition of entropy was introduced by Bowen [4] in 1971 and independently by Dinaburg [9] in 1970. Later, Bowen [5] proved that both definitions are equivalent. Bowen's approach uses a notion of (n, ε)-separated points.

Again, let $f : X \to X$ be a continuous map defined on a compact metric space (X, d). Following Bowen we say that a subset $E \subset X$ is (n, ε)-separated (where n is a positive integer and $\varepsilon > 0$) if the inequality

$$\max\{d(f^i(x), f^i(y)) : i = 0, 1, \ldots, n-1\} \geq \varepsilon$$

holds for any distinct points $x, y \in E$. Since X is a compact space the cardinality $card(A)$ of any (n, ε)-separated set A is finite. Let $s(n, \varepsilon) = \max\{\text{card}(A) : A \text{ is } (n, \varepsilon) - \text{separated subset of } X\}$.

Definition 2 The *topological entropy* of a continuous map $f : X \to X$ defined on a compact metric space (X, d) is defined as

$$h_{top}(f) := \lim_{\varepsilon \to 0^+} \limsup_{n \to \infty} \frac{1}{n} \log s(n, \varepsilon).$$

We recommend textbooks [7, 21] or [10] which treat in details properties of topological and measure-theoretical entropies of classical dynamical systems.

2.3 Katok Formula for Measure-Theoretical Entropy

Denote by $B(x, \varepsilon)$ an open ball in (X, d), centered at $x \in X$ and of radius ε. The sequence of metrics

$$d_n^f(x, y) := \max\{d(f^i(x), f^i(y)) : i = 0, 1, \ldots, n-1\}$$

determines the family of $\varepsilon-$balls centered at $x \in X$, in the d_n^f-metric:

$$B_n^f(x, \varepsilon) := \bigcap_{i=0}^{n-1} f^{-i}(B(f^i(x), \varepsilon)).$$

In 1980, Katok [14] proposed the definition of the measure-theoretical entropy $h_\mu(f)$ of $f : X \to X$, with respect to Borel probability f-invariant measure μ, which mimics the definition of topological entropy given by R. Bowen. His definition reads as follows. For $\varepsilon > 0$ and $\delta \in (0, 1)$, let us denote by $N_f(n, \varepsilon, \delta)$ the minimal number of $\varepsilon-$balls in the d_n^f-metric which cover the set of measure more than or equal to $1 - \delta$. Finally, put

$$h_\mu^{K,\delta}(f) = \lim_{\varepsilon \to 0} \limsup_{n \to \infty} \frac{1}{n} \log N_f(n, \varepsilon, \delta).$$

Using combinatorial arguments A. Katok proves the relation between $h_\mu^{K,\delta}(f)$ and $h_\mu(f)$.

Theorem 1 (Theorem 1.1 in [14]) *For any homeomorphism $f : X \to X$ of a compact metric space (X, d) and for every $\delta > 0$*

$$h_\mu^{K,\delta}(f) = \lim_{\varepsilon \to 0} \limsup_{n \to \infty} \frac{1}{n} \log N_f(n, \varepsilon, \delta) = \lim_{\varepsilon \to 0} \liminf_{n \to \infty} \frac{1}{n} \log N_f(n, \varepsilon, \delta)$$

and

$$h_\mu^{K,\delta}(f) = h_\mu(f).$$

2.4 Variational Principle

Due to the Krilov-Bogoliubov Theorem for a continuous map $f : X \to X$ the set $M(f, X)$ of f-invariant Borel probability measures on X is not empty. The topological entropy and measure-theoretic entropies of f are interrelated. The relation between them is stated in the famous Variational Principle. One inequality in the Variational Principle was proved by Dinaburg [9] and Goodman [11] the other inequality by Goodwyn [12].

Theorem 2 (Variational Principle) *For a continuous map $f : X \to X$ defined on a compact metric space (X, d)*

$$h_{top}(f) = \sup\{h_\mu(f) : \mu \in M(f, X)\}$$

i.e., topological entropy equals the supremum of the Kolmogorov-Sinai entropies $h_\mu(f)$ of f, where μ ranges over the set $M(f, X)$ all f-invariant Borel probability measures on X.

Remark 1 If $h_{top}(f) = h_\mu(f)$ then the f-invariant measure μ is called the measure of maximal entropy. In many cases a measure of maximal entropy exists (see [8]).

3 Topological Entropy of a Solenoid

Let $f_\infty = (f_n : X_n \to X_{n-1})_{n=1}^\infty$ be a sequence of continuous epimorphisms of compact metric spaces X_n. We assume that all spaces X_n coincide with a compact metrizable space X, (i.e. $X_n = X$). Each space X_n is equipped with a metric d_n. In the case of a solenoid, which can be consider as a generalized dynamical system, one can define its topological entropy. Following Bowen [4] we define a topological entropy of a solenoid by (n, ε)-separated sets. For any positive integer n we define a new metric D_n on X_n by

$$D_n(x, y) = \max\{d_{i-1}(f_i \circ f_{i+1} \circ \cdots \circ f_n(x), f_i \circ f_{i+1} \circ \cdots \circ f_n(y)) : i \in \{1, \ldots, n\}\}.$$

We say that a subset $E \subset X_n$ is $(n, \varepsilon)-$ separated if for any distinct points $a_1, a_2 \in E$ the inequality $D_n(a_1, a_2) \geq \varepsilon$ holds. Since (X_n, d_n) is the compact metric space, then any $(n, \varepsilon)-$ separated set E is finite. Let

$$s(n, \varepsilon) := \max\{card(E) : E \text{ is } (n, \varepsilon) - \text{separated subset of } X_n\}.$$

Definition 3 The quantity

$$h_{top}(f_\infty) := \lim_{\varepsilon \to 0^+} \limsup_{n \to \infty} \frac{1}{n} \log s(n, \varepsilon)$$

is called the topological entropy of the solenoid f_∞.

Remark 2 The topological entropy of a solenoid also can be expressed in the language of (n, ε)-spannings sets. A subset $F \subset X_n$ is (n, ε)-spanning if for any $x \in X_n$ there exists $y \in F$ such that $D_n(x, y) < \varepsilon$. Let

$$r(n, \varepsilon) := \min\{card(F) : F \text{ is } (n, \varepsilon) - \text{spanning subset of } X_n\}.$$

Using standard arguments (e.g. [21]) we get an estimation $r(n, \varepsilon) \leq s(n, \varepsilon) \leq r(n, \varepsilon/2)$. Consequently, passing to the suitable limits, we obtain the equality

$$h_{top}(f_\infty) = \lim_{\varepsilon \to 0^+} \limsup_{n \to \infty} \frac{1}{n} \log r(n, \varepsilon).$$

4 Homogeneous Measures

If there exists a homogeneous measure for a solenoid then one can express topological entropy by local measure entropies calculated with respect to this particular homogeneous measure. The metric D_n on X_n given by

$$D_n(x, y) := \max\{d_{i-1}(f_i \circ f_{i+1} \circ \cdots \circ f_n(x), f_i \circ f_{i+1} \circ \cdots \circ f_n(y)) : i \in \{1, \ldots, n\}\}$$

determines a family of sets

$$B_n(x, \varepsilon) := \bigcap_{i=1}^{n} (f_i \circ f_{i+1} \circ \cdots \circ f_n)^{-1}[B_{d_{i-1}}(f_i \circ f_{i+1} \circ \cdots \circ f_n(x), \varepsilon)],$$

where $B_{d_i}(y, r) = \{z \in X_i : d_i(z, y) < r\}$ is a standard ball in (X_i, d_i) centered at y and of radius r. Following Bowen [4] we introduce a notion of a homogeneous measure for a solenoid.

Definition 4 We say that a Borel measure μ on a metric space X is f_∞-homogeneous measure for a solenoid f_∞ if:

(1) $\mu(K) < \infty$ for any compact $K \subset X$,
(2) there exists $K_0 \subset X$ with $\mu(K_0) > 0$ and

(3) for any $\varepsilon > 0$ there exist $\delta > 0$ and $c > 0$ such that the inequality

$$\mu(B_n(y, \delta)) \leq c \cdot \mu(B_n(x, \varepsilon))$$

holds for all $n \in \mathbb{N}$ and all $x, y \in X$.

The authors in [3] provide the following examples of homogeneous measures for solenoids:

Example 1 Choose a closed compact and oriented Riemannian manifold (M, d) with volume form dV. Let $(X_n, d_n) = (M, d)$, for any $n \in N$, and $f_\infty = (f_n : X_n \to X_{n-1})_{n=1}^{\infty}$ be a sequence of isometries of M. The volume form induces a natural measure μ on M :

$$\mu(A) = \int_A 1 \cdot dV,$$

where A is a Borel subset of M, which is f_∞-homogeneous measure.

Example 2 Let G be a compact topological group with a right invariant Haar measure μ then G admits a right invariant metric d. Fix an isomorphism (so a homeomorphism and homomorphism) $H : G \to G$ of topological group and infinite sequence $\{g_n\}_{n \in N}$ of elements of G. Define $f_i := R_{g_i} \circ H$, where $R_{g_i}(x) = x \cdot g_i$ is a right multiplication for any $x \in G$. The sequence $f_\infty = (f_n : X_n \to X_{n-1})_{n \in \mathbb{N}}$, where $X_n = G$, determines a solenoid with a homogeneous measure.

4.1 f_∞-Homogeneous Measures and Topological Entropy

Brin and Katok [6] introduced a notion of the local measure entropy for a single continuous map $f : X \to X$ of a compact metric space X. We adapt this notion of the local measure entropy to a solenoid determined by $f_\infty = (f_n : X_n \to X_{n-1})_{n \in \mathbb{N}}$ in the following way:

Definition 5 For any $x \in X$ and a Borel probability measure μ on X the quantity

$$h^{\mu}_{f_\infty}(x) = \lim_{\varepsilon \to 0} \limsup_{n \to \infty} -\frac{1}{n} \log \mu(B_n(x, \varepsilon))$$

is called a local upper μ-measure entropy at the point x, with respect to f_∞, while the quantity

$$h_{\mu, f_\infty}(x) = \lim_{\varepsilon \to 0} \liminf_{n \to \infty} -\frac{1}{n} \log \mu(B_n(x, \varepsilon))$$

is called a local lower μ-measure entropy at the point x, with respect to f_∞.

The authors of [3] studied the properties of homogeneous measures for a solenoid and obtained the following results:

Theorem 3 (Theorem 3 in [3]) *If μ is an f_∞-homogeneous measure on X then the equalities $h^\mu_{f_\infty}(x) = h^\mu_{f_\infty}(y)$ and $h_{\mu,f_\infty}(x) = h_{\mu,f_\infty}(y)$ hold for any $x, y \in X$.*

Definition 6 If μ is an f_∞-homogeneous measure on X, then the common value of local upper $\mu-$measure entropies is denoted by $h^\mu_{f_\infty}$.

Theorem 4 (Theorem 4 in [3]) *For a solenoid $f_\infty = (f_n : X_n \to X_{n-1})_{n=1}^\infty$ admitting an f_∞-homogeneous measure μ on X, we have*

$$h_{top}(f_\infty) = h^\mu_{f_\infty}.$$

5 Dynamics of Solenoids Via Carathéodory Structures

Dimension theory is a very useful tool in theory of dynamical systems. Bowen [5] pointed out that the topological entropy of a continuous map can be defined in a way similar to the construction of Hausdorff dimension. Twenty five years later, Pesin in [17] discussed the interrelation between dimension theory and the theory of classical dynamical systems, he noticed that the construction of Hausdorff dimension and well-known Carathéodory construction in general measure theory can be generalized. To this aim, Pesin introduced in axiomatic way so called Carathéodory structure, which allows to extend the classical notion of the topological pressure to non-compact or non-invariant sets. Also, a Carathéodory structure generates the Carathéodory dimension, lower and upper capacities of a set. Carathéodory structures applied to dynamical systems are a very powerful tool.

In this section we study entropy of a solenoid from the dimension theory point of view, applying Pesin theory of Carathéodory structures.

5.1 Carathéodory Dimension Structure

Following Pesin [17] we define a Carathéodory structure.

Let Y be a nonempty set. Suppose that a cover $\mathscr{F}$ of a subset of Y and three set functions $\eta, \psi, \xi : \mathscr{F} \to \mathbb{R}_+$ are given. Assume that the following conditions are satisfied:

1. $\emptyset \in \mathscr{F}$ and $\psi(\emptyset) = \eta(\emptyset) = 0$. If $\emptyset \neq U \in \mathscr{F}$ then $\psi(U)\eta(U) > 0$.
2. For every $\delta > 0$ there exists $\varepsilon > 0$ such that $\eta(U) < \delta$ for any $U \in \mathscr{F}$ with $\psi(U) < \varepsilon$.
3. For every $\varepsilon > 0$ there exists a finite or countable subcover $\mathscr{G} \subset \mathscr{F}$ of Y such that $\psi(V) < \varepsilon$, for every $V \in \mathscr{G}$.

A system $\tau = (\mathscr{F}, \xi, \eta, \psi)$ is called a *Carathéodory structure* (or shortly a *C-structure*) on Y. Suppose that the C-structure $\tau = (\mathscr{F}, \xi, \eta, \psi)$ on Y is given. If $\mathscr{G} \subset \mathscr{F}$ is finite or countable subcollection then we write $\mathscr{G} \prec \mathscr{F}$. We put $\psi(\mathscr{G}) = \sup\{\psi(V) : V \in \mathscr{G}\}$.

Let $\alpha \in \mathbb{R}$. Following Pesin, we define an outer measure m_α on Y as follows: Choose a subset $Z \subset Y$, $\varepsilon > 0$ and put

$$M_\alpha(Z, \varepsilon) = \inf\{\sum_{V \in \mathscr{G}} \xi(V)\eta(V)^\alpha : \mathscr{G} \prec \mathscr{F},\ Z \subset \bigcup\nolimits_{V \in \mathscr{G}} V \text{ and } \psi(\mathscr{G}) < \varepsilon\}.$$

One can show that there exists a limit

$$m_\alpha(Z) = \lim_{\varepsilon \to 0^+} M_\alpha(Z, \varepsilon).$$

According to the general measure theory the outer measure m_α induces a $\sigma-$additive measure on Y called the *α-Carathéodory measure*.

It turns out that there exists a critical value $\alpha_C \in [-\infty, \infty]$ such that

$$m_\alpha(Z) = \infty \text{ for } \alpha \leq \alpha_C \text{ and } m_\alpha(Z) = 0 \text{ for } \alpha > \alpha_C.$$

The quantity $\dim_\tau(Z) = \alpha_C$ is called a *C-dimension* of Z with respect to the C-structure τ.

Now suppose that the set function ψ satisfies a stronger condition than 3. Namely, assume that

4. There exists $\varepsilon_0 > 0$ such that for every $\varepsilon_0 > \varepsilon_1 > 0$ there exist $\varepsilon \in (0, \varepsilon_1)$ and a subcover $\mathscr{G} \prec \mathscr{F}$ such that $\psi(V) = \varepsilon$ for every $V \in \mathscr{G}$.

Take $\alpha \in \mathbb{R}$ and $\varepsilon \in (0, \varepsilon_0)$. As before, for any $Z \subset Y$ we define the quantity

$$R_\alpha(Z, \varepsilon) = \inf\{\sum_{V \in \mathscr{G}} \xi(V)\eta(V)^\alpha : \mathscr{G} \prec \mathscr{F},\ Z \subset \bigcup\nolimits_{V \in \mathscr{G}} V \text{ and } \psi(\mathscr{G}) = \varepsilon\}.$$

Due to 4, the quantity $R_\alpha(Z, \varepsilon)$ is well defined. It yields the existence of the limits

$$\underline{r}_\alpha(Z) = \liminf_{\varepsilon \to 0^+} R_\alpha(Z, \varepsilon),$$
$$\overline{r}_\alpha(Z) = \limsup_{\varepsilon \to 0^+} R_\alpha(Z, \varepsilon).$$

As before, there exist $\underline{\alpha}_C, \overline{\alpha}_C \in [-\infty, \infty]$ such that

$$\underline{r}_\alpha(Z) = \infty \text{ for } \alpha \leq \underline{\alpha}_C \text{ and } \underline{r}_\alpha(Z) = 0 \text{ for } \alpha > \underline{\alpha}_C,$$
$$\overline{r}_\alpha(Z) = \infty \text{ for } \alpha \leq \overline{\alpha}_C \text{ and } \overline{r}_\alpha(Z) = 0 \text{ for } \alpha > \overline{\alpha}_C.$$

The quantity $\underline{\alpha}_C$ (resp. $\overline{\alpha}_C$) is called *lower* (resp. *upper*) *C-capacity* of Z with respect to a C-structure τ. We denote lower (resp. upper) C-capacity of Z by $\underline{\mathrm{Cap}}\,(Z)$ (resp. $\overline{\mathrm{Cap}}\,(Z)$), i.e.,

$$\underline{\mathrm{Cap}}\,(Z) = \underline{\alpha}_C \quad \text{and} \quad \overline{\mathrm{Cap}}\,(Z) = \overline{\alpha}_C. \tag{1}$$

Moreover, we assume that the set functions η and ψ are related as follows:

5. If $U, V \in \mathscr{F}$ and $\psi(U) = \psi(V)$ then $\eta(U) = \eta(V)$. In other words, η is constant on each level set $\psi^{-1}(a)$, $a \in \mathbb{R}$, of the set function ψ.

The Carathéodory structure τ is called *Carathéodory-Pesin-structure* (or *CP-structure*), if τ satisfies additionally both conditions 4 and 5.

Let $Z \subset Y$ and $\varepsilon > 0$. Put

$$\Lambda(Z, \varepsilon) = \inf\{\sum_{V \in \mathscr{G}} \xi(V) : \mathscr{G} \prec \mathscr{F},\ Z \subset \bigcup_{V \in \mathscr{G}} V \text{ and } \mathscr{G} \subset \psi^{-1}(\varepsilon)\}.$$

Observe that for every such $\mathscr{G}$ as above $\eta|_{\mathscr{G}}$ is constant. Denote its value by η_ε, i.e., $\eta_\varepsilon = \eta(V)$ if $V \in \psi^{-1}(\varepsilon)$.

Lower and upper capacities determined by CP-structures have the following properties: Let $Z, S \subset Y$ then

$$\underline{\mathrm{Cap}}\,(S \cup Z) = \max\{\underline{\mathrm{Cap}}\,(S), \underline{\mathrm{Cap}}\,(Z)\},$$
$$\overline{\mathrm{Cap}}\,(S \cup Z) = \max\{\overline{\mathrm{Cap}}\,(S), \overline{\mathrm{Cap}}\,(Z)\}.$$

Moreover, lower and upper capacities are related to Λ as follows:

Theorem 5 (Theorem 2.2 in [17]) *If the set function η satisfies Condition A4 then for any subset $Z \subset X$*

$$\underline{\mathrm{Cap}}\,(Z) = \liminf_{\varepsilon \to 0^+} \frac{-\log \Lambda(Z, \varepsilon)}{\log \eta_\varepsilon}, \tag{2}$$

$$\overline{\mathrm{Cap}}\,(Z) = \limsup_{\varepsilon \to 0^+} \frac{-\log \Lambda(Z, \varepsilon)}{\log \eta_\varepsilon}. \tag{3}$$

5.2 *Entropies of a Solenoid Via Carathéodory-Pesin Structures*

The first author and Kozłowski in [2] studied the relation of topological entropy of a solenoid with Carathéodory-Pesin structures. Among others, they noticed that bounding maps of a solenoid determine a Carathéodory-Pesin structure that its upper capacity coincides with the topological entropy of the solenoid. More precisely, they proved the following result for the topological entropy $h_{top}(f_\infty|Z)$ of the solenoid, restricted to a subset $Z \subset X_0$.

Theorem 6 (Theorem 2 in [2]) *For a solenoid $f_\infty = (f_n : X_n \to X_{n-1})_{n=1}^\infty$ described by a sequence of continuous epimorphisms of compact metric spaces X_n there exists a Carathéodory-Pesin structure τ such that*

$$h_{top}(f_\infty|Z) = \overline{\mathrm{CP}_\tau}(Z), \tag{4}$$

where $\overline{\mathrm{CP}_\tau}(Z)$ *is an upper capacity of a subset* $Z \subset X_0$*, with respect to the Carathéodory-Pesin structure* τ*. In particular,*

$$h_{top}(f_\infty) = \overline{\mathrm{CP}_\tau}(X_0). \tag{5}$$

We mimic the definition of measure-theoretic entropy given by Katok for a continuous map $f : X \to X$ with respect to $f-$invariant Borel probability measure.

Definition 7 Given a solenoid $f_\infty = (f_n : X_n \to X_{n-1})_{n=1}^\infty$ described by a sequence of continuous epimorphisms of compact metric spaces X_n, real number $\delta \in (0, 1)$ and Borel probability measure μ on X_0. For $\varepsilon > 0$ let us denote by $N_{f_\infty}(n, \varepsilon, \delta)$ the minimal number of $\varepsilon-$balls in the D_n-metric which cover the set of measure more than or equal to $1 - \delta$. We define measure-theoretic entropy of f_∞ as follows

$$h_\mu^\delta(f_\infty) := \lim_{\varepsilon\to 0} \limsup_{n\to\infty} \frac{1}{n} \log N_{f_\infty}(n, \varepsilon, \delta).$$

Theorem 7 *For a solenoid* $f_\infty = (f_n : X_n \to X_{n-1})_{n=1}^\infty$ *described by a sequence of continuous epimorphisms of compact metric spaces* X_n*, positive number* $\delta \in (0, 1)$ *and Borel probability measure* μ *on* X_0

$$h_\mu^\delta(f_\infty) \le h_{top}(f_\infty). \tag{6}$$

Proof The sequence $f_\infty = (f_n : X_n \to X_{n-1})_{n=1}^\infty$ of continuous epimorphisms of compact metric spaces (X_n, d_n) determines a sequence of D_n-metrics and the family $\mathscr{B}_n(\varepsilon) = \{B_n(z, \varepsilon) : z \in X_0\}$ of $\varepsilon-$balls in D_n-metric. We construct a Pesin-Caratheodory structure as follows. The family $\mathscr{B}_n(r) = \{B_n(z, r) : z \in X_0\}$ is an open cover of X_0. Fix $\gamma > 0$ and let $\mathscr{F}_\gamma = \{\emptyset, \bigcup_{n=0}^\infty \mathscr{B}_n(\gamma)\}$.

Consider set functions $\xi, \eta, \psi : \mathscr{F}_\gamma \to \mathbb{R}$ given by: $\xi(V) = 1$, $\eta(V) = \exp(-n)$ and $\psi(V) = n^{-1}$, for $V = B_n(z, \gamma)$ and $n \ge 1$ and $\xi(V) = \psi(V) = \eta(V) = 1$ if $V = B_0(z, \gamma)$. It is clear that $\tau_\gamma = (\mathscr{F}_\gamma, \xi, \eta, \psi)$ is a Carathéodory-Pesin structure determined by f_∞. To emphasize that all objects depend on γ we will sometimes write Λ_γ, $\overline{\mathrm{Cap}}_\gamma$ etc. instead of Λ, $\overline{\mathrm{Cap}}$.

For any $\alpha \in \mathbb{R}$ we define

$$R_{\alpha,1}(\gamma, m) := \inf\{\sum_{V\in\mathscr{G}} \exp(-m\alpha) : \mathscr{G} \prec \mathscr{B}_m(\gamma), \text{ and } X_0 \subset \bigcup\nolimits_{V\in\mathscr{G}} V\},$$

$$R_{\alpha,2}(\gamma, m) := \inf\{\sum_{V\in\mathscr{G}} \exp(-m\alpha) : \mathscr{G} \prec \mathscr{B}_m(\gamma), \text{ and } \mu(\bigcup\nolimits_{V\in\mathscr{G}} V) > 1 - \delta\}.$$

It is clear that

$$R_{\alpha,2}(\gamma, m) \le R_{\alpha,1}(\gamma, m). \tag{7}$$

Taking limit superior, for $i = 1, 2$ we denote

$$\overline{r_\alpha}(i, \gamma) := \limsup_{m\to\infty} R_{\alpha,i}(\gamma, m). \tag{8}$$

Due to (3), for $Z = X_0$ we obtain

$$\overline{\mathrm{Cap}_\gamma}(i) = \limsup_{n\to\infty} n^{-1} \log \Lambda_\gamma(i, X_0, n^{-1}) = \limsup_{n\to\infty} n^{-1} \log \Lambda_\gamma(i, n^{-1}),$$

where $i = 1, 2$. Following arguments of Pesin [17] we get the existence of limit capacities

$$\overline{\mathrm{CP}}(i) = \lim_{\gamma\to 0^+} \overline{\mathrm{Cap}}_\gamma(i).$$

Consequently,

$$\overline{\mathrm{CP}}(i) = \lim_{\gamma\to 0^+} \limsup_{n\to\infty} \frac{1}{n} \log \Lambda_\gamma(i, \frac{1}{n}).$$

Observe that the definition of Λ yields that:

1. $\Lambda_\gamma(1, n^{-1})$ is equal to $r(n, \gamma)$, the minimal cardinality of (n, γ)-spanned subset of X_0, i.e. minimal number of $\gamma-$balls in D_n-metric which cover X_0. Thus

$$\overline{\mathrm{CP}}(1) = h_{top}(f_\infty) = \lim_{\gamma\to 0^+} \limsup_{n\to\infty} \frac{1}{n} \log r(n, \gamma).$$

2. $\Lambda_\gamma(2, n^{-1})$ is equal to $N_{f_\infty}(n, \gamma, \delta)$, minimal number of $\gamma-$balls in D_n-metric which cover the set of measure more than or equal to $1 - \delta$. Thus

$$\overline{\mathrm{CP}}(2) = h^\delta_\mu(f_\infty) = \lim_{\gamma\to 0^+} \limsup_{n\to\infty} \frac{1}{n} \log N_{f_\infty}(n, \gamma, \delta).$$

The inequality (7) yields that

$$h^\delta_\mu(f_\infty) = \quad \overline{\mathrm{CP}}(2) \leq \quad \overline{\mathrm{CP}}(1) = h_{top}(f_\infty).$$

Acknowledgements The first author was supported by the National Science Centre (NCN) under grant Maestro 2013/08/A/ST1/00275.

References

1. Adler, R., Konheim, A., McAndrew, M.: Topological entropy. Trans. Amer. Math. Soc. **114**, 309–319 (1965)
2. Biś, A., Kozłowski, W.: Some remarks on dynamical systems of solenoids. Taiwanese J. Math
3. Biś, A., Namiecińska, A.: Topological entropy and homogeneous measure for a solenoid, to appear in Bulletin de la Sociéte des Sciences et des Lettres de Łódź **47**, 21–32 (2017)

4. Bowen, R.: Entropy for group endomorphisms and homogeneous spaces. Trans. Amer. Math. Soc. **153**, 401–414 (1971)
5. Bowen, R.: Topological entropy for noncompact sets. Trans. Amer. Math. Soc. **184**, 125–136 (1973)
6. Brin, M., Katok, A.: On, local entropy. In: Geometric Dynamics, Lecture Notes in Math., vol. 1007, pp. 30–38. Springer, Berlin (1983)
7. Brin, M., Stuck, G.: Introduction to Dynamical Systems. Cambrigde Univ. Press, Cambridge (2002)
8. Buzii, J.: Intrinsic ergodicity for smooth interval maps. Israel J. Math. **100**, 125–161 (1997)
9. Dinaburg, E.: On the relations among various entropy characteristics of dynamical systems, Izv. Akad. Nauk SSSR 35, 324–366, (1971), (Math. USSR Izvestija 5 (1971), 337–378)
10. Downarowicz, T.: Entropy in Dynamical Systems. Cambridge Univ, Press (2011)
11. Goodman, T.: Relating topological entropy to measure entropy. Bull. London Math. Soc. **3**, 176–180 (1971)
12. Goodwyn, L.: The product theorem for topological entropy. Trans. Amer. Math. Soc. **158**, 445–452 (1971)
13. Ingram, W., Mahavier, W.: Inverse Limits: From Continua to Chaos. Springer Science+Business Media, LLC (2012)
14. Katok, A.: Lyapunov exponents, entropy and periodic orbits for diffeomorphisms, Publications mathematiques de l'I.H.E.S, **51**, 137–173 (1980)
15. Katok, A.: Fifty years of entropy in dynamics: 1968–2007. J. Mod. Dynam. **1**(4), 545–596 (2007)
16. McCord, C.: Inverse limit sequences with covering maps. Trans. Amer. Math. Soc. **209**, 114–197 (1965)
17. Pesin, Y.: Dimension Theory in Dynamical Systems: Contemporary Views and Applications. The University of Chicago Press (1997)
18. Smale, S.: Differentiable dynamical systems. Bull. of the AMS **73**, 747–817 (1967)
19. Vietoris, L.: Über den höheren Zusammenhang kompakter Räume und eine Klasse von zusammenhangstreuen Abbildungen. Math. Ann. **97**, 454–472 (1927)
20. Walczak, P.: Dynamics of Foliations, Groups and Pseudogroups, Birkh*ä*user (2004)
21. Walters, P.: An Introduction to Ergodic Theory. Springer-Verlag (1982)
22. Williams, R.: Expanding attractors. Publ. Math. IHES **43**, 169–203 (1974)

Lyapunov Functions for Almost Sure Exponential Stability

Hjortur Björnsson and Sigurdur Freyr Hafstein

Abstract We present a generalization of results obtained by X. Mao in his book "Stochastic Differential Equations and Applications" (2008). When studying what Mao calls "almost sure exponential stability", essentially a negative upper bound on the almost sure Lyapunov exponents, he works with Lyapunov functions that are twice continuously differentiable in the spatial variable and continuously differentiable in time. Mao gives sufficient conditions in terms of such a Lyapunov function for a solution of a stochastic differential equation to be almost surely exponentially stable. Further, he gives sufficient conditions of a similar kind for the solution to be almost surely exponentially unstable. Unfortunately, this class of Lyapunov functions is too restrictive. Indeed, R. Khasminskii showed in his book "Stochastic Stability of Differential Equations" (1979/2012) that even for an autonomous stochastic differential equation with constant coefficients, of which the solution is stochastically stable and such that the deterministic part has an unstable equilibrium, there cannot exists a Lyapunov function that is differentiable at the origin. These restrictions are inherited by Mao's Lyapunov functions. We therefore consider Lyapunov functions that are not necessarily differentiable at the origin and we show that the sufficiency conditions Mao proves can be generalized to Lyapunov functions of this form.

Keywords Almost sure exponential stability · Lyapunov function · Almost sure Lyapunov exponent

1 Introduction

Lyapunov methods, as first described in [1], have been widely used to study the behaviour of various dynamical systems, both real-world examples or purely theo-

H. Björnsson (✉) · S. F. Hafstein
University of Iceland, The Science Institute, Dunhagi 5, 107 Reykjavík, Iceland
e-mail: hjb6@hi.is

S. F. Hafstein
e-mail: shafstein@hi.is

J. Awrejcewicz (ed.), *Dynamical Systems in Theoretical Perspective*,
Springer Proceedings in Mathematics & Statistics 248,
https://doi.org/10.1007/978-3-319-96598-7_5

retical ones. This is a very active field due to the complicated dynamics exhibited in several real-world systems, as for example the wobblestone model presented in [2]. Other specific examples include the dynamics of the double [3] or triple pendulum [4, 5], where Lyapunov exponents were used to study the chaotic behavior of the systems. Often it is necessary to modify a dynamical system to include either an unknown force, or to consider the perturbation of the system by some noise, and that is where stochastic differential equations (SDEs) are commonly used. Here in this paper, we are concerned with applying Lyapunov methods for classical dynamical systems to the stochastic framework, as done by Khasminskii [8].

We work in a complete probability space $(\Omega, \mathscr{F}, \mathbf{P})$ with a right continuous filtration $\{\mathscr{F}_t\}_{t\geq 0}$ and such that $\mathscr{F}_0$ contains all $\mathbf{P}$ null sets. In this paper we consider strong solutions of the d-dimensional stochastic differential equation

$$\mathrm{d}x(t) = f(x(t), t)\mathrm{d}t + g(x(t), t)\mathrm{d}B(t) \quad \text{on } t \geq t_0 \tag{1}$$

where $B(t)$ is an m-dimensional Brownian motion. For a more detailed description of the setting cf. [9, Sec. 2.1]. We assume that for any given initial value $x(t_0) = x_0 \in \mathbf{R}^d$ there exists a unique global solution, denoted by $t \mapsto x(t, t_0, x_0)$, with continuous sample paths. Furthermore, we assume that

$$f(0, t) = 0 \quad \text{and} \quad g(0, t) = 0 \quad \text{for all } t \geq t_0.$$

Sufficient condition for the existence of such solutions are, for example, given by the following statement, cf. [9, Thm. 2.3.6].

For any real number $T > 0$ and integer $n \geq 1$, the following hold true:

1. There exists a positive constant $K_{T,n}$, such that for all $t \in [t_0, T]$ and all $x, y \in \mathbf{R}^d$ with $|x| \vee |y| \leq n$,

$$|f(x, t) - f(y, t)|^2 \bigvee |g(x, t) - g(y, t)|^2 \leq K_{T,n}|x - y|^2.$$

2. There exists a positive constant K_T, such that for all $(x, t) \in \mathbf{R}^d \times [t_0, T]$

$$x^\top f(x, t) + \frac{1}{2}|g(x, t)|^2 \leq K_T(1 + |x|^2).$$

Here $|\cdot|$ is the Euclidean norm and the symbols $\wedge$ and $\vee$ are defined to be the minimum and the maximum respectively:

$$a \wedge b := \min(a, b) \quad \text{and} \quad a \vee b := \max(a, b).$$

Corresponding to the initial value $x(t_0) = 0$, we have the solution $x(t) = 0$ for all t. This solution is called the trivial solution. In this paper we are studying the stability of the trivial solution and, more specifically, when it is almost surely exponentially stable. This definition is taken from Mao's book [9, Def. 4.3.1], see also e.g. [6, 11].

Definition 1 The trivial solution of (1) is said to be *almost surely exponentially stable* if

$$\limsup_{t\to\infty} \frac{1}{t} \log |x(t, t_0, x_0)| < 0$$

almost surely, for all $x_0 \in \mathbf{R}^d$.

First, we clarify some of the notation used in the paper. For our purposes all integrals in this paper of the form $\int \cdot \, \mathrm{d}B(s)$ are to be interpreted in the Itô sense. We write $b_n \uparrow a$ if the sequence b_n is increasing and has limit a. We denote by $\mathscr{L}^2(\mathbf{R}_+, \mathbf{R}^{d\times m})$ the family of all $(d \times m)$-matrix valued measurable $\{\mathscr{F}_t\}_{t\geq 0}$-adapted processes $f = \{f(t)\}_{t\geq 0}$ such that

$$\int_0^T |f(t)|^2 \mathrm{d}t < \infty \quad \text{a.s. for every } T > 0$$

and by $\mathscr{M}^2(\mathbf{R}_+, \mathbf{R}^{d\times m})$ the family of all processes $f \in \mathscr{L}^2(\mathbf{R}_+, \mathbf{R}^{d\times m})$ such that

$$\mathbf{E}\left\{\int_0^T |f(t)|^2 \mathrm{d}t\right\} < \infty \quad \text{for every } T > 0.$$

Here $\mathbf{E}$ denotes the expectation and a.s. is an abbreviation for *almost surely* as usual. Let $f \in \mathscr{M}^2(\mathbf{R}_+, \mathbf{R}^{d\times m})$ and consider the process

$$M_t = \int_0^t f(s)\mathrm{d}B(s)$$

then there exists a t-continuous version of the process M_t. Furthermore the process is $\{\mathscr{F}_t\}$ adapted and is a square integrable martingale [10, Thm. 3.2.5]. By the preceding remark, we will assume that $\int_0^t f(s)\mathrm{d}B(s)$ refers to a t-continuous version of the integral.

A sequence of stopping times $\{\tau_k\}_{k\geq 1}$ is called a *localization* if it is non-decreasing and $\tau_k \uparrow \infty$ almost surely. A right continuous adapted process $M = \{M_t\}_{t\geq 0}$ is called a *local martingale* if there exists a localization $\{\tau_k\}_{k\geq 1}$ such that the process $\{M_{\tau_k \wedge t} - M_0\}_{t\geq 0}$ is a martingale for every $k \geq 1$. We denote the quadratic variation of a continuous local martingale M by $\langle M, M\rangle_t$, which is the unique continuous adapted process of finite variation, such that $\{M_t^2 - \langle M, M\rangle_t\}_{t\geq 0}$ is a continuous local martingale which takes the value 0 at $t = 0$.

Let M_t be a continuous martingale of the form

$$M_t = \int_0^t f(s)\mathrm{d}B(s).$$

Then the quadratic variation $\langle M, M \rangle_t$ is given by

$$\langle M, M \rangle_t = \int_0^t |f(s)|^2 \mathrm{d}s$$

almost surely [9, Thm. 1.5.14].

Let τ be a stopping time and let $[[0, \tau]]$ be the stochastic interval

$$[[0, \tau]] = \{(t, \omega) \in \mathbf{R}_+ \times \Omega : 0 \leq t \leq \tau(\omega)\}.$$

We now list a few facts needed to give rigid proofs of our results. For any $f \in \mathscr{L}^2(\mathbf{R}_+, \mathbf{R}^{d\times m})$ we can define a sequence of stopping times

$$\tau_n := n \wedge \inf\{t \geq 0 : \int_0^t |f(s)|^2 \mathrm{d}s \geq n\}.$$

It is easy to see that $\tau_n \uparrow \infty$ almost surely. Let I_A, for $A \subset \mathbf{R}_+ \times \Omega$, be the indicator function, that is $I_A(x) = 1$ if $x \in A$ and zero otherwise. Then we can define the process $g_n(t) = f(t) I_{[[0,\tau_n]]}(t)$. We see that $g_n \in \mathscr{M}^2(\mathbf{R}_+, \mathbf{R}^{d\times m})$ so the integral

$$J_n(t) = \int_0^t g_n(s) \mathrm{d}B(s)$$

is a martingale. That is to say, the process

$$J(t) := \int_0^t f(s) \mathrm{d}B(s)$$

is a local martingale with localization $\{\tau_n\}$, since for any $n \geq 1$

$$J(t \wedge \tau_n) = \int_0^{t\wedge\tau_n} f(s) \mathrm{d}B(s) = \int_0^t f(s) I_{[[0,\tau_n]]}(s) \mathrm{d}B(s) = \int_0^t g_n(s) \mathrm{d}B(s) = J_n(t)$$

is a martingale.

In his book [9], Mao considers Lyapunov functions $V(x, t) \in C^{2,1}(\mathbf{R}^d \times [t_0, \infty[; \mathbf{R}_+)$ where $C^{2,1}(\mathbf{R}^d \times [t_0, \infty[; \mathbf{R}_+)$ is the set of all continuous functions $\mathbf{R}^d \times [t_0, \infty[\to \mathbf{R}_+$, which are continuously differentiable twice in the first coordinate x, with $x \in \mathbf{R}^d$, and once in t with $t \in [t_0, \infty[$. Now define a differential operator L associated with (1) by

$$L = \frac{\partial}{\partial t} + \sum_{i=1}^d f_i(x, t) \frac{\partial}{\partial x_i} + \frac{1}{2} \sum_{i,j=1}^d [g(x, t) g^\top(x, t)]_{ij} \frac{\partial^2}{\partial x_i \partial x_j}, \tag{2}$$

where $[g(x,t)g^\top(x,t)]_{ij}$ is the (i,j)-th component of the $(d \times d)$-matrix $gg^\top$ at (x,t). If $x(t)$ is a solution of (1) then by Itô's formula

$$dV(x(t),t) = LV(x(t),t)\mathrm{d}t + V_x(x(t),t)\mathrm{d}B(t)$$

where $V_x \in \mathbf{R}^{1\times d}$ is the derivative (gradient) of V with respect to x.

Khasminskii showed in his book [8, p. 154–155] that even for SDEs with constant coefficients there cannot exist Lyapunov functions that are differentiable at 0 unless the deterministic part of the SDE is already stable. Therefore we extend the results from Mao's book using the larger class of functions $C_0^{2,1}(\mathbf{R}^d \times [t_0,\infty[\,;\mathbf{R}_+)$ which are continuous, continuously differentiable in t, and twice continuously differentiable in x except at the point $x = 0$.

Below is a theorem taken from Mao's book [9] which we will use in the next chapter. For completeness we give a more worked out proof than in the book.

Theorem 1 [9, Thm. 1.7.4]
Let $g = (g_1,\ldots,g_m) \in \mathscr{L}^2(\mathbf{R}_+, \mathbf{R}^{d\times m})$, and T, α, β be any numbers ≥ 0. Then

$$\mathbf{P}\left\{\sup_{0\leq t\leq T}\left[\int_0^t g(s)\mathrm{d}B(s) - \frac{\alpha}{2}\int_0^t |g(s)|^2\mathrm{d}s\right] > \beta\right\} \leq \mathrm{e}^{-\alpha\beta}. \tag{3}$$

Proof Define the process

$$x(t) = \alpha\int_0^t g(s)\mathrm{d}B(s) - \frac{\alpha^2}{2}\int_0^t |g(s)|^2\mathrm{d}s$$

and for every integer $n \geq 1$, define the stopping time

$$\tau_n = \inf\left\{t \geq 0 : \left|\int_0^t g(s)\mathrm{d}B(s)\right| + \int_0^t |g(s)|^2\mathrm{d}s \geq n\right\}.$$

Then τ_n is a localization, and since

$$\begin{aligned}|x_n(t)| &\leq \alpha\left|\int_0^t g(s)I_{[[0,\tau_n]]}(s)\mathrm{d}B(s)\right| + \frac{\alpha^2}{2}\int_0^t |g(s)|^2 I_{[[0,\tau_n]]}\mathrm{d}s\\ &\leq \alpha n + \frac{\alpha^2}{2}n = n\frac{2\alpha+\alpha^2}{2}\end{aligned}$$

we see that the process $x_n(t) := x(t\wedge\tau_n)$ is bounded.

Apply Itô's formula to $\exp(x_n(t))$ and we obtain

$$\begin{aligned}\exp(x_n(t)) &= 1 + \int_0^t \exp(x_n(s))\mathrm{d}x_n(s) + \frac{\alpha^2}{2}\int_0^t \exp(x_n(s))|g(s)|^2 I_{[[0,\tau_n]]}(s)\mathrm{d}s \\ &= 1 + \left(\alpha\int_0^t \exp(x_n(s))g(s)I_{[[0,\tau_n]]}(s)\mathrm{d}B(s)\right. \\ &\qquad \left. -\frac{\alpha^2}{2}\int_0^t \exp(x_n(s))|g(s)|^2 I_{[[0,\tau_n]]}(s)\mathrm{d}s\right) \\ &\quad + \frac{\alpha^2}{2}\int_0^t \exp(x_n(s))|g(s)|^2 I_{[[0,\tau_n]]}(s)\mathrm{d}s \\ &= 1 + \alpha\int_0^t \exp(x_n(s))g(s)I_{[[0,\tau_n]]}(s)\mathrm{d}B(s).\end{aligned}$$

The term inside the integral is bounded by $n^2\frac{2\alpha+\alpha^2}{2}$ almost surely, therefore the process $\exp(x_n)$ is a non negative martingale with $\mathbf{E}\{\exp(x_n(T))\} = 1$, for all $n \geq 1$. This construction is known as the Doléans-Dade exponential of the local martingale $Y_t := \int_0^t g(s)\mathrm{d}B(s)$, see [8, Thm. 26.8].
By Doob's martingale inequality [9, Thm. 1.3.8] we get that

$$\mathbf{P}\left\{\sup_{0\leq t\leq T}\exp[x_n(t)] \geq \mathrm{e}^{\alpha\beta}\right\} \leq \mathrm{e}^{-\alpha\beta}\mathbf{E}\{\exp(x_n(T))\} = \mathrm{e}^{-\alpha\beta}.$$

Then it follows that

$$\mathbf{P}\left\{\sup_{0\leq t\leq T}\frac{x_n(t)}{\alpha} > \beta\right\} \leq \mathrm{e}^{-\alpha\beta}.$$

Since this inequality holds for any $n \geq 1$, and

$$\lim_{n\to\infty} x_n(t) = x(t)$$

almost surely, we get by the dominated convergence theorem that

$$\mathbf{P}\left\{\sup_{0\leq t\leq T}\frac{x(t)}{\alpha} > \beta\right\} \leq \mathrm{e}^{-\alpha\beta}$$

and the proof is complete. □

2 The Theorems and Their Proofs

As discussed above, we state two theorems from Mao's book [9], more specifically Theorem 4.3.3 and Theorem 4.3.5, except we allow the Lyapunov functions V to be in the $C_0^{2,1}$ space instead of the too restrictive space $C^{2,1}$, like Mao does. The difference

is that in the former space the functions are not required to be differentiable at the origin, while functions in the latter one are smooth everywhere. As already explained before, this makes the results much more relevant and useful.
First we state and proof Theorem 4.3.3 from [9] with the weaker conditions. Note that, like above, $V_x \in \mathbf{R}^{1\times d}$ is the derivative (gradient) of V with respect to x.

Theorem 2 (advancement of Thm. 4.3.3 in Mao)
Assume there exists a function $V \in C_0^{2,1}(\mathbf{R}^d \times [t_0, \infty); \mathbf{R}_+)$ *and constants* $p > 0$, $c_1 > 0$, $c_2 \in \mathbf{R}$, $c_3 \geq 0$, *such that for all* $x \neq 0$ *and* $t \geq t_0$*:*

1. $c_1|x|^p \leq V(x,t)$,
2. $LV(x,t) \leq c_2 V(x,t)$,
3. $|V_x(x,t)g(x,t)|^2 \geq c_3 V^2(x,t)$.

Then

$$\limsup_{t\to\infty} \frac{1}{t} \log|x(t;t_0,x_0)| \leq -\frac{c_3 - 2c_2}{2p} \quad a.s.$$

for all $x_0 \in \mathbf{R}^d$. *In particular, if* $c_3 > 2c_2$, *the trivial solution of Eq.* (1) *is almost surely exponentially stable, see Definition 1.*

The proof here mostly follows Mao's original argument, but with some modifications, since the process $M(t)$ below isn't necessarily a martingale.

Proof Clearly the inequality holds for $x_0 = 0$ since $x(t, t_0, 0) = 0$ for all t. We only need to show the inequality for all $x_0 \neq 0$. Fix any $x_0 \neq 0$ and write $x(t) := x(t; t_0, x_0)$. It is well known that 0 is an inaccessible point, cf. e.g. [9, Lemma 4.3.2], that is to say, $x(t) \neq 0$ for all $t \geq t_0$ almost surely. Thus one can apply Itô's formula and get

$$\begin{aligned}
&\log V(x(t),t) \\
&= \log V(x_0,t_0) + \int_{t_0}^t \frac{LV(x(s),s)}{V(x(s),s)}\mathrm{d}s + M(t) - \frac{1}{2}\int_{t_0}^t \frac{|V_x(x(s),s)g(x(s),s)|^2}{(V(x(s),s))^2}\mathrm{d}s \\
&\leq \log V(x_0,t_0) + c_2(t-t_0) + M(t) - \frac{1}{2}\int_{t_0}^t \frac{|V_x(x(s),s)g(x(s),s)|^2}{(V(x(s),s))^2}\mathrm{d}s
\end{aligned}$$

where we used condition 2 for the last inequality and

$$M(t) := \int_{t_0}^t \frac{V_x(x(s),s)g(x(s),s)}{V(x(s),s)}\mathrm{d}B(s).$$

We claim the process

$$h(s) := \frac{V_x(x(s),s)g(x(s),s)}{V(x(s),s)}$$

is in $\mathscr{L}^2([t_0,\infty[, \mathbf{R}^d)$. Indeed, for almost all $\omega \in \Omega$, the trajectory of $x(t)(\omega)$, $t_0 \leq t \leq T$, is a compact subset of $\mathbf{R}^d \setminus \{0\}$. Hence, for almost all ω, the function $h(s)(\omega)$

is continuous on the compact set $t_0 \leq s \leq T$ and thus bounded. Since this holds true for all T, we have $h(s) \in \mathscr{L}^2([t_0, \infty[, \mathbf{R}^d)$.

Fix an arbitrary $\varepsilon > 0$. We can now use Theorem 1 and get for all $n \in \mathbf{N}$:

$$\mathbf{P}\left\{\sup_{t_0 \leq t \leq t_0+n}\left[M(t) - \frac{\varepsilon}{2}\int_{t_0}^{t}\frac{|V_x(x(s),s)g(x(s),s)|^2}{(V(x(s),s))^2}\mathrm{d}s\right] > \frac{2}{\varepsilon}\log(n)\right\} \leq \frac{1}{n^2}$$

By the Borel Cantelli theorem, cf. e.g. [7, Thm. 3.18], there exists an $n_0(\omega) > 0$ for almost all ω, such that

$$M(t) \leq \frac{2}{\varepsilon}\log(n) + \frac{\varepsilon}{2}\int_{t_0}^{t}\frac{|V_x(x(s),s)g(x(s),s)|^2}{(V(x(s),s))^2}\mathrm{d}s.$$

for all $t_0 \leq t \leq t_0 + n$ if $n > n_0$. By condition 3,

$$\begin{aligned}
&\log V(x(t),t)\\
&\leq \log V(x_0,t_0) + c_2(t-t_0) + \frac{1}{2}(\varepsilon-1)\int_{t_0}^{t}\frac{|V_x(x(s),s)g(x(s),s)|^2}{(V(x(s),s))^2}\mathrm{d}s + \frac{2}{\varepsilon}\log(n)\\
&\leq \log V(x_0,t_0) + c_2(t-t_0) - \frac{1}{2}(1-\varepsilon)c_3(t-t_0) + \frac{2}{\varepsilon}\log(n)\\
&= \log V(x_0,t_0) - \frac{1}{2}((1-\varepsilon)c_3 - 2c_2)(t-t_0) + \frac{2}{\varepsilon}\log(n)
\end{aligned}$$

for all $t_0 \leq t \leq t_0 + n$ if $n > n_0$ for almost all ω. Therefore we have for almost all ω, that

$$\frac{1}{t}\log V(x(t),t) \leq -\frac{t-t_0}{2t}[(1-\varepsilon)c_3 - 2c_2] + \frac{\log V(x_0,t_0) + 2\log(n)/\varepsilon}{t_0+n-1}$$

if $t_0 + n - 1 \leq t \leq t_0 + n$ and $n > n_0$.

Fix ω and let $n \to \infty$, then

$$\limsup_{t\to\infty}\frac{1}{t}\log V(x(t),t) \leq -\frac{1}{2}((1-\varepsilon)c_3 - 2c_2)$$

holds point-wise for almost all ω. Finally using condition 1 we have

$$\limsup_{t\to\infty}\frac{1}{t}\log|x(t)| \leq -\frac{(1-\varepsilon)c_3 - 2c_2}{2p}$$

for almost all ω. Since $\varepsilon > 0$ was arbitrary we have the conclusion. □

Now we state and proof Theorem 4.3.5 from [9] with the weaker conditions.

Theorem 3 (advancement of Thm. 4.3.5 in Mao)
Assume that there exists a function $V \in C_0^{2,1}(\mathbf{R}^d \times [t_0, \infty); \mathbf{R}_+)$, *and constants* $p > 0$, $c_1 > 0$, $c_2 \in \mathbf{R}$, $c_3 > 0$, *such that for all* $x \neq 0$ *and* $t \geq t_0$,

1. $c_1|x^p| \geq V(x,t) > 0$,
2. $LV(x,t) \geq c_2 V(x,t)$,
3. $|V_x(x,t)g(x,t)|^2 \leq c_3 V^2(x,t)$.

Then

$$\liminf_{t\to\infty} \frac{1}{t} \log|x(t;t_0,x_0)| \geq \frac{2c_2 - c_3}{2p} \quad a.s.$$

for all $x_0 \neq 0$ *in* $\mathbf{R}^d$.

The proof again follows the same method Mao used in his book, but here it works without modifications for our weaker assumptions on the function V. For completeness we, however, give a more worked out proof than given in [9].

Proof Just like in the proof of Theorem 2 we fix some $x_0 \neq 0$ and we write $x(t) = x(t;t_0,x_0)$. Furthermore we define $M(t)$ and $h(s)$ as in the proof of Theorem 2, and by Itô's formula we have that

$$\begin{aligned} &\log V(x(t),t) \\ &= \log V(x_0,t_0) + \int_{t_0}^t \frac{LV(x(s),s)}{V(x(s),s)}\mathrm{d}s + M(t) - \frac{1}{2}\int_{t_0}^t \frac{|V_x(x(s),s)g(x(s),s)|^2}{(V(x(s),s))^2}\mathrm{d}s. \end{aligned} \tag{4}$$

By condition 3, we have that $|h(s)|^2 < c_3$, so $h \in \mathscr{M}^2(\mathbf{R}_+, \mathbf{R}^{1\times m})$ and $M(t) = \int_{t_0}^t h(s)\mathrm{d}B(s)$ is a martingale. By Eq. (4) and condition 2

$$\begin{aligned} \log V(x(t),t) &\geq \log V(x_0,t_0) + c_2(t-t_0) - \frac{c_3}{2}(t-t_0) + M(t) \\ &= \log V(x_0,t_0) + \frac{1}{2}(2c_2 - c_3)(t-t_0) + M(t). \end{aligned} \tag{5}$$

Since $M(t)$ is a martingale with quadratic variation

$$\langle M(t), M(t)\rangle = \int_{t_0}^t |h(s)|^2 \mathrm{d}s \leq c_3(t-t_0),$$

we have by the strong law of large numbers, cf. e.g. [9, Thm 1.3.4], that $\lim_{t\to\infty} M(t)/t = 0$ a.s. It therefore follows from (5) that

$$\liminf_{t\to\infty} \frac{1}{t} \log V(x(t),t) \geq \frac{1}{2}(2c_2 - c_3) \quad \text{a.s.}$$

Finally by condition 1 then

$$\liminf_{t\to\infty} \frac{1}{t} \log |x(t; t_0, x_0)| \geq \frac{2c_2 - c_3}{2p}.$$

□

Remark If in the last theorem we have $2c_2 > c_3$, then almost all the sample paths of $t \mapsto |x(t; t_0, x_0)|$ will tend to infinity, and in this case the trivial solution of Eq. (1) is said to be *almost surely exponentially unstable*.

Example Consider the 1-dimensional SDE

$$dX(t) = f(X(t), t)dt + g(X(t), t)dB(t) := \frac{1}{4}X(t)dt + X(t)dB(t) \tag{6}$$

Set $V(x, t) = |x|^{1/2}$, then $V \in C_0^{2,1}$ and, by Eq. (2), the function $LV(x)$ is given by

$$LV(x) = \frac{1}{4}x \cdot (1/2)|x|^{-1/2} + \frac{1}{2}x^2 \cdot (-1/2)(1/2)|x|^{-3/2} = \frac{1}{8}|x|^{1/2} - \frac{1}{8}|x|^{1/2} = 0.$$

Furthermore we see that

$$|V_x(x)g(x, t)|^2 = |(1/2)|x|^{-1/2}x|^2 = \frac{1}{4}(|x|^{1/2})^2 = \frac{1}{4}V(x)^2.$$

Fixing constants $c_1 = 1$, $p = 1/2$, $c_2 = 0$ and $0 < c_3 < 1/4$, we see by Theorem 2 that for any solution $x(t)$ of Eq. (6) the following inequality holds

$$\limsup_{t\to\infty} \frac{1}{t} \log |x(t)| \leq -\frac{c_3 - 2c_2}{2p} = -c_3 < 0 \quad \text{a.s.}$$

In particular the trivial solution of system (6) is almost surely exponentially stable (in fact the solution is stable in probability, see [8, Thm. 5.3]), and the function V we used is not differentiable at 0. Moreover, as shown by Khasminskii [8, p. 154–155], there cannot exists a Lyapunov function for this system that is differentiable at the origin.

3 Conclusions

In his book [9] X. Mao states and proves two theorems, Theorem 4.3.3 and Theorem 4.3.5, where he shows that the existence of a certain auxiliary function, so-called Lyapunov function, implies the *almost sure exponential stability* or, for a different kind of function, the *almost sure exponential instability* respectively of the zero solution of a SDE. Unfortunately, the class of functions $C^{2,1}(\mathbf{R}^d \times [t_0, \infty); \mathbf{R}_+)$

he considers to serve as the foundation for Lyapunov functions is too restrictive as had already been pointed out in the literature [8, p. 154–155]. The adequate class of functions is given by $C_0^{2,1}(\mathbf{R}^d \times [t_0, \infty); \mathbf{R}_+)$ and we formulate and prove Mao's theorems for this wider class of functions. This renders these theorems much more useful for applications.

Acknowledgements This research was supported by the Icelandic Research Fund (Rannís) grant number 152429-051, Lyapunov Methods and Stochastic Stability.

References

1. Lyapunov, A.M.: The general problem of the stability of motion. Int. J. Control **55**(3), 531–534 (1992)
2. Awrejcewicz, J., Kudra, G.: Mathematical modelling and simulation of the bifurcational wobblestone dynamics. Discontinuity, Nonlinearity, and Complexity **3**(2), 123–132 (2014)
3. Awrejcewicza, J., Wasilewskia, G., Kudra, G., Reshmin, S.: An experiment with swinging up a double pendulum using feedback control. J. Comput. Syst. Sci. Int. **51**(2), 176–182 (2012)
4. Awrejcewicz, J., Kudra, G., Wasilewski, G.: Experimental and numerical investigation of chaotic regions in the triple physical pendulum. Nonlinear Dyn. **50**, 755–766 (2007)
5. Awrejcewicz, J., Kudra, G., Wasilewski, G.: Chaotic zones in triple pendulum dynamics observed experimentally and numerically. Appl. Mech. Mater. **9**, 1–17 (2008)
6. Higham, D.J., Mao, X., Yuan, C.: Almost sure and moment exponential stability in the numerical simulation of stochastic differential equations. SIAM. J. Numer. Anal. **45**(2), 592–609 (2007)
7. Kallenberg, O.: Foundations of Modern Probability. Springer Science & Business Media, (2006)
8. Khasminskii, R.: Stochastic stability of differential equations, vol. 66. Springer Science & Business Media (2007)
9. Mao, X.: Stochastic Differential Equations and Applications. Elsevier (2007)
10. Oksendal, B.: Stochastic Differential Equations. Springer (2003)
11. Wu, F., Mao, X., Szpruch, L.: Almost sure exponential stability of numerical solutions for stochastic delay differential equations. Numer. Math. (Heidelb) **115**(4), 681–697 (2010)

Numerical Analysis of Dynamic Stability of an Isotropic Plate by Applying Tools Used in Dynamics

Lukasz Borkowski

Abstract The aim of the study is to analyze an isotropic plate in terms of its dynamic stability (or its instability), by applying tools that are mainly used in the vibrations theory of dynamical systems e.g. in the theory of bifurcation and chaos. The results achieved by using tools such as phase portraits, Poincaré maps, FFT analysis, the largest Lyapunov exponents were compared with the results obtained by using the Volmir criterion.

Keywords Dynamic stability · Dynamic response · Phase portraits · Poincaré maps · FFT analysis · The largest Lyapunov exponents

1 Introduction

Dynamic stability of plates is a subject, the beginning of which can be found in the middle of twentieth century. The first publication on the dynamic stability of plates was published by Zizicas in 1952 [42]. He presented the theoretical solution for the joint supported plate where a time-dependent load was added. In this work, the critical dynamic loads was not calculated and criteria for dynamic stability was not formulated. In subsequent years, intense research on the dynamic stability of plates led to the emergence of criteria by means of which can be estimated the load causing loss of stability. The criteria of dynamic stability can be divided into geometrical [17], energy [33], failure [32].

One of the first criterion of dynamic stability was a Budiansky-Hutchinson criterion [21]. It concerned rods and cylindrical shells with an axial load. They analyzed the load in the form of pulse of a finite and infinite duration. According to authors, the loss of stability of structures under dynamic load occurs when the small load increments cause rapid increase in deflection. A similar criterion for the cylindrical

L. Borkowski (✉)
Department of Strength of Materials, Lodz University of Technology,
Stefanowskiego 1/15, 90-924 Lodz, Poland
e-mail: lukasz.borkowski@p.lodz.pl

J. Awrejcewicz (ed.), *Dynamical Systems in Theoretical Perspective*,
Springer Proceedings in Mathematics & Statistics 248,
https://doi.org/10.1007/978-3-319-96598-7_6

shells with a transverse load was formulated by Budiansky and Roth [15]. Many researchers have implemented the above criterion for plate structures [27, 34, 41]. The adapted Budiansky-Hutchinson criterion says that the loss of stability for the construction with the pulse load corresponds to the amplitude, for which the velocity of rise of deflection is the greatest.

In 2000, Petry and Fahlbusch [32] said that the Budiansky-Hutchinson criterion for plate structures does not allow the full use of capacity of structural elements. They said that the analysis of the stress state should determine the dynamic critical load for the construction with a stable post-critical equilibrium path. Based on this analysis, it is possible to determine the value of the load, for which the destruction of the structure take place. According to the Petry-Fahlbusch criterion, if the condition – a reduced stress is smaller or equal to a boundary stress – is fulfilled at any time and at any point of study structure then a dynamic response of the construction under the pulse load is dynamically stable. Petry and Fahlbusch also defined the dynamic load factor as:

$$DLF_f = \frac{N_f^{dyn}}{N_f^{stat}}, \tag{1}$$

where: N_f^{dyn} – the dynamic failure load, N_f^{stat} – the static failure load.

In 1972, a study for joint supported rectangular plates which were subjected to different pulse loads was presented by Volmir [36]. He analyzed the pulses of a finite duration: a rectangular pulse and an exponentially decreasing pulse, the pulses of an infinite duration and a linearly increasing load. He studied the pulses that caused both compression and shear. The problem of dynamic stability was solved by applying the Bubnov-Galerkin method [30], and the resulting equations by the Runge-Kutta method [16, 18]. Based on the study, Volmir proposed the criterion of dynamic stability assuming that the loss of stability for the pulse load plates occurs when the maximum deflection of the plates are equal to a certain constant value. Most often, the thickness or the half thickness of plate is assumed as the critical value of deflection.

Another criteria of dynamic stability was proposed by Ari-Gur and Simonetta [3]. They described the value of critical load depending on the following parameters: a measured deflection in the middle of length and width of the plate, the intensity of load, for the plates fixed at all edges and loaded a pulse of half-wave shaped (a pulse of finite duration). On the basis of analytical and numerical studies, Ari-Gur and Simonetta suggested four criteria of dynamic stability. The first concerns the value of deflection and the intensity of load pulse – the dynamic buckling occurs when a slight increase the intensity of the load pulse causes a significant increase the value of deflection. Another criterion is based on the analysis of the maximum values of the load pulse and deflection. According to this criterion, the dynamic buckling occurs when a slight increase of the amplitude of load pulse causes a decrease the value of deflection. The following two criteria are the failure criteria, which are based on a response analysis for the loaded edge of a plate – shortening (for load of the force pulse) or reaction (for load of the displacement pulse) at the edges. According to the

third criterion, the dynamic buckling occurs when a small increase of the amplitude of force pulse causes a sudden increase the value of shortening of loaded plate edge. The fourth criterion concerns the case when the load is realized by the displacement pulse and defines the critical intensity of the displacement pulse – the dynamic buckling occurs when a small increase of the intensity of displacement pulse of loaded edge causes the change of sign of reaction at the plate edge.

In 1987, Kleiber, Kotula, Saran [23] analyzed the behavior of rod systems by finite element method. They formulated the quasi-bifurcation criterion of dynamic stability for the construction that are jumping loaded of Heaviside pulse by using the properties of a tangent stiffness matrix in the point of bifurcation. According to this criterion, the structure loses stability and a deflection begin to grow boundlessly when the determinant of the tangent stiffness matrix is equal to zero and the absolute value of the smallest eigenvalue is greater than the absolute value of the nearest maximum, which the smallest eigenvalue reaches. In the stability theory of dynamical systems, a tangent stiffness matrix corresponds to the Jacobi matrix [22].

The above-mentioned criteria are widely used by many researchers, who are engaged in the analysis of dynamic stability of plates and shells [13, 20, 24–26, 28, 29, 31, 38]. Using the dynamic criteria (for example in the theory of bifurcation and chaos) it is also possible to evaluation of stability of system. [1, 2, 19, 35, 37, 39, 40]. An analysis of the stability of plates and shells was presented by Awrejcewicz et al. in many papers [4–11]. In these articles, the dynamic analysis by applying the Bubnov-Galerkin method was implemented. The Bubnov-Galerkin method was used to reduce partial differential equations governing the dynamics of flexible plates and shells to a discrete system with finite degrees of freedom.

In this work, the criteria of phase portraits, Poincaré Maps, FFT analysis, largest Lyapunov exponents are computed and compared with the results obtained by using the Volmir criterion.

2 Analyzed Plate

In this work, a square isotropic plate with dimensions $b = l = 100$ mm, $h = 1$ mm and the material constants $E = 200$ GPa, $\upsilon = 0.3$, joint supported on the all edges (Fig. 1) was examined. Dynamic compressive load in the plane of the plate was included. The dynamic load means the load, which was suddenly introduced and lasted for infinite duration.

Using research done by Volmir [36], the above plate can be described by the following equation:

$$\ddot{\zeta} + \Omega_0^2(1 - k\cos\theta t)\zeta + \eta\zeta^3 = 0 \tag{2}$$

where: $k = \frac{\sigma_t^*/\sigma_{cr}^*}{1-\sigma_0^*/\sigma_{cr}^*}$, $\Omega_0^2 = \omega_0^2(1 - \frac{\sigma_0^*}{\sigma_{cr}^*})$, ζ – deflection of the plate, ω_0 – natural frequency, σ_{cr}^* – critical stress, σ_0^* – medium stress, σ_t^* – stress amplitude, η – parameter, whose value is dependent on the boundary conditions.

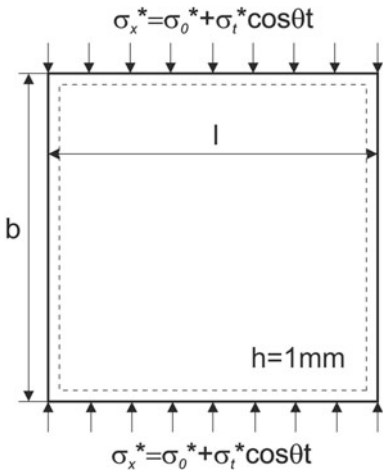

Fig. 1 Analyzed plate

For the studied plate the values of parameters were: $\omega_0 = 3014.3[\text{rad}/s]$, $\sigma^*_{cr} = 72.3$ [MPa], $\eta = 0.23[\text{rad}/s^2]$ - the value of parameter for the plate joint supported on the all edges.

Transforming the Eq. (2) to dimensionless form we get:

$$\ddot{x} + a(1 - k\cos\psi\tau)x + bx^3 = 0 \tag{3}$$

where: $a = 1 - \frac{\sigma_0^*}{\sigma_{cr}^*}$, $b = \frac{\eta}{\omega_0^2}$, $\ddot{x} = \frac{1}{\omega_0^2}\ddot{\zeta}$, $x = \zeta$, $x^3 = \zeta^3$, $\psi = \frac{\theta}{\omega_0}$, τ – dimensionless time. For the purpose of the further numerical analysis, the Eq. (3) was described by two first-order differential equations:

$$\begin{aligned} \dot{x}_1 &= x_2 \\ \dot{x}_2 &= -a(1 - k\cos\psi\tau)x_1 - bx_1^3 \end{aligned} \tag{4}$$

The studies were made for the following initial conditions: $x_1 = 0.01$, $x_2 = 0$.

3 Numerical Analysis of the Study Plate

The analysis of dynamic stability of the plate was made by changing the values of the parameters σ_0 and σ_t. This allowed to create the graph of stability and instability areas.

Figure 2 presents the graphs of dynamic stability and instability (a circled area) of the plate (a) and the timing diagram of stress (b) presented in the Volmir studies [36]. Whereas, Fig. 3 shows the areas of dynamic stability and instability (a circled area) for the analyzed plate obtained by using the criteria of phase portraits (PP), Poincaré maps

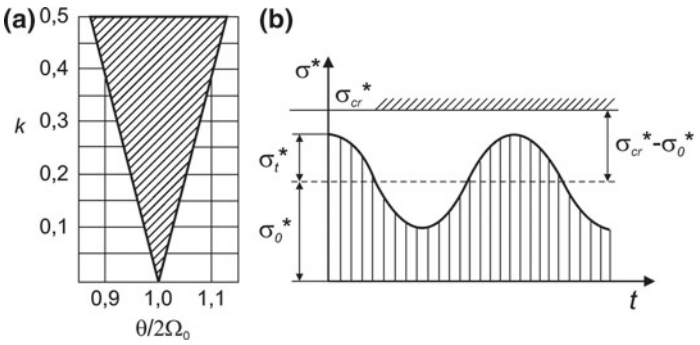

Fig. 2 The graph of dynamic stability and instability of the plate (**a**) and the timing diagram of stress (**b**) presented in the Volmir studies [36]

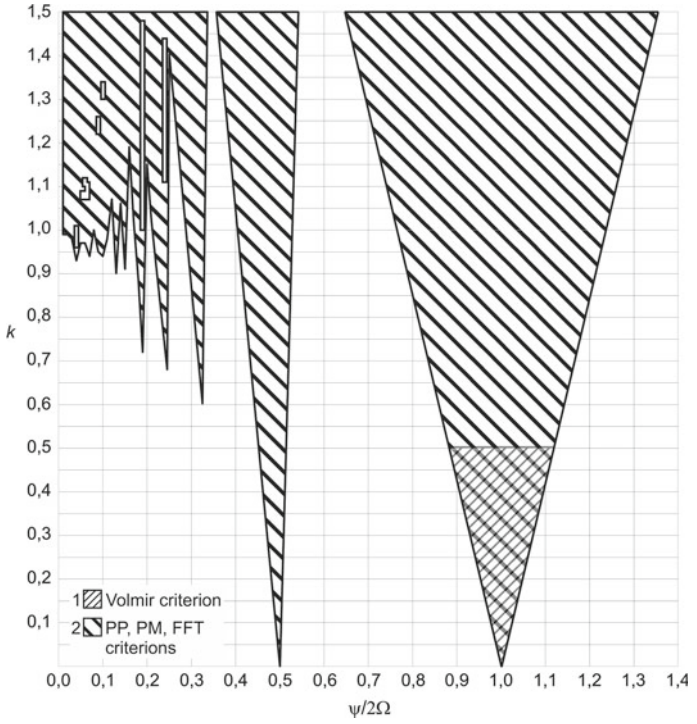

Fig. 3 The graph of dynamic stability and instability areas for the study plate

(PM), FFT analysis (FFT) in the coordinates $k - \psi/2\Omega$ ($\psi = \theta/\omega_0$, $\Omega = \Omega_0/\omega_0$). Calculations for parameters k and $\psi/2\Omega$ changing every 0,01 were made.

This graph shows the extended study which were presented in the Volmir work [36]. Applying tools used in dynamics, it is possible to not only the full agreement with the Volmir results (the area nr 1 in Fig. 3), but also presented the larger areas of

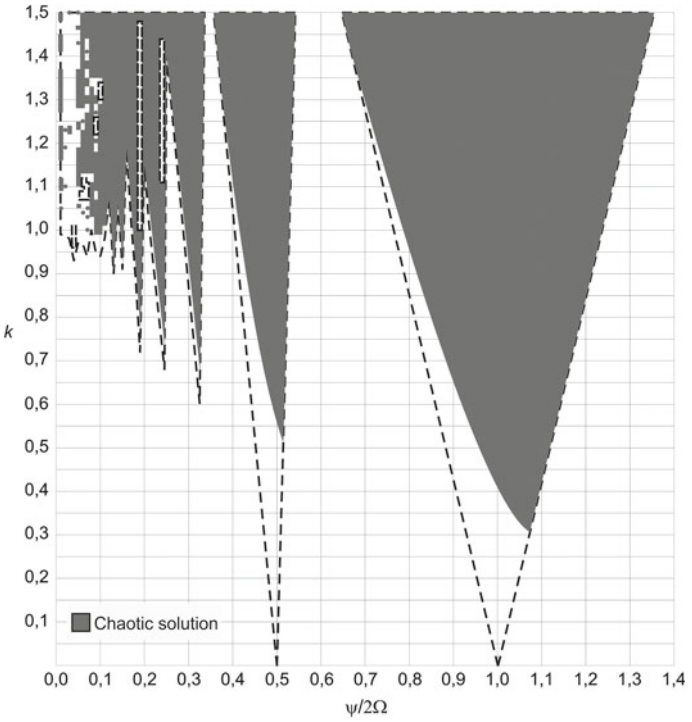

Fig. 4 The graph of the areas representing the chaotic solution – the criteria of Poincaré maps and the largest Lyapunov exponents

dynamic instability (the area nr 2 in Fig. 3). In the areas of dynamic stability quasi-periodic solutions were obtained. Besides, for the areas of dynamic instability quasi-periodic as well as chaotic solutions were observed. Therefore, the graph (Fig. 4) on which were indicated the areas representing the chaotic solution (gray areas) by applying the criteria of Poincaré maps and the largest Lyapunov exponents was made. The dashed line marks the boundary of stability solution which corresponds to the areas of dynamic stability and instability presented in Fig. 3. In addition, magnifying for the above two graphs (Figs. 3 and 4) in the beginning part of $\psi/2\Omega$ parameter was made (Fig. 5). In both figures, it can notice the appearance of small dynamic stability areas within the dynamic instability range. For the initial value of the parameter $\psi/2\Omega$ (for the parameter value up to 0.1) the areas of the chaotic solution are small and occurs for the specific values (marked with gray circles) or ranges (marked with gray rectangles).

For a detailed presentation and description of the results using the dynamic criteria, the results for three selected points were analyzed. These points represent the areas of dynamic stability ($k = 0.5$, $\psi/2\Omega = 0.3$), dynamic instability with a quasi-periodic solution ($k = 0.3$, $\psi/2\Omega = 1.0$), dynamic instability with a chaotic solution ($k = 1.3$, $\psi/2\Omega = 0.5$). The phase portraits (a, d, g), FFT analysis (b, e, h) and Poincaré maps

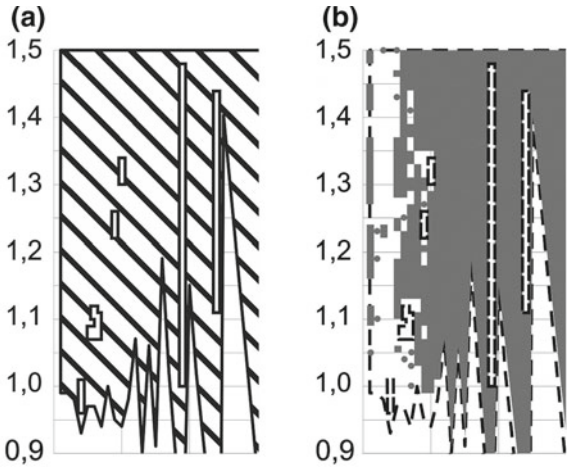

Fig. 5 The detailed graphs of dynamic stability and instability areas (**a**) and the areas representing the chaotic solution (**b**)

(c, f, i) for the areas of dynamic stability (a, b, c), dynamic instability – quasiperiodic solution (d, e, f) and dynamic instability – chaotic solution (g, h, i) were presented on the Fig. 6.

Analyzing the graphs of the phase portraits can be observed that for the assumed initial conditions ($x_1 = 0.01, x_2 = 0$), the loss of dynamic stability (Fig. 6d, g) is represented by a rapid increase the values of the displacement x_1 and velocity x_2 as against the areas of dynamic stability (Fig. 6a). According to the study [12], the coordinate values of the phase trajectory with the loss of dynamic stability are endless. This is when the analysis time of tested structure is close to the period of natural vibration of the structure. From a mathematical viewpoint – as is described in the research – the coordinate values of the phase trajectory are limited if the analysis time of the tested structure far exceeds the period of natural vibration of the analyzed plate. Their maximum values depend on the value of the parameter k. However, from the physical point of view, presented displacement values are unattainable to obtain. Nevertheless, a full compliance of the solutions for the areas of dynamic stability and instability for the short and long durations of analysis for the study plate was obtained.

Using the criterion of FFT analysis, it can be concluded that the areas of the dynamic stability are represented by the signal spectrum, from which the dominant frequencies can be precisely specify (Fig. 6b). In the areas of loss of stability it is not possible to specify the dominant frequencies. For some frequency ranges, the signal spectrum is continuous (Fig. 6e) or is continuous for almost the entire range of the analyzed frequencies (Fig. 6h). The loss of stability is represented also by a substantial increase of the amplitude of the analyzed signal, which has been expressed in decibels.

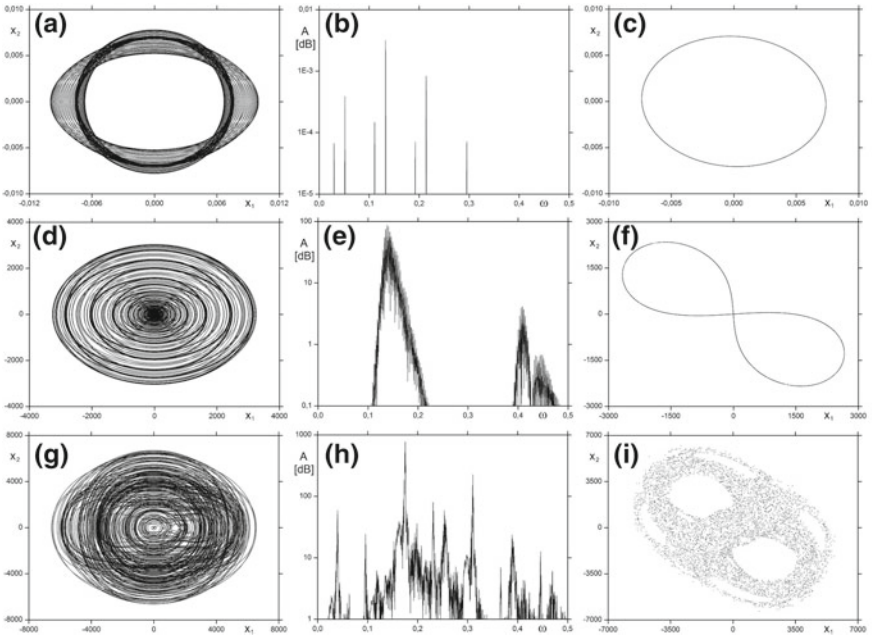

Fig. 6 The phase portraits (Zhejiang, **d**, **g**), FFT analysis (**b**, **e**, **h**) and Poincaré maps (**c**, **f**, *i*) for the areas of dynamic stability (**a**, **b**, **c**), dynamic instability – quasiperiodic solution (**d**, **e**, **f**) and dynamic instability – chaotic solution (**g**, **h**, **i**)

Similar as for the phase portraits graphs, the loss of dynamic stability on the Poincaré maps (Fig. 6f, i) is associated with the rapid growth of the displacement x_1 and velocity x_2. In addition, analyzing the results obtained for the stability area (Fig. 6c), it can be concluded that the solution is quasi-periodic. There are two disproportionate to each other frequencies which form the so-called 2D torus [14]. The existence of 2D torus for a point from the stationary area ($k = 0.5$, $\psi/2\Omega = 0.3$) is confirmed by the zero values of the largest Lyapunov exponents – $\lambda_1 = 0.000002$, $\lambda_2 = -0.000002$. In the areas of the dynamic instability with a quasi-periodic solution ($k = 0.3$, $\psi/2\Omega = 1.0$), the values of the largest Lyapunov exponents are also equal to zero – $\lambda_1 = 0.000004$, $\lambda_2 = -0.000004$. The existence of the torus 2d also in this area was proved. However, it should be noted that the occurrence of the 2D torus in the areas of the dynamic stability is related to the lack of damping in the system. Consequently, there is no attractor (or attractors) to which the trajectory would coincide. Introducing the damping to the system would lead to two negative values of the largest Lyapunov exponents [14]. In the areas of the dynamic instability with a chaotic solution ($k = 1.3$, $\psi/2\Omega = 0.5$), the value of the largest Lyapunov exponent is positive – $\lambda_1 = 0.026312$, $\lambda_2 = -0.026312$. In addition, in order to accurately present the transition from the unstable quasi-periodic solution to the

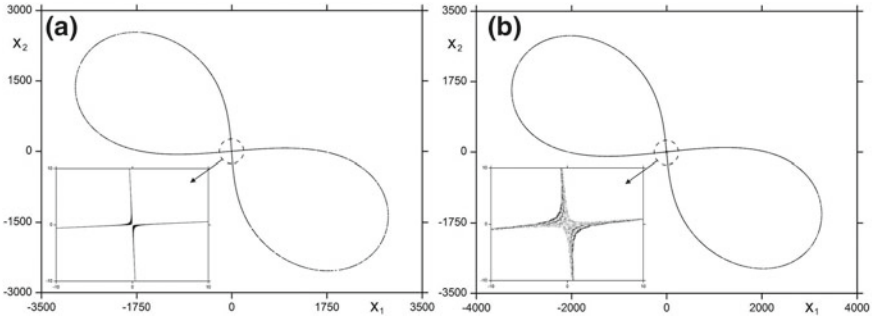

Fig. 7 The Poincaré maps for the areas of dynamic instability – quasiperiodic solution (**a**) and dynamic instability – chaotic solution (**b**)

unstable chaotic solution, the Poincaré maps for the points $k = 0.40$, $\psi/2\Omega = 1.0$ (a) and k=0.42, $\psi/2\Omega = 1.0$ (b) were presented (Fig. 7). The magnified centered part for each graph clearly indicates the nature of the solution.

4 Summary

The aim of the study was to analyze an isotropic plate in terms of its dynamic stability (or its instability), by using the criteria of phase portraits, Poincaré maps, FFT analysis, largest Lyapunov exponents and compared the obtained results with the results received by using the Volmir criterion. Summing up the results, it can be concluded that using the criteria of phase portraits, Poincaré maps, FFT analysis, it is possibile to designate the areas of dynamic stability and instability for the study system. The results obtained with the above criteria are consistent with the results which were presented in the Volmir work [36]. Furthermore, the larger areas of dynamic stability and instability as compared with the Volmir results were presented. In addition, using the criteria of Poincaré maps and the largest Lyapunov exponents the areas in which the solution is chaotic were presented.

For the criteria of phase portraits and Poincaré maps, the loss of stability was associated with a significant increase in the value of the displacement x_1 and velocity x_2 (in comparison with the area of dynamic stability for given initial conditions). On the FFT analysis graphs, the area of dynamic stability is represented by the signal spectrum, from which the dominant frequencies can be precisely specify. On the graphs of the FFT analysis, during the transition into the area of instability, the signal spectrum is continuous (specification of the dominant frequencies is impossible) and significantly increased their amplitude. Besides, applying the criteria of Poincaré maps and the largest Lyapunov exponents can present the complex quasi-periodic and chaotic solutions and precisely determine the values of the parameters for which these solutions appear.

The criteria which were used in this article can be very useful during the following research.

Acknowledgements This work has been supported by the internal grant awarded by the Lodz University of Technology with the Young Scientists Fund.

References

1. Alijani, F., Amabili, M., Karagiozis, K., Bakhtiari-Nejad, F.: Nonlinear vibrations of functionally graded doubly curved shallow shells. J. Sound Vibr. **330**(7), 1432–1454 (2011)
2. Alijani, F., Bakhtiari-Nejad, F., Amabili, M.: Nonlinear vibrations of FGM rectangular plates in thermal environments. Nonlinear Dyn. **66**(3), 251–270 (2011)
3. Ari-Gur, J., Simonetta, S.R.: Dynamic pulse buckling of rectangular composite plates. Compos. Part B: Eng. **28**(3), 301–308 (1997)
4. Awrejcewicz, J., Krysko, V.A.: Feigenbaum scenario exhibited by thin plate dynamics. Nonlinear Dyn. **24**(4), 373–398 (2001)
5. Awrejcewicz, J., Krysko, A.V.: Wavelet-based analysis of parametric vibrations of flexible plates. Int. Appl. Mech. **39**(9), 997–1028 (2003)
6. Awrejcewicz, J., Krysko, V.A., Narkaitis, G.G.: Bifurcations of a thin plate-strip excited transversally and axially. Nonlinear Dyn. **32**(2), 187–209 (2003)
7. Awrejcewicz, J., Krysko, A.V.: Analysis of complex parametric vibrations of plates and shells using Bubnov-Galerkin approach. Arch. Appl. Mech. **73**(7), 495–504 (2003)
8. Awrejcewicz, J., Krysko, V.A., Krysko, A.V.: Complex parametric vibrations of flexible rectangular plates. Meccanica **39**(3), 221–244 (2004)
9. Awrejcewicz, J., Krysko, V. A., Moldenkova, T.: Mathematical model of dissipative parametric vibrations of flexible plates with nonhomogeneous boundary conditions. Math. Probl. Eng. 16 pp. https://doi.org/10.1155/MPE/2006/85623(2006)
10. Awrejcewicz, J., Krysko, A.V., Bochkarev, V.V., Babenkova, T.V., Papkova, I.V., Mrozowski, J.: Chaotic vibrations of two-layered beams and plates with geometric, physical and design nonlinearities. Int. J. Bifurcat. Chaos **21**(10), 2837–2851 (2011)
11. Awrejcewicz, J., Papkova, I.V., Krylova, E.U., Krysko, V.A.: Wavelet-based analysis of the regular and chaotic dynamics of rectangular flexible plates subjected to shear-harmonic loading. Shock Vibr. **19**(5), 979–994 (2012)
12. Bazant, Z.P., Cedolin, L.: Stability of Structures: Elastic, Inelastic. Fracture and Damage Theories. World Scientific, London (2010)
13. Bolotin, V.: Dynamic Stability of Elastic Systems, vol. 1 (1962)
14. Borkowski, L., Perlikowski, P., Kapitaniak, T., Stefanski, A.: Experimental observation of three-frequency quasiperiodic solution in a ring of unidirectionally coupled oscillators. Phys. Rev. E **91**(6), 062906 (2015)
15. Budiansky, B., Roth, R.S.: Axisymmetric dynamic buckling of clamped shallow spherical shells. 597–606 (1962)
16. Collatz, L.: The Numerical Treatment of Differential Equations, vol. 60. Springer, Berlin (2012)
17. Cooley, J.W., Tukey, J.W.: An algorithm for the machine calculation of complex Fourier series. Math. Comput. **19**(90), 297–301 (1965)
18. Fortuna, Z., Macukow, B., Wasowski, J.: Metody Numeryczne. WNT (2005). ISBN 83-204-3075-5
19. Gilat, R., Aboudi, J.: Parametric stability of non-linearly elastic composite plates by Lyapunov exponents. J. Sound Vibr. **235**(4), 627–637 (2000)
20. Hsu, Y.C., Forman, R.G.: Elastic-plastic analysis of an infinite sheet having a circular hole under pressure. J. Appl. Mech. **42**(2), 347–352 (1975)

21. Hutchinson, J.W., Budiansky, B.: Dynamic buckling estimates. AIAA J. **4**(3), 525–530 (1966)
22. Kapitaniak, T., Wojewoda, J.: Bifurkacje i chaos. Wydawnictwo Naukowe PWN, Wydawnictwo Politechniki Lodzkiej (2000)
23. Kleiber, M., Kotula, W., Saran, M.: Numerical analysis of dynamic quasi-bifurcation. Eng. Comput. **4**(1), 48–52 (1987)
24. Kolakowski, Z.: Some aspects of dynamic interactive buckling of composite columns. Thin-Walled Struct. **45**(10), 866–871 (2007)
25. Kolakowski, Z., Kubiak, T.: Interactive dynamic buckling of orthotropic thin-walled channels subjected to in-plane pulse loading. Compos. Struct. **81**(2), 222–232 (2007)
26. Kowal-Michalska, K.: About some important parameters in dynamic buckling analysis of plated structures subjected to pulse loading. Mech. Mech. Eng. **14**(2), 269–279 (2010)
27. Kubiak, T.: Criteria of dynamic buckling estimation of thin-walled structures. Thin-Walled Struct. **45**(10), 888–892 (2007)
28. Kubiak, T., Kolakowski, Z., Kowal-Michalska, K., Mania, R., Swiniarski, J.: Dynamic response of conical and spherical shell structures subjected to blast pressure. In: Proceedings of SSDS'Rio (2010)
29. Mania, R., Kowal-Michalska, K.: Behaviour of composite columns of closed cross-section under in-plane compressive pulse loading. Thin-Walled Struct. **45**(10), 902–905 (2007)
30. Michlin, S.G., Smolnicki, C.L.: Approximate Methods for the Solution of Integral and Differential Equations. PWN (1970)
31. Moorthy, J., Reddy, J.N., Plaut, R.H.: Parametric instability of laminated composite plates with transverse shear deformation. Inte. J. Solids Struct. **26**(7), 801–811 (1990)
32. Petry, D., Fahlbusch, G.: Dynamic buckling of thin isotropic plates subjected to in-plane impact. Thin-Walled Struct. **38**(3), 267–283 (2000)
33. Raftoyiannis, I.G., Kounadis, A.N.: Dynamic buckling of 2-DOF systems with mode interaction under step loading. Int. J. Non-linear Mech. **35**(3), 531–542 (2000)
34. Shariyat, M.: Thermal buckling analysis of rectangular composite plates with temperature-dependent properties based on a layerwise theory. Thin-Walled Struct. **45**(4), 439–452 (2007)
35. Touati, D., Cederbaum, G.: Influence of large deflections on the dynamic stability of nonlinear viscoelastic plates. Acta Mech. **113**(1–4), 215–231 (1995)
36. Volmir, A.S.: Nonlinear Dynamics Plates and Shells. Science, Moscow (1972)
37. Wang, Y.G., Song, H.F., Li, D., Wang, J.: Bifurcations and chaos in a periodic time-varying temperature-excited bimetallic shallow shell of revolution. Arch. Appl. Mech. **80**(7), 815–828 (2010)
38. Wu, G.Y., Shih, Y.S.: Analysis of dynamic instability for arbitrarily laminated skew plates. J. Sound Vib. **292**(1), 315–340 (2006)
39. Yeh, Y.L., Lai, H.Y.: Chaotic and bifurcation dynamics for a simply supported rectangular plate of thermo-mechanical coupling in large deflection. Chaos, Solitons Fractals **13**(7), 1493–1506 (2002)
40. Yuda, H., Zhiqiang, Z.: Bifurcation and chaos of thin circular functionally graded plate in thermal environment. Chaos, Solitons Fractals **44**(9), 739–750 (2011)
41. Zhang, T., Liu, T.G., Zhao, Y., Luo, J.Z.: Nonlinear dynamic buckling of stiffened plates under in-plane impact load. J. Zhejiang Univ. Sci. **5**(5), 609–617 (2004)
42. Zizicas, G.A.: Dynamic buckling of thin plates. Trans. ASME **74**(7), 1257–1268 (1952)

Rigid Jeffcott Rotor Bifurcation Behaviour Using Different Models of Hydrodynamic Bearings

Miroslav Byrtus and Štěpán Dyk

Abstract The paper studies dynamical behaviour of Jeffcott rotor supported by a hydrodynamic bearings. It uses different analytical formulations for hydrodynamic bearing forces acting on Jeffcott rotor. The model is nonlinear due to the presence of hydrodynamic bearings and can show different subharmonic behaviour like oil whip and oil whirl. Such a system is subjected to dynamical analysis using numerical continuation aimed at detection of nonlinear phenomena like bifurcations and unstable behaviours with respect to basic system parameters.

Keywords Rotordynamics · Hydrodynamic bearings · Vibration · Bifurcation

1 Introduction

This paper is focused on dynamics of a modified version of the *Jeffcott rotor* [12], also known as the *Laval rotor* [9], neglecting the shaft bending stiffness. The main motivation for this model is to understand the phenomena resulting from fluid-film bearing forces. The modifications of Jeffcott rotor are widely used to show various rotordynamics phenomena such as influence of rotor clearances and rotor-stator contacts [18], effects of seals [14], parametric vibration caused by cracked shaft [11] or influence of thermo hydrodynamic effects [13]. In general, non-linear phenomena are studied on different mechanical systems [2–4].

Recently, using the developed computer based tools for non-linear dynamic system analysis, existence of equilibria, periodic orbits can be predicted along with various bifurcations [10]. In [1, 8] the numerical continuation is used for an analysis of a Jeffcott rotor model supported by hydrodynamic bearing loaded by the gravity. The bifurcation of equilibria and limit cycles is studied. Numerical continuation

M. Byrtus (✉) · Š. Dyk
University of West Bohemia, Univerzitni 8, Plzen, Czech Republic
e-mail: mbyrtus@kme.zcu.cz

Š. Dyk
e-mail: sdyk@kme.zcu.cz

J. Awrejcewicz (ed.), *Dynamical Systems in Theoretical Perspective*,
Springer Proceedings in Mathematics & Statistics 248,
https://doi.org/10.1007/978-3-319-96598-7_7

method is applied to Jeffcott rotor supported by semi-floating ring bearings in [6]. Different subsynchronous oscillations like oil whirl and oil whip are detected along with various bifurcations of the solutions. Further, authors in [16] studied nonlinear stability of a flexible rotor-bearing system using the Hopf bifurcation theory.

The work presented here is similar in spirit to the analyses performed by numerical continuation mentioned above but the Jeffcott rotor model is moreover completed by the unbalance load. Mathematical model of the system is derived in polar coordinates and the fluid-film bearing forces are adopted for both infinitely long (IL) and infinitely short (IS) hydrodynamic journal bearings (JB) [5]. Both ILJB and ISJB are subjected to stability analysis with gravity load only. And then the continuation of limit cycles is performed for a system loaded by gravity and unbalance forces simultaneously.

2 Mathematical Model of Jeffcott Rotor with Hydrodynamic Journal Bearing

Based on the scheme depicted in Fig. 1, the mathematical model of Jeffcott rotor can be formulated. In the original Jeffcott model, the elastic forces of flexible shaft or elastic forces in the bearing were considered. However, the phenomena occurring in the journal bearings are more complex and the bearing forces can be represented more precisely using an approximate solution of Reynolds equation which describes a pressure distribution in the bearing and which can be transformed to the force acting to the journal.

According to Fig. 1, position of the geometric centre C of journal is described by polar coordinates e (radial displacement) and φ (angular displacement) in the

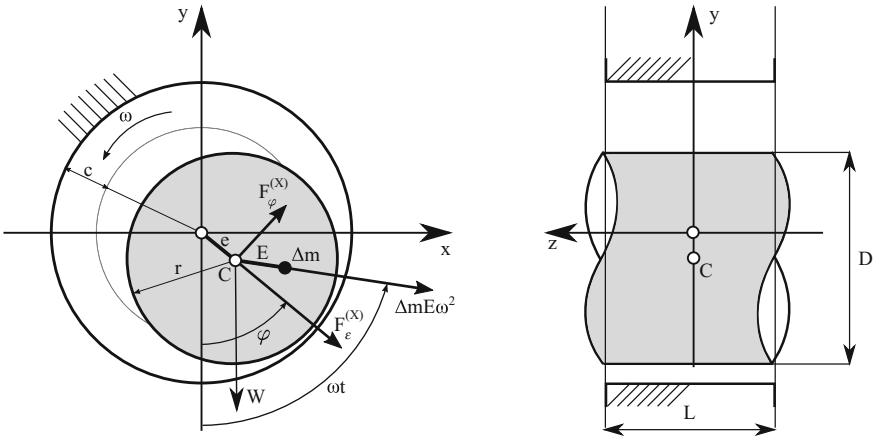

Fig. 1 The scheme of the considered Jeffcott rotor

non-rotating space. The rotor rotates with angular speed ω, it has the mass m and its static unbalance is ΔmE. In central position, the radial clearance between the journal and a bearing is c.

The mathematical model of the Jeffcott rotor in journal bearings can be formulated in polar coordinates considering gravity load [1] and unbalance load in following way

$$\begin{aligned} \varepsilon'' - \varepsilon\varphi'^2 &= \frac{F_{\varepsilon}^{(X)}}{mc\omega^2} + \frac{W}{mc\omega^2}\cos\varphi + \frac{\Delta mE}{mc}\cos(\tau-\varphi), \\ \varepsilon\varphi'' + 2\varepsilon'\varphi' &= \frac{F_{\varphi}^{(X)}}{mc\omega^2} - \frac{W}{mc\omega^2}\sin\varphi + \frac{\Delta mE}{mc}\sin(\tau-\varphi), \end{aligned} \tag{1}$$

where superscripts $X = IL, IS$ correspond to the infinitely long and infinitely short journal bearings. The relative (dimensionless) eccentricity is given as $\varepsilon = e/c$.

The equations of motion (1) are formulated in dependence on dimensionless time $\tau = \omega t$. This assumption results in following relationships for the time derivative of used time-dependent variables $\dot{\square} = \square'\omega$, where $\dot{\square} = \frac{d}{dt}\square$ and $\square' = \frac{d}{d\tau}\square$.

Formulas for forces in HD journal bearings introduced in [17] (IL) and [7, 15] (IS) have been summarized in [5]. Corresponding to the directions indicated in Fig. 1 (the influence of oil film on the shaft), the forces can be expressed in dependence on dimensionless eccentricity and time in following way

$$F_{\varepsilon}^{(IL)} = -6\mu RL\left(\frac{R}{c}\right)^2 \omega \underbrace{\left[(1-2\varphi')\frac{2\varepsilon^2}{(2+\varepsilon^2)(1-\varepsilon^2)} + \frac{\pi\varepsilon'}{(1-\varepsilon^2)^{3/2}}\right]}_{f_{\varepsilon}^{(IL)}}, \tag{2}$$

$$F_{\varphi}^{(IL)} = 6\mu RL\left(\frac{R}{c}\right)^2 \omega \underbrace{\left[(1-2\varphi')\frac{\pi\varepsilon}{(2+\varepsilon^2)(1-\varepsilon^2)^{1/2}} + \frac{4\varepsilon'}{(1+\varepsilon)(1-\varepsilon^2)}\right]}_{f_{\varphi}^{(IL)}}, \tag{3}$$

$$F_{\varepsilon}^{(IS)} = -\mu RL\left(\frac{L}{c}\right)^2 \omega \underbrace{\left[(1-2\varphi')\frac{\varepsilon^2}{(1-\varepsilon^2)^2} + \frac{\pi(1+2\varepsilon^2)\varepsilon'}{2(1-\varepsilon^2)^{5/2}}\right]}_{f_{\varepsilon}^{(IS)}}, \tag{4}$$

$$F_{\varphi}^{(IS)} = \mu RL\left(\frac{L}{c}\right)^2 \omega \underbrace{\left[(1-2\varphi')\frac{\pi\varepsilon}{4(1-\varepsilon^2)^{3/2}} + \frac{2\varepsilon\varepsilon'}{(1-\varepsilon^2)^2}\right]}_{f_{\varphi}^{(IS)}}. \tag{5}$$

The equations of motion (1) along with journal bearing forces expressions (2)–(5) were rewritten in the form

$$\begin{aligned}\varepsilon'' - \varepsilon\varphi'^2 &= -\frac{\lambda^{(X)}}{\overline{\omega}} f_{\varepsilon}^{(X)} + \frac{1}{\overline{\omega}^2}\cos\varphi + \frac{\Delta mE}{mc}\cos(\tau-\varphi),\\ \varepsilon\varphi'' + 2\varepsilon'\varphi' &= \frac{\lambda^{(X)}}{\overline{\omega}} f_{\varphi}^{(X)} - \frac{1}{\overline{\omega}^2}\sin\varphi + \frac{\Delta mE}{mc}\sin(\tau-\varphi),\end{aligned} \tag{6}$$

where the introduced dimensionless parameters are formulated as follows

$$\overline{\omega} = \omega\sqrt{\frac{c}{g}}, \quad \lambda^{(IL)} = \frac{6\mu LR^3}{mc^{2.5}g^{0.5}}, \quad \lambda^{(IS)} = \frac{\mu RL^3}{mc^{2.5}g^{0.5}}. \tag{7}$$

The variable μ stands for the oil viscosity and g corresponds to gravity constant.

3 Computational Analysis

The mathematical model (6) is analysed using time integration and numerical continuation methods using the software MATCONT [10]. Therefore, it needs to be rewritten in the state space

$$\boldsymbol{x}' = \boldsymbol{f}^{(X)}(\boldsymbol{x}, \overline{\omega}, \lambda^{(X)}), \quad X = IS, IL. \tag{8}$$

The state-space is defined by the vector $\boldsymbol{x} = [x_1, x_2, x_3, x_4]^T = [\varepsilon, \varphi, \varepsilon', \varphi']^T$. Particularly, the model (8) states as follows

$$\begin{aligned} x_1' &= x_3,\\ x_2' &= x_4,\\ x_3' &= x_1 x_4^2 - \frac{\lambda^{(X)}}{\overline{\omega}} f_{x_1}^{(X)} + \frac{1}{\overline{\omega}^2}\cos x_2 + \frac{\Delta mE}{mc}\cos(\tau - x_2),\\ x_4' &= \frac{1}{x_1}\left[-2x_3x_4 + \frac{\lambda^{(X)}}{\overline{\omega}} f_{\varphi}^{(X)} - \frac{1}{\overline{\omega}^2}\sin x_2 + \frac{\Delta mE}{mc}\sin(\tau - x_2)\right]. \end{aligned} \tag{9}$$

4 Parametric Study by Numerical Continuation

The mathematical model (8) has two (dimensionless) free parameters: rotational velocity $\overline{\omega}$ and mass-geometric-material parameter $\lambda^{(X)}$ whose form depends on bearing type. These parameters characterize bearing properties in general. Further, dynamical properties of the Jeffcott rotor model are studied in dependence on these two parameters.

The analyses are performed for both considered bearing models (ISJB, ILJB) and two main cases are taken into account: (i) perfectly balanced rotor (only gravity load is considered), (ii) unbalanced rotor (gravity load along with unbalance forces are considered).

4.1 Perfectly Balanced Rotor

By the term *perfectly balanced rotor* we assume such a rotor which is very well balanced and which is operated up to such conditions when the unbalance forces can be neglected in the response. However, the model based on this assumption can reveal basic dynamical properties of the system.

In Fig. 2, different responses of the system (9) for ISJB are plotted. The blue solid lines correspond to equilibrium solutions for different values of the parameter $\lambda^{(IS)}$. One can for example imagine, the higher the parameter λ is the higher the mass of the rotor is. If the rotor rotates with a given angular velocity, the position of the rotor is formed by a stable equilibrium – the eccentricity ε and the angle φ are constant in time. As the velocity increases, the eccentricity decreases up to it reaches the Hopf bifurcation point. Crossing the Hopf point the equilibrium becomes unstable (designated by dashed blue line). All the Hopf points for different form the so called Hopf curve (black line) as the parameter λ changes. The Hopf curve is divided into two parts by the Generalized Hopf bifurcation point. The black solid line contains all Hopf points which give arise to supercritical bifurcation (limit cycles are born).

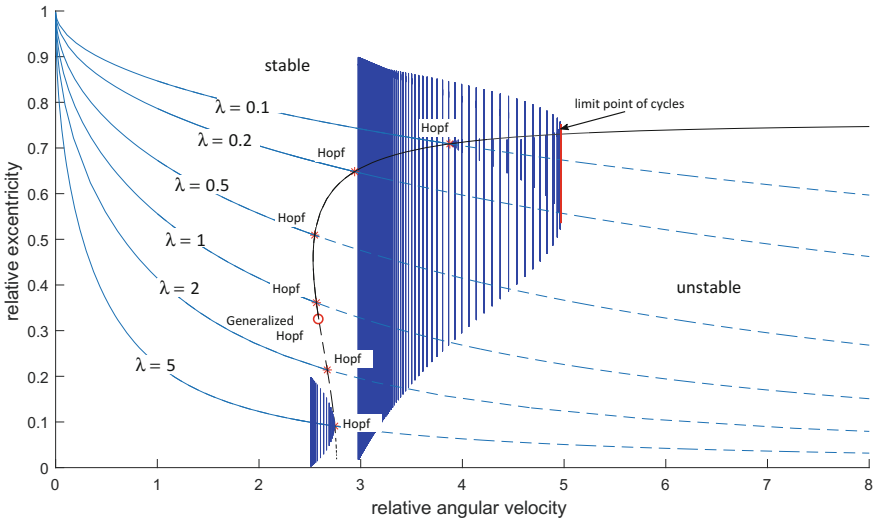

Fig. 2 Equilibrium points of IS bearing

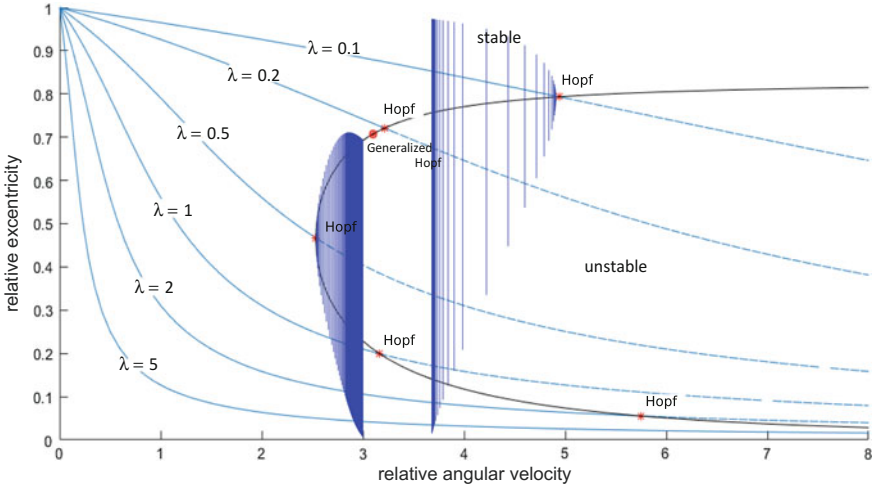

Fig. 3 Equilibrium points of IL bearing

The black dashed line contains Hopf point which give arise to subcritical bifurcation. According to Fig. 2, the supercritical Hopf bifurcation limits at limit point of cycles and forms back subcritically. The limit cycles develop up to a limiting cycle where the eccentricity reaches the limit values ($\varepsilon \in [0, 1]$) within the cycle. The limit cycles bifurcating from Hopf points correspond to the *oil whirl* instability.

In the case of perfectly balanced rotor supported by ILJB presented in Fig. 3, the dynamical behaviour is qualitatively very similar. The operational area is divided into stable and unstable regions of equilibria by the Hopf curve. However, the Hopf curve does not limit to a given angular velocity as the the case of ISJB. The limit cycles arising from Hopf points are even subcritical or supercritical and they do not cross over limit point of cycles.

4.1.1 Sensitivity to Initial Conditions

When the rotor operating speed approaches the border of the stability but still staying in the stable region, the response becomes more sensitive to initial conditions of the system. The set of possible initial conditions (from the position point of view) is divided into two areas (basins of attraction). In Fig. 4, in the plane given by axes named horizontal and vertical direction lay all possible initial conditions. The blue area corresponds to initial conditions which form the equilibrium solution. Initial conditions laying in the yellow area form a stable limit cycle where the eccentricity draws completely the bearing clearance. The basins of attraction evolve with respect to rotor velocity and depend on the bearing model as well.

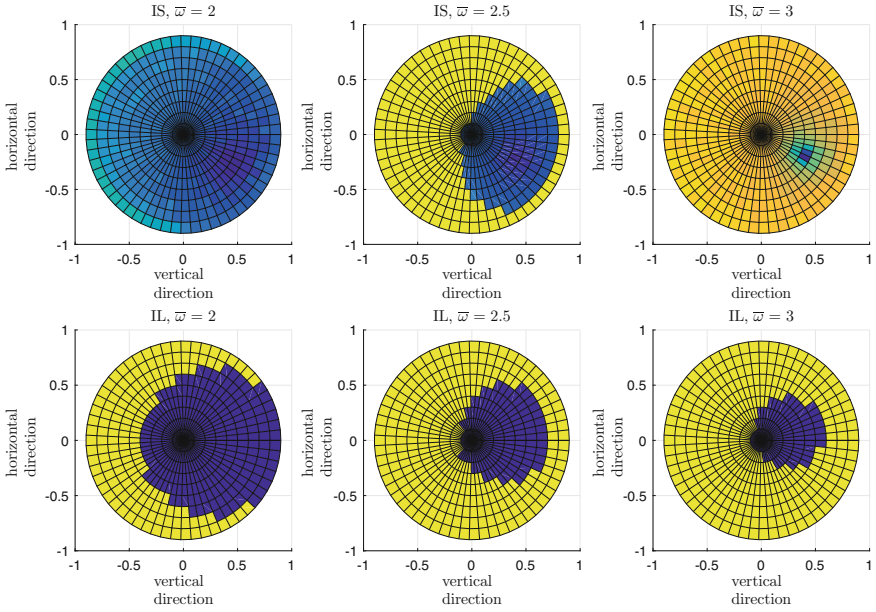

Fig. 4 Basins of attractions

4.2 Unbalanced Rotor - Real Case Study

In real cases, the unbalance is the main source of excitation of rotating systems. Here, the model of Jeffcott rotor is excited by the gravity load and by a rotating force induced by the rotor unbalance.

In the case of unbalanced rotor, continuation of periodic solution is performed for a chosen mass-geometric-material parameter $\lambda^{(IL)} = 1.1577$ and $\lambda^{(IS)} = 0.7718$, these values correspond to rotor parameters which are summarized in Tab. 1. To show the influence how change of the parameter λ influences the behaviour of the system, analyses for $\lambda^{(IL)} = \lambda^{(Is)} = 1$ is performed as well. Figures 5 and 6 correspond to rotor supported by ISJB. The mechanism how the bifurcations arise is the same, the bifurcation point are shifted only with respect to relative angular velocity of the rotor. As the angular velocity increases, the amplitude of the limit cycles grows up to it reaches period doubling point. At this point the solution bifurcates and the 2-period solutions trends to limiting point of cycles and it goes over Neimarck-Sacker point. The 2-period limit cycles then tends to second period doubling point. Between the two period doubling points, there is a neutral saddle on the 1-period solution branch.

Figures 7 and 8 correspond to rotor supported by ILJB. The ILJB model is more sensitive to the change of the parameter λ. Comparing both figures, one can clearly see the formation of period doubling scenarios. The fundamental behaviour of the rotor is similar to the previous model. For small relative angular velocity, the behaviour is moreover comparable to the perfectly balanced rotor, i.e. here, a very small limit

Table 1 Reference parameters of the Jeffcott rotor in HD journal bearings [5]

Parameter	Value
Radial clearance	$c = 0.9 \times 10^{-3}$ m
Unbalance	$\Delta m = 0.01$ kg
Unbalance eccentricity	$E = 0.01$ m
Rotor mass	$m = 3$ kg
Rotor RPM	$n = \langle 0; 8000 \rangle$ rpm
Dynamic viscosity	$\mu = 0.07$ Pa s
Bearing diameter	$D = 47.37 \times 10^{-3}$ m
Bearing axial length	$L = \eta D, \eta = 1$

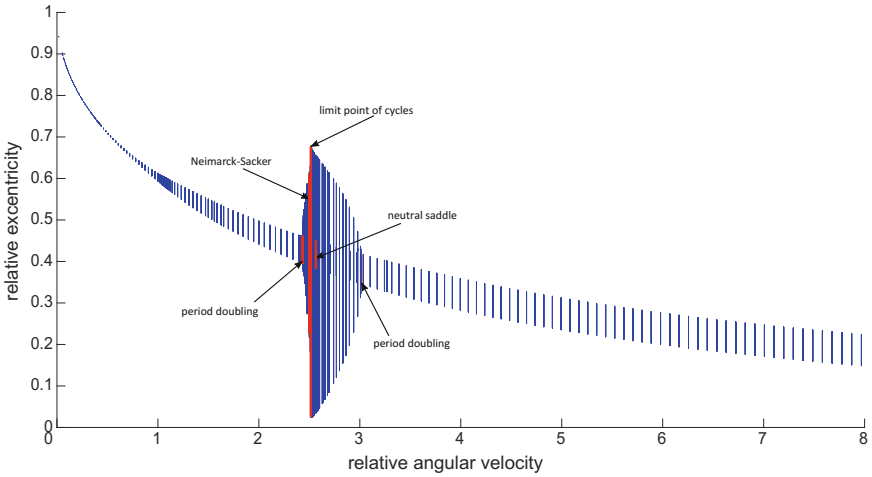

Fig. 5 Response to rotor unbalance ISJB for real parameters given in Table 1 resulting in $\lambda = 0.7718$

cycle develops and grows as the velocity increases up to it reaches the period doubling point. In dependence on the λ parameter the 2-period solution bifurcates either supercritically or subcritically. In case of $\lambda = 1.1577$, the 2-period solutions trends through Neimarck-Sacker point and it limits for angular velocity approx. 4.4. And for the velocity 5.7 another period doubling point appears. The 2-period solution arising form this point is subcritical and at branching point it turns to supercritical one. Taking into account the parameters $\lambda = 1$, in the followed region there appears one period doubling point only. The 2-period solution then disappears for velocity 5, since the 1-period solution disappears around the velocity 7.3. The disappearing of the 1-period solution is influenced by the borders where the model is valid. Since the parameter $\lambda = 1$ correspond to the ration $L/D < 1$, the validity of the model is limited.

The period doubling scenario can be practically explained as the *oil whirl* instability.

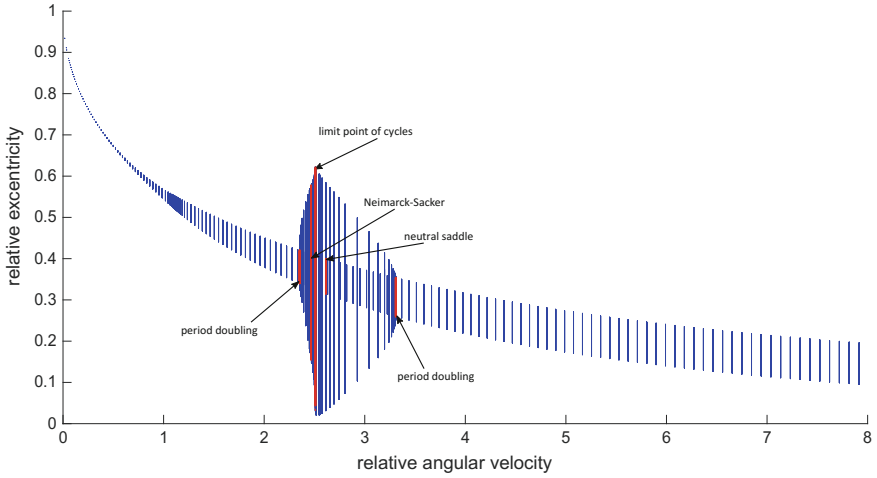

Fig. 6 Response to rotor unbalance ISJB, $\lambda = 1$

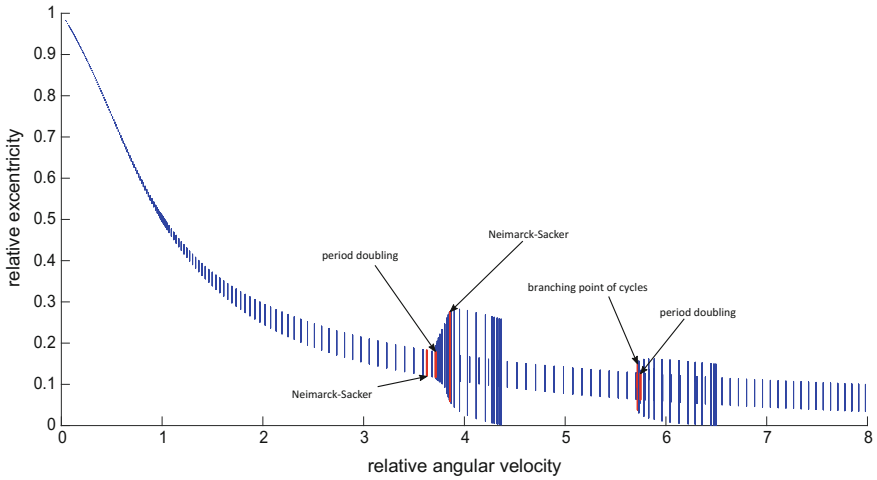

Fig. 7 Response to rotor unbalance ILJB for real parameters given in Table 1 resulting in $\lambda = 1.1577$

5 Conclusions

The paper focuses on the dynamical analysis of modified Jeffcott rotor supported by HD journal bearings using numerical continuation. For the purpose of this paper, two analytical models of hydrodynamic bearing forces are taken into account: i) for infinitely long journal bearing model (ILJB) and ii) for infinitely short journal bearing model (ILJB).

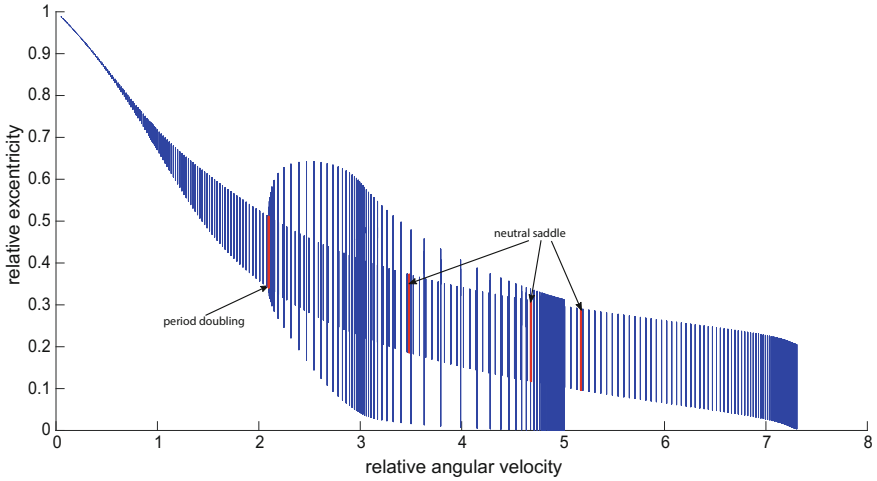

Fig. 8 Response to rotor unbalance ILJB, $\lambda = 1$

Firstly, a stability analyses of both ILJB and ISJB were performed considering the gravity load only. The analyses are performed for a wide range of mass-geometric-material parameter to show its influence on the formation of the stability boundary. For both cases, the stability boundary is formed by so called Hopf curve which is itself divided by Generalized Hopf bifurcation point, i.e. one part of the boundary gives rise to supercritical bifurcation of limit cycles, since the other part forms subcritical limit cycles bifurcation. Numerical experiment further show a strong dependence of the system response to the initial conditions in the vicinity of the border of the stability. Such a behaviour is demonstrated by basins of attraction formed by initial conditions. Two sets were revealed where one set limits to equilibrium since the other one limits to unstable limit cycle completely drawing the bearing clearance.

In the next, a parametric study of a Jeffcott rotor with real parameters were performed. In case of ISJB, an area bounded by period doubling points was detected. The 2-period solutions transit between the period doubling points through limit point of cycles. In case of ILJB, the model is more sensitive to the mass-geometric-material parameter as the presented bifurcation diagrams show.

The analyses of the modified Jeffcott rotor explain the fundamental dynamic properties of the fluid-film journal bearings, especially the stability properties and mechanisms of loosing the stability (oil whirl) have an important impact to engineering applications.

Acknowledgements The work has been supported by the project No. 17-15915S of the Czech Science Foundation entitled Nonlinear dynamics of rotating systems considering fluid film instabilities with the emphasis on local effects.

References

1. Amamou, A., Chouchane, M.: Nonlinear stability analysis of long hydrodynamic journal bearings using numerical continuation. Mech. Mach. Theory **72**, 17–24 (2014)
2. Awrejcewicz, J., Kudra, G.: Mathematical modelling and simulation of the bifurcationalwobblestone dynamics. Discontinuity Nonlinearity Complex. **3**(2), 123–132 (2014)
3. Awrejcewicz, J., Kudra, G., Wasilewski, G.: Experimental and numerical investigation of chaotic regions in the triple physical pendulum. Nonlinear Dyn. **50**(4), 755–766 (2007)
4. Awrejcewicz J., Kudra, G., Wasilewski, G.: Chaotic zones in triple pendulum dynamics observed experimentally and numerically. In: *New Trends in Mechanics and Transport, volume 9 of Applied Mechanics and Materials*, pp. 1–17. Trans Tech Publications, 3 2008
5. Bastani, Y.: A new analytic approximation for the hydrodynamic forces in finite-length journal bearings. J. Tribol. **132**(1), 014502–01–014502–9 (2010)
6. Boyaci, A.: Numerical continuation applied to nonlinear rotor dynamics. Procedia IUTAM **19**(Supplement C), 255–265 (2016). IUTAM Symposium Analytical Methods in Nonlinear Dynamics
7. Buckholz, R.H., Hwang, B.: The accuracy of short bearing theory for newtonian lubricants. J. Tribol. **108**(1), 73–79 (1986)
8. Chouchane, M., Amamou, A.: Bifurcation of limit cycles in fluid film bearings. Int. J. Non-Linear Mech. **46**(9), 1258–1264 (2011)
9. Gasch, R.: Dynamic behaviour of the laval rotor with a transverse crack. Mech. Syst. Sig. Process. **22**(4), 790 – 804 (2008). Special Issue: Crack Effects in Rotordynamics
10. Govaerts, W., Kuznetsov, Y.A., De Vitte, V., Dhooge, A., Meijer, M.G.E., Mestrom, W., Riet, A.M., Sautois, B.: Matcont and cl_matcont: Continuation toolboxes in matlab (2011)
11. Ishida, Y.: Cracked rotors: industrial machine case histories and nonlinear effects shown by simple jeffcott rotor. Mech. Syst. Sig. Process. **22**(4), 805 – 817 (2008). Special Issue: Crack Effects in Rotordynamics
12. Jeffcott, H.H.: Xxvii. the lateral vibration of loaded shafts in the neighbourhood of a whirling speed. The effect of want of balance. Philos. Mag. **37**(219), 304–314 (1919)
13. Kim, S., Palazzolo, A.B.: Effects of thermo hydrodynamic (THD) floating ring bearing model on rotordynamic bifurcation. Int. J. Non-Linear Mech. **95**, 30–41 (2017)
14. Li, W., Yang, Y., Sheng, D., Chen, J.: A novel nonlinear model of rotor/bearing/seal system and numerical analysis. Mech. Mach. Theory **46**(5), 618–631 (2011)
15. Ocvirk, F.W.: Short-bearing approximation for full journal bearings. Technical Report, Cornell University, 10 1952
16. Sghir, R., Chouchane, M.: Nonlinear stability analysis of a flexible rotor-bearing system by numerical continuation. J. Vibr. Control **22**(13), 3079–3089 (2016)
17. Sommerfeld, A.: Zur hydrodynamischen theorie der schmiermittelreibung. Z. Math. Phys. **50**(1–2), 97–155 (1904)
18. Vlajic, N., Champneys, A.R., Balachandran, B.: Nonlinear dynamics of a jeffcott rotor with torsional deformations and rotor-stator contact. Int. J. Non-Linear Mech. **92**, 102–110 (2017)

The Burden of the Coinfection of HIV and TB in the Presence of Multi-drug Resistant Strains

Ana Carvalho and Carla M. A. Pinto

Abstract We introduce a fractional-order model for the coinfection of the immunodeficiency virus and tuberculosis, in the presence of drug resistant tuberculosis strains and treatment for both diseases. We compute the reproduction number of the model. Numerical simulations show the different dynamics of the model for variation of relevant parameters. Moreover, the order of the fractional derivative plays an important role in the severity of the epidemics.

Keywords Tuberculosis · HIV · Resistant strains · Coinfection

1 Introduction

The human immunodeficiency virus (HIV) and the *Mycobacterium tuberculosis* (Mtb) have a synergistic relationship. In coinfected individuals, tuberculosis (TB) causes cell activation and excessive cytokine and chemokine productions. The later stimulates HIV replication and accelerates the progression to acquired immunodeficiency syndrome (AIDS). On the other hand, HIV increases twenty times the odds of TB reactivation and increases the risk of infection by multi-drug resistant strains (MDR-TB) of Mtb, since it expands the number of individuals with active TB [1, 2].

Resurgence of TB in the 1980's is attributed jointly to the emergence of MDR-TB strains and the AIDS pandemic, which led the World Health Organization (WHO) to declare TB as a global emergency in 1983. MDR-TB and, more recently, extensively

A. Carvalho
Faculty of Sciences, University of Porto, Rua do Campo Alegre s/n,
Porto 4440-452, Portugal
e-mail: up200802541@fc.up.pt

C. M. A. Pinto (✉)
School of Engineering, Polytechnic of Porto and Center for Mathematics
of the University of Porto, Rua Dr Ant ónio Bernardino
de Almeida 431, Porto 4200-072, Portugal
e-mail: cap@isep.ipp.pt

J. Awrejcewicz (ed.), *Dynamical Systems in Theoretical Perspective*,
Springer Proceedings in Mathematics & Statistics 248,
https://doi.org/10.1007/978-3-319-96598-7_8

resistant TB (XDR-TB), jeopardize TB control, and rise concerns of a future of non-effective drugs [3].

Several mathematical models have been derived with the purpose of understanding the dynamics of HIV, and TB, and of the coinfection [4–10]. In 1997, Castillo-Chavez and Feng [7], formulated a model for TB where it is possible to determine the survival and spread of naturally resistant strains of TB and resistant strains of TB generated by antibiotics. They concluded that the coexistence of the two strains only occurs in treated individuals and results from the lack of adherence to treatment. In 2012, Sergeev et al. [9] explored the effect of HIV on the dynamics of MDR-TB. An increase in the HIV viral load in coinfected individuals increased the prevalence of MDR-TB within populations. That occurred even as it lowered the average fitness of circulating MDR-TB strains, when compared to similar HIV uninfected populations. Silva and Torres [10] proposed a HIV/TB coinfection model, where treatments for latent and active TB are included. They applied optimal control techniques to derive optimal treatment protocols for HIV/TB coinfected individuals. Numerical results of the model pointed to some measures to reduce the number of individuals developing active TB and AIDS.

Fractional calculus

Fractional calculus (FC) is a generalization of the integer order calculus. It is first mentioned in the literature in 1695 in a letter exchange between L'Hôpital and Leibniz. Since then, the meaning and methods to compute $1/2$-order derivatives or, in general, α-order derivatives, with α non-integer, has been a major research in mathematics [11, 12]. Some well-known mathematicians that have devoted their work to fractional differentiation and integration are Euler, Abel, Liouville, Riemann, Grünwald, Letnikov, Caputo, amongst others [13–18].

Fractional models have been used in the literature to understand the behavior of epidemiological models, where the integer-order models fail to give a complete explanation. Pinto and Carvalho [19] proposed a fractional-order (FO) model for HIV and TB co-infection. They observed that the results from both the integer-order and the FO versions of the model provided biologically feasible results for the coinfection. Sardar et al. [20] derived three mathematical models for a common single strain mosquito-transmitted infection. The first model used ordinary differential equations to describe the patterns of the infection, whereas the other two were based on fractional order equations. The authors found that the model with memory (fractional model), in both the host and the vector population, fitted better epidemic data.

Driven by the aforementioned research, in this paper, we analyze the burden of the coinfection in a non-integer order model for HIV and TB coinfection, in the presence of drug resistant TB strains and treatment for both diseases. In Sect. 2 we introduce the model. Then, in Sect. 3, we simulate the model for distinct values of the order of the fractional derivative and two relevant parameters. The obtained the results are discussed. Finally, we conclude our work and mention future research headlines.

2 The Model

The model is composed of 13 classes. The individuals in the susceptible class, S, are recruited at a rate Λ. They are infected by HIV and TB at rates

$$\lambda_H = \frac{\beta_H(I_H + E_T I_H + RI_H + \eta_H(I_{TH} + T_R I_H))}{N}$$

and

$$\lambda_T = \frac{\beta_T(I_T + \eta_T(T_R + I_{TH} + T_R I_H))}{N}$$

respectively. Parameters β_H and β_T are the effective contact rates for HIV and TB infection, respectively. The modification parameters η_H and η_T account for the increased infectiousness of individuals coinfected with HIV and TB, when compared to individuals solely infected with either HIV or TB. We consider, for simplification, that people showing symptoms of AIDS do not infect others.

The individuals exposed to TB, E_T, develop active TB at rate ε and move to the class of infected individuals, I_T. The exposed, E_T, may also be infected with HIV at a rate λ_H and move to the class of individuals exposed to TB and infected with HIV, $E_T I_H$. Individuals I_T may recover from TB at rate γ and move to the recovered class, R. They are also resistant to the first line of TB treatment at rate σ_T, and move to the MDR-TB drug-resistant individuals' class, T_R. I_T individuals are infected with HIV at rate $\psi_3\lambda_H$, where ψ_3 captures the fact that individuals infected with TB are more infectious than the ones only exposed to TB, and move to the dually infected class, I_{TH}. The individuals infected with the MDR-TB strains, T_R, recover from TB at rate a. The recovered individuals, R, become susceptible to TB at rate ρ.

The individuals infected with HIV, I_H, develop AIDS at a rate σ_H moving to the class of patients showing symptoms of AIDS, A. They are also infected with TB at rate $\psi_1\lambda_T$, where ψ_1 is a modification parameter, and move to class $E_T I_H$. The individuals with AIDS, A, are treated at rate τ_2, and move to class I_H. They are infected with TB at rate $\psi_2\lambda_T$, where $\psi_2 > \psi_1$ are modification parameters, and move to the class of individuals exposed to TB and showing symptoms of AIDS, $E_T A$. The inequality $\psi_2 > \psi_1$ models the fact that the individuals with AIDS are more infectious than those only infected with HIV. The individuals in class $E_T I_H$, and in class $E_T A$, develop active TB at rates $\eta_1\varepsilon$ and $\eta_2\varepsilon$, and move to classes I_{TH} and $I_T A$, respectively. The class $I_T A$ are the dually infected individuals with active TB and AIDS. We note that $\eta_2 > \eta_1$, since patients with AIDS develop active TB faster than individuals infected only with HIV. The patients in class $E_T I_H$ and in class I_{TH} proceed to AIDS at rates $\theta_1\sigma_H$ and $\theta_2\sigma_H$, respectively, where $\theta_2 > \theta_1$. The later translates the fact that individuals infected with TB proceed faster to AIDS than the ones exposed to TB. The individuals in class I_{TH} and the ones in class $I_T A$ are treated at rates γ_1 and γ_2, respectively, and move to class RI_H (patients recovered from TB and infected with HIV). Moreover, patients in classes I_{TH} and $I_T A$ may also

develop MDR-TB strains at rates σ_{T1} and σ_{T2}, respectively, and move to class $T_R I_H$ (individuals dually infected with MDR-TB strains). The later recover from TB at rate a_1.

All individuals die from natural causes at rate μ. Depending on the state of infection, individuals die from the HIV, or TB, or HIV and TB coinfection at rates δ_i, $i = 1, \ldots, 9$.

The nonlinear system of fractional-order differential equations describing the dynamics of the model is:

$$
\begin{aligned}
\tfrac{d^\alpha S}{dt^\alpha} &= \Lambda^\alpha - \lambda_T S - \lambda_H S + \rho^\alpha R - \mu^\alpha S \\
\tfrac{d^\alpha E_T}{dt^\alpha} &= \lambda_T S - (\lambda_H + \varepsilon^\alpha + \mu^\alpha) E_T \\
\tfrac{d^\alpha I_T}{dt^\alpha} &= \varepsilon^\alpha E_T - (\psi_3 \lambda_H + \gamma^\alpha + \sigma_T^\alpha + \mu^\alpha + \delta_1^\alpha) I_T \\
\tfrac{d^\alpha R}{dt^\alpha} &= \gamma^\alpha I_T + a^\alpha T_R - (\rho^\alpha + \mu^\alpha) R \\
\tfrac{d^\alpha T_R}{dt^\alpha} &= \sigma_T^\alpha I_T - (a^\alpha + \mu^\alpha + \delta_2^\alpha) T_R \\
\tfrac{d^\alpha I_H}{dt^\alpha} &= \lambda_H S + \tau_2^\alpha A - (\psi_1 \lambda_T + \sigma_H^\alpha + \mu^\alpha + \delta_3^\alpha) I_H \\
\tfrac{d^\alpha A}{dt^\alpha} &= \sigma_H^\alpha I_H - (\psi_2 \lambda_T + \tau_2^\alpha + \mu^\alpha + \delta_4^\alpha) A \\
\tfrac{d^\alpha E_T I_H}{dt^\alpha} &= \lambda_H E_T + \psi_1 \lambda_T I_H + \tau_2^\alpha E_T A - (\eta_1 \varepsilon^\alpha + \theta_1 \sigma_H^\alpha + \mu^\alpha + \delta_5^\alpha) E_T I_H \\
\tfrac{d^\alpha E_T A}{dt^\alpha} &= \theta_1 \sigma_H^\alpha E_T I_H + \psi_2 \lambda_T A - (\eta_2 \varepsilon^\alpha + \tau_2^\alpha + \mu^\alpha + \delta_6^\alpha) E_T A \\
\tfrac{d^\alpha I_{TH}}{dt^\alpha} &= \eta_1 \varepsilon^\alpha E_T I_H + \psi_3 \lambda_H I_T - (\gamma_1^\alpha + \sigma_{T1}^\alpha + \theta_2 \sigma_H^\alpha + \mu^\alpha + \delta_7^\alpha) I_{TH} \\
\tfrac{d^\alpha I_T A}{dt^\alpha} &= \theta_2 \sigma_H^\alpha I_{TH} + \eta_2 \varepsilon^\alpha E_T A - (\gamma_2^\alpha + \sigma_{T2}^\alpha + \mu^\alpha + \delta_8^\alpha) I_T A \\
\tfrac{d^\alpha R I_H}{dt^\alpha} &= \gamma_1^\alpha I_{TH} + \gamma_2^\alpha I_T A + a_1^\alpha T_R I_H - (\mu^\alpha + \delta_3^\alpha) R I_H \\
\tfrac{d^\alpha T_R I_H}{dt^\alpha} &= \sigma_{T1}^\alpha I_{TH} + \sigma_{T2}^\alpha I_T A - (a_1^\alpha + \mu^\alpha + \delta_9^\alpha) T_R I_H
\end{aligned}
\tag{1}
$$

where $\lambda_H = \frac{\beta_H^\alpha (I_H + E_T I_H + R I_H + \eta_H (I_{TH} + T_R I_H))}{N}$ and $\lambda_T = \frac{\beta_T^\alpha (I_T + \eta_T (T_R + I_{TH} + T_R I_H))}{N}$.

Parameter $\alpha \in (0, 1]$ is the order of the fractional derivative. When $\alpha = 1$, then the model is the integer order counterpart. The fractional derivative of the proposed model is used in the Caputo sense, i.e.:

$$\frac{d^\alpha y(t)}{dt^\alpha} = I^{p-\alpha} y^{(p)}(t), \quad t > 0$$

where $p = [\alpha]$ is the value of α rounded up to the nearest integer, $y^{(p)}$ is the p-th derivative of $y(r)$, I^{p_1} is the Riemann-Liouville fractional integral given by:

$$I^{p_1} z(t) = \frac{1}{\Gamma(p_1)} \int_0^t \left(t - t'\right)^{p_1 - 1} z(t')dt'$$

We compute the reproduction number of model (1), R_0, using the next generation method [21]. R_0 is defined as the number of secondary infections due to an infected individual in a completely susceptible population. The associative basic reproduction number is given by:

$$R_0 = \max\{R_T, R_H\} \tag{2}$$

where

$$R_T = \frac{\varepsilon^\alpha \beta_T^\alpha (\eta_T \sigma_T^\alpha + a^\alpha + \delta_2^\alpha + \mu^\alpha)}{(\varepsilon^\alpha + \mu^\alpha)(\gamma^\alpha + \sigma_T^\alpha + \mu^\alpha + \delta_1^\alpha)(a^\alpha + \mu^\alpha + \delta_2^\alpha)} \tag{3}$$

is the reproduction number for the TB-only submodel.

$$R_H = \frac{\beta_H^\alpha (\tau_2^\alpha + \mu^\alpha + \delta_4^\alpha)}{(\mu^\alpha + \delta_3^\alpha)(\mu^\alpha + \delta_4^\alpha + \tau_2^\alpha) + \sigma_H^\alpha (\mu^\alpha + \delta_4^\alpha)} \tag{4}$$

is the reproduction number for the HIV-only submodel. We have the following lemma:

Lemma 1 *The disease-free equilibrium P_0 is locally asymptotically stable if all eigenvalues λ_i of the linearization matrix of model (1), satisfy $|\arg(\lambda_i)| > \alpha \frac{\pi}{2}$.*

3 Numerical Results

We simulate the model (1) for different values of the order of the fractional derivative, α and for parameters η_H and η_T. The parameters used in the simulations, based on [4, 6], are $\Lambda = 50000$, $\beta_T = 0.75$, $\eta_T = 1.02$, $\beta_H = 0.2$, $\eta_H = 1.05$, $\rho = 0.05$, $\mu = 0.02$, $\psi_3 = 1.03$, $\varepsilon = 0.25$, $\gamma = 0.15$, $\sigma_T = 0.003$, $\delta_1 = 0.01$, $a = 0.11$, $\delta_2 = 0.02$, $\tau_2 = 0.08$, $\psi_1 = 1.1$, $\psi_2 = 1.2$, $\sigma_H = 0.15$, $\delta_3 = 0.01$, $\delta_4 = 0.02$, $\eta_1 = 1.5$, $\theta_1 = 1.02$, $\delta_5 = 0.1$, $\eta_2 = 1.8$, $\delta_6 = 0.03$, $\gamma_1 = 0.13$, $\sigma_{T1} = 0.005$, $\gamma_2 = 0.11$, $\sigma_{T2} = 0.005$, $\alpha_1 = 0.10$, $\theta_2 = 2.5$, $\delta_7 = 0.03$, $\delta_8 = 0.03$, $\delta_9 = 0.03$, and the inicial conditions are: $S(0) = 500$, $E_T(0) = A(0) = 50$, $I_T(0) = 25$, $R(0) = 10$, $T_R(0) = 5$, $I_H(0) = 100$ and $E_T I_H(0) = E_T A(0) = I_{TH}(0) = I_T A(0) = R I_H(0) = T_R I_H(0) = 10$.

In Figs. 1 and 2, it is shown the dynamics of the variables of system (1) for different values of η_T, the parameter that accounts for the increased infectiousness of individuals coinfected with HIV and TB, when compared to individuals solely infected with TB, and for two values of α. We observe that as η_T increases, there

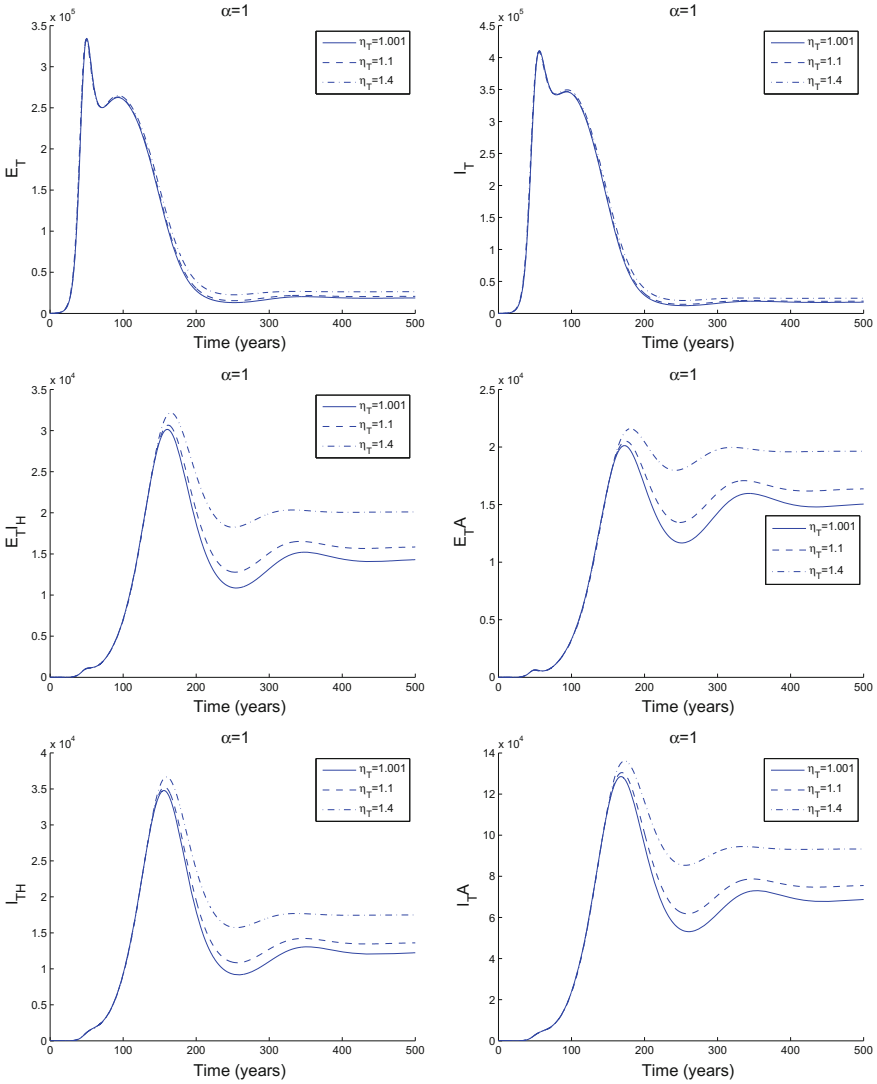

Fig. 1 Dynamics of the relevant variables of system (1) for different values of η_T, which accounts for the increased infectiousness of individuals coinfected with HIV and TB, when compared to individuals solely infected with TB. Parameter values and initial conditions in the text ($\eta_T = 1.001$ - $R_T = 3.8707, R_H = 2.5, R_0 = 3.8707, \eta_T = 1.1$ - $R_T = 3.8783, R_H = 2.5, R_0 = 3.8783, \eta_T = 1.4$ - $R_T = 3.9010, R_H = 2.5, R_0 = 3.9010$)

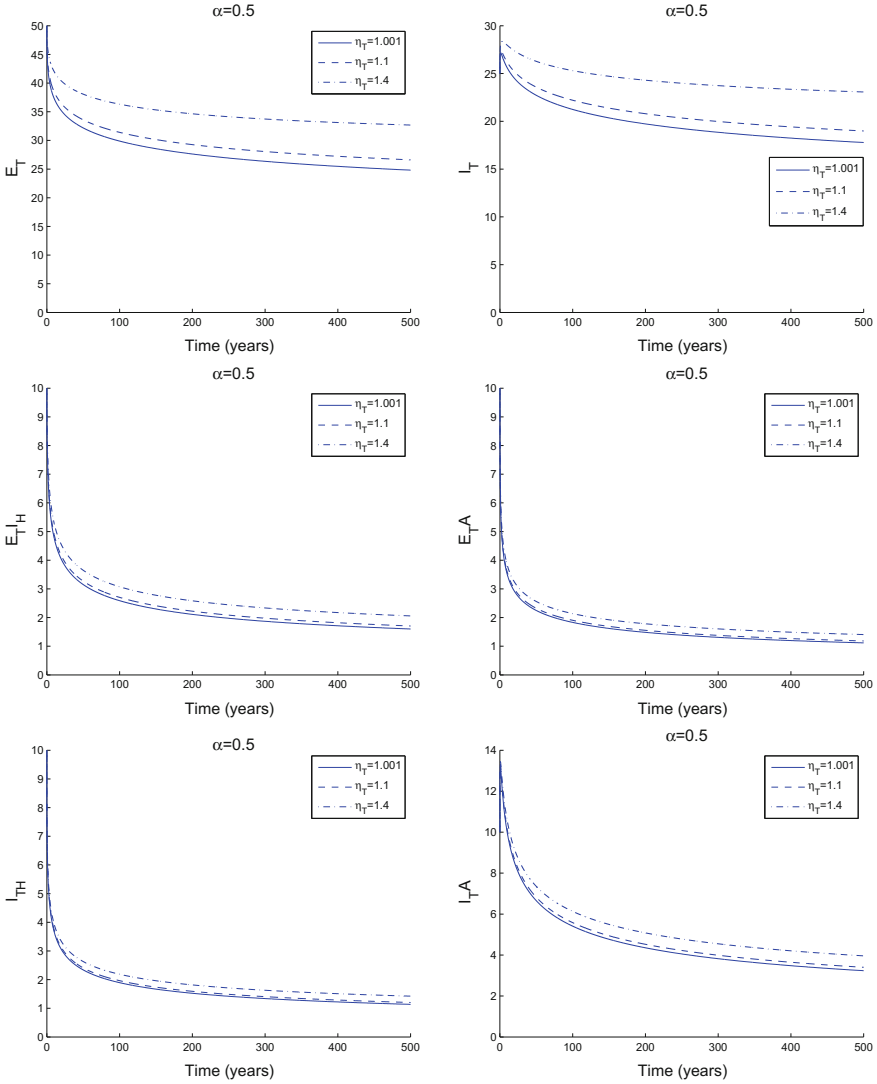

Fig. 2 Dynamics of the relevant variables of system (1) for different values of η_T, which accounts for the increased infectiousness of individuals coinfected with HIV and TB, when compared to individuals solely infected with TB. Parameter values and initial conditions in the text ($\eta_T = 1.001$ - $R_T = 1.0873, R_H = 1.0279, R_0 = 1.0873$, $\eta_T = 1.1$ - $R_T = 1.1440, R_H = 1.0279, R_0 = 1.1440$, $\eta_T = 1.4$ - $R_T = 1.3159, R_H = 1.0279, R_0 = 1.3159$)

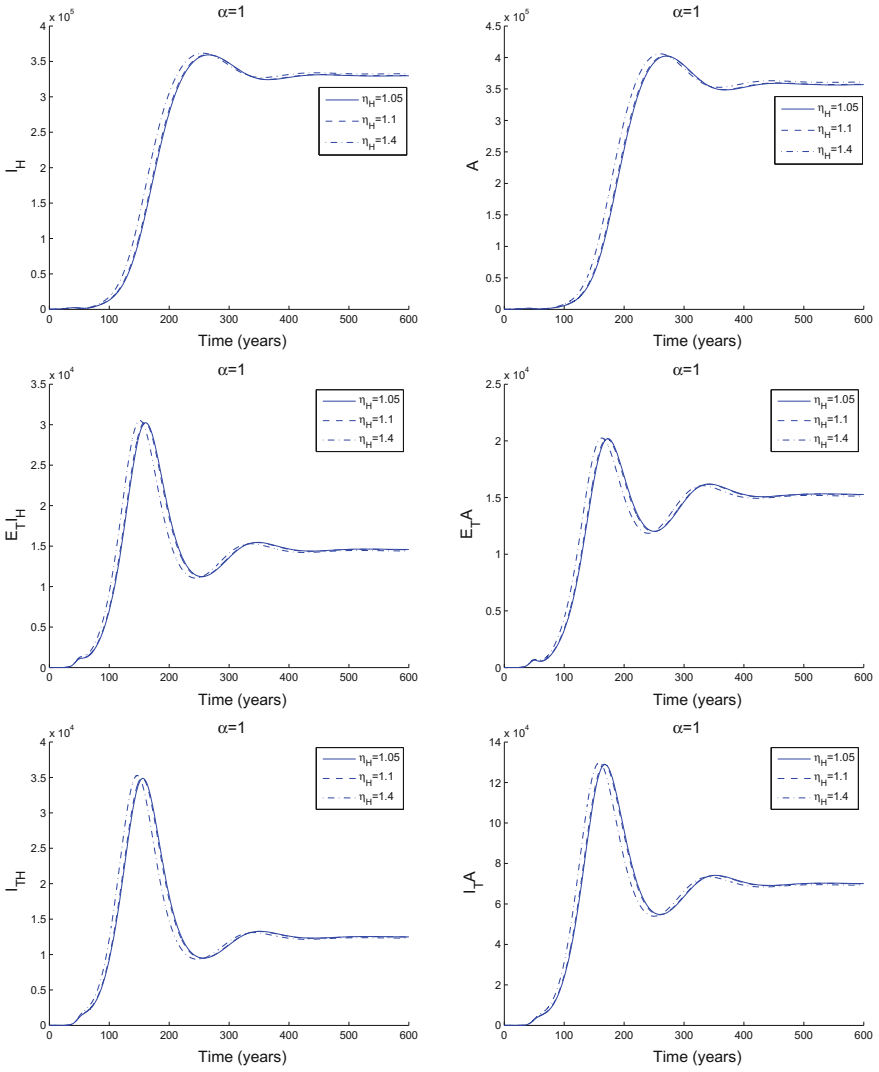

Fig. 3 Dynamics of the relevant variables of system (1) for different values of η_H, which accounts for the increased infectiousness of individuals coinfected with HIV and TB, when compared to individuals solely infected with HIV. Parameter values and initial conditions in the text ($R_T = 3.8722$, $R_H = 2.5$, $R_0 = 3.8722$)

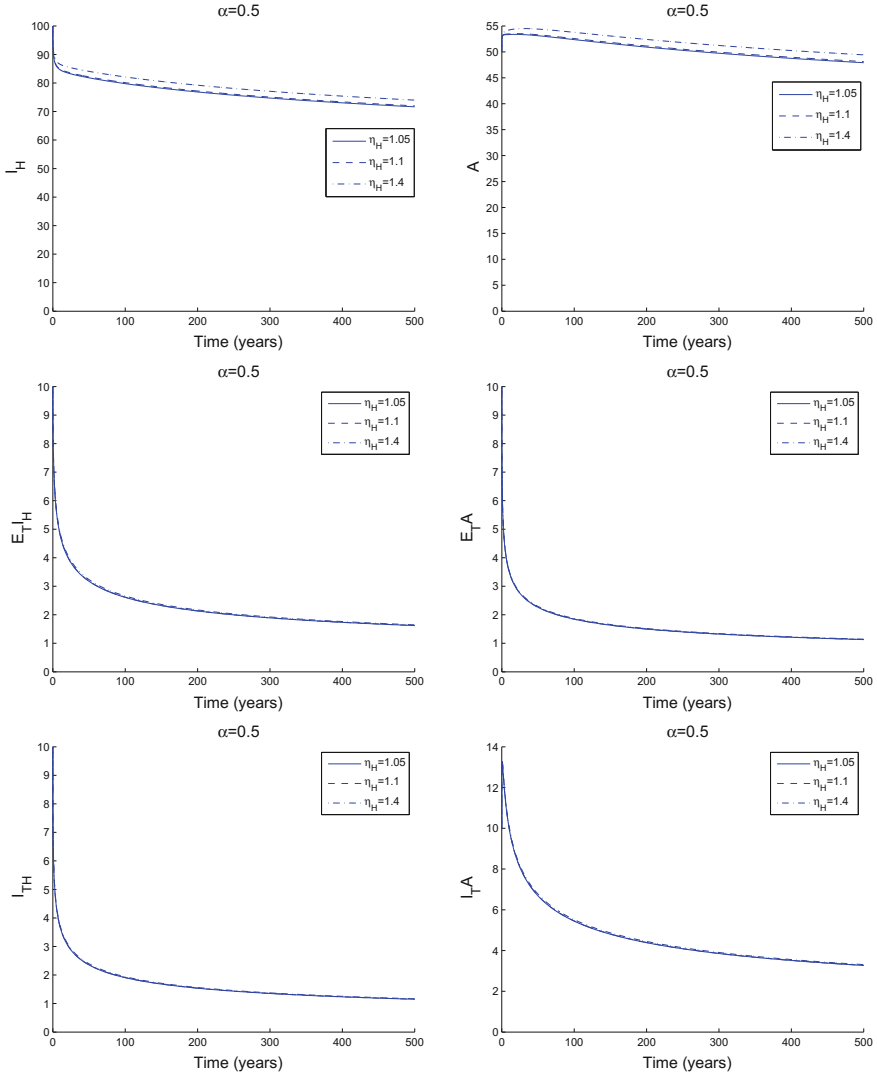

Fig. 4 Dynamics of the relevant variables of system (1) for different values of η_H, which accounts for the increased infectiousness of individuals coinfected with HIV and TB, when compared to individuals solely infected with HIV. Parameter values and initial conditions in the text ($R_T = 1.0982$, $R_H = 1.0279$, $R_0 = 1.0982$)

is an overall increase in individuals, exposed and actively infected with TB and coinfected with HIV and TB, showing or not symptoms of AIDS. This suggests a higher disease burden for coinfected individuals, with AIDS and TB fuelling each other's symptoms. The patterns of the model are similar for the two values of the order of the fractional derivative, α. Though, the severity of the disease (in terms of higher number of infected individuals) decreases with α. The corresponding values of the reproduction number, R_0, are calculated and validate this behaviour, i.e., smaller values of R_0 are obtained for increased values of α.

In Figs. 3 and 4, it is depicted the dynamics of the variables of system (1) for different values of η_H, which refers to the increased infectiousness of individuals coinfected with HIV and TB, when compared to individuals solely infected with HIV, and two values of α. As η_H increases, there is an overall increase of the number of infected individuals, either with HIV, xor TB, or both, in the first few years of the infection. This is epidemiologically relevant since we expect heavier symptoms, due to weakened immune systems, in the presence of both HIV and Mtb in the organism. Then, as time goes by, and people get treatment for TB, they evolve favourably from TB, but infection by HIV persists. Similar dynamics occur for the two simulated values of α.

The results of the model appear to be biologically reasonable. We note that the model may be adjusted to fit real data from HIV and TB solely and coinfected individuals. This will be considered in our future work.

4 Conclusions

We proposed a FO model for the coinfection of HIV and TB, in the presence of MDR-TB strains. We analysed the model's behaviour for distinct values of the order of the fractional derivative, α, and for two epidemiologically relevant parameters η_H and η_T, which accounted for the increased infectiousness of individuals coinfected with HIV and TB, when compared to individuals solely infected with either HIV xor TB. We observed that the coinfection burden (translated by higher values of η_H and η_T) increased the severity of the disease, i.e., augments the number of infected individuals. This was observed for distinct values of α. Moreover, the burden of the coinfection seemed to be reduced with α. In future work, fitting of real data by the proposed model will be considered.

Acknowledgements The authors were partially funded by the European Regional Development Fund through the program COMPETE and by the Portuguese Government through the FCT - Fundação para a Ciência e a Tecnologia under the project PEst-C/MAT/UI0144/2013. The research of AC was partially supported by a FCT grant with reference SFRH/BD/96816/2013.

References

1. Madariaga, M.G., Lalloo, U.G., Swindells, S.: Extensively drug-resistant tuberculosis. Am. J. Med. **121**(10), 835–844 (2008)
2. The World Health Organization (WHO): Global Tuberculosis Report (2016)
3. Gandhi, N.R., Nunn, P., Dheda, K., Schaaf, H.S., Zignol, M., Van Soolingen, D., Jensen, P., Bayona, J.: Multidrug-resistant and extensively drug-resistant tuberculosis: a threat to global control of tuberculosis. Lancet **375**, 1830–1843 (2010)
4. Agusto, F.B., Adekunle, A.I.: Optimal control of a two-strain tuberculosis-HIV/AIDS co-infection model. BioSystems **119**, 20–44 (2014)
5. Bacaër, N.N., Ouifki, R., Pretorius, C., Wood, R., Williams, B.: Modeling the joint epidemics of TB and HIV in a South African township. J. Math. Biol. **57**(4), 557–593 (2008)
6. Bhunu, C.P., Garira, W., Mukandavire, Z.: Modeling HIV/AIDS and tuberculosis coinfection. Bull. Math. Biol. **71**, 1745–1780 (2009)
7. Castillo-Chavez, C., Feng, Z.: To treat or not to treat: the case of tuberculosis. J. Math. Biol. **35**, 629–656 (1997)
8. Denysiuk, R., Silva, C.J., Torres, D.F.M.: Multiobjective approach to optimal control for a tuberculosis model. Optim. Methods Softw. **30**(5), (2015)
9. Sergeev, R., Colijn, C., Murray, M., Cohen, T.: Modeling the dynamic relationship between HIV and the risk of drug-resistant tuberculosis. Sci. Transl. Med. **4**(135), 135–167 (2012)
10. Silva, C.J., Torres, D.F.M.: A TB-HIV/AIDS coinfection model and optimal control treatment. Discrete Continuous Dyn. Syst. - A **35**(9), 4639–4663 (2015)
11. Ezz-Eldien, S.S., Doha, E.H., Bhrawy, A.H., El-Kalaawy, A.A., Machado, J.T.A.: A new operational approach for solving fractional variational problems depending on indefinite integrals. Commun. Nonlinear Sci. Numer. Simul. **57**, 246–263 (2017)
12. Nigmatullin, R.R., Zhang, W., Gubaidullin, I.: Accurate relationships between fractals and fractional integrals: new approaches and evaluations. Fractional Calc. Appl. Anal. **20**(5), 1263–1280 (2017)
13. Carvalho, A.R.M., Pinto, C.M.A., Baleanu, D.: HIV/HCV coinfection model: a fractional-order perspective for the effect of the HIV viral load. Adv. Differ. Equ. **2018**(1), 1–22 (2018)
14. Copot, D., De Keyser, R., Derom, E., Ortigueira, M., Ionescu, C.M.: Reducing bias in fractional order impedance estimation for lung function evaluation. Biomed. Sig. Process. Control **39**, 74–80 (2018)
15. Oldham, K., Spanier, J.: The Fractional Calculus: Theory and Application of Differentiation and Integration to Arbitrary Order. Academic Press, New York, NY (1974)
16. Samko, S., Kilbas, A., Marichev, O.: Fractional Integrals and Derivatives: Theory and Applications. Gordon and Breach Science Publishers, London (1993)
17. Ventura, A., Tejado, I., Valério, D., Martins, J.: Fractional direct and inverse models of the dynamics of a human arm. J. Vibr. Control **22**(9), 2240–2254 (2016)
18. Wu, G.C., Baleanu, D., Huang, L.L.: Novel Mittag-Leffler stability of linear fractional delay difference equations with impulse. Appl. Math. Lett. **82**, 71–78 (2018)
19. Pinto, C.M.A., Carvalho, A.R.M.: New findings on the dynamics of HIV and TB coinfection models. Appl. Math. Comput. **242**, 36–46 (2014)
20. Sardar, T., Rana, S., Bhattacharya, S., Al-Khaled, K., Chattopadhyay, J.: A generic model for a single strain mosquito-transmitted disease memory on the host and the vector. Math. Biosci. **263**, 18–36 (2015)
21. Driessche, P., Watmough, P.: Reproduction numbers and sub-threshold endemic equilibria for compartmental models of disease transmission. Math. Biosci. **180**, 29–48 (2002)

Value Distribution and Growth of Solutions of Certain Painlevé Equations

Ewa Ciechanowicz and Galina Filipuk

Abstract As a result of classification of second order ordinary differential equations without movable branch points, a number of the so-called Painlevé equations was obtained. Among them, six irreducible equations are the best known. They led to the recognition of new functions, called the Painlevé transcendents. The Painlevé equations have numerous applications in modern mathematics and mathematical physics. The solutions of these equations, as they are meromorphic in the complex plane can be studied from the perspective of value distribution and growth theory, with such values as defect, deviation or multiplicity index estimated.

Keywords Meromorphic function · Painlevé equation · Defective value

Mathematics Subject Classification: Primary 30D35 · Secondary 34M05 34M55

1 Introduction

During 1895–1910 Painlevé and his student Gambier studied the problem posed by Picard [15] of finding second order ordinary differential equations of the form

$$f'' = F(z, f, f'),\ f = f(z),\quad ' = \mathrm{d}/\mathrm{d}z, \tag{1}$$

The author gave a presentation of this paper during one of the conference sessions.

E. Ciechanowicz (✉)
Faculty of Mathematics and Physics, University of Szczecin,
ul. Wielkopolska 15, 70-451 Szczecin, Poland
e-mail: ewa.ciechanowicz@usz.edu.pl

G. Filipuk
Faculty of Mathematics, Informatics and Mechanics,
University of Warsaw, Banacha 2, 02-097 Warsaw, Poland
e-mail: filipuk@mimuw.edu.pl

J. Awrejcewicz (ed.), *Dynamical Systems in Theoretical Perspective*,
Springer Proceedings in Mathematics & Statistics 248,
https://doi.org/10.1007/978-3-319-96598-7_9

where F is rational in f, algebraic in f' and analytic in z, with the property that movable singularities (which depend on initial data) of solutions are at most poles. This property was later referred to as the *Painlevé property* and the equations were called *equations of Painlevé type* or *P-type equations*. Painlevé and Gambier found fifty P-type differential equations of the form (1) ([3, 12], see also [8]). Among those, the following six equations are considered to be the most important:

$$f'' = 6f^2 + z, \tag{P_1}$$

$$f'' = 2f^3 + zf + \alpha, \tag{P_2}$$

$$f'' = \frac{(f')^2}{f} - \frac{1}{z}f' + \frac{1}{z}(\alpha f^2 + \beta) + \gamma f^3 + \frac{\delta}{f}, \tag{P_3}$$

$$f'' = \frac{f'^2}{2f} + \frac{3f^3}{2} + 4zf^2 + 2(z^2 - \alpha)f + \frac{\beta}{f}, \tag{P_4}$$

$$f'' = \frac{3f-1}{2f(f-1)}(f')^2 - \frac{1}{z}f' + \frac{1}{z^2}(f-1)^2(\alpha f + \frac{\beta}{f}) + \frac{\gamma f}{z} + \frac{\delta f(f+1)}{f-1}, \tag{P_5}$$

$$\begin{aligned} f'' = {} & \frac{1}{2}\left(\frac{1}{f} + \frac{1}{f-1} + \frac{1}{f-z}\right)(f')^2 - \left(\frac{1}{z} + \frac{1}{z-1} + \frac{1}{f-z}\right)f' \\ & + \frac{f(f-1)(f-z)}{z^2(z-1)^2}\left(\alpha + \beta\frac{z}{f^2} + \gamma\frac{z-1}{(f-1)^2} + \delta\frac{z(z-1)}{(f-z)^2}\right), \end{aligned} \tag{P_6}$$

where $\alpha, \beta, \gamma, \delta$ are fixed complex parameters and $f = f(z)$.

Apart from movable poles and a singularity at infinity, the solutions of P_3, P_5 and P_6 also have a singularity at 0, and P_6 also at 1. This singularity structure suggests that in case of P_1, P_2 and P_4 local solutions can be extended to meromorphic functions in the complex plane. Recent proofs of this fact were given by Hinkkanen and Laine in [7], Steinmetz in [21] and Shimomura in [17]. It follows that the solutions of P_1, P_2, P_4, and, after a suitable substitution, of modified P_3 and P_5 equations are meromorphic functions in the plane and they can be examined by methods of value distribution theory [6]. In this paper we concentrate on P_1, P_2 and P_4 and an additional equation, the so-called P_{34}, given by

$$f'' = \frac{(f')^2}{2f} + 2Bf^2 - Bzf - \frac{A}{2f}, \qquad P_{34}(A, B)$$

where A, B are complex parameters and which is connected with P_2 via the Hamiltonian system. We review the known and present some recent results for these equations.

2 Value Distribution and Growth of Meromorphic Functions

We say that a complex function of a complex variable is meromorphic in a region D if it is holomorphic in D, possibly apart from isolated points where it has poles. In the paper, whenever we say that a function is meromorphic, we mean that it is a function meromorphic in the whole complex plane.

By Picard theorem, a transcendental entire function assumes every finite value possibly except one, whereas a transcendental meromorphic function in the plane assumes every value in $\overline{\mathbb{C}}$ infinitely often apart from at most two exceptions [14]. Here the term *transcendental* simply means non-rational.

2.1 Nevanlinna Theory

Modern theory of value distribution of meromorphic functions was introduced in the 1920's in the papers of Rolph Nevanlinna. A meromorphic function f is characterized by a real-valued function

$$T(r,f) := m(r,\infty,f) + N(r,\infty,f),$$

the Nevanlinna characteristic function of f. Here

$$m(r,\infty,f) = \frac{1}{2\pi}\int_0^{2\pi} \log^+ |f(re^{i\theta})|\mathrm{d}\theta$$

denotes a mean proximity (to infinity) function and

$$N(r,\infty,f) = \int_0^r [n(t,\infty,f) - n(0,\infty,f)]\frac{\mathrm{d}t}{t} + n(0,\infty,f)\log r$$

is a function counting poles ($n(t,\infty,f)$ is the number of poles of f in the disc $\{z : |z| \le t\}$, counted with multiplicity, $n(0,\infty,f)$ is the multiplicity of a pole at zero). The integrated counting function $N(r,\infty,f)$ grows with r, $m(r,\infty,f)$ in general does not. Nevertheless, $T(r,f)$ is a nondecreasing, convex function of $\log r$.

For a number $a \in \mathbb{C}$ we can consider accompanying functions

$$m(r,a,f) := m(r,\infty,\frac{1}{f-a}) \quad \text{and} \quad N(r,a,f) := N(r,\infty,\frac{1}{f-a})$$

measuring mean proximity of f to a on the circle and the density of distribution of $a-$points of f in the disc, respectively. Nevanlinna, applying the notions presented above, transformed the Poisson-Jensen formula into the following form.

Theorem 1 [11] *For any function f meromorphic in $|z| < R \leq \infty$ the equality*

$$m(r,a,f) + N(r,a,f) = T(r,f) + \phi(r,a) \tag{2}$$

holds for each $a \in \overline{\mathbb{C}}$, where $|\phi(r,a)| \leq \log^+ |a| + |\log |c|| + \log 2$, c is the first non-vanishing coefficient of the Laurent expansion of $f - a$ at zero.

Theorem 1, known as the First Main Theorem of Nevanlinna, says that the sum $m(r,a,f) + N(r,a,f)$ is relatively independent from the choice of the value $a \in \overline{\mathbb{C}}$.

The Second Main Theorem of Nevanlinna, on the other hand, shows that for most values a the main role in the invariant sum (2) belongs to the counting function $N(r,a,f)$.

Theorem 2 [11] *Let f be a meromorphic function and $\{a_k\}_{k=1}^q \in \overline{\mathbb{C}}$ be a finite set of distinct values. The following inequality is true*

$$\sum_{k=1}^{q} m(r,a_k,f) \leq 2T(r,f) + O(\log(rT(r,f))) \tag{3}$$

for $r \to \infty$, possibly outside of a set $E \subset [0,\infty)$ of finite linear measure.

Inequality (3) in the Second Main Theorem can also be formulated in the following way:

$$(q-2)T(r,f) \leq \sum_{k=1}^{q} \overline{N}(r,a_k,f) + O(\log(rT(r,f))), \tag{4}$$

where $\overline{N}(r,a,f)$ is the integrated function counting each a-point once, regardless of its multiplicity.

For various purposes it is necessary to estimate not only the sum of multiplicities of a-points, which is done by means of $N(r,a,f)$, but also the number of a-points itself and the number of multiple a-points. Thus, we can introduce the function

$$N_1(r,a,f) := N(r,a,f) - \overline{N}(r,a,f).$$

It means that $N_1(r,a,f)$ does not include simple a-points, and each multiple a point of multiplicity m is counted $m-1$ times. By $\vartheta(a,f)$ we denote the index of multiplicity (ramification index) of a value a,

$$\vartheta(a,f) = \liminf_{r\to\infty} \frac{N_1(r,a,f)}{T(r,f)}.$$

If $\vartheta(a,f) > 0$ we say that a is *a ramified value*. It follows from the inequality (4) that

$$\sum_{a\in\overline{\mathbb{C}}} \vartheta(a,f) \leq 2.$$

Value distribution theory refers to $a \in \overline{\mathbb{C}}$ as a defective (exceptional, deficient) value of f if this value is assumed by f relatively less frequently. This notion does not apply to rational functions, as they take up each value at most a finite number of times. Thus a is *a Picard defective value* of a transcendental function f if f has only a finite number of a-points. *A Nevanlinna defective value*, on the other hand, is a value for which the condition

$$\delta(a,f) := \liminf_{r\to\infty} \frac{m(r,a,f)}{T(r,f)} = 1 - \limsup_{r\to\infty} \frac{N(r,a,f)}{T(r,f)} > 0$$

holds. The First Main Theorem of Nevanlinna implies that for all $a \in \overline{\mathbb{C}}$, *Nevanlinna defect* $\delta(a,f)$ fulfills the inequality

$$0 \le \delta(a,f) \le 1. \tag{5}$$

The Second Main Theorem, on the other hand, means that the set of Nevanlinna defective values is at most countable and

$$\sum_{a\in\overline{\mathbb{C}}} \delta(a,f) \le 2. \tag{6}$$

The rate of growth of a polynomial is fully determined by its degree. The growth of a meromorphic function can be described with respect to the characteristic. Values

$$\rho := \limsup_{r\to\infty} \frac{\log T(r,f)}{\log r} \quad \text{and} \quad \lambda := \liminf_{r\to\infty} \frac{\log T(r,f)}{\log r}$$

are called, respectively, *order* and *lower order* of a meromorphic function f. Thus, all rational functions are of order 0, $\exp z$ is of order 1 and $\exp(\exp z)$ is of infinite order.

2.2 Petrenko's Theory

Proximity of a meromorphic function to a value a may also be estimated by means of a different metric. In 1969 Petrenko introduced the function

$$\mathscr{L}(r,a,f) := \begin{cases} \max\limits_{|z|=r} \log^+ |f(z)| & \text{for } a = \infty, \\ \max\limits_{|z|=r} \log^+ |f(z)-a|^{-1} & \text{for } a \neq \infty. \end{cases}$$

Hence, $a \in \overline{\mathbb{C}}$ is *a defective value in the sense of Petrenko* if

$$\beta(a,f) := \liminf_{r\to\infty} \frac{\mathscr{L}(r,a,f)}{T(r,f)} > 0.$$

The quantity $\beta(a,f)$ is called *Petrenko's deviation*. It is easy to notice that for all $a \in \overline{\mathbb{C}}$ we have $\delta(a,f) \leq \beta(a,f)$. Therefore, the set of defective values in the sense of Nevanlinna is a subset of the set of Petrenko's defective values. If f is of infinite order, it is possible that $\beta(a,f) = \infty$. Indeed, $\beta(\infty, \exp(\exp z)) = \infty$. For meromorphic functions of finite lower order λ we have upper estimates of $\beta(a,f)$ parallel to the Nevanlinna defect relations (5) and (6). In 1969 Petrenko showed [13] that if f is a meromorphic function of finite lower order λ, then for all $a \in \overline{\mathbb{C}}$ we have

$$\beta(a,f) \leq B(\lambda) := \begin{cases} \frac{\pi\lambda}{\sin\pi\lambda} & \text{if } \lambda \leq 0.5\,, \\ \pi\lambda & \text{if } \lambda > 0.5\,, \end{cases} \tag{7}$$

and in 1990 Marchenko and Shcherba proved the inequality [10]

$$\sum_{a\in\overline{\mathbb{C}}} \beta(a,f) \leq 2B(\lambda). \tag{8}$$

Gol'dberg, Eremenko and Sodin in 1987 [4, 5] gave a full answer to the question of the relationship between the sets of defective values in the sense of Nevanlinna and in the sense of Petrenko. They proved that for any two fixed, at most countable sets E_1, E_2 such that $E_1 \subset E_2 \subset \overline{\mathbb{C}}$ and for any fixed number $\rho > 0$ we can find a meromorphic function of order ρ such that E_1 is the set of Nevanlinna's defective values and E_2 is the set of Petrenko's defective values of f.

3 Value Distribution of Painlevé Transcendents

This section is devoted to review of the basic features of transcendental meromorphic solutions of the equations P_1, P_2, P_4 and P_{34}, including the finiteness of order of growth, relatively regular distribution of values and limits for ramification indices. We conclude with a new estimate of Petrenko's deficiency for solutions of P_1.

3.1 Order of Growth

The following theorem gives estimates of growth for solutions of P_1.

Theorem 3 *The solutions of the Painlevé equation P_1 are transcendental meromorphic functions of finite growth order $\rho(f) = 5/2$. Moreover, they are of regular growth, that is $\lambda(f) = \rho(f)$.*

The result was known since 1913–14 and the papers of Boutroux, but the rigorous proofs were given by Steinmetz in 2002 [22] and, independently, by Shimomura in 2001 [16] and in 2003 [17]. The same authors also proved the following estimates of the growth of transcendental solutions of P_2 and P_4.

Theorem 4 *Solutions of P_2 fulfill the condition*

$$T(r,f) = O(r^3) \qquad (r \to \infty),$$

while for solutions of P_4 the equality

$$T(r,f) = O(r^4) \qquad (r \to \infty)$$

holds. Thus, $\rho(f) \leq 3$ in the first case and $\rho(f) \leq 4$ in the second.

Apart from solutions of order 3, equation P_2 may admit rational solutions and solutions of order $3/2$ for some values of the parameter of the equation. Similarly, apart from solutions of order 4, equation P_4 may admit rational solutions and solutions of order 2 for some values of the parameters. Solutions corresponding to order $3/2$ for P_2 and to order 2 for P_4 are classical special function solutions. It is conjectured that, in both cases, no other values of order of solutions are possible.

Ciechanowicz and Filipuk in 2017 [2], applying known results for P_2 presented above, obtained the following estimate of growth of solutions of P_{34}.

Theorem 5 *Solutions of $P_{34}(A, B)$ are meromorphic functions in $\mathbb{C}$, of order $\rho(f) \leq 3$. In particular, if $B = 0$ the solutions are polynomial*

$$f(z) = \frac{(C_1^2 - A)}{4C_2} z^2 + C_1 z + C_2,$$

so $\rho(f) = 0$ in this case.

3.2 Nevanlinna Defective Values

All solutions of equation P_1 are transcendental, that is the equation does not admit rational solutions. The well-known estimates of defects for solutions of P_1 were given by Schubart and Wittich in 1957 [19].

Theorem 6 *For solutions of P_1 for every $a \in \overline{\mathbb{C}}$, we have $m(r, a, f) = O(\log r)$ and $\delta(a, f) = 0$.*

The estimates of defects for transcendental solutions of P_2 were given by Schubart in 1956 [18] and by Schubart and Wittich in 1957 [19].

Theorem 7 *Transcendental solutions of $P_2(\alpha)$ fulfill the conditions:*

1. *if $\alpha \neq 0$, then, for every $a \in \overline{\mathbb{C}}$, we have $m(r,a,f) = O(\log r)$ and $\delta(a,f) = 0$;*
2. *if $\alpha = 0$ for every $a \in \overline{\mathbb{C}} \setminus \{0\}$ we have $m(r,a,f) = O(\log r)$ and $\delta(a,f) = 0$, and for $a = 0$ we have $m(r, \frac{1}{f}) \leq \frac{1}{2}T(r,f) + O(\log r)$ and $\delta(0,f) \leq \frac{1}{2}$.*

Is should be added that Steinmetz in 2013 [23] proved that $\delta(0,f) = 0$ also for all transcendental solutions of $P_2(0)$. Let us now recall the estimates for transcendental solutions of P_4 which were originally given by Steinmetz in 1982 [20].

Theorem 8 *Transcendental solutions of $P_4(\alpha,\beta)$ fulfill the conditions:*

1. *if $\beta \neq 0$, then for $a \in \overline{\mathbb{C}}$ we have $m(r,a,f) = O(\log r)$ and $\delta(a,f) = 0$;*
2. *if $\beta = 0$ and $a \neq 0$, then we have $m(r,a,f) = O(\log r)$ and $\delta(a,f) = 0$;*
3. *if $\beta = 0$ and if f does not satisfy the Riccati differential equation*

$$f' = \pm(f^2 + 2zf),$$

then

$$m(r, \frac{1}{f}) \leq \frac{1}{2}T(r,f) + O(\log r) \quad \text{and} \quad \delta(0,f) \leq \frac{1}{2}.$$

If a solution of $P_4(\alpha,0)$ satisfies $f' = \pm(f^2 + 2zf)$, then $\alpha = \mp 1$ and $\delta(0,f) = 1$.

In the same paper Steinmetz also presented the following example. The equation

$$2ff'' = (f')^2 + 3f^4 + 8zf^3 + 4(z^2-1)f^2 \qquad P_4(1,0)$$

is solved by $f(z) = \left(e^{z^2}\int_0^z e^{-t^2}dt\right)^{-1}$. Here f solves the Riccati equation

$$f' = -(f^2 + 2zf),$$

and $f(z) \neq 0$, so zero is defective in every sense. In particular, $\delta(0,f) = 1$.

Estimates of defects of transcendental solutions of P_{34} were given by Filipuk and Ciechanowicz in [1, 2].

Theorem 9 *Transcendental meromorphic solutions of $P_{34}(A,B)$ satisfy the following conditions:*

1. *$m(r,a,f) = O(\log r)$ and $\delta(a,f) = 0$ for all $a \in \overline{\mathbb{C}} \setminus \{0\}$;*
2. *if $A \neq 0$, then $m(r,1/f) = O(\log r)$ and $\delta(0,f) = 0$;*
3. *if $A = 0$, then $m(r,1/f) \leq \frac{1}{2}T(r,f) + O(\log r)$ and $\delta(0,f) \leq \frac{1}{2}$.*

3.3 Multiplicity and Ramification Indices

Like in the case of defects, the ramification estimates for P_1 were also obtained by Schubart and Wittich in 1957 [19].

Theorem 10 *Transcendental solutions of P_1 fulfill the conditions:*

1. *for every $a \in \mathbb{C}$ we have $N_1(r,a,f) \leq \frac{1}{6}T(r,f) + O(\log r)$ and $\vartheta(a,f) \leq \frac{1}{6}$;*
2. *$N_1(r,f) = \frac{1}{2}T(r,f) + O(\log r)$ and $\vartheta(\infty,f) = \frac{1}{2}$.*

The following estimates of ramification indices for P_2 were given by Kiessling in 1996 [9].

Theorem 11 *Transcendental solutions of P_2 fulfill the conditions:*

1. *for every $a \in \mathbb{C} \setminus \{0\}$ we have $N_1(r, \frac{1}{f-a}) \leq \frac{1}{4}T(r,f) + O(\log r)$ and $\vartheta(a,f) \leq \frac{1}{4}$;*
2. *if $\alpha \neq 0$, then $N_1(r, \frac{1}{f}) \leq \frac{1}{5}T(r,f) + O(\log r)$ and $\vartheta(0,f) \leq \frac{1}{5}$, and if $\alpha = 0$, then $N_1(r, \frac{1}{f}) = 0$ and $\vartheta(0,f) = 0$;*
3. *$N_1(r,f) = 0$ and $\vartheta(\infty,f) = 0$.*

The estimates for transcendental solutions of P_4 were given by Steinmetz in 1982 [20].

Theorem 12 *Transcendental solutions of P_4 fulfill the conditions:*

1. *for every $a \in \mathbb{C} \setminus \{0\}$, $N_1(r, \frac{1}{f-a}) \leq \frac{1}{4}T(r,f) + O(\log r)$ and $\vartheta(a,f) \leq \frac{1}{4}$;*
2. *if $\beta \neq 0$, then $N_1(r, \frac{1}{f}) = 0$ and $\vartheta(0,f) = 0$;*
3. *if $\beta = 0$, then $N_1(r, \frac{1}{f}) = \frac{1}{2}T(r,f) + O(\log r)$ and $\vartheta(0,f) = \frac{1}{2}$;*
4. *$N_1(r,f) = 0$ and $\vartheta(\infty,f) = 0$.*

The description of multiple values of solutions of P_{34} was given in [1].

Theorem 13 *A transcendental meromorphic solution f of $P_{34}(A,B)$ satisfies the following conditions:*

1. *all the poles of f are double and $\vartheta(\infty,f) = 1/2$;*
2. *for $P_{34}(A,B)$, $(A \neq 0)$ all the zeros of f are simple and $\vartheta(0,f) = 0$, for $P_{34}(0,B)$, the zeros are double and $\vartheta(0,f) \leq \frac{1}{2}$;*
3. *if $a \in \mathbb{C} \setminus \{0\}$, we have $\vartheta(a,f) \leq \frac{1}{4}$.*

3.4 Petrenko's Defective Values

Even though for measuring Petrenko's deviation a stronger metrics is applied, transcendental solutions of Painlevé equations do not show any stronger irregularity of

their behaviour towards values in $\overline{\mathbb{C}}$ in comparison to what is known about Nevanlinna defects. Also in this case the only possibly 'troublesome' value remains zero. Moreover, even this exception happens only for particular choice of parameters.

The structure of the sets of defective values in the sense of Petrenko for P_2, P_4 and P_{34} was examined by Ciechanowicz and Filipuk in 2016 [1].

Theorem 14 *Let f be a transcendental meromorphic solution of $P_2(\alpha)$. Then we have the following conditions:*

1. *if $\alpha \neq 0$, then $\mathscr{L}(r,a,f) = S(r,f)$ for all $a \in \overline{\mathbb{C}}$;*
2. *for $P_2(0)$ we have $\mathscr{L}(r,a,f) = S(r,f)$ for all $a \in \overline{\mathbb{C}} \setminus \{0\}$.*

Theorem 15 *Let f be a transcendental meromorphic solution of $P_4(\alpha,\beta)$. Then we have the following conditions:*

1. *if $\beta \neq 0$, then $\mathscr{L}(r,a,f) = S(r,f)$ for all $a \in \overline{\mathbb{C}}$;*
2. *for $P_4(,\alpha,0)$ we have $\mathscr{L}(r,a,f) = S(r,f)$ for all $a \in \overline{\mathbb{C}} \setminus \{0\}$.*

Theorem 16 *Transcendental meromorphic solutions of P_{34} satisfy the condition*

$$\mathscr{L}(r,a,f) = S(r,f) \quad \text{for all} \quad a \in \overline{\mathbb{C}} \setminus \{0\}.$$

If $\alpha \neq 0$ we also have $\mathscr{L}(r,0,f) = S(r,f)$.

Let us add that by $S(r,f)$ we understand any function $s : [0,+\infty) \to \mathbb{R}$ satisfying $s(r) = o(T(r,f))$ $(r \to \infty)$ for r outside a set E of finite linear measure.

Corollary 1 *Transcendental meromorphic solutions of equation $P_2(\alpha)$ when $\alpha \neq 0$, or $P_4(\alpha,\beta)$ when $\beta \neq 0$, or $P_{34}(A,B)$ when $A \neq 0$ for all $a \in \overline{\mathbb{C}}$ fulfill the conditions $\delta(a,f) = 0$ and $\beta(a,f) = 0$. Both the set of defective values in the sense of Nevanlinna, and the set of defective values in the sense of Petrenko are empty. For $P_2(0)$ it has been proved that the set of Nevanlinna defective values is empty. For $P_4(\alpha,0)$ and $P_{34}(0,\beta)$ we have $\delta(a,f) = 0$ and $\beta(a,f) = 0$ for all $a \in \overline{\mathbb{C}} \setminus \{0\}$. In this case, the sets of defective values in both senses may not be empty, with the only possible element being zero.*

3.5 Petrenko's Defective Values and P_1

Finally, let us formulate the following theorem concerning solutions of P_1.

Theorem 17 *Let f be a solution of P_1. Then for all values $a \in \overline{\mathbb{C}}$ we have $\mathscr{L}(r,a,f) = S(r,f)$ and $\beta(a,f) = 0$.*

To prove the theorem we need the following three lemmas. The first of them concerns the estimate of deviation for logarithmic derivative, the other two are analogues of Clunie lemma and Mohon'ko-Mohon'ko lemma.

Lemma 1 [1] *Let f be a meromorphic function. Then, possibly except for r in a set of finite linear measure, for $k = 1, 2, \ldots$ we have*

$$\mathscr{L}\left(r, \infty, \frac{f^{(k)}}{f}\right) = O(\log(rT(r,f))) \qquad (r \to \infty),$$

where $f^{(k)}$ means the k-th derivative of f.

Lemma 2 [1] *Let f be a transcendental meromorphic solution of*

$$f^n P(z,f) = Q(z,f),$$

where n is a positive integer, $P(z,f)$, $Q(z,f)$ are polynomials in f and its derivatives with meromorphic coefficients a_v, b_v, respectively, which are small with respect to f in the sense that

$$\mathscr{L}(r, \infty, a_v) = S(r,f), \qquad \mathscr{L}(r, \infty, b_v) = S(r,f).$$

If the total degree d of $Q(z,f)$ as a polynomial in f and its derivatives is $d \le n$, then

$$\mathscr{L}(r, \infty, P(z,f)) = S(r,f).$$

Lemma 3 [1] *Let $P(z,f,f',\ldots,f^{(n)}) = 0$ be an algebraic differential equation ($P(z, u_0, u_1, \ldots, u_n)$ is a polynomial in all arguments) and let f be its transcendental meromorphic solution. If a constant a does not solve the equation, then $\mathscr{L}(r, a, f) = S(r,f)$ and $\beta(a,f) = 0$.*

Proof of Theorem 17. Equation P_1 can be transformed into

$$f^2 = \frac{1}{6}f'' - \frac{1}{6}z,$$

so it fulfills conditions of Lemma 2 with $P(z,f) = f$, $Q(z,f) = \frac{1}{6}f'' - \frac{1}{6}z$ and $n = 1$. It follows that

$$\mathscr{L}(r,f) = \mathscr{L}(r, P(z,f)) = S(r,f) \qquad (r \to \infty).$$

Next, we need to notice that a constant $a \neq 0$ does not solve P_1, so by Lemma 3, we get $\mathscr{L}(r, \frac{1}{f-a}) = S(r,f)$. Finally, we can estimate

$$\begin{aligned}\mathscr{L}(r,\frac{1}{f}) &\le \mathscr{L}(r,\frac{z}{f}) + \mathscr{L}(r,\frac{1}{z}) \\ &= \mathscr{L}(r,\frac{f''}{f} - 6f) + \mathscr{L}(r,\frac{1}{z}) \\ &\le \mathscr{L}(r,\frac{f''}{f}) + \mathscr{L}(r,f) + O(\log r).\end{aligned}$$

Applying Lemma 1 and the estimate $\mathscr{L}(r,f) = S(r,f)$ completes the proof.

References

1. Ciechanowicz, E., Filipuk, G.: Meromorphic solutions of $P_{4,34}$ and their value distribution. Ann. Acad. Sci. Fenn. Math. **41**, 617–638 (2016)
2. Ciechanowicz, E., Filipuk, G.: Transcendental meromorphic solutions of P_{34} and small targets. In: Filipuk, G., Haraoka, Y., Michalik, S. (eds.) Analytic, Algebraic and Geometric Aspects of Differential Equations, Trends in Mathematics, pp. 307–323. Birkhauser (2017)
3. Gambier, B.: Sur les équations différentielles du second ordre et du premier degré dont lintégrale générale est à points critiques fixés. Acta Math. **33**, 1–55 (1909)
4. Gol'dberg, A.A., Eremenko, A.E., Sodin, M.L.: Exceptional values in the sense of R. Nevanlinna and in the sense of V. Petrenko, I. Teor. Funkts., Funkts. Anal. Prilosh., **47**, 41–51 (1987). Engl. transl.: J. Sov. Math. **48.6**, 648–655 (1990)
5. Gol'dberg, A.A., Eremenko, A.E., Sodin, M.L.: Exceptional values in the sense of R. Nevanlinna and in the sense of V. Petrenko, II. Teor. Funkts. Funkts. Anal. Prilosh. **48**, 58–70 (1987). Engl. transl.: J. Sov. Math. **49.2**, 891–899 (1990)
6. Gromak, V., Laine, I., and Shimomura, S.: Painlevé Differential Equations in the Complex Plane. De Gruyter Studies in Mathematics, vol. 28, Walter de Gruyter, Berlin (2002)
7. Hinkkanen, A., Laine, I.: Solutions of the first and second Painlevé equations are meromorphic. J. d'Analyse Math. **79**, 345–377 (1999)
8. Ince, E.L.: Ordinary Differential Equations. Longmans Green, London (1927)
9. Kiessling, H.: Zur Werteverteilung der Lösungen algebraischer Differentialgleichungen. Ph.D. thesis, Berlin (1996)
10. Marchenko, I.I. and Shcherba, A.I.: On the magnitudes of deviations of meromorphic functions. Mat. Sb. **181**, 3–24 (1990). Engl. transl. in: Math. USSR Sb. **69**, 1–24 (1991)
11. Nevanlinna, R.: Eindeutige Analytische Funktionen. Springer, Berlin (1970)
12. Painlevé, P.: Leçons sur la Théorie Analytique des Équations Différentielles, Profesées à Stockholm, 1895. Hermann, Paris (1897)
13. Petrenko, V.P.: The growth of meromorphic functions of finite lower order. Izv. Akad. Nauk SSSR **33**, 414–454 (1969). (Russian)
14. Picard, E.: Sur une propriété des fonctions entières. C.R. Acad. Sci. Paris **88** (1879)
15. Picard, E.: Mémoire sur la théorie des fonctions algébriques de deux variables. J. de Math. **4–5**, 135–319 (1889)
16. Shimomura, S.: The first, the second and the fourth Painlevé transcendents are of finite order. Proc. Japan Acad. Ser. A **77**, 42–45 (2001)
17. Shimomura, S.: Growth of the first, the second and the fourth Painlevé transcendents. Math. Proc. Cambr. Philos. Soc. **134**(2), 259–269 (2003)
18. Schubart, H.: Zur Wertverteilung der Painlevéschen Transzendenten. Arch. Math. (Basel) **7**, 284–290 (1956)
19. Schubart, H., Wittich, H.: Über die Lösungen der ersten beiden Painlevéschen Differentialgleichungen. Math. Z. **66**, 364–370 (1957)

20. Steinmetz, N.: Zur Wertverteilung der Lösungen der vierten Painlevéschen Differentialgleichung. Math. Z. **181**, 553–561 (1982)
21. Steinmetz, N.: On Painlevé equations I. II and IV. J. d'Analyse Math. **82**, 363–377 (2000)
22. Steinmetz, N.: Value distribution of the Painlevé transcendents. Israel J. Math. **128**, 29–52 (2002)
23. Steinmetz, N.: Sub-normal solutions to Painlevé's second differential equation. Bull. Lond. Math. Soc. **45**, 225–235 (2013)

Numerical-Analytical Algorithms for Nonlinear Optimal Control Problems on a Large Time Interval

Yulia Danik, Mikhail Dmitriev, Dmitry Makarov and Tatiana Zarodnyuk

Abstract Some nonlinear and discrete optimal control problems with phase constraints on a fixed but sufficiently large time interval are considered as singularly perturbed problems. In continuous-time case the state equations are reduced to singularly perturbed equations on a finite time interval and, in discrete-time case, the state equations have the form of systems with a small step. Using the technique for singularly perturbed systems, the formal asymptotic expansions by the corresponding small parameter are constructed which contain the structural information about the solution. That is usually sufficient for most applications to obtain an initial approximation to control in the global optimum neighborhood. The obtained algorithms can be applied to mathematical economics and technical objects control problems with phase and control constraints, and with turnpike effects in the trajectories, where the turnpike trajectories can be discontinuous. The use of traditional algorithms for these problems is inefficient due to the large increase of computational difficulty.

Keywords Large time interval · Singular perturbations · Optimal control problems · Asymptotic expansions · Turnpike trajectories

Y. Danik · M. Dmitriev (✉) · D. Makarov
Federal Research Center "Computer Science and Control" of Russian Academy of Sciences (FRC CSC RAS), pr. 60-letiya Oktyabrya 9, Moscow 117312, Russia
e-mail: mdmitriev@mail.ru

Y. Danik
e-mail: danik@isa.ru

D. Makarov
e-mail: makarov@isa.ru

T. Zarodnyuk
Matrosov Institute for System Dynamics and Control Theory SB RAS, Lermontova str. 134, Irkutsk 664033, Russia
e-mail: tzarodnyuk@gmail.com

J. Awrejcewicz (ed.), *Dynamical Systems in Theoretical Perspective*,
Springer Proceedings in Mathematics & Statistics 248,
https://doi.org/10.1007/978-3-319-96598-7_10

1 Introduction

The existing algorithms [5, 9] of optimal control problems solution use local optimization methods and, therefore, large computing resources are needed to find the optimal control with a given accuracy. In the case of autonomous objects, the problem of effective algorithms development is worsened by the necessity of solving linear and nonlinear control problems with time and resource constraints. Therefore, it is important to create computationally efficient algorithms that with greater probability allow to find in real time the admissible control which is rather close to the global optimum. One of the possible ways to do this is to make use of the specific characteristics of a mathematical model of an optimal control problem. The paper illustrates the possibility of such algorithms creation based on the segregation of formal small parameters in the mathematical models of control objects [3, 4, 6, 7] and on the use of possible turnpike properties of optimal trajectories in control problems with sufficiently large time intervals. On the one hand, accounting for the turnpike nature of optimal trajectories makes it possible to generate initial approximations to the control that are close to the global optimum. On the other hand, the asymptotic analysis of the model generates numerical-analytical procedures that reduce the amount of necessary calculations. In this paper, the possibility of constructing efficient numerical-analytical algorithms for solving such problems using the singular perturbations technique is illustrated for two classes of continuous and discrete time optimal control problems with a large finite horizon.

2 Continuous Large Finite Horizon Problems with Slowly Varying Coefficients

Let us consider the following large finite horizon optimal control problem with slowly varying coefficients

$$J(u) = \varepsilon\phi(y(T)) + \varepsilon \int_0^T F(y, u, s\varepsilon)ds \to \min_u, \; T \gg 1, \; 0 < \varepsilon \ll 1,$$

$$\frac{dy}{ds} = A(s\varepsilon)y + B(s\varepsilon)u + f(s\varepsilon), \quad y \in R^n, u \in R^r, \; y(0) = y^0, \tag{1}$$

where u is the control variable, y is the state vector, ε is a small parameter, $s \in [0, T]$ is the time variable, T is the final time point, $\varepsilon\phi(y(T))$ is the terminal payoff, $F(y, u, s\varepsilon)$ is an integrand function, $J(u)$ is the criterion function, $A(s\varepsilon) \in R^{n\times n}$, $B(s\varepsilon) \in R^{n\times r}$ are time-varying matrices, $f(s\varepsilon) \in R^n$ is a vector function.

Performing the replacement $t = s\varepsilon$ in (1) we get the next singularly perturbed variational problem

$$I_\varepsilon(u) = \varepsilon\phi(y(T_0)) + \int_0^{T_0} F(y,u,t)dt \to \min_u,$$

$$\varepsilon\frac{dy}{dt} = A(t)y + B(t)u + f(t),\ y \in R^n,\ u \in R^r,\ y(0) = y^0, \tag{2}$$

where $T_0 = T\varepsilon, t \in [0, T_0]$ is the modified time variable. Here, because of the nonlinear criterion, the singularly perturbed nonlinear boundary value problem for Pontryagin extremals has the form

$$\varepsilon\frac{dy}{dt} = A(t)y + B(t)u(y,\psi,t) + f(t), \quad \varepsilon\frac{d\psi}{dt} = -A'\psi + F_y,$$
$$y(0) = y^0, \quad \psi(T_0) = -\frac{\partial\phi(y(T_0))}{\partial y}, \tag{3}$$

where $\tilde{\psi}$ is the conjugate variable of the maximum principle, $\psi = \frac{\tilde{\psi}}{\varepsilon}$, $u(y,\psi,t)$ is the maximum point of the corresponding hamiltonian $H = \frac{1}{\varepsilon}\tilde{\psi}'(A(t)y + B(t)u + f(t)) - F(y,u,t)$ with respect to u and the prime denotes transposition.

There can be several equilibrium points (the roots of the right parts) in the corresponding associated system. Let there be three equilibrium points, then the existence of internal transition layers (so-called contrast structures) is possible in the solution of the perturbed problem. For example, this is true when there are two equal Hamiltonian maximum points $u = u(y, \tilde{\psi}, t)$ along the extremal of the next degenerate problem

$$J(y,u) = \int_0^{T_0} F(y,u,t)dt \to \min_{y,u},$$
$$0 = A(t)y + B(t)u + f(t),\ y \in R^n,\ u \in R^r,\ t \in [0, T_0], \tag{4}$$

here we suppose that the solution (4) has one internal point of discontinuity (transition point).

Using the direct scheme [1, 2, 4], we seek the asymptotic approximation of the solution in the next form

$$z(t,\varepsilon)=\begin{cases} y(t,\varepsilon)=\sum\limits_{k=0}^{\infty}\varepsilon^k(\bar{y}_k(t)+\Pi_k y(\tau_0)+R_k^{(-)}y(\tau)) \\ u(t,\varepsilon)=\sum\limits_{k=0}^{\infty}\varepsilon^k(\bar{u}_k(t)+\Pi_k u(\tau_0)+R_k^{(-)}u(\tau)) \end{cases}, 0\le t\le t^*(\varepsilon),$$

$$z(t,\varepsilon)=\begin{cases} y(t,\varepsilon)=\sum\limits_{k=0}^{\infty}\varepsilon^k(\bar{y}_k(t)+R_k^{(+)}y(\tau)+Q_k y(\tau_1)) \\ u(t,\varepsilon)=\sum\limits_{k=0}^{\infty}\varepsilon^k(\bar{u}_k(t)+R_k^{(+)}u(\tau)+Q_k u(\tau_1)) \end{cases}, t^*(\varepsilon)\le t\le T_0, \quad (5)$$

where $z=\begin{pmatrix} y \\ u \end{pmatrix}$, $\bar{z}_i(t)$, $\Pi_i z(\tau_0)$, $Q_i z(\tau_1)$, $R_i^{\binom{+}{-}}z(\tau)$ are the terms of regular, left boundary, right boundary and inner boundary series accordingly. It is assumed that the terms of all boundary series decrease at infinity $\tau_0=\frac{t}{\varepsilon}\to+\infty$, $\tau=\frac{t-t_0}{\varepsilon}\to\pm\infty$, $\tau_1=\frac{t-T_0}{\varepsilon}\to-\infty$, $\varepsilon\to 0$, $t^*(\varepsilon)=t_0+\varepsilon t_1+\cdots$. The direct scheme algorithm for constructing the formal asymptotics of the variational problem solution consists in substituting (5) in (4), expanding all the conditions of the problem into the corresponding series and the solution of the obtained variational problems for the terms of the asymptotics in each approximation.

Thus, we obtain $I=I_0+\varepsilon I_1+\cdots+\varepsilon^m I_m+O\left(\varepsilon^{m+1}\right)$, $m=2n+1$, where in the zero approximation we have the next conditional extremum problem for time-dependent terms of the regular series

$$I_0=\int_0^{T_0}F(\bar{y}_0,\bar{u}_0,t)dt\to\min_{(\bar{y}_0,\bar{u}_0)},\quad y_0^{T_0}=\arg\min_y\phi(y),\quad 0=A(t)y_0+B(t)u_0+f(t).$$

Let us define $\bar{z}_0(t)=\left(\bar{y}_0'(t),\bar{u}_0'(t)\right)'=\begin{cases}\bar{z}_0^-(t), 0<t<t_0,\\ \bar{z}_0^+(t), t_0<t<T_0\end{cases}$, then the optimality conditions take the form $\bar{H}_y(t)=H_y\left(\bar{z}_0,\bar{\psi}_0,t\right)=0$, $\bar{H}_u(t)=H_u\left(\bar{z}_0,\bar{\psi}_0,t\right)=0$, where $H(z,\psi,t)=\psi^T(Ay+Bu)-F(y,u,t)$. Further, we seek all the terms of the asymptotic expansions by solving the corresponding optimal control problems.

So, for example, the boundary layers $\Pi_0 z(\tau_0)$, $Q_0 z(\tau_1)$ and $R_0^{\binom{+}{-}}z(\tau)$ are the trajectories and controls in the auxiliary nonlinear infinite-horizon optimal control problems [1]:

$$\Pi_0 I=-\int_0^{\infty}(H(\tau_0)-H(0))d\tau_0\to\min_{\Pi_0 u},\ \frac{d\Pi_0 y}{d\tau_0}=g(\bar{y}_0(0)+\Pi_0 y,\bar{u}_0(0)+\Pi_0 u,0),$$

$$\Pi_0 y(0)=y^0-\bar{y}_0(0), \quad (6)$$

$$Q_0 I = \int_0^{-\infty} (H(\tau_1) - H(T_0))d\tau_1 \to \min_{Q_0 u},$$

$$\frac{dQ_0 y}{d\tau_1} = g(\bar{y}_0(T_0) + Q_0 y(\tau_1), \bar{u}_0(T_0) + Q_0 u(\tau_1), T_0),\ Q_0 y(0) = y_0^{T_0} - \bar{y}_0(T_0), \tag{7}$$

$$R_0^{\binom{+}{-}} I = \mp \int_0^{\pm\infty} (H(\tau) - H(t_0))d\tau \to \min_{R_0 u},$$

$$\frac{dR_0^{\binom{+}{-}} y}{d\tau} = g\left(\bar{y}_0(t_0) + R_0^{\binom{+}{-}} y(\tau), \bar{u}_0(t_0) + R_0^{\binom{+}{-}} u(\tau), t_0\right),$$

$$R_0^{\binom{+}{-}} y(0) = y_0^* - \bar{y}_0(t_0), \tag{8}$$

where $g = A(t)y + B(t)u + f(t)$ and $y^*(T_0, \varepsilon)$, $y_\varepsilon^{t^*} = y^*(t^*, \varepsilon)$, are the optimal final value of the trajectory and the optimal value of the trajectory at the optimal transition time $t^*(\varepsilon)$ respectively in accordance with the criterion (2). Note that $t^*(\varepsilon)$ is a point of smooth gluing of the left and right approximations of the trajectory and controls $R_0^{\binom{+}{-}} z(\tau)$.

Thus, suppose that all the variational problems obtained by the expansion of the functional in (2) are solvable and that all terms of the asymptotic expansions up to the n-th order are calculated. Let us introduce

Definition A k-th order partial sum of all series for all elements of the problem (1) solution is called a k-th formal asymptotic solution.

Let us state the following

Theorem *Let all functions in problem (2) be sufficiently smooth and, in addition,*

1. *A solution* $\bar{z}_0(t) = \begin{pmatrix} \bar{y}_0(t) \\ \bar{u}_0(t) \end{pmatrix}$ *of the degenerate problem (4) is an isolated stationary solution in the adjoint system for all* t *on intervals* $0 < t < t_0, t_0 < t < T_0$.
2. $\begin{pmatrix} \bar{H}_{yy} \bar{H}_{yu} \\ \bar{H}_{uy} \bar{H}_{uu} \end{pmatrix} < 0$ *along* $\bar{z}_0(t)$ *on each interval* $0 < t < t_0, t_0 < t < T_0$.
3. $\{A(t), B(t)\}$ *is a controllable pair for each* $0 \le t \le T_0$.
4. $y^0 - \bar{y}_0(0) \in G^+, \quad y_0^T - \bar{y}_0(T_0) \in G^-, \quad y_0^* - \bar{y}_0^+(t_0) \in R^+, \quad y_0^* - \bar{y}_0^-(t_0) \in R^-$, *where* G^+, G^-, R^+, R^- *are the corresponding regions of influence in problems (6)–(8).*

Then, for sufficiently small ε, *in addition to the exponential estimates for the boundary functions, the formal asymptotic solution of problem (2) exists in some neighborhood* $\bar{z}_0(t)$ *and the following is*

true $\left\| \varepsilon \frac{dy_k}{dt} - A(t)y_k - B(t)u_k - f(t) \right\|_{C^n_{[0,\,T_0]}} = O(\varepsilon^{k+1})$, $y_k(0,\varepsilon) = y^0 + O(\varepsilon^{k+1}), J(u_k) \le J(u_{k-1}), k = 1, 2, \ldots,$ *where* $J(u_k) < J(u_{k-1})$ *if* $u_k \ne u_{k-1}$.

Thus, the discrepancies in the variational problem constraints decrease with the increase of the order of the formal uniform asymptotic approximation. That allows us to construct minimizing control sequences by the solution of computationally simpler problems: the degenerate finite-horizon problem (4) and the boundary layer problems, the solution of which can also be found on finite intervals because of the exponential nature of the decrease. So there is no significant accumulation of errors.

In the presence of asymptotic estimates of the closeness of the initial and degenerate problems solutions, we can state that the solution of the degenerate problem contains qualitative information about the optimal control. This makes it possible to employ simplified algorithms for optimal control nonlinear problems using, for example, the control structure from the degenerate problem and reducing the initial problem to the problem of non-linear programming, where the global optimum of the criterion can already be found by local optimization methods. This can be done because the initial approximation, as a rule, is in the global optimum neighborhood.

Example 1 Let us have the next minimization problem

$$I(u) = \frac{1}{2}\varepsilon(y(2\pi) - 2)^2 + \int_0^{2\pi} \left(\frac{1}{4}y^4 - \frac{1}{3}y^3 \sin t - \frac{1}{2}y^2 + y \sin t + \frac{1}{2}t^2 + tu + \frac{1}{2}u^2 \right) dt$$

$$\to \min_u,$$

$$\varepsilon \frac{dy}{dt} = u + t, 0 \le t \le 2\pi \, (A = 0; B = 1), \quad y(0,\varepsilon) = 0, T_0 = 2\pi. \tag{9}$$

This example was for the first time considered from the asymptotic analysis point of view in [8]. The solution of the degenerate problem is $\bar{u} = -t$, $\bar{y}(t) = \begin{cases} -1, & 0 \le t \le t_0, \\ 1, & t_0 \le t \le 2\pi \end{cases}$, where the transition point $t_0 = \pi$ is determined from the continuity condition of the corresponding Hamiltonian of the Pontryagin maximum principle. It is obvious now that the optimal control in (9) can be described at the qualitative level by the next zero order uniform asymptotic approximation

$u_0(t,\varepsilon) = \bar{u}_0(t) + \Pi_0 u(\tau_0) + Q_0 u(\tau_1) + R_0^- u\left(\tau_{t_0}^-\right) + R_0^+ u\left(\tau_{t_0}^+\right)$, $\tau_{t_0}^- \to -\infty$, $\tau_{t_0}^+ \to +\infty, \varepsilon \to 0$. Let $\varepsilon = 0.1$. First, take $u(t) = 0$, the criterion value in (9) is 2.662×10^8 for $u(t) = 0$, i.e. the problem is very "stiff". This "stiffness" is conditioned by not only the value of ε, but also the presence of an internal transition point in the trajectory. It turns out that by successively finding the elements of the zeroth approximation of the control we obtain a set of first terms of the minimizing control sequence in the variation problem (9). Let us introduce the sequence $\{u_i(t,\varepsilon)\}, i = 1, \ldots, 5$, where $u_1 = \bar{u}_0(t) = -t$, $u_2 = \bar{u}_0(t) + \tilde{R}_0^- u\left(\tau_{t_0}^-\right)$, $u_3 = \bar{u}_0(t) + \tilde{\Pi}_0 u(\tau_0) + \tilde{R}_0^- u\left(\tau_{t_0}^-\right)$, $u_4 = \bar{u}_0(t) + \tilde{\Pi}_0 u(\tau_0) + \tilde{R}_0^- u\left(\tau_{t_0}^-\right) + \tilde{R}_0^+ u\left(\tau_{t_0}^+\right)$, $u_5 = \bar{u}_0(t) + \tilde{\Pi}_0 u(\tau_0) + \tilde{R}_0^- u\left(\tau_{t_0}^-\right) +$

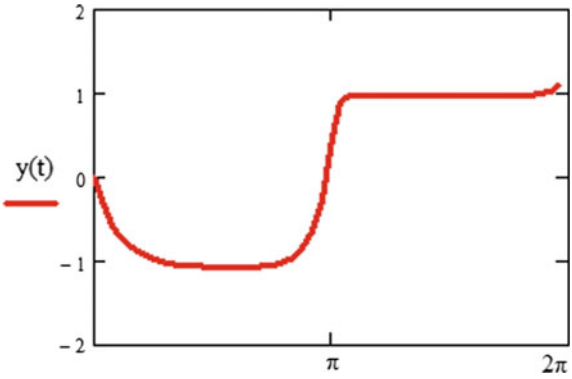

Fig. 1 The state trajectory corresponding to u_5

$\tilde{R}_0^+ u\left(\tau_{t_0}^+\right) + \tilde{Q}_0 u(\tau_1)$, and $\tilde{\Pi}_0 u(\tau_0) = L_1 e^{-\frac{a_1 t}{\varepsilon}}$, $\tilde{Q}_0 u(\tau_1) = L_2 e^{\frac{a_2(t-T_0)}{\varepsilon}}$, $\tilde{R}_0^+ u\left(\tau_{t_0}^+\right) = \begin{cases} L_3 e^{\frac{a_3(t-t_0)}{\varepsilon}}, if\ t \le t_0 \\ 0, otherwise \end{cases}$,

$\tilde{R}_0^- u\left(\tau_{t_0}^-\right) = \begin{cases} L_3 e^{-\frac{a_4(t-t_0)}{\varepsilon}}, if\ t \ge t_0 \\ 0, otherwise \end{cases}$, $L_1 = -0.325, a_1 = 0.303, L_2 = 0.414, a_2 = 1, L_3 = 0.784, a_3 = 0.507, a_4 = 1.567$. We obtain the following criterion values along these controls $I(u_{adm} = 0) = 2.662 \times 10^8 > I(u_1) = 0.2 > I(u_2) = -1.081 > I(u_3) = -2.536 > I(u_4) = -3.968 > I(u_5) = -3.988$. This sequence of criterion values corresponds to the successive use of information about the structure of the exact solution taken from the structure of the degenerate problem solution.

Note, that here $\tilde{\Pi}_0 u(\tau_0)$, $\tilde{R}_0^- u\left(\tau_{t_0}^-\right)$, $\tilde{Q}_0 u(\tau_1)$, $\tilde{R}_0^+ u\left(\tau_{t_0}^+\right)$ are rough two-parameter approximations, which are in the form of decreasing scalar exponents for the corresponding external and internal boundary functions. Optimizing the free coefficients in each term we can improve the quality of the minimizing control sequence. The state trajectory is presented in Fig. 1.

The best functional value of $I_\varepsilon^* \approx -4.0125$ was found using OPTCON software with the initial condition $u = 0.1$ and required the solution of the specified Cauchy problem approximately 3298 times. The usage of $\bar{u}_0(t)$ as the initial condition allows to reduce the amount of calculations to 1938 times. In contrast, the presented approximate solution $u_5(t, \varepsilon)$ required to solve the same Cauchy problem only 26 times.

3 Discrete Optimal Control Problems with a Small Step

Optimal control problems with large finite horizon often have one common property, i.e. their trajectories lie in a small neighborhood of the so-called turnpikes, which are the trajectories of certain degenerate problems on almost the entire time horizon.

If the optimal trajectory is connected with the turnpike, then this trajectory can be approximated by a trajectory consisting of three sections: a section of a transition to the turnpike, a section of a turnpike neighborhood, and a section of a transition from a turnpike neighborhood to the end point neighborhood. Such structure of the solution is typical for singularly perturbed optimal control problems [4] in the classical formulation, that is, there are no control and state constraints in them. Here on the example of a class of discrete finite-horizon optimal control problems or the problems with a large number of steps on a given time interval we show that the singular perturbations technique allows to propose algorithms for their solution even in the presence of control or state constraints.

Let us consider the following problem

$$J(u) = (x(1) - x_{fix})^T F(x(1) - x_{fix}) \to \min_u, \tag{10}$$

$$x(t+\varepsilon) = Ax(t) + Bu(t) + f(t), x(0) = x^0, \quad x, f \in R^n, u \in R^r, \tag{11}$$

$$Cu(t) \le x(t), \quad u(t) \ge 0, x(t) \ge 0, \tag{12}$$

where x is the state vector, x_{fix} is the desired final state, u is the control vector, $J(u)$ is the criterion function, $A \in R^{n\times n}$, $B \in R^{n\times r}$, $C \in R^{n\times r}$ are constant matrices, $f(t)$ is a vector function, $t \in T_\varepsilon = \{t : t = k\varepsilon, k = 0, 1, \ldots, N-1\} \in [0, 1]$, $N = \frac{1}{\varepsilon}, \varepsilon > 0$ is a small step, $F > 0$ is a symmetric positive definite matrix. The known results in literature [4] related to the direct scheme method deals with the cases where the optimal control is unique in the degenerated problem and the optimization problems for the terms of asymptotic approximations have only one solution. But in our case, because of the specific form of the criterion, it does not appear in some of the obtained problems or these problems have a nonunique solution.

The problem (10)–(12) is singularly perturbed as in both continuous- and discrete-time case if $\varepsilon = 0$, then there is a loss of additional boundary conditions required for the determination of original problem trajectories. So, there are fast-change zones in the solution (so called boundary layers) to compensate for this loss. As above, using the direct scheme and substituting the expansions for x and u into all conditions (11)–(12) and into the cost function (10) and expanding these conditions into the corresponding series we obtain the relations for the formal zeroth uniform asymptotic approximation of the solution for the defined variational problem [4].

Assuming that the terms of the boundary series have the corresponding exponential estimates. As in the continuous case, assuming that the terms of the boundary series have the corresponding exponential estimates, we have

$$J(u) = (\bar{x}_0(T) + Q_0 x(0) - x_{fix})^T F(\bar{x}_0(T) + Q_0 x(0) - x_{fix}) + \ldots, \tag{13}$$

$$\bar{x}_0(t) + \Pi_0 x(\tau_0 + 1) + Q_0 x(\tau_1 + 1) + \ldots = A[\bar{x}_0(t) + \Pi_0 x(\tau_0) + Q_0 x(\tau_1) + \ldots] + B[\bar{u}_0(t) + \Pi_0 u(\tau_0) + Q_0 u(\tau_1) + \ldots] + f(t), \tag{14}$$

$$\bar{x}_0(0) + \Pi_0 x(0) + \ldots = x^0,$$

$$C(\bar{u}_0(t) + \Pi_0 u(\tau_o) + Q_0 u(\tau_1) + \ldots) \le \bar{x}_0(t) + \Pi_0 x(\tau_o) + Q_0 x(\tau_1) + \ldots;$$
$$\bar{u}_0(t) + \Pi_0 u(\tau_o) + Q_0 u(\tau_1) + \ldots \ge 0; \bar{x}_0(t) + \Pi_0 x(\tau_o) + Q_0 x(\tau_1) + \ldots \ge 0,$$

where $\tau_0 = 0, 1, 2 \ldots, \tau_1 = 0, -1, -2, \ldots$

Then from (13), (14) we have the following expressions for the terms of the regular series

$$\bar{x}_0(t) = (E - A)^{-1} B \bar{u}_0(t) + (E - A)^{-1} f(t), \tag{15}$$
$$C\bar{u}_0(t) \le \bar{x}_0(t), \bar{u}_0(t) \ge 0, \bar{x}_0(t) \ge 0. \tag{16}$$

Let us introduce a condition which is, in particular, satisfied if the unit cost matrix is productive

I. The matrix $(E - A)^{-1}$ exists and the system of constraints (15), (16) is uniquely solvable.

For the left boundary layer we obtain a system of difference equations

$$\Pi_0 x(\tau_0 + 1) = A\Pi_0 x(\tau_0) + B\Pi_0 u(\tau_0), \bar{x}_0(0) + \Pi_0 x(0) = x^0, \tag{17}$$

under the next constrains

$$C(\bar{u}_0(t) + \Pi_0 u(\tau_0)) \le \bar{x}_0(t) + \Pi_0 x(\tau_0), \bar{u}_0(t) + \Pi_0 u(\tau_0) \ge 0$$
$$\bar{x}_0(t) + \Pi_0 x(\tau_0) \ge 0. \tag{18}$$

Then we have a simple optimization problem for finding $Q_0 x(0)$

$$(\bar{x}_0(1) + Q_0 x(0) - x_{fix})^T F(\bar{x}_0(1) + Q_0 x(0) - x_{fix}) \to \min_{Q_0 x(0)}.$$

Here, $Q_0 x(0) = x_{fix} - \bar{x}_0(1)$ is the solution of this problem and we obtain the following system of equalities and inequalities for $Q_0 x(\tau_1)$, $Q_0 u(\tau_1)$

$$Q_0 x(\tau_1) = A^{\tau_1}(x_{fix} - \bar{x}_0(1)) - \sum_{s=\tau_1}^{-1} A^{\tau_1 - s - 1} B Q_0 u(s), \tag{19}$$

$$C(\bar{u}_0(t) + Q_0 u(\tau_1)) \le \bar{x}_0(t) + Q_0 x(\tau_1), \bar{u}_0(t) + Q_0 u(\tau_1) \ge 0, \bar{x}_0(t) + Q_0 x(\tau_1) \ge 0. \tag{20}$$

Let us introduce the condition

II. There exist the sets of admissible continuous controls $\Pi_0 u(\tau_0)$, $Q_0 u(\tau_1)$ satisfying the constraints (15), (16) and (17), (18) respectively for all $\tau_0 = 0, 1, 2, \ldots, \tau_1 = 0, -1, -2, \ldots$ and there exist constants $K > 0, \alpha > 0$, such that the estimates

$$(\|\Pi_0 x(\tau_0)\|, \|\Pi_0 u(\tau_0)\|) \le K e^{-\alpha\tau_0}, \tau_0 = 0, 1, 2, \ldots,$$
$$(\|Q_0 x(\tau_1)\|, \|Q_0 u(\tau_1)\|) \le K e^{\alpha\tau_1}, \tau_1 = 0, -1, -2, \ldots \quad (21)$$

are true for all admissible pairs $\Pi_0 x(\tau_0)$, $\Pi_0 u(\tau_0)$ and $Q_0 x(\tau_1)$, $Q_0 u(\tau_1)$, and at the same time the control

$$u_0(t, \varepsilon) = \bar{u}_0(t) + \Pi_0 u(\tau_0) + Q_0 u(\tau_1), \tau_0 = 0, 1, 2, \ldots, \tau_1 = 0, -1, -2, \ldots \quad (22)$$

is admissible in problem (10)–(12) for all sufficiently small $\varepsilon > 0$.

Now, because of the asymptotic approximations properties, taking into account the estimates (21) and the representations for $\bar{x}_0(t)$, $\bar{u}_0(t)$, $\Pi_0 x(\tau_0)$, $Q_0 x(\tau_1)$ obtained from (15), (17), (19), we can state that the conditions discrepancies in problem (10)–(12) strictly decrease along the control sequence $u_0(t, \varepsilon_{k-1}) \ne u_0(t, \varepsilon_k), k = 1, 2, \ldots$ under conditions I and II for any strictly decreasing sequence $\{\varepsilon_k\}, k = 0, 1, 2, \ldots$ and sufficiently small numbers $\varepsilon_0 > \varepsilon_1 > \varepsilon_2 \ldots$..

The noted property of the formal asymptotic approximation can be used in another heuristic approximate solution algorithm. Firstly, we find an admissible control $u_0(t, \varepsilon_0)$ for some fixed time step which is significantly greater than the initial step. Of course, $u_0(t, \varepsilon_0)$ will be a rough approximation to the exact control, but it is calculated much faster and, at the same time, it may have a similar structure as the exact solution. Then the number of steps is successively increased, i.e. either the time horizon is expanded or the step becomes smaller. The step is changed until we reach the initial small step. Such iterations can be combined with the local descent method in nonlinear programming problems on each step. This can be done using the control vector coordinates values defined in grid nodes as initial values for the unknown variables. Thus, performing fairly "cheap" calculations based on the analytical representations, we obtain a solution with a given accuracy within time acceptable for various applications.

Example 2 Let us consider problem (10)–(12), where

$$A = \begin{pmatrix} 0,56 & 0,33 \\ 0,37 & 0,45 \end{pmatrix}, B = \begin{pmatrix} 1.12 & 0.13 \\ 0.1 & 1.11 \end{pmatrix} \left(\frac{5+\sqrt{165}}{20} \begin{pmatrix} 0.6 & 0.2 \\ 0.1 & 0.7 \end{pmatrix} - \begin{pmatrix} 0.3 & 0.5 \\ 0.4 & 0.2 \end{pmatrix} \right)$$
$$\approx \begin{pmatrix} 0.223 & -0.305 \\ -0.321 & 0.439 \end{pmatrix}, x^0 = \begin{pmatrix} 0,5 \\ 0,4 \end{pmatrix}, x_{fix} = \begin{pmatrix} 0,8 \\ 1 \end{pmatrix}, f(t) = \begin{pmatrix} 0,12 \\ 0,1 \end{pmatrix} t^\beta,$$
$$\beta = 1.005, \quad N = 12, \quad t \in [0, 1].$$

In general, the pair $\bar{x}_0(t), \bar{u}_0(t)$ is chosen from (15), (16). In the particular case when the quadratic matrix B is degenerate, we may have $\bar{u}_0(t) = p(t)u_A$, where $p(t)$ is a scalar function. From (15) we obtain $\bar{x}_0(t) = (E - A)^{-1} f(t)$ "which reminds the output trajectory in Leontiev's balance equation" if input-output matrix A is

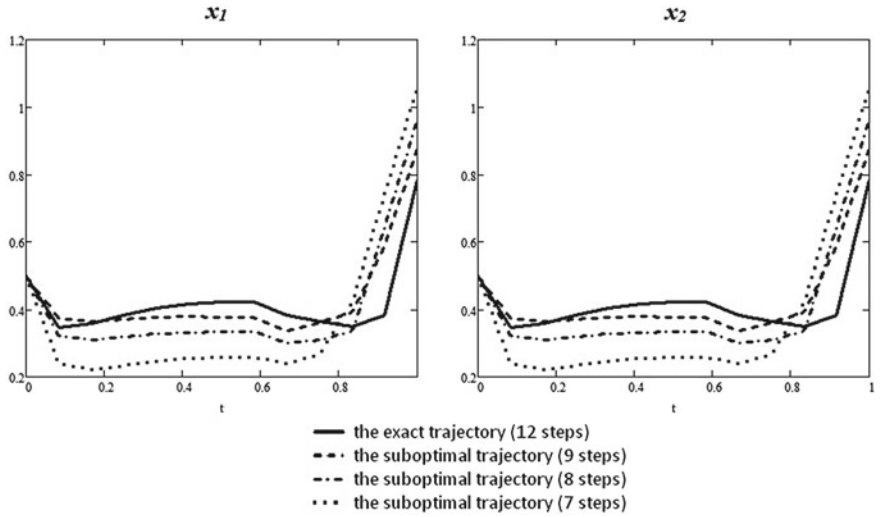

Fig. 2 The trajectories for the different control strategies

productive and $f(t)$ is the vector of final demand. Now we get the representation of the control function

$$u_0(t, \varepsilon, p(t), \Pi_0 u(\tau_0), Q_0 u(\tau_1)) = \bar{u}_0(t, p(t)) + \Pi_0 u\left(\frac{t}{\varepsilon}\right) + Q_0 u\left(\frac{t-1}{\varepsilon}\right). \quad (23)$$

This approach allows us to propose additional procedures for the sequential improvement of the obtained approximation within the found structure. Taking into account the supposed exponential nature of boundary functions decrease, it is possible to assume without loss of generality that the boundary functions identically equal zero on a certain part of the time horizon at some distance from the corresponding boundaries. This assumption reduces the amount of computation and simplifies the admissible control calculation. We solve the initial problem using the zero-approximation structure (23) for increasing number of steps (N = 7; 8; 9) and get the corresponding minimizing control sequence (Fig. 2).

It can be seen from the graphs that suboptimal trajectories approach the exact ones during the process of the uniform zero control approximation correction, and the sum of deviation squares between the exact trajectory, and the resulting suboptimal trajectories along the three optimal control approximations successively take the values 1.388, 0.468, 0.188 and the corresponding criterion values sequence is 0.194, 0.092, 0.035.

4 Conclusions

Specific algorithms for the solution of continuous- and discrete-time optimal control problems on a large finite time interval based on the singular perturbations theory methods are proposed. These algorithms use the zero order uniform asymptotic approximations which describe the structure of the global optimal control and, by so, significantly reduce the computational difficulty and simplify the finding of the approximate suboptimal control with high accuracy. The examples illustrating the work of algorithms for problems where trajectories contain fast internal transitions, or the so-called contrast structures, and the problems with control and state constraints are presented.

Acknowledgements Research was supported by the Russian Science Foundation (project No. 17-11-01220) and the calculations on OPTCON software carried out in the example 1 of section 2 were supported by the Russian Foundation for Basic Research (project No. 17-07-00627).

References

1. Belokopytov, S.V., Dmitriev, M.G.: Direct scheme in optimal control problems with fast and slow motions. Syst. Control Lett. **2**, 129–135 (1986)
2. Belokopytov, S.V., Dmitriev, M.G.: Solution of classical optimal control problems with a boundary layer. Autom. Remote Control. **7**, 907–917 (1989)
3. Chernous'ko, F.L., Kolmanovskii, V.B.: Computational and approximate methods of optimal control. J. Soviet Math. **3**, 310–353 (1979)
4. Dmitriev, M.G., Kurina, G.A.: Singular perturbations in control problems. Autom. Remote Control **1**, 1–43 (2006)
5. Fedorenko, R.P.: Approximate Solution of Some Optimal Control Problems. Nauka, Moscow (1978) (in Russian)
6. Gornov, A.Y., Dmitriev, M.G., Tyatyushkin, A.I.: Recent Advances in Solving Optimal Control Problems with a Boundary Layer, vol. **8441-B85**. Dep. in VINITI (1985) (in Russian)
7. Gornov, A.Y., Dmitriev, M.G., Zarodnyuk, T.S.: Improving the efficiency of the optimal control search in nonlinear problems basing on the selection of the initial approximation. In: Proceedings of the XII National Conference on Control Problems (VSPU), pp. 2408–2414 (2014) (in Russian)
8. Mingkang, N., Dmitriev, M.G.: Steplike contrast structure in an elementary optimal control problem. Comput. Math. Math. Phys. **8**, 1312–1323 (2010)
9. Tyatyushkin, A.I.: A multimethod technique for solving optimal control problem. Optim. Simul. Control **7**, 275–288 (2013)

The Dynamic Behavior of the Vehicle Wheels Under Impact Loads—FEM and Experimental Researches

Irina Demiyanushko, Aleksandr Vakhromeev, Evgeny Loginov and Violetta Mironova

Abstract Results of the analysis of dynamic impact effect for vehicle light alloy wheels of various types, which may occur in various road situations (head-on crash, drift, collision with another car) are given. This study applied to simulate the impact behavior caused by a dynamic loading of vehicle wheels by impact testing according to the scheme of certification tests with static and dynamic strain measurement for definition of deformation fields and impact stresses. New approach to creation of FEM model of virtual impact tests of wheels with use of program complex of nonlinear dynamics Ls-Dyna is developed and validation of models by comparison with results of dynamic strain-gaging is carried out.

Keywords Finite element method · Wheel · Dynamic impact

1 Introduction

Aluminum alloy wheels, both cast and forged, are used for cars. While it is critical for car safety, such wheels' behavior at dynamic impact has not been adequately explored. Impact effects occur in a variety of emergencies (head-on crash, drift, collision with another car etc.). Statistic studies of typical accidents show that the average head-on crash angle is 27.6°. Impact loading of aluminum cast wheels at 30° angle (so called "oblique impact") is a mandatory phase of car wheel certification

I. Demiyanushko (✉) · A. Vakhromeev · E. Loginov · V. Mironova
Moscow Automobile and Road Construction State Technical University (MADI),
125319 Moscow, Russia
e-mail: demj-ir@mail.ru

A. Vakhromeev
e-mail: ilka92@mail.ru

E. Loginov
e-mail: emloginov@yandex.ru

V. Mironova
e-mail: violettmir@gmail.com

J. Awrejcewicz (ed.), *Dynamical Systems in Theoretical Perspective*,
Springer Proceedings in Mathematics & Statistics 248,
https://doi.org/10.1007/978-3-319-96598-7_11

testing [1, 2]. Standard oblique impact test simulates a 1t car going at 60 km/h, running with its wheel over a fixed obstacle at an angle of 30°. Complicated design of modern wheels, especially cast ones, requires analysis of the space stress/strain state (SSS) that normally uses the finite elements method in static position (FEM) [3–5]. Experimental impact tests of wheels are carried out on specific benches, which design is conventionally reflected in regulatory documents, however, it may affect the results significantly. Moreover, such impact testing requires considerable computational efforts, especially when the cast wheel configuration needs to be varied in design analysis.

This paper contains the results of computational studies of stress/strain state of an aluminum cast wheel for a car in case of oblique impact. The object under investigation was a 7JX16H2 modern standard aluminum cast wheel. Experimental SSS study of the wheels was made by strain measurement. Of interest, therefore, are calculation/experimental research of static and dynamic behavior of a cast aluminum wheel, when loaded in impact bench testing, to identify FEM model adequacy and possibility to use the dynamic factor for preliminary comparative structure analysis based on static calculation to evaluate their behavior at impact, without detailed dynamic option analyses. The dynamic factor is the ratio of the maximum impact deformation to deformation caused by similar static loading.

2 Experimental Study

The study was carried out on an impact test bench (see Fig. 1a) both for static and dynamic loading that was applied to the wheel rim against (see Fig. 1b) and between the spokes (see Fig. 1c). The wheel was mounted on the impact bench support at 30° to the horizontal surface and rigidly secured to the bearing surface with bolts. The tests were carried out both with a tired and bare wheel.

Two loads (basic mass and striking bar) represented the loading element with the total weight amounting to one t interconnected via a spring simulating a car suspension. The wheel was turned about its mounting axis to ensure various test load applications. The height of the striking bar above the tire is determined by the maximum static loading F_v applied to wheel being subject to investigation [1].

Resistive strain gages were mounted on the disks to measure deformations (strain gages' register surface—3 mm) on flat areas in radial axis of the spokes, and on the rim along the wheel axis (see Fig. 2) [6]. Areas chosen for installation of the strain gages were next to the highest expected deformation points. Impact deformations were recorded at strain-measuring channel polling frequency.

16-channel strain-measuring equipment was used for measurement and digital recording of loaded wheel deformation values. In case of static tests, a load was slowly applied to the wheel rim edge. Dispersion and mean values were calculated in result of automated test data statistical processing. Bare wheel static loading results are shown in Fig. 3 in form of deformation curves measured by 16 resistive strain gages. Testing data analysis proved no after flow and showed that tired and bare

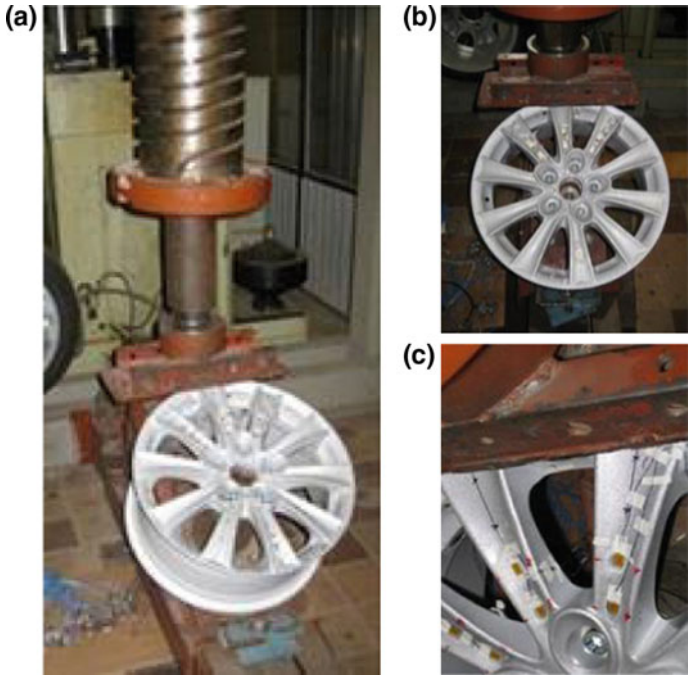

Fig. 1 **a** Impact test bench and installation diagram of resistive strain gages on **b** outer and **c** inner surface of the wheel

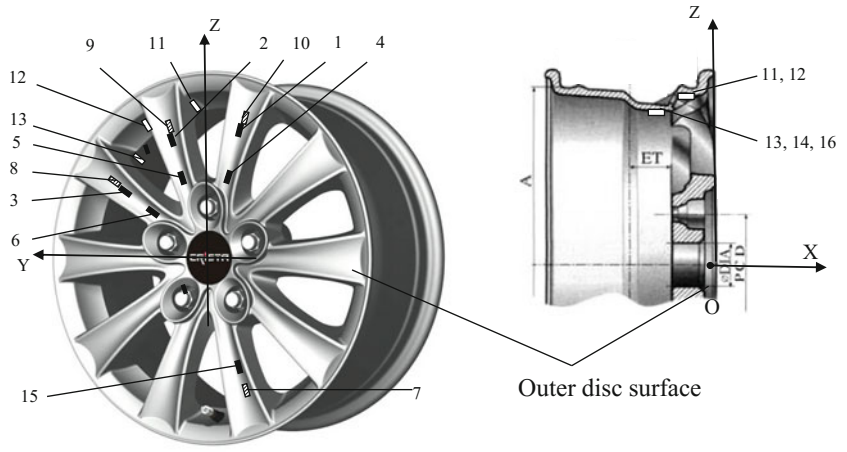

Fig. 2 Installation diagram of resistive strain gages on outer and inner surfaces of the wheel

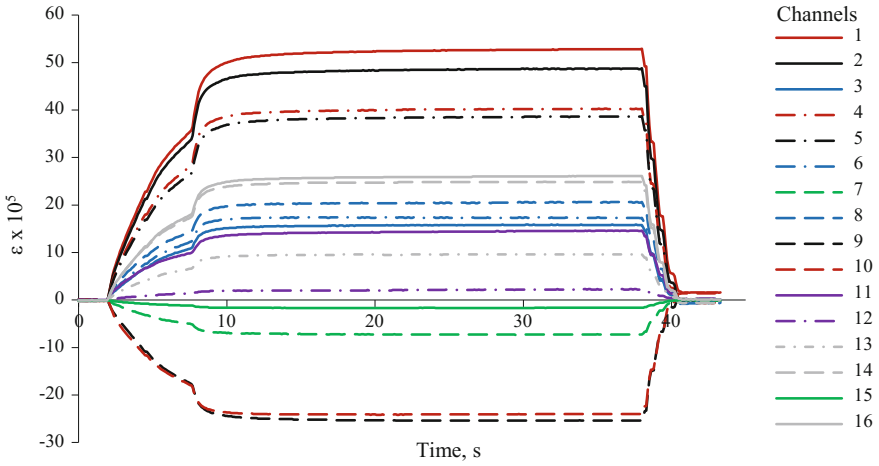

Fig. 3 Deformation curves for static loading

wheel deformations were practically the same under static loading (spread in values, when applying loading to a tired and bare wheel spoke did not exceed 5 and 7% for inter-spoke impact).

Impact loading was also performed in two areas: against and between spokes. The obtained research results are represented as impact load deformation curves in Fig. 4. For all loading options, it is found that rapidly, damping oscillations similar to harmonic ones occur after an impact impulse. Analysis of resistive strain gage readings allowed to identify that complete damping of oscillations takes place within ca. 2.5 s. Oscillation time and damping in all measurement points turned out to be virtually the same: averaged by all measurement points, the oscillation time T = 0.256 s. Determination of damping logarithmic decrement (1) value was based on comparison of subsequent oscillation amplitudes resulting in assessment of the conventional absorption factor value φ of the wheel material which amounted to ca. 0.6–0.7. The obtained value indicates a substantial internal friction in the wheel aluminum cast material leading to significant absorption of impact energy [7]. Additionally oscillation processes could be analyzed using technique designed and described in [8].

$$\delta = ln\, A_s / A_{s+1} \tag{1}$$

Maximum impact-caused deformations occur in the spoke middle on the wheel face. No considerable impact-caused permanent plastic deformations or breakages occur. Research results (see Table 1) allowed establishing the ratios of impact-caused deformations ε_{din} to deformations caused by static loading ε_{st}, which turned out to be practically the same regardless of the measurement points. Thus, an approximate engineering judgment of impact-caused wheel SSS can be recommended by using the obtained average value of dynamic factor (2) and static loading computation results [9].

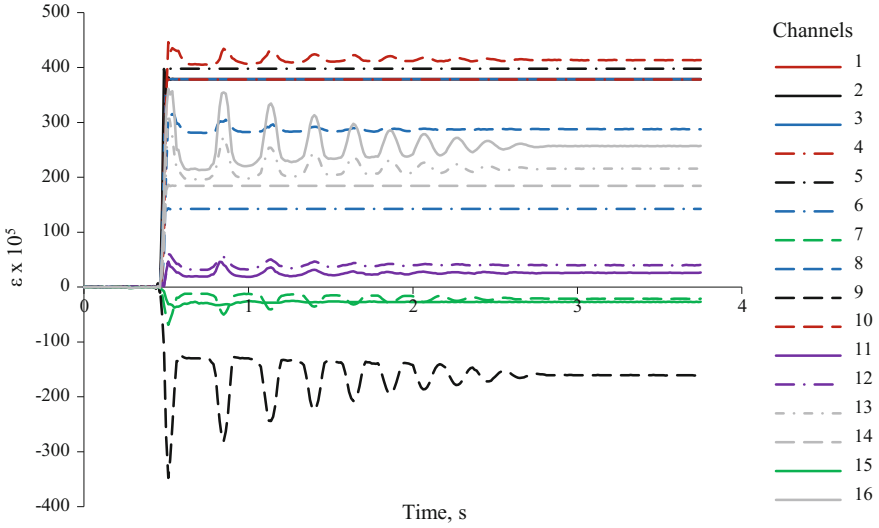

Fig. 4 Deformation curves for impact loading

Table 1 Static and impact loading caused deformations measurements

Strain gage no.	Impact $\varepsilon_{din} \times 10^5$	Static $\varepsilon_{st} \times 10^5$	Dynamic factor K_D
1	378.6	37.6	10.07
3	378.5	34.7	10.91
4	378.4	36.8	10.28
5	397.8	39.8	9.99
6	350.0	28.7	12.20
13	197.3	14.8	13.33
14	184.7	15.3	12.07
16	354.4	31.2	11.36
		Average value K_D:	11.28

$$K_D = \varepsilon_{din}/\varepsilon_s \tag{2}$$

3 Structural Analysis SSS at Static Loading and Dynamic Impact Using FEM

Calculation of wheel impact SSS was done using LS-Dyna multifunction software package [10], designed for solving nonlinear dynamics tasks. Description of the elements motion was based on Lagrange formulation, the solution of the system of

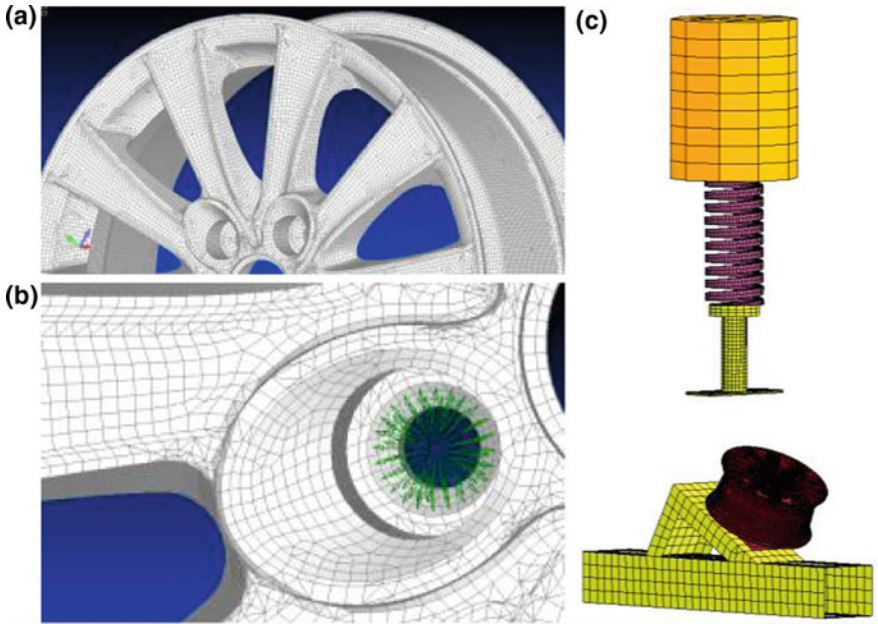

Fig. 5 Computed FE model of the **a**, **b** wheel and **c** impact test bench

dynamic equations and state equations performed using of the explicit integration method [11].

As shown by our research, the calculation results depend on materially on the quality of wheel FE [12, 13]. The computed finite-element model (see Fig. 5a) of a wheel under static loading applied at an angle of 30° (oblique impact conditions) accounts for the main mechanical properties of the wheel, its geometrical peculiarities, holding forces (see Fig. 5b). The comparison of tests and the calculation results carried out without regard for the tire. 3-D FE model consisted of 224,175 nodes and 483,910 components which average size amounted to 3 mm. 8-node hexagonal components prevailed in the model volumewize. The external edge of the flange-secured model was statically loaded at an angle of 300 to the wheel plane and uniformly distributed at 25 points where the striking element contacts with the outer wheel edge.

For dynamic loading the FE model of the wheel consisted of 48,281 nodes and 38,480 elements, with 8-node hexagonal elements prevailing in the construction both in quantity and in volume. Moreover, FE-model comprises test bench components [12, 13] making possible to account for their stiffness, location and conditions of wheel fastening on the test bench support (see Fig. 5c), so that studies are in fact virtual experiment [14]. The wheel support consists of a cylinder system made of 8-node hexagonal components and channel welded structure modelled by 4-node shell members. The impact load consists of three parts comprising 8-node hexagonal

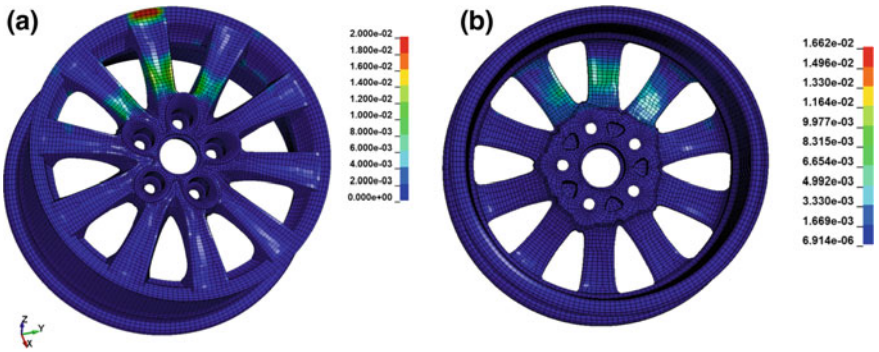

Fig. 6 Distribution of deformation rate on the **a** outer and **b** inner wheel surface

Table 2 Comparison of the main oscillatory process parameters obtained in result of calculations and experiment/test

Parameter	Calculation	Experiment	Inaccuracy (%)
Oscillation time T, s	0.246	0.260	5.4
Oscillation frequency ν, rad^{-1}	25.559	24.127	5.9
Damping logarithmic decrement	≈0.27	≈0.31	≈13

components. The wheel is bonded to the support surface of the test bench using of equivalent compressing force applied from two sides to the system of rigid beam elements of the support. In the design model, the wheel is exposed to permanent loads occurring when tightening the fastening bolts, as well as variable loads resulting from contact interaction with the impact element.

In the course of calculations, an impact was simulated both against and between spokes just as during the test. The height of load fall complied with certification test requirements and test conditions.

SSS components in the wheel are determined based on the values of deformation velocity in each node. In order to account for effect of deformation velocity on the form and key points of the wheel's material deformation curve, including the dynamic yield stress, the calculation uses Cowper-Symonds stiffening condition [15]. Damping properties of materials are accounted for as well. Figure 6 shows the deformation rate values obtained with impact on the wheel rim in the spoke area.

For comparison with test results, the calculation estimated values of oscillation frequency, oscillation time and the damping logarithmic decrement for the first six amplitude deformation values. These values shown in Table 2 and Fig. 7. The difference between the calculated and experimentally recorded values of oscillation frequency, oscillation time and damping logarithmic decrement is within 13%.

Table 3 shows comparison of the maximum deformation rate values under static and dynamic loading. Results obtained within impact computational simulation

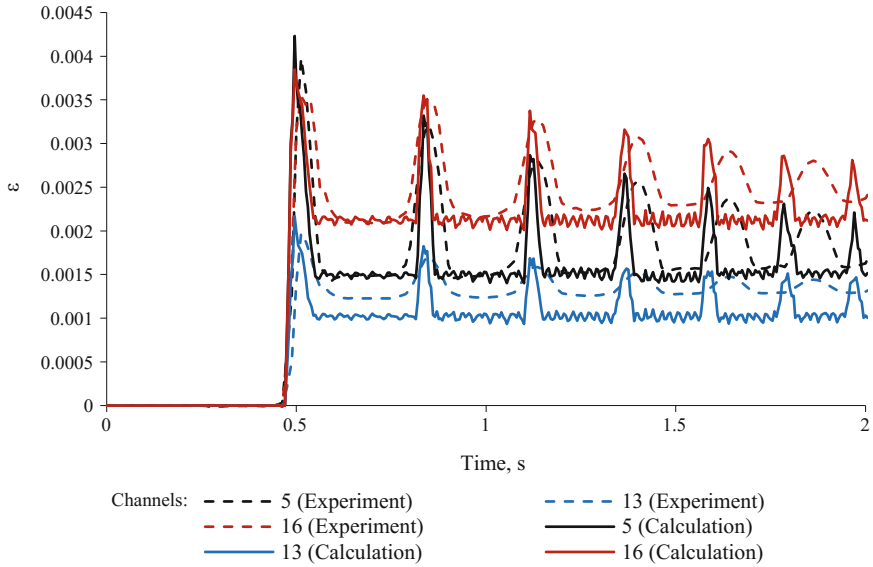

Fig. 7 Calculation and experimental deformation values over time

Table 3 Comparison of the maximum deformation values under static and dynamic loading

Strain gage no.	Impact ε_{din} (calculation)	Impact ε_{din} (experiment)	Inaccuracy (%)	Static ε_{st} (calculation)	K_D
1	0.4478	0.3786	18	0.0549	11.06
3	0.4274	0.3785	13	0.0165	11.07
4	0.4203	0.3784	11	0.0449	9.77
5	0.4232	0.3978	6	0.0449	9.08
6	0.3875	0.3500	11	0.0182	12.26
13	0.2167	0.1973	10	0.0104	11.22
14	0.2003	0.1847	8	0.0314	10.75
16	0.3848	0.3544	9	0.0296	10.87

reflect ca. 11% deviation from the test results in respective measurement points. Analyses of comparative results of deformation calculations under static and impact loading conditions (with loads been applied against the spoke) show, that the average value of ratio between the impact calculated deformations and calculated deformations in similar areas under static loading, close to $K_D = 10.94$ with the standard deviation of 0.82. These value, in fact, fully concurs with the same result obtained during the testing.

4 Conclusion

The carried out comprehensive calculation and experimental researches of deformed condition of aluminum cast wheels under static and impact loads applied to different areas of a wheel rim demonstrated the adequacy of the wheel design FE models and possibility to carry out a virtual impact test when creating and elaborating new structures. Moreover, the research made it possible to establish the mean value of the dynamic factor for aluminum cast wheels under an impact which amounts to ca. $K_D \approx 10$ (ratio between dynamic and static deformation). This ratio can used for all cast wheels made from aluminum-silicon alloys in the approximate engineering analysis. It established that the dynamic behavior of a cast wheel at an oblique impact does not practically depend on the availability of the tire and determined mainly by mechanical properties of the material and the design.

References

1. GOST R 50511-93: Light Alloy Wheels for Air Tires. GOSSTANDART RF, Moscow (1993)
2. Demiyanushko, I.: The current state of design analysis of vehicle wheel integrity and durability. Veh. Road Infrastruct. Online Mag. **1**(3), (2015). http://www.adi-madi.ru/index.php/madi/article/view/105. Last accessed 12 Nov 2017
3. Demyanushko, I., Esenovsky-Lashkov, Y., Vakhromeev, A.: Cast aluminum wheels for cars: designing, manufacture, quality control. Avtomobilnaya Promyshlennost **9**(12), 29–31 (2002)
4. Demiyanushko, I.: Light alloy wheels—From sketch to metal. Avtomobilnaya Promyshlennost **7**(12), 9–10 (1999)
5. Demiyanushko, I., Yudin, M.: Information technologies and creation of automobile designs. Avtomobilnaya Promyshlennost **9**(12), 3–5 (2003)
6. Mironova, V.: Analysis of stress-strained state of vehicle cast wheels under impact loads. Ph.D. thesis, Moscow Automobile and Road Construction State Technical University (MADI), Moscow (2012)
7. Tirelli, M., Colosio, M., Santos, J.: Evaluation of aluminum wheels with focus on specification materials and manufacturing. SAE Technical Paper 2011-36-0267 (2011)
8. Olejnik, P., Awrejcewicz, J.: Coupled oscillators in identification of nonlinear damping of a real parametric pendulum. Mech. Syst. Sig. Process. **98**, 91–107 (2018). https://doi.org/10.1016/j.ymssp.2017.04.037
9. Demiyanushko, I., Mironova, V., Loginov, E.: Analysis of stress-strained state of vehicle cast wheels under impact loads. Mech. Eng. Tech. Educ. **1**(30), 42–49 (2015)
10. LS-DYNA Keyword User's Manual. Version 971 Release 4. Livermore Software Technology Corporation, Livermore, California (2009)
11. Dietenberger, M., Buyuk M., Kan, C-D.: Development of a high strain-rate dependent vehicle model. In: LS-DYNA Anwenderforum, B-III-1-10, Bamberg (2005)
12. Loginov, E.: Development of a comprehensive method for estimation of motor vehicle wheel integrity and durability. Extended abstract of Ph.D. thesis, Moscow Automobile and Road Construction State Technical University (MADI), Moscow (2017)
13. Loginov, E.M.: Development of a comprehensive method for estimation of motor vehicle wheel integrity and durability. Ph.D. thesis, Moscow Automobile and Road Construction State Technical University (MADI), Moscow, 2017

14. Chang, C., Yang, S.: Finite element simulation of wheel impact test. J. Achievements Mater. Manuf. Eng. **28**(2), 167–170 (2008)
15. Biderman, V.L.: Theory of Mechanical Oscillations. NIC Regular and Chaotic Dynamics, Moscow-Izhevsk (2009)

Optimal Control for Robot Manipulators with Three-Degress-of-Freedom

Jose Adenilson Gonalves Luz Junior, Angelo Marcelo Tusset, Frederic Conrad Janzen, Rodrigo Tumolin Rocha, Jose Manoel Balthazar and Airton Nabarrete

Abstract This work presents the modeling and simulation of a manipulator robot with three degrees of freedom and considering its structures with rigid behavior. The concepts of kinematics for the mathematical deduction and the Lagrangian mechanics were used to obtain the dynamic models of the manipulator and the DC actuators with permanent magnet. Due to nonlinearity and dynamics characteristics, both the states observer and the control used were based on State Dependet Ricatti Equation (SDRE). The simulations made for constant performance parameters demonstrated the effectiveness of the optimal control applied to the manipulator and to the chosen DC actuator models. The applications of trajectories to the manipulator enrich the applicability of the project and the results obtained with the techniques chosen show his efficiency.

Keywords Robot manipulator · Control design · Nonlinear dynamics

J. A. G. Luz Junior · A. M. Tusset · F. C. Janzen · R. T. Rocha
Federal University of Technology - Parana, Ponta Grossa, PR 84016-210, Brazil
e-mail: jose.adg@hotmail.com

A. M. Tusset
e-mail: tusset@utfpr.edu.br

F. C. Janzen
e-mail: fcjanzen@utfpr.edu.br

R. T. Rocha
e-mail: digao.rocha@gmail.com

J. M. Balthazar (✉) · A. Nabarrete
Aeronautics Technological Institute, Sao Jose dos Campos, SP 12228-900, Brazil
e-mail: jmbaltha@gmail.com

A. Nabarrete
e-mail: nabarret@ita.br

J. Awrejcewicz (ed.), *Dynamical Systems in Theoretical Perspective*,
Springer Proceedings in Mathematics & Statistics 248,
https://doi.org/10.1007/978-3-319-96598-7_12

1 Introduction

Robotic systems are composed of several parts that can be considered linear such as mechanical structures and some types of actuators. However, when the physical structure presents high nonlinear and complex interactions, the linear system or a system with linearized modes of vibration may present a very different result from the desired model [1]. Even if linear control can be used in the actuators, in a robot, it is not feasible [2].

The inclusion of nonlinearities inherent in a robot is a very complex process and raises the need to apply more refined techniques in the model and control process [3]. In [1, 4, 5] the SDRE controller has a great applicability for systems with a complex dynamics. Using optimal control allows to have more precision and good performance on consumption of energy [6].

Generally, friction applications in a robot have been strongly considered in the joints for, due to the contact of the link of the joints, it generates such friction in which breaks the robot motion. According to [7], such friction phenomenon is related to dissipation of energy, for example as heat, and leads to friction and wear on surfaces of contact bodies, that is, the contact of the links of the robot joints generates a dry friction phenomenon. There exist many well-designed mathematical models to dry friction model, as for example, Bay-Wanheim, Dahl and many others.

Therefore, in this paper is proposed the optimal control for a planar robot with three-degrees-of-freedom, considering the influence of the friction phenomenon by a mechanical differential equation as in [8]. The efficiency of the control was tested with fixed points simulation and path planning.

2 Equations of Motion

Several approaches can be made to find the mathematical representation of the manipulator, which will depend on the structure, model and its use. Denavit-Hartenberg algorithm is a very widespread approach on robotics because of its universality and applicability [9]. Cartesian, polar or cylindrical coordinates are other ways of representing points and structures in space. Each one of them have advantages and disadvantages always depending on the model and its possible movements. Using the correct coordinate system can simplify the mathematical model.

2.1 Manipulator Model/Kinematics Model

The robot manipulator which was used is of three-degrees-of-freedom and can be represented by Fig. 1. In this deduction, the link length is l_n, the center of mass is cm_n and the position angles θ_n.

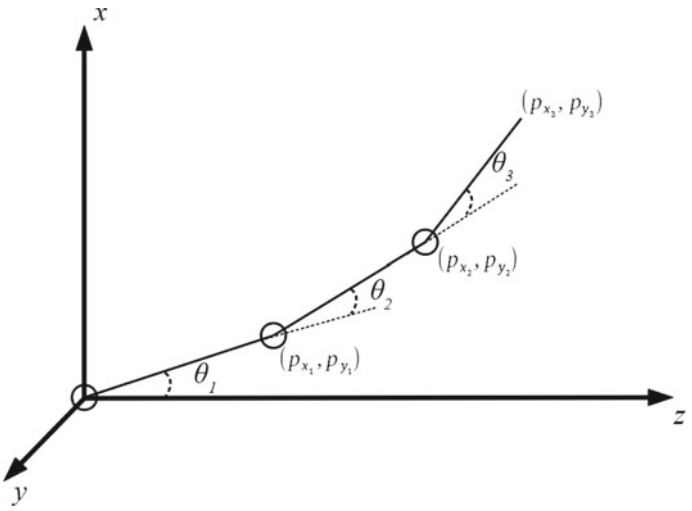

Fig. 1 Structure of the manipulator with three planar degrees of freedom

As the manipulator can only move in two of the three possible axes, by coherence, the positions of the manipulator were deduced based on the cartesian representation [10]. The kinect energy was deduced through the links, i.e., the place where the actuators are coupled in the manipulator structure as Eqs. (1)–(6).

$$p_{x_1} = l_1 cm_1 \cos\theta_1 \tag{1}$$
$$p_{y_1} = -l_1 cm_1 \sin\theta_1 \tag{2}$$
$$p_{x_2} = l_1 \cos\theta_1 + l_2 cm_2 \cos(\theta_1 + \theta_2) \tag{3}$$
$$p_{y_2} = -l_1 \sin\theta_1 - l_2 cm_2 \sin(\theta_1 + \theta_2) \tag{4}$$
$$p_{x_3} = l_1 \cos\theta_1 + l_2 cm_2 \cos(\theta_1 + \theta_2) + l_3 cm_3 \cos(\theta_1 + \theta_2 + \theta_3) \tag{5}$$
$$p_{y_3} = -l_1 \sin\theta_1 - l_2 cm_2 \sin(\theta_1 + \theta_2) - l_3 cm_3 \cos(\theta_1 + \theta_2 + \theta_3) \tag{6}$$

where l_i is the length of each link, cm_i is the center of mass of each link and θ_i is the angular position of each link, being that $i = 1, 3$ are the first, second and third links of the robot arm.

2.2 Dynamic Model

The dynamic model can be obtained using the Lagranges energy method which consists of the Lagranges function and Euler-Lagrange equation based on the energy balance of the kinematics and potential components of the body:

$$L = \sum_{k=1}^{n} E_{kinetic} - \sum_{k=1}^{n} E_{potential} \; n = 1, 2, 3 \ldots \tag{7}$$

Euler-Lagrange equation is expressed in terms of the non-conservative generic force (τ_k), which do not depend on the space variable (q_k) used in mathematical deduction, and by considering a non-damping system [10]:

$$\frac{d}{dt}\left(\frac{\partial L}{\partial \dot{q}_k}\right) - \left(\frac{\partial L}{\partial q_k}\right) = \tau_k \;\; k = 1, 2, \ldots, n \tag{8}$$

For all k degrees-of-freedom of the dynamic system (Fig. 1), a differential equation is generated. Therefore, the total kinetic and potential energies are a sum of the 3DOFs of the body and the Lagrangian function is expressed as:

$$\begin{aligned} L = {} & \dot{\theta}_2^2 \Omega_1 + \dot{\theta}_2^2 \Omega_2 + \dot{\theta}_2^2 \Omega_3 + \dot{\theta}_1 \dot{\theta}_2 \Omega_4 + \dot{\theta}_1 \dot{\theta}_2 \Omega_5 + \dot{\theta}_1 \dot{\theta}_2 \Omega_6 \\ & - g \left(\cos\theta_2 \left(m_2 cm_2 l_2 + m_3 l_2\right) + \cos\theta_3 \left(l_3 cm_3 m_3\right)\right. \\ & \left. + \cos\theta_1 \left(m_1 cm_1 l_1 + m_2 l_1 + l_1 m_3\right)\right) \end{aligned} \tag{9}$$

Substituting Eq. (9) into Euler-Lagrange equation to each coordinate, the non-conservative generalized forces of the three links are given by:

$$\tau_1 = \dot{\theta}_1 \dot{\theta}_2 \left(-\sin\theta_2 \left(2cm_2 l_1 l_2 m_2 + 2l_1 l_2 m_3\right)\right) - \sin\left(\theta_1 + \theta_2 + \theta_3\right) l_3 cm_3 m_3 \tag{10}$$

$$\tau_2 = \dot{\theta}_1 \dot{\theta}_2 \left(-\sin\theta_2 \left(cm_2 l_1 l_2 m_2 + l_1 l_2 m_3\right)\right) - \sin\left(\theta_1 + \theta_2 + \theta_3\right) l_3 cm_3 m_3 \tag{11}$$

$$\begin{aligned} \tau_3 = {} & \ddot{\theta}_1 \Omega_5 + \ddot{\theta}_2 \Omega_6 + \ddot{\theta}_3 \Omega_3 - \dot{\theta}_1 \dot{\theta}_2 \sin\left(\theta_2 + \theta_3\right) \\ & + g \sin\left(\theta_1 + \theta_2 + \theta_3\right) l_3 cm_3 m_3 \end{aligned} \tag{12}$$

In the following, the accelerations are isolated to be highlighted in each respective equation, i.e., the equation of motion of the first link will be only dependent on the component $\ddot{\theta}_1$ (excluding $\ddot{\theta}_2$ and $\ddot{\theta}_3$). To rewrite, the system was exceptionally compared to a linear system composed by the acceleration multiplied by a constant and an additional constant that summarizes all the other terms:

$$\tau_1 = \ddot{\theta}_1 c_1 + \ddot{\theta}_2 c_2 + \ddot{\theta}_3 c_3 + c_4 \tag{13}$$

$$\tau_2 = \ddot{\theta}_1 c_5 + \ddot{\theta}_2 c_6 + \ddot{\theta}_3 c_7 + c_8 \tag{14}$$

$$\tau_3 = \ddot{\theta}_1 c_9 + \ddot{\theta}_2 c_{10} + \ddot{\theta}_3 c_{11} + c_{12} \tag{15}$$

Therefore, the isolated accelerations are obtained by solving the system of equations of Eqs. (13), (14) and (15). Hence, the final representation is denoted by:

$$\begin{aligned} \ddot{\theta}_1 = {} & \frac{\tau_1 \left(c_{10} c_7 - c_{11} c_6\right) + \tau_2 \left(c_{11} c_2 - c_{10} c_3\right) + \tau_3 \left(c_3 c_6 - c_2 c_7\right)}{c_1 c_{10} c_7 - c_1 c_{11} c_6 - c_{10} c_3 c_5 + c_{11} c_2 c_5 - c_2 c_7 c_9 + c_3 c_6 c_9} \\ & + \frac{c_{10} \left(c_3 c_8 - c_4 c_7\right) + c_{11} \left(c_4 c_6 - c_2 c_8\right) + c_{12} \left(c_2 c_7 - c_3 c_6\right)}{c_1 c_{10} c_7 - c_1 c_{11} c_6 - c_{10} c_3 c_5 + c_{11} c_2 c_5 - c_2 c_7 c_9 + c_3 c_6 c_9} \end{aligned} \tag{16}$$

$$\ddot{\theta}_2 = \frac{\tau_1 (c_{11}c_5 - c_7c_9) + \tau_2 (c_3c_9 - c_1c_{11}) + \tau_3 (c_1c_7 - c_3c_5)}{c_1c_7c_{11} - c_1c_7c_{11} - c_{10}c_3c_5 + c_{11}c_2c_5 - c_2c_7c_9 + c_3c_6c_9} + \frac{c_1 (c_8c_{11} - c_{12}c_7) + c_5 (c_{12}c_3 - c_{11}c_4) + c_9 (c_3c_8 - c_4c_7)}{c_1c_7c_{11} - c_1c_7c_{11} - c_{10}c_3c_5 + c_{11}c_2c_5 - c_2c_7c_9 + c_3c_6c_9} \quad (17)$$

$$\ddot{\theta}_3 = -\frac{\tau_1 (c_{10}c_5 - c_6c_9) + \tau_2 (c_2c_9 - c_1c_{10}) + \tau_3 (c_1c_6 - c_2c_5)}{c_1c_10c_7 - c_1c_{11}c_6 - c_{10}c_3c_5 + c_{11}c_2c_5 - c_2c_7c_9 + c_3c_6c_9} + \frac{c_1 (c_{10}c_8 - c_{12}c_6) + c_5 (c_{12}c_2 - c_{10}c_4) + c_9 (c_4c_6 - c_2c_8)}{c_1c_10c_7 - c_1c_{11}c_6 - c_{10}c_3c_5 + c_{11}c_2c_5 - c_2c_7c_9 + c_3c_6c_9} \quad (18)$$

2.3 Dissipation components

In this model, every dissipation in the system was summarized in a mechanical differential equation based on the variables of movement and a constant denoted by [8]:

$$D(t)_n = \frac{1}{2}\sum_{i=1}^{n}\sum_{j=1}^{n} c_{ij}\dot{q}_i\dot{q}_j = \frac{1}{2}\mu_1\dot{\theta}_1^2 + \frac{1}{2}\mu_2\left(\dot{\theta}_1 + \dot{\theta}_2\right)^2 + \frac{1}{2}\mu_3\left(\dot{\theta}_1 + \dot{\theta}_2 + \dot{\theta}_3\right)^2 \quad (19)$$

2.4 State-Space representation

In [1, 4, 5], to use optimal control, it is necessary to represent the system in state-space notation, as given by:

$$\dot{x} = A(x)x + B(x)u_f + G \quad (20)$$

$$y = C(x)x + D(x)u_f \quad (21)$$

where $A(x)$ and $B(x)$ are based on the state of the system and G summarizes all the non-state dependent components [11]. The final matrices of the systems can be represented, with the elements based on Eqs. (16), (17) and (18), by:

$$A(x) = \begin{bmatrix} 0 & 1 & 0 & 0 & 0 & 0 \\ 0 & 0 & 0 & \varphi_{24} & 0 & \varphi_{63} \\ 0 & 0 & 0 & 1 & 0 & 0 \\ 0 & & 0 & \varphi_{44} & 0 & \varphi_{64} \\ 0 & 0 & 0 & 0 & 0 & 1 \\ 0 & 1 & 0 & \varphi_{46} & 0 & \varphi_{66} \end{bmatrix} \quad B(x) = \begin{bmatrix} 0 & 0 & 0 \\ \beta_{21} & \beta_{22} & \beta_{23} \\ 0 & 0 & 0 \\ \beta_{41} & \beta_{42} & \beta_{43} \\ 0 & 0 & 0 \\ \beta_{61} & \beta_{62} & \beta_{63} \end{bmatrix} \quad G = \begin{bmatrix} 0 \\ \psi_1 \\ 0 \\ \psi_2 \\ 0 \\ \psi_3 \end{bmatrix} \quad (22)$$

The values used in $C(x)$, Eq. (23), were defined by the output requirement. The elements of the main diagonal are associated with the system states; δ_{11} associated

with the state x_1, δ_{22} associated with x_2 and so on. If the state is needed in the output, the respective element turns to 1 and if it is dispensable, the element turns to 0.

$$C = \begin{bmatrix} \delta_{11} & 0 & 0 & 0 & 0 & 0 \\ 0 & \delta_{22} & 0 & 0 & 0 & 0 \\ 0 & 0 & \delta_{33} & 0 & 0 & 0 \\ 0 & 0 & 0 & \delta_{44} & 0 & 0 \\ 0 & 0 & 0 & 0 & \delta_{55} & 0 \\ 0 & 0 & 0 & 0 & 0 & \delta_{66} \end{bmatrix} \tag{23}$$

By the system of control, the vector of states and vector of input are defined as $x = \left(\theta_1, \theta_2, \theta_3, \dot{\theta}_1, \dot{\theta}_2, \dot{\theta}_3\right)$ and $u(x) = (\tau_1, \tau_2, \tau_3)$, respectively.

3 Optimal Control

The optimal control represented in state-space form uses the matrices $A(x)$, $B(x)$ and $C(x)$ to determine if the control is possible and to reach the feedback control law. For a controller, there exist the matrices (A, B) that must be controllable (stabilizable). Equation (24) shows how to define the controllability.

$$M_c = \begin{bmatrix} B & AB & A^2B & \ldots & A^{n-1}B \end{bmatrix} \tag{24}$$

With the value of M_c, the rank (r) of M_c is calculated. For the system to be controllable, if the rank of the matrix (M_c) is six, the system is controllable and the SDRE solution use the actual value for the matrix $A(x)$ [6]. If r is lower or higher than the system size, the last controllable value for $A(x)$ is used in SDRE solution.

Once the controllability was verified, the control law can be determined by [5]:

$$u(t) = R^{-1}B(x)^T P(x)x(t) \tag{25}$$

The matrix $P(x)$ is based on the solution of Riccati equation:

$$\begin{aligned} A\left(x_n\right) P(x)_{n+1} + P(x)_{n+1} A\left(x_n\right) - P(x) B\left(x_n\right) R\left(x_n\right)^{-1} B\left(x_n\right)^T P(x)_{n+1} \\ + Q(x) = 0 \end{aligned} \tag{26}$$

The matrices $Q(x)$ and $R(x)$ must be defined positive. The values used in the matrices are defined by the planner and control guidelines to perform the minimization of a functional:

$$J\left(x_0, u\right) = \frac{1}{2} \int_0^{\infty} \left(x^T Q x + u^T R u\right) dt \tag{27}$$

As the considered system is nonlinear and possesses a high state dependence, the controllability needs to be recalculated in all interactions defined in the simulation

of the parameters. Basically, the controllability and the matrices $A(x)$, $B(x)$ and $C(x)$ are recalculated every step of the numerical solution [6].

For the matrices Q and R two fronts were addressed. First, Q was deemed as the multiplication of C by C^T. When all states are considered in C, this first approach leads Q to an identity matrix. With the first results using Q as $C \cdot C^T$, some elements of Q were tuned in to improve the final response. This process of refinement is guided by the need to improve the responses of the output of each state. In Q, the columns and rows are associated with the system states [6]. Then, the values used in the elements of Q dictate the control gains for every system state. The tune is chosen to increase or decrease the pitch in the states. If the planner wants more attention on the position of the first link and less in speed, the elements on the first column should be increased and so on.

To follow the changes and improvements, the matrix R, Eq. (29), was kept constant with the same number of columns as $B(x)$. The elements r_{11}, r_{22} and r_{33} were kept as 1. As R is multiplied by Q, in this case, keeping R constant or floating makes no difference if Q is already floating.

$$Q(x) = \begin{bmatrix} q_{11} & 0 & 0 & 0 & 0 & 0 \\ 0 & q_{22} & 0 & 0 & 0 & 0 \\ 0 & 0 & q_{33} & 0 & 0 & 0 \\ 0 & 0 & 0 & q_{44} & 0 & 0 \\ 0 & 0 & 0 & 0 & q_{55} & 0 \\ 0 & 0 & 0 & 0 & 0 & q_{66} \end{bmatrix} \tag{28}$$

$$R = \begin{bmatrix} r_{11} & 0 & 0 \\ 0 & r_{22} & 0 \\ 0 & 0 & r_{33} \end{bmatrix} \tag{29}$$

4 Nonlinear States Observer and Estimation

The State Observer is designed to estimate the robot state variables [12]. In this paper, it is analyzed the estimation for the robot speed, in this case, the second and fourth system states. The system represented in Eqs. (20) and (21) is used as the basis for the observer. Assuming that the state x_i can be estimated by the state $\hat{x}_i$ [11], the observer can be represented in the form of:

$$\dot{x} = A(x) + Bu_f - K_0(\hat{x})\left(C(x) - C(\hat{x})\right) \tag{30}$$

$$\hat{y} = C\hat{x}(t) + Du_f \tag{31}$$

To define if the system is Observable, a similar approach used for Controllability is used, however using the matrix C(x) instead of matrix B(x) [12]. Equation (32) shows how to define the observability.

$$M_o = \begin{bmatrix} C \\ CA \\ CA^2 \\ \cdots \\ CA^{n-1} \end{bmatrix} \tag{32}$$

The rank (r) of the matrix M_o is calculated, if the result is six the system is completely Observable. If the rank is lower than six, that means there are states of the system that are not observable.

The Observer Gain is denoted by K_0 given by Eq. (33). The matrix size must be such that the dynamic behavior matrices are stable and the values of K_0 can be obtained by the implementation of optimal feedback control.

$$K_0 = -R^{-1}CP(\hat{x})\hat{x} \tag{33}$$

By using optimal feedback control, the matrix $P(\hat{x})$ is determined by the solution of the Riccati equation, as shown in Eq. (26).

The matrix $\hat{Q}$ is based on the same previously discussed statements on Eq. (28). Otherwise, the matrix $\hat{R}$ is defined as the same number of columns as $C(x)$ shown in Eq. (23).

$$\hat{R} = \begin{bmatrix} r_{11} & 0 & 0 & 0 & 0 & 0 \\ 0 & r_{22} & 0 & 0 & 0 & 0 \\ 0 & 0 & r_{33} & 0 & 0 & 0 \\ 0 & 0 & 0 & r_{44} & 0 & 0 \\ 0 & 0 & 0 & 0 & r_{55} & 0 \\ 0 & 0 & 0 & 0 & 0 & r_{66} \end{bmatrix} \tag{34}$$

Subtracting the Eqs. (20) and (21) and (30) and (31), which are the system and the observer representation, respectively, the observer error is given by:

$$\hat{e}_0 = \left(A(x) - K_0(\hat{x})C\right)x - \left(A(\hat{x}) - K_0(\hat{x})C\right)\hat{x} \tag{35}$$

$$\hat{e}_0 = x(t) - \hat{x}(t) \tag{36}$$

The dynamic behavior of the error vector is determined by the eigenvalues of the matrices:

$$\left[A(x) - K_0(\hat{x})C(x)\right] \tag{37}$$

$$\left[A(\hat{x}) - K_0(\hat{x})C(x)\right] \tag{38}$$

where

$$A(x) = \begin{bmatrix} 0 & 1 & 0 & 0 & 0 & 0 \\ 0 & 0 & 0 & \varphi_{24} & 0 & \varphi_{63} \\ 0 & 0 & 0 & 1 & 0 & 0 \\ 0 & & 0 & \varphi_{44} & 0 & \varphi_{64} \\ 0 & 0 & 0 & 0 & 0 & 1 \\ 0 & 1 & 0 & \varphi_{46} & 0 & \varphi_{66} \end{bmatrix} \qquad C(x) = \begin{bmatrix} \delta_{11} & 0 & 0 & 0 & 0 & 0 \\ 0 & \delta_{22} & 0 & 0 & 0 & 0 \\ 0 & 0 & \delta_{33} & 0 & 0 & 0 \\ 0 & 0 & 0 & \delta_{44} & 0 & 0 \\ 0 & 0 & 0 & 0 & \delta_{55} & 0 \\ 0 & 0 & 0 & 0 & 0 & \delta_{66} \end{bmatrix}$$

$$K_0 = -R^{-1}CP(\hat{x})\hat{x}$$

5 Path Planning

To analyze the effectiveness of the control, the model was tested by placing values for the three possible variables of each link: position, speed and acceleration [13].

For this purpose, a fifth order polynomial was used. To the position, the fifth order was used and for speed and acceleration were used the first and the second derivatives, respectively:

$$q_i(t) = a_{i5}t^5 + a_{i4}t^4 + a_{i3}t^3 + a_{i2}t^2 + a_{i1}t + a_{i0} \tag{39}$$

$$\dot{q}_i(t) = 5a_{i5}t^4 + 4a_{i4}t^3 + 3a_{i3}t^2 + 2a_{i2}t + a_{i1} \tag{40}$$

$$\ddot{q}_i(t) = 20a_{i5}t^3 + 12ai4t^2 + 6a_{i3}t + 2a_{i2} \tag{41}$$

6 Numerical Simulations

In the simulations for path planning, the matrix of control without the State Observer is considered as:

$$k_{ij} = \begin{bmatrix} k_{11} & k_{12} & k_{13} & k_{14} & k_{15} & k_{16} \\ k_{21} & k_{22} & k_{23} & k_{24} & k_{25} & k_{26} \\ k_{31} & k_{32} & k_{33} & k_{34} & k_{35} & k_{36} \end{bmatrix} \tag{42}$$

The elements of k_i are used to determine the error in the control law. As each element is associated with one of the system states and one control law equation, the elements of k_{ij} are in the $(ij)^{ht}$ state and n^{ht} control law. For example, the element k_{12} is associated with the speed, $\dot{\theta}_2$, of the first link and the first control law, u_1. Such elements and error are denoted by Eqs. (43)–(46). In the simulation, the 4th order

Table 1 Parameters for SDRE control with path planning without state observer

Parameters	Symbol	Unit	Final value
Initial time	t_0	s	0
Final time	t_f	s	0.1
Initial position—link 1	θ_{01}	rad	0
Desired position—link 1	θ_{f1}	rad	0.1745 (10°)
Initial position—link 2	θ_{02}	rad	0
Desired position—link 2	θ_{f2}	rad	0.5236 (30°)
Initial position—link 3	θ_{03}	rad	0
Desired position—link 3	θ_{f3}	rad	0.5236 (30°)
Initial speed—link 1, 2 and 3	ω_0	rad/s	0
Desired speed—link 1, 2 and 3	ω_f	rad/s	0
Initial acceleration—link 1, 2 and 3	$\dot{\omega}_0$	rad/s^2	0
Desired acceleration—link 1, 2 and 3	$\dot{\omega}_f$	rad/s^2	0

Runge-Kutta method was used in the integration of all the presented equations of motion, using the parameters of Table 1.

$$e_{x_n} = x_n = x_{n_d} \tag{43}$$

$$u_1 = -k_{11}(x_1 - x_{1_d}) - k_{16}(x_6 - x_{6_d}) \tag{44}$$

$$u_2 = -k_{21}(x_1 - x_{1_d}) - k_{26}(x_6 - x_{6_d}) \tag{45}$$

$$u_3 = -k_{31}(x_1 - x_{1_d}) - k_{36}(x_6 - x_{6_d}) \tag{46}$$

Figures 2 show the path planning simulation without state observer. The curves show the efficiency of the controller in leading the position of the three links to the desired position with a small time and low levels of velocity, in this way, not compromising the controller.

The state observer was used to estimate separately two system states related to velocity of the first and the second link, x_2 and x_4 without path planning. The analysis of Observability, Eq. (32), indicated these two states allow to apply the State Observer. The gain matrix of the State Observer was product of the matrix A(x) and C(x) and the generic result is shown in Eq. (47).

$$K_{0i} = \begin{bmatrix} K_{011} & K_{012} & K_{013} & K_{014} & K_{015} & K_{016} \\ K_{021} & K_{022} & K_{023} & K_{024} & K_{025} & K_{026} \\ K_{031} & K_{032} & K_{033} & K_{034} & K_{035} & K_{036} \\ K_{041} & K_{042} & K_{043} & K_{044} & K_{045} & K_{046} \\ K_{051} & K_{052} & K_{053} & K_{054} & K_{055} & K_{056} \\ K_{061} & K_{062} & K_{063} & K_{064} & K_{065} & K_{066} \end{bmatrix} \tag{47}$$

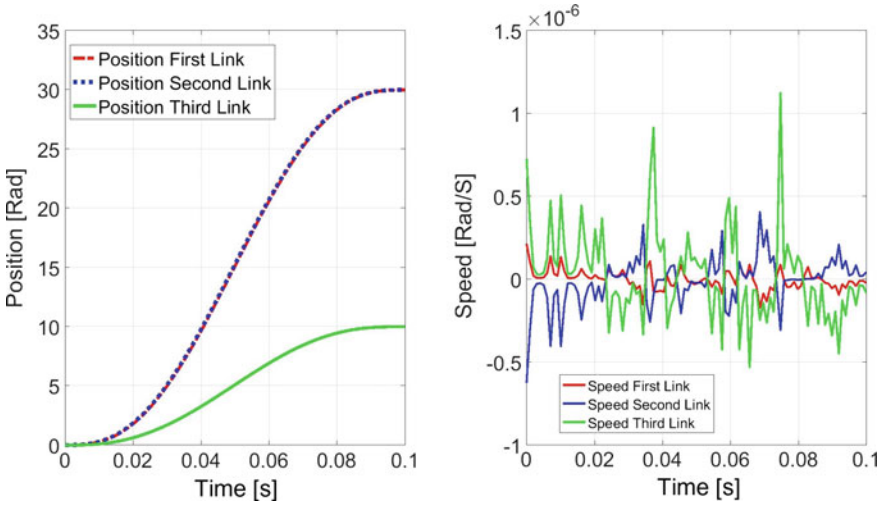

Fig. 2 Position and speed path following for all the system states

The control action L_{0i} used on the state observer control was found Eq. (49) based on the product of $C(x)$, the matrix of the error estimation γ_i, Eq. (48), and the matrix K_{0i}.

$$\gamma_i = \begin{bmatrix} x_1 - \hat{x}_1 \\ x_2 - \hat{x}_2 \\ x_3 - \hat{x}_3 \\ x_4 - \hat{x}_4 \\ x_5 - \hat{x}_5 \\ x_6 - \hat{x}_6 \end{bmatrix} \tag{48}$$

$$\delta_{0i} = \begin{bmatrix} \gamma_{11}C_{11}K_{011} & \gamma_{22}C_{22}K_{012} & \gamma_{33}C_{33}K_{013} & \gamma_{44}C_{44}K_{014} & \gamma_{55}C_{55}K_{015} & \gamma_{66}C_{66}K_{016} \\ \gamma_{11}C_{11}K_{021} & \gamma_{22}C_{22}K_{022} & \gamma_{33}C_{33}K_{023} & \gamma_{44}C_{44}K_{024} & \gamma_{55}C_{55}K_{025} & \gamma_{66}C_{66}K_{026} \\ \gamma_{11}C_{11}K_{031} & \gamma_{22}C_{22}K_{032} & \gamma_{33}C_{33}K_{033} & \gamma_{44}C_{44}K_{034} & \gamma_{55}C_{55}K_{035} & \gamma_{66}C_{66}K_{036} \\ \gamma_{11}C_{11}K_{041} & \gamma_{22}C_{22}K_{042} & \gamma_{33}C_{33}K_{043} & \gamma_{44}C_{44}K_{044} & \gamma_{55}C_{55}K_{045} & \gamma_{66}C_{66}K_{046} \\ \gamma_{11}C_{11}K_{051} & \gamma_{22}C_{22}K_{052} & \gamma_{33}C_{33}K_{053} & \gamma_{44}C_{44}K_{054} & \gamma_{55}C_{55}K_{055} & \gamma_{66}C_{66}K_{056} \\ \gamma_{11}C_{11}K_{061} & \gamma_{22}C_{22}K_{062} & \gamma_{33}C_{33}K_{063} & \gamma_{44}C_{44}K_{064} & \gamma_{55}C_{55}K_{065} & \gamma_{66}C_{66}K_{066} \end{bmatrix} \tag{49}$$

Each one of the six equations of the state observer, represented by the i index on the matrices, receives one element of the matrix L_{0i}, given by Eq. (50).

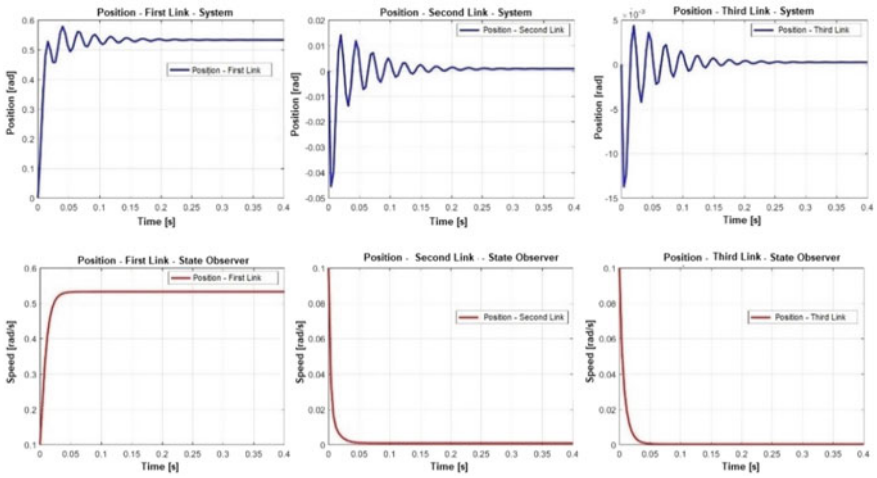

Fig. 3 Position with state observer in the second system state

$$L_{0i} = \begin{bmatrix} \sum_{n=1}^{6} \delta_{n_1} \\ \sum_{n=1}^{6} \delta_{n_2} \\ \sum_{n=1}^{6} \delta_{n_3} \\ \sum_{n=1}^{6} \delta_{n_4} \\ \sum_{n=1}^{6} \delta_{n_5} \\ \sum_{n=1}^{6} \delta_{n_6} \end{bmatrix} \tag{50}$$

The matrix $C(x)$ presented in Eq. (23) is changed to define the systems states used in the State Observer. The main diagonal of $C(x)$ variates the values to define the states in the Observer, if the state was used on the observer, the index was 0 and if the state is not used, the index was 1. Based on that the element δ_2 turns to 0 when the observer was estimated to the second system state and the element δ_4 turns to 0 when estimating the fourth system state.

Figures 3 and 5 show the positioning of the system and the position of the state observer in the second and fourth system state, respectively. The SDRE control showed to be effective in guide the position of the manipulator and control the speed. It is shown by the errors minimized to almost zero, presented in Figs. 4 and 6.

7 Conclusions

In this paper, a robot manipulator of three-degrees-of-freedom and a nonlinear control law based on the SDRE (State Dependent Riccati Equation) was used for positioning control. The application of the robot was analyzed proposing a path for all positions, as illustrated in Fig. 2, and delimitations for speed and acceleration.

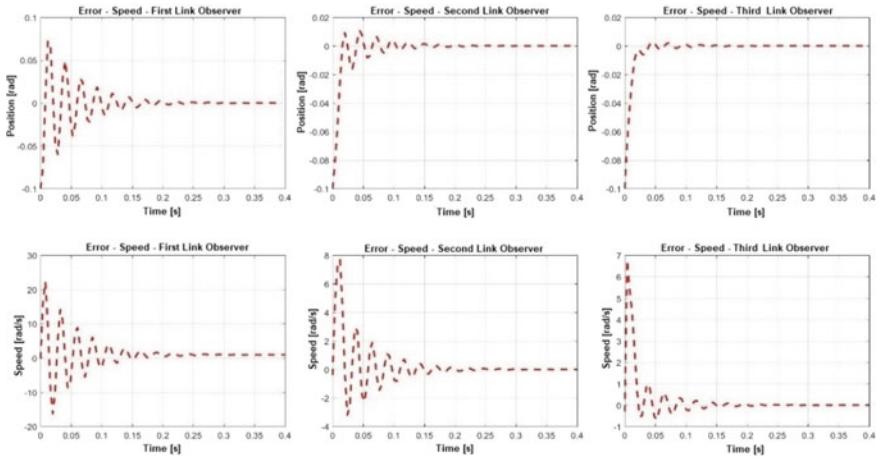

Fig. 4 Error of the observer in the second system state

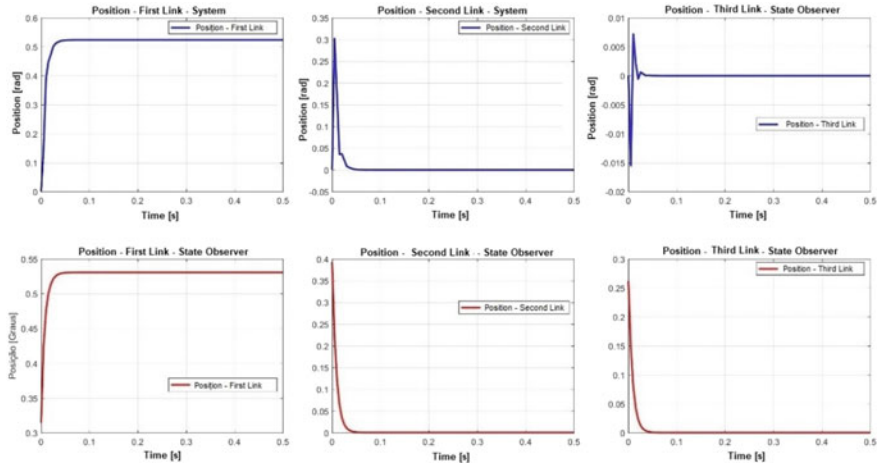

Fig. 5 Position with state observer in the fourth system state

The use of the State Observer showed its efficacy in the solution for the control of the manipulator, as illustrated in Figs. 3 and 5. The analysis of the Observability indicated the possibility to use the state observer only be a two-states system. The results showed that the SDRE control was effective to guide the position motion and control the speed.

The application of the state observer in some combination of the system states require a new approach and union between the equations of the actuator, DC motor, and the manipulator on the same application, which are some of the next steps of this research.

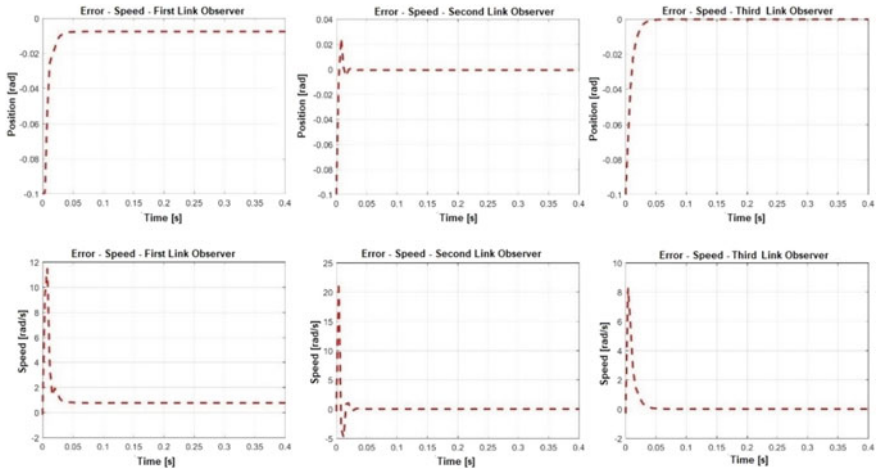

Fig. 6 Error of the observer in the fourth system state

Acknowledgements The authors acknowledge support by CNPq (GRANT:306525/2015-1) and (GRANT:447539/2014-0), CAPES and FAPESP (GRANT 2015/20363-6) both Brazilian research funding agencies.

References

1. Doosthoseini, M., Kadkhodaei, B., Korayem, M.H., Shafei, A.M.: An experimental electronic interface design for a two-link elastic robotic arm. In: 2013 XXIV International Symposium on Information, Communication and Automation Technologies (ICAT), pp. 1–4. IEEE (2013). https://doi.org/10.1109/ICAT.2013.6684084
2. Hummadi, R.M.A.M.: Simulation of optimal speed control for a DC motor using linear quadratic regulator (LQR). J. Eng. **18**(3), 340–346 (2012)
3. Erdem, E.B., Alleyne, A.G.: Experimental real-time SDRE control of an underactuated robot. In: Proceedings of the 40th IEEE Conference on Decision and Control, vol. 3, pp. 2986–2991. IEEE (2001). https://doi.org/10.1109/CDC.2001.980731
4. Korayem, M.H.: Dynamics of flexible manipulators and applications to determine load carrying capacity. Ph.D. thesis, University of Wollongong, Australia (1994)
5. Korayem, M.H., Nekoo, S.R.: Suboptimal tracking control of nonlinear systems via state-dependent differential Riccati equation for robotic manipulators. In: 2015 3rd RSI International Conference on Robotics and Mechatronics (ICROM), pp. 025–030 (2015). https://doi.org/10.1109/ICRoM.2015.7367755. IEEE
6. Katsev, S.: Streamlining of the state-dependent Riccati equation controller algorithm for an embedded implementation. Ph.D. thesis, Rochester Institute of Technology, New York (2006)
7. Olejnik, P., Fečkan, M., Awrejcewicz, J.: Modeling. Analysis and Control of Dynamical Systems with Friction and Impacts. World Scientific Publishing Company (2017). https://doi.org/10.1142/10577
8. Galicki, M.: An adaptive regulator of robotic manipulators in the task space. IEEE Trans. Autom. Control **53**(4), 1058–1061 (2008). https://doi.org/10.1109/TAC.2008.921022

9. Mohammed, A.A., Sunar, M.: Kinematics modeling of a 4-DOF robotic arm. In: 2015 International Conference on Control, Automation and Robotics (ICCAR), pp. 87–91. IEEE (2015). https://doi.org/10.1109/ICCAR.2015.7166008
10. Janzen, F.C., Koslopp, D., Carneiro, T.T., Nascimento, C.B., Cruz, F.B.C., Tusset, A.M., Balthazar, J.M.: Position control of robotic manipulator joints with two degrees of freedom using SDRE control. Proc. Ser. Braz. Soc. Comput. Appl. Math. **1**(1) (2013). https://doi.org/10.5540/03.2013.001.01.0058
11. Tusset, A.M., Bueno, A.M., Nascimento, C.B., dos Santos, M.K., Balthazar, J.M.: Nonlinear state estimation and control for chaos suppression in MEMS resonator. Shock Vibr. **20**(4), 749–761 (2013). https://doi.org/10.3233/SAV-130782
12. Dorf, R.C., Bishop, R.H.: Modern Control Systems. Pearson, Prentice Hall (2011)
13. Zhang, X., Fang, Y.: Set-oriented optimal path planning of mobile robots by a polynomial rootfinder. In: 2013 IEEE International Conference on Control Applications (CCA), pp. 778–783. IEEE (2013). https://doi.org/10.1109/CCA.2013.6662844

Optimal Control of Automotive Multivariable Dynamical Systems

Jacek Jackiewicz

Abstract Two distinctive features of challenging control engineering problems are commonly taken into consideration in design of dynamical, mechatronics systems, namely operation ranges, of such systems with nonlinear effects, which are not always near to equilibrium states, as well as a fairly high level of uncertainties of their physical description with which controllers have to cope despite a lack of knowledge on the all system parameters although physical modeling allows to identify their particular nonlinear effects. It should be noted that usage of nonlinear physical modeling in real-time control systems can be computationally very demanding. Hence, it seems to be suitable to use robust control methods based on linearized models with adaptive updating algorithms. However, usually strong nonlinearities can reduce the effectiveness of control methods, and thus of adaptive control algorithms. The controller gains can be often updated by using the estimated parameters. In this contribution the adaptive control systems for automotive applications, which are based on indirect (or self-tuning) controller strategies are discussed. The modeling issue of indirect optimal controller strategies is illustrated by the application example.

Keywords Control systems · Adaptive systems · Cruise control · Nonlinear optimal control

1 Introduction

From its beginnings in the middle of the 20th century, a multidisciplinary field of dynamical systems and feedback control has rapidly become an attractive research area for both scientists and engineers. Nowadays, the field of science that includes mainly a combination of mechanical engineering, electronics, computer engineering, systems engineering and control engineering is known as mechatronics. Thus, mechatronics relates to design of systems, which are often understood as an amal-

J. Jackiewicz (✉)
Faculty of Mathematics, Physics & Technical Sciences,
Kazimierz Wielki University, Chodkiewicza 30, 85-064 Bydgoszcz, Poland
e-mail: jacek.jackiewicz@ukw.edu.pl

J. Awrejcewicz (ed.), *Dynamical Systems in Theoretical Perspective*,
Springer Proceedings in Mathematics & Statistics 248,
https://doi.org/10.1007/978-3-319-96598-7_13

gamation of components acting together to accomplish certain objectives and, at the same time, which are aimed at achieving an optimal balance between basis mechanical structure and its overall control.

Electronic control systems engineering has become the backbone enabling automotive industry products to meet quality and functionality criteria regarding the cars' fuel consumption, improvement of vehicle dynamic properties and also safety. Recently, according to the statement of manufacturers [1], about 90% of all innovations in the automobile industry are implemented thanks to remarkable technological progress in electronics. In consequence, new series of actuators are introduced again and again into the automotive systems due to progressive increase in the requirements for the emission reduction as well as the power and safety. As has been indicated in [1], all aspects of the ultimate performance of any types of vehicles are increasingly dependent on the development of control technology. However, in this paper only aspects of cruise control systems are considered.

2 Automatic Cruise Control

Automatic cruise control can be considered as an example of a feedback control system applied in many modern vehicles. The purpose of the conventional cruise control system is to maintain a constant vehicle speed despite external disturbances, such as changes in wind or road grade. This aim is accomplished through measuring the vehicle speed, comparing it to the desired or reference speed, and automatically adjusting the throttle according to a control law.

The vehicle (see Fig. 1), of mass m, is acted on by a motive force, F, which represents the force generated at the road/tire interface. The force, F, available at the drive wheels is:

$$F = \frac{T}{\mathrm{r}} i_{\mathrm{TOT}} \eta_{\mathrm{TOT}} = \frac{P}{v} \eta_{\mathrm{TOT}}, \tag{1}$$

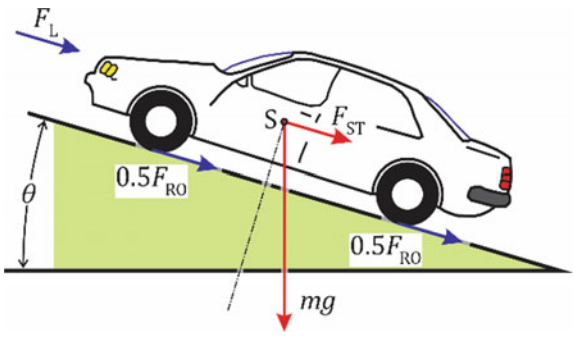

Fig. 1 Forces acting on a vehicle

where T is the motive torque, P the motive power, i_{TOT} the total transmission ratio, r the tire radius, η_{TOT} the total drive-train efficiency, and v is the vehicle velocity. For this simplified model, it is assumed that the force, F, can be controlled directly.

Referring to Fig. 1, the total running resistive force, F_W, acts in the direction opposite to the vehicle's motion and is calculated as $F_W = F_L + F_{RO} + F_{ST}$, where F_L is the aerodynamic drag, F_{RO} the rolling resistance and F_{ST} is the climbing resistance. The drag, F_L, is proportional to the square of the sum of car velocity, v, and the head-wind velocity, v_{HW}, (or $(v + v_{HW})^2$) as shown in the following equation:

$$F_L = 0.5\rho\, C_W\, A(v + v_{HW})^2, \tag{2}$$

where ρ it the air density, C_W the coefficient of aerodynamic drag, and A is the largest cross-section of the vehicle. The other two resistances, F_{RO} and F_{ST}, are functions of vehicle weight, m g, and the gradient of the road (given by the gradient angle, θ). These resistances can be calculated as follows:

$$F_{RO} = f\, \mathrm{m\,g} \cos\theta, \tag{3}$$

$$F_{ST} = \mathrm{m\,g} \sin\theta, \tag{4}$$

where f is the dimensionless coefficient of rolling resistance (or the coefficient of rolling friction—CRF), and g is the gravitational acceleration.

A simple nonlinear model of the vehicle dynamics can be obtained by summing external forces in the direction of the vehicle velocity (i.e., the longitudinal direction) and by applying the Newton's 2nd law in the following form:

$$F^*_{NL} = -\mathrm{m}\frac{dv}{dt} + F - 0.5\,\rho\, C_W A(v + v_{HW})^2 - f\, \mathrm{m\,g} \cos\theta - \mathrm{m\,g} \sin\theta = 0, \tag{5}$$

Equation 5 is nonlinear in the forward velocity, $v(t)$. Difficulties in design of the cruise-control system stem mainly from two uncertainties, which might be beyond control due to: (i) change of vehicle weight, or due to (ii) external disturbances caused by road grade [2]. Thus, a good cruise-control algorithm should work well under these uncertainties.

Three approaches are often taken in analysis of nonlinear systems:

1. replacing nonlinear elements by their linear equivalents
2. directly solving nonlinear models of these systems
3. linearizing equation systems of nonlinear models for small perturbations.

Considering accurate results and the cost of their computation, the third approach seems to be the most rational. The purpose of linearization is to replace nonlinear Eq. 5 with its linear approximation, like linearizing the nonlinear function, $F_{NL}(x)$, means replacing it locally with an approximating straight line. However, such a formulation of the linearization process is not precise and may yield inaccurate results, unless restrictions are placed on its use. In particular, a limit must be somehow established for the small variation, $\hat{x}$, of its variable, $x \stackrel{\text{def}}{=} \bar{x} + \hat{x}$, from its average value, $\bar{x}$, at the

operating point. This limit on the range of acceptable variation of the independent variable, x, is influenced by the shape of the nonlinear function curve and the location of the operating point on the curve. The term "operating point" used here refers to the condition of a system when it is in a state of equilibrium with the input variables constant and equal to their mean values averaged over time. At equilibrium (i.e., when $d\bar{v}/dt = 0$), Eq. 5 can be solved for:

$$\overline{F}^*_{\mathrm{NL}} = \overline{F} - 0.5\,\rho\,\mathrm{C_W}\,\mathrm{A}(\bar{v} + \bar{v}_{\mathrm{HW}})^2 - f\,\mathrm{m}\,\mathrm{g}\cos\bar{\theta} - \mathrm{m}\,\mathrm{g}\sin\bar{\theta} = 0. \tag{6}$$

Hence, the value of the nonlinear function, $\overline{F}^*_{\mathrm{NL}}$, at the "operating point" could be defined as

$$\overline{F}^*_{\mathrm{NL}} \stackrel{\mathrm{def}}{=} F^*_{\mathrm{NL}}\left(\overline{\left(\frac{dv}{dt}\right)}, \overline{F}, \bar{v}, \bar{v}_{\mathrm{HW}}, \bar{\theta}\right). \tag{7}$$

Equation 5 may be linearized by using the first order Taylor series approximation of F^*_{NL} about the specified operating (i.e., equilibrium) state:

$$\begin{aligned}
&F^*_{\mathrm{NL}}\left(\left(\frac{dv}{dt}\right), F, v, v_{\mathrm{HW}}, \theta\right) \\
&\quad\equiv F^*_{\mathrm{NL}}\left(\overline{\left(\frac{dv}{dt}\right)} + \widehat{\left(\frac{dv}{dt}\right)}, \overline{F} + \widehat{F}, \bar{v} + \hat{v}, \bar{v}_{\mathrm{HW}} + \hat{v}_{\mathrm{HW}}, \bar{\theta} + \hat{\theta}\right) \\
&\quad\approx \overline{F}^*_{\mathrm{NL}} + \left.\frac{\partial F^*_{\mathrm{NL}}}{\partial\left(\frac{dv}{dt}\right)}\right|_{\left(\overline{\left(\frac{dv}{dt}\right)}, \overline{F}, \bar{v}, \bar{v}_{\mathrm{HW}}, \bar{\theta}\right)} \cdot \widehat{\left(\frac{dv}{dt}\right)} \\
&\quad + \left.\frac{\partial F^*_{\mathrm{NL}}}{\partial F}\right|_{\left(\overline{\left(\frac{dv}{dt}\right)}, \overline{F}, \bar{v}, \bar{v}_{\mathrm{HW}}, \bar{\theta}\right)} \cdot \widehat{F} + \left.\frac{\partial F^*_{\mathrm{NL}}}{\partial v}\right|_{\left(\overline{\left(\frac{dv}{dt}\right)}, \overline{F}, \bar{v}, \bar{v}_{\mathrm{HW}}, \bar{\theta}\right)} \cdot \hat{v} \\
&\quad + \left.\frac{\partial F^*_{\mathrm{NL}}}{\partial v_{\mathrm{HW}}}\right|_{\left(\overline{\left(\frac{dv}{dt}\right)}, \overline{F}, \bar{v}, \bar{v}_{\mathrm{HW}}, \bar{\theta}\right)} \cdot \hat{v}_{\mathrm{HW}} + \left.\frac{\partial F^*_{\mathrm{NL}}}{\partial \theta}\right|_{\left(\overline{\left(\frac{dv}{dt}\right)}, \overline{F}, \bar{v}, \bar{v}_{\mathrm{HW}}, \bar{\theta}\right)} \cdot \hat{\theta}
\end{aligned} \tag{8}$$

with the following derivatives evaluated at the equilibrium state:

$$\left.\begin{aligned}
&\left.\frac{\partial F^*_{\mathrm{NL}}}{\partial\left(\frac{dv}{dt}\right)}\right|_{\left(\overline{\left(\frac{dv}{dt}\right)},\overline{F},\bar{v},\bar{v}_{\mathrm{HW}},\bar{\theta}\right)} = -\mathrm{m} && \text{(a)}\\
&\left.\frac{\partial F^*_{\mathrm{NL}}}{\partial F}\right|_{\left(\overline{\left(\frac{dv}{dt}\right)},\overline{F},\bar{v},\bar{v}_{\mathrm{HW}},\bar{\theta}\right)} = 1 && \text{(b)}\\
&\left.\frac{\partial F^*_{\mathrm{NL}}}{\partial v}\right|_{\left(\overline{\left(\frac{dv}{dt}\right)},\overline{F},\bar{v},\bar{v}_{\mathrm{HW}},\bar{\theta}\right)} = -\rho\,\mathrm{C_W}\,\mathrm{A}\,(\bar{v}+\bar{v}_{\mathrm{HW}}) && \text{(c)}\\
&\left.\frac{\partial F^*_{\mathrm{NL}}}{\partial v_{\mathrm{HW}}}\right|_{\left(\overline{\left(\frac{dv}{dt}\right)},\overline{F},\bar{v},\bar{v}_{\mathrm{HW}},\bar{\theta}\right)} = -\rho\,\mathrm{C_W}\,\mathrm{A}\,(\bar{v}+\bar{v}_{\mathrm{HW}}) && \text{(d)}\\
&\left.\frac{\partial F^*_{\mathrm{NL}}}{\partial \theta}\right|_{\left(\overline{\left(\frac{dv}{dt}\right)},\overline{F},\bar{v},\bar{v}_{\mathrm{HW}},\bar{\theta}\right)} = -\mathrm{m\,g}\,\cos\bar{\theta} + f\,\mathrm{m\,g}\,\sin\bar{\theta} && \text{(e)}
\end{aligned}\right\}. \qquad (9)$$

So, the linearized governing differential equation is

$$\mathrm{m}\widehat{\left(\frac{dv}{dt}\right)} + \rho\,\mathrm{C_W}\,\mathrm{A}(\bar{v}+\bar{v}_{\mathrm{HW}})\left(\hat{v}+\hat{v}_{\mathrm{HW}}\right) - \widehat{F} - \mathrm{m\,g}\left(f\,\sin\bar{\theta} - \cos\bar{\theta}\right)\hat{\theta} = 0, \qquad (10)$$

which might be rearranged to a more compact form:

$$\tau\widehat{\left(\frac{dv}{dt}\right)} + \hat{v} = K\left(\widehat{F} + \hat{d}\right), \qquad (11)$$

where the estimates of incremental, or perturbated, variables are defined as: $F(t) \stackrel{\text{def}}{=} \overline{F} + \hat{F}(t)$, $\theta(t) \stackrel{\text{def}}{=} \bar{\theta} + \hat{\theta}(t)$, $v(t) \stackrel{\text{def}}{=} \bar{v} + \hat{v}(t)$, and $v_{\mathrm{HW}} \stackrel{\text{def}}{=} \bar{v}_{\mathrm{HW}}$ (because of $\hat{v}_{\mathrm{HW}} \approx 0$). Furthermore, in Eq. 11 the following function: $\hat{d}(t) \stackrel{\text{def}}{=} \mathrm{m\,g}\left(f\,\sin\bar{\theta} - \cos\bar{\theta}\right)\hat{\theta}(t)$ represents uncertainties and external disturbances, while $K \stackrel{\text{def}}{=} 1/(\rho\,\mathrm{C_W}\,\mathrm{A}(\bar{v}+\bar{v}_{\mathrm{HW}}))$ and $\tau \stackrel{\text{def}}{=} \mathrm{m}\,K$ are both parameters, which vary with operating conditions (e.g., mass, speed, and wind velocity).

The next step is to take the Laplace transform of the linearized differential equation, assuming zero initial conditions [3]. The signal, $x(t)$, and its associated Laplace transform, $X(s)$, form the following Laplace transform pair:

$$X(s) = \mathcal{L}[x(t)], \qquad (12)$$

where the operator notation, $\mathcal{L}$, means to multiply the signal being operated upon, $x(t)$, by the complex exponential, e^{-st}, and then to integrate that product over the time interval $(-\infty, +\infty)$, as follows: $\int_{-\infty}^{+\infty} x(t)\,e^{-st}dt$. The operator of time-domain differentiation has then been found to correspond to a multiplication by s in the Laplace variable s-domain. The Laplace transform of differential signal, $dx(t)/dt$, from the t-domain into the s-domain is

$$\mathcal{L}\left[\frac{dx(t)}{dt}\right] = s\,X(s). \qquad (13)$$

The Laplace transform of Eq. 11 can now be written as:

$$(\tau s + 1)V(s) = K\big[F^*(s) + D(s)\big], \tag{14}$$

where $V(s) = \mathcal{L}\big[\hat{v}(t)\big]$, $F^*(s) = \mathcal{L}\Big[\hat{F}(t)\Big]$, and $D(s) = \mathcal{L}\Big[\hat{d}(t)\Big]$ are the associated Laplace transforms.

Finally, in Eq. 14 the input variables, $F^*(s)$ and $D(s)$, and the output variable, $V(s)$, are separated, and then the vehicle transfer function, $G_{\mathrm{V}}(s)$, takes the form:

$$G_{\mathrm{V}}(s) = \frac{K}{\tau s + 1}. \tag{15}$$

The transfer function of any linear system, $T(s)$, (represented here by Eq. 15) can be considered as a ratio of polynomials [4]:

$$T(s) = \frac{B(s)}{A(s)}, \tag{16}$$

where the polynomials $A(s)$ and $B(s)$ take the following form:

$$\left.\begin{array}{ll} A(s) = \mathrm{a_n}s^n + \cdots + \mathrm{a_1}s + \mathrm{a_0} & \text{(a)} \\ B(s) = \mathrm{b_m}s^m + \cdots + \mathrm{b_1}s + \mathrm{b_0} & \text{(b)} \end{array}\right\}. \tag{17}$$

For such system, the roots of the system characteristic equation (which are the poles of the system transfer function) are the same as the roots of the equation $A(s) = 0$.

Compensation is the process of modifying a closed-loop control system (usually by adding a compensator or controller) in such a way that the compensated system satisfies a given set of design specifications [5]. The design specifications of control systems are often used to describe some design criteria that the compensated system should achieve (e.g., a vehicle should be able to accelerate up to specified velocities at designated times taking into account actuator limitations encountered in control systems engineering). These specifications are unique to each individual application and often include specifications about relative stability, steady-state accuracy (error), transient-response characteristics, and frequency-response characteristics. The design of control systems can be carried out in either the time domain (e.g., the steady-state control accuracy is often specified with respect to a step input, a ramp input, or a parabolic input) or the frequency domain (e.g., by means of frequency-domain specifications, which should be used in conjunction with such tools as the Bode plot, polar plot, gain-phase plot, and Nichols chart).

In general, the dynamics of a controlled process can be represented by the block diagram of a typical negative feedback system illustrated in Fig. 2. This system consists of a simplified vehicle model and a proportional-plus-integral (PI) controller. The transfer function of the PI controller is given by

$$G_{\mathrm{C}}(s) = K_{\mathrm{P}} + \frac{K_{\mathrm{I}}}{s}, \tag{18}$$

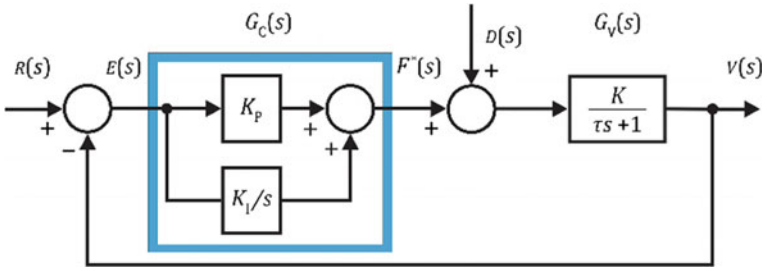

Fig. 2 Block diagram of a closed-loop system with a series PI controller

where K_P is the proportional gain and K_I is the integral gain (note that both gains are tuning parameters).

The transfer function of the feedback system shown in Fig. 2 is

$$T_{CL}(s) = \frac{G_C(s)G_V(s)}{1 + G_C(s)G_V(s)}, \tag{19}$$

where $G_C(s) = N_{GC}(s)/D_{GC}(s)$ and $G_V(s) = N_{GV}(s)/D_{GV}(s)$. Thus, the system characteristic equation is

$$1 + G_C(s)G_V(s) = 0 \quad \text{or} \quad N_{GC}(s)N_{GV}(s) + D_{GC}(s)D_{GV}(s) = 0. \tag{20}$$

All roots of Eq. 20 must be located in the left half of the complex plane for asymptotic stability of the system and, moreover, the controller gains (i.e., parameters K_P and K_I) must be selected to achieve good performance for the closed-loop system.

3 Design of an Optimal Adaptive Cruise Controller

Not only dynamic but also static properties of controlled processes may often change in time. In such cases, there is a need to use adaptive control techniques, which enable an adaptation to unknown and changing process behavior [6]. Adaptive algorithms may be used to compute directly the gains of the controller (for direct adaptive control), as well as indirectly. So, adaptive controllers can be classified as either indirect or direct. The direct adaptive control can be, in essence, implemented in several ways. One of them is the self-tuning control based on pole placement [2]. The pole-placement procedure places all poles of the closed-loop transfer function (or all roots of the closed-loop system characteristic equation) at desirable locations. The pole-placement procedure is a feasible design technique only for systems that are controllable. Furthermore, for a robust closed loop system, the poles and zeros of the process impose severe restrictions on the location of the closed loop poles.

Having regard to the closed-loop system illustrated in Fig. 2 with models of the vehicle and the PI controller (note that their transfer functions are given by Eqs. 15 and 18, respectively), the loop transfer function of this system takes the following form:

$$L(s) \stackrel{\text{def}}{=} G_{\mathrm{C}}(s)G_{\mathrm{V}}(s) = \frac{K(K_{\mathrm{P}}s + K_{\mathrm{I}})}{s(\tau s + 1)} \tag{21}$$

and hence the corresponding closed-loop characteristic polynomial can be written as follows

$$s(s + 1/\tau) + (K/\tau)(K_{\mathrm{P}}s + K_{\mathrm{I}}) = s^2 + (1/\tau + K_{\mathrm{P}}K/\tau)s + K_{\mathrm{I}}K/\tau. \tag{22}$$

If the desired closed-loop characteristic polynomial is rewritten in the factored form: $(s + p_1)\,(s + p_2)$, then the controller gains are given by:

$$K_{\mathrm{P}} = \frac{p_1 + p_2 - 1/\tau}{K/\tau}, \quad K_{\mathrm{I}} = \frac{p_1 p_2}{K/\tau}. \tag{23}$$

However, as parameters for the vehicle model (i.e., K and τ) cannot be determined successfully by means of physical quantities, which are directly ascertained by measurements, a recursive parameter identification algorithm might be used to estimate indirectly unspecified quantities assuming that the vehicle model is linear, and then the indirect adaptive controller design is based on the parameters so identified (for indirect adaptive control). An example block diagram showing an indirect self-tuning discrete-time control system of a single variable process is demonstrated on Fig. 3.

The self-tuning control system with a discrete-time controller estimates process model parameters of a given structure, and then calculates new controller gains in each sampling instant. Afterwards, a manipulated variable is calculated. The identi-

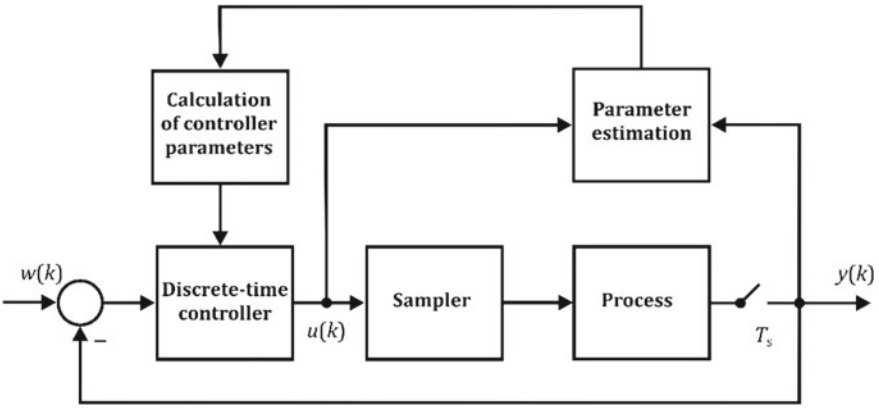

Fig. 3 Block diagram of an indirect self-tuning discrete-time control system

fied parameters, as well as the manipulated variable, remain constant until the new sampling time.

Several following approaches can be considered for deriving parameter adaptation algorithms: least squares minimization, reconciliation with Kalman filter, gradient technique, stability approach, and heuristic approach [7]. Thus, indirect adaptive controllers employ an estimation algorithm to determine the unknown system parameters and adaptive controller gains. It should be noted that many adaptive control techniques are nonlinear adaptive analogues of pole-placement methods in some form [8].

The classical controller design procedures are based on a transfer-function model of a system. However, modern controller design procedures are based on a state-variable model of the vehicle.The state-variable model for a single-input–single-output vehicle model can be mathematically written as:

$$\begin{cases} \frac{d\mathbf{x}(t)}{dt} = \mathbf{A}\,\mathbf{x}(t) + \mathbf{B}\,u(t) \\ y(t) = \mathbf{C}\,\mathbf{x}(t) \end{cases} \tag{24}$$

where $\mathbf{x}(t)$ is the n $\times$ 1 state vector, $u(t)$ is the vehicle input signal, $y(t)$ is the vehicle output signal, $\mathbf{A}$ is the n $\times$ n system matrix, $\mathbf{B}$ is the n $\times$ 1 input matrix, and $\mathbf{C}$ is the 1 $\times$ n output matrix. The vehicle transfer function, $G_{\mathrm{V}}(s)$, can be considered as an input-output model. The function, $G_{\mathrm{V}}(s)$, is related to the state model, defined by Eq. 24, by

$$G_{\mathrm{V}}(s) = \mathbf{C}(s\,\mathbf{I} - \mathbf{A})^{-1}\mathbf{B}. \tag{25}$$

Note that the state model yields the same input-output model and, in addition, includes an internal model of the system. Moreover, this model is without difficulty adaptable to a multiple-input–multiple-output system. For this case, $\mathbf{u}(t)$ and $\mathbf{y}(t)$ are vectors.

In general, in modern controller design procedures [9] a common method for negative feedback is to multiply the estimated state vector, $\hat{\mathbf{x}}(t)$, by a 1 $\times$ n feedback-gain matrix, $\mathbf{K}$, wherein the states of the system are estimated from the measurement of the output vector, $\mathbf{y}(t)$. In addition to feedback, an input vector, $\mathbf{r}(t)$, can be added such that

$$\mathbf{u}(t) = \mathbf{r}(t) - \mathbf{K}\,\hat{\mathbf{x}}(t), \tag{26}$$

where $\mathbf{u}(t)$ is the input (or control) vector. The feedback-gain matrix, $\mathbf{K}$, is determined based on the following relationship:

$$|s\,\mathbf{I} - (\mathbf{A} - \mathbf{B}\,\mathbf{K})| = (s - \mu_1)(s - \mu_2)\ldots(s - \mu_{\mathrm{n}}), \tag{27}$$

where $\mu_1, \ldots, \mu_{\mathrm{n}}$ are the desired pole locations. For the observer pole-placement controller design the course of this mathematical operation is depicted in Fig. 4.

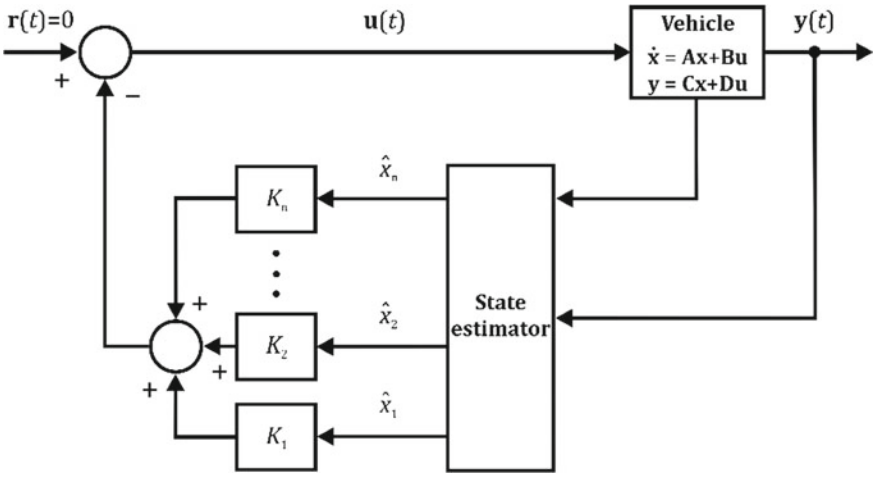

Fig. 4 Implementation of the observer pole-placement controller design

In general, there are three basic approaches, which relate to problems of optimal control [10, 11], namely: (a) indirect methods (b) direct methods, and (c) dynamic programming. Indirect methods of optimal control rely on the Pontryagin maximum principle [12]. According to these methods, the optimal control problem is turned into a two point boundary value problem containing the same mathematical information as the original one by means of necessary conditions of optimality. Then, the boundary value problem is discretized by some numerical technique to get a solution. It can be stated that indirect methods follow a "*first optimize*, *then discretize*" scheme. Numerical techniques for solving the two point boundary value problem of optimal control can be categorized as indirect collocation [13], gradient methods [14], and indirect shooting and indirect multiple shooting [15]. Direct methods of optimal control can be applied without deriving the necessary condition of optimality, and they are based on a finite dimensional parameterization of the infinite dimensional problem (i.e., they convert the original infinite dimensional problem of optimal control into a problem with a finite set of variables). Then, the finite dimensional problem is solved by means of an optimization method, known as the technique of nonlinear programming problem. Thus, direct methods follow an approach known as "*first discretize*, *then optimize*" [16]. The dynamic programming approach applied to optimal control uses the optimality criteria in continuous time, which are based on the Hamilton-Jacobi-Belman partial differential equation [17]. The solution of this equation is treated as the value function, which gives the minimum cost for a given dynamical system with an associated cost function. According to dynamic programming the problem is subdivided and solved in a number of stages. Each stage is associated with one subproblem and the subproblems are linked together by a recurrence relation. Thus, using recursive computations the solution of the whole problem is obtained by solving the subproblems [17].

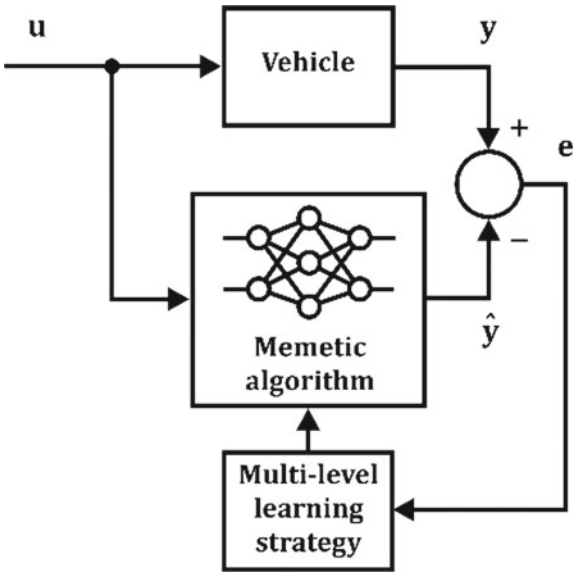

Fig. 5 Forward system identification approach

In spite of the fact that some key theoretical problems continue to exist in application of memetic algorithms based on genetic algorithm [18–20] with artificial neural networks to design of an optimal adaptive cruise controller, properties of these algorithms demonstrate that they have great promise in the modeling of nonlinear systems. An open problem in system identification is whether a system under study can be properly represented within a given model structure. As a rule, it is assumed that the system under consideration belongs to a certain class of systems, which the chosen network is able to represent. Two kinds of system identification techniques can be distinguished: forward modeling and inverse modeling. A schematic diagram of the procedure of training a neural network to represent the forward dynamics of a system is shown in Fig. 5. The neural network is placed in parallel with the system, and the error vector, **e** between the system output vector, **y**, and the network output vector, $\hat{\mathbf{y}}$, is used to train the network. This diagram illustrates a classical supervised learning problem for which the teacher (i.e., the system) provides target values (i.e., system outputs) directly in the output coordinate system of the learner (i.e., the network model).

The inverse modeling structure depicted in Fig. 6 is supposed to provide the opportunity to represent the inverse of the vehicle model by network. However, there are potential drawbacks to this approach. The training signal must be chosen to sample over a wide range of system inputs, and the actual operational inputs may be difficult to define a priori. A second drawback is that an incorrect inverse model can be obtained if the nonlinear system mapping is not one-to-one. An approach called specialized inverse modeling has been proposed in an effort to overcome these problems [21]. The neural network identification models can be used in the

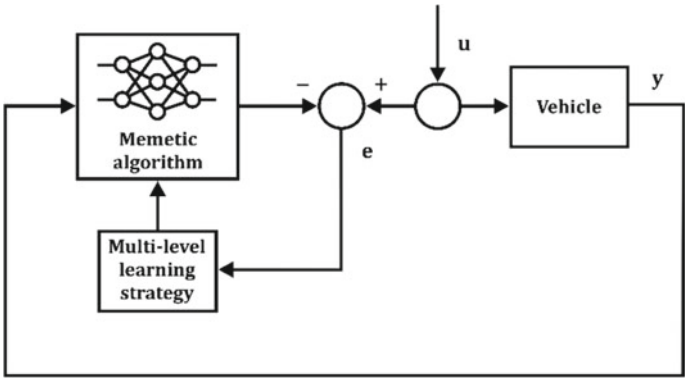

Fig. 6 Direct inverse system identification approach

adaptive control of vehicles for which their models do not have known values of parameters.

4 Application Example

As an application example is considered the design of the adaptive cruise controller for a model of the two-door, two-seater sports car: 16MY Jaguar F-Type. The vehicle parameters are taken from [22]. The parameters of the car model give a good match compared with the advertised vehicle parameters. For a 60 s simulation, the maximum vehicle speed is 253 kph, as shown at Fig. 7.

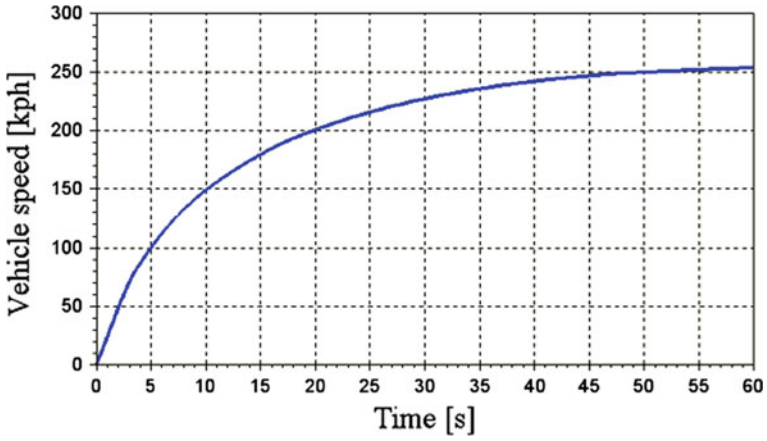

Fig. 7 Vehicle speed plot for the 16MY Jaguar F-Type (Xcos simulation results)

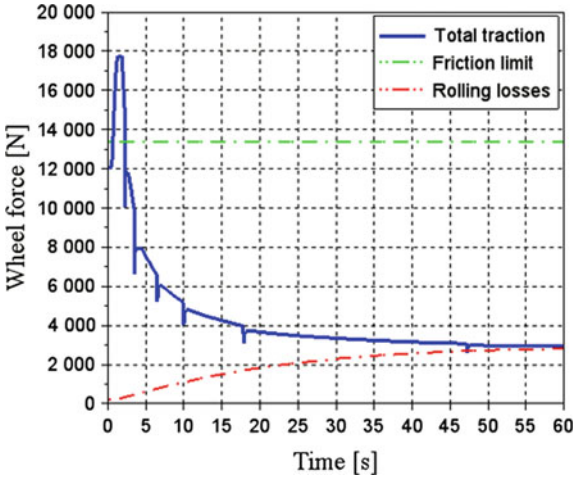

Fig. 8 Wheel forces plot for the 16MY Jaguar F-Type (Xcos simulation results)

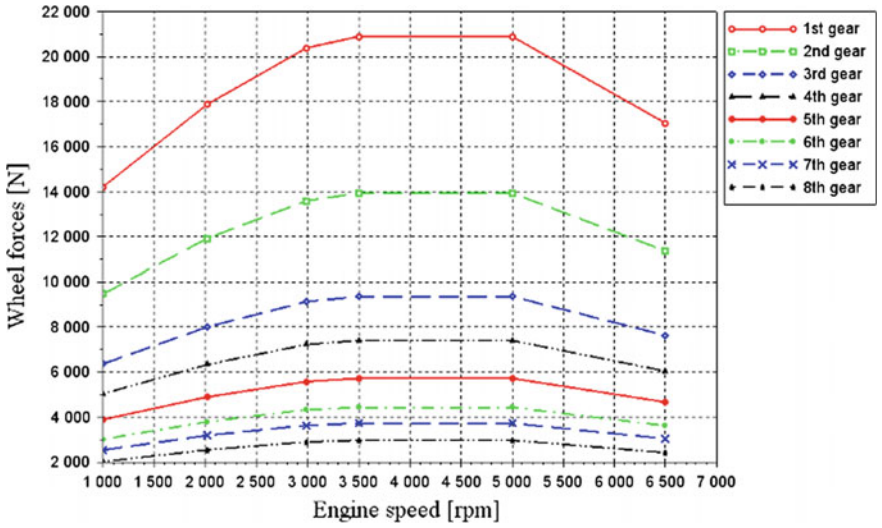

Fig. 9 Wheel forces at full load function of engine speed and gear for the 16MY Jaguar F-Type (Scilab simulation results)

According to Fig. 8, the total force of 17,766 N, available at the wheels for traction, is obtained in 1st gear. However, since of the maximum traction force is limited by the friction force to the value of 13,383 N the wheels cannot deploy a higher motive force on the road, even if, according to Fig. 9, the engine and transmission are capable to deliver this amount of force.

In a computer controlled system, the control applied to the vehicle is not continuous and varies discontinuously at the sampling instants (see [23]). In addition, a sample of the control signal is constant and hold between the sampling instants (effect of the zero order hold). Therefore, it is important to relate the vehicle transfer function, $G_{\mathrm{V}}(s)$, of the continuous-time system to the corresponding sampled model. The converted continuous time Laplace transfer function of $G_{\mathrm{V}}(s)$ to a discrete time z transfer function is

$$G_{\mathrm{V}}(z) = \frac{\mathrm{b}\, z^{-1}}{1 + \mathrm{a}\, z^{-1}}, \tag{28}$$

where the parameters $\mathrm{a} \stackrel{\text{def}}{=} 1/\tau$ and $\mathrm{b} \stackrel{\text{def}}{=} K/\tau = 1/\mathrm{m}$ are estimated by means of a recursive least squares (RLS) parameter-estimation method.

A deadbeat-like procedure is adopted for the design of a digital controller, $D(z)$. According to a desired discrete transfer function, $G_{\mathrm{M}}(z)$, of the system for the overall control loop, the controller transfer function, $D(z)$, can be expressed in the following form:

$$G_{\mathrm{M}}(z) \stackrel{\text{def}}{=} \frac{Y(z)}{V(z)} = \frac{D(z)G_{\mathrm{V}}(z)}{1 + D(z)G_{\mathrm{V}}(z)} \stackrel{\text{hence}}{\longrightarrow} D(z) = \frac{G_{\mathrm{M}}(z)}{G_{\mathrm{V}}(z)[1 - G_{\mathrm{M}}(z)]}, \tag{29}$$

with

$$G_{\mathrm{M}}(z) = \frac{(1 + c_1 + c_2)z^{-1}}{1 + c_1 z^{-1} + c_2 z^{-2}}, \tag{30}$$

where

$$c_1 \stackrel{\text{def}}{=} \mathrm{e}^{-\zeta\omega_{\mathrm{n}} k \mathrm{T_s}} \cos\left(\omega_{\mathrm{n}}\sqrt{1-\zeta^2} k \mathrm{T_s}\right), \quad c_2 \stackrel{\text{def}}{=} \mathrm{e}^{-2\zeta\omega_{\mathrm{n}} k \mathrm{T_s}}, \tag{31}$$

$V(z)$ stands for the desired reference input, $Y(z)$ represents the output of the process, k is the sample number, $\mathrm{T_s}$ is the sampling period, while ζ (i.e., the damping coefficient) and ω_{n} (i.e., the natural frequency) are parameters used to specify the desired response.

The Scilab program is used to generate the results shown in Figs. 10, 11, 12, 13, 14 and 15. The implementation is digital, so a discrete-time process model is used, obtained for two different sampling rates, $\mathrm{T_s}$, both of 0.1 s and of 1 s, as well. As can be seen in Figs. 11 and 14, the parameter estimates converge quickly (i.e., well below 4 s), despite the fact that the unknown parameters a and b are initialized to two different values.

During the computer calculations, it was assumed that $\zeta = 0.95$ and $\omega_{\mathrm{n}} = 0.1$.

It should be noted that the sampling time ($\mathrm{T_s} = 0.1$ s), taken to calculations, is too small for the power transmission capacity of the drive system of the modeled vehicle.

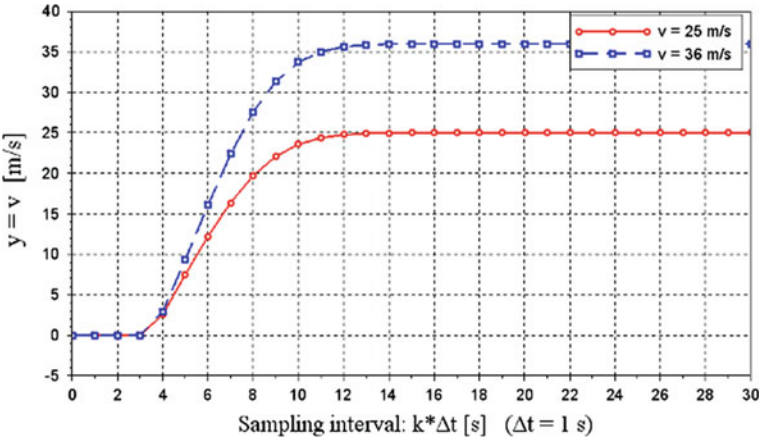

Fig. 10 Vehicle speed change for the 16MY Jaguar F-Type (Scilab simulation results)

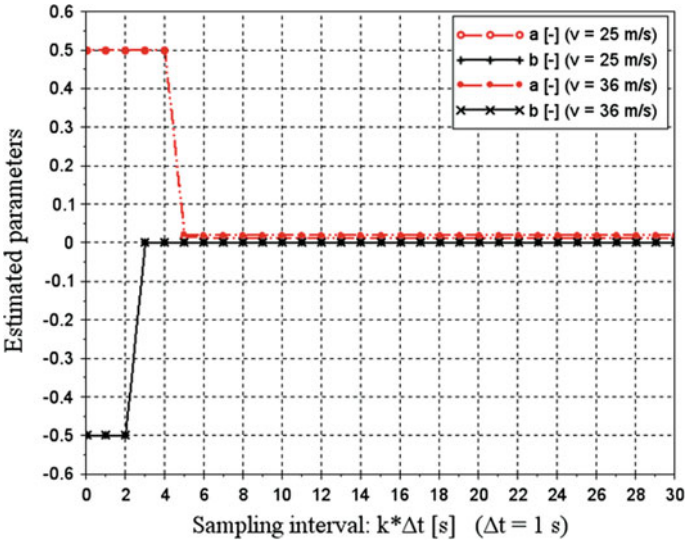

Fig. 11 Change of the parameters, a and b, over time during control for the model of 16MY Jaguar F-Type (Scilab simulation results). (for v = 25 m/s, a (required): 0.0137206, a (established): 0.0137265, b (required): 0.0005241, b (established): 0.0005241, for v = 36 m/s, a (required): 0.0197576, a (established): 0.0197605, b (required): 0.0005241, b (established): 0.0005241)

5 Conclusions

The applied adaptive control method based on the RLS algorithm for estimating the parameters of the nonlinear systems is very efficient and has the ability to adjust quickly the control parameters. In addition, expanding the possibilities of this method

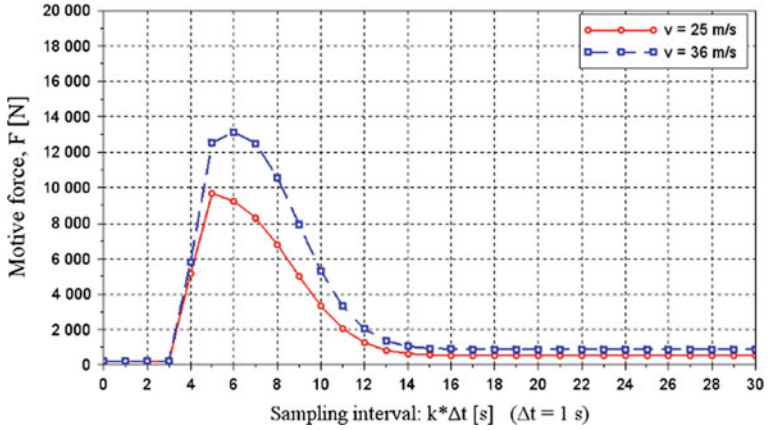

Fig. 12 Controlling motive force of the 16MY Jaguar F-Type (Scilab simulation results)

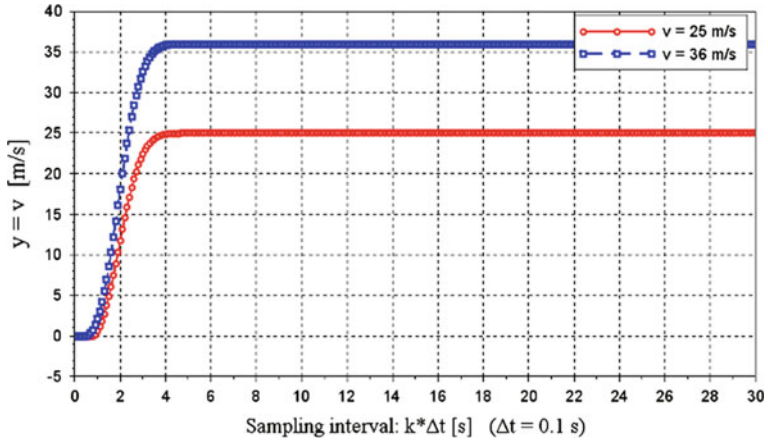

Fig. 13 Vehicle speed change for the 16MY Jaguar F-Type (Scilab simulation results)

by the usage of memetic algorithms based on genetic algorithm with artificial neural networks can improve process controller performance for variety automotive multivariable dynamical systems. Nowadays, the implementation of systems of optimal control is relatively easy taking into account the widespread availability of microcontrollers.

However, the engineering practice usually demonstrates that the best choose is the implementation of the simplest possible controller that meets all the design specifications. In most cases, the more complex a controller is, the less reliable it could be, the more it could cost, and, first of all, the more difficult it could be to design. Furthermore, choosing a specific controller for a specific application is sometimes based on the designer's intuition and quite often past experience. Considering that

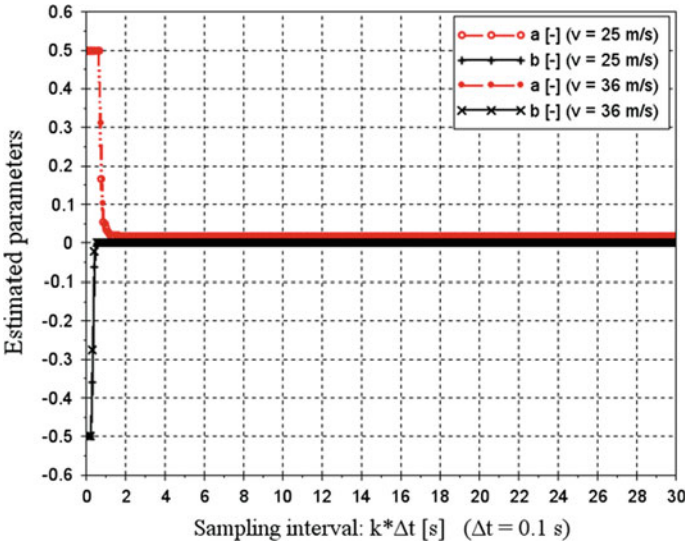

Fig. 14 Change of the parameters, a and b, over time during control for the model of 16MY Jaguar F-Type (Scilab simulation results). (for v = 25 m/s, a (required): 0.0137206, a (established): 0.0137377, b (required): 0.0005241, b (established): 0.0005241, for v = 36 m/s, a (required): 0.0197576, a (established): 0.0197665, b (required): 0.0005241, b (established): 0.0005241)

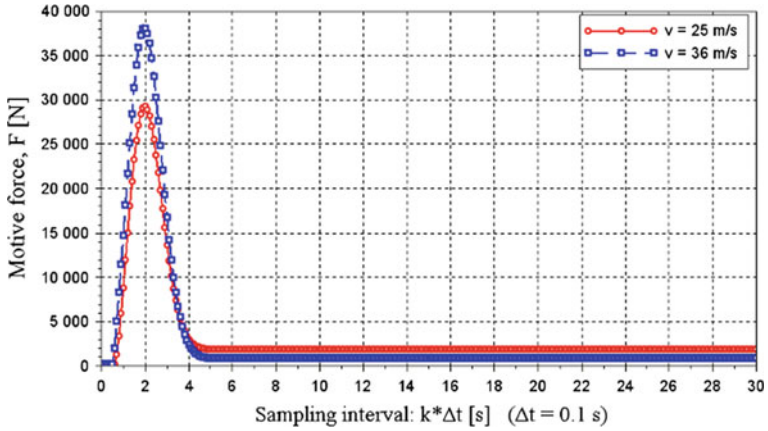

Fig. 15 Controlling motive force of the 16MY Jaguar F-Type (Scilab simulation results)

for a novice, any task of design of an optimal adaptive controller may be initially found difficult to achieve, it cannot be forgotten about using appropriate software, which supports the designer's work to a large extend.

References

1. Chen, H., Gong, X., Hu, Y.-F., Liu, Q.-F., Gao, B.-Z., Guo, H.-Y.: Automotive control: the state of the art and perspective. Acta Autom. Sin. **39**, 322–346 (2013)
2. Ulsoy, A.G., Peng, H., Çakmakci, M.: Automotive Control Systems. Cambridge University Press, Cambridge (2012)
3. Nise, N.S.: Control Systems Engineering. Wiley, Jefferson City (2011)
4. Kulakowski, B.T., Gardner, J.F., Shearer, J.L.: Dynamic Modeling and Control of Engineering Systems. Cambridge University Press, Cambridge (2007)
5. Golnaraghi, M.F., Kuo, B.C.: Automatic Control Systems. Wiley, Rochester (2010)
6. Mikleš, J., Fikar, M.: Process Modelling, Identification, and Control. Springer, Berlin Heidelberg (2007)
7. Landau, I.D., Lozano, R., M'Saad, M., Karimi, A.: Adaptive Control—Algorithms, Analysis and Applications. Springer, London (2011)
8. Kaufman, H., Bar-Kana, I., Sobel, K.: Direct Adaptive Control Algorithms: Theory and Applications. Springer, NYC (1994)
9. Dorf, R.C.: The Electrical Engineering Handbook. CRC Press LLC, Boca Raton (2000)
10. del Re, L., Allgöwer, F., Glielmo, L., Guardiola, C., Kolmanovsky, I.: Automotive Model Predictive Control—Models, Methods and Applications. Springer, Berlin Heidelberg (2010)
11. García-Heras, J., Soler, M., Sáez, F.J.: A comparison of optimal control methods for minimum fuel cruise at constant altitude and course with fixed arrival time. Procedia Eng. **80**, 231–244 (2014)
12. Pontryagin, L.S., Boltyanskii, V.G., Gamkrelidze, R.V., Mishchenko, E.F.: The Mathematical Theory of Optimal Processes. Interscience Publishers (Wiley), NYC London (1962)
13. Ascher, U., Christiansen, J., Russell, R.: A collocation solver for mixed order systems of boundary value problems. Math. Comput. **33**, 659–679 (1979)
14. Kelley, H.: Gradient theory of optimal flight paths. AIAA J. **30**, 947–954 (1960)
15. Stoer, J., Bulirsch, R.: Introduction to Numerical Analysis. Springer, NYC (2002)
16. Nocedal, J., Wright, S.: Numerical Optimization. Springer, NYC (1999)
17. Bertsekas, D.P.: Dynamic Programming and Optimal Control, 3rd edn. Athena Scientific, Nashua (2007)
18. Pecháč, P., Sága, M.: Memetic algorithm with normalized RBF ANN for approximation of objective function and secondary RBF ANN for error mapping. Procedia Eng. **177**, 540–547 (2017)
19. Jackiewicz, J.: Manufacturing of instructional aids for students at low cost by means of 3D printing. Mater. Manuf. Processes **32**, 1116–1130 (2017)
20. Neri, F., Cotta, C., Moscato, P.: Handbook of Memetic Algorithms. Springer, Berlin Heidelberg (2012)
21. Psaltis, D., Sideris, A., Yamamura, A.A.: A multilayered neural network controller. IEEE Contr. Syst. Mag. **8**(2), 17–21 (1988)
22. https://x-engineer.org/projects/vehicle-acceleration-maximum-speed-modeling-simulation/
23. Landau, I.D., Zito, G.: Digital Control Systems Design, Identification and Implementation. Springer, London (2006)

Mathematical Model of Two Types of Atrioventricular Nodal Reentrant Tachycardia: Slow/Fast and Slow/Slow

Beata Jackowska-Zduniak and Urszula Foryś

Abstract Proposed model consisting of two coupled van der Pol equations is considered as a description of the heart's action potential. System of ordinary differential equations with time delay is used to recreate pathological behaviour in the heart's conducting system such as slow/fast and slow/slow type of atrioventricular nodal reentrant tachycardia (AVNRT). In our study, introducing the feedback loops and couplings entails the creation of waves which can correspond to the re-entry waves occurring in the AVNRT. Our main aim is to study solutions of the given equations and take into consideration the influence of feedback and delays which occur in these pathological modes. Analytical results are illustrated by some numerical examples of the model dynamics.

Keywords Delay differential equation · Stability analysis · Model of tachycardia · Van der Pol equation

1 Introduction

In this paper, we propose a mathematical model which allows to reconstruct pathological behaviours in the system of the heart. We consider a system of ordinary differential equations with time delays which is based on the van der Pol equations. We try to model two types of pathology such as: slow/fast and rare slow/slow AVNRT. The structure of the AV node has a multi-level architecture in which there may be many pathways (slow and fast) at different locations in the AV node; cf. [6, 7]. This knowledge of architecture helped to recognise many types of AVNRT, which previously were understood as one, although the mechanisms of action are different. We can

B. Jackowska-Zduniak (✉)
Warsaw University of Life Sciences, Nowoursynowska 159, 02-776 Warsaw, Poland
e-mail: beata_jackowska_zduniak@sggw.pl

U. Foryś
University of Warsaw, Banacha 2, 02-097 Warsaw, Poland
e-mail: urszula@mimuw.edu.pl

J. Awrejcewicz (ed.), *Dynamical Systems in Theoretical Perspective*,
Springer Proceedings in Mathematics & Statistics 248,
https://doi.org/10.1007/978-3-319-96598-7_14

distinguish five different forms of the AVNRT (typical: slow/fast, atypical: fast/slow, and other forms: slow/slow, more than two re-entries waves, one fast pathway with depolarisation of slow pathway) [2, 3, 8, 9]. Part of the population has abnormal accessory pathways: fast and slow. The pathways in the AV node are anatomical and functional contributions of the most popular supra-ventricular tachycardia, which is a re-entry tachycardia from the AV node. The pathways connect at two points within the AV node so as to form a circle. One pathway conducts impulses quickly but has a long refractory period. The other conducts impulses slowly but recovers quickly from depolarisation. Because of the existence of the accessory conducting pathway outside the AV node, a flutter wave starts to circle. The motivation for this paper was that there is a problem with making the appropriate diagnosis, and therefore with treating patients with this disease effectively. This kind of problem is observed mainly in different types of AVNRT. The mechanisms of these pathologies are not fully understood. Moreover, the symptoms are often mistakenly taken for other heart diseases. As a result, an ablation therapy is often done, which does not give expected effect. Especially, when slow/slow type of AVNRT is diagnosed as a slow/fast, then ablation therapy is used only for one slow pathway instead of two or more. This implies that the re-entry circuits are not destroyed and tachycardia can return. We propose mathematical models of a rare or rarely diagnosed type of AVNRT: slow/slow and also slow/fast. We try to distinguish and show the main difference between the action potential in both pathologies. We hope it will allow to understand these arrhythmias better.

1.1 Typical AVNRT

The most common form of the AVNRT, is slow anterograde and fast retrograde pattern (slow/fast type), which is shown in Fig. 1a.

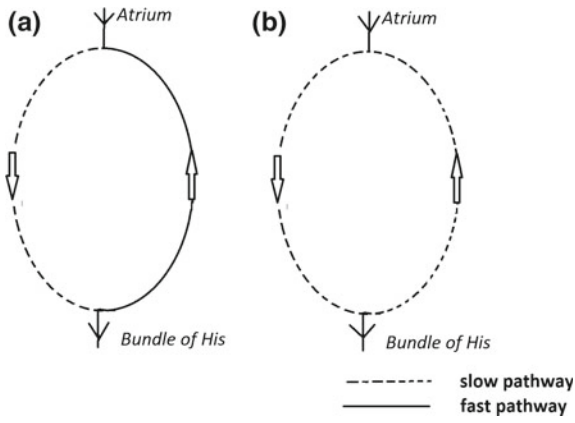

Fig. 1 **a** Sketch of the typical location of the slow/fast AVNRT; **b** uncommon form of AVNRT: slow/slow

In Fig. 1a, we can observe a re-entry circus in which an action potential goes by the slow pathway in the anterograde direction and by the fast pathway in the retrograde direction. Typical AVNRTs are easily inducible during incremental atrial pacing as well as atrial extra stimulation techniques. This type of AVNRT is about 85% of all cases of AVNRT.

1.2 Slow/Slow Type of AVNRT

The next type of AVNRT modelled in this paper is slow/slow type AVNRT. It involves the anterograde slow and retrograde slow pathways; c.f. Fig. 1b. It is very rare and difficult to distinguish from other arrhythmias AVNRT. However, it is about 12% of all types of AVNRT. It is associated with atypical, non-physiological structure of the atrio-ventricular node and multiple pathways of slow conduct. In slow/slow AVNRT and slow/fast AVNRT with programmed atrial pacing, tachycardia occurs after a sudden increase in period ("jump"). Patients often present "jump" in the atrio-ventricular conduction curve during atrial pacing with additional pulse due to the presence of multiple slow pathways; [7]. The distinction between slow/slow and slow/fast AVNRT is important for at least two reasons: ablation technique of the fast pathway does not eliminate slow/slow AVNRT and part of relapse after ablation of the slow pathway is higher for slow/slow AVNRT.

2 Model Construction

The van der Pol model is a relaxation oscillator, which is very useful in the description of the heart dynamics because it easily adjusts its frequency to excitation frequency. The van der Pol equation provides rich dynamical behaviour which we would like to exploit in the modelling of the heart action; cf. [5]. At the beginning, we present the modified van der Pol system, which can be applied to model either SA or AV node. The main property of this oscillator is the mutual interaction of a limit cycle which is present around an unstable focus with a saddle and a stable node. This allows reproducing correctly the refraction period and non-linear phase sensitivity of an action potential of node cells. The modified van der Pol equation in its two-dimensional first order form reads

$$\begin{aligned} \dot{x} &= y, \\ \dot{y} &= -a(x^2 - 1)y - fx(x + d)(x + e), \end{aligned} \tag{1}$$

where a influences time intervals between pulses, f corresponds to a harmonic oscillator's frequency, e and d regulate the location of steady states in the phase space.

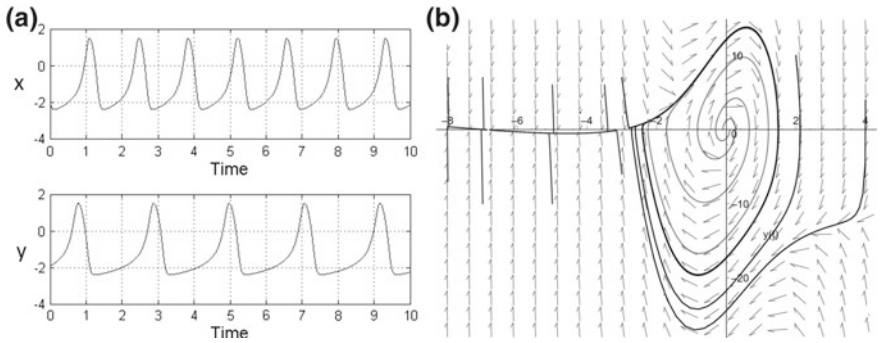

Fig. 2 **a** Dynamics of action potential for Eqs. (1). **b** Phase space portrait with the vector field: [5]

The selection of physiological values of parameters was done after a verification in [4]. The reference model has the following parameter values:

$$a = 5, \quad f = 3, \quad d = 3, \quad e = 7.$$

A solution of this system in time presents the action potential; cf. Fig. 2a. Figure 2b presents a phase portrait with a very important feature – limit cycle appearing in the phase space. In this system, there are three steady states: $x_1 = 0$ (an unstable focus), $x_2 = -d$ (a saddle) and $x_3 = -e$ (a stable node).

A model consisting of two coupled modified van der Pol systems is considered in this paper. For the slow/fast and slow/slow types of AVNRT we model the fast pathway as the first modified van der Pol system and the slow pathway (or slow pathways) as the second one. The difference between these systems is related to the length of period of oscillations – the slow pathway is modelled as slower, so we fit parameter e as to be equal to 4.5 (three steady states of the type described above exist). In the first system all parameters are the same as the reference values. We introduce a feedback and time delay in order to reproduce slow/fast and slow/slow types of AVNRT. Introducing feedback loops entails the creation of waves which can correspond to re-entry waves, which is presented in Fig. 1. The feedback is introduced to the third equation because the re-entry wave is from the slow pathway to the fast one (or from the slow pathway to the slow one). Moreover, small delays are observed in this type of AVNRT. The time when a wave goes along uncontrolled in order to return to the node is reflected by the delay which is added to the feedback part. Including this time delay in the feedback we obtain the final version of the model. Therefore, we consider the following system of ordinary differential equations with time delay

$$\begin{aligned}
\dot{x}_1 &= y_1 - k_1 x_2, \\
\dot{y}_1 &= -a({x_1}^2 - 1)y_1 - f x_1(x_1 + d)(x_1 + e_1), \\
\dot{x}_2 &= y_2 - k_2(x_2 - x_2(t - T)), \\
\dot{y}_2 &= -a({x_2}^2 - 1)y_2 - f x_2(x_2 + d)(x_2 + e_2),
\end{aligned} \tag{2}$$

where k_1 and k_2 denote coupling coefficients, and T is time delay. The values of parameters are given as: $k_1 = 0.75, k_2 = 0.3, a = 5, f = 3, d = 3, e_1 = 7$ and $e_2 = 4.5$.

In the analysis of differential equations, steady states and their stability are one of the most important aspects. Notice, that each of uncoupled van der Pol systems (i.e. subsystems (x_1, y_1) and (x_2, y_2) for $k_1 = k_2 = 0$) has three steady states $(0, 0)$, $(0, -e_i)$, $(0, -d)$, $i = 1, 2$. Recall that $(0, 0)$ is an unstable focus, and for $e_i > d$, $(0, -d)$ is a saddle, $(0, -e_i)$ is a stable node. In the following, we assume $e_i > d_i > 1$.

3 Analysis of Equations (2)

3.1 Existence of Steady States

We start the analysis of Eqs. (2) for $k_i > 0$ with checking the number of steady states. First notice that at any steady state $x_2(t) = x_2(t - T)$, and therefore from the third equation we have $\dot{x}_2 = 0$ if $y_2 = 0$. Hence, from the fourth equation we obtain $x_2 = 0$ or $x_2 = -d$, or $x_2 = -e_2$.

• *Consider* $x_2 = 0$.

In this case we have $y_1 = 0$ and this yields $x_1 = 0$ or $x_1 = -d$, or $x_1 = -e_1$, like in the uncoupled case. Therefore, we obtain three steady states $S_1 = (0, 0, 0, 0)$, $S_2 = (-d, 0, 0, 0)$, $S_3 = (-e_1, 0, 0, 0)$ and these states exist independently of the model parameters.

• *Consider* $x_2 = -d$.

Then we obtain $y_1 = -k_1 d$, which yields $adk_1\big(x_1^2 - 1\big) - fx_1\big(x_1 + d\big)\big(x_1 + e_1\big) = 0$. Let us denote

$$G_1(x) = adk_1\big(x^2 - 1\big), \quad G_2(x) = fx\big(x + d\big)\big(x + e_1\big),$$

and $G(x) = G_1(x) - G_2(x)$. At the steady state we have $G_1(x_1) = G_2(x_1)$, or equivalently $G(x_1) = 0$, where x_1 is the first coordinate of this state. Possible cross-sections of G_1 and G_2, yielding different number of steady states, are shown in Fig. 3.

It is obvious that there is at least one x such that $G(x) = 0$, namely $x = x^I \in (-d, 0)$; cf. Fig. 3. Next, we can show that for small values of k_1 there are three zeros of G; except x^I there are two additional zeros $x^{II}, x^{III} \in (-e_1, -d)$. Moreover, we can check that the condition

$$ak_1 < f\frac{e_1}{2} \tag{3}$$

is sufficient for G has no positive zeros, while the sufficient condition of the existence of two zeros of G in the interval $(-e_1, -d)$ reads

$$\begin{aligned} G_1(x_{\max}) &= adk_1\left(\left(\frac{2(d+e_1)+\sqrt{\Delta}}{6}\right)^2 - 1\right) \\ &< -f\frac{2(d+e_1)+\sqrt{\Delta}}{6}\left(d - \frac{2(d+e_1)+\sqrt{\Delta}}{6}\right)\left(e_1 - \frac{2(d+e_1)+\sqrt{\Delta}}{6}\right) = G_2(x_{\max}). \end{aligned} \tag{4}$$

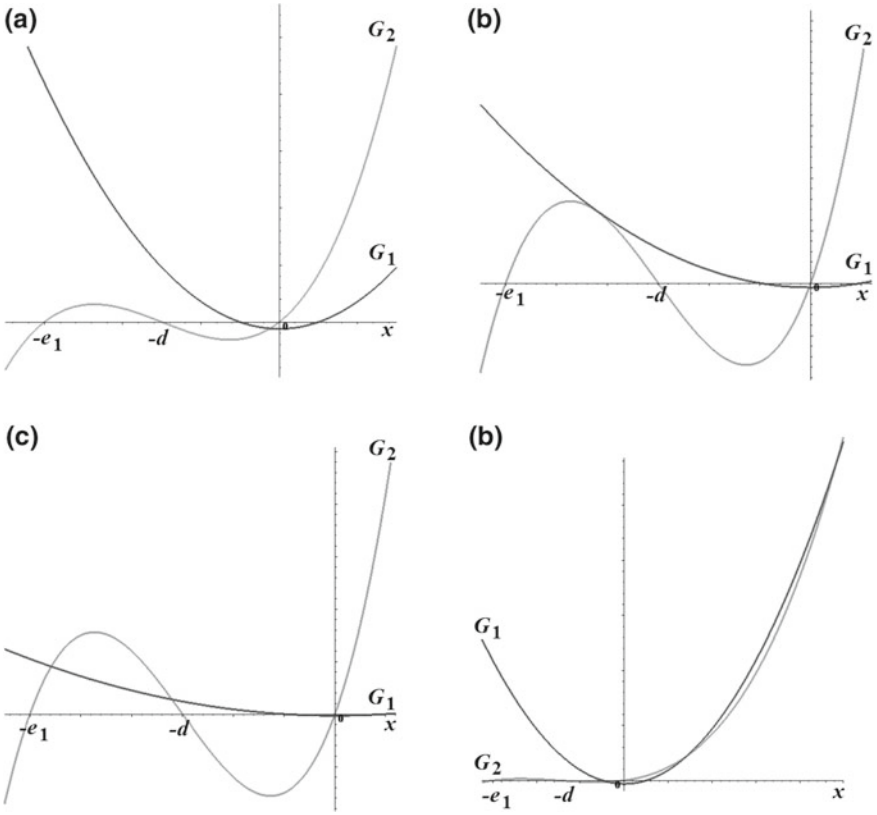

Fig. 3 Various possibilities of the cross-sections of G_1 and G_2. **a** There is one cross-section for intermediate values of k_1. **b** Bifurcation between 2 and 3 cross-sections. **c** There are three cross-sections with $x < 0$ for k_1 small. **d** There are three cross-sections for k_1 large, two of them with $x > 0$.

Let us denote $D = d + e_1 + \sqrt{d^2 + e_1^2 - de_1}$. Using this notation $x_{\max} = -D/3$ and the sufficient condition for the existence of three negative zeros x^I, x^{II}, x^{III} has the following form

$$ak_1 < f \min\left\{\frac{D(D-3d)(3e_1-D)}{3d(D^2-9)}, \frac{e_1}{2}\right\}. \tag{5}$$

• *Consider* $x_2 = -e_2$.

Then we obtain $y_1 = -k_1 e_2$, which yields $ae_2k_1\big(x_1^2 - 1\big) - fx_1\big(x_1 + d\big)\big(x_1 + e_1\big) = 0$. Let us denote

$$\tilde{G}_1(x) = ae_2k_1\big(x^2 - 1\big), \quad \tilde{G}(x) = \tilde{G}_1(x) - G_2(x),$$

and in the case we consider there is $\tilde{G}_1(x) > G_1(x)$ for $|x| > 1$. Moreover, the analysis for G_1 could be repeated for $\tilde{G}_1$. We easily see that Condition (3) changes to

$$ak_1 < f\frac{de_1}{2e_2}, \tag{6}$$

while Condition (5) could be rewritten as

$$ak_1 < f \min\left\{\frac{D(D-3d)(3e_1-D)}{3e_2(D^2-9)}, \frac{de_1}{2e_2}\right\}, \tag{7}$$

and this is the sufficient condition for the existence of three zeros of $\tilde{G}$:

$$\tilde{x}^I \in (-d,-1), \tilde{x}^{II}, \tilde{x}^{III} \in (-e_1, d).$$

Notice, that if both Conditions (5) and (7) are satisfied, then there are nine steady states which is a simple consequence of the dynamics of uncoupled van der Pol subsystems. However, these Conditions are not independent.

Analysing relations between these inequalities we are able to formulate our first result.

Theorem 1 *If* $ak_1 < f \min\left\{\frac{D(D-3d)(3e_1-D)}{3e_2(D^2-9)}, \frac{de_1}{2e_2}\right\}$, *then Eqs. (2) has exactly nine steady states:*

$$\begin{array}{lll}
(0,0,0,0), & (-d,0,0,0), & (-e_1,0,0,0),\\
(x^I,-dk_1,-d,0), & (x^{II},-dk_1,-d,0), & (x^{III},-dk_1,-d,0),\\
(\tilde{x}^I,-e_2k_1,-e_2,0), & (\tilde{x}^{II},-e_2k_1,-e_2,0), & (\tilde{x}^{III},-e_2k_1,-e_2,0),
\end{array}$$

where $x^I, \tilde{x}^I \in (-1,0)$ *and* $x^{II}, \tilde{x}^{II}, x^{III}, \tilde{x}^{III} \in (-e_1,-d)$.

Corollary 1 *If* $d > 2$ *and* $e_1 \geq \frac{2d}{d-2}$, *then the statement of Corollary 1 holds true for* $ak_1 < f\frac{D(D-3d)(3e_1-D)}{3e_2(D^2-9)}$.

On the other hand, one can be also interested in the case when there is only five steady states, which is the smallest possible number. To get the sufficient condition for it we only need to study the behaviour of the function G for $x < 0$ and the behaviour of $\tilde{G}$ for $x > 0$. Both functions tend to $+\infty$ as $x \to -\infty$ and to $-\infty$ as $x \to +\infty$. As the sufficient condition for $\tilde{G}(x) > 0$ for $x > 0$ is formulated above, we turn to the analysis of $G(x)$ for $x < 0$. In fact, we are only interested in the sign of this function in the interval $(-x_{\max}, -d) \subset (-e_1, -d)$, because it is clear that $G(x) > 0$ for $x < x_{\max}$ if $G(x_{\max}) > 0$ (G is decreasing in the whole interval $(-\infty, x_{\max})$ as G_1 is decreasing and G_2 is increasing), while in the interval $(-d, 0)$ there is one zero x^I.

We have $G'(x) = -\Big(3fx^2 + 2\big(f(d+e_1) - adk_1\big)x + fde_1\Big)$, and we can check that

- if $f \in (f_1, f_2)$, then G' has no zeros, G is decreasing for all x and there is only one zero of G;

- if $f \in (0, f_1) \cup (f_2, \infty)$, then G' has two zeros, $x_1^G < x_2^G$, so G has minimum at $x = x_1^G$, and if $x_1^G > -d$, then $G(x) > 0$ for $x < -d$;

where $f_1 = adk_1 \frac{d+e_1-\sqrt{3de_1}}{d^2+e_1^2-de_1}$, $f_2 = adk_1 \frac{d+e_1+\sqrt{3de_1}}{d^2+e_1^2-de_1}$.

Let us calculate x_1^G. We have $x_1^G = \frac{2\left(adk_1 - f(d+e_1)\right)-\sqrt{\Delta_{G'}}}{6f}$, where $\Delta_{G'}$ is the discriminant of G'. Therefore $x_1^G > -d \Leftrightarrow \sqrt{\Delta_{G'}} < 2\Big(adk_1 - 2f(e_1 - 2d)\Big)$.

Analysing this inequality we arrive at the sufficient condition for G has only one negative zero.

Corollary 2 *If one of the following conditions holds*

1. $e_1 > 2d$ *and* $f < \min\left\{\frac{2adk_1}{e_1-d}, \frac{adk_1}{2(e_1-2d)}\right\}$;
2. $e_1 \le 2d$ *and* $f < \frac{2adk_1}{e_1-d}$;

then Eqs. (2) has only one steady state with $y_1 = -dk_1$ *and* $x_1 < 0$.

Analysing conditions of Corollary 2 for $e_1 \le \frac{7}{3}d$ and $e_1 > \frac{7}{3}d$ and combining these results with Condition (6) guaranteeing that both $\tilde{G}$ and G have no positive zeros we are in a position to formulate our final result.

Theorem 2 *Assume that*

H1 $e_1 > \frac{7}{3}d$ *and* $ak_1\frac{2e_2}{de_1} < f < ak_1\frac{d}{2(e_1-2d)}$;
H2 $\frac{7}{3}d \ge e_1 > 2d$ *and* $ak_1\frac{2e_2}{de_1} < f < ak_1\frac{2d}{e_1-d}$.

If H1 or H2 is satisfied, then Eqs. (2) has exactly 5 steady states:

$$(0,0,0,0),\ (-d,0,0,0),\ (-e_1,0,0,0),\ (x^I,-dk_1,-d,0),\ (\tilde{x}^I,-e_2k_1,-e_2,0),$$

where $x^I, \tilde{x}^I \in (-1, 0)$.

Notice that for our reference parameter values assumption *H2* is satisfied. Clearly, $e_1 = 7 \le \frac{7}{3}d$ and

$$ak_1\frac{2e_2}{de_1} = 5\cdot\frac{3}{4}\cdot\frac{2\cdot 4.5}{3\cdot 7} = \frac{45}{28} < 3 = f < ak_1\frac{2d}{e_1-d} = 5\cdot\frac{3}{4}\cdot\frac{2\cdot 3}{7-3} = 3\cdot\frac{45}{16},$$

which implies that for these parameter values there are 5 steady states, as stated in Theorem 2. These steady states have the following coordinates:

$(0,0,0,0)$, $(-3,0,0,0)$, $(-7,0,0,0)$, $(-0.188866899, -2.25, -3, 0)$, $(-0.283518286, -3.375, -4.5, 0)$.

At the end of this section we should mark that Theorems 1 and 2 do not exhaust a topic of the existence and number of steady states. However, as we are mainly interested in the dynamics of Eqs. (2) for our reference parameter values, we decided to present only Theorems 1 and 2.

3.2 Stability of the Steady States

In this section we turn to the analysis of stability of the steady states focusing on the influence of time delay T. In general this analysis is complex, so we focus on the case when only 5 steady states exist, as for our reference parameter values.

Case T = 0. Calculating Jacobian matrix for Eqs. (2) with $T = 0$ we easily see that it has a specific block form. Hence, the characteristic polynomial separates into the polynomials for two van der Pol subsystems

$$\begin{aligned} W(\lambda) = \det\left(J - \lambda I\right) = \left(\lambda^2 + a(x_1^2 - 1)\lambda - A_1\right)\left(\lambda^2 + a(x_2^2 - 1)\lambda - A_2\right), \\ -A_i = 3fx_i^2 + 2\left(f(d + e_i) + ay_i\right)x_i + de_i f, \quad i = 1,\ 2. \end{aligned} \tag{8}$$

Looking at Eq. (8) we easily see that if at least one of A_i, $i = 1, 2$, is positive, then corresponding steady state is unstable (a saddle). Moreover, any steady state with $|x_i| < 1$, $i = 1$ or $i = 2$ is also unstable, independently of the sign of corresponding A_i.

• *Consider* $(0, 0, 0, 0)$.
For this state (8) reads

$$W(\lambda) = \left(\lambda^2 - a\lambda + de_1 f\right)\left(\lambda^2 - a\lambda + de_2 f\right),$$

yielding instability. Moreover, for $a^2 < 4de_2 f$ (the case of our reference parameter values) it is an unstable focus in both directions.

• *Consider* $(-d, 0, 0, 0)$.
For this state (8) reads

$$W(\lambda) = \left(\lambda^2 + a(d^2 - 1)\lambda - fd(e_1 - d)\right)\left(\lambda^2 - a\lambda + de_2 f\right).$$

Hence, it is a saddle.

• *Consider* $(-e_1, 0, 0, 0)$.
For this state (8) reads

$$W(\lambda) = \left(\lambda^2 + a(e_1^2 - 1)\lambda + fd(e_1 - d)\right)\left(\lambda^2 - a\lambda + de_2 f\right),$$

yielding instability.

• *Consider* $(x^I, -dk_1, -d, 0)$, $x^I \in (-1, 0)$.
For this state (8) reads

$$W(\lambda) = \left(\lambda^2 + a\left((x^I)^2 - 1\right)\lambda - A_1)(\lambda^2 + a(d^2 - 1)\lambda - fd(e_2 - d)\right)$$

with $A_1 = -\Big(3f(x^I)^2 + 2\big(f(d+e_1) - adk_1\big)x^I + de_1 f\Big)$. From the second van der Pol subsystem we obtain that it is a saddle. For our reference parameter values we have $A_1 \approx -56.23852764$ and the eigenvalues are complex ($\lambda_{1,2} \approx 2.410823236 \pm 7.101158987\, i$), so that it is an unstable focus in this direction.

• *Consider* $(\tilde{x}^I, -e_2k_1, -e_2, 0)$, $\tilde{x}^I \in (-1, 0)$.

For this state (8) reads

$$W(\lambda) = \Big(\lambda^2 + a\Big(\big(\tilde{x}^I\big)^2 - 1\Big)\lambda - A_1\Big)\Big(\lambda^2 + a\left(e_2^2 - 1\right)\lambda + fe_2(e_2 - d)\Big)$$

with $A_1 = -\Big(3f\big(\tilde{x}^I\big)^2 + 2\big(f(d+e_1) - ae_2k_1\big)\tilde{x}^I + de_1f\Big)$. The second subsystem yields stability, while the first one has the same properties as above, i.e. we have instability in the (x_1, y_1) direction. For the reference parameter values $A_1 \approx -56.28109$ and we have unstable focus in this direction ($\lambda_{1,2} \approx 2.29904 \pm 7.14111\, i$), and a stable node in (x_2, y_2) direction ($\lambda_3, \lambda_4 < 0$).

Case T > 0. To check stability of the steady states for $T > 0$ we use the method proposed by Cooke and Driessche [1]. Characteristic quasi-polynomial for Eqs. (2) reads

$$\begin{aligned} W(\lambda) =& \lambda^4 + \Big(B + k_2\left(1 - \mathrm{e}^{-\lambda T}\right)\Big)\lambda^3 + \Big(C - A_1 - A_2 + k_2B\left(1 - \mathrm{e}^{-\lambda T}\right)\Big)\lambda^2 \\ &- \Big(a\left(A_2(x_1^2 - 1) + A_1(x_2^2 - 1)\right) - k_2\left(1 - \mathrm{e}^{-\lambda T}\right)(C - A_1)\Big)\lambda + A_1A_2 \\ &- aA_1k_2\left(1 - \mathrm{e}^{-\lambda T}\right)(x_2^2 - 1), \end{aligned} \tag{9}$$

where A_i are as above, and $B = a(x_2^2 + x_1^2 - 2)$, $C = a^2(x_1^2 - 1)(x_2^2 - 1)$.

Now, following the method described in [1] we rewrite the characteristic quasi-polynomial (9) as $W(\lambda) = P(\lambda) + Q(\lambda)\mathrm{e}^{\lambda T}$ and define an auxiliary function as

$$F(\omega^2) = |P(i\omega)|^2 - |Q(i\omega)|^2.$$

The change of stability can occur only if $F(z) = 0$ for some $z > 0$. Moreover, the direction of movement of eigenvalues in the complex plane is determined by the sign of the derivative F' at the considered zero point–positive derivative means movement from left to right, while negative one means movement in the opposite direction.

For any steady state (x_1, y_1, x_2, y_2) we calculate

$$\begin{aligned} P(i\omega) =& \omega^4 - (k_2B + C - A_1 - A_2)\,\omega^2 - ak_2A_1(x_2^2 - 1) + A_1A_2 \\ &- \Big((B + k_2)\omega^3 - \big(k_2(C - A_1) - aA_2(x_1^2 - 1) - aA_1(x_2^2 - 1)\big)\,\omega\Big)i, \\ Q(i\omega) =& k_2B\omega^2 + ak_2A_1(x_2^2 - 1) + \Big(k_2\omega^3 - k_2\,(C - A_1)\,\omega\Big)i\,. \end{aligned}$$

Hence

$$\begin{aligned} lclF(\omega^2) =& \Big(\omega^4 - (C - A_1 - A_2)\,\omega^2 + A_1A_2\Big)^2 \\ & - 2\Re\big(Q(i\omega)\big)\Big(\omega^4 - (C - A_1 - A_2)\,\omega^2 + A_1A_2\Big) \\ & + \Big(B\omega^3 + a\left(A_2(x_1^2 - 1) + A_1(x_2^2 - 1)\right)\omega\Big)^2 \\ & + 2\Im\big(Q(i\omega)\big)\Big(B\omega^3 + a\left(A_2(x_1^2 - 1) + A_1(x_2^2 - 1)\right)\omega\Big), \end{aligned}$$

where

$\Re\big(Q(i\omega)\big) = k_2\Big(B\omega^2 + aA_1(x_2^2 - 1)\Big)$, $\Im\big(Q(i\omega)\big) = k_2\Big(\omega^2 - (C - A_1)\Big)\omega$.

Notice that in general

$$F(z) = z^4 + c_3z^3 + c_2z^2 + c_1z + c_0,$$

where

$c_0 = A_1^2A_2^2 - 2ak_2A_1^2A_2(x_2^2 - 1) = A_1^2A_2\left(A_2 - 2ak_2(x_2^2 - 1)\right)$,

$c_3 = B^2 - 2(C - A_1 - A_2) = a^2\left((x_1^2 - 1) + (x_2^2 - 1)\right) + 2\,(A_1 + A_2)$.

Hence, the sign of c_0 does not depend on the sign of A_1.

Analysis of the auxiliary function F is complex and could be not possible for the whole range of parameter values. As an example of this analysis, below we present results obtained for the trivial steady state and next we formulate the final result for the reference parameter values.

For the trivial steady state the auxiliary function takes the form

$$\begin{aligned} F(z) = & z^4 + 2(a^2 + A_1 + A_2)z^3 \\ & + \left(a^4 + 2a^2(A_1 + A_2) + 2ak_2A_2 + 4A_1A_2 + A_1^2 + A_2^2\right)z^2 \\ & + \left(2a^3k_2A_2 + a^2(A_1^2 + A_2^2) + 2A_1A_2(A_1 + A_2 + 2ak_2)\right)z \\ & + A_1^2A_2(A_2 + 2ak_2), \end{aligned}$$

with $A_1 = -de_1f$, $A_2 = -de_2f$. Notice that whenever $2ak_2 < -A_2 = de_2f$, the free term is positive. Notice also, that Condition (6) implies this condition under the assumption $e_1 < e_2^2$, as then $ak_2 < f\frac{de_1}{2e_2} < f\frac{de_2}{2}$. Moreover, this is the case of Assumption H1 of Theorem 2.

For sufficiently large $|A_1|$, $|A_2|$ we expect four changes of the signs of coefficients of F. Clearly the coefficient of cubic term $a^2 + A_1 + A_2 < 0$ iff $a^2 < df\,(e_1 + e_2)$. Next, the coefficient of squared term $a^4 + 2a^2(A_1 + A_2) + 2ak_2A_2 + (A_1 + A_2)^2 + 2A_1A_2 = a^4 + (A_1 + A_2)(2a^2 + A_1 + A_2) + 2A_2(ak_2 + A_1) > 0$ for $ak_2 < de_1f$ and $a^2 < df\frac{e_1+e_2}{2}$. The first inequality follows from the positivity of the free term as $e_2 < e_1$. Eventually, the coefficient of linear term $2a^3k_2A_2 + 4ak_2A_1A_2 + a^2(A_1 + A_2)^2 - 2a^2A_1A_2 + 2A_1A_2(A1 + A2) = 2a^3k_2A_2 + 2aA_1A_2(2k_2 - a) + (a^2(A_1 + A_2) + 2A_1A_2)(A1 + A2) < 0$ for $a^2 < 2df\frac{e_1e_2}{e_1+e_2}$ and $k_2 < \frac{a}{2}$.

To sum up, if $e_1 < 3e_2$ and $k_2 < \frac{a}{2}$, then to get four changes of signs it is enough to assume

$$a^2 < 2df\frac{e_1e_2}{e_1+e_2}.$$

Clearly, $a^2 < 2df\frac{e_1e_2}{e_1+e_2} \leq df\frac{e_1+e_2}{2}$. Moreover, as $a > 2k_2$, we obtain $2ak_2 < a^2 < df\frac{e_1+e_2}{2} < 2dfe_2 < 2dfe_1$.

According to Descarte's Rule of Signs four changes of signs mean that F has an even number of positive zeros. Hence, in general there are 0, 2 or 4 positive zeros. It is obvious that if there is no positive zero then stability switches do not occur. In this case (0, 0, 0, 0) is unstable independently of the delay. It could be checked that there is no real zeros for reference parameter values meaning that the state (0, 0, 0, 0) is always unstable. In the case when 2 positive zeros $0 < z_1 < z_2$ exist, we have two pairs of purely imaginary eigenvalues $\pm\sqrt{z_1}i$ and $\pm\sqrt{z_2}i$ for corresponding critical delays T_1 and T_2, which could be found from the characteristic quasi-polynomial (8), that is we are able to calculate sinus and cosinus of ωT.

However, in a general case it is not easy to check the relation between T_1 and T_2.

Assuming $T_1 < T_2$ we have the following dynamics of eigenvalues with respect to delays. For $T < T_1$ we have four eigenvalues in the right-hand complex half-plane (due to continuous dependence and presence of these eigenvalues for $T = 0$). At $T = T_1$ a pair of eigenvalues moves from right to left (according to the negative derivative of F at z_1), but still two eigenvalues remain on right, so the state is unstable. Next, for $T = T_2$ a pair of eigenvalues goes from right to left, so again the number of eigenvalues on right increases implying instability. The only possibility of getting stable steady state is when $2T_1 < T_2$. In such a case at $T = 2T_1$ there is no eigenvalues on right and the pair of purely imaginary eigenvalues goes to left implying stability. However, this stability will be lost at $T = T_2$.

Assuming $T_2 < T_1$ we obtain that for $T < T_2$ we have four eigenvalues on right, at $T = T_2$ next two eigenvalues move from left to right, so in this case the switch of stability is impossible.

When there are 4 positive zeros of F, then the situation is even more complex and stability switches are more probable than in the case of 2 zeros.

On the other hand, when a is large comparing to $|A_1|$ and $|A_2|$, then the signs of coefficients of F could be different. Assume $a^2 > 2df(e_1 + e_2)$ and $ak_2 < df\frac{e_2}{2}$. Then the free term $A_1^2A_2(2ak_2 + A_2) > 0$, the cubic coefficient $a^2 + A_1 + A_2 > 0$, and the square coefficient $a^2\left(a^2 + 2(A_1 + A_2)\right) + A_2(2ak_2 + A_2) + 4A_1A_2 + A_1^2 > 0$. Hence, there could be either 0 or 1 change of signs, implying 0 or 1 positive zero of F. If there is no positive zero, then switches of stability are impossible. If there is one positive zero z_1, we have the corresponding delay T_1 and for $T < T_1$ we have 4 eigenvalues on right, while at $T = T_1$ a pair of eigenvalues moves from left to right implying increasing number of eigenvalues on right. Therefore, stability switch is also impossible in this case. Hence, for such parameter values (0, 0, 0, 0) remains unstable for all $T > 0$.

Making similar analysis for other steady states we are able to formulate our main result.

Proposition 1 *For the reference parameter values the stability of steady states does not change with increasing delay.*

Proof For the reference parameter values and five possible steady states auxiliary functions have no positive zeros or there is one zero but eigenvalues go through the imaginary axis in the direction which does not allow the change of stability.

4 Numerical Analysis

In this section we illustrate analytical results presented above by numerical simulations for given parameters. Now we consider slow/fast AVNRT pathology. In this case, we have coexistent conduction by two pathways. We assume that the fast pathway is described by the first van der Pol system but the slow pathway is treated as an action potential in other characteristic, so we use the second van der Pol model to describe this pathway. We treat a re-entry wave from slow pathway as an external pulse which is added to the main pathway, so it is reflected by the kx_2 term. As a result, we obtain faster rhythm than reference one (model as a physiological rhythm), which is a typical behaviour for this kind of pathology (during this type of tachycardia, the rhythm of the heart is about 35% more frequent than normal rhythm, which is in accordance with our results), Fig. 4. In Fig. 4c, we see a longer period in the initial phase of the rhythm, which is described as "jump" in the literature. It is the phenomenon often observed before appearing of tachycardia, especially in slow/fast and slow/slow types of AVNRT.

To model additional slow pathways which create new re-entry waves in given system, we assume bigger value of k_2 parameter, which corresponds to the sum of consecutive re-entry waves. In this pathology, the presence of more than two conduction paths is possible which is associated with more re-entry waves. The behaviour is similar to the previous one – we can also observe shortening of the period of oscillations but bi-period behaviour appears in this case. Increasing the number of feedbacks modelling re-entry waves of the slow pathways causes a progressive shortening of the period of oscillation, while the rhythm remains almost regular.

5 Conclusions

The main aim of the paper was to propose the system of differential equations describing the dynamics of action potential that accompanies various types of AVNRT (slow/fast and slow/slow). In this work, by using proposed models we were able to reproduce the most important physiological properties of the discussed pathologies. We try to continue the validation of these models with the use of medical data. However, to collect the necessary data, only the invasive methods can be used, which constitutes an important difficulty.

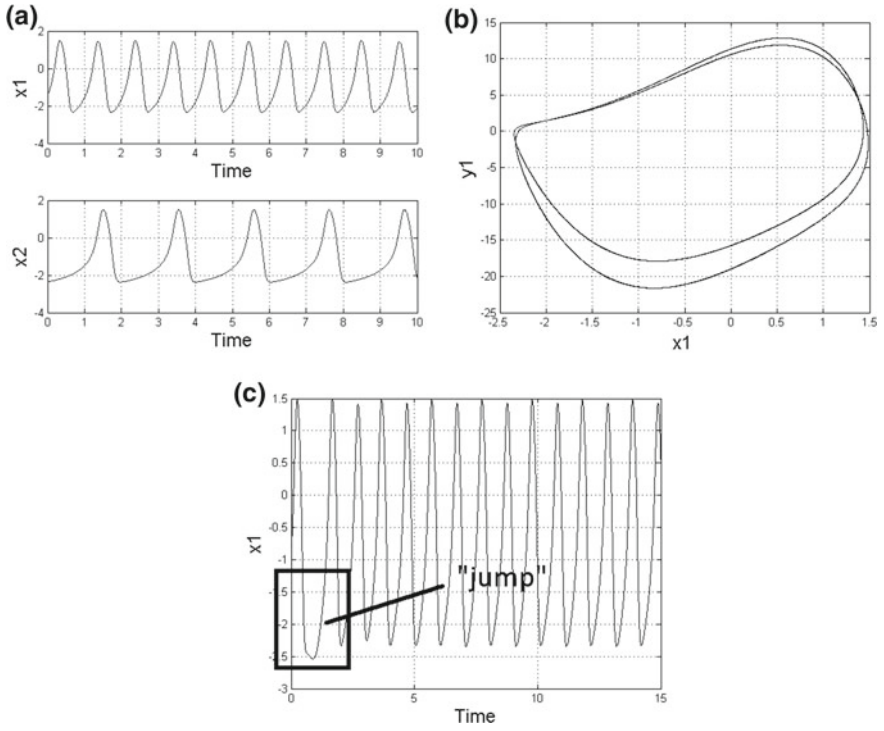

Fig. 4 **a** Dynamics of action potential for Eqs. (2) with $k_2 = 0.3$. **b** Solution in (x_1, y_1) plane. **c** Jump in the initial phase

References

1. Cooke, K.L., van den Driessche, P.: On zeroes of some transcedental equations. Funkcj. Ekvacioj. **29**, 77–90 (1986)
2. Dabrowska, B., Gajewski, P.: Postepowanie u chorych z nadkomorowymi zaburzeniami rytmu Wytyczne American College of Cardiology, American Heart Association European Society of Cardiology. Medycyna Praktyczna **6**, 1–62 (2004)
3. Freedman, R.A., Mason, J.W.: Sustained ventricular tachycardia, clinical aspects. Cardiac pacing and electrophysiology. In: W.B. Sanders Co., Philadelphia (1991)
4. Grudziński, K.: Modeling the Electrical Activity of the Heart Conduction. Warsaw University of Technology, Warsaw (2007)
5. Jackowska-Zduniak, B., Bodnar, M., Foryś, U.: A modified van der Pol equation with delay in a description of the heart action. Int. J. Appl. Math. Comput. Sci. **24**, 853–863 (2014)
6. Katritsis, D.G., Josephson, M.E.: Classification of electrophysiological types of atrioventricular nodal re-entrant tachycardia: a reappraisal. Europace **15**, 1231–1240 (2013)
7. Malaczynska, K., Blaszczyk, K.: Atrioventricular nodal reentrant tachycardia. Polish Rev. Cardiol. **14**, 196–203 (2012)
8. Shenasa, M.: Electrocardiography of complex arrhythmias. In: Elsevier, London (2014)
9. Stevenson, W.G.: Exploring postinforction reentrant ventrivular tachycardia with entertainment mapping. J. Am. Coll. Cardiol. **29**, 1180–1189 (1997)

Two-Frequency Averaging in the Problem of Motion of a Counter-Rotating Vertical Axis Wind Turbine

Liubov Klimina, Ekaterina Shalimova, Marat Dosaev, Boris Lokshin and Vitaly Samsonov

Abstract Motion of a small-scale Darrieus counter-rotating vertical axis wind turbine (VAWT) in a steady wind flow is studied. The system consists of two turbines that rotate in opposite directions. The shaft of the first turbine is rigidly joined to the rotor of a generator and the shaft of the second turbine is rigidly joined to the stator. A closed few-parametric mathematical model that takes into account the changeable electrical load in the local circuit of the generator is constructed. The corresponding dynamical system is a two-frequency system. In order to describe operating modes of the model, the system is averaged over two angles under the assumption that both frequencies are bounded away from zero. It is shown that passage through resonances has no crucial effect on the system behavior in the considered range of the parameters of the model.

Keywords Counter-rotating darrieus wind turbine · Closed dynamical model · Steady motions

1 Introduction

The idea of extracting energy from the flow using counter rotating turbines is rapidly developed in different ways. Counter rotating horizontal axis wind turbines become

L. Klimina (✉) · E. Shalimova · M. Dosaev · B. Lokshin · V. Samsonov
Institute of Mechanics, LMSU, Michurinsky prosp., 1, 119192 Moscow, Russia
e-mail: klimina@imec.msu.ru

E. Shalimova
e-mail: ekateryna-shalimova@yandex.ru

M. Dosaev
e-mail: dosayev@imec.msu.ru

B. Lokshin
e-mail: blokshin@imec.msu.ru

V. Samsonov
e-mail: samson@imec.msu.ru

J. Awrejcewicz (ed.), *Dynamical Systems in Theoretical Perspective*,
Springer Proceedings in Mathematics & Statistics 248,
https://doi.org/10.1007/978-3-319-96598-7_15

more and more popular and attract attention of researchers and industry [1–5]. For these turbines, the rotor of generator is attached to one of the propellers, the stator is attached to the other, so the relative angular speed of the rotor with respect to the stator increases. Moreover, one propeller is located in the wake of the other, so aerodynamic torque acting on the rear propeller is influenced greatly by the front propeller. Thus, for such turbines, both electromechanical interaction between two counter-rotating parts and aeromechanical interaction are present.

The situation with the counter rotating vertical axis wind turbines (VAWTs) is rather different. At least two classes of such turbines can be distinguished. It is supposed that in models of the first class very essential aeromechanical interaction between counter-rotating turbines [6, 7] without any electromechanical interaction takes place. For the second class the electromechanical interaction takes place [8] while the aeromechanical interaction can be neglected (for example, one turbine is located above the other). The scheme including both types of interaction can be obtained from a turbine of the first class using additional gears in such a way that one turbine will drive the rotor of the generator and the other will drive the stator of the same generator.

In this paper we focus on the second class of counter-rotating VAWTs. They have the following advantage compared to classical VAWTs: the relative speed of the rotor of the generator with respect to the stator increases without using a gear. Significance of increase in the relative angular speed was discussed earlier (see [9]). Moreover, counter-rotating VAWTs have the following advantage compared to counter-rotating HAWTs: VAWTs do not need to be orientated with respect to the wind direction.

A small-scale counter-rotating VAWT of the Darrieus type is studied (Fig. 1). A closed few-parametric mathematical model of this system that takes into account changeable electrical load in the local circuit of the generator is constructed. The similar model for a single-turbine Darrieus setup was discussed in [10]. Such kind of model allows performing detailed parametric analysis of operation modes of the turbine. In [10] the single-frequency averaging method is applied to analyse the behavior of the system. However, two-frequency averaging is needed to perform a similar study in the case of a counter-rotating VAWT. Further, the general conditions, under which the two-frequency averaging in the model of a counter-rotating VAWT is correct, are provided, the qualitative parametric analysis of the averaged system is performed, the results of the study are discussed.

2 Description of the Mechanical System

The system consists of two Darrieus type vertical axis wind turbines, one of which is mounted above the other (Fig. 1). The wind-receiving blades are orientated in such a way that they maintain the counter rotation of turbines. The shaft of one of the turbines carries a rotor of an electric generator; the shaft of the other is joined to a stator of the same generator. The generator is connected to a local electric circuit with a changeable external resistance.

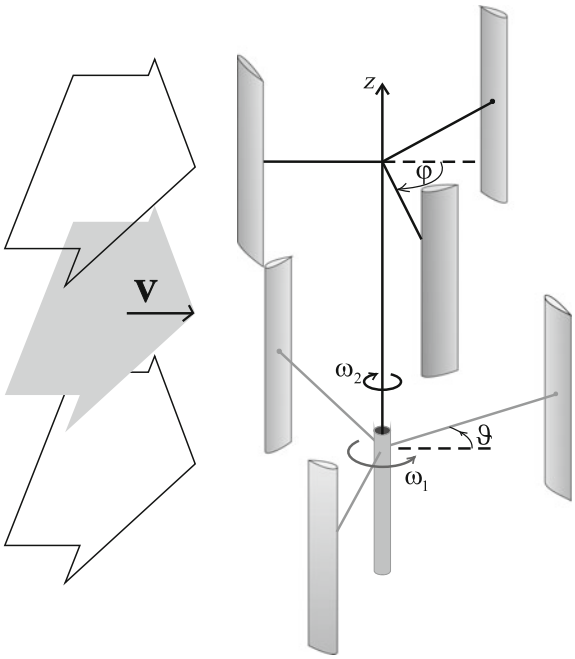

Fig. 1 The scheme of the Darrieus type counter-rotating VAWT

Let θ and φ be the angles of rotation of the lower and upper turbines, respectively. These angles are counted counterclockwise and clockwise, correspondingly, if observe from the tip of the axis z of rotation. Each turbine has n blades (in the figure each turbine has 3 blades). It is supposed that θ is the angle between the direction of the wind and the holder of one of the blades of the lower turbine, which is chosen as the first blade. Then the angle between the wind direction and the holder of the blade number k is $(\theta + 2\pi(k-1)/n)$. Similar formulas hold for the angles of location of the blades of the upper turbine with φ instead of θ.

Let r be the radius, h be the height, J be the moment of inertia about the axis of rotation z for each turbine. Assume that each blade has a character area S. The airfoil of each blade is characterized by the coefficients $C_d(\alpha)$, $C_l(\alpha)$ of drag and lift aerodynamic forces, respectively, where α is the instantaneous angle of attack.

The system is located in a steady horizontal wind flow of the speed $\mathbf{V}$. Let ρ be the air density, $\omega_1 = r\dot{\theta}/V$ be the tip speed ratio (t.s.r.) of the lower turbine, $\omega_2 = r\dot{\varphi}/V$ be the t.s.r. of the upper turbine. Notice, that these two tip speed ratios are counted in the opposite directions.

The quasi-steady model [11, 12] is used to describe the aerodynamic forces acting upon each blade. Further D is the drag force, L is the lift force, U is the airspeed of the point of the blade located at distance r from the axis z, values u and w are intermediate variables, k is the number of the blade:

$$D_k = 0.5\rho S U_k^2 C_d(\alpha_k), \quad L_k = 0.5\rho S U_k^2 C_l(\alpha_k), \quad U_k^2 = u_k^2 + w_k^2,$$

$$\alpha_k = \begin{cases} \arctan\left(\frac{u_k}{w_k}\right), & \text{if } w_k \geq 0, \\ \arctan\left(\frac{u_k}{w_k}\right) + \pi, & \text{if } w_k < 0, \end{cases} \tag{1}$$

$$u_k = \cos\left(\theta + \frac{2\pi}{3}k\right), \quad w_i = \left(\omega_1 + \sin\left(\theta + \frac{2\pi}{3}k\right)\right) - \text{for the lower turbine;}$$

$$u_k = \cos\left(\varphi + \frac{2\pi}{3}k\right), \quad w_i = \left(\omega_2 + \sin\left(\varphi + \frac{2\pi}{3}k\right)\right) - \text{for the upper turbine.}$$

An electromagnetic torque T is responsible for the interaction between the rotor and the stator of the generator. This torque is supposed to be a linear function of the angular speed $(\omega_1 + \omega_2)$ of the rotor with respect to the stator [11]:

$$T = \frac{C}{\sigma + R}\frac{V}{r}(\omega_1 + \omega_2). \tag{2}$$

Here C is the coefficient of electromechanical interaction, σ is the inner resistance of the generator, R is the external resistance in the local electric circuit of the generator.

3 Equations of Motion and Statement of the Problem

The equations of motion of the system can be represented in the following dimensionless form:

$$\begin{cases} \dot{\theta} = \omega_1, \\ \dot{\varphi} = \omega_2, \\ \dot{\omega_1} = \varepsilon(f(\theta, \omega_1) - c(\omega_1 + \omega_2)), \\ \dot{\omega_2} = \varepsilon(f(\varphi, \omega_2) - c(\omega_1 + \omega_2)), \end{cases} \quad \text{where } \varepsilon = \frac{\rho S r^3}{2J}, \quad c = \frac{2C}{V\rho S r^2(\sigma + R)}, \tag{3}$$

$$f = \sum_{k=1}^{3} \sqrt{u_k^2 + w_k^2}(C_i(\alpha_k)u_k - C_d(\alpha_k)w_k).$$

The system (3) is closed by the relations (1).

The external load coefficient c is responsible for changeable conditions of operation of the counter-rotating VAWTs, namely, for the wind speed and the external resistance. The more consumers are in the circuit, the smaller R and the larger c are.

The solution of (3) with quasi-periodically changing $\omega_1(t)$, $\omega_2(t)$ corresponds to the autorotation of both turbines. If this regime is stable, it represents the operation mode of the device.

The problem is to find and describe quasi-steady solutions $\omega_1(t)$, $\omega_2(t)$ of the system (3) under the assumption that ε is a small parameter. In practice, sufficiently small values of ε can be obtained by increasing of the moment of inertia J.

4 The Averaging Approach, Passing Through Resonances

Assume that ε is a small parameter of the system (3). Then both angles θ and φ are fast variables, and both t.s.r. ω_1 and ω_2 are slow variables. Consider the behavior of the system in the phase domain $G = \{\omega_1 > \omega_0 > 0, \omega_2 > \omega_0 > 0\}$, where ω_0 is some positive value.

To perform a constructive parametric analysis of quasi-periodic phase trajectories of (3), it is convenient to begin with the averaging with respect to both fast variables. The formal averaging leads to the following system:

$$\begin{cases} \dot{\omega}_1 = \varepsilon(F(\omega_1) - c(\omega_1 + \omega_2)), \\ \dot{\omega}_2 = \varepsilon(F(\omega_2) - c(\omega_1 + \omega_2)), \end{cases} \quad \text{where } F(\omega) = \frac{1}{2\pi}\int_0^{2\pi} f(x, \omega)dx. \tag{4}$$

However, to prove the correspondence between the behavior of systems (3) and (4), we should check how the passing through resonances happens in (3): whether trajectories can be trapped into resonances [13–18].

4.1 Passing through resonances

In the domain G, the angle θ can be chosen as a new time in the system (3):

$$\begin{cases} \dfrac{d\varphi}{d\theta} = \dfrac{\omega_2}{\omega_1}, \\ \dfrac{d\omega_1}{d\theta} = \dfrac{\varepsilon}{\omega_1} f_1(\theta, \omega_1, \omega_2), \\ \dfrac{d\omega_2}{d\theta} = \dfrac{\varepsilon}{\omega_1} f_2(\varphi, \omega_1, \omega_2), \end{cases} \tag{5}$$

where

$$f_1(\theta, \omega_1, \omega_2) = f(\theta, \omega_1) - c(\omega_1 + \omega_2), \quad f_2(\varphi, \omega_1, \omega_2) = f(\varphi, \omega_2) - c(\omega_1 + \omega_2).$$

Both functions f_1 and f_2 are 2π-periodic with respect to the first argument, and they are indefinitely differentiable with respect to all arguments. In our case functions f_1 and f_2 are in fact similar, but this does not affect the calculations in this paragraph.

Suppose that the system is in the ε-vicinity of a resonance:

$$m\omega_1 - n\omega_2 = \varepsilon g(\omega_1, \omega_2). \tag{6}$$

Here m, n are the natural numbers, $g(\omega_1, \omega_2)$ is some indefinitely differentiable function of the order $O(1)$ or less.

Introduce a new angle coordinate:

$$\psi = m\theta - n\varphi, \quad \frac{d\psi}{d\theta} = \frac{\varepsilon}{\omega_1} g(\omega_1, \omega_2). \tag{7}$$

The coordinate ψ is a slow variable. Rewrite the system (5) in the variables ψ, ω_1, ω_2:

$$\begin{cases} \dfrac{d\psi}{d\theta} = \dfrac{\varepsilon}{\omega_1} g(\omega_1, \omega_2), \\ \dfrac{d\omega_1}{d\theta} = \dfrac{\varepsilon}{\omega_1} f_1(\theta, \omega_1, \omega_2), \\ \dfrac{d\omega_2}{d\theta} = \dfrac{\varepsilon}{\omega_1} f_2(\dfrac{m}{n}\theta - \dfrac{1}{n}\psi, \omega_1, \omega_2). \end{cases} \tag{8}$$

All variables of the system (8) are slow variables, all functions in the right-hand side are indefinitely differentiable, the period of the right-hand side with respect to θ is $2\pi n$. Apply the classical single-frequency averaging to the system (8):

$$\begin{cases} \dfrac{d\psi}{d\theta} = \dfrac{\varepsilon}{\omega_1} g(\omega_1, \omega_2), \\ \dfrac{d\omega_1}{d\theta} = \dfrac{\varepsilon}{\omega_1} F_1(\omega_1, \omega_2), \\ \dfrac{d\omega_2}{d\theta} = \dfrac{\varepsilon}{\omega_1} F_2(\omega_1, \omega_2), \end{cases} \tag{9}$$

where

$$F_1(\omega_1, \omega_2) = \frac{1}{2\pi} \int_0^{2\pi} f_1(x, \omega_1, \omega_2) dx,$$

$$F_2(\omega_1, \omega_2) = \frac{1}{2\pi n} \int_0^{2\pi n} f_2(\frac{m}{n}x - \frac{1}{n}\psi, \omega_1, \omega_2) dx.$$

Due to [19], steady points of the system (9) correspond to quasi-periodic trajectories of (8); moreover, if all real parts of eigenvalues at a steady point are negative, then the corresponding quasi-periodic trajectory of (8) is attracting, if at least one of the eigenvalues has a negative real part, then the corresponding quasi-periodic trajectory of (8) is repelling.

Notice, that the first equation of (9) is separated from the two others, so equations that describe the change of ω_1, ω_2 can be studied without taking into consideration the angle ψ. Moreover, the following holds:

$$F_2(\omega_1,\omega_2)=\frac{1}{2\pi n}\int\limits_0^{2\pi n} f_2\left(\frac{m}{n}x-\frac{1}{n}\psi,\omega_1,\omega_2\right)dx=\frac{1}{2\pi n}\frac{n}{m}\int\limits_{-\frac{1}{n}\psi}^{2\pi m-\frac{1}{n}\psi} f_2(y,\omega_1,\omega_2)dy$$
$$=\frac{1}{2\pi}\frac{1}{m}\int\limits_0^{2\pi m} f_2(y,\omega_1,\omega_2)dy=\frac{1}{2\pi}\int\limits_0^{2\pi} f_2(y,\omega_1,\omega_2)dy. \tag{10}$$

Thus, the two last equations of (9) transform to the following system:

$$\begin{cases}\dfrac{d\omega_1}{d\theta}=\dfrac{\varepsilon}{\omega_1}F_1(\omega_1,\omega_2),\\ \dfrac{d\omega_2}{d\theta}=\dfrac{\varepsilon}{\omega_1}F_2(\omega_1,\omega_2),\end{cases} \tag{11}$$

where

$$F_1(\omega_1,\omega_2)=\frac{1}{2\pi}\int\limits_0^{2\pi} f_1(x,\omega_1,\omega_2)dx,\quad F_2(\omega_1,\omega_2)=\frac{1}{2\pi}\int\limits_0^{2\pi} f_2(x,\omega_1,\omega_2)dx.$$

The system (11) coincides exactly with the result of the direct two-frequency averaging of the system (5). The system (11) does not depend on the resonance number n/m. Thus, it is shown that in the domain G all the resonances are passed without a capture.

5 Quasi-Steady Motions

In the initial problem the averaged system (11) takes the form (4). Thus, as it was noticed above, the operation modes of the counter-rotating VAWT correspond to the steady points of (4) with eigenvalues with negative real parts.

The system of the form (4) was discussed in [5] in the frames of model of a counter-rotating horizontal axis turbine neglecting aerodynamic interaction between propellers. The condition of existence of a steady point $\omega_1\equiv\Omega_1\equiv const$, $\omega_2\equiv\Omega_2\equiv const$ is:

$$F(\Omega_1)=F(\Omega_2),\quad \frac{F(\Omega_1)}{\Omega_1+\Omega_2}=c. \tag{12}$$

The conditions of stability of the corresponding autorotation mode are the following (the prime denotes differentiation with respect to ω):

$$\begin{cases} G_1 = -F'(\Omega_1) - F'(\Omega_2) + 2c > 0, \\ G_2 = F'(\Omega_1)F'(\Omega_2) + c(-F'(\Omega_1) - F'(\Omega_2)) > 0, \end{cases} \tag{13}$$

where $F'(\Omega_1) = F'|_{\omega=\Omega_1}, \quad F'(\Omega_2) = F'|_{\omega=\Omega_2}$

The characteristic polynomial corresponding to the steady point of (4) is: $\lambda^2 + \varepsilon G_1 \lambda + \varepsilon^2 G_2 = 0$.

If $G_1 < 0$ or $G_2 < 0$, then the corresponding autorotation motion is unstable.

Figure 2 represents the qualitative shape of the curve $F(\omega)$.

Qualitative dependence of t.s.r. Ω_1, Ω_2 corresponding to autorotations on the parameter c is shown in Fig. 3. Solid branches correspond to attracting motions, thin branches correspond to repelling motions. The diagram is constructed for $\Omega_1 \leq \Omega_2$ due to the symmetry of the system.

The part of the diagram, where Ω is close to zero, represents the behavior not of the initial system (3), but of the averaged system (4). For small Ω the behavior of the system (3) can be more complicated that of the averaged system.

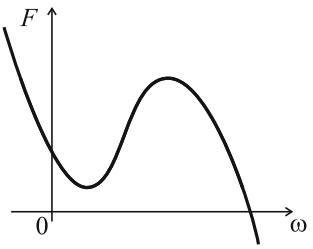

Fig. 2 The qualitative view of the function $F(\omega)$

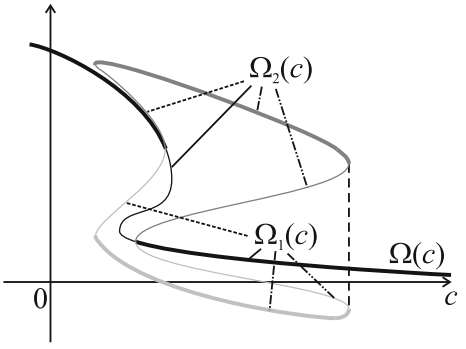

Fig. 3 The qualitative bifurcation diagram of averaged t.s.r. at autorotations depending on the parameter c

6 Discussion

The obtained diagram corresponds to the averaged system. So for every given value of ε, if ω_1 and ω_2 become too small, there is no correspondence between the averaged system (4) and the initial system (3). Thus, there is some area near the abscissa axis, for which the diagram is not valid for the initial system. This area depends on ε: the smaller ε is, the more narrow this area is.

Three types of quasi-steady motions are possible: the motion for which the averaged tip speed ratios are equal $\Omega_1 = \Omega_2 = \Omega(c)$, the motion for which the averaged Ω_2 is larger than the averaged Ω_1, and the motion for which the averaged Ω_1 is larger than the averaged Ω_2 (not shown in Fig. 3). Each of these kinds of quasi-steady motions can be attracting or repelling.

For a given value of the parameter c there can exist from one up to five quasi-steady motions. If only one quasi-steady motion exists, then it is stable.

7 Conclusions

The closed dynamical model of a counter-rotating Darrieus type VAWT is constructed. The system consists of two turbines driving the same generator. The relative angular speed of the rotor of the generator with respect to the stator is the sum of angular speeds of turbines.

The corresponding dynamical system possesses two angular coordinates. The two-frequency averaging over these coordinates is performed. The fact that each angle appears only in the differential equation for its angular speed leads to simplicity of passing through resonances.

The domain of phase space where the correspondence between averaged and precise system takes place is described.

Sufficient conditions of the existence and stability of quasi-steady motions are obtained. The qualitative bifurcation diagram is constructed.

Acknowledgements This work was partially supported by the Russian Foundation for Basic Research, projects NN 15-01-06970, 16-31-00374, and 17-08-01366.

References

1. Stobart, A.: Wind turbine. International Patent WO1992012343 (1992)
2. Shen, W.Z., Zakkam, V.A.K., Sorensen, J.N., Appa, K.: Analysis of counter-rotating wind turbines. J. Phys. Conf. Ser. **75**, 012003 (2007)
3. Farthing, S.P.: Robustly optimal contra-rotating HAWT. Wind Eng. **34**(6), 733–742 (2010)
4. Cho, W., Lee, K., Choy, I., Back, J.: Development and experimental verification of counter-rotating dual rotor/dual generator wind turbine: generating, yawing and furling. Renew. Energy **114**, 644–654 (2017)

5. Klimina, L.A., Shalimova, E.S., Dosaev, M., Garziera, R.: Closed dynamical model of a double propeller HAWT. Procedia Eng. **199**, 577–582 (2017)
6. Dabiri, J.O.: Potential order-of-magnitude enhancement of wind farm power density via counter-rotating vertical-axis wind turbine arrays. J. Renew. Sustain. Energy **3**, 4, 043104 (2011)
7. Tjiu, W., Marnoto, T., Mat, S., Ruslan, M.H., Sopian, K.: Darrieus vertical axis wind turbine for power generation I: assessment of Darrieus VAWT configurations. Renew. Energy **75**, 50–67 (2015)
8. Flaherty, R.A., A. Burton, C.A.: Counter-rotating vertical axis wind turbine assembly. US Patent US 20120148403 A1 (2011)
9. Dosaev, M., Holub, A., Klimina, L., Selyutskiy, Y., Gritsenko, D., Tsai, M.-C., Yang, H.-T.: Power output estimation of steady regimes of a HAWT with differential gearbox. In: Dynamical Systems Applications. TU of Lodz Press, Lodz 647–656 (2013)
10. Klimina, L., Lokshin, B., Samsonov, V.: Parametrical analysis of the behaviour of an aerodynamic pendulum with vertical axis of rotation. In: Modelling, Simulation and Control of Nonlinear Engineering Dynamical Systems. State-of-the-Art, Perspectives and Applications, pp. 211–220. Springer (2009)
11. Dosaev, M.Z., Samsonov, V.A., Seliutski, Y.D.: On the dynamics of a small-scale wind power generator. Dokl. Phys. **52**(9), 493–495 (2007)
12. Dosaev, M.Z., Lin, C.-H., Lu, W.-L., Samsonov, V.A., Selyutskii, Y.D.: A qualitative analysis of the steady modes of operation of small wind power generator. J. Appl. Math. Mech. **73**(3), 259–263 (2009)
13. Arnold, V.I.: Geometrical methods in the theory of ordinary differential equations. Springer, New York (1988)
14. Arnold, V.I.: Mathematical methods of classical mechanics. Springer, New York (1989)
15. Sanders, J.A., Verhulst, F.: Averaging methods in nonlinear dynamical systems. Springer, New York (1985)
16. Sanders, J.A., Verhulst, F., Murdock, J.: Averaging methods in nonlinear dynamical systems. Springer, New York (2007)
17. Awrejcewicz, J., Andrianov, I.V., Manevitch, L.I.: Asymptotic approaches in nonlinear dynamics: new trends and applications. Springer, Berlin, Heidelberg (1998)
18. Neishtadt, A.I.: Averaging, passage through resonances, and capture into resonance in two-frequency systems. Russ. Math. Surv. **69**(5), 771–843 (2014)
19. Bogolyubov, N.N., Mitropolsky, Y.A.: Asymptotic Methods in the Theory of Non-Linear Oscillations. (2 addition, Russian) Nauka, Moscow (1974)

Process-Oriented Approach to the Design of Cyber-Physical Systems

Lech Knap, Jędrzej Mączak and Michał Trojgo

Abstract The paper is focused on the problem of lack of the uniform method of CPS systems description. In this paper a new, task-oriented, method of designing the CPS systems is proposed. The method is based on the process approach and continuous improvement of the design. This new method should be considered as extremely versatile and useful in the design and construction of the CPSs. The proposed method of the description of CPSs is based on the assumption that the task to be realized by the system is nothing more than the goal of one or more processes that should be implemented in the system. Processes, in turn, are collections of activities carried out by resource groups (components) and the tasks performed by one resource (a single element of the CPS). Activities and tasks can be carried out both in series and in parallel. Division for operations and tasks allows you to use the description of the process at different levels of detail in accordance with the requirements of the design phase of the CPS.

Keywords Cyber-physical systems · CPS · Design method · Task-oriented method · Process identification · Security threat · Risk

Lech Knap, Ph.D.: The author gave a presentation of this paper during one of the conference sessions.

L. Knap · J. Mączak (✉) · M. Trojgo
Institute of Vehicles, Warsaw University of Technology, Narbutta 84, 02-524 Warsaw, Poland
e-mail: jma@simr.pw.edu.pl

L. Knap
e-mail: l.knap@simr.pw.edu.pl

M. Trojgo
e-mail: m.trojgo@mechatronika.net.pl

J. Awrejcewicz (ed.), *Dynamical Systems in Theoretical Perspective*,
Springer Proceedings in Mathematics & Statistics 248,
https://doi.org/10.1007/978-3-319-96598-7_16

1 Introduction

This work is dedicated to issues related to the design, construction and operation of the Cyber-Physical Systems that combine and coordinate the computational and physical resources.

In the world surrounding us, for the last decade or two, an increasingly growing use of mechatronic systems consisting of mechanical systems cooperating with electronic systems, has been observed. In the human environment, many such systems can be found, supporting people in their duties or just providing a better quality of life. Even though many of these systems fulfill vital functions, such as controlling drivetrains, vehicle active safety systems, robots, vehicle traffic, etc., they still remain mostly invisible and we often do not realize their existence [1–4, 20]. Most frequently, these invisible mechatronic systems are called embedded systems working under the control of the embedded software. Combination of mechanical systems with electronic ones offers numerous advantages but also poses a series of potential threats and challenges—not only for the users of these systems but for their designers and people in their surroundings, too.

Nowadays, almost every new vehicle is equipped with mechatronic systems supporting the operator's work. Each of these systems can constitute an individual mechatronic system or, in combination with other systems, it can compose a greater system of the whole vehicle, for example a tractor. Each of the mentioned mechatronic systems is characterized by typical features, i.e. has an electronic control unit and physical interfaces allowing for the mechatronic system's influence on its environment. The electronic unit works under the control of the software, i.e. control algorithms, and accounts for the main component of the so-called cybernetic layer.

The cyber layer is connected with the physical layer by means of physical interfaces, which comprise sensors of physical magnitudes allowing for observation of phenomena taking place in the environment of the mechatronic system, as well as actuators enabling the mechatronic system's affecting the physical processes occurring in the physical layer. Such mechatronic systems (Fig. 1), integrating the cyber layer with the physical layer, and characterized by a new level of "integrated intelligence" enabling interaction and coordination of many physical processes at the same time, are customarily named cyber-physical systems or CPS [5–8].

One of the important problems the CPS designers have to face is lack of universal and widely acceptable methods of description of these systems' design and their components. This can be seen as resulting from a particularly high degree of complexity of their design and the necessity of applying various forms of requirement description among designers from different domains.

This is why a task-oriented method for designing the CPSs has been proposed in this work. It is based on the process approach and the constant improving of the project. This work illustrates how this new method should be deemed exceptionally universal and user-friendly in the process of design and building of the CPSs.

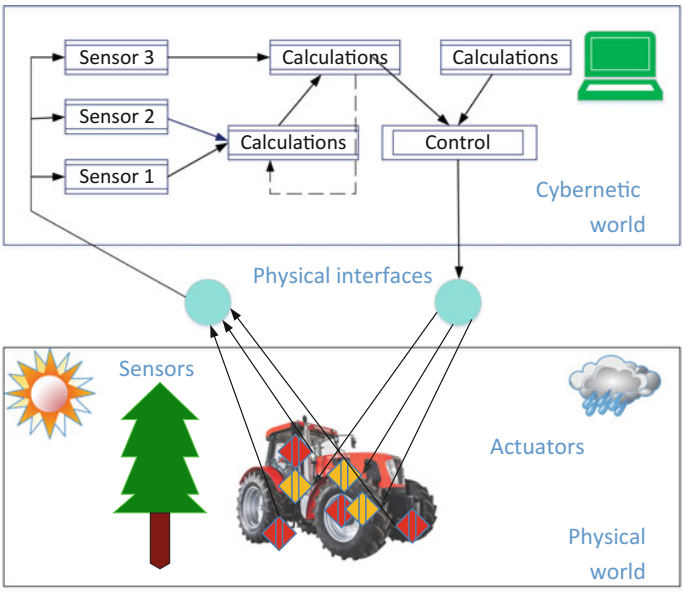

Fig. 1 Simplified example of the cyber-physical system of the agricultural tractor

2 Applied Models of System Design

Models play a key role in the process of designing the CPSs because they allow for dividing the area of the designed system into components connected with particular science domains. Thanks to this arrangement, it is possible to design a system or its components in parallel by various teams of designers from different domains and providing mechanisms for integration of all the components into a fully operative system.

Nowadays, as far as the CPS system design is concerned, there is practically no single, commonly acknowledged method of the model creation and design. Many centers and scientists working on CPS suggested several methods but currently none of them is unequivocally dominating. What is interesting, practically each of these methods depicts the way of the CPS model creation considering a different factor as crucial. The most popular methods of designing the systems, based on development of the system's model [9], include: business-model-based design [10], model-based design and model-driven development, actor-oriented design [11], adaptive discrete event model (temporal and spatial properties of events model) [12].

One of the most popular ways of designing based on the so-called model-based method, described by Jensen et al. [9], can be divided into several stages: problem description, model of physical processes, problem characteristics, developing the control algorithm, selection of the model of computation—MoC), selection of the equipment platform, simulations, construction, developing the software and its ver-

ification, validation, and testing. This model is focused on the system designing and testing stages, systematizing activities so that the created system is well-composed and efficiently operating. Many of the abovementioned steps are sets of general rules which should be taken successively. Additionally, the possibility of using the model is limited to the stage of system verification and testing, without considering the stage of practical operation, which should be included in the stage of designing. It could allow for the elimination of factors disturbing the system's work under normal operating conditions. Similar problems were observed during modeling the software development, and in recent years, it led to the creation of practical new models including: Agile [13] or DevOps [14], based on a different approach to the processes of design, verification, implementation, and practical operation.

The CPS design, based on the other models indicated above, can also render very good results due to the possibility of the profound comprehension of the CPS functionality. However, it can be burdened with limitations resulting from the necessity of identification of all events and participants, as early as during the designing stage. In real life, the CPS design requires the precise determination of the system's functionality in the project's initial phase. These functionalities together with completion of the project often change as a result of "new" requirements of the end users (unidentified and undefined in the early phase of the project), or of the staff responsible for the system's maintenance. Meeting these requirements at the later stages of the project often leads to discrepancies of goals for different groups of interested parties and to discarding of the project having incurred substantial costs.

Despite the existence of the CPS design and construction methods mentioned before, the complex approach comprising the majority of problems to be encountered in the course designing the CPS is still missing. Complexity and interdisciplinary character of the CPSs indicates the need of developing a more complex character which can be based on the selected elements of the modeling methods mentioned above.

3 Process-Oriented Approach to the Design of Cyber-Physical Systems

The process-oriented approach in organization management has undergone changes and transformations over the years, recently, however, it has been subject to development and revival again [15]. It means employing the system of processes in the organization together with identification and interaction, as well as managing these processes. According to the assumptions of the theory of process management, their use should lead to achieving goals efficiently and effectively. In order to provide for the correct operation of the process, it is necessary to identify the numerous connections and interactions that can take place within the process or among processes. Fulfilling the tasks in turn, as part of the process, is possible due to controlling the necessary resources. In the process-oriented approach, resources are defined as, for

example: financial means, workers (providing competencies and in possession of the know-how), equipment, machines, etc.

Taking into consideration the possibility of ensuring efficient and effective realization of the processes, it is also necessary to determine the methods of monitoring the process, thus of achieving the goals. Monitoring the processes is most frequently based on coefficients, which are determined and measured on an ongoing basis in the course of the process. Thanks to the carefully selected process indicators, taking decisions regarding correctness of the process functioning or necessity of its modification is possible—which is understood as perfecting of the process functioning.

Functioning of the main processes—i.e. the processes realizing the values for the client—almost always requires that the management processes and support processes should function. The task for the management processes will be controlling and providing the resources and controlling the efficient and effective realization of the remaining processes (for example monitoring and calibrating the activity of the CPS components). The task of the support processes however, is ensuring the resources and other assets necessary for the functioning of the main processes (e.g. providing the appropriate supply voltage in situations related to normal or emergency operation). The diagram illustrating the range of processes and their possible relations and interconnections is often called the process map.

An example of application of the process approach has been discussed using0 the case of designing the system controlling the main transmission of the agricultural tractor [16]. One of the main tasks to be performed by the discussed system is selection of an appropriate gear and the method of its shifting. Building such a system is complicated because it involves ensuring the operation of a few dozens of processes, including securing adequate safety procedures, for example the automatic disconnecting of the PTO drive.

The first step of designing the CPS for the tractor's main transmission requires determining the set of tasks to be performed by the system. For instance, the following functional requirements can be considered: Power Shuttle (drive control providing the gear shifting under load conditions), Power Shift (semiautomatic control with the system adapted to the automatic control system), accelerating and stopping the vehicle, control of the differential lock of the rear axle, connecting/disconnecting of the front drive, connecting/disconnecting of the PTO shaft, blocking of selected gears with the Creeper gear option on, managing the Brake & Clutch function (depressing the brake pedal results in disconnecting the drive), control of the tractor's maximal speed, providing the diagnostics, on-board communications, storage of work parameters of the transmission, enabling the cooperation of the gear unit control system with the EHR system, etc. On the basis of identification of tasks and requirements, it is possible to develop processes to be performed by the system and their depiction on the process map, illustrating possible connections among processes (Fig. 2). Nevertheless, the figure shows a simplified version of the basic processes related to functionalities which are desirable and required by the tractor manufacturer, and supporting the Power Shift gear unit. In the subsequent considerations, the authors will discuss one of the functionalities, connected with shifting the gear in the section of the gear unit where shifting gears takes place under load. To perform this activity,

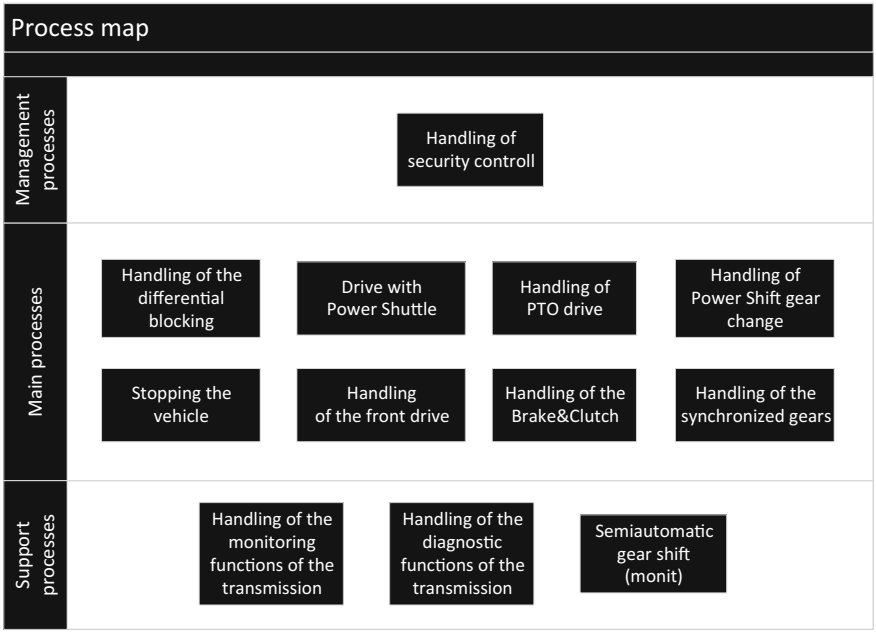

Fig. 2 Exemplary fragment of the process map of the transmission CPS of an agricultural tractor

it is necessary to select properly characteristics of the valves: the one controlling the work of engaging the clutch with the new gear and the one controlling disengaging of the clutch. The decision regarding selection of control signals is taken after the operator decides to shift the gear.

Based on the sensors mounted on the tractor, as well as on information from the ECU (Engine Control Unit), values of adequate signals controlling the valves of neighboring gears (controlling operation of multiplate clutches) are computed so as to keep the break in transmission of the driving force accordingly small. In some cases, admission of work of both clutches in parallel is necessary, which means that before one gear is disengaged, another one is engaged, in spite of the lack of kinematic compatibility. In such a case, clutch slipping is acceptable throughout a short period of shifting time.

A signal to start the process of shifting is the moment when the driver pushes the button initiating the sequential gear shift. The system should then measure the information signals: the settings of high and low gears, the engaged gear in the manually operated gear unit, as well as the signals of engine settings (speed, momentary fuel dose, engine moment), received from the ECU by means of the CAN bus. The next activity is signal analysis allowing for determination and generation of the signals controlling actuators of the clutches engaging the current gear and the gear selected by the operator.

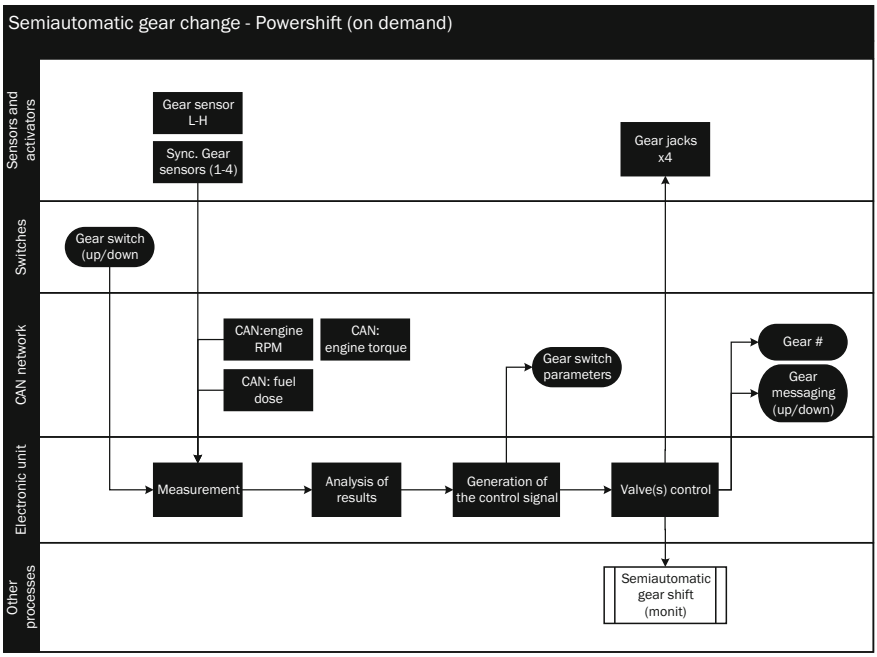

Fig. 3 Example of description of the gear shifting process in the power shift section

In accordance with the manufacturer's indications, for the service purposes, the necessity of generating information about conditions under which the shifting took place should also be taken into consideration. In the end, after overdriving the actuators with the CAN bus, the process makes the signals available, allowing for changing the information shown on the operator's dashboard or storage for diagnostic reasons. In parallel, the information is generated for the associated process of the monitoring of the semiautomatic gear change. This is a continuous process, whose purpose is an on-line monitoring of the tractor's work parameters, of the engine in particular, and indicating the information about the gear unit work state to the operator. Figure 3 shows the simplified process where the relationships and the sequence of the task fulfillment through the resources are also shown.

To illustrate the process, the following basic elements of the description were used:

⬬ indicates the beginning or the end of a given process in the CPS, often the beginning or the end of a given process is connected with the change in the actuator state, e.g. as a result of the change in the state of the system's physical layer. In the discussed example, this symbol is used to observe the change in the state of position of the gear shift lever—upwards or downwards. Similarly, this symbol was used to generate in the CAN bus the appropriate information packets about the gear shift.

This information can be used by other electronic systems, including appliances used to diagnose the transmission work;
▬ depending on the complexity of the process diagram, this symbol indicates a single action (sometimes a set) of the resource, e.g. generating the signal realized by the gear shift lever;
◆ most frequently this symbol describes the so-called "decision block" in the process, on the basis of which the successive activities arranged into various paths can be differently realized. Often, in designing the process, this symbol is used during taking decision about switching on and off the given actuator or verification of the correctness of the system components' operation. Even though the diagram does not show this symbol, it can be used, for example after more detailed account of the activity was given—Analysis of Conditions– e.g. when there is no change in the state of the lever, no action is taken and the process is terminated;
▯▯▯ this symbol is used most frequently to illustrate the relations between the described process and the other process performed by the system. It can be a connection with both the process performed in parallel and in sequence. Symbols of this kind are important because they show the flow of signals (information) between individual processes.

It should be indicated, that for the process description, a series of other symbols can be used, e.g. connections with external data bases, creation of archived data, delay to meet the needs of the synchronizing the tasks performed in parallel, the alternative task or activity, preparation or collection of data, etc.

The featured process enables meeting yet another requirement in future, i.e. making possible the automation of gear shifting and shifting gears without operator's involvement. Connection with the supporting process of monitoring is important because due to the maintenance data, i.e. information from the history of gear-shifting, taking corrective actions possible, regarding the algorithm determining values of the signals controlling actuators of clutches for individual gears.

Another advantage present in the suggested approach is using in the process diagram, in individual rows, the resources to be applied during its realization. For example, in the considered process, in the first stage of designing, it was assumed that the following resources will be used:

- in the field of integration of the cybernetic and physical layers: sensors and switches, as well as actuators (hydraulic cylinders together with valves and multiplate clutches),
- in the field of internal structure of the controller: electronic system in a broad sense,
- in the field of transmission: internal network—the CAN bus.

Certainly, at the initial stage of designing, it is difficult to define precisely the construction of, for example, an electronic system. The first stage of designing, based on the processes, enables selection of the majority of main (or all) physical interfaces necessary to complete the process. On the basis of the specified sensors, it is possible to select and design an electronic system ensuring the supply for the

sensors, measurement of physical quantities, and generating the signals controlling the proportional valves. This is what makes it possible performing the subsequent stages of designing, allowing for increasingly precise selection of all components of the system.

Together with the development of the CPS project description, it is necessary to modify the process diagram, which will thus become growingly complete, but also more and more detailed. It is clear that from the beginning of the cyclic designing the process indicates also, how the algorithm will have to work in the controller. The algorithm needs to complete the actions in the successive steps, which were defined in the process diagram (Fig. 3). It is thus apparent that the process diagram can be used by the engineers specializing in designing the physical as well as the cybernetic layers. The process approach is therefore a designing method that can be employed by engineers from various domains and allows for finding a common ground while building a system at the level of integration of different domains.

The concept of using the activities interrelated with the resources in the description of processes is similar and contains the aspects of different approaches to the CPS design. For example, it comprises the elements of the model-based design and model-driven development, and actor-oriented design. It also includes the selected elements of the methodology of the IT project development of the kind of DevOps as well as methods of constraints that were not mentioned before.

Comparing the model-oriented design with the process approach enables identification of several common areas. In the model-oriented design, the concept of the CPS design consisting of many phases emerges; the alternating phases are analyzed and realized in the process approach with every single process. In the user-oriented modeling, a considerable emphasis is laid on the director, actor, and the defining of relations between actors. In the presented process approach, relations between the successive activities performed by different resources within the processes are also defined. If the definition of an actor is adopted describing them as the resource acting within the CPS, the process approach becomes an approach similar very close, and in many cases very much the same as the user-oriented modeling. Employing a deterministic or stochastic approach [17] to describe the CPS model is possible, too, as well as the connection in serial or in parallel. The process approach—as can be seen on the diagram of the exemplary process—also allows for the locating in time of the events realized by particular resources.

Applying the process approach in the CPS design offers a lot of advantages, which result from the identification of processes and interactions among these processes. These advantages include

- understanding and meeting functional requirements set for the system,
- ensuring the running monitoring of the relationships among individual processes within the system, as well as of their combinations and mutual influence,
- ensuring the possibility of measurement with the correctness of process functioning,
- ensuring the possibility of continuous improving the processes on the basis of the objective measurement,

- ensuring the possibility of integrating the work of engineers from different domains, due to the simplicity of the description of connections between tasks and resources,
- ensuring identification of the resources and their parameters, necessary to provide for the given process functioning,
- possibility of determination of the effects resulting from events in the course of the process.

As seen above, the process approach can be successfully used in the design of the task-oriented CPSs. This means concentrating attention on the processes reflecting the functionalities expected by the client and enables the adequate control of the processes. The concept of the process approach may offer new possibilities of creating competitive advantage in building the CPSs. It has also the merit consisting in the possibility of being employed at building the systems which must undergo the process of certification—i.e. verification that the design and construction have been carried out in accordance with the requirements of the industry. In the certification process, the focus is on correct documentation of the process of designing and building the systems that interacts with the operator.

4 CPS Safety Context at the Design Stage Using a Process Approach

Problems of safety connected with the use of the CPSs have been in certain countries subject to research for the last few years. Its purpose is protecting these systems from an unauthorized access and ensuring the system resistance to the majority of attacks. This is why in some countries, where the remote control of the CPSs is not isolated from the environment, e.g. from different networks, the objectives for designing such systems have been developed, aiming at the system's security. For example, in the NIST directives [18] an increased emphasis is put on many aspects to be taken into consideration at the designing stage, e.g. efficiency requirements, availability of the systems, risk management, system and software management, change management, communication management. It is apparent that much significance is being attached to the typical elements of the IT infrastructure, i.e. issues related to the life cycle of the equipment and software.

The issue of safety, considered as early as at the stage of designing, seems to be justified because already in an early phase it is possible to consider the security aspects, for example, during selection of the components or determination of the software functional requirements. Such an approach can lead to lowering the maintenance costs in the operation of the mass-produced CPSs. An approach to the security aspects, as signaled by the NIST, is not the only one to be employed. Tools and an approach to security can be used, as formulated in the information security management systems in Europe, i.e. based on the standard of the ISO/IEC-27000 series requirements that can be integrated with the considered process approach in

an almost natural way. This approach is also based on the identification of activities within the processes. Thus, it is possible to place the security requirements on the key locations in the processes realized by the CPS. One of the main requirements of the ISO27000 series that can be transmitted onto the designing stage of the CPS relatively easy, are the requirements related to the risk analysis. The starting point for the risk analysis can be directives of the ISO/IEC-27005 [19], regarding the risk assessment in IT systems. The risk analysis is based on acquiring information about possible threats and their influence on the future activity of processes, the CPS system, and its surrounding, as well as determination of the effects resulting from current events that can affect security of the CPS functioning. Security is understood in this approach in a much broader sense than usual and regards not only the confidentiality but also efficiency, integrity, availability of functionalities realised by the designed CPS.

5 Conclusions

The presented approach to designing and building the CPSs allows for creation of the universal description of the system's project, which can be seen as a kind of language, the so-called "meta-description". Applying this description allows for interchangeability of components within the CPSs—assuming that the processes within would realise the same goals. In the custom software, this corresponds to the possibility of using different libraries, which despite being different still realise the same goal.

The suggested method of the CPS description is based on the assumption that its task is nothing short of the goal of one or many processes. The processes are, in turn, sets of activities realised by individual CPS components. The activities can be performed both in serial or in parallel, and the proposed record allows for envisaging this fact. The key advantage of the discussed method is drawing special attention to identification not only of the connections between resources but also determination of precise requirements of all the interested parties as early as possible.

The presented approach enables describing the CPS project in a simple way, comprehensible for engineers in different fields. This is exactly the simplicity and universality that make it useful in solving a series of problems connected with designing and building the task-oriented CPSs.

An additional advantage of the presented process approach, in view of the discussed threats that can affect the cyber-physical system, is the possibility of taking into consideration the security aspects. Identification of activities taking place within the process also enables identification of threats which can influence individual components, connections between these components (e.g. networks connecting the components) or the cyber-layer supporting the component (e.g. services of the software) or the whole system (e.g. environmental threats).

Acknowledgements The authors wish to express their thankfulness to the BogArt Sp. z o.o. company for help carrying out the project.

References

1. Ge, Y., Dong, Y., Zhao, H.: A cyber-physical energy system architecture for electric vehicles charging application. In: Xi'an, 12th International Conference on Quality Software (QSIC) (2012)
2. Li, Q., Negi, R.: Distributed scheduling in cyber-physical systems: the case of coordinated electric vehicle charging. Huston, IEEE GLOBECOM Workshops (GC Wkshps) (2011)
3. Loos, S., Platzer, A., Nistor, L.: Adaptive cruise control: hybrid, distributed, and now formally verified. Berlin, Formal Methods. FM 2011. Lecture Notes in Computer Science, Springer, vol. 6664, pp. 42–56 (2011)
4. Mo, Y., et al.: Cyber–physical security of a smart grid infrastructure. In: Proceedings of the IEEE 100 (2011)
5. Conti, M., et al.: Looking ahead in pervasive computing: challenges and opportunities in the era of cyber–physical convergence. Pervasive Mobile Comput. Issue 8, pp. 2–21 (2012)
6. Khaitaan, S.K., McCalley, J.D.: Design techniques and applications of cyber physical systems: a survey. IEEE Syst. J. **9**(2) (2015)
7. Lee, E.A., Seshia, S.A.: Introduction to Embedded Systems, A Cyber-Physical Systems Approach. MIT Press, Los Angeles (2011)
8. US National Science Fundation. Cyber-Physical Systems (CPS). Available at: https://www.nsf.gov/publications/pub_summ.jsp?ods_key=nsf16549&org=NSF. Access 2017 09 01
9. Jensen, J.C., Chang, D.H., Lee, E.A.: A model-based design methodology for cyber-physical systems. In: Istambul, 7th International Wireless Communications and Mobile Computing Conference (IWCMC) (2011)
10. Osterwalder, A., Pigneur, Y.: Business Model Generation: A Handbook for Visionaries, Game Changers, and Challengers. Willey (2010)
11. Ptolemaeus, C.: System Design, Modeling, and Simulation using Ptolemy II. Los Angeles: Ptolemy.org. (2014)
12. Yue, K., et al.: An adaptive discrete event model for cyber-physical system. Guilin, Analytic Virtual Integration of CPS Workshop (2010)
13. Hajjdiab, H., Taleb, A.S.: Adopting agile software development: issues. Int. J. Managing Value Supply Chains **2**(3), 1–10 (2011)
14. Samer, I.M.: DevOps shifting software engineering strategy Value based perspective. IOSR J. Comput. Eng. **17**(2), 51–57 (2015)
15. Bitkowska, A.: Business Process Management in the Enterprise. Vizja Press&IT, Warsaw (2009)
16. Knap, L.: Design and construction of the task-oriented cyber-physical system. The Institute for Sustainable Technologies—National Research Institute (2017) (in Polish)
17. Elishakoff, I., Soize, C.: Nondeterministic Mechanics. International Centre for Mechanical Sciences, Udine (2012)
18. Special Publication 800-82. Guide to Industrial Control Systems (ICS) Security. Supervisory Control and Data Acquisition (SCADA) Systems, Distributed Control Systems (DCS), and Other Control System Configurations such as Programmable Logic Controllers (PLC), NIS National Institute of Standards and Technology (2015)
19. PN-ISO/IEC-27005. Information technology. Safety technology. Risk management in information security (2015)

An Inverse Dynamics Analysis of the Remote Controlled Artillery-Missile System Under the Influence of Disturbances

Zbigniew Koruba, Daniel Gapiński and Piotr Szmidt

Abstract The paper presents a dynamic model of hypothetical missile-artillery system mounted on a moving object (e.g. mobile platform or warship). Model inputs are driving torques for the azimuth and elevation angle, and the angular and linear displacements of the set base relative to the given stationary coordinate system. The output of the model is the resulting position of the line of sight relative to the mentioned stationary coordinate system. The effect of disturbances (motion) from the moving object was studied and the reverse dynamic analysis of the presented system under the influence of the disturbances was performed. This has been investigated to check if the set's drive systems will be able to work out the required torque in time to maintain the desired line of sight. Simulations were made using the SciLab environment. Some results of numerical simulation tests was presented in graphical form.

Keywords Control · Artillery-missile system · Nonlinear system · Kinematic disturbances

1 Introduction

In today's battlefield, there is a constant need for increased combat capabilities including speed, target detection and identification, as well as firefighting capabilities by short range artillery missile systems. The challenge is to be able to successfully fire such systems in response to disturbance not only from the cannon side but also from the moving platform on which the cannon and homing missiles are mounted.

Z. Koruba · D. Gapiński · P. Szmidt (✉)
Kielce University of Technology, Al. Tysiąclecia PP 7 St, 25-314 Kielce, Poland
e-mail: pszmidt@tu.kielce.pl

Z. Koruba
e-mail: ksmzko@tu.kielce.pl

D. Gapiński
e-mail: tu_daniel_kielce@wp.pl

J. Awrejcewicz (ed.), *Dynamical Systems in Theoretical Perspective*,
Springer Proceedings in Mathematics & Statistics 248,
https://doi.org/10.1007/978-3-319-96598-7_17

In addition, this is a system with variable mass because in a short time can be fired from a few to dozens or even hundreds of bullets—so we are dealing with a strongly nonlinear system with variable parameters (non-stationary). The aim of this paper is to investigate problem of stabilizing artillery-missile system (AMS) on which external forces and kinematic extortions are acting. Manually maintaining desired line of sight in such conditions, e.g. AMS mounted on warship or moveable platform, is in principle impossible. Furthermore, training operators is expensive and time consuming [8] and they are in addition exposed to the aggressor's fire. The development of automated guidance systems and precision tracking of the target by moving system is a current research problem. For example 35 mm canons are being tested in this area in Poland [2, 3].

For the work presented in this study, the ZU-23-2MR artillery-missile system was chosen. This is a widely used naval set manufactured in Poland. The system is equipped with two 23 mm cannons as well two GROM missiles and is designed to combat lightly armoured aircraft, helicopters or other air or land targets. The actual rate of fire is 400 shots per minute, and the maximum effective fire range is 1.5 km for vertical targets up to 3 km for land targets [11].

2 Artillery-Missile System Dynamics Model

Prior to determining the equations of motion of the set, a 3D model was constructed to obtain physical parameters such as mass and moments of inertia. This model is shown in Fig. 1 along with the designation of the most important elements.

Figure 2 shows a diagram of a mechanical model. It was assumed that the generalized torque M_1 rotates the body 1 by an azimuth angle θ_1 about the axis z_1. Further, the generalized torque M_2 rotates the body 2 by the elevation angle θ_2 about the axis y_2 that moves along with the body 1.

Designations presented in Fig. 2: θ_1—azimuth angle, θ_2—elevation angle, Q_i—generalised torque impacting on i-th element, I_1—constant mass inertia moment of body 1 in relation to z_1 axis, $I_s(n)$—variable mass inertia moment of body 1 in relation to z_1 axis depending on a number of cartridges n in boxes, I_2—constant

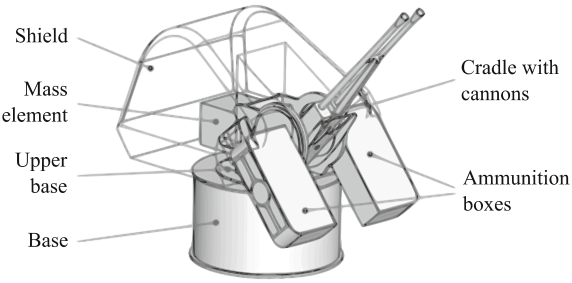

Fig. 1 General view of 3D model

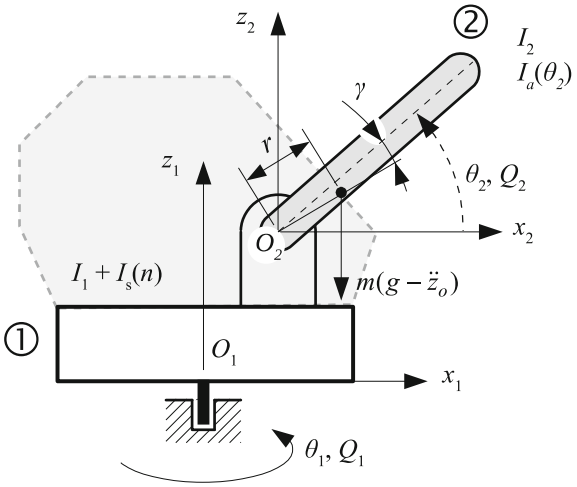

Fig. 2 Artillery-missile system mechanical model

mass inertia moment of body 2 in relation to y_2 axis, $I_a(\theta_2)$—variable mass inertia moment of body 2 in relation to z_1 axis depending on elevation angle θ_1, m—mass of body 2, g—gravitational acceleration, $\ddot{z}_0$—acceleration of set's base vertical displacement, r—distance from the centre of gravity of body 2 in relation to y_2 rotation axis, γ—angular displacement of the centre of gravity of body 2 in relation to an axis of a gun barrel.

The nonlinear differential equations of generalized torques Q_1 and Q_2 are given by (1) and (2). Some simplifications has been made. The model assumes that kinematic disturbances from the moving object on which the system is located may appear as roll and pitch angles to relatively the longitudinal and transverse axes of the carrier and as the linear displacement in the vertical direction (parallel to the action of gravity). Furthermore, acceleration in the horizontal plane is negligible and centre of gravity of the body 1 lies on the z_1 axis and does not significantly alter its position.

$$Q_1 = \left(3a\theta_2^2 + 2b\theta_2 + c\right)\dot{\theta}_1\dot{\theta}_2 + \left(I_1 + pn + q + a\theta_2^3 + b\theta_2^2 + c\theta_2 + d\right)\ddot{\theta}_1 \tag{1}$$

$$Q_2 = I_2\left(\ddot{\theta}_2 + \ddot{\tau}_x \sin\theta_1 + \ddot{\tau}_y \cos\theta_1\right) - \frac{1}{2}\left(3a\theta_2^2 + 2b\theta_2 + c\right)\dot{\theta}_1^2 \cdots + mr\left(\ddot{z}\cos\tau_x \cos\tau_y - g\right)\cos\left(\theta_2 + \gamma + \tau_x \sin\theta_1 + \tau_y \cos\theta_1\right) \tag{2}$$

where: τ_x—roll angle, τ_y—pitch angle, $Q_i = M_i - T_i$ and M_i—driving torque of motor with reduction gear, T_i—friction torque; a, b, c, d, q, p—parameters of the set described in detail in the paper [6].

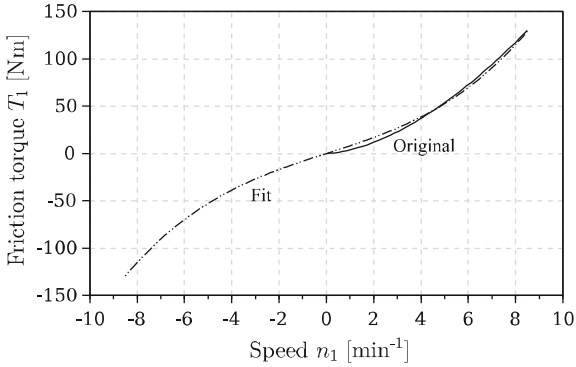

Fig. 3 Original friction curve and fitted polynomial

2.1 Friction Model

In real systems, especially in those where very precise control is required, friction plays an important role. An example of interesting works, in which this friction phenomenon in dynamic systems is analyzed in depth are works [1, 10]. For considered AMS the assumed friction model is nonlinear and is given by (3). This is a viscosity model based on empirical and geometrical parameters. Because of the fractional power in the equation, the friction domain is only positive arguments (i.e. velocity n_i). Thus, the friction value for negative velocities cannot be calculated without the abs() and sign() functions.

$$T_i(n_i) = f_0 \cdot 10^{-7} \cdot n_i \cdot (\nu n_i)^{\frac{2}{3}} \cdot d_i^3 \tag{3}$$

where: f_0—coefficient depended of bearing, n_i—rotational speed of body i, ν—kinematic viscosity, d_i—mean diameter of i-th body bearing

Function fitting was used for simplifying and speeding up calculations during simulations. The third degree polynomial was chosen to obtain the odd function shape and then the polynomial coefficients were found by the least squares method. The found functions are $T_1 = 86.15n_1^3 + 77.44n_1$ and $T_2 = 8.98n_2^3 - 8.04n_2$. As example the original and the fitted function of T_1 are shown in the Fig. 3. As we can see, the polynomial of the third degree fairly accurately maps the graph of the friction torque calculated from the original formula.

3 Target Coordinates

In fixed Cartesian coordinate system $Oxyz$ (Fig. 4) there is missile-artillery system at the origin and target described by vector $\mathbf{v}_T$ with coordinates x_T, y_T and z_T. For our purposes let us suppose that the target denotes the point in the space on which the line of sight should be directed, i.e. ballistic and weather correction are already

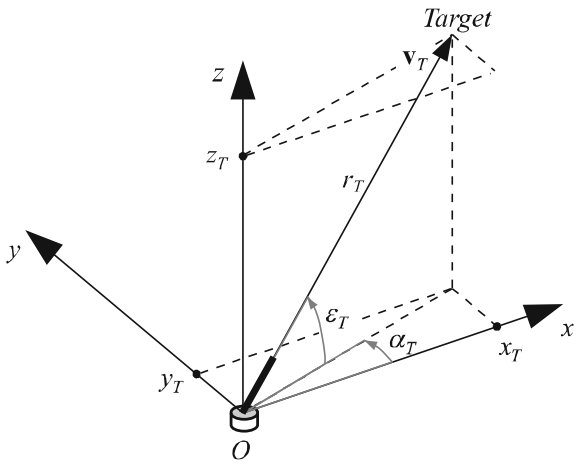

Fig. 4 Target coordinates in fixed coordinate system

included. The position of the target can also be specified by spherical coordinates, which is actually done. These are: deviation in azimuth α_T, tilt in elevation ε_T, and distance r_T.

Target observations coordinates can be obtained, for example, from an optoelectronic scanning seeker head [4] mounted on the artillery system. Since the geometry of the set is much smaller than the target distance r_T, we can assume that the angles of the azimuth and the elevation of the cannons must be equal to the angles of the target observation. Therefore we can write (4) and (5) but these equations are true only if the observation coordinate system and AMS coordinate system are identical.

$$\theta_1 = \alpha_T \tag{4}$$

$$\theta_2 = \varepsilon_T \tag{5}$$

In case where kinematic disturbances start acting on the set, set starts to move and above equations are not true if we know target observation angles α_T and ε_T in fixed or other than AMS coordinate system. Target observation angles must be given in the new coordinate system $O'x'y'z'$ (Fig. 5) which is stiff associated with the AMS, i.e. $x'y'$ plane is where azimuth θ_1 is generated and elevation θ_2 is generated in plane perpendicular to $x'y'$ plane. Let the new spherical azimuth, elevation and distance coordinates be α_T^c, ε_T^c and r_T^c respectively as they compensate for set displacement. Cartesian coordinates of the target in $O'x'y'z'$ coordinate system are x_T^c, y_T^c and z_T^c.

To express the coordinates of a target in a AMS coordinate system, we must first move from spherical coordinates to Cartesian coordinates in fixed coordinate system $Oxyz$ by formulas (6), (7) and (8). Note that Eqs. (6) and (7) are different from its standard form [7] since nonstandard convection was used to specify elevation angle ε_T.

$$x_T = r_T \cos\varepsilon_T \cos\alpha_T \tag{6}$$

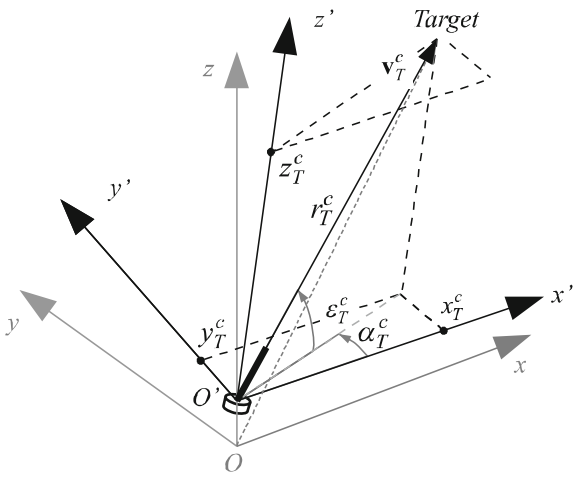

Fig. 5 Target coordinates in displaced coordinate system

$$y_T = r_T \cos\varepsilon_T \sin\alpha_T \tag{7}$$

$$z_T = r_T \sin\varepsilon_T \tag{8}$$

Now we can formulate Cartesian target coordinates as a vector $\mathbf{v}_T$ (9). Next, target coordinates transition to the set's $O'x'y'z'$ coordinate system is given by formula (10). The rotation matrices $\mathbf{R}_x$ and $\mathbf{R}_y$ [5] are already transposed because we do not rotate point in fixed coordinates but we rotate coordinate system while the point (target) remains at the same place.

$$\mathbf{v}_T = \begin{bmatrix} x_T \\ y_T \\ z_T \end{bmatrix} \tag{9}$$

$$\mathbf{v}_T^c = \mathbf{R}_x\mathbf{R}_y(\mathbf{v}_T - \mathbf{T}_z) = \mathbf{R}_{xy}(\mathbf{v}_T - \mathbf{T}_z) \tag{10}$$

where:

$$\mathbf{R}_x = \begin{bmatrix} 1 & 0 & 0 \\ 0 & \cos\tau_x & \sin\tau_x \\ 0 & -\sin\tau_x & \cos\tau_x \end{bmatrix} \tag{11}$$

$$\mathbf{R}_y = \begin{bmatrix} \cos\tau_y & 0 & -\sin\tau_y \\ 0 & 1 & 0 \\ \sin\tau_y & 0 & \cos\tau_y \end{bmatrix} \tag{12}$$

$$\mathbf{T}_z = \begin{bmatrix} 0 \\ 0 \\ z \end{bmatrix} \tag{13}$$

$$\mathbf{R}_{xy} = \begin{bmatrix} \cos\tau_y & 0 & -\sin\tau_y \\ \sin\tau_x \sin\tau_y & \cos\tau_x & \sin\tau_x \cos\tau_y \\ \cos\tau_x \sin\tau_y & -\sin\tau_x & \cos\tau_x \cos\tau_y \end{bmatrix} \tag{14}$$

Target position vector $\mathbf{v}_T^c$ in displaced coordinate system $O'x'y'z'$ contains Cartesian coordinates x_T^c, y_T^c and z_T^c (15).

$$\mathbf{v}_T^c = \begin{bmatrix} x_T^c \\ y_T^c \\ z_T^c \end{bmatrix} \tag{15}$$

To go back to spherical coordinates, (16), (17) and (18) formulas are used.

$$r_T^c = \sqrt{x_T^{c2} + y_T^{c2} + z_T^{c2}} \tag{16}$$

$$\varepsilon_T^c = \arcsin \frac{z_T^c}{r_T^c} \tag{17}$$

$$\alpha_T^c = \arctan \frac{y_T^c}{x_T^c} \tag{18}$$

Finally, we can write that cannons position in azimuth (19) and elevation (20) should be equal to target observation angles in AMS coordinate system.

$$\theta_1 = \alpha_T^c \tag{19}$$

$$\theta_2 = \varepsilon_T^c \tag{20}$$

4 An Inverse Analysis of AMS Dynamics

As an example of inverse analysis of AMS dynamics let's consider a case where the target remains in a position $\alpha_T = 15$ deg, $\varepsilon_T = 30$ deg and $r_T = 500$ m in fixed coordinate system and the system is mounded on a warship. The kinematic disturbances are given by rotations angles τ_x and τ_y as shown in Fig. 6. Waveforms (Fig. 7) of rotations angles τ_x and τ_y were generated by inverse Fourier transform and linear amplitude scaling. Coefficients have been selected so that the graphs are similar in their character to those shown in the work [4] but with the difference that the extortions gradually increase.

In Fig. 8 there are angular displacements, velocities and accelerations both for azimuth and elevation that have to be generated by AMS to maintain target at line of sight. And, therefore, the barrels will trace a fairly complicated trajectory, as shown in Fig. 9. The simulations were conducted for fully armament system.

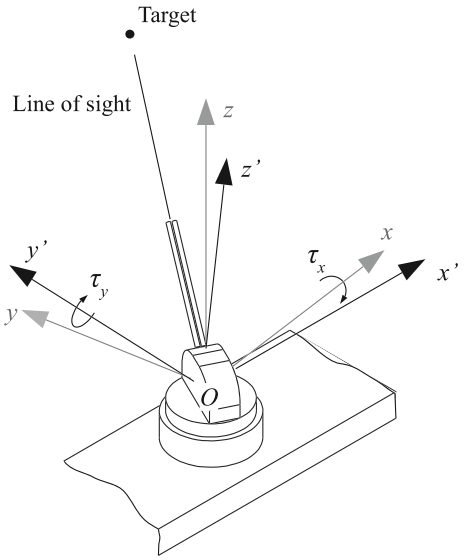

Fig. 6 System rotations for considered case

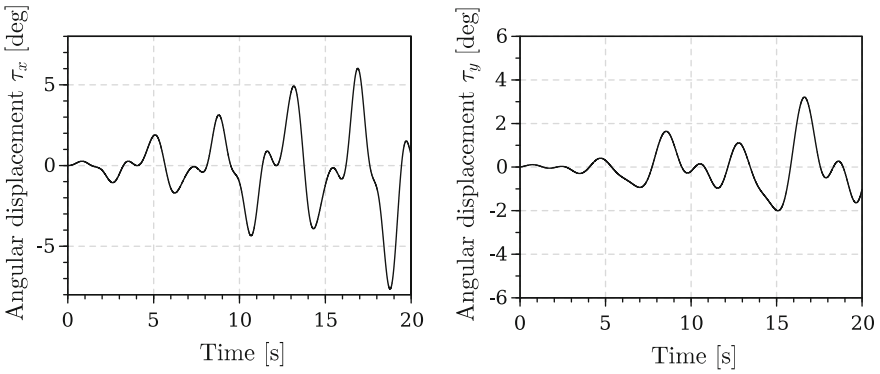

Fig. 7 Assumed angular disturbances (rotations) τ_x and τ_y

As a result of inverse dynamic analysis, driving torque M_1 which must be applied to body 1 to produce proper azimuth angle in time was calculated and is shown in Fig. 10.

The gray lines (Fig. 10) indicates the maximum and minimum torque that the SBL 4-0530 motor with reducer at the instantaneous speed can produce. As we can see the required torque is safely within acceptable limits. In Fig. 11 there is presented peak torque-speed curve for used motors. The graph has been drawn on the basis of the data contained in the catalogue [9]. At speeds above 2000 rpm the maximum peak torque generated by motor starts to drop significantly with increasing speed.

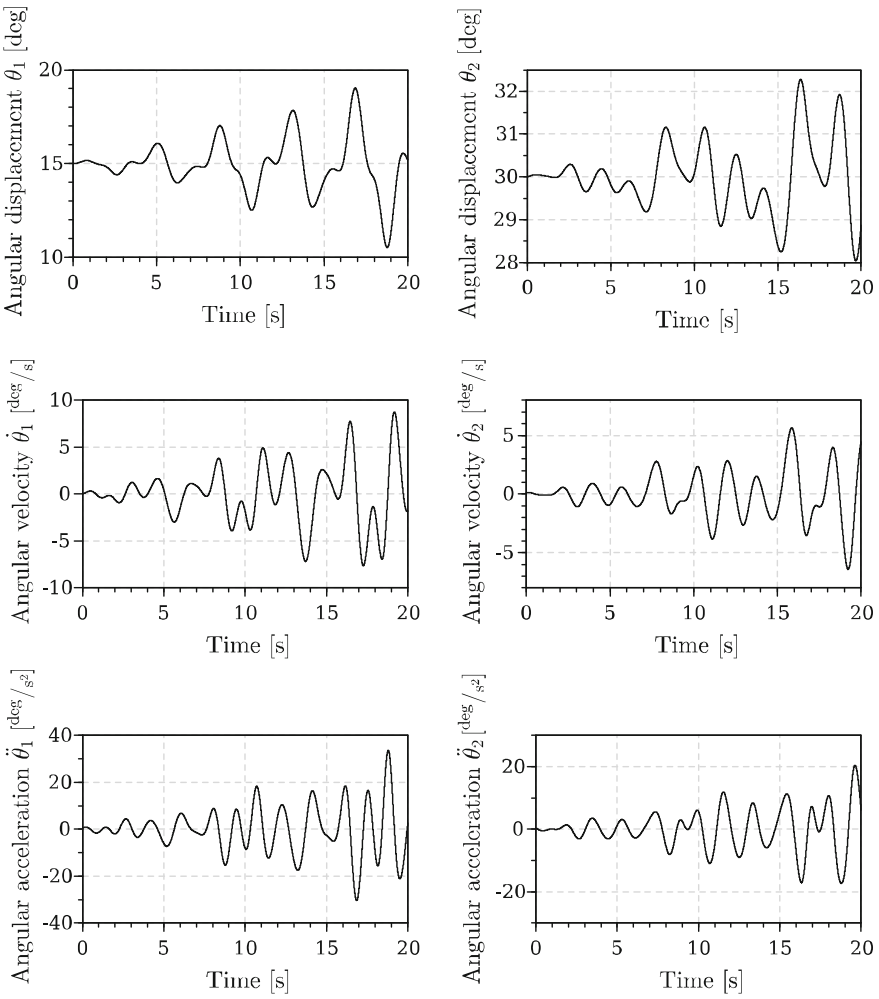

Fig. 8 Required angular displacements, velocities and accelerations of azimuth θ_1 and elevation θ_2 angles

Although this occurrence in the elevation driving system does not occur, the required driving torque M_2 exceeds the drive limits. There are some peaks marked with arrows in the Fig. 12. It should be noted that Figs. 10 and 12 illustrate the driving torques already taking into account the transmission ratios of $i_1 = 52$ and $i_2 = 38$ respectively in the azimuth and elevation system and with included 95% efficiency.

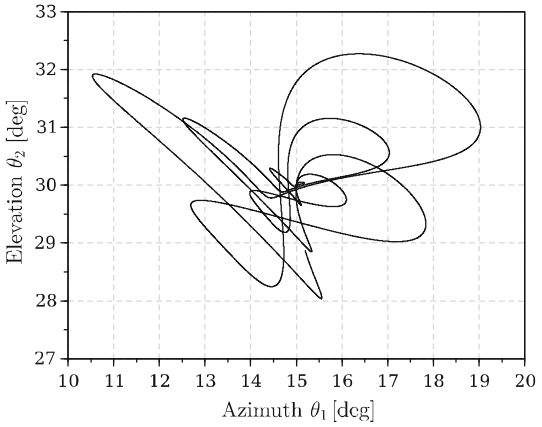

Fig. 9 Required line of sight trajectory

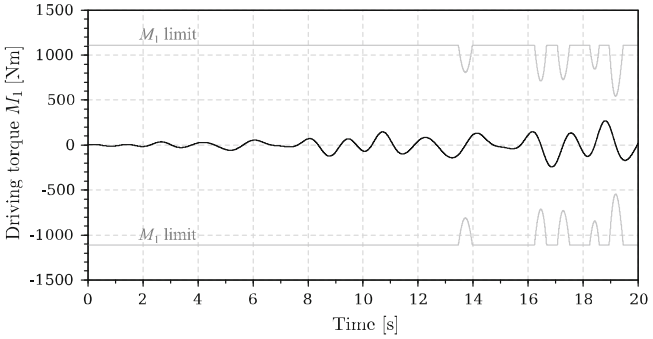

Fig. 10 Required driving torque M_1

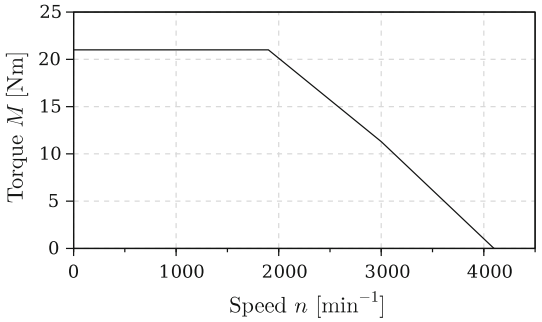

Fig. 11 Peak torque-speed curve for the SBL 4-0530 servo-motor

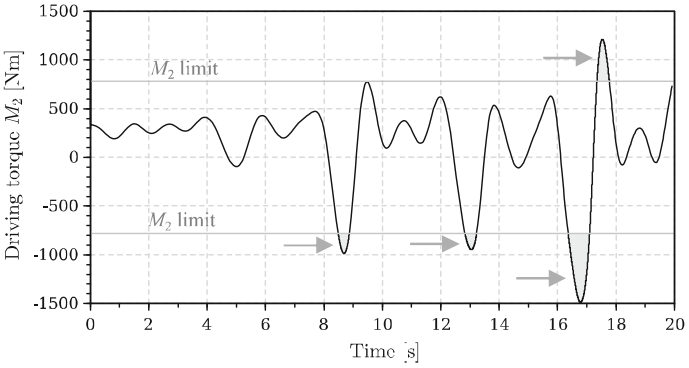

Fig. 12 Required driving torque M_2

5 Conclusions

The paper presents a mathematical model of a ZU 23-2MR system on a moveable object. Some simplifications have been made, however, the model allows to estimate the forces acting on the system. For the preliminary study that was conducted pseudo random kinematic signals acting on the system were generated. Efforts were made that the waveforms are similar to those that may occur in the actual movement of the warship on the sea wave. Obviously, it would be preferable to know the real waveforms for a given class of ship and apply them in simulations.

A procedure was proposed to determine the corrections of azimuth and elevations angles during kinematic disturbances acting on the system. Maintaining motionless target at line of sight was chosen as primary case to investigate required driving torques. As a result of the tests it can be stated that in the case of azimuth, the driving motor with a maximum torque of 20 Nm will be able to work out appropriate compensating movements. In case of elevation the power of motor will not be sufficient in certain moments. This is mainly due to the lower gear ratio in the drive system of the elevation. Also, the character of disturbances has strong impact and for the case under study, especially accelerations. Full attainment of the target in the elevation was possible for compensating angle up to about $\pm 1^\circ$ for considered kinematic disturbances. Still, most of the time of the simulation (about 80–85%) motors theoretically should be able to drive the elevation system properly. This would be a significant improvement over the control system without compensating for kinematic disturbances.

An additional very important issue is the dynamics of the drives themselves. If there are any delays or too high inertia in the drive systems, it may not be possible to properly compensate for the disturbances. The drive torque will then be unable to keep up with the quick changes required. In the preliminary tests, the AMS control was simulated with different controllers, PID and SMC, and the drive models assumed as first order inertia systems with the time constant $T = 0.02$ s. The system control

was correct. However, for the time constant $T = 0.05$ s and larger, there were already slight oscillations of the output variables. Therefore, it can be expected that for the stability of the entire control system, not only the controllers, but also the driving systems will be essential.

References

1. Awrejcewicz, J., Olejnik, P.: Analysis of dynamic systems with various friction laws. Appl. Mech. Rev. **58**(6), 389–411 (2005)
2. Dura, M.: *Armata 35 mm Tytron dla Kormorana* (*35 mm Tytron Cannon for Kormoran)* (on-line) (2016). http://www.defence24.pl/292995,fbm-armata-35-mm-tryton-dla-kormorana. Accessed 02 Sep 2017
3. Gacek, J., Gwardecki, J., Kobierski, J., Leciejewski, Z., Łuszczak, S., Milewski, S., Świętek, T., Woźniak, R., Wójcik, Z.: Struktura oraz innowacyjne technologie polskiego okrętowego systemu uzbrojenia kalibru 35 mm. In: Conference materials of 11th International Armament Conference on Scientific Aspects of Armament & Safety Technology, pp. 246–247 (2016)
4. Gapiński, D.: *Zmodyfikowana optyczna głowica skanujaco-śledząca jako układ do poszukiwania, identyfikacji i śledzenia celów powietrznych*. Ph.D. thesis, Kielce University of Technology (2016)
5. Koruba, Z.: Dynamika i sterowanie żyroskopem na pokładzie obiektu latającego (Gyroscope control and dynamics on flying object). Kielce University of Technology Publishing House, Kielce (2001)
6. Koruba, Z., Gapiński, D., Szmidt, P.: *The analysis of optimal PID controllers parameters selection for missile-artillery system*. In: Fuis, V. (ed.) Engineering Mechanics 2017, pp. 970–973 (2017)
7. Koruba, Z., Osiecki, J.W.: Mechanika elementarna (Elementary mechanics). Kielce University of Technology Publishing House, Kielce (2005)
8. Milewski, S., Kobierski, J.W.: Szkolenie funkcyjnych okrętowych systemów rozpoznawczo-ogniowych z wykorzystaniem trenażera ZU-23-2MR. Mech. Aviat. **I**, 241–254 (2012)
9. Motor Technology Ltd., *SBL/K Motor Catalogue* (on-line) http://docplayer.net/5976825-Sbl-k-motor-catalogue-2002.html. Accessed 02 Sep 2017
10. Olejnik, P., Awrejcewicz, J., Fečkan, M.: Modeling, Analysis and Control of Dynamical Systems: With Friction and Impacts. Singapore World Scientific Publishing (2018)
11. Zakłady Mechaniczne Tarnów, *23 mm Naval anti-aircraft gun and missile system ZU-23-2MR*, (on-line) http://www.zmt.tarnow.pl/wordpress/item/23mm-przeciwlotniczy-morski-zestaw-artyleryjsko-rakietowy-zu-23-2mr/. Accessed 02 Sep 2017

Approximate Identification of Dynamical Systems

Jan Kozánek, Štěpán Chládek, Jaroslav Zapoměl and Lucie Švamberová

Abstract Usually, as the input data of the parametric identification methods in the frequency domain, the corresponding pairs of the "unit harmonic force excitation"—"steady state harmonic response" are considered. This paper deals with approximate identification of linear dynamical systems by time response on unknown initial displacement (or velocity) with the help of the Fourier transform. In this paper, basic analytical relationships and identification alternatives are analyzed. Formulae are completed and presented with special consideration given to the simplest one mass dynamical system.

Keywords Linear dynamical systems · Parametric identification · Time response · Fourier transform · One mass dynamical system

1 Introduction

We suppose a mathematical model of vibrating discrete dynamical system as the $n\,(n \geq 1)$ 2nd order linear non-homogeneous differential equations, written (see [1–4]) in matrix form as

$$\mathbf{K}\,\tilde{\mathbf{v}}(t) + \mathbf{B}\,\dot{\tilde{\mathbf{v}}}(t) + \mathbf{M}\,\ddot{\tilde{\mathbf{v}}}(t) = \tilde{\mathbf{f}}(t) \tag{1}$$

J. Kozánek (✉) · Š. Chládek · J. Zapoměl · L. Švamberová
Department of Dynamics and Vibrations, Institute of Thermomechanics AS CR,
Dolejskova 5, 18200 Prague 8, Czech Republic
e-mail: kozanek@it.cas.cz

Š. Chládek
e-mail: chladek@it.cas.cz

J. Zapoměl
e-mail: jaroslav.zapomel@vsb.cz

L. Švamberová
e-mail: lucie.svamberova@seznam.cz

J. Awrejcewicz (ed.), *Dynamical Systems in Theoretical Perspective*,
Springer Proceedings in Mathematics & Statistics 248,
https://doi.org/10.1007/978-3-319-96598-7_18

with generally real non-symmetric stiffness, viscous damping and mass matrices $\mathbf{K}, \mathbf{B}, \mathbf{M} \in \mathrm{R}^{n,n}$ of order n, where $\mathbf{M}$ is supposed to be non-singular. The position vectors (linear or angular displacements in different points and directions), velocities, accelerations $\tilde{\mathbf{v}}(t)$, $\dot{\tilde{\mathbf{v}}}(t)$, $\ddot{\tilde{\mathbf{v}}}(t) \in \mathrm{R}^n$ are real time vector functions. On the right hand side of Eq. (1) there is a real vector of excitation forces (moments) $\tilde{\mathbf{f}}(t) \in \mathrm{R}^n$ depending on time t. We assume that our mathematical model is asymptotically stable (all corresponding eigenvalues have negative real parts). The initial position and velocity vectors we write as real vectors

$$\tilde{\mathbf{v}}(t=0) = \mathbf{v}_0 \in \mathrm{R}^n, \ \dot{\tilde{\mathbf{v}}}(t=0) = \mathbf{v}_{d0} \in \mathrm{R}^n. \tag{2}$$

The homogeneous matrix equation to the (1) will be for zero right hand part $\tilde{\mathbf{f}}(t) = \mathbf{o} \in \mathrm{R}^n$

$$\mathbf{K}\,\mathbf{v}_h(t) + \mathbf{B}\,\dot{\mathbf{v}}_h(t) + \mathbf{M}\,\ddot{\mathbf{v}}_h(t) = \mathbf{o}. \tag{3}$$

Supposing the homogeneous solution of the (3) as "exponential type"

$$\mathbf{v}_h(t) = \mathbf{v}_{ha} e^{st}, \quad s \in C,$$

we obtain the non-linear (with respect to s)—quadratic eigenvalue problem

$$(\mathbf{K} + s\mathbf{B} + s^2\mathbf{M})\,\mathbf{v}_{ha} = \mathbf{o}. \tag{4}$$

Defining the 2n order matrices

$$\mathbf{P} = \begin{bmatrix} \mathbf{B} & \mathbf{K} \\ -\mathbf{M} & \mathbf{0} \end{bmatrix}, \ \mathbf{N} = \begin{bmatrix} \mathbf{M} & \mathbf{0} \\ \mathbf{0} & \mathbf{M} \end{bmatrix} \in \mathrm{R}^{2n,2n}, \ (\mathbf{0} \in \mathrm{R}^{n,n} \text{ is zero matrix}),$$

the above quadratic eigenvalue problem can be transformed to the helping linear (the so called generalized) eigenvalue problem (in 2n state space)—see [2–4]

$$(\mathbf{P} + s\mathbf{N}) \begin{bmatrix} \mathbf{v}_{ha} s \\ \mathbf{v}_{ha} \end{bmatrix} = (\mathbf{P} + s\mathbf{N})\mathbf{u}_{ha} = \mathbf{o}_2 \tag{5}$$

($\mathbf{o}_2 \in \mathrm{R}^{2n}$ is 2n-dimension zero vector) and 2nd order n linear non-homogeneous differential equations (1) are replaced by 2n first order equations

$$\mathbf{P}\tilde{\mathbf{u}}(t) + \mathbf{N}\dot{\tilde{\mathbf{u}}}(t) = \tilde{\mathbf{p}}(t), \tag{6}$$

where $\tilde{\mathbf{u}}(t) = \begin{bmatrix} \dot{\tilde{\mathbf{v}}}(t) \\ \tilde{\mathbf{v}}(t) \end{bmatrix}$, $\tilde{\mathbf{p}}(t) = \begin{bmatrix} \tilde{\mathbf{f}}(t) \\ \mathbf{o} \end{bmatrix}$ with $\tilde{\mathbf{u}}(t=0) = \begin{bmatrix} \mathbf{v}_{d0} \\ \mathbf{v}_0 \end{bmatrix} = \mathbf{u}_0$. Similarly, the homogeneous equation to Eq. (6) will be

$$\mathbf{P}\mathbf{u}_h(t) + \mathbf{N}\dot{\mathbf{u}}_h(t) = \mathbf{o}_2. \tag{7}$$

Supposing

$$\mathbf{u}_h(t) = \mathbf{u}_{ha} e^{st},$$

the (linear) eigenvalue problem is

$$(\mathbf{A} - s\mathbf{I}_{2n})\,\mathbf{u}_{ha} = \mathbf{o}_2, \tag{8}$$

where

$$\mathbf{A} = -\mathbf{N}^{-1}\mathbf{P} = \begin{bmatrix} -\mathbf{M}^{-1}\mathbf{B} & -\mathbf{M}^{-1}\mathbf{K} \\ \mathbf{I}_n & \mathbf{0} \end{bmatrix} \in R^{2n,\,2n},\ \mathbf{I}_n, \mathbf{I}_{2n}$$

are identity matrices of order n, 2n, respectively. The eigenvalues and eigenvectors of $\mathbf{A}$ can give the solutions of Eqs. (1) and (3). If we for simplicity suppose that matrix $\mathbf{A}$ is non-derogatory (Jordan normal form of $\mathbf{A}$ is diagonal) and that all its eigenvalues have non-zero and increasing imaginary parts and "small" damping, we can write its complex and diagonal spectral matrix as

$$\mathbf{D} = \begin{bmatrix} \mathbf{S} & \\ & \overline{\mathbf{S}} \end{bmatrix},$$

where diagonal matrix of order n is

$$\mathbf{S} = [\backslash s_v \backslash],\ s_v = -\alpha_v + i\omega_v,\ \omega_v \gg \alpha_v > 0,\ v = 1, 2, \ldots, n,\ i = \sqrt{-1},$$
$$\omega_{v-1} < \omega_v,\ v = 2, \ldots, n,$$

where $\alpha_v,\ \omega_v,\ v = 1, 2, \ldots n$ are eigendampings and eigenfrequencies, respectively. The notation $\overline{\mathbf{S}}$ is complex conjugate of the matrix $\mathbf{S}$ and similarly for the other matrices further in the text. Corresponding eigenvectors of the matrix $\mathbf{A}$ are the columns of the complex matrix $\mathbf{U} \in C^{2n,\,2n}$:

$$\mathbf{A}\mathbf{U} = \mathbf{U}\mathbf{D}, \tag{9}$$

where the submatrix form of the matrix

$$\mathbf{U} = \begin{bmatrix} \mathbf{V}\mathbf{S} & \overline{\mathbf{V}}\,\overline{\mathbf{S}} \\ \mathbf{V} & \overline{\mathbf{V}} \end{bmatrix}$$

and for the complex non-singular matrix $\mathbf{V} \in C^{n,\,n}$ holds:

$$\mathbf{KV} + \mathbf{BVS} + \mathbf{MVS}^2 = \mathbf{0}, \tag{10}$$

where zero matrix $\mathbf{0} \in \mathrm{R}^{\mathrm{n,\,n}}$. From Eq. (9) follows that

$$\mathbf{PU} + \mathbf{NUD} = \mathbf{0}_2 = \mathbf{P}^T\mathbf{Z} + \mathbf{N}^T\mathbf{ZD}, \tag{11}$$

where $\mathbf{0}_2 \in \mathrm{R}^{2\mathrm{n},\,2\mathrm{n}}$ is zero matrix and

$$\mathbf{Z}^{\mathrm{T}} = \mathbf{U}^{-1}\mathbf{N}^{-1}$$

and $\mathbf{Z}^{\mathrm{T}}$ is the transposition of the matrix $\mathbf{Z} \in \mathrm{C}^{2\mathrm{n},\,2\mathrm{n}}$ and

$$\mathbf{Z}^{\mathrm{T}}\mathbf{NU} = \mathbf{I}_{2\mathrm{n}},\ \mathbf{Z}^{\mathrm{T}}\mathbf{PU} = -\mathbf{D}. \tag{12}$$

The submatrix form of the matrix

$$\mathbf{Z} = \begin{bmatrix} \mathbf{W} & \overline{\mathbf{W}} \\ \mathbf{Q} & \overline{\mathbf{Q}} \end{bmatrix},\ \mathbf{W}, \mathbf{Q} \in \mathrm{C}^{\mathrm{n},\,\mathrm{n}},$$

and

$$\mathbf{W}^{\mathrm{T}}\mathbf{K} + \mathbf{SW}^{\mathrm{T}}\mathbf{B} + \mathbf{S}^2\mathbf{W}^{\mathrm{T}}\mathbf{M} = \mathbf{0} = \mathbf{K}^{\mathrm{T}}\mathbf{W} + \mathbf{B}^{\mathrm{T}}\mathbf{WS} + \mathbf{M}^{\mathrm{T}}\mathbf{WS}^2.$$

From Eq. (12) we can also simply prove the very important equation

$$\mathrm{Re}\,(\mathbf{VW}^{\mathrm{T}}) = \mathbf{0}.$$

Then the solution of (7) is

$$\mathbf{u}_{\mathrm{h}}(\mathrm{t}) = \mathbf{U}\mathrm{e}^{\mathbf{D}\,\mathrm{t}}\,\mathbf{Z}^{\mathrm{T}}\mathbf{Nu}_0 \tag{13}$$

and the solution of homogeneous Eq. (4) is

$$\begin{aligned}\mathbf{v}_{\mathrm{h}}(\mathrm{t}) &= \mathbf{V}\mathrm{e}^{\mathbf{St}}(\mathbf{W}^{\mathrm{T}}\mathbf{Mv}_{\mathrm{d0}} + \mathbf{Q}^{\mathrm{T}}\mathbf{Mv}_0) + \overline{\mathbf{V}}\mathrm{e}^{\overline{\mathbf{S}}\mathrm{t}}(\overline{\mathbf{W}}^{\mathrm{T}}\mathbf{Mv}_{\mathrm{d0}} + \overline{\mathbf{Q}}^{\mathrm{T}}\mathbf{Mv}_0) \\ &= \sum_{\mathrm{v}=1}^{n} \mathbf{v}_{\mathrm{v}}(\mathbf{w}_{\mathrm{v}}^{\mathrm{T}}\mathbf{Mv}_{\mathrm{d0}} + \mathbf{q}_{\mathrm{v}}^{\mathrm{T}}\mathbf{Mv}_0)\,\mathrm{e}^{s_{\mathrm{v}}\,\mathrm{t}} + \sum_{\mathrm{v}=1}^{\mathrm{n}} \overline{\mathbf{v}}_{\mathrm{v}}(\overline{\mathbf{w}}_{\mathrm{v}}^{\mathrm{T}}\mathbf{Mv}_{\mathrm{d0}} + \overline{\mathbf{q}}_{\mathrm{v}}^{\mathrm{T}}\mathbf{Mv}_0)\mathrm{e}^{\overline{s}_{\mathrm{v}}\,\mathrm{t}}\end{aligned} \tag{14}$$

where vectors $\mathbf{v}_{\mathrm{v}}, \mathbf{w}_{\mathrm{v}}, \mathbf{q}_{\mathrm{v}} \in \mathrm{C}^{\mathrm{n}}$ and complex conjugate $\overline{\mathbf{v}}_{\mathrm{v}}, \overline{\mathbf{w}}_{\mathrm{v}}, \overline{\mathbf{q}}_{\mathrm{v}} \in \mathrm{C}^{\mathrm{n}}$ are columns of matrices $\mathbf{V} = [-\mathbf{v}_{\mathrm{v}}-], \mathbf{W} = [-\mathbf{w}_{\mathrm{v}}-], \mathbf{Q} = [-\mathbf{q}_{\mathrm{v}}-], \overline{\mathbf{V}} = [-\overline{\mathbf{v}}_{\mathrm{v}}-], \overline{\mathbf{W}} = [-\overline{\mathbf{w}}_{\mathrm{v}}-], \overline{\mathbf{Q}} = [-\overline{\mathbf{q}}_{\mathrm{v}}-] \in C^{n,n}$, respectively.

Note also, that the right- ($\mathbf{v}_{\mathrm{v}}$, $\overline{\mathbf{v}}_{\mathrm{v}}$) and left-eigenvectors ($\mathbf{w}_{\mathrm{v}}$, $\overline{\mathbf{w}}_{\mathrm{v}}$) satisfy the above quadratic eigenvalue problems (4):

$$(\mathbf{K} + s_v\mathbf{B} + s_v^2\mathbf{M})\mathbf{v}_v = \mathbf{o} \quad \text{and} \quad \mathbf{w}_v^T(\mathbf{K} + s_v\mathbf{B} + s_v{}^2\mathbf{M}) = \mathbf{o}^T,$$
$$(\mathbf{K} + \bar{s}_v\mathbf{B} + \bar{s}_v^2\mathbf{M})\bar{\mathbf{v}}_v = \mathbf{o} \quad \text{and} \quad \bar{\mathbf{w}}_v^T(\mathbf{K} + \bar{s}_v\mathbf{B} + \bar{s}_v^2\mathbf{M}) = \mathbf{o}^T, \ v = 1, 2, \ldots, n.$$

Harmonic excitation of dynamical system modelled by Eqs. (1) and (6) with angular frequency $\omega > 0$ in complex ("mathematical") form reads:

$$\tilde{\mathbf{f}}(t) = \mathbf{f}e^{i\,\omega t} \text{ and } \tilde{\mathbf{p}}(t) = \begin{bmatrix} \mathbf{f} \\ \mathbf{o} \end{bmatrix} e^{i\,\omega t} = \mathbf{p}e^{i\,\omega t},$$

and the solution of Eq. (6) with non-zero initial condition $\tilde{\mathbf{u}}(t = 0) = \mathbf{u}_0$ we can write as

$$\tilde{\mathbf{u}}(\omega, t) = \mathbf{U}e^{\mathbf{D}\,t}\mathbf{a}_0 + \mathbf{U}(i\omega\mathbf{I}_{2n} - \mathbf{D})^{-1}\begin{bmatrix} \mathbf{W} & \overline{\mathbf{W}} \end{bmatrix}^T \mathbf{f}e^{i\,\omega\,t}, \tag{15}$$

where

$$\mathbf{a}_0 = \mathbf{Z}^T\mathbf{N}\mathbf{u}_0 - (i\omega\mathbf{I}_{2n} - \mathbf{D})^{-1}\begin{bmatrix} \mathbf{W} & \overline{\mathbf{W}} \end{bmatrix}^T \mathbf{f}.$$

The steady state (after the disappearance of the influence of the initial conditions) harmonic solution of Eqs. (1) and (6) will be less complicated than (15). The displacement vector

$$\tilde{\mathbf{v}}(\omega, t) = \mathbf{v}(\omega)e^{i\omega t}$$

with time independent complex amplitude vector $\mathbf{v}(\omega)$ satisfies the equation:

$$(\mathbf{K} + i\omega\mathbf{B} - \omega^2\mathbf{M})\mathbf{v}(\omega) = \mathbf{f} \text{ with the solution } \mathbf{v}(\omega) = (\mathbf{K} + i\omega\mathbf{B} - \omega^2\mathbf{M})^{-1}\mathbf{f}, \tag{16}$$

where the relationship between the real displacement vector $\tilde{\mathbf{v}}(t)$ and the complex "mathematical" amplitude vector $\mathbf{v}(\omega) \in C^n$ is unambiguous, $\tilde{\mathbf{v}}(\omega, t) = \mathrm{Re}(\mathbf{v}(\omega)e^{i\,\omega\,t})$.

In the steady state harmonic regime, the complex amplitudes $\mathbf{v}(\omega)$, $\mathbf{v}_v(\omega)$, $\mathbf{v}_a(\omega)$ of displacements $\tilde{\mathbf{v}}(\omega, t) = \mathbf{v}(\omega)e^{i\omega\,t}$, velocities $\dot{\tilde{\mathbf{v}}}(\omega, t) = \mathbf{v}_v(\omega)e^{i\omega\,t}$, and accelerations $\ddot{\tilde{\mathbf{v}}}(\omega, t) = \mathbf{v}_a(\omega)e^{i\omega\,t}$ are related by simple relations:

$$\mathbf{v}_v(\omega) = i\omega\mathbf{v}(\omega) \quad \text{and} \quad \mathbf{v}_a(\omega) = i\omega\mathbf{v}_v(\omega) = -\omega^2\mathbf{v}(\omega). \tag{17}$$

Similarly, in a steady state regime, the complex amplitude $\mathbf{u}(\omega)$ of the solution

$$\tilde{\mathbf{u}}(\omega, t) = \mathbf{u}(\omega)e^{i\omega\,t}$$

for harmonic excitation

$$\tilde{\mathbf{p}}(t) = \mathbf{p}e^{i\omega t}$$

satisfies the equation: $(\mathbf{P} + i\omega\mathbf{N})\mathbf{u}(\omega) = \mathbf{p}$ with the solution

$$\mathbf{u}(\omega) = (\mathbf{P} + i\omega\mathbf{N})^{-1}\mathbf{p}. \tag{18}$$

The resolvent formulae (16) and (18) are disadvantageous because the spectral characteristics (resonance positions, spectrum density, or possible different damping of the individual modes of vibration) and modal properties (vibration modes, orthogonality or "parallelity" of the excitation vector $\mathbf{f}$ in relation to structure eigenmodes) are included in the complex matrices

$$(\mathbf{K} + i\omega\mathbf{B} - \omega^2\mathbf{M})^{-1} \text{ and } (\mathbf{P} + i\omega\mathbf{N})^{-1}$$

in implicit (non-transparent) form. Therefore, we express the above formulae in a more transparent way, by using partial fraction decomposition with the help of eigenvalue problem (9). According to Eq. (15), in 2n state space we can the steady state solution write as

$$\mathbf{u}(\omega) = \mathbf{U}(i\omega\mathbf{I}_{2n} - \mathbf{D})^{-1}\left[\mathbf{W}\ \overline{\mathbf{W}}\right]^{T}\mathbf{f}. \tag{19}$$

The resolvent (16) can then be expressed in a "matrix" compact form, or in "vector" expansion form (as Green resolvent with the expansion of the excited harmonic displacement to the eigenmodes of the vibrating system):

$$\begin{aligned}\mathbf{v}(\omega) &= (\mathbf{V}(i\omega\mathbf{I}_n - \mathbf{S})^{-1}\mathbf{W}^{T} + \overline{\mathbf{V}}(i\omega\mathbf{I}_n - \overline{\mathbf{S}})^{-1}\overline{\mathbf{W}}^{T})\mathbf{f} \\ &= \sum_{\nu=1}^{n}\mathbf{v}_\nu\frac{\mathbf{w}_\nu^{T}\mathbf{f}}{i\omega - s_\nu} + \sum_{\nu=1}^{n}\overline{\mathbf{v}}_\nu\frac{\overline{\mathbf{w}}_\nu^{T}\mathbf{f}}{i\omega - \overline{s}_\nu}\end{aligned} \tag{20}$$

2 The Parametric Identification Methods and Approximate Identifications

The parametric identification of machines can be defined as the creation of a mathematical model, which well defines its dynamical behaviour in the given frequency interval of the harmonic excitation frequencies $< \omega >$ and for all excitation forces $\mathbf{f} \in R^n$, described by means of excited displacements or by spectral and modal properties—[1, 5–7].

The so called "direct methods" determine directly the coefficient matrices $\mathbf{K}, \mathbf{B}, \mathbf{M} \in R^{n,n}$, where n is a small number mostly not exceeding $n = 4$ because this problem is frequently very badly numerically conditioned. On the other hand, in the determination of spectral and modal properties (modal analysis methods), i.e. com-

plex eigenvalues s_v, $v = 1, 2, \ldots n$ and corresponding right- and left- eigenvectors $\mathbf{v}_v$, $\mathbf{w}_v$, $v = 1, 2, \ldots n$, the number n is not limited—[4, 8].

2.1 *Dynamical Experiments with Known and Unknown Excitations*

Most of the current measurement methods in the field of vibration are based on known force (moment) excitations. The known harmonic or pulse excitation is used and the corresponding complex amplitude of the harmonic steady-state excited displacement, velocity or acceleration are measured or subsequently evaluated.

As the input data of the identification methods in the frequency domain—see [9], corresponding pairs of "unit harmonic excitation"—"steady state harmonic response" related to the angular frequency ω, i.e. the response-vectors of the complex amplitude $\mathbf{v}(\omega)$, $\mathbf{v}(\omega) = [-v_j(\omega)-]^T$:

$$\left\{\omega,\ \mathbf{f}(t) = \mathbf{f}\, e^{i\omega t}\right\} \rightarrow \{\mathbf{v} = \mathbf{v}(\omega,\ \mathbf{f})\} \tag{21}$$

are considered, e.g. see Figs. 1 and 2. In the case of known impulse excitation, the harmonic components of harmonic response are determined by application of the Fourier transform of the known time excitation and of the measured time response.

In many practical situations, it is possible that the dynamical system is excited by a given but unknown force (moment) excitation or is excited by an unknown non-zero initial displacement or velocity. These two above situations can even be considered as a single case, because when a force (moment) impulse ceases to operate, we consider a new time origin in which the system is excited by some non-zero initial displacement or velocity.

Let us now consider the response of the dynamical system on unknown non-zero initial displacement, velocity,

$$\tilde{\mathbf{v}}(t = 0) = \mathbf{v}_0 \neq \mathbf{o},\ \dot{\tilde{\mathbf{v}}}(t = 0) = \mathbf{v}_{d0} \neq \mathbf{o},\ \text{respectively.}$$

In this above context we can define the approximate identification as the determination of the complex eigenvalues (eigendampings and eigenfrequencies, where the eigenfrequencies are from a given frequency interval, most often, the eigenvalues with lowest eigenfrequencies) s_v, $v = 1, 2, \ldots m < n$ and corresponding approximate right-eigenvectors $\mathbf{v}_v$, $v = 1, 2, \ldots m$.

As follows from Eq. (14), the time displacement of the dynamical system will be

$$\mathbf{v}_h(t) = \sum_{v=1}^{n} \mathbf{v}_v c_v e^{s_v t} + \sum_{v=1}^{n} \overline{\mathbf{v}}_v \overline{c}_v e^{\overline{s}_v t}, \tag{22}$$

where $c_v = c_v(\mathbf{v}_0, \mathbf{v}_{d0}) = \mathbf{w}_v^T \mathbf{M} \mathbf{v}_{d0} + \mathbf{q}_v^T \mathbf{M} \mathbf{v}_0$, e.g. in Fig. 3.

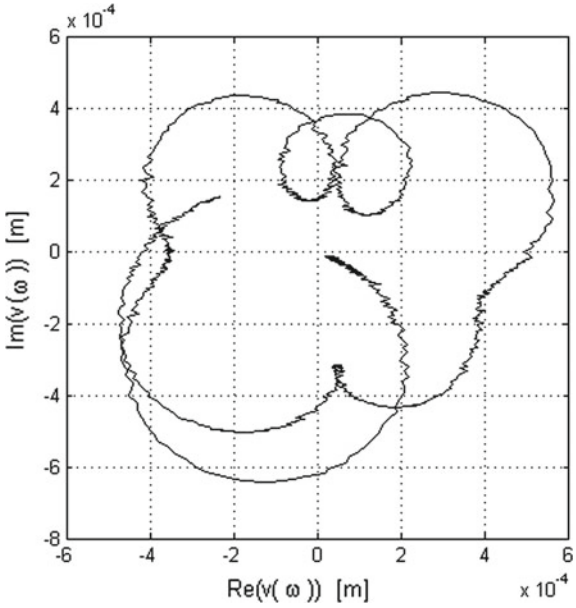

Fig. 1 Nyquist diagram $v(\omega) \in C$ in some measured point of the dynamical system with simulated experimental errors about 2%

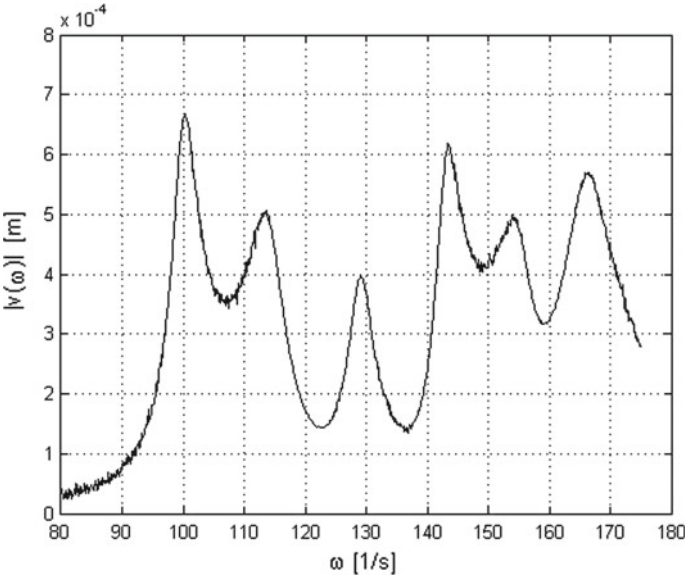

Fig. 2 Amplitude-frequency response function $|v(\omega)|$ corresponding to Fig. 1

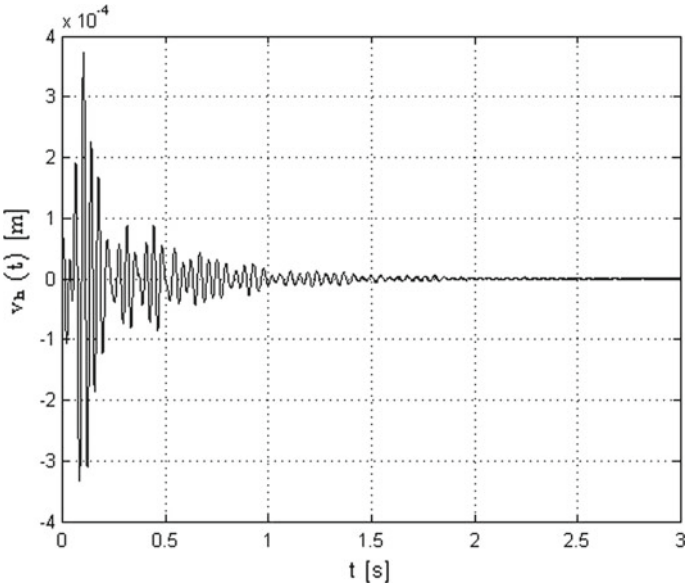

Fig. 3 Time-response $v_h(t)$ in the same measured point as in Fig. 1 on some initial displacement and with simulated experimental errors about 2%

For some m ($1 \leq m < n$) Eq. (22) can be rewritten as an approximate form

$$\mathbf{v}_h(t) = \sum_{v=1}^{m} \mathbf{v}_v c_v e^{s_v t} + \sum_{v=1}^{m} \overline{\mathbf{v}}_v \overline{c}_v e^{s_v t} + \Delta \mathbf{v}_h(t), \tag{23}$$

where the residual vector $\Delta \mathbf{v}_h(t)$ is small enough:

$$\|\Delta \mathbf{v}_h(t)\| \ll \|\mathbf{v}_h(t)\|, \; t > 0.$$

2.2 The Relation Between Homogeneous Solution and Steady State Harmonic Response

If we define the Fourier transform of a time vector function $\mathbf{g}(t) \in C^n$, $t \geq 0$, $\mathbf{g}(t) = 0$, $t < 0$ as

$$\hat{\mathbf{g}}(\omega) = \int_0^{\infty} \mathbf{g}(t) e^{-i\omega t} dt,$$

then Fourier transform of the homogeneous solution (23) will be

$$\hat{\mathbf{v}}_h(\omega) = \sum_{v=1}^{m} \mathbf{v}_v \frac{c_v}{i\omega - s_v} + \sum_{v=1}^{m} \overline{\mathbf{v}}_v \frac{\overline{c}_v}{i\omega - \overline{s}_v} + \int_0^{\infty} \Delta \mathbf{v}_h(t) e^{-i\omega t} dt. \tag{24}$$

For dynamical systems with small damping and for $\omega \in < 0, \omega_m >$ will be

$$\frac{1}{|i\omega - \overline{s}_v|} \ll \frac{1}{|i\omega - s_v|}, \quad v = 1, 2, \ldots, m$$

and we can approximately write Eq. (24) as

$$\hat{\mathbf{v}}_h(\omega) = \sum_{v=1}^{m} \mathbf{v}_v \frac{c_v}{i\omega - s_v} + \Delta \hat{\mathbf{v}}_h(\omega), \tag{25}$$

where the vector $\Delta \hat{\mathbf{v}}_h(\omega)$ is small enough:

$$\left\| \Delta \hat{\mathbf{v}}_h(\omega) \right\| \ll \left\| \hat{\mathbf{v}}_h(\omega) \right\|, \quad \omega \in < 0, \omega_m > .$$

The steady state harmonic response (20) for $\omega \in < 0, \omega_m >$ will be approximately

$$\begin{aligned} \mathbf{v}(\omega) &= \sum_{v=1}^{n} \mathbf{v}_v \frac{\mathbf{w}_v^T \mathbf{f}}{i\omega - s_v} + \sum_{v=1}^{n} \overline{\mathbf{v}}_v \frac{\overline{\mathbf{w}}_v^T \mathbf{f}}{i\omega - \overline{s}_v} \\ &= \sum_{v=1}^{m} \mathbf{v}_v \frac{\mathbf{w}_v^T \mathbf{f}}{i\omega - s_v} + \Delta \mathbf{v}(\omega) = \sum_{v=1}^{m} \mathbf{v}_v \frac{d_v}{i\omega - s_v} + \Delta \mathbf{v}(\omega), \end{aligned} \tag{26}$$

where $d_v = \mathbf{w}_v^T \mathbf{f} \in C$, $v = 1, 2, \ldots, m$ and $\|\Delta \mathbf{v}(\omega)\| \ll \|\mathbf{v}(\omega)\|$, $\omega \in < 0, \omega_m >$.

When comparing Eqs. (25) and (26) it is evident that (except for different coefficients c_v, d_v, $v = 1, 2, \ldots, m$) the steady state harmonic response on a known force (moment) harmonic excitation and Fourier transform of a time response of dynamical system on unknown non-zero initial displacement and (or) velocity (Fourier transform of homogeneous solution) give a similar expression.

This means that a time response of dynamical system on unknown non-zero initial displacement or velocity can be theoretically used as input data for spectral and modal identification methods, as well as the steady state harmonic response—see Fig. 4.

Fourier and wavelet spectra of quasi-periodic, chaotic and periodic vibrations have been investigated for example in [10].

The fundamental difference here is in the fact that while in Eqs. (20) and (26) the steady state harmonic response occurs the right- and left-eigenvectors $\mathbf{v}_v$, $\mathbf{w}_v$ in "symmetric" form, in Eqs. (22) and (25) the left-eigenvectors $\mathbf{w}_v$ (see [11]) are in implicit form through coefficients

$$c_v = \mathbf{w}_v^T \mathbf{M} \mathbf{v}_{d0} + \mathbf{q}_v^T \mathbf{M} \mathbf{v}_0.$$

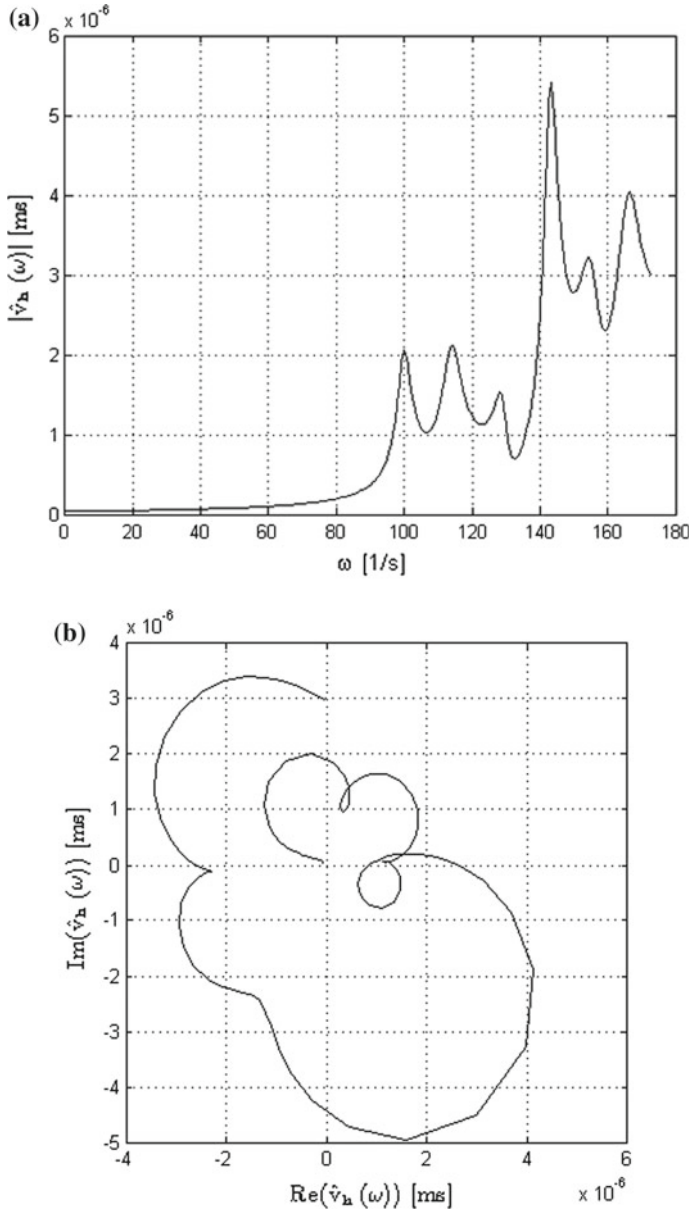

Fig. 4 Amplitude of the Fourier transform $\left|\widehat{v}_h(\omega)\right|$- a) and complex Fourier transform $\widehat{v}_h(\omega)$- b) of the time-response $v_h(t)$ from Fig. 3. The resonance locations in this figure and in Fig. 2 are the same, the amplitudes of corresponding eigenmodes are different, but this fact is not relevant for the identification of eigenmodes

This results in the fact, that for unknown excitation forces it is not possible to even approximate identification of left-eigenvectors.

We recall that from steady state harmonic responses $\mathbf{v}(\omega,\ \mathbf{f})$ (for known excitation $\mathbf{f}$)

$$\mathbf{v}(\omega,\ \mathbf{f}) = \sum_{v=1}^{m} \mathbf{v}_v \frac{\mathbf{w}_v^T \mathbf{f}}{i\omega - s_v} + \Delta\mathbf{v}(\omega,\ \mathbf{f})$$

we can identify left-eigenvectors $\mathbf{w}_v$ by the following way. We select some coordinate (for example, j) of the vector

$$\mathbf{v}(\omega,\ \mathbf{f}) = [v_1(\omega,\ \mathbf{f}), v_2(\omega,\ \mathbf{f}), \ldots, v_n(\omega,\ \mathbf{f})]^T$$

and we will write it for all unit excitation forces

$$\mathbf{f} = \mathbf{e}_k = [0, 0, \ldots 1 \ldots 0]^T,\ k = 1, 2, \ldots, n,\ (1 \text{ is in } \quad k\text{-th position})$$

as the following row vector

$$[v_j(\omega,\ \mathbf{f} = \mathbf{e}_1), v_j(\omega,\ \mathbf{f} = \mathbf{e}_2), \ldots, v_j(\omega,\ \mathbf{f} = \mathbf{e}_n)] = \sum_{v=1}^{m} \mathbf{w}_v^T \frac{b_v}{i\omega - s_v} + \Delta\mathbf{w}^T(\omega). \tag{27}$$

Another, much more serious problem in the case of using time response of dynamical system on unknown non-zero initial displacement or velocity as possible input data for spectral and modal identification methods, is the exponential time function

$$e^{-\alpha_v t},\ \alpha_v > 0$$

derived from the function $e^{s_v t} = e^{-\alpha_v t}(\cos(\omega_v t) + i \sin(\omega_v t))$ in Eq. (23). In this equation the numerically non zero components will only be components corresponding in absolute value to the smallest real parts of eigenvalues $s_v,\ v = 1, 2, \ldots$. In practice, we should take advantage of $\mathbf{v}_h(t)$ corresponding to a very small time interval and therefore with the least (technically possible) time step. Another possibility is the use of frequency filters, analog and (or) digital, selectively "drawing" investigated eigenmodes. Vanishing motions of triple pendulum as a non-linear dynamical system have been studied numerically and experimentally in [12].

2.3 One Mass Dynamical System

The mathematical model of one mass ($n = 1$) vibrating dynamical system can be written in scalar form as one 2nd order linear non-homogeneous differential equation

$$k\,\tilde{v}(t) + b\,\dot{\tilde{v}}(t) + m\,\ddot{\tilde{v}}(t) = \tilde{f}(t) \tag{28}$$

with real stiffness $k > 0$, viscous damping $b > 0$ and mass $m > 0$ ($k/m \gg (b/2m)^2$) and with position $\tilde{v}(t)$ and external force (moment) $\tilde{f}(t)$ as in Eq. (1). The scalar initial conditions are generally

$$\tilde{v}(t=0) = v_0 \in R,\ \dot{\tilde{v}}(t=0) = v_{d0} \in R.$$

The corresponding homogeneous scalar equation is

$$k\,v_h(t) + b\dot{v}_h(t) + m\,\ddot{v}_h(t) = 0 \tag{29}$$

and for an "exponential type solution"

$$v_h(t) = v_{ha}e^{s\,t},\ s \in C$$

we have the simple quadratic equation

$$k + sb + s^2 m = 0$$

with the solution, two complex conjugated eigenvalues

$$s_1, \bar{s}_1 \in C,\ s_1 = -\frac{b}{2m} + i\sqrt{\frac{k}{m} - \left(\frac{b}{2m}\right)^2} = -\alpha_1 + i\omega_1,\ \omega_1 \gg \alpha_1 > 0.$$

The solution of the homogeneous Eq. (29) with the above initial conditions is

$$\begin{aligned} v_h(t) &= \frac{-i}{2\omega_1}\left[(e^{s_1 t} - e^{\bar{s}_1 t})v_{d0} + (s_1 e^{\bar{s}_1 t} - \bar{s}_1 e^{s_1 t})v_0\right] \\ &= \frac{i(\bar{s}_1\,v_0 - v_{d0})}{2\,\omega_1}e^{s_1 t} + \frac{-i(s_1\,v_0 - v_{d0})}{2\,\omega_1}e^{\bar{s}_1 t} \\ &= e^{-\alpha_1 t}\left[\frac{v_{d0}}{\omega_1}\sin(\omega_1 t) + \left(\cos(\omega_1 t) + \frac{\alpha_1}{\omega_1}\sin(\omega_1 t)\right)v_0\right] \end{aligned}$$

and its Fourier transform will be

$$\hat{v}_h(\omega, v_{d0}, v_0) = \int_0^\infty v_h(t)e^{-i\omega t}dt = \frac{c_1}{i\,\omega - s_1} + \frac{\bar{c}_1}{i\,\omega - \bar{s}_1},\quad c_1 = \frac{i(\bar{s}_1\,v_0 - v_{d0})}{2\,\omega_1}, \tag{30}$$

corresponding to the general case for $n \geq 1$ in Eq. (22). This mean that Fourier transform of the homogeneous time solution (a response to an unknown non-zero

excitation of the investigated dynamical system) $v_h(t)$ can be used as an input data for spectral identification in frequency domain.

For special initial conditions—with zero initial position $\tilde{v}(t=0) = v_0 = 0$ and non-zero initial velocity $\dot{\tilde{v}}(t=0) = v_{d0} \neq 0$ we have

$$v_h(t) = \frac{-i}{2\omega_1}(e^{s_1 t} - e^{\bar{s}_1 t})v_{d0} = \frac{v_{d0}}{\omega_1} e^{-\alpha_1 t} \sin(\omega_1 t) \tag{31}$$

and just in this special case is Fourier transform of the homogeneous solution (30) up to the multiplicative constant equal to the steady state harmonic solution of one mass vibrating system because

$$\widehat{v}_h(\omega, v_{d0}) = \int_0^\infty v_h(t) e^{-i\omega t} dt = \frac{m\, v_{d0}}{k + i\,\omega\, b - \omega^2 m}. \tag{32}$$

We recall that in the above derivation

$$k/m = \alpha_1^2 + \omega_1^2 \text{ and } b/m = 2\alpha_1.$$

Apparently, the steady state harmonic solution of Eq. (28) for

$$\tilde{f}(t) = f e^{i\omega t},\ f > 0$$

is

$$\tilde{v}(\omega, t) = v(\omega)\, e^{i\omega t}$$

and

$$v(\omega) = \frac{f}{k + i\,\omega\, b - \omega^2 m}, \tag{33}$$

or in partial fraction resolvent form

$$v(\omega) = \frac{a_1}{i\,\omega - s_1} + \frac{\bar{a}_1}{i\,\omega - \bar{s}_1}, \quad a_1 = \frac{-i\,f}{2\,m\,\omega_1} \tag{34}$$

with purely imaginary coefficient

$$a_1 \in C,\ \mathrm{Re}(a_1) = 0$$

and with negative imaginary part

$$\mathrm{Im}(a_1) < 0.$$

Let's go back now to the general case of a discrete dynamical system with $n \geq 1$ and let us consider the scalar case of the measured position in one point (direction) excited by a force (moment) applied also at a single point (direction). One (j-th) coordinate $v_{jk}(\omega)$ of steady state harmonic response (20) on special force excitation

$$\mathbf{f} = \mathbf{e}_k = [0, 0, \ldots 1 \ldots 0]^T \text{ (in k-th point)}$$

we can write in "scalar form" as

$$v_{jk}(\omega) = \sum_{v=1}^{n} \frac{a_{vjk}}{i\omega - s_v} + \sum_{v=1}^{n} \frac{\bar{a}_{vjk}}{i\omega - \bar{s}_v}, \tag{35}$$

where "modal parameters"

$a_{vjk} = \mathbf{v}_{vj} w_{vk} \in C$ and $\mathbf{v}_v = [-v_{vj}-]^T, j = 1, 2, \ldots n, w_v = [-w_{vk}-]^T, k = 1, 2, \ldots n$

For $\omega \in < 0, \omega_m >$ we have approximately

$$v_{jk}(\omega) = \sum_{v=1}^{m} \frac{a_{vjk}}{i\omega - s_v} + \Delta v_{jk}(\omega), \tag{36}$$

where $1 \leq m < n$, $\|\Delta v_{jk}(\omega)\| \ll \|v_{jk}(\omega)\|$. In both cases (35) and (36), we therefore have the steady state harmonic response $v_{jk}(\omega)$ composed of more components corresponding to each eigenmodes either of the type

$$\frac{a_{vjk}}{i\omega - s_v}, \quad \text{or} \quad \frac{a_{vjk}}{i\omega - s_v} + \frac{\bar{a}_{vjk}}{i\omega - \bar{s}_v}, \; a_{vjk} \in C. \tag{37}$$

Let us now question whether it is possible to model this $v-$ th term (37) using one mass dynamical system (28)—see Figs. 5 and 6, where one selected eigenmode is underlined. By comparing Eqs. (34) with (37), it is understood that the answer is in general case unfavourable. Only in the special case when vth modal coefficient $a_{vjk} \in C$ has a zero real part and a negative imaginary part, we can define real and positive parameters k,b,m i.e., the alternative one mass dynamical system. In this context, it is very interesting that Fourier transform of one mass dynamical system (31) for initial condition with non zero initial position $v_0 \neq 0$ gives "steady state harmonic response" of the "general, $n > 1$ type (37)" for which there are no corresponding system coefficients k, b, $m > 0$ because $\mathrm{Re}(c_1) \neq 0$.

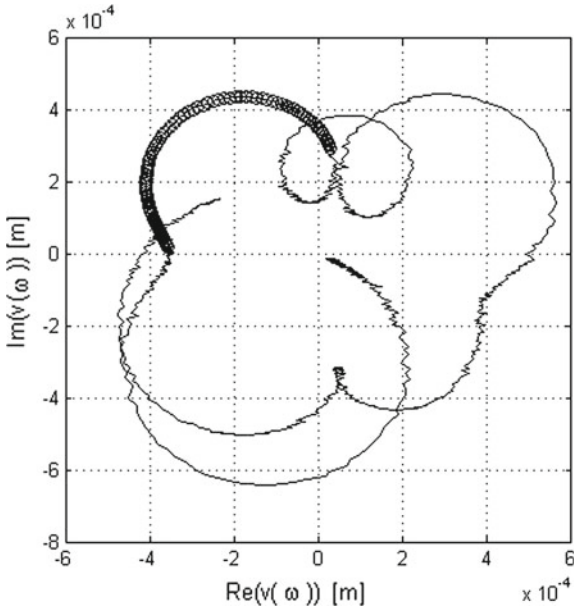

Fig. 5 Nyquist diagram v(ω) from Fig. 1, where the second eigenmode is underlined. In this case it is not possible to model the underlined part using one mass dynamical system with real k, b, m > 0

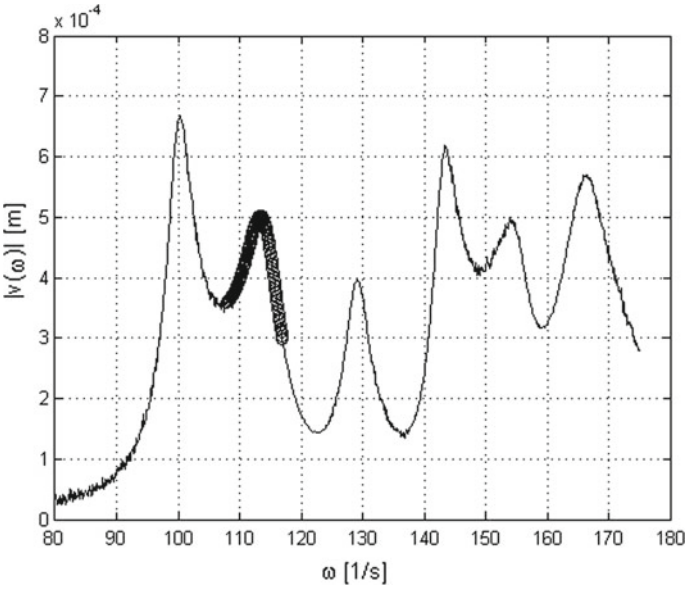

Fig. 6 Amplitude-frequency response function |v(ω)| corresponding to Fig. 5

3 Conclusions

In this contribution the theoretical possibility of using the time response on unknown initial displacement (or velocity) as input data for identification methods in frequency domain is studied. The harmonic steady state solution and homogeneous solution of discrete dynamical systems with real stiffness, viscous damping and mass matrices of order n via state space 2n formulation were derived. The Fourier transform of homogeneous solution is (up to multiplicative coefficients) formally the same as steady state harmonic solution. The dynamical experiments with known harmonic or pulse excitations are compared with frequent practical situations, when the excitation of an investigated dynamical system is unknown. The relation between the response on unknown excitation and on known harmonic excitation was formulated by the Fourier transform.

The time response of dynamical system on unknown non-zero initial displacement or velocity can be theoretically used as input data for spectral and modal identification methods, as well as the steady state harmonic response. It seems hard to believe that this simple fact has not yet been described in detail in the literature. At least the authors of this article are not aware of its previous publication.

The simplest one mass damped dynamical system is compared with its general case and the necessary condition for modelling of the one eigenmode of general dynamical systems by the one mass model with real stiffness, damping and mass was formulated.

Acknowledgements This contribution was elaborated under a pilot project of Institute of Thermomechanics AS CR, included in a frame of conceptual development of the research organization RVO: 61388998 and by the project of the Czech Academy of Sciences "Strategy AV21 - Efficient Energy Transformation and Storage" and by "Open Science" of the Czech Academy of Sciences 6.173 "Inversion problem of damped dynamical systems".

References

1. Daněk, O.: Identification methods in the dynamics of machines. J. Mech. Eng. **48**(5), 297–314 (1997)
2. Kozánek, J.: Resolvent of matrix polynomials, pseudospectra and inversion problems. Selcuk J. Appl. Math. **3**(1), 49–80 (2002)
3. Gohberg, I., Lancaster, P., Rodman, L.: Matrix Polynomials. Academic Press, New York (1982)
4. Daněk, O., Kozánek, J.: Mathematical models of dynamic systems with general structure. J. Mech. Eng. **49**(2), 81–96 (1998)
5. He, J., Fu, Z.-F.: Modal Analysis. Linacre House, Jordan Hill, Oxford (2001)
6. Kozánek, J., Zapoměl, J.: Parametric identification in mechanical engineering. In: Proceedings Dynamics of Machines and Mechanical Systems with Interactions, DYMAMESI 2017, Inter. Colloquium, Cracow, pp. 27–34 (2017)
7. Fillod, R., et al.: Global method of modal identification. In: Proceedings of the 3rd International Modal Analysis Conference, Orlando, Florida, pp. 1145–1151 (1985)
8. Kozánek, J.: The evaluation of the frequency transfer function from experimental data. J. Mech. Eng. **33**(3), 281–289 (1982)

9. Kennedy, C.C., Pancu, C.D.P.: Use of vectors in vibration measurement and analysis. J. Aeronaut. Sci. **14**(11), 603–625 (1947)
10. Awrejcewicz, J., Kudra, G., Wasilewski, G.: Experimental and numerical investigation of chaotic regious in the triple physical pendulam, J. Comput. Nonl. Dyn. **50**(4), 755–766 (2007)
11. Zhang, Q., Lallement, G.: Relations between left and right hand side eigenvectors in non-self adjoint structures, applications to axi-symmetrical rotors. J. Mech. Syst. Sig. Proces. **2**(1), 97–103 (1989)
12. Awrejcewicz, J., Supet, B., Lamarqwe, C-H, Kudra, G., Wasilewski, G., Olejnik, P.: Numerical and experimental study of regular and chaotic motion of triple physical pendulum. Int. J. Bifurcat. Chaos **18**(10), 2883–2915 (2008)

Algorithm for Damping Control in Vehicle Suspension Equipped with Magneto-Rheological Dampers

Michal Makowski

Abstract This paper is devoted to developing the control algorithms of semi-active systems of vehicle suspensions. In order to accomplish the goal, a vehicle was equipped with controlled magneto-rheological (MR) dampers. The model of a vehicle with the controlled suspension was developed. It was assumed that controlling the force in the suspension will be based on two criteria: ride comfort and safety. On the basis of the adopted evaluation criteria, the algorithm for controlling the damping force of vehicle vibrations. The mathematical vehicle model and the control algorithm helped develop a simulation programme. The coefficients adopted in the model were determined empirically. The numerical study of the vehicle model with the controlled suspension was conducted in the Matlab/Simulink programme. As a result of the performed work, the control algorithm was developed, taking into account two conflicting criteria of the drive comfort and safety. A vehicle with the controlled suspension can be driven in the conditions of maximal comfort and safety. A compromise solution was suggested, where a weight factor of the influence of individual control criteria is introduced. In this paper, some sample results of the numerical tests of a vehicle with the MR dampers are presented.

Keywords Magneto-rheological damper · Control algorithms
Mathematical model · Vehicle · Vibration control · Ride comfort

1 Introduction

The presented subject matter of this work comprises semi-active systems of vibration damping in mechanical systems. Development of active and semi-active systems is closely related to development of electronic control systems. These solutions made possible building mechanical systems in which change in the damping force takes

M. Makowski (✉)
Institute of Vehicles, Warsaw University of Technology,
Narbutta 84 Street, 02-524 Warsaw, Poland
e-mail: michal.makowski@simr.pw.edu.pl

J. Awrejcewicz (ed.), *Dynamical Systems in Theoretical Perspective*,
Springer Proceedings in Mathematics & Statistics 248,
https://doi.org/10.1007/978-3-319-96598-7_19

place within a few milliseconds. These properties contributed to application of the semi-active systems of vibration damping in vehicles, machines, and building constructions [1, 3, 4, 10].

Nowadays, in motor vehicles, electronic systems of driving control are widespread, for example. Operation of the active safety systems is influenced to a great extent by the vertical wheel load and lateral forces occurring in the wheel–road contact [11] or wheel–rail contact [2]. Reducing the body vibrations significantly improves the ride comfort. The solution consists of a system improving the ride comfort. This problem was discussed in works [5, 8], where the control system taking into account the ride comfort was presented (minimising the module of the body vertical accelerations).

In this work, the strategy of the compromise choice of the control parameters for the vehicle suspension has been presented. The developed control algorithm takes into account two criteria: of comfort and safety. In the two-criterion control system, an improvement in comfort while keeping the constant value of driving safety is possible. A mathematical model of the vehicle was developed to enable the investigation. This model takes into account the possibility of the wheels losing contact with the road surface. Magneto-rheological dampers were used in the vehicle suspension. Then, the friction force in the dampers is dependent upon the control parameter, i.e. the current. The range of values of the damper friction forces which are possible to obtain was determined on the basis of the earlier experimental research. The simulation programme in the Matlab/Simulink environment was created based on the mathematical vehicle model and the control algorithm. The numerical research was conducted with various kinematic excitations which reflect different conditions of the vehicle motion. During the tests, it was indicated that improving the ride comfort and safety is possible in the controlled system compared to the system without control. The tests with a double-criterion function were also conducted. Analysis of the results showed that improving comfort is possible while maintaining a high level of safety.

2 Mathematical Model of the Vehicle with Controlled MR Dampers

The suggested vehicle model is shown in Fig. 1. The coordinates of the position-defining characteristic points were adopted. The mechanical system is shown in the gravitational field, and the coordinates define the vehicle in the equilibrium position.

The adopted vehicle model was described in the coordinates:

$$X := \left[z, \Phi_x, \Phi_{y,} x_{01}, x_{02}, x_{03}, x_{04}\right]^T \tag{1}$$

The equation of motion of the mechanical system was shown in the form:

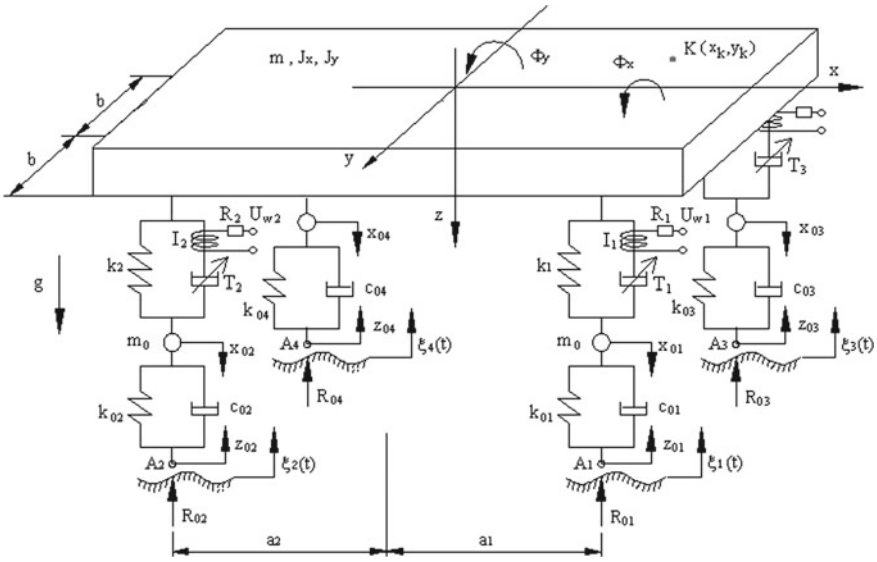

Fig. 1 Vehicle model in generalised coordinates

$$M\ddot{X} + H(S + T) = Q \tag{2}$$

Interaction of the vehicle wheels with the road surface is described in the form of an equation:

$$S_0 + T_0 = R_0 \tag{3}$$

The inertia matrix of the system is described as:

$$M := diag\big(m, J_x, J_y, m_0, m_0, m_0, m_0\big) \tag{4}$$

The gravitational forces vector is shown in the form of:

$$Q := [mg, 0, 0, m_0 g, m_0 g, m_0 g, m_0 g]^T \tag{5}$$

The vectors of the spring forces S and friction forces T, presenting the suspension with the wheels are described in the form:

$$S = [S_1, S_2, S_3, S_4, S_{01}, S_{02}, S_{03}, S_{04}]^T, \quad T = [T_1, T_2, T_3, T_4, T_{01}, T_{02}, T_{03}, T_{04}]^T. \tag{6}$$

Vector H defines the directions of activity of forces S and T

$$H = [H_1, H_2, H_3, H_4, H_{01}, H_{02}, H_{03}, H_{04}]^T \tag{7}$$

where vectors H_i $(i = 1, \ldots, 4)$ define the directions of activity of the forces in the suspension:

$$\begin{aligned} H_1 &= [1, +b, -a_1, -1, 0, 0, 0]^T \quad H_2 = [1, +b, +a_2, 0, -1, 0, 0]^T \\ H_3 &= [1, -b, -a_1, 0, 0, -1, 0]^T \quad H_4 = [1, -b, +a_2, 0, 0, 0, -1]^T \end{aligned}, \tag{8}$$

vectors H_{0i} $(i = 1, \ldots, 4)$ define the directions of forces acting in tyres:

$$\begin{aligned} H_{01} &= [0, 0, 0, 1, 0, 0, 0]^T \quad H_{02} = [0, 0, 0, 0, 1, 0, 0]^T \\ H_{03} &= [0, 0, 0, 0, 0, 1, 0]^T \quad H_{04} = [0, 0, 0, 0, 0, 0, 1]^T \end{aligned}, \tag{9}$$

The spring forces vector in the tyres and the vector of damping forces in the tyres were described in the form:

$$S_0 = [S_{01}, S_{02}, S_{03}, S_{04}]^T, \quad T_0 = [T_{01}, T_{02}, T_{03}, T_{04}]^T. \tag{10}$$

The vector of the response forces, presenting the wheel vertical force on the road surface:

$$R_0 = [R_{01}, R_{02}, R_{03}, R_{04}]^T, \tag{11}$$

The spring and damping forces in the suspension are determined on the basis of the equations:

$$S_i = k_i U_i, \quad T_i = \mathbb{F}(V_i,\ I_i), \quad i = 1, \ldots, 4. \tag{12}$$

where $\mathbb{F}$—is function of $(V_i,\ I_i)$ and described the control damping forces.

However, the spring and damping forces in the wheels are determined on the basis of the equations:

$$S_{0i} = k_0 U_{0i}, \quad T_{0i} = c_0 V_{0i}, \quad i = 1, \ldots, 4. \tag{13}$$

Values of the U_i springs deformations and the deformation velocity of the V_i dampers representing the suspension are shown in the form:

$$U_i = H_i^T X + u_{ist}, \quad V_i = H_i^T \dot{X}, \quad i = 1, \ldots, 4 \tag{14}$$

where u_{ist} is the static deformation of springs caused by the forces of gravity.

Magnitudes of the tyre deformations and the deformation velocities have the form:

$$U_{0i} = H_{0i}^T X + z_{0i} + u_{0ist}, \quad V_{0i} = H_i^T \dot{X} + \dot{z}_{0i}, \quad i = 1, \ldots, 4. \tag{15}$$

where u_{0ist} is a static tyre deformation.

Vector of the position of the wheel points of contact with the road surface is described as:

$$z_0 = [z_{01}, z_{02}, z_{03}, z_{04}]^T, \tag{16}$$

Kinematic excitations of the vehicle vibrations were presented in the form of a vector:

$$\xi = [\xi_1, \xi_2, \xi_3, \xi_4]^T, \tag{17}$$

where ξ_i $(i = 1, \ldots, 4)$—are kinematic excitations and $\xi_1 \neq \xi_2 \neq \xi_3 \neq \xi_4$.

To solve the system of equations describing the vehicle vibrations, the relations were determined describing interaction of the wheels with the road surface, which was shown as:

$$R_{0i} = 0 \quad \text{where } z_{0i} - \xi_i \geq 0 \quad \text{and } R_{0i} \geq 0 \quad \text{where } z_{0i} - \xi_i = 0, \tag{18}$$

where $i = 1, \ldots, 4$.

In the case where the relation $z_{0i} - \xi_i = 0$ takes place, the vertical wheel force on the road surface R_{0i} is determined on the basis of the relation:

$$c_{0i}(\dot{z}_{0i} - \dot{\xi}_i) + F_i = R_{0i}, \quad F_i := c_{0i}\dot{x}_{0i} + c_{0i}\dot{\xi}_i + k_{0i}x_{0i} + k_{0i}z_{0i} + k_{0i}u_{0ist}, \tag{19}$$

Next, the conditions of the cooperation between the wheel and the road surface are verified on the basis of the relation:

$$\dot{z}_{0i} - \dot{\xi}_i \geq 0, \quad R_{0i} \geq 0, \quad R_{0i}(\dot{z}_{0i} - \dot{\xi}_i) = 0, \tag{20}$$

On the basis of the conditions shown above, the value of the force R_{0i} and velocity $\dot{z}_{0i}$ can be unequivocally determined:

$$R_{0i} = \begin{cases} 0 & when\ F_i < 0 \\ F_i & when\ F_i \geq 0 \end{cases} \quad when\ z_{0i} - \xi_i = 0, \tag{21}$$

The presented task serves the purpose of determining the conditions of the interaction between the wheel and the road surface, and it is repeated for every wheel. In the discussed case, the task is repeated four times. The abovementioned relations allow for simultaneous determination of values of the forces of the tyre response to the road surface in cases when the response force is greater than zero and equal to zero.

The equations of motion of the mechanical system describe the vibrating motion of the vehicle body and suspension, with the wheel masses taken into consideration. The reaction of the wheels to the road surface was described on the basis of relations

illustrating the interactions of the ith vehicle wheel. On the basis of the derived equations of motion, it is possible to determine the vehicle body accelerations.

The vehicle was equipped with controlled MR dampers so as to control the friction force in the suspension. The equations describing phenomena taking place in the electric system were used to illustrate the phenomena occurring in the magneto-rheological damper. Change in the current supplying the coil influences the friction force in the mechanical system. These relations were determined on the basis of the experimental investigations.

Supplying the MR dampers takes place with the help of the electronic system. An assumption was made that the signal generator does not introduce the decelerations. Then, the MR damper coil is supplied with the control voltage value determined on the basis of the control algorithm.

The model of the electric system is presented by the currents supplying the coils in MR dampers, where the current vector is shown as:

$$I = [I_1, I_2, I_3, I_4], \tag{22}$$

The equation of an electrical system assumes the form:

$$L\dot{I} + RI = U_w, \tag{23}$$

It was assumed that the electric parameters of the coils are the same and have inductiveness L, and resistance R. The vector of voltages supplying the coil circuit is described as:

$$U_w = [U_{w1}, U_{w2}, U_{w3}, U_{w4}], \tag{24}$$

The value of the controlling voltage is generated on the basis of the displacement signals in the mechanical system. Then, the value of the controlling voltage for the i-th damper assumes the form:

$$U_{wi} = R\mathbb{F}^{-1}(H_i^T \dot{X}, T_{wi}), \quad i = 1, \ldots, 4. \tag{25}$$

However, the value of the friction forces is determined on the basis of the algorithm:

$$T_w = \mathcal{A}(H^T X, H^T \dot{X}), \tag{26}$$

where $\mathcal{A}$ is an operator determining the vector of the friction forces on the basis of the adopted control criterion.

Then, the vector of the friction forces takes the form:

$$T_w = [T_{w1}, T_{w2}, T_{w3}, T_{w4}]. \tag{27}$$

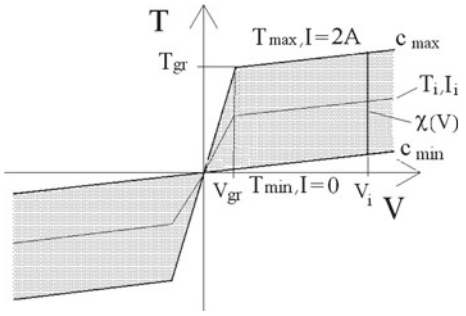

Fig. 2 MR damper characteristics

The relation between the control voltage and the friction force in the MR damper was schematically illustrated in Fig. 2. The characteristics was developed on the basis of experimental research presented in [7]. The presented characteristics was generated based on the Grzesikiewicz model [6]. In this figure, the dependence of the friction forces T_w on the current supplying the windings of the coils of the MR damper was shown, at the present velocity of the damper deformation.

The value of the friction forces determined on the basis of the control algorithm. The force is limited by the obtainable currents supplying the damper coil. The limit values of the currents I_{min} and I_{max} determine the limit values of the damper friction forces T_{wmin} and T_{wmax}.

The mathematical vehicle model with the controlled magneto-rheological dampers consists of the equations describing the operation of the mechanical and electric systems. In the vehicle mechanical system, there are described: the motion of the vehicle body, displacements of the suspension, and the contact of the wheels with the road surface.

3 Algorithm for Determination of Forces in MR Dampers

Controlling the magneto-rheological dampers takes place by means of the developed algorithm taking into account the assumed criterion. It was assumed that the friction force will be determined based on two criteria: drive comfort and safety.

In the control system, under the criterion of comfort, the module of vertical accelerations is minimised of the selected point on the vehicle body. This point was marked with letter K, and is shown in Fig. 1. The friction forces in the dampers are selected so that the vertical acceleration module is minimal at K point.

To evaluate the system's control under the comfort criterion, the ISO 2631 standard was used. The lined amplitude spectrum of the acceleration signal defined by the Discrete Fourier Transform is evaluated here. The standard shows three levels of vibration effect on humans: the lowest acceptable values of acceleration regard the

comfort, higher values are related to nuisance, and the highest values determine the level of harmfulness.

In the control algorithm, an indicator was used, i.e. the acceleration module at a selected point on the vehicle body:

$$\mathcal{K}(T) = \left|a_0 + D^T T\right|. \tag{28}$$

The value of acceleration in the chosen K point, located on the body (Fig. 1) is determined from the relation:

$$a_K = G^T \ddot{X}, \tag{29}$$

where vector $G = [1, x_k, y_k, 0, 0, 0, 0]^T$ defines the vector characterising the location of point K.

Relations (29) can be shown in the form:

$$a_K = -G^T M^{-1} H(S + T), \tag{30}$$

where forces in the spring elements are measured from the position of equilibrium.

The relation describing acceleration at the point K was transformed into:

$$a_K = -G^T M^{-1} H(S + T), \tag{31}$$

where the following was denoted:

$$D^T := -G^T M^{-1} H \in R^4 \tag{32}$$

$$a_0 := D^T S \in R^1 \tag{33}$$

The friction forces in the system are selected based on the comfort criterion so that the value of the vertical accelerations module at the point K could be at a minimum.

Next, to control the system, the criterion of the vehicle ride safety was adopted, where the ratio was represented by the variability of the wheel vertical forces on the road surface (change in the dynamic loads in the suspension). Change in the vertical forces is caused by the kinematic excitations and vehicle vibrations. Evaluation of the control is conducted on the basis of the minimalization of the difference in the wheel vertical forces acting on the road surface. The ratio of the drive safety was adopted, which is constituted by the mean value of the integral of the difference in the vertical forces in relation to the vehicle static load.

The form of the criterion function relative to the safety criterion was adopted in the form:

$$W = \frac{1}{Q_{st}} \sqrt{\sum_{i=1}^{N} (\Delta S_i + T_i - F_{wi})^2} \tag{34}$$

where: Q_{st}—is the static load, ΔS_i—is the spring force change, T_i—is the friction force in magneto-rheological device, N—number of wheels, F_{wi}—is the force of inertia of a vehicle wheel.

The index W defined above can be employed to quantify the efficacy of minimizing variations of the wheel vertical forces (forces in the suspension) of a vehicle. W takes into account the value of the sum of changes of spring forces ΔS_i, but not the entire spring force which is equal:

$$\Delta S_i = k_i H_i^T X \tag{35}$$

Force of inertia of a vehicle is described:

$$F_{wi} = m_{0i} \ddot{x}_{0i} \tag{36}$$

Determining the optimum friction forces requires solving optimisation problems. In the following considerations, the criterion functions will be addressed as functional. In further discussion criterion functions are addressed as functionals.

In the first optimisation task, the friction force vector T_K is determined, for which the value of the first functional $\mathcal{K}$ reaches the minimum. It should be noted that the $\mathcal{K}$ functional is not strictly convex. It means that there exists a set of arguments, for which the $\mathcal{K}$ functional reaches the minimum. In the considered case, this set has a form of a linear variety (hyperplane).

In the considered problem, the limitations of the friction forces occur, resulting from the characteristics shown in Fig. 2. An illustration can be the situation in which the damper is stretched with the velocity V, then the set of permissible values of the friction force has the form of a section $\chi(V)$ marked in the plot of the characteristics. In the task discussed here, a set of permissible friction forces is as follows:

$$\Omega(V) := \left\{T \in R^4 : T_i \in \chi(V_i)\right\} = \left\{T_i \in R^4 : T_{min}(V_i) \leq T_i \leq T_{max}(V_i)\right\} \tag{37}$$

where: V_i—stretching velocity of the ith—damper, $i = 1, \ldots, 4$, T_{min}, T_{max}—functions describing the limit values of the friction force depending on the stretching velocity.

The description of the first optimisation task is shown as follows:

$$T_K \in Argmin_{T \in \Omega(V)} \mathcal{K}(T). \tag{38}$$

where $Arg\,min$ is an operator which determines the set of arguments the $\mathcal{K}$ functional in the set Ω. A detailed description of the solution of the optimization task was presented in the paper [5].

The presented task consists in determining the vector of the friction forces in the damper, that is comprised in the set determined from the comfort criterion. On the basis of the solution to the optimisation task, the vector of the friction forces is determined in the form:

$$T_K = [T_{K1}, T_{K2}, T_{K3}, T_{K4}] \tag{39}$$

The second task includes the minimalisation of the functional $\mathcal{N}$ on the set Ω this task is described with the safety criterion taken into consideration. The functional is strictly convex and was described with the relation in the form:

$$T_N \in \underset{T \in \Omega(V)}{arg\,min}\, \mathcal{N}(T). \tag{40}$$

in this case $arg\,min$ is an operator, which determines the only argument minimising the functional $\mathcal{N}$. On the basis of the task solution, the friction force vector is determined in the form:

$$T_N = [T_{N1}, T_{N2}, T_{N3}, T_{N4}] \tag{41}$$

On the basis of the vectors of the friction forces obtained from the optimisation tasks, an optimisation task is determined, which is a double-criterion task with an influence coefficient and determined by the formula:

$$T_w = \alpha T_K + (1 - \alpha) T_N. \tag{42}$$

where α is an influence coefficient $0 \leq \alpha \leq 1$.

The solution to the double-criterion optimisation task described above determines the value of the $\mathcal{A}$ operator described by Eq. (26).

4 Simulation Research of the Vehicle with Controlled Dampers

The simulation research of the vehicle with the controlled MR dampers was carried out on the basis of the described mathematical model of the vehicle, and on the basis of the algorithm for determining the friction forces. To conduct the tests, the simulation programme in the Matlab/Simulink environment was developed. The numerical tests were performed with the assumption that the vehicle model is symmetrical relative to the x- and y- axes, and the centre of mass is located in the geometric centre of the system. The vehicle body is represented by the object with the parameters in Table 1.

Table 1 The parameters values of vehicle body

Parameter	m	J_x	J_y	$k_{1,\ldots,4}$	$a_{1,2}$	b	x_k	y_k
Unit	(kg)	(kg m^2)	(kg m^2)	(N/m)	(m)	(m)	(m)	(m)
Value	2400	1536	6144	47,500	1.6	0.8	0.7	0.3

Table 2 The parameters values of suspension and MR damper with electric circuits supplying

Parameter	$m_{01,..,04}$	$k_{01,\ldots,04}$	$c_{01,\ldots,04}$	c_{min}	c_{max}
Unit	(kg)	(N/m)	(Ns/m)	(Ns/m)	(Ns/m)
Value	20	47,500	240	750	80,000
Parameter	$_{gr}$	V_{gr}	R	L	
Unit	(N)	(m/s)	(Ω)	(mH)	
Value	800	0.01	2	6	

The simulation research with controlling the damping force was performed based on the characteristics shown in Fig. 2, where the set of permissible solutions is determined by the limit values of the friction forces T_{min} and T_{max}. The suspension and MR damper with electric circuits supplying vehicle body is represented by the parameters in Table 2.

In order to compare the controlled system, the tests were conducted of the system with the constant damping coefficient (with no control). Due to the limited volume of this paper, a simple Newton's model of friction was adopted for comparative research. The subject literature offers insight into other friction models, e.g. the Maxwell's, Kelvin's, or the fractional model [9, 12]. The value of the damping coefficient was assumed at $c_1, \ldots, c_4 = 4500\,\text{Ns/m}$ this value was determined on the basis of the dimensionless damping ratio $\gamma = 0.3$.

The friction force in the system with no control is determined on the basis of the relation:

$$T_i = c_i V_i, i = 1, \ldots, 4. \tag{43}$$

The simulation investigations were conducted under kinematic excitation ξ defined by the harmonic function with amplitude $A = 0.02\,\text{m}$ and frequency of 1.5 Hz. This excitation corresponds to the ride on the rough road with the velocity $V_0 = 60\,\text{km/h}$.

The effectiveness of the control algorithm is measured by the index value of W_G which can be calculated by the following formula:

$$W_G = \frac{1}{Q_{st} N} \int_0^t \sqrt{\sum_{i=1}^{N} (\Delta S_i + T_i - F_{wi})^2} \tag{44}$$

where: W—is the value of index W_G in time step described by sample, N—is the total number of time step samples.

Figure 3 shows the curve of the acceleration module, which is a result of the simulation research. The accelerations were determined at point K located on the vehicle body. Two curves are presented here: with control and with the comfort criterion taken into account (alpha = 1), and without control. In the controlled system, reduction of the module of vertical accelerations of the selected point K was obtained.

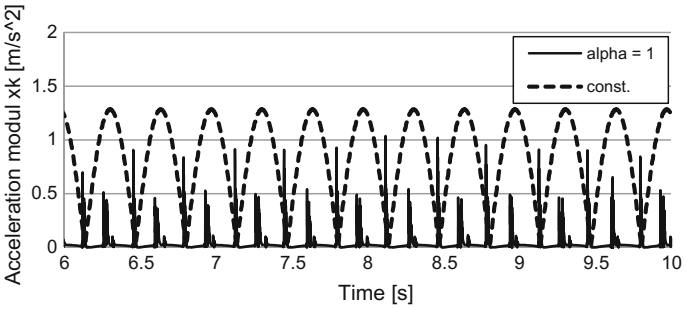

Fig. 3 Acceleration module at the point K under harmonic excitation, with control, given the comfort criterion (alpha = 1), and with no control (const.)

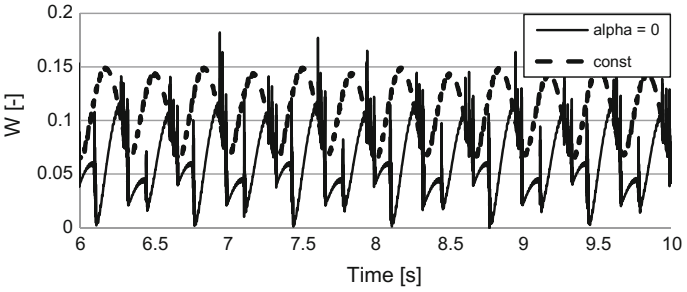

Fig. 4 Curve of the vertical force change ratio under harmonic excitation, with control, given the criterion of safety (alpha = 0), and with no control (const.)

The evaluation of the acceleration curves was performed on the basis of the ISO-2631 standard. The exposure time was extended in the conditions of comfort, from 6 min in the system with no control, to the value above 9 h in the system with the controlled MR dampers.

The vehicle numerical research was conducted taking into account the criterion of safety. Figure 4 shows the curve of the vertical force change ratio under harmonic excitation. Two curves are shown: with control under the criterion of safety (alpha = 0), and the system with the constant damping (const). On the basis of the analysis, the dynamic load ratios W_G were determined: with no control 1.08×10^{-1}, and with control 6.61×10^{-2}. In the system with control, there was the improvement obtained in the ratio by 38.5%.

5 Conclusion

The suggested control algorithm enables combining two opposing criteria for controlling the vehicle suspension: minimising the acceleration module (comfort) and minimising the dynamic loads (safety).

Using the MR damper control with the comfort criterion taken into account allowed for minimising the acceleration module relative to the system without control. On the basis of the analysis of the tests results, a significant extension of exposure time was observed in the system with the friction force control. The analysis of test results conducted with the safety criterion taken into consideration indicates the decrease in vertical force changes under individual vehicle wheels.

Acknowledgements This work was supported by the Polish National Center for Research and Development allocated on the basis of the decision number project PBS3/B6/34/2015.

References

1. Bajkowski, J., Jasiński, M., Mączak, J., Radkowski, S., Zalewski, R.: The active magnetorheological support as an element of damping of vibrations transferred from the ground to large-scale structure supports. Key Eng. Mater. **518**, 350–357 (2012)
2. Bogacz, R., Czyczuła, W., Konowrocki, R.: Effect of periodicity of railway track and wheel–rail interaction on wheelset–track dynamics. Arch. Appl. Mech. **85**(9), 1321–1330 (2014)
3. Holnicki-Szulc, J., Pawłowski, P., Mikułowski, M., Graczykowski, C.: Adaptive impact absorption and applications to landing devices. Adv. Sci. Technol. **56**, 609–613 (2008)
4. Konowrocki, R., Pręgowska, A., Szolc, T.: Experimental and numerical investigations for the controlled rotary damper dynamically interacting with the electromechanical rotating system. Solid State Phenom. **240**, 198–205 (2016)
5. Makowski, M.: Investigation of control of magnetorheological damper influence in car suspension on comfort. Ph.D. thesis, Warsaw University of Technology (2009)
6. Makowski, M., Knap, L., Grzesikiewicz, W., Pokorski, J.: Steuernmöglichekeiten eines schwinungssystems mit magnetorheologischen dämpfer (MR). Proc. Inst. Veh. **4**(63), 73–80 (2006)
7. Makowski, M., Knap, L.: Reduction of wheel force variations with magneto-rheological devices. J. Vib. Control **20**, 1552–1564 (2014)
8. Makowski, M., Zalewski, R.: Vibration analysis for vehicle with vacuum packed particles suspension. J. Theor. Appl. Mech. **53**(1), 109–117 (2015)
9. Olejnik, P., Awrejcewicz, J., Fečkan, M.: Modeling, analysis and control of dynamical system with friction and impact. Word Sci. Nonlinear Sci. Ser. A **92** (2018)
10. Sapiński, B.: Theoretical analysis of magnetorheological damper characteristics in squeeze mode. Acta Mech. et Automatica **9**(2), 89–92 (2015)
11. Sar, H., Reński, A., Pokorski, J.: Investigation of the tyre characteristics under non-steady-state conditions on the basis of road tests. Proc. Inst. Mech. Eng. Part D: J. Automobile Eng., 1–13 (2016). https://doi.org/10.1177/0954407016629517
12. Yang, X., Chen, W., Xiao, R., Ling, L.: A fractional model for time-variant non-Newtonian flow. Thermal Sci. **21**(1A), 61–68 (2017). https://doi.org/10.2298/tsci160426245y

Shadowing, Entropy and Minimal Sets

Piotr Oprocha

Abstract In this review paper we describe some consequences of the shadowing property for global and local aspects of dynamics. We will put additional emphasis on approximation of invariant measures by ergodic measures with additional properties of their supports (minimality, positive entropy, mixing).

Keywords Shadowing · Entropy · Transitive · Mixing · Minimal · Odometer Invariant measure · Poulsen simplex

1 Introduction

Theory of shadowing (or tracing) of approximate trajectories by exact trajectories is an important part of modern theory of dynamical systems. Beginnings of the notion of pseudo-trajectory, which is fundamental for our considerations, can be derived from old papers of Birkhoff [2].

Suppose that we are given a dynamical system (X, T), that is a compact metric space (X, d) together with a continuous map $T: X \to X$. One of the classical objects studied in dynamics are *recurrent points*, that is points $x \in X$ such that for any open neighborhood $U \ni x$ there is an integer $n > 0$ such that $T^n(x) \in U$. A natural generalization of these are *nonwandering* points, i.e. points $x \in X$ such that there is a sequence $(x_k)_{k\in\mathbb{N}} \subset X$ and an increasing sequence of integers $(n_k)_{k\in\mathbb{N}}$ such that $\lim_{k\to\infty} x_k = x$ and $\lim_{k\to\infty} T^{n_k}(x_k) = x$. Generalizing the above approximation property even further we come to the definition of chain-recurrent point. Given $\delta > 0$ we say that a finite sequence $(x_0, \ldots, x_n)$ is a δ-*pseudo orbit* from x to y if $x_0 = x$,

P. Oprocha (✉)
Faculty of Applied Mathematics, AGH University of Science and Technology,
al. Mickiewicza 30, 30-059 Kraków, Poland
e-mail: oprocha@agh.edu.pl

P. Oprocha
National Supercomputing Centre IT4Innovations,
Division of the University of Ostrava, Institute for Research and Applications
of Fuzzy Modeling, 30. dubna 22, 70103 Ostrava, Czech Republic

J. Awrejcewicz (ed.), *Dynamical Systems in Theoretical Perspective*,
Springer Proceedings in Mathematics & Statistics 248,
https://doi.org/10.1007/978-3-319-96598-7_20

$x_n = y$ and $d(T(x_k), x_{k+1}) < \delta$ for $k = 0, \ldots, n-1$. A point x is *chain-recurrent* if for every $\delta > 0$ there is a δ-pseudo orbit from x to x. It is not hard to check that the set of chain-recurrent points (denoted $\mathrm{CR}(T)$) is always closed and T-invariant. The same can be said about the set of non-wandering points $\Omega(T)$. On the other hand, the set of recurrent points $\mathrm{Rec}(T)$ does not have to be closed, so it is worth to consider so-called Birkhoff center $\overline{\mathrm{Rec}(T)}$. It is clear from definitions that

$$\mathrm{Rec}(T) \subset \overline{\mathrm{Rec}(T)} \subset \Omega(T) \subset \mathrm{CR}(T).$$

Unfortunately it may happen in practice that all of the above inclusions are strict. When searching for the property under which $\mathrm{Rec}(T) = \mathrm{CR}(T)$ we arrive in a natural way to the definition of shadowing property. A point x is *ε-tracing* a pseudo-orbit $(x_0, \ldots, x_n)$ if $d(T^i(x), x_i) < \varepsilon$ for $i = 0, \ldots, n$. A dynamical system (X, T) has the *shadowing property* if for any $\varepsilon > 0$ there is $\delta > 0$ such that any finite δ-pseudo orbit $(x_0, \ldots, x_n)$ can be ε-traced. Roughly speaking, if a dynamical system has the shadowing property then orbits calculated with sufficiently small error (e.g. these visualized in numerical simulations) very well approximate real trajectories, and the error of this approximation depends only on magnitude of error in single step but not on the number of steps in simulation.

In this paper we will present selected results on consequences of shadowing property for the dynamics.

2 Preliminaries

In this section we are going to recall a few basic concepts from topological dynamics. For a more extensive exposition, the reader is referred to a standard textbook, such as [1, 7]. An accessible treatment of dynamical systems with view towards shadowing property can be found in monographs [1, 11–13].

By the *orbit* of a point $x \in X$ we as usual mean the set $O^+(x) = \{T^n(x) : n \geq 0\}$. Point is *periodic* if $T^n(x) = x$ for some $n > 0$ and its *period* is $m = \min\{n : T^n(x) = x\}$. Point of period 1, that is point satisfying $T(x) = x$ is called a *fixed point*.

If it is clear from the context that $M \subset X$ and we are restricted to this smaller set, we write T instead of $T|_M$. In particular, for any closed and T-invariant set M (i.e. $T(M) \subset M$) we write (M, T) instead of $(M, T|_M)$.

2.1 Recurrence, Minimality and Mixing

The definition of recurrence leads us immediately to the following standard global properties. A dynamical system (X, T) is:

– *transitive* when for any two nonempty open sets U, V there is $n > 0$ such that $T^n(U) \cap V \neq \emptyset$;
– *totally transitive* if (X, T^n) is transitive for each $n = 1, 2, \ldots$;
– *weakly mixing* if $(X \times X, T \times T)$ si transitive;
– *mixing* if for any two nonempty open sets U, V there is $N > 0$ such that $T^n(U) \cap V \neq \emptyset$ for every $n > N$.

It is well known that the above ordering is strict, i.e. each property is implied by the next in the list, but there is no converse implication in general (e.g. cyclic permutation of finite set is transitive but not totally transitive).

As an example of a transitive map we may consider $x \mapsto 4x(1-x)$ acting on $[0, 1]$. It is not hard to deduce that this example is transitive but some points are not even recurrent. On the other hand, by Baire category theorem, the set of points whose orbit is dense is residual in X for every transitive dynamical system (X, T).

If orbit of every point is dense in X then we say that (X, T) is *minimal*. Equivalently it means that there are no proper, nonempty, closed and invariant sets $A \subset X$ (*invariant* means $T(A) \subset A$). A subset $M \subset X$ is *minimal* if it is closed, invariant and (M, T) is a minimal dynamical system.

There are many natural examples of minimal systems. Probably the most known is rotation of the unit circle by an irrational angle (also note that rotation is totally transitive, but not weakly mixing). The other less popular, however crucial for our further considerations are so-called *adding machines* or *odometers*. The formal definition is as follows.

Let $\mathbf{s} = (s_n)_{n\in\mathbb{N}}$ be a nondecreasing sequence of positive integers such that s_n divides s_{n+1}. For each $n \geq 1$ define $\pi_n \colon \mathbb{Z}_{s_{n+1}} \to \mathbb{Z}_{s_n}$ by the natural formula $\pi_n(m) = m \pmod{s_n}$. These maps define in a natural way the following inverse limit

$$G_{\mathbf{s}} = \varprojlim_n (\mathbb{Z}_{s_n}, \pi_n) = \left\{ x \in \prod_{i=1}^{\infty} \mathbb{Z}_{s_n} : x_n = \pi_n(x_{n+1}) \right\},$$

where each $\mathbb{Z}_{s_n}$ is given the discrete topology, and on $\prod_{i=1}^{\infty} \mathbb{Z}_{s_n}$ we have the Tychonoff product topology (thus is compact metrizable space).

On $G_{\mathbf{s}}$ we define a natural map $T_{\mathbf{s}} \colon G_{\mathbf{s}} \to G_{\mathbf{s}}$ by $T_{\mathbf{s}}(x)_n = x_n + 1 \pmod{s_n}$. It is not hard to see that $G_{\mathbf{s}}$ is closed and $T_{\mathbf{s}}$ is a homeomorphism, therefore $(G_{\mathbf{s}}, T_{\mathbf{s}})$ is a dynamical system. Note that each coordinate in this inverse limit is periodic under action of $T_{\mathbf{s}}$ which easily shows that each odometer is a minimal dynamical system. It is also not hard to see that odometers (when not reduced to a single point) are transitive but not totally transitive. Note that if the sequence $\mathbf{s}$ is bounded, then constructed system is in fact a periodic orbit. Some authors do not call these "degenerate" systems odometers, but we do not put this restriction here.

There are many equivalent ways to define odometers, for example we can also represent them on the space of sequences with dynamics defined by addition by 1 witch "carry". Probably this definition is responsible for the name "adding machine". A detailed exposition on odometers and their properties can be found in [6] (see also [7]).

A dynamical system (X, T) is an *almost 1-1 extension* of an odometer (Y, S) if there exists a surjection $\pi : X \to Y$ such that $\pi \circ T = S \circ \pi$ and the set $\{x \in X : \pi^{-1}(\pi(x)) = \{x\}\}$ is residual in X. Clearly, almost 1-1 extension of an odometer is a minimal system.

2.2 Chain Recurrence

Given two points $x, y \in X$, we write $x \sim y$ if for every $\delta > 0$ there is a δ-pseudo orbit from x to y and from y to x. Observe that the relation $\sim$ is an equivalence relation of the set $\mathrm{CR}(T)$. We call equivalence classes under $\sim$ the *chain-recurrent classes*. The most desirable case is when we have $[x]_\sim = \mathrm{CR}(T)$ for some (thus every) $x \in \mathrm{CR}(T)$. If $X = [x]_\sim$ for some $x \in X$, we say that (X, T) is *chain-transitive*. It is clear that chain-recurrent classes are always closed however it may happen that there are infinitely many of them. To see this, it is enough to consider identity map on the Cantor set (note that this map has the shadowing property as well). We say that (X, T) is *chain mixing* if for every $\delta > 0$ there is N such that for every $x, y \in X$ and any $n \geq N$ there exists a δ-pseudo orbit from x to y consisting exactly of n elements.

It is not hard to verify that $T(\mathrm{CR}(T)) = \mathrm{CR}(T)$. It is much less obvious that $\mathrm{CR}(T) = \mathrm{CR}(T|_{\mathrm{CR}(T)})$, see [15]. By the above we see that $([x]_\sim, T)$ is a dynamical system for any $x \in \mathrm{CR}(T)$. In general not much can be said about dynamics on these classes, so usually additional assumptions on dynamics are made.

The following theorem is among strongest properties that can be proven about chain-recurrent classes (see [14]).

Theorem 2.1 *Suppose that (X, T) is chain transitive. Then one of the following assertions hold:*

1. *there exists $n > 0$ such that (X, T) permutes cyclically n closed and open chain-recurrent classes of (X, T^n) and (X, T^n) is chain mixing on each of these classes;*
2. *(X, T) factors onto odometer.*

2.3 Invariant Measures

Let (X, T) be a dynamical system, let $\mathcal{B} = \mathcal{B}_X$ denote the Borel σ-algebra on X and denote by $M(X)$ the space of all Borel probability measures on X. It is well known that $M(X)$ endowed with weak* topology is convex and compact metrizable space. We say that a measure $\mu \in M(X)$ is *T-invariant* if $\mu(T^{-1}(A)) = \mu(A)$ for every $A \in \mathcal{B}$. The set of all T-invariant measures will be denoted by $M_T(X)$. It is standard fact that $M_T(X)$ is convex and compact subset of $M(X)$, and by Krylov-Bogolyubov theorem it is also nonempty (see [18] for more details).

For $x \in X$ and $n \in \mathbb{N}$, define the nth *empirical measure* of x as

$$\mathcal{E}_n(x) := \frac{1}{n} \sum_{j=0}^{n-1} \delta_{T^j(x)}$$

and observe that any limit points of the sequence $(\mathcal{E}_n(x))_{n\in\mathbb{N}} \subset M(X)$ is T-invariant measure. Since $M(X)$ is compact, always at least one accumulation point exists (in fact, it is the main idea behind the proof of Krylov-Bogolyubov theorem).

An invariant measure $\mu \in M_T(X)$ is *ergodic* if for any $A \in \mathcal{B}$ condition $T^{-1}(A) = A$ implies $\mu(A) = 0$ or $\mu(A) = 1$. The set of all ergodic measures will be denoted by $M_T^e(X)$. A useful property of $M_T^e(X)$ is that it coincides with the set of extreme points of $M_T(X)$. A dynamical system (X, T) is called *uniquely ergodic* if $M_T(X)$ is a singleton, and *strictly ergodic* if (X, T) is minimal and uniquely ergodic. If (X, T) is an odometer or an irrational rotation on the circle, then we may view T as a translation in a compact metrizable group. Therefore these dynamical systems are strictly ergodic, with the Haar measure as the only invariant measure (e.g. see [18, Theorem 6.20]).

A point $x \in X$ is *generic* for measure $\mu \in M_T(X)$ if $\mathcal{E}_n(x) \to \mu$ as $n \to \infty$. If μ is ergodic, then Birkhoff ergodic theorem implies that μ-almost every point is *generic*. It is also clear that if (X, T) is uniquely ergodic, then every point is generic, because $\mathcal{E}_n(x)$ must have the unique measure as its only accumulation point. If μ is not ergodic, then it may be the case that none of the points in X is generic for it.

For each $\mu \in M_T(X)$ there exists a Borel probability measure τ on $M_T^e(X)$ such that (see Remark (2) in page 153 of [18])

$$\mu = \int_{M_T^e(X)} \nu d\tau(\nu). \tag{1}$$

We call (1) the *ergodic decomposition* of μ.

2.4 Entropy

Let (X, T) be a dynamical system. For any two finite covers $\mathcal{U}, \mathcal{V}$ of X we define their refinement $\mathcal{U} \vee \mathcal{V}$ by the formula $\mathcal{U} \vee \mathcal{V} = \{U \cap V \ : \ U \in \mathcal{U}, \ V \in \mathcal{V}, U \cap V \neq \emptyset\}$ and for each $n = 0, 1, 2, \ldots$ we denote $T^{-n}(\mathcal{U}) = \{T^{-n}(U) \ : \ U \in \mathcal{U}\}$.

Fix a finite open cover $\mathcal{U}$ of X. For any $A \subseteq X$ let $r(\mathcal{U}, A)$ denote the minimal cardinality of cover of A consisting of elements of $\mathcal{U}$. The *topological entropy of* $\mathcal{U}$ is the number

$$h_{\text{top}}(f, \mathcal{U}) = \lim_{n\to\infty} \frac{1}{n} \log r\left(\bigvee_{i=0}^{n-1} T^{-i}(\mathcal{U}), X\right) = \inf_{n\in\mathbb{N}} \frac{1}{n} \log r\left(\bigvee_{i=0}^{n-1} T^{-i}(\mathcal{U}), X\right).$$

It is well known that the above limit always exist. Then the *topological entropy of* (X, T) is defined as $h_{\text{top}}(T) = \sup_{\mathcal{U} \in \mathcal{C}_X} h_{\text{top}}(T, \mathcal{U})$, where, $\mathcal{C}_X$ denotes the set of all possible finite open covers of X.

For a finite Borel partition $\mathcal{A} = \{A_1, \ldots, A_n\}$ of X and a measure $\mu \in M_T(X)$ define its entropy $H(\mathcal{A}) = -\sum_{i=1}^{n} \mu(A_i) \log(\mu(A_i))$ and entropy of T with respect to $\mathcal{A}$ is $h_\mu(T, \mathcal{A}) = \lim_{n\to\infty} \frac{1}{n} H(\bigvee_{i=0}^{n-1} T^{-i}(\mathcal{A}))$. Let us emphasize that we always consider partitions without degenerate elements, that is $\mu(A_i) \neq 0$ for every i. Again, by standard argument the above limit always exist. Entropy of an invariant measure μ is defined by $h_\mu(T) = \sup_{\mathcal{A} \in \mathcal{P}_X} h_\mu(T, \mathcal{A})$, where $\mathcal{P}_X$ denotes the set of all finite Borel partitions of X. One of the most useful tools to deal with entropy is variational principle:

$$h_{\text{top}}(X, T) = \sup_{\mu \in M_T(X)} h_\mu(T) = \sup_{\mu \in M_T^e(X)} h_\mu(T). \tag{2}$$

Another important tool, which works when $h_\mu(T) < \infty$ is the ergodic decomposition of the entropy (see [18, Theorem 8.4 (ii)]), which can be stated as

$$h_\mu(T) = \int_{M_T^e(X)} h_\nu(T) d\tau(\nu) \tag{3}$$

where τ is the measure from ergodic decomposition of μ. In fact (2) and (3) are among most effective tools when constructing measures approximating given entropy. An example of their utility can be found in [9].

We refer the reader to the textbooks [5] or [18] for basic properties of entropy.

3 Specification Property

Let (X, T) be a dynamical system with surjective T and consider inverse limit

$$X_T = \varprojlim (X, T) = \left\{ x \in \prod_{i=0}^{\infty} X : T(x_{i+1}) = x_i \text{ for all } i \geq 0 \right\}$$

where $\prod_{i=0}^{\infty} X$ is endowed with Tychonoff product topology (hence we may regard it as a compact metric space). Clearly X_T is compact and additionally we have a natural homeomorphism σ of X_T defined by the formula $\sigma(x)_i = x_{i+1} = T(x_i)$ for very $i \geq 0$. We call (X_T, σ) a *natural extension* of (X, T). Natural extension shares many properties with original dynamical system, such as density of periodic points, value of topological entropy or the shadowing property (see [4, 19]). It also allows us to extend the standard definition of expansive homeomorphism to continuous surjections (many authors call such maps c-expansive, e.g. see [1]). An invertible dynamical system (X, T) is *expansive* if there exists $\lambda > 0$ (an *expansive constant*)

such that for every $x \neq y$ there is $n \in \mathbb{Z}$ such that $d(T^n(x), T^n(y)) \geq \lambda$. We say that (X, T), with T surjective, is *expansive* is (X_T, σ) is expansive. It is clear that for homeomorphism both definitions coincide.

Expansiveness combined with shadowing property has strong consequences for the dynamics. Among most beautiful examples of its utility is the following theorem (see Theorem 3.4.4 in [1]).

Theorem 3.1 (Topological decomposition theorem) *Let (X, T) be a dynamical system with T surjective. Assume additionally that (X, T) is expansive with the shadowing property. Then the following assertions hold.*

1. *(Spectral decomposition due to Smale) There are finitely many closed, T-invariant and pairwise disjoint sets $B_1, \ldots, B_l \subset \Omega(T)$ such that:*
   (a) $\Omega(T) = \sum_{i=1}^{l} B_i$,
   (b) *Each dynamical system (B_i, T) is topologically transitive.*

   Sets B_i are called basic sets.
2. *(Spectral decomposition due to Bowen) For each basic set B there is k and a finite sequence of pairwise disjoint closed sets $C_0, \ldots, C_{k-1}$ such that:*
   (a) $T(C_i) = C_{i+1}$ *for* $i = 0, \ldots, k-1$, *where for technical reasons* $C_k = C_0$,
   (b) $B = \sum_{i=0}^{k-1} C_i$,
   (c) (C_i, T^k) *is topologically mixing for each* i.

   Sets C_i are called elementary sets.

We say that a dynamical system (X, T) satisfies the *periodic specification property* if for any $\varepsilon > 0$ there exists $M > 0$ such that for any $k \geq 2$, any sequence of k points $x_1, x_1, \ldots, x_k \in X$, any non-negative integers $0 \leq a_1 \leq b_1 < a_2 \leq b_2 < \cdots < a_k \leq b_k$ with $a_i - b_{i-1} \geq M$ for each $i = 2, 3, \ldots, k$ and any integer $p \geq M + b_k - a_1$, there exists a periodic point $z \in X$ with $T^p(z) = z$ and $d(T^j(z), T^j(x_i)) < \varepsilon$ for all $a_i \leq j \leq b_i$ and $1 \leq i \leq k$. We say that (X, T) satisfies the *specification property* if the point z from the definition of periodic specification property is not any more requested to be periodic (i.e. we drop the requirement that $T^p(z) = z$).

The following result summarizes relations between various mixing properties in dynamical systems with shadowing property. Dependences between shadowing and stronger forms of mixing were known to specialists in the field for some time (see [3, 5]); in particular relation between mixing and specification property was first provided by Bowen. We present a longer list of such dependences after [8].

Theorem 3.2 *If (X, T) is a dynamical system with the shadowing property, then the following conditions are equivalent:*

1. *(X, T) is totally transitive,*
2. *(X, T) is weakly mixing,*
3. *(X, T) is mixing,*
4. *T is surjective and (X, T) has the specification property,*

If any of the above conditions is satisfied and (X, T) *is expansive then it has the periodic specification property.*

Then as we see, mixing on elementary sets from the decomposition theorem is in fact the specification property (or even periodic specification property). Motivated by works of Bowen, Sigmund in a series of papers [16, 17] presented deep results on relations between specification property and the structure of the set of invariant measures. Among most classical is the following (see [1, 5]).

Theorem 3.3 *If* (X, T) *has the periodic specification property then the set of ergodic measures supported on periodic points is dense in* $M_T(X)$.

Sigmund also proved that the set of ergodic measures, the set of non-atomic measures, the set of measures positive on all open sets, and the set of measures vanishing on all proper closed invariant subsets in residual in the set of all invariant measures (e.g. see [5]). In particular, by Baire theorem there always exists a fully supported ergodic measure in that case. On the other hand, strongly mixing measures form a set of the first category in the space of invariant measures, therefore it cannot be guaranteed that a map with specification property has such a measure.

4 Shadowing Property and Local Dynamics

In is not surprising that the shadowing property can exists without expansiveness. In fact, there are many cases when expansiveness is not very common or even is not admissible (the simplest example is the class of interval maps [1]). On the other hand, shadowing itself is enough to induce interesting consequences for properties of dynamics and the structure of invariant measures. In fact, a slightly weaker version of Theorem 3.3 is still valid for systems with the shadowing property as seen in the following two theorems, which are the main results of [9].

Theorem 4.1 *Suppose that a dynamical system* (X, T) *is transitive and has the shadowing property. Then the collection of ergodic measures which are supported on odometers is dense* $M_T(X)$. *In particular ergodic measures form a residual subset of* $M_T(X)$.

Theorem 4.2 *Suppose that a dynamical system* (X, T) *is transitive and has the shadowing property. Then for every invariant measure* $\mu \in M_T(X)$ *and every* $0 \leq c \leq h_\mu(T)$ *there exists a sequence of ergodic measures* $(\mu_n)_{n=1}^{\infty} \subset M_T(X)$ *supported on almost 1-1 extensions of odometers such that* $\lim_{n\to\infty} \mu_n = \mu$ *and* $\lim_{n\to\infty} h_{\mu_n}(T) = c$.

In [9] the authors constructed an example of a dynamical system with the shadowing property and positive topological entropy which is not weakly mixing (so in particular, transitive dynamical system with the shadowing property is not necessarily totally transitive). In that example, every minimal system has an odometer as a factor.

In [10, Question 3] the following question was stated:

Question: *Does every non-wandering sensitive dynamical system with shadowing property contain an equicontinuous minimal subsystem?*

The answer to this question can be easily derived from result of [9], which is a local version of Theorem 4.1.

Theorem 4.3 *Suppose that* (X, T) *has the shadowing property and* $\mu \in M_T(X)$. *If* $\text{supp}(\mu)$ *is contained in a single chain-recurrent class, then for every* $\varepsilon > 0$ *there is an ergodic measure* ν *supported on an odometer such that* $\rho(\nu, \mu) < \varepsilon$, *where* ρ *is a metric on* $M(X)$ *compatible with weak* topology.*

We have an immediate Corollary from this result (recall that with our notation, periodic orbits are also odometers), providing a positive answer to the above question form [10].

Corollary 4.4 *If* (X, T) *has the shadowing property then it contains an odometer as a minimal subset (recall that according to our definition periodic points are odometers).*

Proof First recall that by Krylov-Bogolyubov theorem there is always an invariant measure, and then by ergodic decomposition theorem always $M_T^e(X) \neq \emptyset$. Therefore, let us fix an ergodic measure μ. If $\text{supp}(\mu)$ is an odometer then we are done, so assume it is not the case. But $(\text{supp}(\mu), T)$ is a transitive dynamical system, hence $\text{supp}(\mu)$ is contained in a chain-recurrent class. Now, we can apply Theorem 4.3 and find ν supported on an odometer.

We finish this section by announcing the following two results (Theorem 4.5 and 4.6). The complete proofs of these statement will be published in a separate paper.

Theorem 4.5 *There exists a topologically mixing dynamical system* (X, T) *with the shadowing property and a unique fixed point p, such that if* $M \subset X$ *is minimal and* (M, T) *is weakly mixing then* $M = \{p\}$.

The above system is not proximal (in fact it cannot be), but any of its (numerous) minimal systems is either degenerate or not weakly mixing. It is worth mentioning at this point another [10, Question 2]:

Question: *Does every weakly mixing dynamical system with shadowing contain a weakly mixing minimal subsystem.*

While our Theorem 4.5 does not answer this question completely, at least it shows that sometimes there are no nontrivial such subsets.

While there is no chance for minimal weakly mixing sets to be dense in the space, still a little weaker version of weak mixing is present in the dynamical system from Theorem 4.5. Price we must pay is that we no more require that the invariant set on which we have weak mixing is minimal (which in fact cannot be required).

Theorem 4.6 *Suppose that a dynamical system* (X, T) *is topologically mixing and has the shadowing property. Then, for every invariant measure* $\mu \in M_T(X)$ *there exists a sequence of ergodic measures* $(\mu_n)_{n=1}^{\infty} \subset M_T^e(X)$ *such that* $\lim_{n\to\infty} \mu_n = \mu$ *and each* $(\mathrm{supp}(\mu_n), T)$ *is weakly mixing.*

It would be nice to know whether measures μ_n in the above sequence can be weakly mixing measures. Unfortunately, we do not know the answer for this question. Surely, by Theorem 4.5 dynamical systems $(\mathrm{supp}(\mu_n), T)$ are not minimal in general.

Acknowledgements Research of P. Oprocha was supported by National Science Centre, Poland (NCN), grant no. 2015/17/B/ST1/01259.

References

1. Aoki, N., Hiraide, K.: Topological Theory of Dynamical Systems. Recent Advances. North-Holland Mathematical Library, vol. 52. North-Holland Publishing Co., Amsterdam (1994)
2. Birkhoff, G.: An extension of Poincares last geometric theorem. Acta Math. **47**, 297–311 (1926)
3. Bowen, R.: Periodic points and measures for axiom A diffeomorphisms. Trans. Am. Math. Soc. **154**, 377397 (1971)
4. Chen, L., Li, S.: Shadowing property for inverse limit spaces. Proc. Am. Math. Soc. **115**, 573–580 (1992)
5. Denker, M., Grillenberger, C., Sigmund, K.: Ergodic Theory on Compact Spaces. Lecture Notes in Mathematics, vol. 527. Springer, Berlin (1976)
6. Downarowicz, T.: Survey of Odometers and Toeplitz Flows. Algebraic and Topological Dynamics. Contemporary Mathematics, vol. 385, pp. 7–37. American Mathematics Society, Providence (2005)
7. Kurka, P.: Topological and Symbolic Dynamics. Cours Spécialisés, 11. Société Mathématique de France, Paris (2003)
8. Kwietniak, D., Oprocha, P.: A note on the average shadowing property for expansive maps. Topol. Appl. **159**, 19–27 (2012)
9. Li, J., Oprocha, P.: Properties of invariant measures in dynamical systems with the shadowing property. Erg. Th. Dynam. Syst. https://doi.org/10.1017/etds.2016.125
10. Moothathu, T.K.S., Oprocha, P.: Shadowing, entropy and minimal subsystems. Monatsh. Math. **172**, 357–378 (2013)
11. Pilyugin, S.: Pilyugin, Shadowing in Dynamical Systems. Lecture Notes in Mathematics, vol. 1706. Springer, Berlin (1999)
12. Pilyugin, S., Sakai, K.: Shadowing and Hyperbolicity. Lecture Notes in Mathematics, vol. 2193. Springer International Publishing, Basel (2017)
13. Palmer, K.: Shadowing in Dynamical Systems. Theory and Applications. Mathematics and its Applications, vol. 501. Kluwer Academic Publishers, Dordrecht (2000)
14. Richeson, D., Wiseman, J.: Chain recurrence rates and topological entropy. Topol. Appl. **156**, 251–261 (2008)
15. Robinson, C.: Stability theorems and hyperbolicity in dynamical systems. Rocky Mountain J. Math. **7**, 425–437 (1977)
16. Sigmund, K.: Generic properties of invariant measures for Axiom A diffeomorphisms. Invent. Math. **11**, 99–109 (1970)
17. Sigmund, K.: On dynamical systems with the specification property. Trans. Am. Math. Soc. **190**, 285–299 (1974)

18. Walters, P.: An Introduction to Ergodic Theory. Graduate Texts in Mathematics, vol. 79. Springer, New York (1982)
19. Ye, X.: Topological entropy of the induced maps of the inverse limits with bonding maps. Topol. Appl. **67**, 113–118 (1995)

Analysis of Vibrations of an Oscillator Using Statistical Series

Ozga Agnieszka

Abstract Solving of a problem for systems subjected to random series of impulses is aimed at determining an approximate distribution of the strength of stochastic impulses forcing vibrations of an oscillator with damping. The difficulties that arose in connection with interpretation of experimental data forced us to search for a mathematical model, where algorithms were applied based on precise solutions. Under appropriate assumptions regarding random variables: the time of action of impulse and their strength, the deviation of the oscillator from its balanced position is a process which, in the limit as time tends to infinity, is stationary and ergodic. At the first stage of the simulation study discussed in this paper, classification of the elements of the structure of statistical series is necessary. The work was inspired by attempts at constructing a measuring device that would control granularity of the medium in a dust pipeline. The device had to signal appearance of big or small particles in excessive quantity in the transported dust.

Keywords Random series of impulses · Stochastic impulses · Random vibrations · Statistical series

1 Introduction

The discussed problem is connected with an attempt at designing and construction of a measuring device controlling homogeneity of granularity of the medium in a dust pipe. To be more precise, the device had to signal appearance of big or small particles in excessive quantity in the transported dust, at a given mean input value in a real technological system.

A mathematical model the inverse identification problem [18] that allows for determining the distribution of strength of impulses forcing the vibrations of the

O. Agnieszka (✉)
Department of Mechanics and Vibroacoustics, Faculty of Mechanical Engineering and Robotics, AGH University of Science and Technology, Al. Mickiewicza 30, 30-059, Kraków, Poland
e-mail: aozga@agh.edu.pl

J. Awrejcewicz (ed.), *Dynamical Systems in Theoretical Perspective*,
Springer Proceedings in Mathematics & Statistics 248,
https://doi.org/10.1007/978-3-319-96598-7_21

system was developed in several stages and was constructed on the basis of linear differential equations [14–17] using the ergodic theory together with the basics of the theory of dynamic systems, measure theory, group theory, probability calculus and the theory of stochastic processes based on it [2–4]. This universal mathematical model will enable us to perform a statistical interpretation of the measurement data. It can be applied both for discrete systems and for continuous ones.

The problem of control of medium homogeneity may be solved by examining the motion of a vibrating system that is influenced by this medium. The motion of such a system is a stochastic process that can be mathematically described in the following way:

$$\varepsilon(t, x) = \sum_{0<t_i<t} G(x, \eta_i, \varepsilon_i, t - t_i) \tag{1}$$

where G is a function dependent on the choice of the vibrating system [10],

x—coordinates of the point of the vibrating system,

η_i is the value of strength of ith impulse, and η_i is a sequence of independent identically random variables with finite expectation,

ε_i is the place where the ith impulse acts,

t_i—ith moment of excitation of the movement.

$$\tau_i = (t_i - t_{i-1}) \tag{2}$$

$\{\tau_i\}_{-\infty}^{+\infty}$ is a sequence of independent identically distributed random variables with exponential distribution.

$$F(\tau) = \begin{cases} 1 - \exp(-\lambda\tau) & \text{if } \tau \geq 0 \\ 0 \qquad\quad \text{if} \quad \tau < 0 \end{cases} \tag{3}$$

The constant λ [6] is the impulse rate.

The intervals between the impulses $\{\tau_i\}_{-\infty}^{+\infty}$ and strength of the impulses $\{\eta_i\}_{-\infty}^{+\infty}$ are independent random variables [11].

The force $f(t)$ exciting vibrations of the system is defined as a series of random impulses with strength η_i occurring at random instants of time t_i:

$$f(t) = \sum_{t_i<t} \eta_i \delta(t - t_i) \tag{4}$$

In the case of the oscillator with damping function G and $f(t)$ do not depend on ε_i,

$$\frac{d^2x}{dt^2} + 2b\frac{dx}{dt} + a^2x = \sum_{t_i<t} \eta_i \delta(t - t_i) \tag{5}$$

with the following initial conditions

$$\mathrm{x}(0)=0 \text{ and } \mathrm{x}'(0)=0 \tag{6}$$

and parameters of the vibrating system the damping coefficient b [1, 7, 8, 13] and the frequency c.

$$c = \sqrt{a^2 - b^2} \tag{7}$$

Using the assumptions listed above it was proved that the motion of a vibrating system for $\mathrm{t} \to \infty$ is ergodic and stationary [5, 9]. The ergodic theorem allows for approximately calculating all jth stochastic moments $m_j(t)$ of location $x(t)$ of the vibrating system.

$$x(t) = \frac{1}{c} \sum_{0<t_i<t} \eta_i \, \exp(-b(t - t_i)) \sin(c(t - t_i)) \tag{8}$$

$$m_j(t) \cong \frac{1}{[t/h]} \sum_{lh<t} x^j(lh) \tag{9}$$

where l is the counter, $h = 10^{-6}$ is the sampling interval and t is a present time.

Statistical moments, in turn, distinctly show the distributions of the random variable from the Eqs. (7) and (8)

$$\sum_{i=1}^{k} \bar{p}_i \left[(m_n m_1 - m_{n+1})\eta_i + \sum_{j=1}^{n} \binom{n}{j} m_{n-j} m_1 \eta_i^{j+1} \frac{C(j+1)}{C(1)c^j} \right] = 0 \tag{10}$$

$$\sum_{i=1}^{k} \bar{p}_i = 1 \tag{11}$$

where k is the number of the sought values of random variable η_k, and for $j>1$ and even j

$$C(j) = \frac{j!}{\prod_{r=0}^{j/2-1} \left((jb/c)^2 + (2r)^2 \right)} \frac{c}{jb} \tag{12}$$

whereas for odd $j>0$,

$$C(j) = \frac{j!}{\prod_{r=0}^{(j-1)/2-1} \left((jb/c)^2 + (2r+1)^2 \right)}. \tag{13}$$

2 Investigations

In this case the mathematical model of an oscillator is understood in accord with the terminology used for defining statistical models as a formalized description of a certain theory or causal situation that are assumed to generate the observed data.

The simulations executed, among others with the use of PLGrid Infrastructure allowed for assessment of difficulty of statistical analysis of the obtained data in the context of the c and b parameters of the oscillating system. This simplified image of reality makes it possible to observe (Table 1) the interdependence between:

1. oscillators with five different values of damping b [12]
2. oscillators with five different vibration frequency c.

The goal of the study presented here is to analyze twenty five one-dimensional vibrating systems for two different distributions of impulses strength η_i (Fig. 1) for the strike impulse rate $\lambda = 50{,}000$ (Table 2).

The object studied is the influence of the smallest values of strength of stochastic impulses η_i in the distribution forcing the vibrations of the oscillator on the differences between the distribution $\eta_i \tilde{p}_i$ executed by the program and the distribution $\eta_i \bar{p}_i$ calculated for model. The algorithm selecting random impulses $\widetilde{p}_i$ is similar to,

Table 1 Parameters and numbers of twenty five one-dimensional vibrating systems

The damping b	The frequency c				
	288,588	240,490	192,392	144,294	96,196
231,000	1	6	11	16	21
92,400	2	7	12	17	22
46,200	3	8	13	18	23
23,100	4	9	14	19	24
4620	5	10	15	20	25

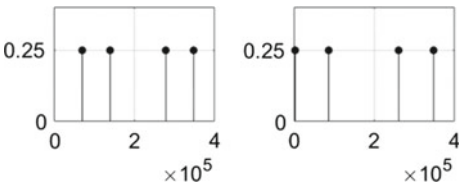

Fig. 1 Probability distribution function. Probabilities and impulses strength used in the distributions Φ_1 and Φ_2

Table 2 Parameters of distributions of the random variables η_i

Distribution/Parameter	Φ_1	Φ_2
Expected value	209,011.75	175,047.38
Standard deviation	110,158.73	136,600.9
Changeability coefficient (%)	52.7	78.0
Asymmetry coefficient	0	0.011

Table 3 Strength η_i of the random impulses used in algorithm

	η_1	η_2	η_3	η_4
Φ_1	η	0.8η	0.4η	0.2η
Φ_2	η	0.75η	0.25η	0.01η

but not identical with, the imposed distributions Φ_1 and Φ_2. The results are saved in the file at every second of the motion, hence $\tilde{p}_i$ assumes different values depending on time.

To achieve this goal we pose two research questions:

1. *What is the influence of the introduced change of the distributions calculated from the model if the vibrations are forced at the same random time interval?*
2. *Will this influence be independent of the parameters of the vibrating system?*

In order to answer the questions posed above, the results of the simulation have to be comparable. It should be remembered that $x(t)$ are realizations of a random variable. In the algorithm used to execute the study, the time of a hit and the impulse are selected at random. In both cases in the imposed distributions Φ_1 and Φ_2 the time remains the same while the strength depends on which of the distributions is analyzed. Accordingly with the algorithm settings, if the impulse of the highest strength η_1 is randomly selected in the first distribution, in the second distribution it will involve the same, strongest impulse of the value $\eta = 348, 353$. The difference becomes significant at the weakest impulse, since the strength in the distribution Φ_1 amounts to 0.2η, while in Φ_2 it is 0.01η. The middle impulses in the distribution Φ_2 have lower strength than those occurring in the distribution Φ_1, and their values are presented in Table 3. The computations were executed in MATLAB software.

3 Classification of the Elements of the Structure of Statistical Series Used In the Analysis of One-Dimensional Dynamic Systems. Simulations

The data in the form of time series including sequences of observation of the examined phenomenon are saved in files as the distribution $\eta_i \widetilde{p}_i$ executed by the program and the distribution $\eta_i \bar{p}_i$ calculated for the model. For each sample the results from each oscillator were saved in a different file. The files are composed of eight vectors including the calculated and executed distributions for four values of η_i forcing the oscillator vibrations. The differences between $\bar{p}_i$ and $\widetilde{p}_i$ define the error of calculations from the model issuing from the selected time section between 1 and 1800 s [9]. For $t \to \infty$ this error would equal zero regardless of the oscillator parameters or the distribution forcing the oscillator vibration, because the deviation of the oscillator from its balanced position is a process which, in the limit as time tends to infinity, is stationary and ergodic. Sample values of $\bar{p}_i - \widetilde{p}_i$ for tone test are presented in panel charts 2–3.

Analyzing the vertical panels we can notice the following properties:

1. For different values of η_i at the same time, different values of error in model application were calculated from the model. The biggest errors were recorded for the weakest impulse in the distribution Φ_2, while the smallest error—for the strongest impulse in the distribution Φ_1 (Figs. 2 and 3).

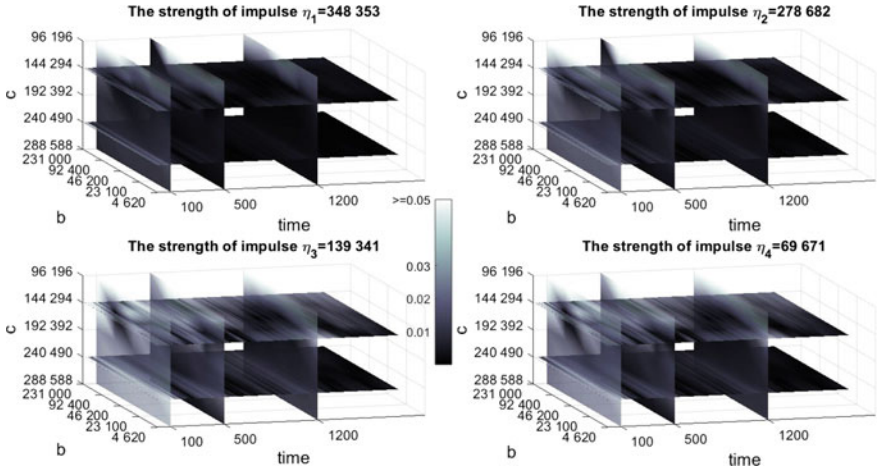

Fig. 2 A panel chart containing a string of observations of formation of the studied phenomenon in subsequent time intervals for twenty-five oscillators with five different values *b* and five different values *c*. The data are for the distribution of Φ_1 impulse forcing

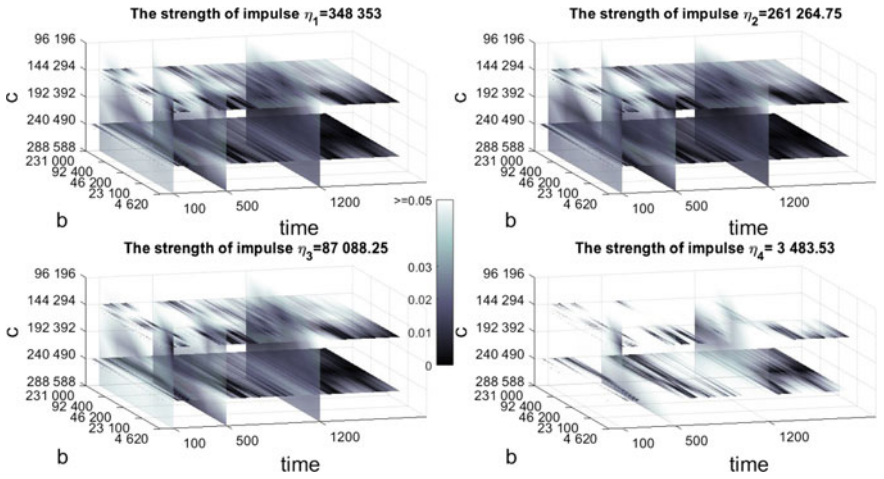

Fig. 3 A panel chart containing a string of observations of formation of the studied phenomenon in subsequent time intervals for twenty five oscillators with five different values *b* and five different values *c*. The data are for the distribution of Φ_2 impulse forcing

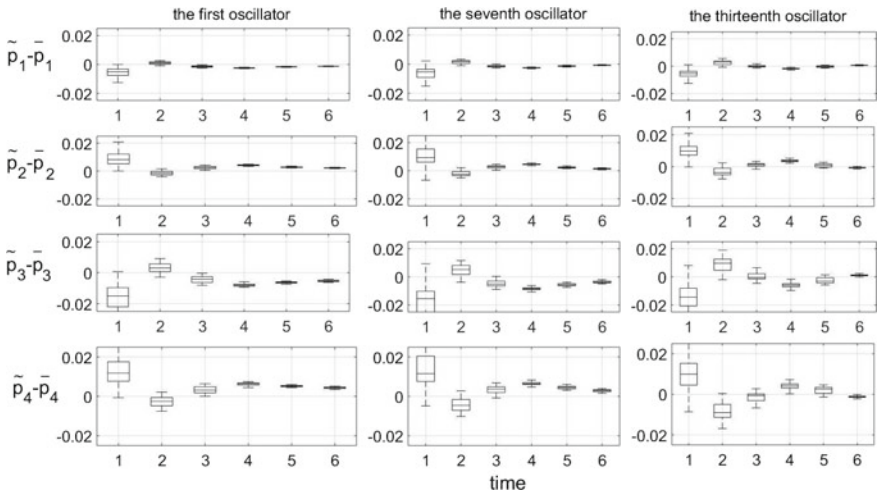

Fig. 4 Errors in the determined distributions of the forced vibrations of an oscillator. Each of the obtained time series for the distribution Φ_1 was divided into six five-minute intervals

Answering the first of the research questions posed in the introduction,

1. For the same oscillators, bigger errors in application of the model were observed for the distributions including impulses with lesser strength, and therefore lesser expected value and greater standard deviation, changeability coefficient and asymmetry coefficient.

The content of the horizontal panels shows that the changes in $\bar{p}_i - \tilde{p}_i$ fluctuate. The changes are visible when each time series is divided into five-minute intervals and the obtained results are compared using boxplot graphs (Figs. 4 and 5). The great differences can be noticed for the first two time intervals from 0 to 600 s, but the greatest one for the twenty-fourth oscillator (Figs. 6 and 7). Analyzing the data obtained for the first, seventh, thirteenth, sixteenth, twentieth and the twenty-fourth oscillator we can give a positive answer to the questions asked at the beginning. We can confirm that a change in the distribution of impulse strength influences significantly the errors in the distributions determined from the model, and the scope of these changes is dependent on the b and c parameters of the vibrating system.

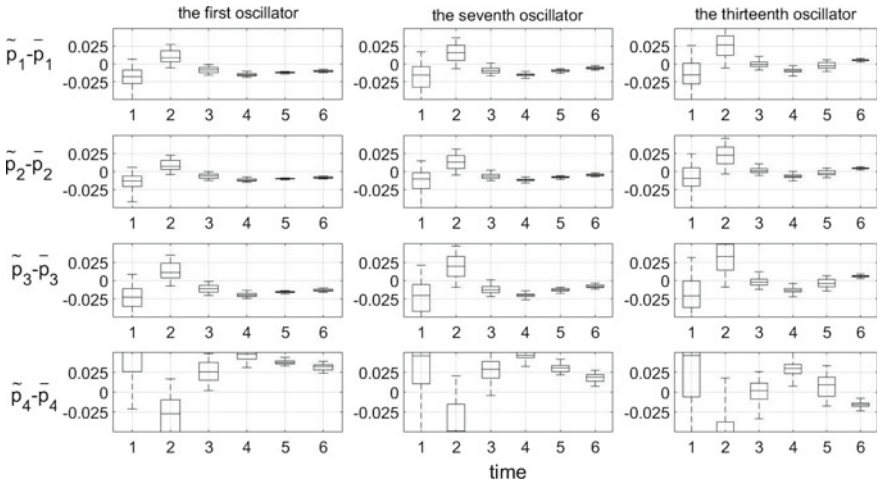

Fig. 5 Errors in the determined distributions of the forced vibrations of an oscillator. Each of the obtained time series for the distribution Φ_1 was divided into six five-minute intervals

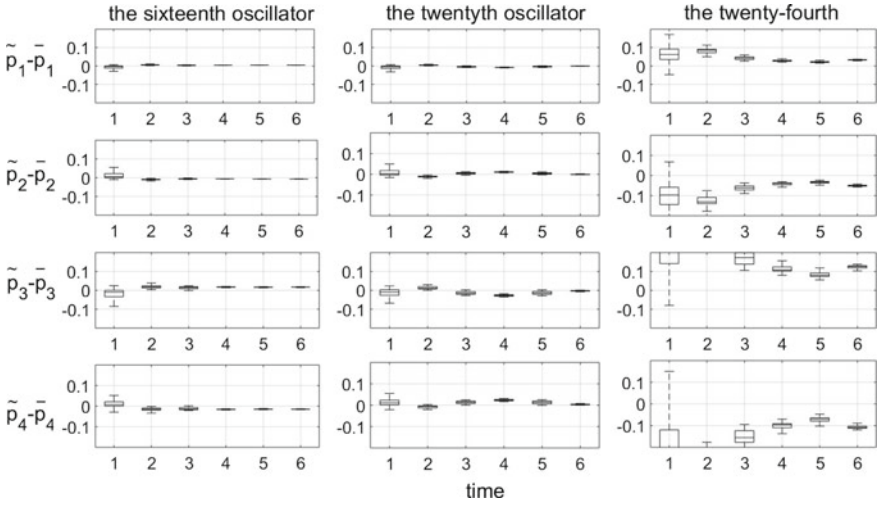

Fig. 6 Errors in the determined distributions of the forced vibrations of an oscillator. Each of the obtained time series for the distribution Φ_1 was divided into six five-minute intervals

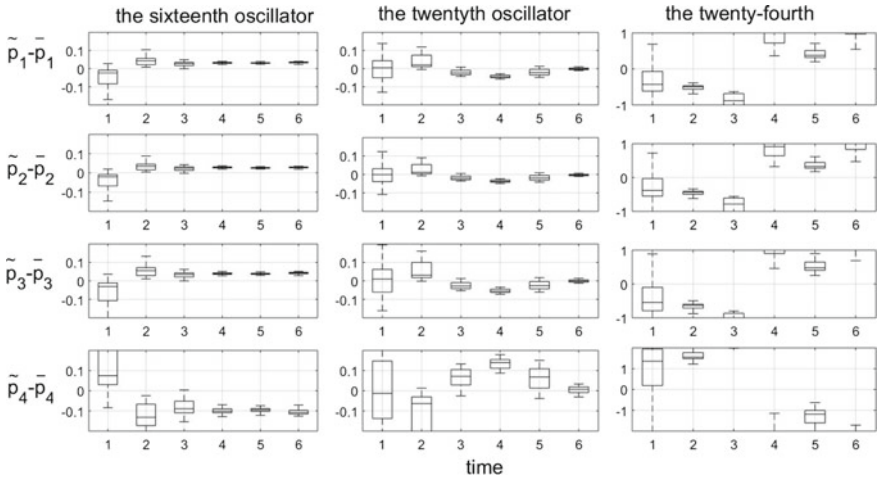

Fig. 7 Errors in the determined distributions of the forced vibrations of an oscillator. Each of the obtained time series for the distribution Φ_2 was divided into six five-minute intervals

4 Conclusions

The applied model of investigations has pointed out the source of some difficulties connected with interpretation of the obtained results. For the same systems whose vibrations are forced by various distributions of impulses we observe increased differences between the distribution generated in simulation and the distribution computed from the model in the situation when the distribution includes impulses of small strength. The decrease of the difference is possible for appropriately selected parameters—the frequency c of vibrations of the oscillator and the damping coefficient b, which will be subjected to extended study.

Acknowledgements The project described in this paper has been executed within the project No. 11.11.130.955.
This research was supported in part by PLGrid Infrastructure.

References

1. Awrejcewicz, J., Kudra, G., Wasilewski, G.: Chaotic zones in triple pendulum dynamics observed experimentally and numerically. Workshop on Advances in Mechanics and Transport Location. Applied Mechanics and Materials, vol. 9 (2008)
2. Jabłoński, M., Ozga, A.: Statistical characteristics of the damped vibrations of a string excited by stochastic forces. Arch. Acoust. **34**(4), 601–612 (2009)
3. Jabłoński, M.: Ozga,: A. Distribution of stochastic impulses acting on an oscillator as a function of its motion. Acta Phys. Pol. A **118**(1), 74–77 (2010)

4. Jabłoński, M., Ozga, A.: Distribution of random pulses acting on a vibrating system as a function of its motion. Agh-Univ Sci & Technol, Krakow (2010)
5. Jabłoński, M., Ozga, A.: Determining the distribution of stochastic impulses acting on a high frequency system through an analysis of its vibrations, Acta Phys. Pol. A (2011)
6. Jabłoński, M., Ozga A.: Determining the distribution of values of stochastic impulses acting on a discrete system in relation to their intensity. Acta Phys. Pol. A (2012)
7. Olejnik, P., Awrejcewicz, J.: Coupled oscillators in identification of nonlinear damping of a real parametric pendulum. Mech. Syst. Signal Process. **98** (2018)
8. Ozga, A.: Determining parameters of an RLC circuit response to a single pulse. Acta Phys. Pol. A (2013). https://doi.org/10.12693/APhysPolA.123.1034
9. Ozga, A.: Distribution of random pulses forcing a damped oscillator determined in a finite time interval. Acta Phys. Pol. A (2014). https://doi.org/10.12693/APhysPolA.125.A-159
10. Ozga, A.: Expanding the mathematical model for recognizing the distribution of values of pulses forcing vibrations of discrete and continuous systems. 7th Forum Acusticum—book of abstracts and programme (2014)
11. Ozga, A.: The effect of pulse amplitudes on quality of determining distribution of pulses forcing vibration of an damped oscillator. Acta Phys. Pol. A (2015). https://doi.org/10.12693/APhysPolA.128.A-67
12. Ozga, A.: Optimization of parameters for a damped oscillator excited by a sequence of random pulses. Arch. Acoust. **39**(4), 645–652 (2014)
13. Pietrusiak, D., Smolnicki, T., Stannco, M.: The influence of superstructure vibrations on operational loads in the undercarriage of bulk material handling machine. Arch. Civil Mech. Eng. **17**(4), 855–862 (2017)
14. Rice, S.: Mathematical analysis of random noise I. Bell. Syst. Tech. J. **23** (1944)
15. Roberts, J.B.: On the harmonic analysis of evolutionary random vibrations. J. Sound Vibr. **2**(3), 336–351 (1965)
16. Roberts, J.B.: The response of linear vibratory systems to random impulses. J. Sound Vibr. **2**(4), 375–390 (1965)
17. Roberts, J.B.: System response to random impulses. J. Sound Vibr. **24**(1), 23–34 (1972)
18. Uhl, T.: The inverse identification problem and its technical application. In: Conference: 8th International Conference on Dynamical Systems Location: Lodz Univ, Lodz. Arch. Appl. Mech. **77**(5), 325–337 (2007)

On Local Aspects of Entropy

Ryszard J. Pawlak and Ewa Korczak-Kubiak

Abstract Although the notion of an entropy has a global character, in many cases the value of an entropy depends on the behaviour of a function near some point. For that reason, in many papers various versions of a notion of "entropy point" are considered. We will examine properties and relations between full entropy points and focal entropy points. Moreover, we will introduce the notion of a full* entropy point and unbalanced point and examine the possibility of graph approximation of some kind of functions by functions having either full* entropy point or unbalanced point.

Keywords Entropy · Discrete dynamical system · $\mathscr{F}$-focal entropy point · Full entropy point · full* entropy point · Unbalanced point · Almost (approximately) continuous function

MSC 2010: 37B40 · 54C70 · 26A18 · 37A05

1 Introduction

The notion of entropy has been introduced with respect to the issues connected with thermodynamics as a result of observations concerning "energy loss" and "lost information" [13, 20]. It led to examining an entropy connected with invariant measures (see e.g. [23]). As the next step in the development of this concept in mathematics, there appeared a notion of a topological entropy (for discrete dynamical systems) which is based on two classical definitions: formulated by Adler et al. [1] using the cover theory for compact spaces and by Bowen [4] and Dinaburg [7] for suitable

R. J. Pawlak (✉) · E. Korczak-Kubiak
Faculty of Mathematics and Computer Science, Łódź University,
Banacha 22, 90-238 Łódź, Poland
e-mail: rpawlak@math.uni.lodz.pl

E. Korczak-Kubiak
e-mail: ekor@math.uni.lodz.pl

J. Awrejcewicz (ed.), *Dynamical Systems in Theoretical Perspective*,
Springer Proceedings in Mathematics & Statistics 248,
https://doi.org/10.1007/978-3-319-96598-7_22

metric spaces. In many papers, the notion of a topological entropy is joined with the chaos theory. Although the notion of an entropy has a global character, in many cases the value of an entropy depends on the behaviour of a function around some point. For that reason, in many papers various versions of a notion of "entropy point" are considered (e.g. [8, 10, 14, 19, 24]). In this paper we will examine properties and relations between full entropy points [24] and focal entropy points [10].

An original impulse for our investigation were the problems posed by prof. P. Walczak during the conference Foliations 2016 (7-th European Congress of Mathematics, Satellite Conference), Będlewo, July 11–17, 2016. Consider selfmaps which are almost continuous or Darboux Baire class one and for such a function f look into the points with the property that f is constant on a "big set" lying near these points and for any function g lying "close enough" to f (in the sense of the metric of uniform convergence) these points are simultaneously focal entropy points and full entropy points of g (according to Theorem 1 it is known that the requirements may be reduced to the demand that x_0 is a focal entropy point). The questions are as follows:

[PW1] What can we say about the family of functions having such kind of points?
[PW2] May the set of such points be big (for example in the sense of measure)?

The last two theorems presented in this paper are connected with the above questions.

2 Preliminaries

Throughout the paper we will use the letters $\mathbb{N}$, $\mathbb{Z}$ and $\mathbb{R}$ to denote the set of all positive integers, the set of all integers and the set of all real numbers, respectively. Moreover, for any $x \in \mathbb{R}$ let us introduce the notation $E(x) := \max\{k \in \mathbb{Z} : k \leq x\}$. The symbol λ will stand for the Lebesgue measure on $\mathbb{R}$ and the symbol D for the class of all Darboux functions.

Let $(a_n)_{n\in\mathbb{N}}, (b_n)_{n\in\mathbb{N}}, (c_n)_{n\in\mathbb{N}}, (d_n)_{n\in\mathbb{N}} \subset [0, 1]$ be sequences such that $\lim_{n\to\infty} a_n = \lim_{n\to\infty} b_n = \lim_{n\to\infty} c_n = \lim_{n\to\infty} d_n = x_0 \in (0, 1)$ and $a_n < b_n < a_{n+1} < x_0 < d_{n+1} < c_n < d_n$, for $n \in \mathbb{N}$. Then the sets $A_l = \bigcup_{n\in\mathbb{N}}(a_n, b_n)$ and $A_p = \bigcup_{n\in\mathbb{N}}(c_n, d_n)$ will be called *left-sided* and *right-sided interval set at the point* x_0, respectively. For $x_0 = 0$ and $x_0 = 1$ we define one-sided interval sets in analogous way. For a Lebesgue measurable set $A \subset \mathbb{R}$ the number $d(A, x_0) = \lim_{h\to 0^+} \frac{\lambda(A\cap[x_0-h,x_0+h])}{2h}$ ($d^+(A, x_0) = \lim_{h\to 0^+} \frac{\lambda(A\cap[x_0,x_0+h])}{h}$, $d^-(A, x_0) = \lim_{h\to 0^+} \frac{\lambda(A\cap[x_0-h,x_0])}{h}$) is called a density (right-sided density, left-sided density) of the set A at the point x_0, respectively.

Throughout the paper, writing X we will always mean a compact metric space (equipped with the metric ρ).

Let $A \subset X$. The symbols $\mathrm{int}(A)$ and $\mathrm{cl}(A)$ will stand for the interior and for the closure of the set A, respectively and by $\#(A)$ we will denote the cardinality of A. We will use the symbol $O(x_0)$ to denote the family of all open neighbourhoods of

$x_0 \in X$. By a closed neighbourhood of a point $x_0 \in X$ we will mean any closed set containing a set from the family $O(x_0)$. We will use the symbol $B(x_0, r)$ ($\overline{B}(x_0, r)$) to denote an open (closed) ball with the centre at $x_0 \in X$ and radius r. The symbol $f \restriction A$ will stand for the restriction of a function $f : X \to Y$ to a set $A \subset X$ and by $\Gamma(f)$ we will denote the graph of f. The set of all fixed points of a function f will be denoted by $\mathrm{Fix}(f)$. We will say that a set A f-covers a set B (denoted by $A \underset{f}{\to} B$) if $B \subset f(A)$.

Based on [6, 9] we adopt the following definition of the entropy. Let $f : X \to X$, $\varepsilon > 0, n \in \mathbb{N}$ and $A \subset X$ be a nonempty compact set. A set $K \subset A$ is (n, ε)-*separated* for f if for each $x, y \in K$, $x \neq y$ there is $0 \leq i < n$ such that $\rho(f^i(x), f^i(y)) > \varepsilon$. A *topological entropy of* $f \restriction A$ is the number

$$h(f \restriction A) = \lim_{\varepsilon \to 0} \limsup_{n \to \infty} \left(\frac{1}{n} \log s_n^A(\varepsilon, f) \right),$$

where

$$s_n^A(\varepsilon, f) = \max\{\#(K) : K \subset A \text{ is } (n, \varepsilon)\text{-separated set for } f\}.$$

If $A = X$ then we simply write *a topological entropy of* f and we denote it by $h(f)$.

The notion of an $\mathscr{F}$-focal entropy point was introduced in [10]. The main idea of this definition was based on tending to express such kind of focusing entropy at a point that would depend mainly on the behaviour of a function in sufficiently small neighbourhoods of that point. We present below a precise definition of this notion.

Throughout the paper the symbol $\mathscr{F}$ will stand for a family of nonempty subsets of X such that each nonempty open set contains some set from the family $\mathscr{F}$. Whenever we consider $X = [0, 1]$ with the natural metric, we assume that $\mathscr{F}$ is the family of nondegenerate closed subintervals of $[0, 1]$.

By $\vartheta_{\mathscr{F}}^Y$ we will denote the family of all finite sequences of sets from $\mathscr{F}$ contained in $Y \subset X$ such that their closures are pairwise disjoint i.e. $F = (A_1, \ldots, A_m) \in \vartheta_{\mathscr{F}}^Y$ iff $A_i \in \mathscr{F}$, $A_i \subset Y$ for any $i \in \{1, \ldots, m\}$ and $\mathrm{cl}(A_i) \cap \mathrm{cl}(A_j) = \emptyset$ for any $i, j \in \{1, \ldots, m\}$ and $i \neq j$. For simplicity of notation, let $\vartheta_{\mathscr{F}}$ stand for $\vartheta_{\mathscr{F}}^X$. Moreover, $\mathscr{F}|Y = \{K \cap Y : K \in \mathscr{F}\}$.

Let $n, m \in \mathbb{N}$, $f : X \to X$ and $F = (F_1, F_2, \ldots, F_{m-1}, F_1)$, where $F_i \in \mathscr{F}$ for $i \in \{1, \ldots, m-1\}$. If $F_i \underset{f^n}{\to} F_{i+1}$ for $i \in \{1, \ldots, m-2\}$ and $F_{m-1} \underset{f^n}{\to} F_1$ then we will denote this sequence F by $[F_1, F_2, \ldots, F_{m-1}, F_1]_{f^n}$.

We shall say that $f \in J(\mathscr{F})$ if for any $n, m \in \mathbb{N}$ and any sequence $[F_1, F_2, \ldots, F_{m-1}, F_1]_{f^n}$ there exists $x_0 \in F_1$ such that $f^{n(m-1)}(x_0) = x_0$ and $f^{n \cdot i}(x_0) \in F_{i+1}$ for $i \in \{1, 2, \ldots, m-1\}$, where $F_m = F_1$.

If $F = (A_1, \ldots, A_m) \in \vartheta_{\mathscr{F}}$ and $f : X \to X$ is a function then for $i, j \in \{1, \ldots, m\}$ put $a_{ij} = 1$ if $A_i \underset{f}{\to} A_j$ and $a_{ij} = 0$ otherwise. The matrix $\mathscr{M}_{F,f} = [a_{ij}]_{i,j=1}^m$ will be called a structural matrix.

A generalized entropy of f with respect to the sequence $F \in \vartheta_{\mathscr{F}}$ is the number

$$H_f(F) = \begin{cases} \log \sigma(\mathscr{M}_{F,f}) & \text{if } \sigma(\mathscr{M}_{F,f}) > 0, \\ 0 & \text{if } \sigma(\mathscr{M}_{F,f}) = 0, \end{cases}$$

where $\sigma(\mathscr{M}_{F,f}) = \limsup_{n\to\infty} \sqrt[n]{\operatorname{tr}(\mathscr{M}^n_{F,f})}$ (cf. [18]).

Let $Y \subset X$ be a nonempty open set. We define the number $H_{\mathscr{F},f}(Y) = \sup\left\{\frac{1}{n} H_{f^n}(F) : F \in \vartheta^Y_{\mathscr{F}} \wedge n \in \mathbb{N}\right\}$.

Next one can consider quantities

$$d(\mathscr{F}, f, Y) = \begin{cases} \frac{H_{\mathscr{F},f}(Y)}{h(f)} & \text{if } h(f) \in (0, \infty), \\ 1 & \text{if } H_{\mathscr{F},f}(Y) = \infty \text{ or } h(f) = 0, \\ 0 & \text{if } H_{\mathscr{F},f}(Y) \in [0, \infty) \text{ and } h(f) = \infty, \end{cases}$$

and $E_{\mathscr{F},f}(x_0) = \inf\{d(\mathscr{F}, f, V) : V \in O(x_0)\}$.

Obviously we have $0 \le E_{\mathscr{F},f}(x_0) \le 1$. We say that $x_0 \in X$ is an *$\mathscr{F}$-focal entropy point of f* if $E_{\mathscr{F},f}(x_0) = 1$. The set of all $\mathscr{F}$-focal entropy points of f will be denoted by $E_{\mathscr{F}}(f)$.

Complexity of the definition of a focal entropy point causes that a natural question arises: what kind of functions have such a point? A partial answer to this question is contained in [10]. We will formulate it in the following way:

Lemma 1 *Let $f : [0, 1] \to [0, 1]$ be a continuous function. Then $E_{\mathscr{F}}(f) \neq \emptyset$.*

In [24], the notion of a full entropy point has been introduced. A point $x_0 \in X$ is called a *full entropy point of a function f* if $h(f \restriction K) = h(f) > 0$ for each closed neighbourhood K of x_0.

Notice that if $h(f) = 0$ then we may consider $\mathscr{F}$-focal entropy points of f (each point of the domain of f is its $\mathscr{F}$-focal entropy point) but we may not consider full entropy points.

The below-presented notions connected with properties of dynamical systems at a point are commonly known (see [2, 3]). Let $f : X \to X$. We say that a point $x_0 \in X$ is a *wandering point of f* if there exists a set $U \in O(x_0)$ such that $U \cap f^i(U) = \emptyset$ for any $i \in \mathbb{N}$. A point which is not a wandering point of f is called *nonwandering point of f*. We say that a point $x_0 \in X$ is a *recurrent point of f* if for any $U \in O(x_0)$ there exists $n \in \mathbb{N}$ such that $f^n(x_0) \in U$. The set of all recurrent points of f will be denoted by $\operatorname{Rc}(f)$. The closure $\operatorname{cl}(\operatorname{Rc}(f))$ of the set of all recurrent points of f will be called a *centre of f*.

In 1959 Stalling distinguished a new class of functions - *almost continuous functions* [21] - which arose in the context of the research connected with the fixed point theory (if X is a Hausdorff space with the fixed point property then each almost continuous function $f : X \to X$ has a fixed point). It may be also joined with some kind of approximation.

Let $f : X \to Y$ and $\mathscr{K}$ be some class of functions from X to Y. We say that a function f is *Γ-approximated by functions from the class $\mathscr{K}$* if for every open set $U \subset X \times Y$ containing the graph of f there exists a function $g \in \mathscr{K}$ such that the graph of g is contained in U.

A function $f : X \to Y$ is *almost continuous* if it is Γ-approximated by continuous functions. The class of all almost continuous functions will be denoted by $\mathscr{A}$.

A function $f : [0, 1] \to [0, 1]$ is turbulent provided there exist closed nondegenerate disjoint intervals $J, K \subset [0, 1]$ such that $J \cup K \subset f(J) \cap f(K)$.

The method of proof presented in [6] or the results contained in [17] allow to formulate the following lemma.

Lemma 2 *If $f : [0, 1] \to [0, 1]$ is turbulent, then $h(f) \geq \log 2$.*

In many considerations connected with real functions of real variables, a special role is played by functions from Baire class one i.e. functions which are pointwise limits of continuous functions (this class is denoted by B_1). However, sometimes it is essential to consider discontinuous functions, but "closer to continuity" than functions from Baire class one. For that reason, there were distinguished the class B_1^* [15] and B_1^{**} [16] (we will only use the class B_1^{**}).

B_1^* is the class of all functions $f : [0, 1] \to \mathbb{R}$ such that for every perfect set P there exists a portion T (i.e. nonempty set of the form $T = P \cap (a, b)$) such that $f \restriction T$ is continuous. A function $f : [0, 1] \to \mathbb{R}$ belongs do the class B_1^{**} if the restriction of f to the set of all discontinuity points of f is a continuous function. Notice that if C denotes the class of all continuous functions then $C \subset B_1^{**} \subset B_1^* \subset B_1$ [16]. Let us consider functions $f_i : [0, 1] \to [0, 1]$ (for $i \in \{0, 1\}$) given by the formulas:

$$f_0(x) = \begin{cases} 0 & \text{for } x \in \{0\} \cup \bigcup_{n=1}^{\infty} (\frac{1}{n+1}, \frac{1}{n}), \\ 1 & \text{for } x \in \{\frac{1}{n} : n = 1, 2, \dots\} \end{cases} \quad \text{and} \quad f_1(x) = \begin{cases} 0 & \text{for } x \in \bigcup_{n=1}^{\infty} (\frac{1}{n+1}, \frac{1}{n}), \\ 1 & \text{for } x \in \{0\} \cup \{\frac{1}{n} : n = 1, 2, \dots\}. \end{cases}$$

Then $f_0 \in B_1^* \setminus B_1^{**}$ and $f_1 \in B_1^{**} \setminus C$.

3 Full* Entropy Points

We will start this section with presenting the connections between $\mathscr{F}$-focal entropy points and full entropy points of a function f. Next we will introduce the notion of a full* entropy point.

Theorem 1 *Let $f : X \to X$ be a function (not necessarily continuous) and $h(f) > 0$. If $x_0 \in X$ is an $\mathscr{F}$-focal entropy point of f then x_0 is a full entropy point of f.*

Proof Let K be an arbitrary closed neighbourhood of the point x_0. We need to show that

$$h(f) = h(f \restriction K). \tag{1}$$

Take $\eta > 0$ such that $\alpha_\eta = h(f) - \eta > 0$.

Obviously, we have $H_{\mathscr{F},f}(\mathrm{Int}(K)) > \alpha_\eta$, which gives that there exists $l \in \mathbb{N}$ and $\mathscr{T} = (A_1, \ldots, A_k) \in \vartheta_{\mathscr{F}}^{\mathrm{Int}(K)}$, where $k > 1$, such that $\frac{1}{l} H_{f^l}(\mathscr{T}) > \alpha_\eta$. Let $\sigma > 0$ denote the minimum of the distances between closures of sets belonging to $\mathscr{T}$. Fix a strictly increasing sequence $\{\mu_n\}$ of positive integers such that $\log \sqrt[\mu_n]{\mathrm{tr}(\mathscr{M}_{\mathscr{T},f^l}^{\mu_n})} > l\,\alpha_\eta$ and set $\mathscr{M}_{\mathscr{T},f^l}^{\mu_n} = [z_{i,j}^{\mu_n}]_{1\le i,j\le k}$. Fix $n_0 \in \mathbb{N}$. We see at once that $\log \mathrm{tr}(\mathscr{M}_{\mathscr{T},f^l}^{\mu_{n_0}}) > \mu_{n_0} l\,\alpha_\eta$ and, consequently, we have $\mathscr{J} = \{m \in \{1, \ldots, k\} : z_{m,m}^{\mu_{n_0}} > 0\} \neq \emptyset$. For each $m \in \mathscr{J}$ there are $z_{m,m}^{\mu_{n_0}}$ different sequences $[A_m, A_{s_1}, \ldots, A_{s_{\mu_{n_0}-1}}, A_m]_{f^l}$, where $s_1, \ldots, s_{\mu_{n_0}-1} \in \{1, \ldots, k\}$. Let $\mathfrak{B}_m^{\mu_{n_0}} = \{B_1^m, \ldots, B_{z_{m,m}^{\mu_{n_0}}}^m\}$ be the set of these sequences. Denote $B_i^m = [A_m, A_{s_1}^i, \ldots, A_{s_{\mu_{n_0}-1}}^i, A_m]_{f^l}$ for $i \in \{1, \ldots, z_{m,m}^{\mu_{n_0}}\}$. Then for any $i \in \{1, \ldots, z_{m,m}^{\mu_{n_0}}\}$ one can find points b_p^i for $p \in \{0, 1, \ldots, \mu_{n_0}\}$ such that $b_0^i, b_{\mu_{n_0}}^i \in A_m$, $b_j^i \in A_{s_{\mu_{n_0}-j}}^i$ for $j \in \{1, \ldots, \mu_{n_0} - 1\}$ and $f^l(b_j^i) = b_{j-1}^i$ for $j \in \{1, \ldots, \mu_{n_0}\}$.

For each $m \in \mathscr{J}$ and $i \in \{1, \ldots, z_{m,m}^{\mu_{n_0}}\}$ we can assign an element $b_{\mu_{n_0}}^i$ to the set $B_i^m \in \mathfrak{B}_m^{\mu_{n_0}}$, and so we create an injection $\Phi_m : \mathfrak{B}_m^{\mu_{n_0}} \to A_m$ ($m \in \mathscr{J}$). Obviously, for any $m \in \mathscr{J}$ we have $\Phi_m(B_i^m) \in A_m$, $(f^l)^j(\Phi_m(B_i^m)) \in A_{s_j}^i$ for each $j \in \{1, \ldots, \mu_{n_0} - 1\}$ and $(f^l)^{\mu_{n_0}}(\Phi_m(B_i^m)) \in A_m$, for $i \in \{1, \ldots, z_{m,m}^{\mu_{n_0}}\}$. Note that

$$\#(\Phi_m(\mathfrak{B}_m^{\mu_{n_0}})) = z_{m,m}^{\mu_{n_0}} \text{ for } m \in \mathscr{J}. \tag{2}$$

Let us denote $\mathfrak{P}_{\mu_{n_0}} = \bigcup_{m\in\mathscr{J}} \Phi_m(\mathfrak{B}_m^{\mu_{n_0}}) \subset \mathrm{Int}(K)$.

Now we prove that

$$\mathfrak{P}_{\mu_{n_0}} \text{ is a } (\mu_{n_0}, \delta)\text{-separated set for } f^l \text{ for each } \delta \in (0, \sigma). \tag{3}$$

Let $x_1, x_2 \in \mathfrak{P}_{\mu_{n_0}}$ and $x_1 \neq x_2$. So, there exist $m_{x_1}, m_{x_2} \in \mathscr{J}$ such that $x_1 \in \Phi_{m_{x_1}}(\mathfrak{B}_{m_{x_1}}^{\mu_{n_0}}) \subset A_{m_{x_1}}$ and $x_2 \in \Phi_{m_{x_2}}(\mathfrak{B}_{m_{x_2}}^{\mu_{n_0}}) \subset A_{m_{x_2}}$. Obviously $\rho(x_1, x_2) \ge \sigma > \delta$, if $m_{x_1} \neq m_{x_2}$. In the opposite situation $m_{x_1} = m_{x_2} = \tau$. So, there exist $i_{x_1}, i_{x_2} \in \{1, \ldots, z_{\tau,\tau}^{\mu_{n_0}}\}$ such that $x_1 = \Phi_\tau(B_{i_{x_1}}^\tau)$ and $x_2 = \Phi_\tau(B_{i_{x_2}}^\tau)$. Obviously, $B_{i_{x_1}}^\tau \neq B_{i_{x_2}}^\tau$. Thus there is $p \in \{1, \ldots, \mu_{n_0} - 1\}$ such that $A_{s_p}^{i_{x_1}} \cap A_{s_p}^{i_{x_2}} = \emptyset$. Consequently, we have $(f^l)^p(x_1) \in A_{s_p}^{i_{x_1}}$ and $(f^l)^p(x_2) \in A_{s_p}^{i_{x_2}}$, so $\rho((f^l)^p(x_1), (f^l)^p(x_2)) \ge \sigma > \delta$. Finally, we obtain $\rho((f^l)^\nu(x_1), (f^l)^\nu(x_2)) > \delta$ for some $\nu \in \{0, \ldots, \mu_{n_0} - 1\}$.

Since $\Phi_{m_1}(\mathfrak{B}_{m_1}^{\mu_{n_0}}) \cap \Phi_{m_2}(\mathfrak{B}_{m_2}^{\mu_{n_0}}) = \emptyset$ for any $m_1, m_2 \in \mathscr{J}$ and $m_1 \neq m_2$, by (2) we obtain $\#(\mathfrak{P}_{\mu_{n_0}}) = z_{1,1}^{\mu_{n_0}} + \cdots + z_{k,k}^{\mu_{n_0}} = \mathrm{tr}(\mathscr{M}_{\mathscr{T},f^l}^{\mu_{n_0}})$, which finishes the proof of (3).

In consequence, we have

$$\log s_{\mu_{n_0}}^{\mathrm{Int}(K)}(\delta, f^l) \ge \log(\#(\mathfrak{P}_{\mu_{n_0}})) = \log(\mathrm{tr}(\mathscr{M}_{\mathscr{T},f^l}^{\mu_{n_0}})) > \mu_{n_0} l\,\alpha_\eta$$

for any $\delta \in (0, \sigma)$.

Since $n_0 \in \mathbb{N}$ was chosen arbitrarily, we obtain $\log s_{\mu_n}^{\mathrm{Int}(K)}(\delta, f^l) > \mu_n l\,\alpha_\eta$ for any $\delta \in (0, \sigma)$ and any $n \in \mathbb{N}$. Consequently,

$$\limsup_{\nu\to\infty}\frac{1}{\nu}\log s_{\nu}^{\mathrm{Int}(K)}(\delta,f^l)\geq\limsup_{n\to\infty}\frac{1}{\mu_n}\log s_{\mu_n}^{\mathrm{Int}(K)}(\delta,f^l)\geq l\,\alpha_\eta$$

for any $\delta\in(0,\sigma)$. Therefore,

$$h(f^l\restriction K)\geq h(f^l\restriction\mathrm{Int}(K))=\lim_{\delta\to0^+}\limsup_{\nu\to\infty}\frac{1}{\nu}\log s_{\nu}^{\mathrm{Int}(K)}(\delta,f^l)\geq l\,\alpha_\eta,$$

so by Proposition 3.6 [6] we have $l\,h(f\restriction K)\geq l\,\alpha_\eta$ which means that $h(f\restriction K)\geq h(f)-\eta$ and it easily leads to our assertion. □

For further considerations, it seems to be interesting to distinguish points which are full entropy points of a function but simultaneously are not $\mathscr{F}$-focal entropy points of this function. Such points will be called *full* entropy points of f*.

One can show that there exists a function with positive entropy which does not have any full* entropy point (in order to avoid repetition of analogous notations, a suitable example will be shown after the proof of Theorem 2). With reference to the definition of almost continuity, it seems to be interesting whether there is a possibility of Γ- approximation of functions belonging to $\mathscr{A}$ by continuous functions with full* entropy points.

Lemma 3 *Let $f:X\to X$, $x_0\in X$. Assume that $y_0\in X$ is a full entropy point of f, $f(x_0)=y_0$ and $y_0\in\mathrm{int}(f(B(x_0,r)))$, for some $r>0$. Then x_0 is a full entropy point of f.*

Proof Obviously $h(f)>0$. Let F be an arbitrary closed neighbourhood of x_0. There exist $r_0>0$ such that $B(x_0,r_0)\subset F$ and $r_1>0$ such that $y_0\in\overline{B}(y_0,r_1)\subset\mathrm{int}(f(B(x_0,r_0)))$. Let $S\subset\overline{B}(y_0,r_1)$ be an (n,ε)-separated set for $f\restriction\overline{B}(y_0,r_1)$ with a maximal possible cardinality $s_n^{\overline{B}(y_0,r_1)}(\varepsilon,f)$. For each $\alpha\in S$ choose $x_\alpha\in f^{-1}(\alpha)\cap B(x_0,r_0)$ and put $S_1=\{x_\alpha:\alpha\in S\}$. One can show that S_1 is an $(n+1,\varepsilon)$-separated set for $f\restriction F$. So, we have $s_{n+1}^F(\varepsilon,f)\geq\#(S_1)=\#(S)=s_n^{\overline{B}(y_0,r_1)}(\varepsilon,f)$. Consequently

$$h(f\restriction F)\geq\lim_{\varepsilon\to0}\limsup_{n\to\infty}\left(\frac{1}{n}\log s_n^{\overline{B}(y_0,r_1)}(\varepsilon,f)\right)=h(f\restriction\overline{B}(y_0,r_1)).\tag{4}$$

Obviously $h(f\restriction\overline{B}(y_0,r_1))=h(f)$. Therefore, using (4) we conclude $h(f\restriction F)\geq h(f)$. Clearly, we have also $h(f\restriction F)\leq h(f)$. □

Theorem 2 *Each almost continuous $f:[0,1]\to[0,1]$ can be Γ-approximated by continuous functions having a full*-entropy point.*

Proof To simplify the notation of the proof, let us accept:

- the symbol $w_{a,b}^n$ to denote a function $w_{a,b}^n:[a,b]\to[a,b]$ fulfilling the following conditions: $(w_{a,b}^n)^{-1}(a)=\{a+\frac{2k(b-a)}{n}:k=0,1,\ldots,E(\frac{n}{2})\}$, $(w_{a,b}^n)^{-1}(b)=\{a+\frac{(2k+1)(b-a)}{n}:k=0,1,\ldots,E(\frac{n-1}{2})\}$, $w_{a,b}^n$ is linear on the intervals $[a+\frac{k(b-a)}{n},a+\frac{(k+1)(b-a)}{n}]$, where $k\in\{0,1,\ldots,n-1\}$;

- the symbol $w_{c,d}$ to denote a function $w_{c,d} : [c, d] \to [c, d]$ such that $w_{c,d}(d) = d$ and $w_{c,d}(x) = w^{2j+1}_{c+\frac{(2^j-1)(d-c)}{2^j}, c+\frac{(2^{j+1}-1)(d-c)}{2^{j+1}}}(x)$, dla $x \in [c + \frac{(2^j-1)(d-c)}{2^j}, c + \frac{(2^{j+1}-1)(d-c)}{2^{j+1}}]$, $j \in \mathbb{N} \cup \{0\}$.

Let $U \subset [0, 1] \times [0, 1]$ be open in $[0, 1] \times [0, 1]$ and such that $\Gamma(f) \subset U$. There exist a continuous function $f_c : [0, 1] \to [0, 1]$ such that $\Gamma(f_c) \subset U$ and a point $x_0 \in \mathrm{Fix}(f_c) \cap (0, 1)$. Let $\delta_1 > 0$ be such that $[x_0 - \delta_1, x_0 + \delta_1] \times [x_0 - \delta_1, x_0 + \delta_1] \subset U$. Choose a number $\delta \in (0, \frac{\delta_1}{2})$ such that $f_c([x_0 - 2\delta, x_0 + 2\delta]) \subset [x_0 - \delta_1, x_0 + \delta_1]$.

Let $g : [0, 1] \to [0, 1]$ be defined as follows: $g(x) = f_c(x)$ for $x \in [0, x_0 - 2\delta] \cup [x_0 + 2\delta, 1]$, g linear on $[x_0 - 2\delta, x_0 - \frac{3\delta}{2}]$, $g(x) = -x + 2x_0$ for $x \in [x_0 - \frac{3\delta}{2}, x_0]$, $g(x) = w_{x_0,x_0+\delta}(x)$ dla $x \in [x_0, x_0 + \delta]$, $g(x) = x$ for $x \in (x_0 + \delta, x_0 + \frac{3\delta}{2})$, g linear on $[x_0 + \frac{3\delta}{2}, x_0 + 2\delta]$. It is easy to observe that $\Gamma(g) \subset U$ and g is continuous.

Now, we will show that $x_0 - \delta$ is a *full** entropy point of g.

First notice that $x_0 - \delta$ is not a focal entropy point of g. Indeed, aiming for a contradiction, suppose that $x_0 - \delta$ is a focal entropy point of g. Then, by ([10], Proposition 3.3), $x_0 - \delta$ is a nonwandering point of g. On the other hand $g^i((x_0 - \frac{3\delta}{2}, x_0 - \frac{\delta}{2})) \subset [x_0 + \frac{\delta}{2}, x_0 + \frac{3\delta}{2}]$ $(i \in \mathbb{N})$, which contradicts the fact that $x_0 - \delta$ is a nonwandering point of g and we can conclude that $x_0 - \delta$ is not a focal entropy point of g.

We have $g(x_0 - \delta) = x_0 + \delta$. Let $r > 0$. Put $\varepsilon = \min\{r, \frac{\delta}{4}\}$. Then $g(B(x_0 - \delta, r)) \supset (x_0 + \delta - \varepsilon, x_0 + \delta + \varepsilon)$, so $x_0 + \delta \in \mathrm{int}(g(B(x_0 - \delta, r)))$. Let K be an arbitrary closed neighbourhood of $x_0 + \delta$. There exists $k_0 \in \mathbb{N}$ such that $[x_0 + \frac{(2^{k_0}-1)\delta}{2^{k_0}}, x_0 + \delta] \subset K$. Denote $Y_j = [x_0 + \frac{(2^j-1)\delta}{2^j}, x_0 + \frac{(2^{j+1}-1)\delta}{2^{j+1}}]$ for $j \geq k_0$. Then $\log(2j - 1) \leq h(g \restriction K)$, for $j \geq k_0$ ([2], Theorem 4.2.4). Thus $h(g \restriction K) = +\infty = h(g)$, which means that $x_0 + \delta$ is a full entropy point of g.

Hence and by Lemma 3 we conclude that $x_0 - \delta$ is a *full** entropy point of g. □

Now, we will present the example which was announced before Lemma 3.

Consider the function $f : [0, 1] \to [0, 1]$, $f(x) = w_{0,1}(x)$ (see notations introduced at the beginning of the proof of Theorem 2). We have $h(f) = \infty$ ([2]) and 1 is a full entropy point of f (see proof of Theorem 2). We will show that 1 is the only one full entropy point of f. Let $x_0 \neq 1$. Consider the following cases:

1. $x_0 \notin \{\frac{2^k-1}{2^k} : k = 0, 1, \dots\}$. Then, there exists $k_0 \in \mathbb{N}$ such that $x_0 \in (\frac{2^{k_0}-1}{2^{k_0}}, \frac{2^{k_0+1}-1}{2^{k_0+1}})$. The interval $K = [\frac{2^{k_0}-1}{2^{k_0}}, \frac{2^{k_0+1}-1}{2^{k_0+1}}]$ is a closed neighbourhood of x_0. We have $h(f \restriction K) = \log(2k_0 + 1) \neq \infty = h(f)$. Thus x_0 is not a full entropy point of f.
2. $x_0 = \frac{2^{k_1}-1}{2^{k_1}}$ for some $k_1 \in \{1, 2, \dots\}$. Then $K = [\frac{2^{k_1-1}-1}{2^{k_1-1}}, \frac{2^{k_1+1}-1}{2^{k_1+1}}]$ is a closed neighbourhood of x_0. Put $Y_{k_1-1} = [\frac{2^{k_1-1}-1}{2^{k_1-1}}, \frac{2^{k_1}-1}{2^{k_1}}]$ and $Y_{k_1} = [\frac{2^{k_1}-1}{2^{k_1}}, \frac{2^{k_1+1}-1}{2^{k_1+1}}]$. Clearly $K = Y_{k_1-1} \cup Y_{k_1}$. Moreover, the sets Y_{k_1-1} and Y_{k_1} are closed and f-invariant. We have $h(f \restriction K) = \max\{h(f \restriction Y_{k_1-1}), h(f \restriction Y_{k_1})\} = \max\{\log(2k_1 - 1), \log(2k_1 + 1)\} \neq \infty = h(f)$. Thus x_0 is not a full entropy point of f.
3. $x_0 = 0$. Put $K = [0, \frac{1}{2}]$. Then $h(f \restriction K) = 0 \neq h(f)$, so $x_0 = 0$ is not a full entropy point of f.

We have shown that 1 is the only one full entropy point of f. By Theorem 1 no point $x \neq 1$ is a focal entropy point of f. Moreover, by Lemma 1 we know that the set of all focal entropy points of f is nonempty, thus 1 is a focal entropy point of f.

4 Focal Entropy Points - Unbalanced Points

It has been mentioned that a lot of considerations regarding discrete dynamical systems are concentrated on functions mapping the closed unit interval into itself (piecewise monotonne functions, unimodal functions, etc.). In this case, it is also worth to examine classes of functions which are important in real analysis [5, 12]. Note that if $f : [0, 1] \to [0, 1]$ then the following implications hold:

$$f \text{ is approximately continuous } \Rightarrow f \text{ is a derivative } \Rightarrow$$

$$f \text{ is a Darboux Baire class one function } \Rightarrow f \text{ is almost continuous.}$$

In the further part of the paper, the facts connected with $\mathscr{F}$-focal entropy points will be examined under as weak as possible assumptions imposed on considered functions. We will start with proving the following theorem.

Theorem 3 *Let $f \in DB_1$ and $h(f) > 0$. Then the set of all $\mathscr{F}$-focal entropy points of f is contained in the centre of f.*

Proof Let x_0 be an $\mathscr{F}$-focal entropy point of f and $U \in O(x_0)$. It is sufficient to show that $U \cap \mathrm{Rc}(f) \neq \emptyset$. We have $h(f) > 0$. Let $\beta \in (0, h(f))$. Then $H_{\mathscr{F},f}(U) > \beta$. We have $H_{\mathscr{F},f}(U) = \sup\{\frac{1}{n} H_{f^n}(F) : F \in \vartheta_{\mathscr{F}}^U \wedge n \in \mathbb{N}\} > \beta$, thus there exist $n_0 \in \mathbb{N}$ and $F_0 = (I_1, \ldots, I_k) \in \vartheta_{\mathscr{F}}^U$ such that $H_{f^{n_0}}(F_0) > n_0\beta$. This gives the existence of strictly increasing sequence $\{d_n\}_{n\in\mathbb{N}}$ of positive integers such that

$$\log \sqrt[d_n]{\mathrm{tr}(\mathscr{M}_{F_0,f^{n_0}}^{d_n})} > n_0\,\beta. \tag{5}$$

Let us adopt the following notation: $\mathscr{M}_{F_0,f^{n_0}}^{d_n} = [a_{i,j}^{d_n}]_{1\le i,j\le k}$ and fix $n_* \in \mathbb{N}$. By (5) we have

$$\mathrm{tr}(\mathscr{M}_{F_0,f^{n_0}}^{d_{n_*}}) > d_{n_*} n_0\,\beta. \tag{6}$$

Set $\Pi = \{m \in \{1, \ldots, k\} : a_{m,m}^{d_{n_*}} > 0\}$. Condition (6) implies $\Pi \neq \emptyset$. Fix $m_0 \in \Pi$. There exists a sequence $[I_{m_0}, I_{s_1}, \ldots, I_{s_{d_{n_*}-1}}, I_{m_0}]_{f^{n_0}}$, where $s_1, \ldots, s_{d_{n_*}-1} \in \{1, \ldots, k\}$. By Remark 2.4 [22] there is $x \in I_{m_0} \subset U$ such that $(f^{n_0})^{d_{n_*}}(x) = x$. Thus $x \in U \cap \mathrm{Rc}(f)$ and the proof is finished. □

Let us note that the assumption $h(f) > 0$ in Theorem 3 is essential. Consider the function $f(x) = \log_2(x + 1)$. Then each point of the interval $(0, 1)$ is an $\mathscr{F}$-focal entropy point of f and simultaneously it does not lie in the centre of f.

One can construct an example of a function with a positive entropy and such that it has an $\mathscr{F}$-focal entropy point which is not a recurrent point.

As it was mentioned in the introduction, it is commonly thought that the basic criterion for dynamical system to be chaotic is a positive entropy of this system. Thus, the fact that x_0 is a focal entropy point of f suggests that f is "chaotic" in the neighbourhood of x_0. What is more, this fact may cause an effect of a "black hole", i.e. each function which is "close" to f is also chaotic in the neighbourhood of x_0. Simultaneously, such a function may be "non-chaotic" (even constant) on a big set (in the sense of Lebesgue measure) lying close to x_0. It leads to the definition of an *unbalanced point*.

Let f be a Darboux function such that $h(f) > 0$. We say that a point $x_0 \in (0, 1)$ (respectively $x_0 = 0, x_0 = 1$) is an *unbalanced point of* f if

[U1] f is approximately constant at x_0, i.e. there is a Lebesgue measurable set A such that $d(A, x_0) = 1$ (respectively $d^+(A, x_0) = 1$, $d^-(A, x_0) = 1$) and $f(x) = f(x_0)$ for $x \in A$;

[U2] there exists $\sigma > 0$ such that for any $g \in B_{\rho_u}(f, \sigma) \cap D$ we have $h(g) > 0$ and $x_0 \in E_{\mathscr{F}}(g)$.

The set of all unbalanced points of a function f will be denoted by $\mathbb{U}(f)$. It is not difficult to notice that if a point x_0 is an unbalanced point of a function f then it is a 0-approximate continuity point of f and f attracts positive entropy at x_0 (see definitions presented in [11]).

The following theorem is connected with the question [PW1] formulated in the introduction.

Theorem 4 *Each almost continuous function can be Γ-approximated by approximately continuous functions having an unbalanced point.*

Proof Let f be an almost continuous function and $U \subset [0, 1] \times [0, 1]$ be an open set in $[0, 1] \times [0, 1]$ containing $\Gamma(f)$.

Clearly, there exist a continuous function $f_c : [0, 1] \to [0, 1]$ such that $\Gamma(f_c) \subset U$ and a point $x_0 \in \mathrm{Fix}(f_c) \cap (0, 1)$. Moreover, there is a number $\delta_1 > 0$ such that $[x_0 - \delta_1, x_0 + \delta_1] \times [x_0 - \delta_1, x_0 + \delta_1] \subset U$. By continuity of f_c, one can choose $\delta_2 \in (0, \delta_1)$ such that $f_c([x_0 - \delta_2, x_0 + \delta_2]) \subset [x_0 - \delta_1, x_0 + \delta_1]$.

Let $A_p = \bigcup_{n=1}^{\infty} (c_n, d_n) \subset (x_0, x_0 + \frac{\delta_2}{2})$ be a right-sided interval set at the point x_0 such that $d^+(A_p, x_0) = 1$. Put $A = (x_0 - \frac{\delta_2}{2}, x_0) \cup A_p$, $x_n = \frac{3d_{n+1} + c_n}{4}$ and $y_n = \frac{3c_n + d_{n+1}}{4}$, for $n \in \mathbb{N}$.

Define f_0 as follows: $f_0(x) = f_c(x)$ for $x \in [0, 1] \setminus (x_0 - \delta_2, x_0 + \delta_2)$, $f_0(x) = x_0$ for $x \in \mathrm{cl}\,(A) \cup (d_1, x_0 + \frac{\delta_2}{2}]$, $f_0(x) = x_0 + \frac{\delta_2}{2}$ for $x = y_n, n \in \mathbb{N}$, $f_0(x) = x_0 - \frac{\delta_2}{2}$ for $x = x_n, n \in \mathbb{N}$, f_0 linear respectively on the intervals $[d_{n+1}, x_n]$, $[x_n, y_n]$, $[y_n, c_n]$, $n \in \mathbb{N}$. Obviously $\Gamma(f_0) \subset U$ and f_0 is an approximately continuous function.

We will show that x_0 is an unbalanced point of f_0.

It is easy to check that f_0 is a turbulent function, so by Lemma 2 we have $h(f_0) > 0$. Moreover, $d(A, x_0) = 1$ and $f_0(x) = x_0$, for $x \in A$.

It remains to prove that there exists $\sigma > 0$ such that for any function $g \in B_{\rho_u}(f, \sigma) \cap D$ we have $h(g) > 0$ and $x_0 \in E_{\mathscr{F}}(g)$.
Let us put $\sigma = \frac{\delta_2}{4}$. Let $g \in B_{\rho_u}(f, \sigma) \cap D$. First observe that $g(y_n) > x_0 + \frac{\delta_2}{4}$ and $g(x_n) < x_0 - \frac{\delta_2}{4}$. The function g is Darboux, so $[x_0 - \frac{\delta_2}{4}, x_0 + \frac{\delta_2}{4}] \subset g([x_n, y_n])$. Notice that there exists $n_1 \in \mathbb{N}$ such that $[x_n, y_n] \subset [x_0 - \frac{\delta_2}{4}, x_0 + \frac{\delta_2}{4}]$ for $n \geq n_1$. Let $n^*, n^{**} \geq n_1$ and $n^* \neq n^{**}$. Then $[x_{n^*}, y_{n^*}] \cap [x_{n^{**}}, y_{n^{**}}] = \emptyset, [x_{n^*}, y_{n^*}] \cup [x_{n^{**}}, y_{n^{**}}] \subset [x_0 - \frac{\delta_2}{4}, x_0 + \frac{\delta_2}{4}] \subset g([x_{n^*}, y_{n^*}]) \cap g([x_{n^{**}}, y_{n^{**}}])$. Thus g is a turbulent function and by Lemma 2 we conclude that $h(g) > 0$.

We will show now that $x_0 \in E_{\mathscr{F}}(g)$. Let $V \in O(x_0)$ and $n_2 > n_1$ be such that $y_{n_2} \in V$. Put $F_k = \{[x_n, y_n] : n = n_2, \ldots, n_2 + k\}$ for $k \in \mathbb{N}$. Clearly $\bigcup F_k \subset V$. Fix $k \in \mathbb{N}$. We have $g([x_n, y_n]) \supset [x_0 - \frac{\delta_2}{4}, x_0 + \frac{\delta_2}{4}] \supset [x_m, y_m]$, for $n, m \in \{n_2, \ldots, n_2 + k\}$. This means that $[x_n, y_n] \underset{g}{\to} [x_m, y_m]$ for $n, m \in \{n_2, \ldots, n_2 + k\}$, so $\mathscr{M}_{F_k,g}$ is a $(k+1) \times (k+1)$ matrix whose all entries are equal to 1. Hence, for any $i \in \mathbb{N}$ the matrix $\mathscr{M}^i_{F_k,g}$ is a $(k+1) \times (k+1)$ matrix whose all entries are of the form $(k+1)^{i-1}$. Therefore for any $i \in \mathbb{N}$ we have $\operatorname{tr}(\mathscr{M}^i_{F_k,g}) = (k+1)^i$. Thus $H_g(F_k) = \log(k+1)$. Moreover

$$H_{\mathscr{F},g}(V) \geq \sup\{H_g(F_k) : k \in \mathbb{N}\} = \sup\{\log(k+1) : k \in \mathbb{N}\} = \infty,$$

so $x_0 \in E_{\mathscr{F}}(g)$. This completes the proof of the fact that x_0 is an unbalanced point of f_0. □

The answer to the question [PW2] is the following theorem.

Theorem 5 *For any $\alpha \in [0, 1)$ there exists a function $f : [0, 1] \to [0, 1]$ such that $f \in DB_1^{**}$ and $\lambda(\mathbb{U}(f)) = \alpha$.*

Proof Let us first consider the case $\alpha \in (0, 1)$. Let $C \subset [0, 1]$ be a Cantor set such that $\lambda(C) = \alpha$. Define a function $f : [0, 1] \to [0, 1]$ in the following way: $f(x) = 0$ for $x \in C$; for each component (a, b) of the complement of C put $f(\frac{a+b}{2}) = 1$ and let f be linear on the intervals $[a, \frac{a+b}{2}]$ and $[\frac{a+b}{2}, b]$.

It is easy to see that $f \in DB_1^{**}$ and $h(f) > 0$.

Let $C^* \subset C$ be the set of all density points of C. By Lebesgue Density Theorem we have $\lambda(C^*) = \lambda(C) = \alpha$. We will show that $\mathbb{U}(f) = C^*$. It is clear that $\mathbb{U}(f) \subset C^*$. Let $x_0 \in C^*$. Then $f(x_0) = 0$. The function f is approximately constant at x_0, because C is a Lebesgue measurable set such that $d(C, x_0) = 1$ and $f(x) = 0 = f(x_0)$, for $x \in C$.

Put $\sigma = \min\{\frac{x_0}{2}, \frac{1-x_0}{2}\}$. Let $g \in B_{\rho_u}(f, \sigma) \cap D$. We need to show that $h(g) > 0$ and $x_0 \in E_{\mathscr{F}}(g)$. This follows by the same method as in the proof of Theorem 4.

We now turn to the case $\alpha = 0$. Let $x_0 \in (0, 1)$ and $A_p = \bigcup_{n=1}^{\infty} (c_n, d_n) \subset (0, 1)$ be a right-sided interval set at x_0 such that $d^+(A_p, x_0) = 1$. Put $A = [0, x_0) \cup A_p$ and $x_n = \frac{d_{n+1}+c_n}{2}$, $n \in \mathbb{N}$. Define $f : [0, 1] \to [0, 1]$ as follows: $f(x) = 0$ for $x \in \operatorname{cl}(A)$, $f(x) = 1$ for $x = x_n$, $n \in \mathbb{N}$ and f is linear on the intervals $[d_{n+1}, x_n]$, $[x_n, c_n]$, $n \in \mathbb{N}$.

Clearly $f \in DB_1^{**}$ and $h(f) > 0$. If we apply similar reasoning as before, we obtain $\mathbb{U}(f) = \{x_0\}$ and consequently $\lambda(\mathbb{U}(f)) = 0$. □

References

1. Adler, R.L., Konheim, A.G., McAndrew, M.H.: Topological entropy. Trans. Am. Math. Soc. **114**, 309–319 (1965)
2. Alsedá, L., Llibre, J., Misiurewicz, M.: Combinatorial Dynamics and Entropy in Dimension One, 2nd edn. World Scientific, Singapore (2000)
3. Block, L.S., Coppel, W.A.: Dynamics in One Dimension. Springer, Berlin (1992)
4. Bowen, R.: Entropy for group endomorphisms and homogeneous spaces. Trans. Am. Math. Soc. **153**, 401–414 (1971)
5. Bruckner, A.M.: Differentiation of Real Functions. Springer, Berlin (1978)
6. Čiklová, M.: Dynamical systems generated by functions with connected G_δ graphs. Real Anal. Exch. **30(2)**, 617–638 (2004/2005)
7. Dinaburg, E.I.: Connection between various entropy characterizations of dynamical systems. Izv. Akad. Nauk SSSR **35**, 324–366 (1971). (in Russian)
8. Fiebig, D., Fiebig, U., Nitecki, Z.: Entropy and preimage sets. Ergodic Theory Dyn. Syst. **23**(6), 1785–1806 (2003)
9. Kolyada, S., Snoha, L.: Topological entropy of nonautonomous dynamical systems. Random Comput. Dyn. **4**(2& 3), 205–233 (1996)
10. Korczak-Kubiak, E., Loranty, A., Pawlak, R.J.: On focusing entropy at a point. Taiwanese J. Math. **20**(5), 1117–1137 (2016)
11. Loranty, A., Pawlak, R.J.: On functions attracting positive entropy. Bull. Aust. Math. Soc. https://doi.org/10.1017/S0004972717000855
12. Łojasiewicz, S.: An Introduction to the Theory of Real Functions. Wiley, New York (1988)
13. Müller, I.: Entropy: a subtle concept in thermodynamics. In: Greven, A., Keller, G., Warnecke, G. (eds.) Entropy. Princeton University Press, Princeton (2003)
14. Nitecki, Z.: Topological entropy and the preimage structure of maps. Real Anal. Exch. **29**(1), 9–42 (2003)
15. O'Malley, R.J.: Baire*1, Darboux functions. Proc. Am. Math. Soc. **60**, 187–192 (1976)
16. Pawlak, R.J.: On some class of functions intermediate between the class B_1^* and the family of continuous functions. Tatra Mt. Math. Publ. **19**, 135–144 (2000)
17. Pawlak, R.J.: Entropy of nonautonomous discrete dynamical systems considered in GTS and GMS, to appear in Bull. Soc. Sci. Lett. de Łódź. Sér. Rech. Déform
18. Pawlak, R.J., Loranty, A.: The generalized entropy in the generalized topological spaces. Topol. Appl. **159**, 1734–1742 (2012)
19. Pawlak, R.J., Loranty, A., Bąkowska, A.: On the topological entropy of continuous and almost continuous functions. Topol. Appl. **158**, 2022–2033 (2011)
20. Shannon, C.E.: A mathematical theory of communication. Bell Syst. Tech. J. **27**, 379–423, 623–656 (1948) (Republished, University of Illinois Press Urbana, IL, 1963)
21. Stallings, J.: Fixed point theorem for connectivity maps. Fund. Math. **47**, 249–263 (1959)
22. Szuca, P.: Sharkovskii's theorem holds for some discontinuous functions. Fund. Math. **179**, 27–41 (2003)
23. Walters, P.: An Introduction to Ergodic Theory. Springer, Berlin (1982)
24. Ye, X., Zhang, G.: Entropy points and applications. Trans. Am. Math. Soc. **359**(12), 6167–6186 (2007)

Optimal Control of Hybrid Systems with Sliding Modes

Radosław Pytlak, Damian Suski and Tomasz Tarnawski

Abstract This paper concerns the numerical procedure for solving hybrid optimal control problems with sliding modes. The proposed procedure has several features which distinguish it from the other procedures for the problem. First of all a sliding mode is coped with differential–algebraic equations (DAEs) and that guarantees accurate tracking of the sliding motion surface. The second important feature is the calculation of cost and constraints functions gradients with the help of adjoint equations. The adjoint equations presented in the paper take into account sliding motion. The third feature is the integration of the presented procedure with the Interactive Dynamic Optimization Server (IDOS) which is a computing environment dedicated to optimal control problems. IDOS user interface relies on Dynamic Optimization Modeling Language (DOML) which is an extension of Modelica language. In the paper we discuss the elements of DOML which help defining hybrid optimal control problems. The paper presents the application of the proposed procedure to an optimal control problem related to a mechanical system with dry friction.

Keywords Hybrid systems · Optimal control · Adjoint equations

R. Pytlak (✉)
Faculty of Mathematics and Information Science,
Warsaw University of Technology, 00-665 Warsaw, Poland
e-mail: r.pytlak@mini.pw.edu.pl

D. Suski
Institute of Automatic Control and Robotics,
Warsaw University of Technology, 02-525 Warsaw, Poland
e-mail: d.suski@mchtr.pw.edu.pl

T. Tarnawski
Department of Quantitative Methods and Information Technology,
Kozminski University, 03-301 Warsaw, Poland
e-mail: ttarnawski@kozminski.edu.pl

J. Awrejcewicz (ed.), *Dynamical Systems in Theoretical Perspective*,
Springer Proceedings in Mathematics & Statistics 248,
https://doi.org/10.1007/978-3-319-96598-7_23

1 Introduction

Hybrid systems are systems with mixed discrete–continuous dynamics [1]. In this work we use a definition of a hybrid system given in [2], which is similar to many other definitions given in the literature e.g. [1, 3–6]. We restrict our analysis to systems with autonomous transitions and without state jumps during transitions

Definition 1 A hybrid system $\mathscr{H}$ is a tuple

$$\mathscr{H} = (\mathscr{Q}, \mathscr{U}, \mathscr{I}, \mathscr{F}, \mathscr{T}, \mathscr{G}) \tag{1}$$

where

- $\mathscr{Q}$ is a finite set of discrete states. Its elements are denoted by q.
- $\mathscr{U}$ is a set of admissible controls. The elements of $\mathscr{U}$ are measurable functions $u : I \to U$, where I can be any closed interval of $\mathbb{R}$ and U is a fixed subset of $\mathbb{R}^m$.
- $\mathscr{I}$ is a function which assigns to every discrete state q a set

$$\mathscr{I}(q) = \left\{x \in \mathbb{R}^n : h_q(x) \le 0\right\},\ h_q : \mathbb{R}^n \to \mathbb{R}^{n_{\mathscr{I}_q}} \tag{2}$$

  such that as long as a hybrid systems is in a discrete state q the continuous state trajectory x stays in $\mathscr{I}(q)$. We therefore say that $\mathscr{I}(q)$ is an *invariant set* for a discrete state q.
- $\mathscr{F}$ is a function which assigns to every discrete state q a function $f_q : \mathscr{I}(q) \times U \to \mathbb{R}^n$ such that in a discrete state q the continuous state evolves according to a differential equation

$$x' = f_q(x, u) \tag{3}$$

- $\mathscr{T}$ is a subset of $\mathscr{Q} \times \mathscr{Q}$, which collects all pairs of discrete states (q, q') such that the transition from a state q to a state q' is possible.
- $\mathscr{G}$ assigns to each pair $(q, q') \in \mathscr{T}$ a subset of $\mathscr{I}(q)$ boundary such that when a continuous state trajectory is about to leave $\mathscr{I}(q)$ through its boundary at a point $x_t \in \mathscr{G}(q, q') \subset \partial\mathscr{I}(q)$ a discrete state changes from q to q'. We call such an event a *transition* and $\mathscr{G}$ plays a role of a *transition guard*.

2 Sliding Mode

In our work we consider hybrid systems with sliding modes. For the sake of simplicity let us consider a hybrid system with two discrete states collected in a set $\mathscr{Q} = \{1, 2\}$. Let us assume that the invariant sets are $\mathscr{I}(1) = \{x \in \mathbb{R}^n : h(x) \le 0\}$ and $\mathscr{I}(2) = \{x \in \mathbb{R}^n : h(x) \ge 0\}$ where $h : \mathbb{R}^n \to \mathbb{R}$. If the hybrid system starts its evolution from a discrete state $q = 1$ the continuous state evolves according to an equation $x' = f_1(x, u)$. At a transition time t_t the continuous state trajectory reaches the boundary of

an invariant set and we have $h(x(t_t)) = 0$. The first order condition which guarantees that the continuous state trajectory will leave the invariant set $\mathscr{I}(1)$ is [2, 3]

$$h_x(x(t_t))f_1(x(t_t), u(t_t)) > 0 \tag{4}$$

where $h_x^T(x)$ is the normal vector to a surface

$$\Sigma = \{x \in \mathbb{R}^n : h(x) = 0\} \tag{5}$$

at x. If at a transition time we have

$$h_x(x(t_t))f_2(x(t_t), u(t_t)) > 0 \tag{6}$$

then the discrete state changes from $q = 1$ to $q = 2$ and the continuous state continues the evolution according to an equation $x' = f_2(x, u)$. If at a transition time we have

$$h_x(x(t_t))f_2(x(t_t), u(t_t)) < 0 \tag{7}$$

then both vector fields $f_1(x, u)$ and $f_2(x, u)$ points towards the surface Σ and we face the *sliding motion* phenomenon [7].

The sliding motion can be handled with the concept of *Filippov solutions* [7]. We say that a continuous state trajectory is a Filippov solution of the considered hybrid system if

$$x' = \begin{cases} f_1(x, u) & \text{if } h(x) < 0 \\ f_F(x, u) & \text{if } h(x) = 0 \\ f_2(x, u) & \text{if } h(x) > 0 \end{cases}$$

where $f_F(x, u)$ is a convex combination of $f_1(x, u)$ and $f_2(x, u)$

$$f_F(x, u) = (1 - \alpha)f_1(x, u) + \alpha f_2(x, u), \ \alpha \in [0, 1] \tag{8}$$

During the sliding motion the continuous state trajectory must stay in the surface Σ, so the condition

$$h_x(x)f_F(x, u) = 0 \tag{9}$$

must be satisfied. From (8) and (9) it is easy to find the formula for α coefficient

$$\alpha(x, u) = \frac{h_x(x)f_1(x, u)}{h_x(x)\,(f_1(x, u) - f_2(x, u))} \tag{10}$$

The hybrid system exits the sliding motion when one of the vector fields $f_1(x, u)$ and $f_2(x, u)$ stops pointing towards the surface Σ. It is easy to track that event by checking the value of $\alpha(x, u)$. If at a moment t_t we have

$$\alpha(x(t_t), u(t_t)) = 0 \tag{11}$$

$$\frac{d}{dt}\alpha(x(t_t), u(t_t)) < 0 \tag{12}$$

the hybrid system transits to a discrete state $q = 1$ [7]. If at a moment t_t we have

$$\alpha(x(t_t), u(t_t)) = 1 \tag{13}$$

$$\frac{d}{dt}\alpha(x(t_t), u(t_t)) > 0 \tag{14}$$

the hybrid system transits to a discrete state $q = 2$ [7].

During the sliding motion the continuous state trajectory should stay in a set Σ. To keep this condition satisfied during the numerical integration, we follow the approach proposed in [8] and integrate the differential-algebraic equations (DAEs)

$$x' = f_F(x, u) + h_x^T(x)z \tag{15}$$

$$0 = h(x) \tag{16}$$

instead of ODEs

$$x' = f_F(x, u) \tag{17}$$

Equations (15)–(16) are index two DAEs under the assumption that at each $x \in \Sigma$

$$h_x(x) \neq 0 \tag{18}$$

The hidden algebraic equation resulting from differentiation of Eq. (16) is

$$0 = h_x(x)\left(f_F(x, u) + h_x^T(x)z\right) \tag{19}$$

From Eqs. (9), (18) and (19) we get that $z = 0$ for an exact solution of Eqs. (15)–(16).

3 Calculating the Optimal Control

Taking into account the considerations and definitions presented in the previous section, in particular including the possibility of the system entering (and spending some time) in the sliding mode, we now put down the optimal control problem of interest, as follows:

$$\min_{u \in U} \phi(x(t_1)) \tag{20}$$

$$x(t_0) = x_0 \tag{21}$$

$$x' = \begin{cases} f_1(x,u) & \text{if } h(x) < 0 \\ f_F(x,u) & \text{if } h(x) = 0 \\ f_2(x,u) & \text{if } h(x) > 0 \end{cases}$$

$$g_i^1(x(t_1)) = 0, \text{ for } i \in E \tag{22}$$

$$g_j^2(x(t_1)) \leq 0, \text{ for } j \in I. \tag{23}$$

The admissible control is a function $u : [t_0, t_1] \to U$.

To calculate the optimal control for hybrid systems with sliding modes we follow the approach presented in [9, 10] for systems described by DAEs and in [2] for hybrid systems without sliding modes. The numerical algorithm calculates the gradients of cost and constraint functionals with the help of adjoint equations. Here we formulate the adjoint equations for two cases, which complement the formulation of adjoint equations presented in [2]. The adjoint equation are derived on the basis of a variational approach presented in [11].

In the first case we assume that in the time interval $[t_0, t_t]$ the system evolves according to the equation $x' = f_1(x,u)$. At a transition time t_t the continuous state trajectory meets the switching surface and we have $h(x(t_t)) = 0$. After the transition the system evolves according to DAEs (15)–(16) up to an ending time t_1. The adjoint equations have the following form
for $t \in [t_0, t_t]$

$$\lambda_f' = -(f_1)_x^T(x,u)\lambda_f \tag{24}$$

for $t \in [t_t, t_1]$ [10]

$$\lambda_f' = -(f_F)_x^T(x,u)\lambda_f - \left(h_x^T(x)z\right)_x^T \lambda_f + h_x^T(x)\lambda_h \tag{25}$$

$$0 = h_x(x)\lambda_f \tag{26}$$

Let us notice that the adjoint Eqs. (25)–(26) are also index two DAEs under the condition (18). The hidden algebraic equation resulting from differentiation of Eq. (26) is

$$0 = (h_x(x))'\lambda_f - h_x(x)(f_F)_x^T(x,u)\lambda_f - h_x(x)\left(h_x^T(x)z\right)_x^T\lambda_f + h_x(x)h_x^T(x)\lambda_h. \tag{27}$$

The DAEs (25)–(26) have to be consistently initialized. To provide the consistent endpoint conditions for the adjoint variables λ_f, λ_h we utilize the approach presented in [12] and solve the following system of equations at time t_1 for the variables $\lambda_f, \lambda_h, \nu$

$$\phi_x^T(x(t_1)) + \lambda_f(t_1) = \nu_1 h_x^T(x(t_1)) \tag{28}$$

$$0 = h_x(x(t_1))\lambda_f(t_1) \tag{29}$$

$$0 = (h_x(x(t_1)))'\,\lambda_f(t_1) \tag{30}$$

$$\begin{aligned} &-h_x(x(t_1))\,(f_F)_x^T\,(x(t_1), u(t_1))\lambda_f(t_1) - h_x(x(t_1))\left(h_x^T(x(t_1))z(t_1)\right)_x^T\lambda_f \\ &+h_x(x(t_1))h_x^T(x(t_1))\lambda_h(t_1) \end{aligned} \tag{31}$$

where ν_1 is some real number.

At the transition time t_t the adjoint variable λ_f undergoes a jump. To calculate the value of $\lambda_f(t_t^-)$ the following system of equations have to be solved for the variables $\lambda_f(t_t^-),\ \pi$ (t_t^- and t_t^+ are instant of times after and before the jump)

$$\lambda_f(t_t^-) = \lambda_f(t_t^+) - \pi h_x^T(x(t_t)) \tag{32}$$

$$\begin{aligned} &\lambda_f^T(t_t^-)f_1(x(t_t^-1), u(t_t^-)) = \lambda_f^T(t_t^+)f_F(x(t_t^+), u(t_t^+)) \\ &+\lambda_f^T(t_t^+)h_x^T(x(t_t^+))z(t_t^+) - \lambda_h^T(t_t^+)h(x(t_t^+)) \end{aligned} \tag{33}$$

where π is an additional Lagrange multiplier (see the analysis in [11]).

Once we solve Eqs. (24)–(33) we get the adjoint variables λ_f and λ_h. Now we can calculate the first variation of a cost function $\delta\phi$ as a function of a control function variation δu as follows

$$\delta\phi(\delta u) = \int_{t_0}^{t_t} -\lambda_f^T\,(f_1)_u\,(x,u)\delta u\,dt - \int_{t_t}^{t_1} \lambda_f^T\,(f_F)_u\,(x,u)\delta u\,dt. \tag{34}$$

In the second case we assume that in the time interval $[t_0, t_t]$ the system evolves according to DAEs (15)–(16). At a transition time t_t the continuous state trajectory leaves the switching surface with the condition $\alpha(x(t_t), u(t_t)) = 0$ satisfied. After the transition the system evolves according to the equation $x' = f_1(x,u)$ up to an ending time t_1. The adjoint equations are (25)–(26) for $t \in [t_0, t_t]$ and (24) for $t \in [t_t, t_1]$.

The endpoint condition for an adjoint variable λ_f is

$$\lambda_f(t_1) = -\phi_x^T(x(t_1)) \tag{35}$$

To calculate the consistent values of $\lambda_f(t_t^-)$ and $\lambda_h(t_t^-)$ the following system of equations have to be solved for the variables $\lambda_f(t_t^-),\ \lambda_h(t_t^-),\ \pi,\ \nu_t$

$$\lambda_f(t_t^-) - \lambda_f(t_t^+) + \pi h_x^T(x(t_t^-)) = \nu_t h_x^T(x(t_t^-)) \tag{36}$$

$$\begin{aligned} &\lambda_f^T(t_t^-)f_F(x(t_t^-), u(t_t^-)) + \lambda_f^T(t_t^-)h_x^T(x(t_t^-))z(t_t^-) \\ &\quad -\lambda_h^T(t_t^-)h(x(t_t^-)) - \pi\alpha_u(x(t_t^-), u(t_t^-))u'(t_t^-) \\ &= \lambda_f^T(t_t^+)f_1(x(t_t^+), u(t_t^+)) \end{aligned} \tag{37}$$

where π and ν_t are some real numbers.

Once we solve the adjoint equations we get the adjoint variables λ_f and λ_h. Now we can calculate the first variation of a cost function $\delta\phi$ as a function of a control function variation δu as follows

$$\delta\phi(\delta u) = \int_{t_0}^{t_t} -\lambda_f^T \left(f_F\right)_u (x,u)\delta u \, dt - \int_{t_t}^{t_1} \lambda_f^T \left(f_1\right)_u (x,u)\delta u \, dt + \pi\alpha_u(x(t_t^-), u(t_t^-))\delta u(t_t^-). \tag{38}$$

4 Numerical Results

Our code for solving optimal control problems with hybrid systems is based on RADAU5 procedure which is the implementation of the implicit Radau IIA Runge–Kutta method [13, 14]. The RADAU5 procedure is modified in two ways. First, the subroutine for evaluating adjoint equations is added in the way given in [15]. The subroutine does also take into account jumps of adjoint variables if applied to hybrid systems–how the switching condition looks in the case of a discrete time dynamics is described in [16]. Secondly, the integration procedure is supplemented by the subroutine which effectively determines switching times locations, these subroutines were borrowed from LSODE package. We have made several modifications to these subroutines in order to allow state variables to be in several discrete states during a simulation process—LSODE package (and its successor CVODE) does not allow that, if the discrete state changes the integration process is terminated. As a result, we have used our unique software for integrating hybrid systems.

The optimal control of hybrid systems is much more complicated process than its simulation. We are strongly convinced that the numerical treatment of the process must be based on variable stepsize selection procedure for equations evaluation. The first reason for that is that we can guarantee a desired accuracy through a single run of a simulation. Secondly, due to switching points location, stepsizes evaluated during hybrid system integration will not be equal. The direct implication of using variable stepsizes integration procedures is the elimination of the direct approach (i.e., the approach based on an a'priori discretization of system equations and then on the transformation of an optimal control problem into, possibly large-scale, non-linear programming problem) as a potential approach for solving an optimal control problem with hybrid systems. Therefore, we are limited to procedures that use the numerical integration (with possibly high accuracy) of hybrid differential equations on each optimization step.

As a result of numerical integration of hybrid equations we have state trajectories whose values depend on current values of controls which will change during the optimization process. In order to apply efficient optimization procedures we need at least gradients of all functional defining an optimal control problem. For that purpose we can either apply sensitivity equations, or adjoint equations. The use of

sensitivity equations [17] is not advised when control variables are approximated using mesh points (each mesh point introduces the set of sensitivity equations of dimension equal to the dimension of the original equations), therefore we based our optimization approach on adjoint equations. Having adjoint trajectories one can calculate the gradient of any problem functional with respect to control variables and, consequently, efficient optimization procedures for constrained problems can be used.

As the optimization procedure we have used the exact penalty method which is presented in [18] (see also [19]) which have been modified by replacing the procedure for direction finding subproblems—we have applied the interior point method OOQP [20].

Example 1 The example concerns the Coulomb–Stribeck friction model. We have a mass m attached to inertial space by a spring k. The mass is moving on a belt at constant velocity v_{dr} (see Fig. 6.4a in [21]).The relative velocity of the mass with respect to the belt is equal to $v_{rel} = v - v_{dr}$. Between the mass and the belt there is the dry friction with a friction force F_T. In the slip phase it is the function of v_{rel} and is given by the relation

$$F_T = -\frac{\mu_s}{1 + \delta|v_{rel}|} F_N \text{sign}(v_{rel}). \tag{39}$$

Here, $F_N = mg$. Furthermore, in the stick phase the friction force is limited by the relation $|F_T| \leq F_s = \mu_s mg$. Eventually the function f_1, f_2 and h in are given as

$$f_1(x,u) = \begin{bmatrix} x_2 \\ -\frac{k}{m}x_1 + \frac{1}{m}\frac{F_s}{1+\delta|x_2 - v_{dr}|} + x_3 \\ u \end{bmatrix},$$

$$f_2(x,u) = \begin{bmatrix} x_2 \\ -\frac{k}{m}x_1 - \frac{1}{m}\frac{F_s}{1+\delta|x_2 - v_{dr}|} + x_3 \\ u \end{bmatrix}$$

and

$$h(x) = x_2 - v_{dr}. \tag{40}$$

Here, x_1 corresponds to the mass position, x_2 to its velocity and x_3 influences the mass movement through the control u.

The optimal control problem is as follows.

$$\min_{u \in U} x_2(x(t_1)) \tag{41}$$

$$\text{s.t.} \tag{42}$$

$$x(t_0) = x_0 \tag{43}$$

$$x' = \begin{cases} f_1(x,u) & \text{if } h(x) < 0 \\ f_F(x,u) & \text{if } h(x) = 0 \\ f_2(x,u) & \text{if } h(x) > 0 \end{cases}$$

and

$$x_1 - 0.6 = 0, \tag{44}$$

with the additional constraint which follow from the assumption that u must lie in the interval $[-2.5\ 2.5]$. Furthermore, we set

$$U = \left\{ u \in \mathscr{L}_1^1[0,t_1] : \ -2.5 \le u(t) \le 2.5 \text{ a.e. on } [0,t_1] \right\}.$$

$t_1 = 1.0$.

The optimal control is shown in Fig. 2 and the optimal trajectories in Fig. 1. One can observe that from the time $t \approx 0.8$ the system is in the sliding mode. The program needed 4 iterations to find the solution with the accuracy 10^{-8}. The results have been obtained by using piecewise–constant approximations to the control function with $N = 100$ subintervals. The system equations have been integrated with absolute and relative accuracies equal to 10^{-9}.

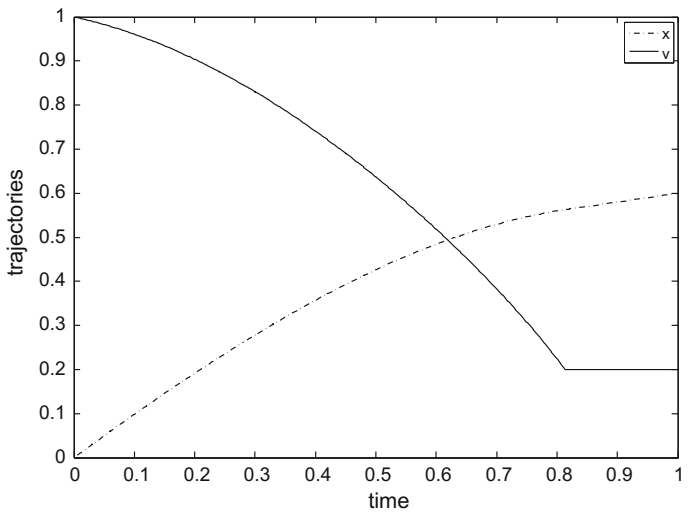

Fig. 1 Mass–spring example–optimal trajectories (variable x corresponds to x_1 and variable v to x_2 in the model)

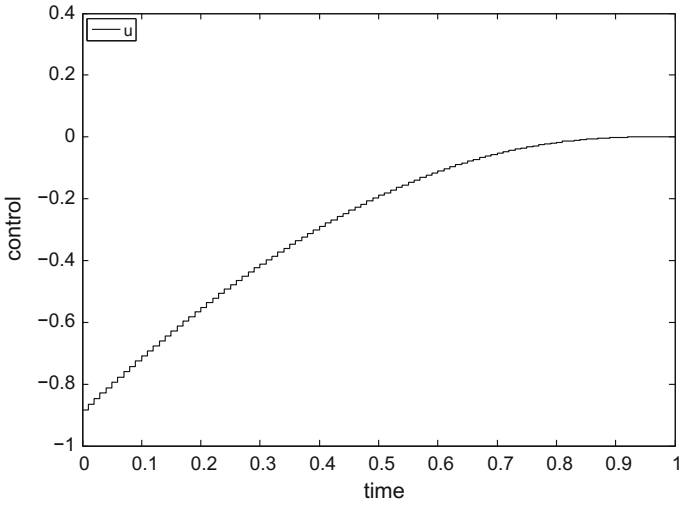

Fig. 2 Mass–spring example–optimal control

5 Conclusions

The paper presents the computational approach to hybrid optimal control problems with sliding modes. To much extent the approach is automated. For the lack of space we do not present here how our numerical procedures could be integrated with our server IDOS (Interactive Dynamic Optimization Server, [22]) dedicated to solving optimal control problems. The server IDOS requires representing optimal control problems as scripts of our language DOML (Dynamic Optimization Modeling Language [23]) for modeling and optimization of dynamical systems. Once the optimal control problem is represented by a DOML script the other calculations are carried out at the IDOS server. In particular it is not necessary to provide gradients of functions defining the problem. It will be shown elsewhere how hybrid optimal control problem can be described in DOML—to some extents it is described in [24].

References

1. van der Schaft, A., Schumacher, H.: An Introduction to Hybrid Dynamical Systems. Springer, London (2000)
2. Suski, D., Pytlak, R.: The weak maximum principle for hybrid systems. In: Proceedings of the 24th IEEE MED, Athens, Greece, pp. 338–343 (2016)
3. Lygeros J., Johansson K.H., Sastry S.S., Egerstedt, M.: On the existence of executions of hybrid automata. In: Proceedings of the 38th IEEE CDC, Phoenix, Arizona, pp. 2249–2254 (1999)
4. Olejnik, P., Awrejcewicz, J.: Application of Hénon method in numerical estimation of the stick-slip transitions existing in Filippov-type discontinuous dynamical systems with dry friction. Nonlinear Dyn. **73**, 723–736 (2013)

5. Olejnik, P., Awrejcewicz, J.: Low-speed voltage-input tracking control of a DC-motor numerically modelled by a dynamical system with stick-slip friction. Differ. Equ. Dyn. Syst. **21**, 3–13 (2013)
6. Shaikh, M.S.: Optimal Control of Hybrid Systems: theory and Algorithms, Ph.D. dissertation. McGill University, Montreal (2004) http://digitool.library.mcgill.ca/R/?func=dbin-jump-full&object_id=85095&local_base=GEN01-MCG02
7. Dieci, L., Lopez, L.: Sliding motion in filippov differential systems: theoretical results and a computational approach. SIAM J. Numer. Anal. **47**, 2023–2051 (2009)
8. Ascher, U., Petzold, L.: Computer Methods for Ordinary Differential Equations and Differential-Algebraic Equations. Society for Industrial and Applied Mathematics, Philadelphia (1998)
9. Pytlak, R.: Optimal control of differential-algebraic equations of higher index, Part 1: first order approximations. J. Optim. Theory Appl. **134**, 61–75 (2007)
10. Pytlak, R.: Optimal control of differential-algebraic equations of higher index, Part 2: necessary optimality conditions. J. Optim. Theory Appl. **134**, 77–90 (2007)
11. Bryson, A., Ho, Y.: Applied Optimal Control. Hemisphere, New York (1975)
12. Cao, Y., Li, S., Petzold, L., Serben, R.: Adjoint sensitivity analysis for differential-algebraic equations: the adjoint DAE system and its numerical solution. SIAM J. Sci. Comput. **24**, 1076–1089 (2000)
13. Hairer, E., Lubich, Ch., Roche, M.: The Numerical Solution of Differential-Algebraic Equations by Runge-Kutta Methods. Springer, Berlin (1989)
14. Hairer, E., Wanner, G.: Solving Ordinary Differential Equations II. Springer, Berlin (1996)
15. Pytlak, R., Zawadzki, T.: On solving optimal control problems with higher index DAEs. Optim. Methods Softw. **29**, 1139–1162 (2014)
16. Pytlak, R., Suski, D.: On solving hybrid optimal control problems with higher index DAEs. Optim. Methods Softw. **32**, 940–962 (2017)
17. Hiskens, I.A., Pai, M.A.: Trajectory sensitivity analysis of hybrid systems. IEEE Trans. Circuits Syst. **47**, 204–220 (2000)
18. Pytlak, R.: Numerical Methods for Optimal Control Problems with State Constraints. Lecture Notes in Mathematics, vol. 1707. Springer, Heidelberg (1999)
19. Pytlak, R., Vinter, R.B.: A feasible directions type algorithm for optimal control problems with state and control constraints. SIAM J. Control Optim. **36**, 1999–2019 (1998)
20. Gertz, E.M., Wright, S.J.: Object-Oriented Software for Quadratic Programming. ACM Trans. Math. Softw. **29**, 58–81 (2003)
21. Leine, R., Nimeijer, H.: Dynamics and Bifurcations of Non-smooth Dynamical Systems. Springer, Berlin (2004)
22. Pytlak, R., Tarnawski, T., Fajdek, B., Stachura, M.: Interactive dynamic optimization server-connecting one modelling language with many solvers. Optim. Methods Softw. **29**, 1118–1138 (2014)
23. Tarnawski, T., Pytlak, R.: DOML - a compiler environment for dynamic optimization supporting multiple solvers. In: Proceedings of the 10th Modelica Conference, Lund, Sweden, pp. 1007–1016 (2014)
24. Pytlak, R., Suski, D., Tarnawski, T., Zawadzki, T.: Defining and solving hybrid optimal control problems with higher index DAEs. In: Proceedings of the 12th Modelica Conference, Prague, Czech Republic, pp. 265–273 (2017)

Study of the High-Amplitude Solutions in the System of Magnetic Sliding Oscillator with Many Degrees of Freedom

Andrzej Rysak, Magdalena Gregorczyk, Konrad Chwełatiuk and Daniel Gąska

Abstract Magnetic interactions are strongly non-linear, especially for small distances between magnets. Their implementation to the oscillator gives it the ability to display complex non-linear and chaotic behaviours. These phenomena under certain conditions can lead to widening of the vibration bandwidth of the system which in the case of energy harvesting systems increases their efficiency, especially under varying excitation conditions. In this paper we compare the numerical and experimental study of different systems of longitudinal magnetic oscillators with one and many degrees of freedom. Tested oscillator configurations differ in magnet parameters and system rigidity. In systems modelling we look for conditions in which the high-amplitude solutions occur over a wide frequency range. Predictions of models are next verified in experimental investigations.

Keywords Magnetic interactions · Energy harvesting · Nonlinear vibrations Magnetic oscillator

1 Introduction

The system of levitating magnet has a simple design, but due to the nonlinearity of magnetic interactions, their various implementations are characterized by complex dynamics. In one of the first works dedicated to this, Heddle [1] suggested that the arrangement of levitating ring magnets could be used to study the properties of magnetic oscillators. He also pointed out that such magnets allow for stabilization of theirs position by a simple mechanical construction. More recently, Mann and Sims [2] were the first to use such a system to the analytical and experimental exploration of the possibility of improving its energy efficiency through exploiting the nonlinear phenomenon. They have shown that nonlinearity is the source of high-amplitude

A. Rysak (✉) · M. Gregorczyk · K. Chwełatiuk · D. Gąska
Faculty of Mechanical Engineering, Lublin University of Technology,
Nadbystrzycka 36, 20-618 Lublin, Poland
e-mail: a.rysak@pollub.pl

J. Awrejcewicz (ed.), *Dynamical Systems in Theoretical Perspective*,
Springer Proceedings in Mathematics & Statistics 248,
https://doi.org/10.1007/978-3-319-96598-7_24

solutions that can occur over a wide frequency range. However, they pointed out that the mechanical damping of the magnets movement raises the excitation threshold at which the system is induced to the high-amplitude vibrations. Various configurations of the levitating magnet system were tested mainly for energy efficiency. In work [3], the free oscillations of the levitating ring magnet were studied. By comparison with the analytical results, the authors have verified that the magnetic field of large ring magnets is significantly different from the magnetic dipole field. They also noticed that a friction significantly effects the vibrations of the coupled magnets. For a levitating cylindrical magnet and single coil, Santos et al. [4] have developed a semi-analytical model that enables geometric optimization of such a energy harvester system, even prior to design and fabrication. Foisal et al. [5] examined the horizontal and vertical layouts of mechanically connected independent electromagnetic generators. Each generator was built with a levitating cylindrical magnet and coil. The slight modification of the magnets of the individual generators resulted in the widening of the frequency band of the efficient energy harvesting. In this work, mechanical friction was reduced by placing the moving magnets in plastic straws with a smooth outer surface. In turn, Munaz et al. [6] investigated the energy efficiency of a single-coil system with the levitating multi-pole cylindrical magnet. The multi-pole magnet was built as a screwed stack of several magnets arranged in a repelling configuration. Wang et al. [7] analysed a similar levitating system with a stack consisted of two separated magnets. Using the FEM method, they found that the setting of magnets in configuration with opposite pole facing each other produces a stronger magnetic field in their surroundings than in the configuration of setting with the same poles facing each other. Next, they checked that the voltage generated by the device in a more efficient magnetic configuration almost does not change when changing the distance between the magnets.

Current research focuses on the system of several levitating ring magnets arranged in a repelling configuration that can move individually along a vertical plastic tube. The whole is enclosed in a plexiglas tube. At the ends of the tube are attached two fixed magnets which act as magnetic springs. The purpose of this work is to study the dynamics of the system, especially in the mode of high-amplitude vibration. Because the dynamics of such a system depends on many variables and parameters, only the selected results are discussed for the configuration with two moving magnets. The next section presents the system geometry and equations that govern its dynamics as well as the base parameters of the magnets available in reported research. Section 3 describes the details of the measuring system. The experimental results presented in Sect. 4 are divided into two parts. Section 4.1 shows the results directly measured in the experiment and describes the normalization method, which partially eliminates the effect of large changes in excitation amplitude. The next subsection discusses the results of a series of measurements obtained for different values of the system stiffness. Also Sect. 5, dedicated to numerical analysis, has been divided into two parts. Section 5.1 describes the studies of forces acting between magnets. The results obtained are used in the next subsection for the numerical modeling of the investigated system. The last section gives a brief summary of the results.

2 System Geometry and Its Mathematical Description

The investigated one-way magnetic oscillator has a simple mechanical construction. The scheme of the device is sketched in Fig. 1a. The main supporting element is a plastic tube along which movable magnets are located on the low friction sliding sleeves (Fig. 1b). All of the studied magnets were ring type *NdFeB* of *N*35 and *N*38 grades. The tube with movable magnets is enclosed in an outer tubular casing made of transparent plexiglass. Fixed magnets are mounted in the lower and upper part of the casing and act as magnetic springs. The upper fixed magnet is attached to the end of the threaded cylinder and its position can be adjusted by screwing. In this way, the mechanical stiffness of the entire oscillator can be regulated. The inner diameter of the housing pipe is 36 mm. The diameter of the guide tube is 10 mm.

In the modeling, on moving magnets act magnetic forces, gravity, inertia, and damping, whereas friction is not included. In this report, it was adopted the convention of naming magnets with Roman numerals. M_{II} and M_{III} are movable magnets, the first one being the bottom magnet and the other the top one. The bottom and top coils are denoted by C_3 and C_4, respectively. Casing tubes of different lengths could be used in the experiment. The set was used which enabled to change the stiffness of the system L in the range of 50–160 mm. In the case of the considered system with two degrees of freedom, vectors of forces in the reference system associated with the housing of the device are shown in Fig. 2. Based on this figure, the equations of motion of both moving magnets can be written as:

$$\begin{aligned} m_2\ddot{x}_2 &= F_{12}(x_2) - F_{32}(x_3 - x_2) - c_2\dot{x}_2 - m_2 g - m_2 a \\ m_3\ddot{x}_3 &= F_{23}(x_3 - x_2) - F_{43}(L - x_3) - c_3\dot{x}_3 - m_3 g - m_3 a, \end{aligned} \tag{1}$$

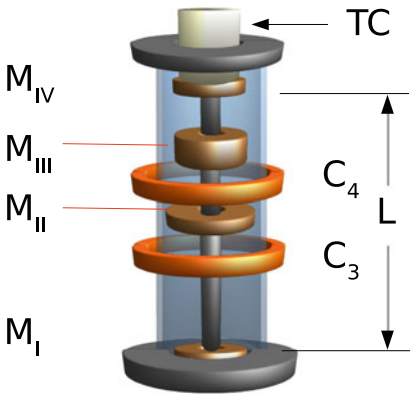

Fig. 1 The scheme of the investigated magnetic slider (**a**), M_1, M_{IV} - magnets fixed to the housing. The position of the M4 magnet determines the stiffness of the system (L). M_{II} and M_{III} - moving magnets, C_3, C_4 - electromagnetic coils, TC - threaded cylinder. **b** magnet $M5$ located on the sliding sleeve

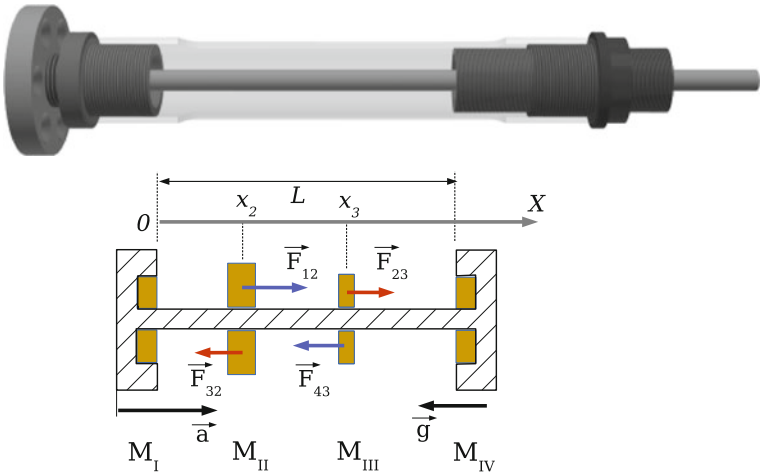

Fig. 2 The frame of the device with the central guide tube is shown in the top drawing. For better readability, no coils and magnets were drawn. The layout of magnets relative to the device frame is sketched in the lower figure, which also shows the forces acting on the moving magnets M_{II} and M_{III}. Acceleration vectors **g** and **a** generally represent gravity and inertia forces. Distance L determines the mechanical stress of the system

Table 1 Magnets markings and their parameters

Magnet	Grade	Mass (kg)	Height (m)	Diameter (m)	Inner diameter (m)
M1	N35	0.02212	0.0050	0.030	0.012
M2	N38	0.01526	0.0060	0.025	0.014
M3	N38	0.02246	0.0080	0.025	0.012
M4	N38	0.02087	0.0080	0.024	0.012
M5	N38	0.04109	0.0160	0.024	0.012
M6	N35	0.05465	0.0145	0.030	0.012

where c_2, c_3 are the damping factors and m_2, m_3 are the masses of both magnets M_{II} and M_{III}, respectively. Several different ring magnets were used in the experimental studies. Their markings and parameters are listed in Table 1. In the model under consideration, we neglect friction and interactions between coils and magnets. With such assumptions, the dynamics of the system is determined by the characteristics of the magnets, the interactions between them, and by the stiffness L. In all conducted tests of the two-degree of freedom system, the magnets $M3$ of Table 1 were used as permanent magnets M_I and M_{IV}. Therefore, to fully specify a particular system configuration, it is enough to give the types of magnets M_{II} and M_{III} as well as the distance L between unmovable magnets. Hence, in the further part of the work the configuration of the system is marked in simplified form, eg: $M5M3 : L90$ or $M5M3$. Where the description of the first magnet ($M5$) relates to the bottom magnet and the second ($M3$) refers to the top magnet. The dimension L is expressed in mm.

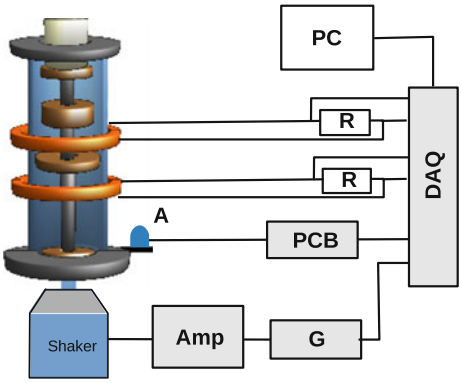

Fig. 3 The scheme of the measuring system. *PC* - computer, *DAQ* - data acquisition card, *R* - coils' loads, *A* - accelerometer, *PCB* - signal conditioner, *G* - voltage generator, *Amp* - shaker amplifier

3 Experiment

The scheme of the experiment is presented in Fig. 3. In the experimental system the following scientific equipment were used: data acquisition card *AdvantechPCI* − 1742*u*, shaker *TIRA TV*51110, shaker amplifier *TIRA BAA*120, function generator *Rigol DG*5071, accelerometer *PCB* 352*C*03 and signal conditioner *PCB* 482*C*05. All measured values are collected by the acquisition card *DAQ* and written by the computer system *PC* with a sampling rate of 10000 S/s per channel. The casing of the device is accelerated by the shaker which is driven by the voltage of generator G. In reported results the generator frequency is programmed to sweep in the range of f_0 to f_k at a constant rate. In all experiments, the amplitude of generator G voltage was constant and equal to 200 mV peak-to-peak. An experimental data processing program calculated the instantaneous values of frequencies based on a time-dependent generator voltage. The A accelerometer measured the acceleration of the casing. Both identical coils were loaded with resistances R having an optimal values for the generated electric power. In the system with small 'L' (high stress) both magnets are moved downward. As a result, they are located near the bottom coil and far away from the upper one. For this reason, the voltage generated in the upper coil is much smaller than the voltage of the bottom coil, what is clearly visible in the measurement results.

4 Experimental Results

4.1 Data Normalization

The small maximum shaker force (100 N) and the relatively large mass of the test system (0.880 kg) cause large variations in the excitation amplitude in the measurement mode in which the voltage controlling the shaker amplifier has a constant amplitude at varying frequency. Figure 4a shows changes in the excitation amplitude

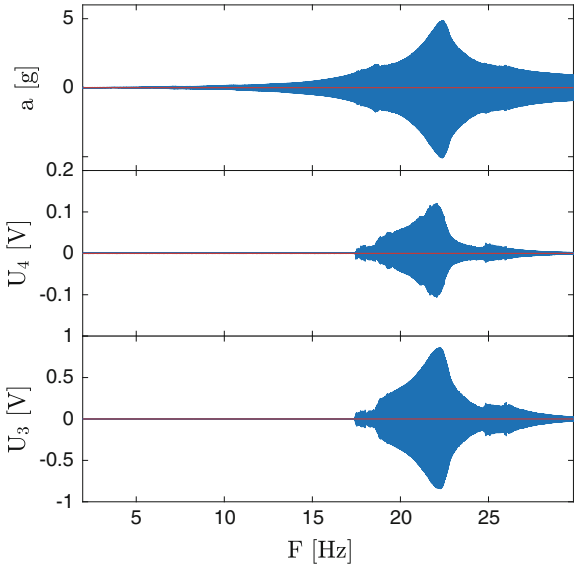

Fig. 4 Changes in the excitation amplitude along with the frequency variation (a). The power generated by the coils: top (U_4) and bottom (U_3) as a function of frequency. The system configuration: $M5M4 : L80$

along with the frequency variation for the system configuration $M5M4 : L80$. This strongly affects the quantitative and qualitative results obtained from the nonlinear system. Therefore, the experimental data has been processed in such a way as to reduce the effect of non-stationary excitation and to show how the electric power generated in the coils varies with respect to the square of the excitation acceleration unit. For this purpose, the following conversions were made. Firstly, the window was moved along the time axis with discrete values corresponding to the measuring points. The width of the window equals n points on time axis and the length of the shift step is Δt_s. Next, for each window was calculated the square of the standard deviation of the excitation σ_a^2 which was expressed in $(\mathrm{m/s^2})^2$. For both coil voltages, the average normalized electrical power in the window was calculated according to the formula:

$$\overline{P} = \frac{1}{nR\sigma_a^2} \sum_{i=1}^{n} U_i^2, \tag{2}$$

where σ_a is a standard deviation of excitation acceleration. The results of these transformations for the system configuration $M5M4 : L80$ are presented in Fig. 5. where $\overline{P}_3$ and $\overline{P}_4$ are normalized powers generated on the bottom and top coil, respectively. The curves in Figs. 5 were obtained by moving the time window of width 0.1 s with a shift step $\Delta t_s = 0.05$ s in the time range corresponding to a frequency change of $f_0 = 2$ Hz to $f_k = 30$ Hz. The final curves show how the mean power generated in the coil changes with the frequency, relative to the square of the excitation unit. The results obtained in this way for different system configurations are compared and analysed in the next subsection.

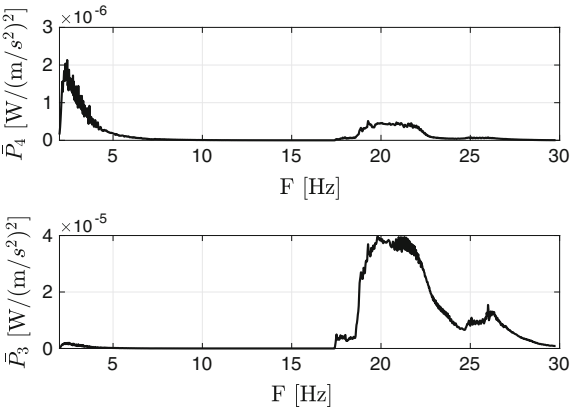

Fig. 5 Changes in amplitude of shaker excitation (a) and coil voltages ($b - c$) depending on frequency. The system configuration: $M5M4 : L80$

4.2 Influence of the System Stiffness on Generated Power

One-way magnetic oscillator dynamics study was performed for several magnets and stiffness configurations (different pairs of magnets and values of the stiffness L). The dynamics of the magnets and the energy efficiency of the system clearly depend on its specific configuration. The experiments were performed in series. For each pair of magnets a number of measurements were carried out for different values of system stiffness as this is one of the most important parameters on which the oscillator dynamics depends. Here, is applied a convention whereby the results of each series are presented on a common $3D$ chart, separately for each coil.

Out of many of the obtained results, two particular are discussed in this work.The first one, obtained for a one-magnet system and the second for the system with two relatively heavy magnets differing in mass. As a point of reference for further study, the results obtained for a single magnet configuration were assumed. The $M5$ magnet was chosen for this study. Next, are presented the measurement results of the system in the $M6M5$ configuration.

The measuring results obtained for the bottom coil in the tests of the one-magnet system when the stiffness was changed from $L = 60$ mm to $L = 160$ mm are shown in Fig. 6. The average power values $\overline{P}$ were obtained by normalizing the measured power with respect to the square of the acceleration unit in accordance with the formula (2). As it is seen, in this basic measurement series the average power has significant values only in a narrow range of a high system stiffness ($L = 60$–70 mm). In this range of stiffness, a broadband power spectrum with maximum values of about 5×10^{-4} mW/(m/s^2)^2 was registered. A clear resonance peak of a maximum value equals to approximately 2×10^{-3} mW/(m/s^2)^2 (for $L = 70$) is superimposed on the broad spectrum and decreases with increasing system stiffness.

In the next series of measurements, the $M5M6$ magnets configuration was tested for different stiffness and frequency values. The $M6$ (top) magnet is heavier than the bottom one. Obtained results after normalization are shown in Fig. 7. Comparing

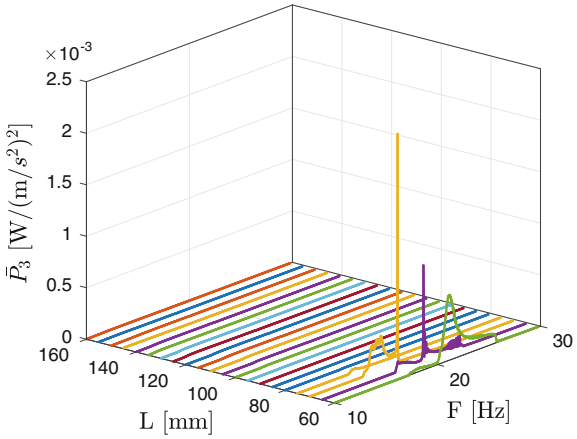

Fig. 6 Average power of the bottom coil for the one-magnet ($M5$) system

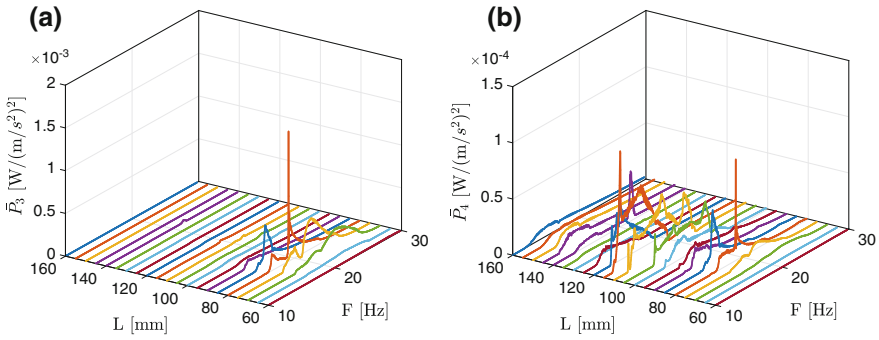

Fig. 7 Power of the bottom (**a**) and top (**b**) coils. System in configuration with two magnets different in mass: M5 - bottom, M6 - top. The M6 magnet is heavier than the M5 magnet

these results with previous ones (obtained for $M5$ configuration) shows that the lower coil generated higher power in a wider range of stress and frequency. In both coils, narrow and high power peaks were detected under various experimental conditions. The top coil generated less power due to its non-optimal position. However, this coil generated relatively high average power in almost full range of the system stiffness. Particularly high energy efficiency in a very wide frequency band was measured for a range of stiffness L from 105 to 120 mm.

The discussed here selected experimental results demonstrate the possibility of modifying the characteristics of the tested system by easy modification of its configuration. Changes of magnets type and in the system stiffness strongly affect the frequency band in which high-amplitude magnets vibrations occur.

5 Numerical Results

5.1 Characterization of Magnetic Forces

Numerical studies of the oscillator require knowledge of the relationship between magnetic force and distance $F(x)$ for all magnets pairs of the system. In this section the experimental results of F(x) measurements for different magnets configurations are presented and discussed. Based on the measured characteristics $F(x)$ analytical formulas describing the interaction between pairs of magnets were derived. Let us start with the mathematical description of the forces acting between the magnets with the equation:

$$F(x) = A\left(\frac{1}{x^2} + \frac{1}{(x+2h)^2} - \frac{2}{(x+h)^2}\right), \tag{3}$$

which was developed in [8] to describe the magnetic interaction between two identical cylindrical magnets oriented coaxially and located at a considerable distance from each other. h is the height of each one. In the present study, magnetic forces characteristics were determined experimentally by using special stand (Fig. 8). In contrast to the case described by (3), the examined magnets are of ring type and have different diameters and heights. Moreover, during high amplitude vibrations, they can come close together at short distances. Therefore, the formula suitable for the applied magnets was sought by testing several expressions similar to (3). Many of the conducted fitting tests had shown that the best formula describing this interaction for different pairs of ring magnets is as follows:

$$F(x) = A\left(\frac{1}{(x+2h)^2} - \frac{b}{(x+h)^2}\right), \tag{4}$$

where A, b, and h are three fitting parameters. The proposed form is simpler than the starting one (3) and gives satisfactory results for the different pairs of ring magnets. Figure 9 shows the results of fitting (4) to the experimental points for three different configurations of magnets: two identical ($M1M1$) (a), smaller lightweight - bigger heavier ($M1M6$) (b), and two heavy, differing in masses and dimensions ($M5M6$) (c). The fitting process gives back values of all three parameters (A, b, h).

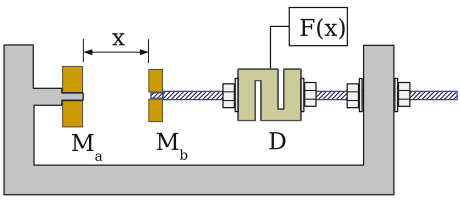

Fig. 8 A stand for measuring the interactions between magnets. D - dynamometer

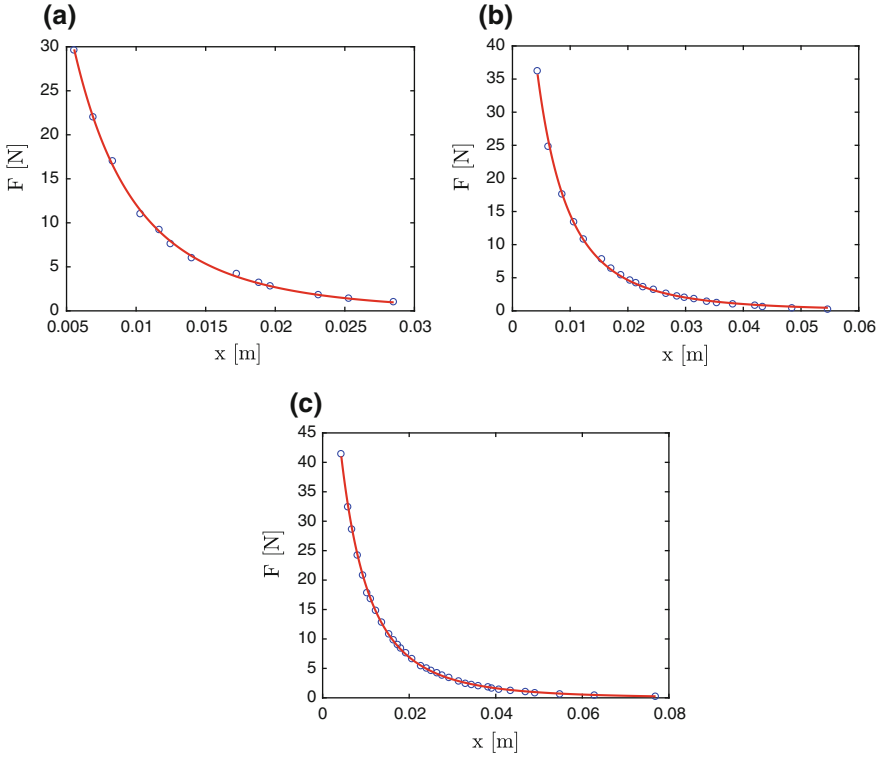

Fig. 9 Results of fitting (4) to the experimental points for three different configurations of ring magnets pairs: **a** two identical lightweight ($M1M1$), **b** one lightweight and one heavy ($M1M6$), and **c** two heavy differing in mass ($M5M6$)

Values of the fitting parameters obtained for all measured characteristics of interactions between pairs of magnets are listed in Table 2. Designated interactions between magnets enable modeling of all these system configurations for which the needed forces $F_{ij}(x)$ (in (1)) are known.

The analytical formula adopted in this article to describe magnetic interactions is an alternative to other approaches, such as, for example, the polynomial dependence used by Kęcik [9] in the study of a similar system with one cylindrical magnet and one coil. The basics of magnetism and magnetic interactions are described in detail in Chap. 3 of monograph [10].

5.2 *Modeling*

Simulations of the dynamics of magnets described by equations (1) were made using MATLAB program and the *ode*45 solver. In the experimental studies, the amplitude

Table 2 Parameters of fitting of the curve described by (4) to the results of magnetic force measurements for different pairs of magnets

Bottom magnet	Top magnet	A (Nm^2)	b	h (m)
M1	M1	−0.010380	0.8292	0.006321
M1	M2	−0.003943	1.0190	0.006362
M1	M3	−0.005694	1.0470	0.007754
M1	M6	−0.010990	0.9385	0.009027
M2	M3	−0.004534	0.9872	0.006912
M2	M6	−0.004730	1.1720	0.007290
M3	M4	−0.002459	1.4970	0.005472
M3	M5	−0.004790	1.3290	0.006634
M3	M6	−0.010280	1.0050	0.008740
M4	M5	−0.007051	1.0710	0.007484
M4	M6	−0.011010	0.9525	0.009923
M5	M6	−0.020640	0.8725	0.012200

of the acceleration was frequency dependent. As was mentioned out, the dynamics of a nonlinear systems also depends on the excitation amplitude. Wherefore, presented in this paper numerical calculations were made for two different excitation modes. In the $a10$ mode, which simulates the typical results of an experiment with excitation control, the excitation acceleration amplitude had a constant value of 10 m/s^2. In the *aEXP* mode the amplitude of the excitation acceleration was changed with frequency in the way according to the function $a(F)$ which is the experimental excitation profile obtained from the measurement of the system in the $M5M6L075$ configuration. Therefore, in further numerical research were used parameters with values corresponding to this reference experimental settings. As a result, the numerical analysis can be narrowed down to the study of changes of the magnets dynamics that follow the variation of both viscous damping coefficients (c_2, c_3). The purpose of these analyses is to examine how the dynamics of the system depends on the viscous damping coefficients and to determine their values in the measured reference configuration.

Normalized powers obtained experimentally for $M5M6L075$ system are presented in Fig. 10. Figure 11 shows the excitation amplitude profile which was derived from this measurement. For both excitation modes, numerical calculations were performed for the decreasing values of viscous damping coefficients (c_2, c_3) of both magnets. Since the difference in values between the two damping coefficients less influence the dynamics of the magnets than their values, it was assumed that both coefficients have the same value in the all discussed numerical tests. Based on the results obtained from modeling, the kinetic energies of both magnets are calculated. The kinetic energy of the magnet is proportional to the square of its velocity, and the power generated on the coils is in turn proportional to the square of the voltage. Since the rate of change of the magnetic flux passing through the coil depends on the speed of the magnet (nonlinearly), Faraday's equation $\mathscr{E} = -\dot{\Phi}$ transfers this

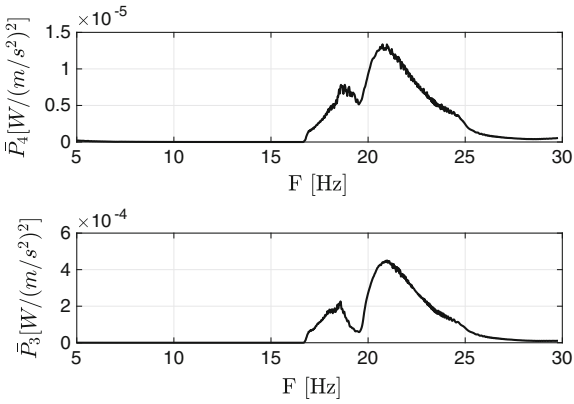

Fig. 10 Normalized average power of $M5M6L75$ oscillator as a function of frequency. $\overline{P}_3$ - power generated by the bottom coil, $\overline{P}_4$ - by the top one

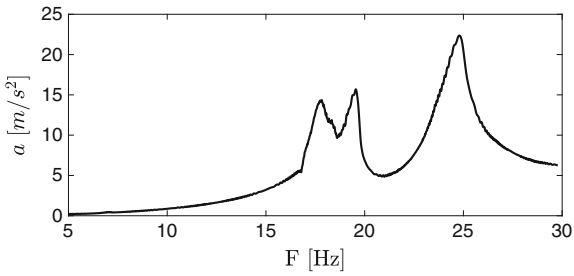

Fig. 11 Profile of the excitation acceleration amplitude as derived from measurement of the system in $M5M6L075$ configuration

relation to the relation between the kinetic energy of the magnet and the electric power generated in the coil. Although comparable variables (E_k, P) are not directly and linearly dependent, both are closely related to vibrations of the magnets. For both modes of numerical simulations: $a10$ and *aEXP*, the calculated energy on time dependencies were normalized in the same way as the powers measured in experiments. $\overline{E}_2$ and $\overline{E}_4$ are the average normalized kinetic energies of the bottom and top magnets, respectively.

Modeling results of the system excited in the $a10$ mode are shown in Fig. 12. The average normalized vibration energy of the bottom magnet ($\overline{E}_2$), obtained for c = 0.3, represents the excitation peak in the narrow frequency band, approximately from $F = 12.5$ to $F = 14.5$ Hz. Comparing it with the results obtained experimentally, it can be seen that the high-amplitude vibration bandwidth obtained in the measurement is clearly wider. Moving towards the lower c-values, it is observed systematic increase of the high-amplitude frequency band. The left limit of the band does not change its value; the extension of the band is made by shifting the right boundary towards higher frequency values. In the case of 'c', the frequency band of the high-amplitude vibrations is comparable to the band recorded experimentally. In parallel with the decreasing of the damping coefficients' values, there is an increase in the vibration energy of the magnets. Analysing changes in the numerical results

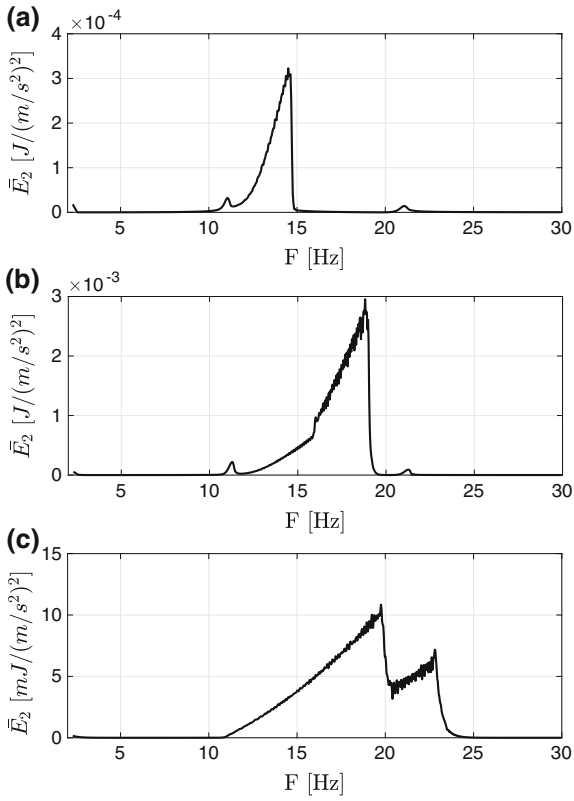

Fig. 12 The average energy of the bottom coil obtained in simulations of system *M5M6L075* for $c = 0.3$ Ns/m (**a**), $c = 0.1$ Ns/m (**b**), and $c = 0.03$ Ns/m (**c**). Please note that the energy of the *Y* axis in case (c) is scaled in *mJ*

obtained in the *aEXP* excitation mode with the decrease in the damping coefficient c (Fig. 13), it can be noticed that the high-amplitude vibrations frequency band evolve in the similar way as is observed in the $a10$ excitation mode. Right boundary of the high-amplitude frequency band is moving toward higher frequencies, giving a clear increase of the bandwidth. The result (c) obtained for $c = 0.03$ Ns/m is very similar to the experimental result, not only due to the approximately the same width of the excitation band, but also to the qualitatively similar changes of energy (in model) and power (in experiment) with frequency.

By analysing the presented numerical results obtained for both excitation modes, there are some general changes in dynamics of the system under consideration. Presented curves of energy on frequency dependencies make it possible to observe that the reduction of the viscous damping coefficients causes new vibration modes to rise at higher frequencies. Figure 12a shows one weak mod in the frequency range from 12 to 14 Hz. The second mod appears in case (b) in the range of 14–19 Hz and its vibrations have much higher values of energy. Figure (c) shows another strong mod that grows in the range of 20–23 Hz. Results obtained for $a10$ excitations mode differ from these calculated for *aEXP* mode because of the nonlinearity of the

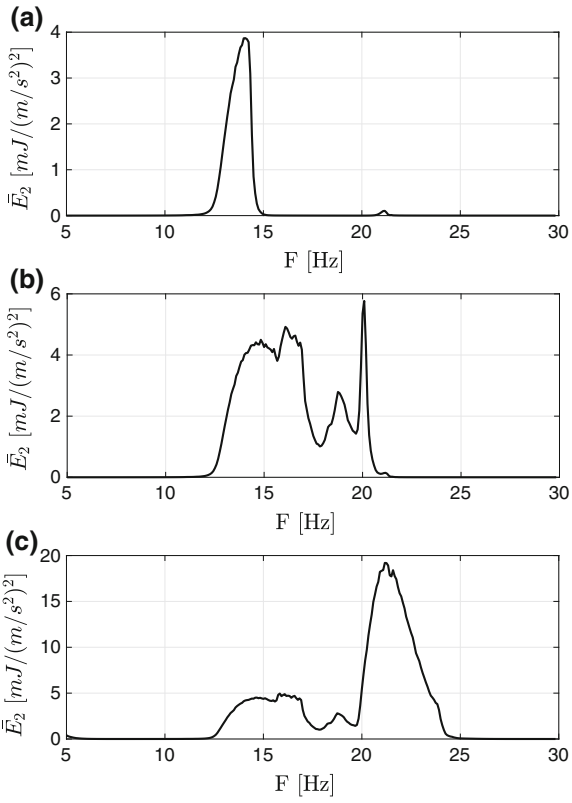

Fig. 13 Energy of the bottom coil obtained in simulations of system *M5M6L075* for $c = 0.3$ Ns/m (**a**), $c = 0.1$ Ns/m (**b**), and $c = 0.03$ Ns/m (**c**)

system. But still, a similar tendency for new mods to appear, with reducing values of damping coefficients, is noticeable. Based on this observation, it can be assumed that the further reduction of the damping coefficient will generate additional modes of high amplitude vibrations at higher frequencies. In order to prove this, numerical calculations were performed, for which the values $c = 0.02$ were assumed for both damping coefficients. The results obtained (Fig. 14) confirm this assumption. New vibration mode appeared in the frequency range from 25 to 30 Hz.

The numerical tests described in this section dealt with a system with the selected magnets configuration and a fixed stress value. They focused mainly on the study of the effect of viscous damping on the dynamics and effectiveness of the system. Comparison of numerical results (Fig. 13c) with experimental (Fig. 10) shows their apparent qualitative similarity. As was shown by the conducted tests, viscous damping greatly influences the dynamics of the system. This may indicate that the system is also sensitive to change in sliding friction occurring in the movement of the magnets but the considered model does not take it take into account. Incorporation of the friction into modeling should bring significant modifications that will make the numerical results more closely matched to real ones.

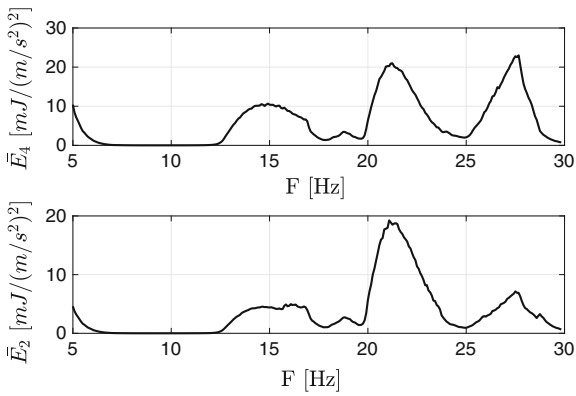

Fig. 14 Numerical results obtained for the considered system with $c = 0.02$ Ns/m. Decreasing the damping coefficient extends the range of effective vibrations up to 30 Hz

6 Conclusions

The paper presents the results of investigation of the one-way magnetic oscillator, with the possibility to easily modify its various parameters, including the number of degrees of freedom. The experimental part of the work shows changes in the dynamics of the system following variations in the configuration of magnets, system stiffness as well as in the amplitude and frequency of excitation. The results change considerably under the influence of system modifications. The numerical research focus on the system with two degrees of freedom. Characteristics of interactions between magnets were determined experimentally and the relevant relationships approximated by (4) were used in modeling. Experiments were performed without control of the excitation level, so the procedure for normalizing the results against the square of the acceleration unit was performed. To allow comparison of the experimental and numerical results some of calculations were made using the excitation profile $a(F)$ which was measured in the corresponding experiment.

The results show that reducing viscous damping leads to an increase in vibration energy and a widening of the frequency band in which the vibrations have a high amplitude. In addition, the comparison of numerical results with experimental data allowed to estimate the value of viscous damping of the real system.

The carried out analysis concerned only a narrow range of parameters selected among many which influence the properties of the system. Obtained results show that the frequency range of high-frequency vibrations and hence the dynamics and efficiency of the system are altered not only by damping and friction but also by several other factors and parameters related to the magnets configuration and system rigidity. That's why the tested device, despite the simplicity of its construction, is well suited for the applications where the control and tuning capabilities are of particular importance.

Acknowledgements This work was supported by the Polish National Science Center under the grant Agreement No. DEC-2013/11/D/ST8/03308.

References

1. Heddle, D.W.O.: Oscillators using ring magnets. Phys. Educ. **5**, 244–245 (1970)
2. Man, B.P., Sims, N.D.: Energy harvesting from the nonlinear oscillatins of magnetic levitation. J. Sound Vib. **319**(1–2), 515–530 (2009)
3. Kewei, L., Jiahuang, L., Yang, K.Z., Liang, S.Y.W., Juan, J.W.S.: The vertical oscillations of coupled magnets. Eur. J. Phys. **32**, S1–S14 (2011)
4. Soares dos Santos, M.P., Ferreira, J.A.F., Simões, J.A.O., Pascoal, R., Tarrão, J., Xue, X., Furlani, E.P.: Magnetic levitation-based electromagnetic energy harvesting: a semi-analytical non-linear model for energy transduction. Sci. Rep. **6**, 18579 (2016). https://doi.org/10.1038/srep18579
5. Foisal, A.R., Hong, C., Chung, G.-S.: Multi-frequency electromagnetic energy harvester using a magnetic spring cantilever. Sensor. Actuators A Phys. **182**, 106–113 (2012)
6. Munaz, A., Lee, B.-C., Chung, G.S.: A study of an electromagnetic energy harvester using multi-pole magnets. Sensor. Actuators A Phys. **201**, 134–140 (2013)
7. Wang, W., Cao, J., Zhang, N., Lin, J., Liao, W.-H.: Magnetic-spring based energy harvesting from human motions: design, modelling and experiments. Energy Convers. Manage. **132**, 187–197 (2017)
8. Vokoun, D., Beleggia, M., Heller, L., Sittner, P.: Magnetic interactions and forces between cylindrical permanent magnets. J. Magn. Magn. Mater. **321**, 3758–3763 (2009)
9. Kęcik, K.: Energy recovery from a non-linear electromagnetic system. Acta Mech. Autom. **12**(1), 11–18 (2018)
10. Awrejcewicz, J., Lewandowski, D., Olejnik, P.: Dynamics of Mechatronics Systems. Modeling, Simulation, Control, Optimization and Experimental Investigations. World Scientific Publishing, Singapore (2017)

Theoretical Investigations on the Behavior of Artificial Sensors for Surface Texture Detection

Moritz Scharff, Maximilian Darnieder, Joachim Steigenberger, Jorge H. Alencastre and Carsten Behn

Abstract Animal vibrissae are used as natural inspiration for artificial tactile sensors, e.g., the mystacial vibrissae enable rodents to perform several tasks in using these tactile hairs: object shape determination and surface texture discrimination. Referring to the literature, the Kinetic Signature Hypothesis states that the surface texture detection is a highly dynamic process. It is assumed that the animals gather information about the surface texture out of a spatial, temporal pattern of kinetic events. This process has to be analyzed in detail to develop an artificial tactile sensor with similar functionalities. Hence, we set up a mechanical model for theoretical investigations of the process. This model is analyzed in two different directions using numerical simulations: at first a quasi-static and then a fully dynamic description.

Keywords Vibrissa · Tactile sensing · Surface texture · Friction · Dynamical model

M. Scharff
Department of Mechanical Engineering, Technische Universitt Ilmenau,
Max-Planck-Ring 12, 98693 Ilmenau, Germany
e-mail: moritz.scharff@tu-ilmenau.de

M. Darnieder
Department of Mechanical Engineering, Technische Universitt Ilmenau,
Gustav-Kirchhoff-Platz 2, 98693 Ilmenau, Germany
e-mail: maximilian.darnieder@tu-ilmenau.de

J. Steigenberger
Institute of Mathematics, Technische Universitt Ilmenau,
Weimarer Straße 25, 98693 Ilmenau, Germany

J. H. Alencastre
Department of Engineering, Pontificial Catholic University of Peru,
Avenida Universitaria No 1801, San Miguel, Lima, Peru
e-mail: jalenca@pucp.edu.pe

C. Behn (✉)
Department of Engineering and Natural Sciences, Merseburg University
of Applied Sciences, Eberhard-Leibnitz-Straße 2, 06217 Merseburg, Germany
e-mail: carsten.behn@hs-merseburg.de

J. Awrejcewicz (ed.), *Dynamical Systems in Theoretical Perspective*,
Springer Proceedings in Mathematics & Statistics 248,
https://doi.org/10.1007/978-3-319-96598-7_25

1 Introduction

The mystacial vibrissae are part of the somatosensory system of rodents. They are powerful tactile sensors. Using these sensors, the animals can detect the distance to an object and recognize the object's shape. Furthermore, the surface texture of the object can be detected also [3]. Each mystacial vibrissa is characterized by a generic geometric shape, e.g., a slender conical body, an inherent pre-curvature and is supported by its own elastic follicle-sinus complex (FSC) [14]. The FSC includes various types of mechanoreceptors to transduce the mechanical stimuli around the vibrissa shaft to a neuronal potential for further processing at the neuronal level [17]. All mystacial vibrissae are arranged in a fixed spatial pattern, on both sides of the animal's muzzle [5]. With this sophisticated sensory system the mentioned tasks can be performed on a high level, e.g., surface texture elements down to a size of 30 μm can be identified [4].

For the procedure of surface texture detection there are two hypotheses: The *Resonance Hypothesis* relates the surface information to a vibro-tactile signal in the FSC, this signal is scaled by the natural frequencies of the different vibrissa [7]. Following, the *Kinetic Signature Hypothesis*, a surface texture is coded in a sequence of velocity and acceleration events depending on time. So, surface texture detection is a dynamical process [1, 16]. To design an artificial tactile sensor for surface texture detection inspired by the natural mystacial vibrissa, the process is analyzed out of the mechanical point of view. The authors of [13] discretize the vibrissa within the limits of the Finite-Element Method as a straight, cylindric, linear elastic beam and model the surface in representation of a spatial distribution of spaces and gaps. Here, the support of the beam is quasi-statical displaced, all inertial effects are neglected. In [8], a quasi-static motion is assumed, too. Using a Multi-Body System, the beam has a tapered shape with an inherent pre-curvature. In a further step, the authors include inertial effects and damping [9]. Both works analyze the initial contact with an object and not the process of surface texture detection. For this case, the quasi-static simulation matches the dynamic one for a very slow displacement of the support of the beam. Another approach is done in [15]: the cylindrical, inherent per-curved Euler-Bernoulli beam is loaded by a periodic time-varying force. The force acts at the beam's tip and represents the surface texture. This model is analyzed in context to parametric resonance of the beam and corresponding amplification of the signals at the support of the beam. The connection between the acting force and properties of the surface texture, like friction, is not analyzed. In [2], the natural vibrissa is assumed as Euler-Bernoulli beam respecting large deflections under quasi-static conditions. These large deflections are superposed with small deformation induced by vibrations. The surface is characterized by a fixed pattern of spaces and gaps. The contact between beam and surface is a point contact underlying the influence of Coulomb's Law of friction. The information for the surface texture is only generated out of the macroscopic effects of the spaces and gaps. Friction is assumed as a disturbance and not as source of information. The work [12] focuses on the coefficient of static friction as source of information for the surface texture. The vibrissa is modeled

within the limits of the nonlinear Euler-Bernoulli beam theory and has a straight, cylindrical shape. The beam is one-sided clamped and touches the surface at the other side. Between beam tip and surface there is a point contact. The contact forces result out of Coulomb's Law of friction. The clamping is displaced quasi-statically, out of the resulting support reactions the coefficient of static friction can be determined. This model is advanced and further analyzed in [10, 11] and is the starting point for the present work.

All mentioned examples analyze different aspects of surface texture detection. But, there is no information if the quasi-static simulations consider all effects of the dynamic process for the procedure of surface texture detection. Considering one example, this work discusses the limits of validity of the quasi-static simulation and the need of full dynamic simulations. First, the different simulations are introduced in Sect. 2. In Sect. 3, the simulations are compared for different parameter sets. The differences between the simulations are discussed. Finally, Sect. 4 summarizes the results.

2 Modeling

Three different types of numerical simulations are used to analyze the process of surface texture detection. First, the vibrissa is modeled as an Euler-Bernoulli beam with continuum behavior, respecting large deflections and a quasi-static displacement (QS), see Sect. 2.1. To consider all dynamic effects of the process, the vibrissa is approximated as a Multi-Body system (MBS), see Sect. 2.2 and with the Finite-Element-Method (FEM) as well, see Sect. 2.3. Since both ways of approximation include different peculiarities and effects, every parameter set is performed with both types.

For all simulations, the process of surface texture detection is assumed as follows:

- The vibrissa is modeled as slender, straight (length L), cylindrical (diameter d) beam.
- The FSC is simplified to a clamping.
- The contact between vibrissa and surface is assumed as a point contact within the limits of Coulomb's Law of friction (1) at the point (x_L, y_L).

$$\tan(\alpha) = \frac{|F_x|}{|F_y|} = \mu \leq \mu_0 = \tan(\alpha_0) \tag{1}$$

- In the initial position, the beam is bent and in contact with the surface (clamping to surface distance η). Hence, the contact force consists only of a vertical component.
- Out of the initial position, the clamping gets translationally displaced against the beam's curvature. The beam's tip is sticking to the surface until the coefficient of static friction μ_0 is reached.

Table 1 System parameters

d (m)	L (m)	$E\left(\frac{\mathrm{N}}{\mathrm{m}^2}\right)$	$G\left(\frac{\mathrm{N}}{\mathrm{m}^2}\right)$	$\rho\left(\frac{\mathrm{kg}}{\mathrm{m}^3}\right)$	η (m)
$4e^{-4}$	0.1	$0.211e^{12}$	$0.769e^{11}$	$0.785e^{4}$	0.09

- After sticking, the tip starts to slide over the surface and is loaded by a friction force in dependence on the kinetic friction coefficient μ_k.
- During the procedure, the reaction forces and moments are gathered and used the characterize surface properties.

The parameters in Table 1 are used for every simulation.

Remark 1 The following brief description of the three models gives no overview of all details, considered in the simulations. Only the most important facts are reported.

2.1 Continuum System (QS)

Since, there is a quasi-static displacement of the clamping the outer equilibrium state (2) is given for all times with:

$$\left.\begin{array}{rlll} \rightarrow: & F_x + f_x & = 0 & \Longleftrightarrow F_x = -f_x \\ \uparrow: & F_y + f_y & = 0 & \Longleftrightarrow F_y = -f_y \\ \circlearrowleft: & M_z + f_y \cdot x_L - f_x \cdot y_L & = 0 & \Longleftrightarrow M_z = -f_y \cdot x_L + f_x \cdot y_L \end{array}\right\} \tag{2}$$

with: $f_x = \sin(\alpha) \cdot f \quad ; \quad f_y = -\cos(\alpha) \cdot f$

According to the nonlinear Euler-Bernoulli beam theory, the following nonlinear system of Eq. (3) describes the elastic line of the beam, see Fig. 1b:

$$\left.\begin{array}{l} x'(s) = \cos(\varphi(s)) \\ y'(s) = \sin(\varphi(s)) \\ \varphi'(s) = \dfrac{f}{E \cdot I_z} \left(\sin(\alpha)\,(y(s) - y_L) + \cos(\alpha)\,(x(s) - x_L)\right) \end{array}\right\} \tag{3}$$

with I_z as second moment of area and the boundary conditions (4):

$$\left.\begin{array}{lll} x(0) = x_0 & ; & x(L) = x_L \\ y(0) = 0 & ; & y(L) = y_L \\ \varphi(0) = \dfrac{\pi}{2} & ; & \varphi(L) = \varphi_L \end{array}\right\} \tag{4}$$

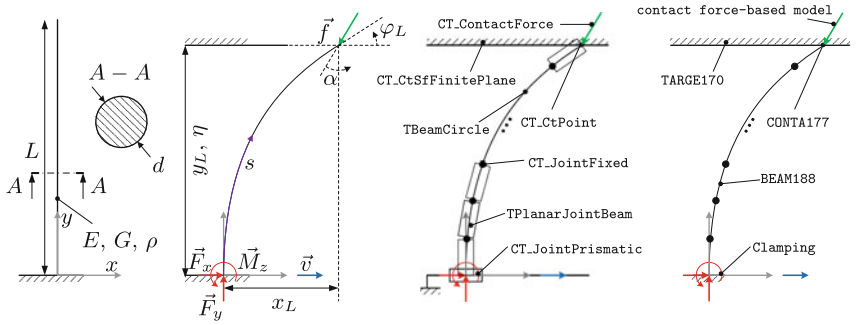

Fig. 1 Beam models: **a** illustates the model without load; **b** shows the QS model and related parameters; **c** summarizes the used elements for the MBS model and **d** for the FEM model; all with E as Young's modulus, G as shear modulus, ρ as density and v as velocity

A sequence of $x_0 = 0 : \Delta x_0 : x_{0_{max}}$ is given for the quasi-static displacement. For every increment Δx_0, (3) is solved. The clamping is displaced until the given μ_0 is reached. In this state, the beam tip starts so slide over the surface. Also, this movement is assumed as a quasi-static one. Here, a sequence of $x_L = x_{L_{initial}} : \Delta x_L : x_{L_{max}}$ is used under the influence of μ_k, while $\mu_k < \mu_0$. The beam tip slides until the present friction force prevents a further movement and a new period of sticking starts.

2.2 Multi-Body System (MBS)

For the MBS simulation the software *ALASKA v.9.1* is used. Figure 1c shows the used elements incorporated in the software and their arrangement. The MBS model consists of 10 beam elements while one beam element consists of various rigid bodies, torsional springs and normal springs, in turn. The beam element is based on the Euler-Bernoulli beam theory. The beam elements are connected by fixed joints. The contact elements are realized by a point contact at the tip of the beam, along the central axis and a contact plane as representation of the surface. The contact between these two elements is subjected to friction and characterized by corresponding forces. To switch from μ_s to μ_k the *magic formula* is used. Using a prismatic joint, the clamping of the beam is displaced.

2.3 Finite-Element System (FEM)

The FEM simulation is done using *ANSYS 16.0*. The beam is discretized with 100 beam elements respecting the Timoshenko-Beam theory and a quadratic shape func-

tion. The mass properties are considered by the consistent mass matrix. Using the contact and target elements (Fig. 1d) the contact is subjected to friction an related forces, again. Here, the switch from μ_s to μ_k is implemented by a *jump function* incorporated into the software.

2.4 Verification

The verification of the three models is done with respect to three criteria:

- large deflection (nonlinear theory) of the tip of the beam under a direction preserving load at the beam tip, see Fig. 2,
- large deflection (nonlinear theory) of the tip of the beam under a angle preserving load at the beam tip, see Fig. 3,
- the first three eigenfrequencies of the vibrations with small amplitude (linear theory), see Fig. 4.

The three criteria are chosen to show that the large deflection of the beam as well as the dynamic properties are nearly equal for all three models. All model properties are identical to the given information in the previous section. Only, the loaded and the boundary conditions are modified. For the verification, the beam is one side clamped and the beam tip is loaded, free, respectively. Three different magnitudes for load and the first three eigenfrequencies are considered.
The first criterion is analyzed in Fig. 2. The deflection of the beam tip under a direction preserving load shows a good matching of the different models for all three forces.

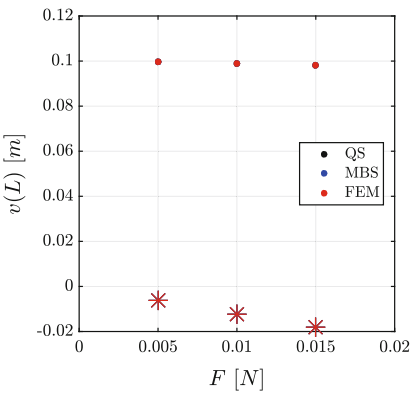

(a) Deflection $v(L)$ of the beam tip.

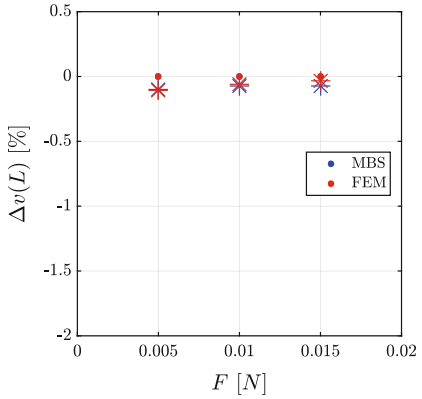

(b) Relative deviation of $v(L)$.

Fig. 2 Part **a** shows the total deflection $v(L)$ of the beam tip that is loaded with a direction preserving force. Part **b** shows the corresponding relative deviation of the solution with the MBS- and FEM model to the QS model. The symbol "·" marks a deflection of the tip in x-direction, an "$*$" one in y-direction

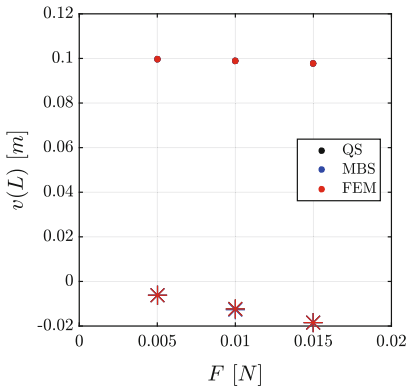

(a) Deflection $v(L)$ of the beam tip.

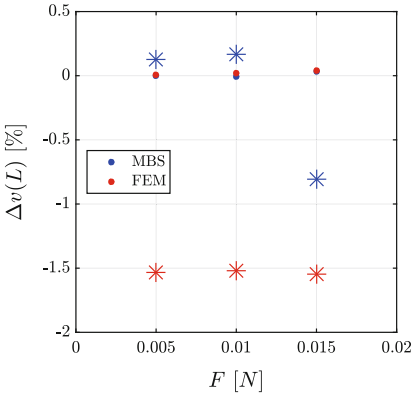

(b) Relative deviation of $v(L)$.

Fig. 3 Part **a** shows the total deflection $v(L)$ of the beam tip that is loaded with a angle preserving force. Part **b** shows the corresponding relative deviation of the solution with the MBS- and FEM model to the QS model. The symbol "$\cdot$" marks a deflection of the tip in x-direction, an "$*$" one in y-direction

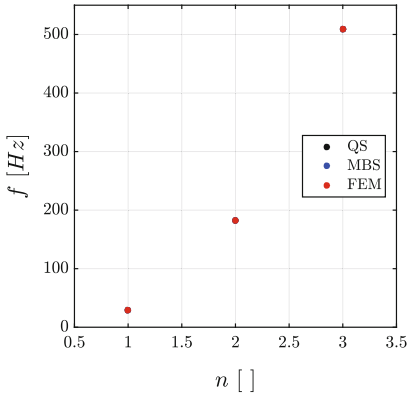

(a) Total values of the eigenfrequencies.

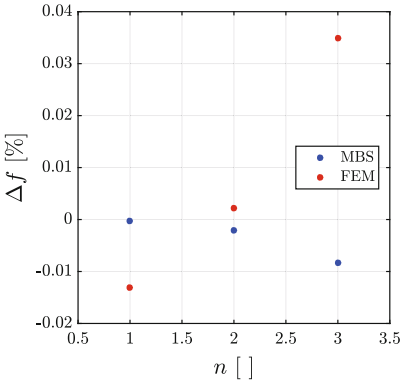

(b) Relative deviation of the eigenfrequencies.

Fig. 4 Part **a** shows the total values for the eigenfrequencies of all three models. Part **b** illustrates the relative deviation of the solution with the MBS- and FEM model to the continuum model

The results for the case of the angle preserving load are more divergent, see Fig. 3. Especially in the case of the FEM model there is a constant deviation to the QS model. The MBS model matches the QS model in a good way, exclusive for the largest force. There are several possibilities to explain this deviation, but since they are still small they are acquiesced.

Remark 2 For the MBS simulation it has to be noted, that $v(L)$ is alternating in a small range. The mean value of this alternating signal is used for the verification.

Figure 4 illustrates the results for the first three eigenfrequencies. The total values for all models and corresponding eigenfrequencies are nearly equal. The values for the MBS model are smaller than the one for the QS model. In contrast to the well known fact that eigenfrequencies determined by FEM are larger than the one of the continuum model, the first eigenfrequency of the FEM model is smaller than the one of QS model. This is caused by the fact that the continuum model is an Euler-Bernoulli beam and the FEM model a Timoshenko one [6]. This discrepancy counteracts the effect of the discretization method itself.

Summarizing the verification, all three models matches in a sufficient way the chosen verification criteria.

3 Simulations

Performing the simulations, the signals at the clamping are shown in Fig. 5. Starting with a sticking phase, the typical behavior of the stick-slip effect is in evidence. Qualitatively, there is a good matching of the signals.

In the case of the amplitude of the signals, they are smaller for the QS model than for the MBS- and FEM one. The MBS- and FEM model are nearly equal.

In contrast, for the stick-slip frequency there is a discrepancy. The discrepancy between the QS model and the other ones is caused by the influence of v. For larger v there are higher stick-slip frequencies, see Table 2. For the offset between the MBS- and FEM model there are several possible reasons, e.g., different mass matrices or differences in the contact and friction model. But, the general behavior, tendencies and influences of different values for v, μ_s and μ_s are similar, see Fig. 6 and Table 2.

To determine μ_s and μ_k, (1) is evaluated for all values of the clamping reactions F_x and F_y, see Fig. 7 and Table 2.

Nearly all results are in the same order of magnitude like the initially assumed values. Only for small velocities there discrepancies and conspicuities for the MBS- and FEM model. The dynamic simulations show that every parameter combination of v, μ_s and μ_k results in a specific stick-slip frequency.

4 Conclusions

The procedure of surface texture detection with an artificial tactile sensor is successfully reproduced by the quasi-static model, the Multi-Body-System and the Finite Element Method simulation. The influences of different magnitudes of velocities and friction coefficients are analyzed. For a certain range of velocities, the simulations with the quasi-static model gather the principal effects of the procedure of surface

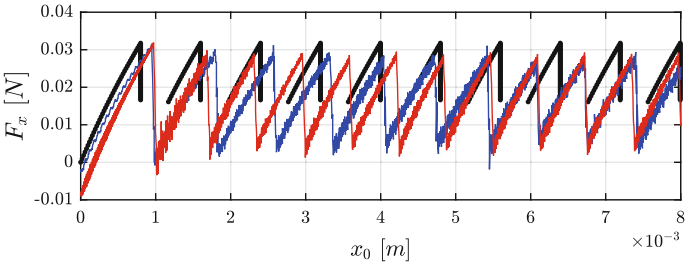

(a) F_x over x_0.

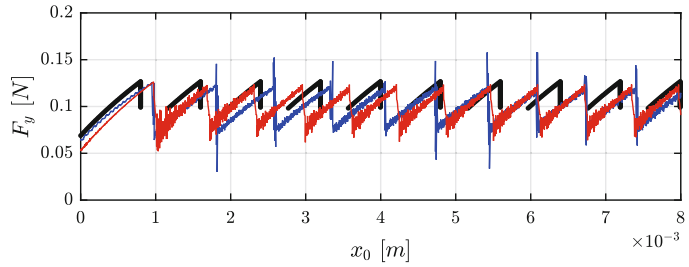

(b) F_y over x_0.

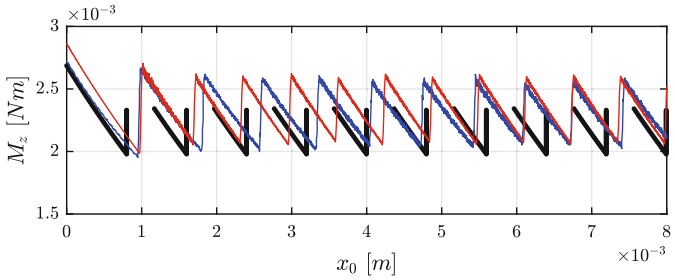

(c) M_z over x_0.

Fig. 5 The simulations **a–c** illustrates the magnitude of the reaction forces and moments in dependence on x_0 for $v = 0.005\ \frac{\text{m}}{\text{s}}$ and $\mu_s = 0.2500$, $\mu_k = 0.1666$. The colors are assigned as follows: black - QS, blue - MBS, red - FEM

texture detection and qualitative statements of the corresponding influences could be done. So, this model could be used to study further refinements of the geometrical shape etc., with respect to the natural vibrissa. The results of the Multi-Body System and Finite Element model show that the parameter velocity has a strong influence on the signals at the clamping and has to be taken into account for analyses of real measurement tasks.

In further works, the effects of varying conditions for the contact and damping will be analyzed, also the validation of the theoretic results by experimental data.

Table 2 Parameter studies

$\frac{\mu_s}{\mu_k}$	$v\left(\frac{\text{m}}{\text{s}}\right)$	μ_s (−)			μ_k (−)			f_1 (Hz)	
		QS	MBS	FEM	QS	MBS	FEM	MBS	FEM
$\frac{0.2500}{0.1666}$	0.001	0.2506	0.3035	0.2500	0.1641	0.1648	0.1362	0.2674	0.1750
	0.005	0.2506	0.2513	0.2589	0.1641	0.1607	0.1617	6.8966	8.000
	0.010	0.2506	0.2586	0.2785	0.1641	0.1689	0.1568	13.2184	16.9091
	0.015	0.2506	0.2459	0.2753	0.1641	0.1691	0.1659	40.8046	40.6363
$\frac{0.2000}{0.1333}$	0.001	0.2027	0.2151	0.2000	0.1334	0.1379	0.079	0.5348	1.0633
	0.005	0.2027	0.2308	0.2105	0.1334	0.1305	0.1318	9.1954	14.2727
	0.010	0.2027	0.2343	0.2185	0.1334	0.1344	0.1283	45.4023	34.0001
	0.015	0.2027	0.2463	0.2459	0.1334	0.1360	0.1329	59.1954	52.9090

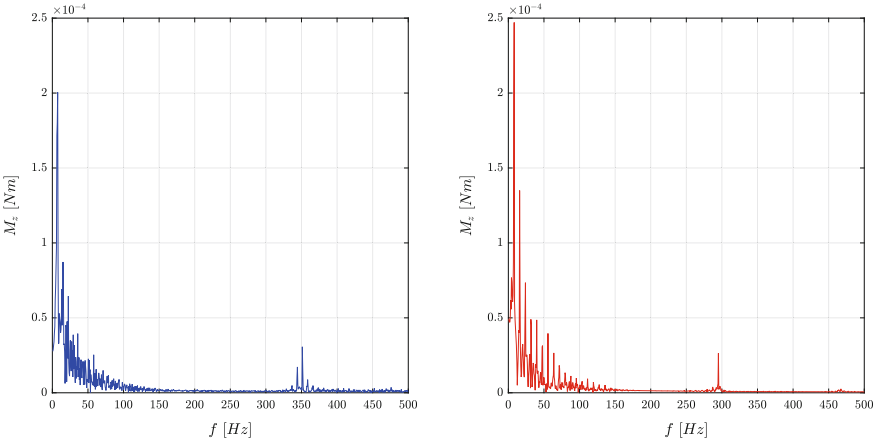

(a) Amplitude spectrum of $M_z(t)$ for the MBS model.

(b) Amplitude spectrum of $M_z(t)$ for the FEM model.

Fig. 6 The plots **a** and **b** show the amplitude spectra of the MBS- and FEM model for $v = 0.005\ \frac{\text{m}}{\text{s}}$ and $\mu_s = 0.2500$, $\mu_k = 0.1666$

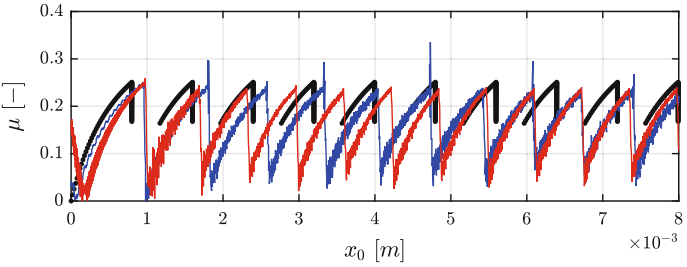

Fig. 7 Comparison of the trend of μ for $v = 0.005\ \frac{\text{m}}{\text{s}}$

Acknowledgements This work was done in cooperation of the Technische Universität Ilmenau, Germany and the Pontificial Catholic University of Peru. Special thanks goes to Dr. Erik Gerlach from Technische Universität Ilmenau for his support and discussions.

References

1. Arabzadeh, E., Zorzin, E., et al.: Neuronal encoding of texture in the whisker sensory pathway. PLoS Biol. **3**, e17 (2005)
2. Boubenec, Y., Claverie, L.N., et al.: An amplitude modulation/demodulation scheme for whisker-based texture perception. J. Neurosci. **34**(33), 10832–10843 (2014)
3. Brecht, M., Preilowski, B., et al.: Functional architecture of the mystacial vibrissae. Behav. Brain Res. **84**(1–2), 81–97 (1997)
4. Carvell, G.E., Simons, D.J.: Biometric analyses of vibrissal tactile discrimination in the rat. J. Neurosci. **10**(8), 2638–2648 (1990)
5. Dörfl, J.: The musculature of the mystacial vibrissae of the white mouse. J. Anat. **135**(1), 147–154 (1982)
6. Labuschagne, A., van Rensburg, N.F.J., et al.: Comparison of linear beam theories. Math. Comput. Model. **49**(1–2), 20–30 (2009)
7. Moor, C.I., Andermann, M.L.: The vibrissa resonance hypothesis. In: Ebner, F.F. (ed.) Neural Plasticity in Adult Somatic Sensory-Motor Systems. Frontiers in Neuroscience. CRS Press, Taylor & Francis (2005)
8. Quist, B.W., Hartmann, M.J.Z.: Mechanical signals at the base of a rat vibrissa: the effect of intrinsic vibrissa curvature and implications for tactile exploration. J. Neurophysiol. **107**(9), 2298–2312 (2012)
9. Quist, B.W., Hartmann, M.J.Z., et al.: Modeling forces and moments at the base of a rat vibrissa during noncontact whisking and whisking against an object. J. Neurosci. **34**(30), 9828–9844 (2014)
10. Scharff, M., Behn, C., et al.: Towards the development of tactile sensors for surface texture detection. In: Proceedings of the 5th International Conference on Intelligent Systems and Applications (INTELLI), Barcelona, Spain (2016)
11. Scharff, M., Darnieder, M., et al.: Towards the development of tactile sensors for determination of static friction coefficient to surfaces. In: Zentner, L., Corves, B., Jensen, B., Lovasz, E.C. (eds.) Microactuators and Micromechanisms. Mechanisms and Machine Science, vol. 45. Springer, Cham (2017)
12. Steigenberger, J., Behn, C., et al.: Mathematical model of vibrissae for surface texture detection. Preprint No. M 15/03. Institute of Mathematics, Technische Universität Ilmenau, Germany (2015)
13. Vaziri, A., Jenks, R.A., et al.: Flexible probes for characterizing surface topology: from biology to technology. Exp. Mech. **47**(3), 417–425 (2007)
14. Voges, D., Carl, K., et al.: Structural characterization of the whisker system of the rat. IEEE Sens. J. **12**(2), 332–339 (2012)
15. Volkova, T., Zeidis, I., et al.: Analysis of the vibrissa parametric resonance causing a signal amplification during whisking behaviour. J. Bionic Eng. **13**(2), 312–323 (2016)
16. Wolfe, J., Hill, D.N., et al.: Texture coding in the rat whisker system: slip-stick versus differential resonance. PLoS Biol. **6**(8), e215 (2008)
17. Zucker, E., Welker, W.I.: Coding of somatic sensory input by vibrissae neurons in the rat's trigeminal ganglion. Brain Res. **12**(1), 138–156 (1969)

Dynamic Analysis of a Compliant Tensegrity Structure for the Use in a Gripper Application

Susanne Sumi, Philipp Schorr, Valter Böhm and Klaus Zimmermann

Abstract The use of compliant tensegrity structures in robotic applications offers several advantageous properties. In this work the dynamic behaviour of a planar tensegrity structure with multiple static equilibrium configurations is analysed, with respect to its further use in a two-finger-gripper application. In this application, two equilibrium configurations of the structure correspond to the opened and closed states of the gripper. The transition between these equilibrium configurations, caused by a proper selected actuation method, is essentially dependent on the actuation parameters and on the system parameters. To study the behaviour of the dynamic system and possible actuation methods, the nonlinear equations of motion are derived and transient dynamic analyses are performed. The movement behaviour is analysed in relation to the prestress of the structure and actuation parameters.

Keywords Compliant tensegrity structure · Multiple states of self equilibrium Dynamic behaviour · Dynamic system · Gripper application

1 Introduction

The use of compliant, mechanically prestressed structures in robotic applications is a recently discussed topic [1, 2, 4, 12]. Compliant free standing tensegrity structures are one class of such structures. Tensegrity structures consist of a group of discon-

S. Sumi (✉) · P. Schorr · V. Böhm · K. Zimmermann
Technical Mechanics Group, Technische Universität Ilmenau,
Max-Planck-Ring 12, 98693 Ilmenau, Germany
e-mail: Susanne.Sumi@tu-ilmenau.de

P. Schorr
e-mail: Philipp.Schorr@tu-ilmenau.de

V. Böhm
e-mail: Valter.Boehm@tu-ilmenau.de

K. Zimmermann
e-mail: Klaus.Zimmermann@tu-ilmenau.de

J. Awrejcewicz (ed.), *Dynamical Systems in Theoretical Perspective*,
Springer Proceedings in Mathematics & Statistics 248,
https://doi.org/10.1007/978-3-319-96598-7_26

nected compressed members connected with compliant tensioned members. Robots based on these structures have a high strength to weight ratio, shock absorbing capabilities and they are lightweight and deployable. An overview of recent development directions can be found in [3, 11, 13].

Known robotic systems use conventional tensegrity structures with only one state of self-equilibrium (equilibrium configuration) [5, 7–9]. In contrast to that, so called multistable tensegrity structures, have more than one state of self-equilibrium and different mechanical properties within these equilibrium configurations. In literature only few structures of this kind are reported [6, 10, 16]. The potential use of these structures in robotic applications is promising in several aspects: The shape change can be realised by transformation between the equilibrium configurations and the structures have different mechanical properties in different equilibrium configurations.

In this work a planer multistable tensegrity structure is investigated, with respect to its future use in a gripper application. This article is based on preliminary studies in [14, 15]. It is composed as follows: After the introduction, in Sect. 2, a parameter study is done: the influence of the member parameters to the existence, stability and shape of the equilibrium configurations is considered. In Sect. 3, the equations of motion are derived and in Sect. 4 two actuation methods are discussed exemplarily. In the first example the time and amplitude of the actuation force is varied, in the second example the influence of the prestress of the structure to the actuation is investigated. Finally conclusions and research directions are given.

In this paper a planar tensegrity structure is analysed. If the parameters are chosen carefully, this is a multistable tensegrity structure (see parameter study in Sect. 2). With suitable parameters the structure has three different static stable equilibrium configurations. The used notations and the three equilibrium configurations are qualitatively depicted in Fig. 1.

This tensegrity structure can be used in a gripper application. Therefor gripper arms are added to obtain a compliant two-finger-gripper. Two of the equilibrium configurations (A and B) represent the opened and the closed state of the gripper, see Fig. 2. An actuation is needed to change between both equilibrium configurations. Different actuation principles are discussed in Sect. 4. This gripper has been introduced in [14, 15].

2 Parameter Study

In this chapter the influence of the member parameters to the existence, stability and shape of the equilibrium configurations is considered.

The compressed members of the tensegrity structure are assumed to be rigid, with the centre of gravity in the middle of each member. The tensioned members are assumed to be massless linear springs. Parallel to each tensioned member a linear damper is modelled.

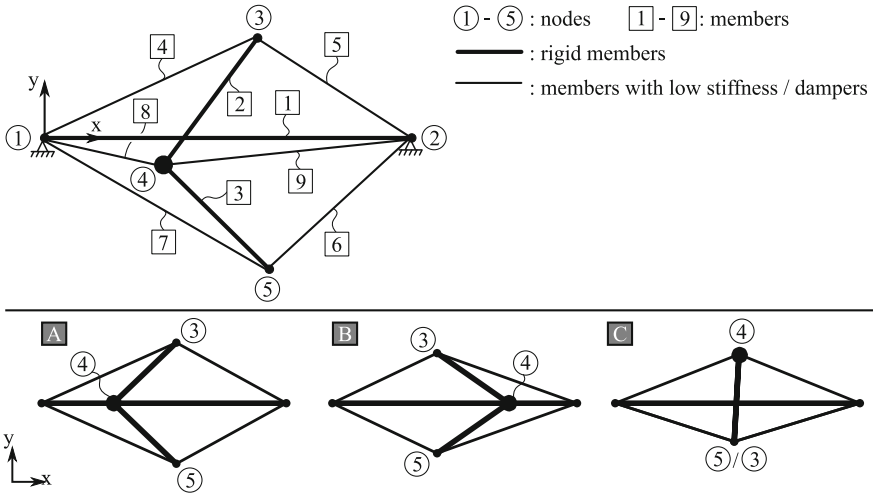

Fig. 1 The tensegrity structure with the used notations and three equilibrium configurations

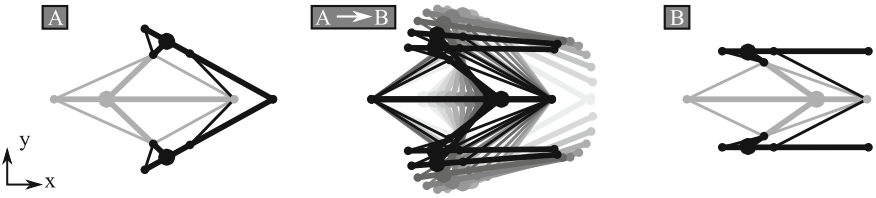

Fig. 2 Design of a two-finger-gripper based on the tensegrity structure

The tensegrity structure has a degree of freedom of 4, for the depicted bearing. The used coordinates $(x_4, y_4, \varphi_2, \varphi_3) \in \mathbb{R}^4$ are shown in Fig. 3. To obtain symmetry and with respect to the application, there are some assumption on the parameters of the tensegrity structure:

- lengths of members 2 and 3 are equal,
- free-lengths and stiffnesses of members 4 and 7 are equal,
- free-lengths and stiffnesses of members 5 and 6 are equal,
- free-lengths and stiffnesses of members 8 and 9 are equal.

For the specific application equilibrium configuration C (see Fig. 1) is not needed, so node 4 is set to be on the x-axis: $y_4 := 0$. Due to symmetry it applies that $\varphi_3 = -\varphi_2$. So the degree of freedom is reduced to two: $(x_4, \varphi_2) \in \mathbb{R}^2$.

Neglecting the gravitational forces, the (static) equilibrium configurations can be determined with the sum of the potential energy of the tensile members. Every sta-

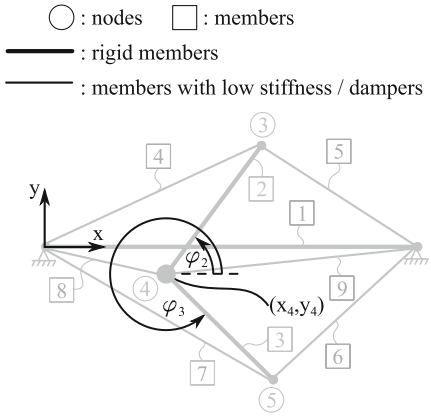

$k_4 = k_7 = 0.482$ N/mm
$k_5 = k_6 = 0.568$ N/mm
$k_8 = k_9 = 0.256$ N/mm
$L_1 = 140$ mm $\quad L_2 = L_3 = 50$ mm
$L_{04} = L_{07} = 59.0$ mm
$L_{05} = L_{06} = 64.2$ mm
$L_{08} = L_{09} = 36.7$ mm
$m_2 = m_3 = 100$ g
$d_4 = d_5 = d_6 = d_7 = d_8 = d_9 = 0.002$ Ns/mm

Fig. 3 Used coordinates to determine the position of the nodes and parameters of the members

tionary point of the energy function is an equilibrium configuration of the tensegrity structure. The potential energy of the structure may be calculated with

$$U = \frac{1}{2} \sum_{f=4}^{9} k_f (L_f - L_{0f})^2, \tag{1}$$

where $L_f \in \mathbb{R}$ are the deformed lengths of the tensile members.

The basis of this study are the parameters listed in Fig. 3. The dependency of the equilibrium configurations on the segment parameters is investigated, while the stiffness of member 8 (k_8) is set to 0.8 N/mm and the stiffness of member 9 (k_9) is varied between 0.05 and 0.60 N/mm with a step size of 0.001 N/mm. The results are plotted in Fig. 4. It shows the number of different static equilibrium configurations and the coordinates (x_4, φ_2) within these equilibrium configurations. The stable equilibrium configurations are marked in black and the instable in grey. Note, that the equilibrium configurations with $\varphi_2 < 0$ are symmetric to the equilibrium configurations with $\varphi_2 > 0$, and have the same mechanical properties. There are regions for k_9, in which only one stable equilibrium configuration exists: if $k_9 < 0.338$ N/mm only equilibrium configuration A exists and if $k_9 > 0.401$ N/mm, only equilibrium configuration B exists. If $k_9 \in [0.338, 0.401]$ N/mm both stable equilibrium configurations A and B exist, with an unstable equilibrium configuration (D) in between.

It can be concluded, that it is possible to obtain parameters that both equilibrium configurations, A and B, are stable and exist, but these parameters have to be chosen carefully.

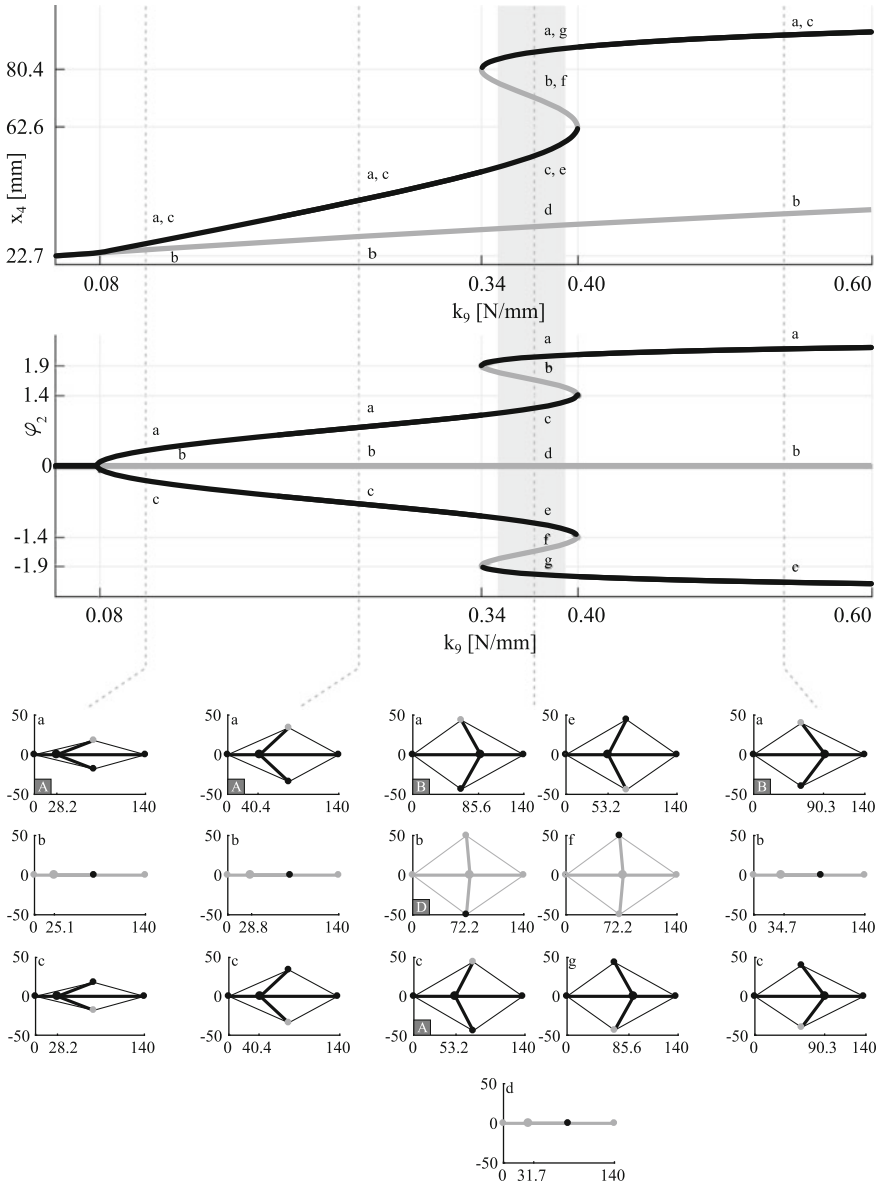

Fig. 4 Diagram, with a variation of k_9 and the corresponding shapes of the tensegrity structure. Black: stable-, grey: unstable equilibrium configurations

The two stable equilibrium configurations A and B and the unstable equilibrium configuration D between A and B, with the segment parameters as listed in Fig. 3 are:

$$P_A = (41.016\text{ mm}, 0\text{ mm}, 0.765\text{ rad}, -0.765\text{ rad}), \tag{2}$$

$$P_B = (100.908\text{ mm}, 0\text{ mm}, 2.531\text{ rad}, -2.531\text{ rad}), \tag{3}$$

$$P_D = (68.585\text{ mm}, 0\text{ mm}, 1.546\text{ rad}, -1.546\text{ rad}) =: (x_{crit}, y_{crit}, \varphi_{crit}, -\varphi_{crit}). \tag{4}$$

3 The Equations of Motion

The planned application of the tensegrity structure is a two-finger-gripper. Two equilibrium configurations correspond to the opened and closed states of the gripper. To study possible actuation methods and the dynamic system behaviour, the nonlinear equations of motion are derived (see [14]). The equations of motion can be determined with the Lagranges equations of the second kind for non-conservative forces:

$$\frac{d}{dt}\frac{\partial \mathscr{L}}{\partial \dot{q}_a} - \frac{\partial \mathscr{L}}{\partial q_a} = -\frac{\partial D}{\partial \dot{q}_a} + Q_a, \qquad \text{with } a = 1, \ldots, n \tag{5}$$

where

- n: degree of freedom of the tensegrity structure,
- q_a: generalised coordinates, $\dot{q}_a$: generalised velocities,
- $\mathscr{L} = T - U$: Lagrangian function,
- T: kinetic energy of the tensegrity structure,
- U: potential energy of the tensegrity structure,
- D: damping of the tensegrity structure.

The degree of freedom has been discussed in Sect. 2. The generalised coordinates are (see Fig. 3):

$$(q_1, q_2, q_3, q_4) := (x_4, y_4, \varphi_2, \varphi_3). \tag{6}$$

The potential energy of the tensile members can be calculated with (1). The damping is assumed as

$$D = \tfrac{1}{2}\sum_{i=4}^{9} d_i \dot{r}_{p_i}^{\top} \dot{r}_{p_i}, \tag{7}$$

where d_i are the damping coefficients of the dampers and $\dot{r}_{p_i} \in \mathbb{R}^2$ are the relative velocities of the dampers.

Furthermore, $Q_{q_a} \in \mathbb{R}$ are the generalised forces. Let $F_k \in \mathbb{R}^2$ be external loads (for example actuation forces) applied to the tensegrity structure and let $r_k \in \mathbb{R}^2$ be the position vector to the corresponding external load F_k. The generalised forces Q_{q_a} are calculated with

$$Q_{q_a} = \sum_k F_k^\top \frac{\partial r_k}{\partial q_a}, \qquad \text{with } a = 1, \ldots, n. \tag{8}$$

Starting with (5) and exploiting (1), (6), (7) and (8) the equation of motion is given by:

$$M \begin{pmatrix} \ddot{x}_4 \\ \ddot{y}_4 \\ \ddot{\varphi}_2 \\ \ddot{\varphi}_3 \end{pmatrix} = b, \qquad M \in \mathbb{R}^{4\times 4},\ b \in \mathbb{R}^4 \tag{9}$$

with

$$M := \begin{pmatrix} m_2 + m_3 & 0 & -c_2\cos(\varphi_2) & -c_3\sin(\varphi_3) \\ 0 & m_2 + m_3 & c_2\cos(\varphi_2) & c_3\cos(\varphi_3) \\ -c_2\sin(\varphi_2) & c_2\cos(\varphi_2) & \frac{1}{3}m_2L_2^2 & 0 \\ -c_3\sin(\varphi_3) & c_3\cos(\varphi_3) & 0 & \frac{1}{3}m_3L_3^2 \end{pmatrix} \tag{10}$$

$$b := \begin{pmatrix} c_2\cos(\varphi_2)\dot{\varphi}_2^2 + c_3\cos(\varphi_3)\dot{\varphi}_3^2 - \frac{\partial U}{\partial x_4} - \frac{\partial D}{\partial \dot{x}_4} + Q_{x_4} \\ c_2\sin(\varphi_2)\dot{\varphi}_2^2 + c_3\sin(\varphi_3)\dot{\varphi}_3^2 - \frac{\partial U}{\partial y_4} - \frac{\partial D}{\partial \dot{y}_4} + Q_{y_4} \\ -\frac{\partial U}{\partial \varphi_2} - \frac{\partial D}{\partial \dot{\varphi}_2} + Q_{\varphi_2} \\ -\frac{\partial U}{\partial \varphi_3} - \frac{\partial D}{\partial \dot{\varphi}_3} + Q_{\varphi_3} \end{pmatrix} \tag{11}$$

and $c_2 := \frac{1}{2}m_2L_2$ and $c_3 := \frac{1}{2}m_3L_3$.

Observe that (9) is an implicit, coupled, nonlinear differential equation system.

4 Actuation

In this chapter different actuation principles are examined. The aim of this chapter is to obtain actuation principles, so that the tensegrity structure changes between equilibrium configuration A and B, and vice versa. The actuation force is applied to node 4 in direction of the x-axis. According to whether the change is from A to B or from B to A, the actuation force is positive or negative, respectively.

The unstable equilibrium configuration (P_D, see (4)) is between equilibrium configuration A and B. If node 4 is slightly over the critical position (x_{crit}, y_{crit}) or if the angles φ_2 and φ_3 are slightly over the critical position φ_{crit} a snap-through happens and no further force is needed to reach the other equilibrium configuration. So there are two different actuation principles:

1. an unforced change,
2. a forced change.

In the unforced change, the actuation force is zero before the tensegrity structure reaches the critical position. The change into the other equilibrium happens because of the inertia of the structure. In the forced change the actuation force is not zero in the critical position, so it is a guided change between the equilibrium configurations.

4.1 Example 1: Sinusoidal Actuation

In this section a sinusoidal force is applied to node 4. It is investigated, which maximal force and duration of the actuation leads to a change between A and B, and B to A.

The actuation force is assumed to be continuous. It is symmetric and starts and ends with 0 N. More precisely the actuation force is $F_1 := (F(t), 0)^\top$ with maximal force $F_{\max} \in \mathbb{R}$ and duration of the actuation $t_{\max} \in \mathbb{R}$:

$$F(t) := \begin{cases} \frac{F_{\max}}{2} \sin\left(t \frac{2\pi}{t_{\max}} - \frac{\pi}{2}\right) + \frac{F_{\max}}{2}, & t \le t_{\max} \\ 0, & \text{else,} \end{cases} \tag{12}$$

and $r_1 := (x_4, y_4)^\top$.

If the initial configuration ($t = 0$ s) is A (P_A, see (2)), the actuation force is F_1 and if the initial configuration is B (P_B (see (3)), the actuation force is $-F_1$. The initial velocities ($t = 0$ s) are zero.

The maximal force $F_{\max}$ is varied between -200 and 200 N with a step size of 0.1 N. The duration of the actuation $t_{\max}$ is varied between 0.01 and 0.1 s with a step size of 0.001 s. The results are depicted in Fig. 5. In the upper picture the unforced change between the equilibrium configurations is considered: if the actuation force is not zero while x_{crit} is reached, the point is marked in white. If, after the actuation, the tensegrity structure is again in its initial configuration, it is marked in dark grey. If the structure moves into the other initial configuration, the point is marked in black (this is the case that is needed for application). And if node 3 and 5 change their position (in Fig. 3 the region with $\varphi_2 < 0$), the point is marked in light grey. In the lower picture in Fig. 5, there is not distinguished between the unforced (1) and the forced change (2). The colours correspond to the upper picture, but white means, that the tensegrity structure changes more than one time between the equilibrium configurations. If both cases happen (node 3 and 5 change their position and several changes between the equilibrium configurations), the colour white is used, too.

In Fig. 6 the case $F_{\max} = 30$ N is analysed in more detail. Five different durations of the actuation are considered: $t_{\max} \in \{0.011, 0.015, 0.019, 0.023, 0.03\}$ s and the initial configuration is P_A, see (2). The actuation force is depicted in Fig. 6 in the upper left picture. In the upper middle and upper right pictures phase portraits are plotted. If the duration is small (maximal 0.015 s), the structure is in equilibrium

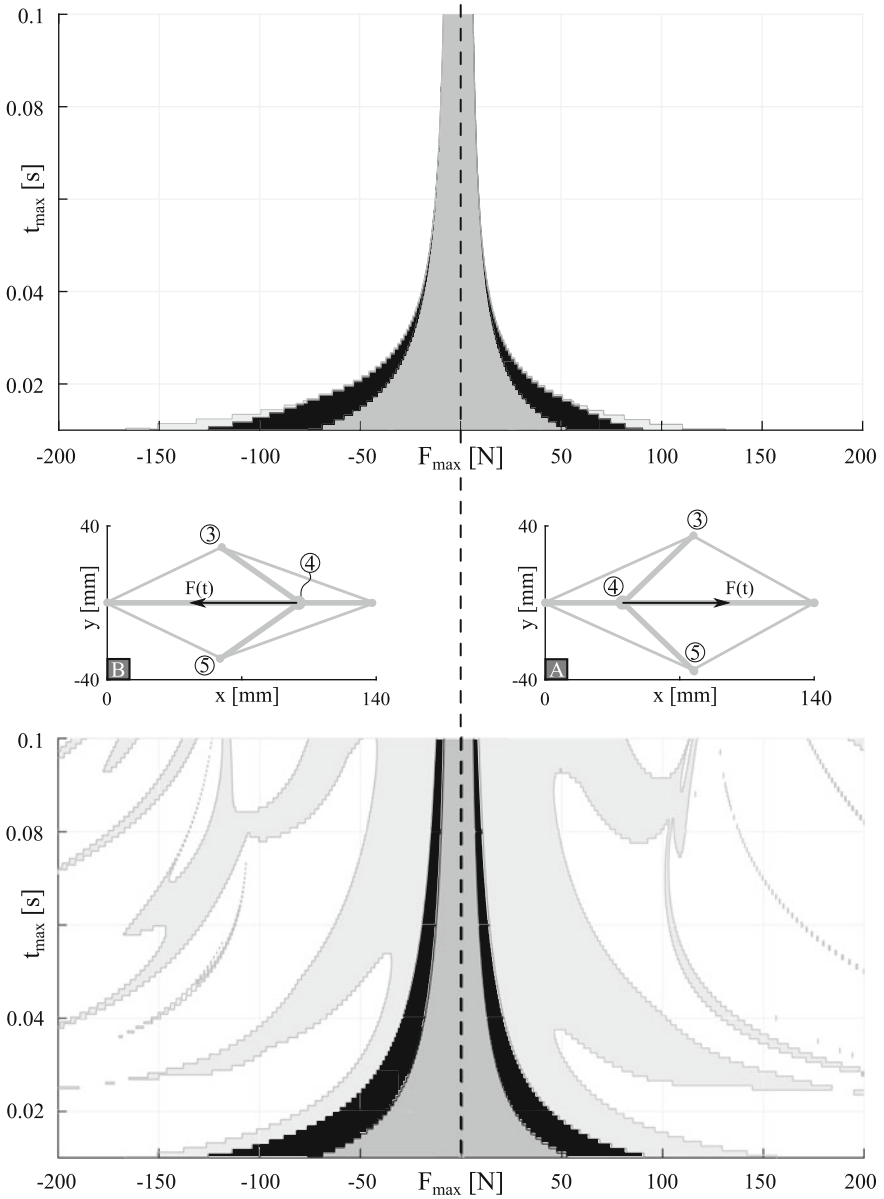

Fig. 5 Behaviour of the tensegrity structure during and after actuation with varied maximal forces and actuation durations

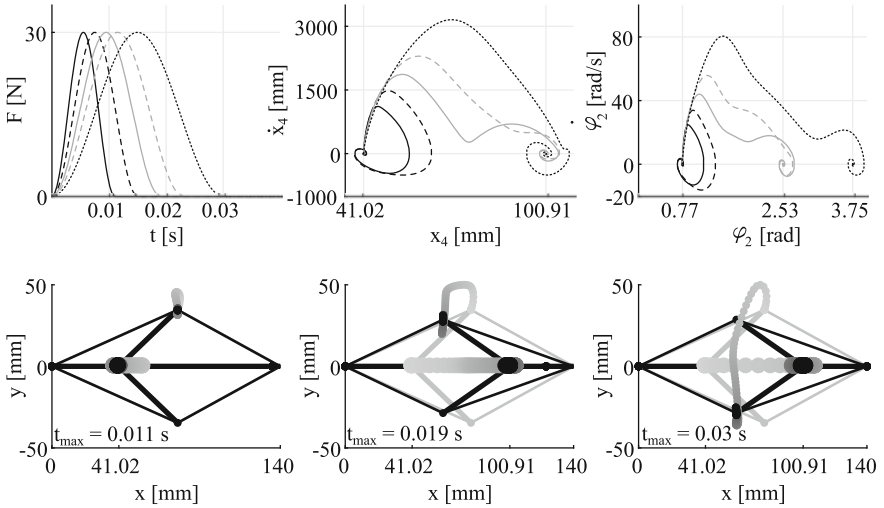

Fig. 6 Actuation force, phase portraits and movement of the nodes during different durations of actuation

configuration A again, after actuation. These points are marked in dark grey in Fig. 5. The movement of the nodes is depicted in the lower left picture. If the duration is larger (at least 0.019 s) the tensegrity structure changes from A to B. These points are marked in black in Fig. 5 and the movement of the nodes is depicted in the lower middle picture in Fig. 6. If the duration is too large (0.03 s), the structure changes from A to B, but nodes 3 and 5 change their positions, see the movement of the nodes in Fig. 6, lower right picture. In Fig. 5 in the upper diagram this point is marked white, since the actuation force is not zero at x_{crit} and in the lower picture this point is marked light grey, since node 3 and 5 change their positions.

This example shows that it is possible to change between both equilibrium configurations with the given sinusoidal actuation force. But the duration of the actuation and the maximal force have to be chosen carefully. If one of both parameters is too small, nothing happens and if it is too big, different unwanted effects occur. The force that is needed to change from A to B is smaller than from B to A. This can be used in the gripper design if distinguished behaviour while opening and closing the gripper is desired.

4.2 Example 2: Constant Actuation and Variation of the Prestress

In this chapter, as a second possibility for the gripper actuation, a constant force $F_{\max}$ is applied for a duration $t_{\max}$ at node 4. The force $F_{\max}$ and the prestress of the

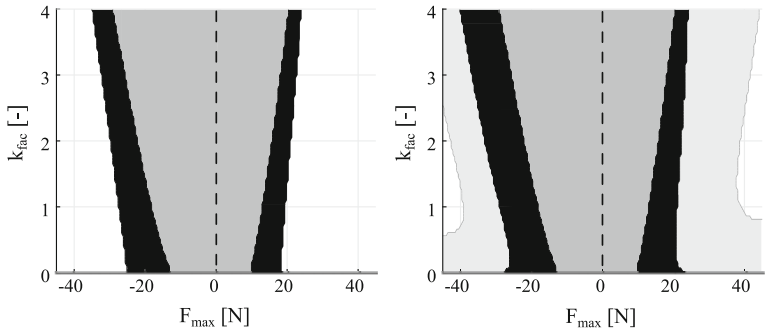

Fig. 7 Behaviour of the tensegrity structure during actuation with varied maximal forces and prestress

structure is varied and the movement of the structure is investigated. More precisely the actuation force is $F_1 = (F(t), 0)^\top$, with

$$F(t) := \begin{cases} F_{\max}, & t \leq t_{\max} \\ 0, & \text{else} \end{cases}, \tag{13}$$

and $r_1 := (x_4, y_4)^\top$.

The maximal force is varied between -45 and 45 N with a step size of 0.5 N. The duration of the actuation is exemplarily set to 0.02 s. To investigate the dependency of the prestress of the structure to the dynamical system behaviour, the prestress of the structure is varied while scaling the stiffnesses of the tensile members by a factor k_{fac}. The factor k_{fac} lies between 0.05 and 4 with a step size of 0.05. The results are depicted in Fig. 7. The meaning of the colours is the same as in Fig. 5. In the right picture in Fig. 7 the black region is bigger than in the left picture (unforced actuation). This shows that it is possible, that the structure changes between both equilibrium configurations in a forced actuation, too.

For all considered prestress states of the structure it is possible to change between both equilibrium configurations with the force defined in (13). If the prestress is larger, a larger force is needed to change between the equilibrium configurations.

5 Conclusions

In this article the equations of motion of a tensegrity structure have been derived. Therewith the motion behaviour can be determined. This has been done for two different kinds of actuation.

The parameter study showed, that this tensegrity structure can be a multistable tensegrity structure, if the parameters are suitable. The analysis of the dynamic system

behaviour showed, that it is possible to change between both equilibrium configurations, if the actuation force is big enough but not too big. It also showed, that the dynamic system behaviour is dependent on the prestress of the structure.

In a future study this could be done with the whole gripper, not only with the underlying tensegrity structure.

Acknowledgements This work is supported by the Deutsche Forschungsgemeinschaft (DFG project BO4114/2-1).

References

1. Boehler, Q., et al.: Definition and computation of tensegrity mechanism workspace. J. Mech. Robot. **7**(4), 044502 (2015)
2. Böhm, V., et al.: Vibration-driven mobile robots based on single actuated tensegrity structures. In: Proceeedings of the IEEE International Conference on Robotics and Automation, pp. 5455–5460 (2013)
3. Böhm, V., et al.: An approach to the dynamics and control of a planar tensegrity structure with application in locomotion systems. Int. J. Dyn. Control **3**(1), 41–49 (2015)
4. Caluwaerts, K., et al.: Design and control of compliant tensegrity robots through simulation and hardware validation. J. R. Soc. Interf. **11**, 98 (2014)
5. Chen, L., et al.: Soft spherical tensegrity robot design using rod-centered actuation and control. In: ASME International Design Engineering Technical Conferences and Computers and Information in Engineering Conference (2016)
6. Defossez, M.: Shape memory effect in tensegrity structures. Mech. Res. Commun. **30**(4), 311–316 (2003)
7. Friesen, J.M., et al.: The second generation prototype of a duct climbing tensegrity robot, DuCTTv2. In: IEEE International Conference on Robotics and Automation, pp. 2123–2128 (2016)
8. Hustig-Schultz, D., et al.: Morphological design for controlled tensegrity quadruped locomotion. In: IEEE International Conference on Intelligent Robots and Systems, pp. 4714–4719 (2016)
9. Lessard, S., et al.: A bio-inspired tensegrity manipulator with multi-DOF, structurally compliant joints. In: Proceedings of the International Conference on Intelligent Robots and Systems, Daejeon, Korea (2016)
10. Micheletti, A.: Bistable regimes in an elastic tensegrity system. Proc. R. Soc. A **469**, 2154 (2013)
11. Mirats Tur, J.M., et al.: Tensegrity frameworks: dynamic analysis review and open problems. Mech. Mach. Theory **44**(1), 1–18 (2009)
12. Rieffel, J.A., et al.: Morphological communication: exploiting coupled dynamics in a complex mechanical structure to achieve locomotion. J. R. Soc. Interf. **7**, 613–621 (2010)
13. Skelton, R.E., et al.: Tensegrity Systems. Springer, Berlin (2009)
14. Sumi, S., et al.: A multistable tensegrity structure with a gripper application. Mech. Mach. Theory **114**, 204–217 (2017)
15. Sumi, S., et al.: A Novel Gripper Based on a Compliant Multistable Tensegrity Mechanism. Microactuators and Micromechanisms, pp. 115–126. Springer, Berlin (2017)
16. Xu, X., et al.: Multistable tensegrity structures. J. Struct. Eng. **137**(1), 117–123 (2011)

Synchronisation Analysis of a De-Tuned Three-Bladed Rotor

Zofia Szmit, Jerzy Warmiński and Jarosław Latalski

Abstract The aim of the paper is to study a synchronisation phenomenon as observed in a rotating structure consisting of three composite beams and a hub. The beams are made of eighteen carbon-epoxy prepreg material layers stacked in a specific sequence. In the performed analysis it is assumed one of the beams is de-tuned due to small misalignment of its reinforcing fibers orientation with regard to the two remaining nominal design blades. The non-classical effects like transverse shear, material anisotropy, non-uniform torsion and cross-section warping are taken into account in the mathematical model of the blades. The partial differential equations of motion of the structure are derived by the Hamilton principle; next the reduction to the ordinary differential ones is done by the Galerkin method. Finally, the equations are solved numerically and the resonance curves for the hub and the individual beams are plotted. In the performed studies two possible variants of the rotor excitation are considered: (a) driving torque expressed by a harmonic function or (b) torque given by a chaotic oscillator formula. The analysis of the synchronisation phenomenon of the hub and the blades motion is based on the study of the resonance curves and time histories in the prepared graphs. The analysis of the structure driven by chaotic oscillator revealed the existence of the strange chaotic attractor for every beam of the rotor; in the particular, nominal beams are fully synchronised, but the de-tuned one is synchronised with a small difference in amplitude.

Keywords Synchronisation phenomenon · Mistunning · Chaotic oscillations · Rotor dynamics · Composite beams

Z. Szmit (✉) · J. Warmiński · J. Latalski
Department of Applied Mechanics, Lublin University of Technology,
Nadbystrzycka 36, 20-618 Lublin, Poland
e-mail: z.szmit@pollub.pl

J. Warmiński
e-mail: j.warminski@pollub.pl

J. Latalski
e-mail: j.latalski@pollub.pl

J. Awrejcewicz (ed.), *Dynamical Systems in Theoretical Perspective*,
Springer Proceedings in Mathematics & Statistics 248,
https://doi.org/10.1007/978-3-319-96598-7_27

1 Introduction

The synchronisation phenomenon was discovered by Christiaan Huygens in XVII century, who found out that pendulums of two clocks hanging on the same beam moved synchronously after some transient time. The studies on synchronisation effect for different types of pendulums and structures were continued over the next centuries. This topic is now well established within scientific community and still stays the subject of continuing research. For instance, the Huygens experiment was repeated recently by Kapitaniak et al. and discussed in detail in the paper [6]. The authors used two clocks as identical as possible and observed the behaviour of their pendulums. Furthermore, they performed computer simulations to check the influence of any possible differences in clocks on the synchronisation process. The synchronous motion of two pendulums mounted on the horizontally excited platform was analysed later in the research [7]. The authors proved that the pendulums could exhibit synchronous oscillatory and rotation motion. Moreover, it was shown the stable in-phase and anti-phase synchronous states always co-existed. The synchronisation effect in the structure consisting of two double pendulums was studied by Koluda et al. in [8]. The authors derived the mathematical conditions that allowed to explain the types of observed synchronisation scenarios in the analysed system.

However, all the above mentioned papers discussed the dynamics and synchronisation of pendulums rotating in a vertical plane. As opposed to these studies a system consisting of two pendulums attached to a rigid hub and rotating in a horizontal plane was examined by Warminski et al. in [16]. The nonlinear dynamics of the full rotor structure as well as the synchronisation phenomenon were investigated. Similar studies were performed on rotors consisting of a rigid hub and a flexible beam. In particular, in the paper [15] the system of a beam and a heavy tip mass was investigated. The proposed nonlinear mathematical model of the blade bending accounted for high curvatures arising from large transversal displacements. Similar studies were performed by Yigit et al. [17] who derived fully coupled non-linear equations of motion considering the hub and beam interactions. Moreover, a torque profile function was used to represent the rotor drive so that the rigid body motion of the structure was not known a priori.

The idea of studying a non-perfect excitation source was adopted by other researches studying the dynamics of flexible beams. In particular, Awrejcewicz et al. [1] investigated the chaotic dynamics of straight as well as curved Euler-Bernoulli beams in geometrically non-linear regime. A series of tests for different boundary conditions were carried out. Time histories, phase and modal portraits, as well as a compression factor of the phase volume of an attractor were investigated. These studies were continued later to incorporate thermal effects and the influence of electrical potential generated on the specimen surface [9].

Most of the presented above studies on rotating structures were motivated by aerospace and mechanical engineering problems; typical examples might be helicopter rotors, aircraft propellers, jet engines etc. A specific nonlinear model of rotating beam dedicated to the helicopter blades was presented by Crespo da Silva in

the papers [2, 3]. This model was derived assuming the homogeneity and isotropic properties of the specimen material. Another model of rotating flexible beams was proposed by Librescu and Song [11]. In contrast to Crespo da Silva their approach accounted for directional properties of the specimen material. However, the presented formulation was limited to the linear regime only.

The current research paper is inspired by the evolution of materials used in mechanical and aerospace engineering. Especially composite materials are becoming more and more popular because of their unique mechanical and physical properties. The multilayered laminates made of unidirectional orthotropic laminas are used due to their directional dependent properties that can be exploited to design a material dedicated for the specific engineering needs. However, independently of their anisotropic properties, the laminated composites can also be used for designs where the fully isotropic properties of the material are called for. For instance, when a thin specimen is subjected to various loading conditions, a macroscopically isotropic composite can be well suited for the purpose, especially if weight of the structure is an additional design constraint. These types of applications require specific combinations of fibres orientations and plies stacking sequences resulting in macroscopic material isotropy. Several exemplary material designs were discussed by Fukunaga [4], and by Vannucci and Verchery [14].

One of the principal weaknesses of the multilayered laminates is their susceptibility to any deviations from the tight manufacturing technology regimes. These include precise prepreg laying orientation, appropriate temperature, pressure and curing time, proper prepreg storage and handling conditions etc. All these factors might be a source of potential error, resulting in deterioration of the composite mechanical characteristics. In certain specific cases also physical macroscopic properties of the material may be affected. For instance in-plane to out-of-plane mechanical coupling might be induced due to deviated orientation of individual laminas. This in turn may lead to inappropriate structural behaviour and/or unexpected dynamic phenomena.

To address the aforementioned issues the current paper studies the problem of the influence of inaccurate multilayered lamination scheme in nominally isotropic laminated material on the dynamic properties of three-bladed composite rotor. In the presented consideration it is assumed that one of the beams is de-tuned due to misalignment of reinforcing fibres angles in subsequent laminate layers, while the other two blades stay nominal. This deviation from the standard design results in different mechanical properties of the affected blade. In particular, the inherent mechanical coupling of in-plane to out of plane deformation is observed.

2 Mathematical Model of the Structure and Equations of Motion

Let us consider a rotor consisting of three slender, straight, and elastic composite beams of solid section clamped at the rigid hub of radius R_0 and inertia J_h rotating about a fixed frame vertical axis CZ_0 as shown in Fig. 1.

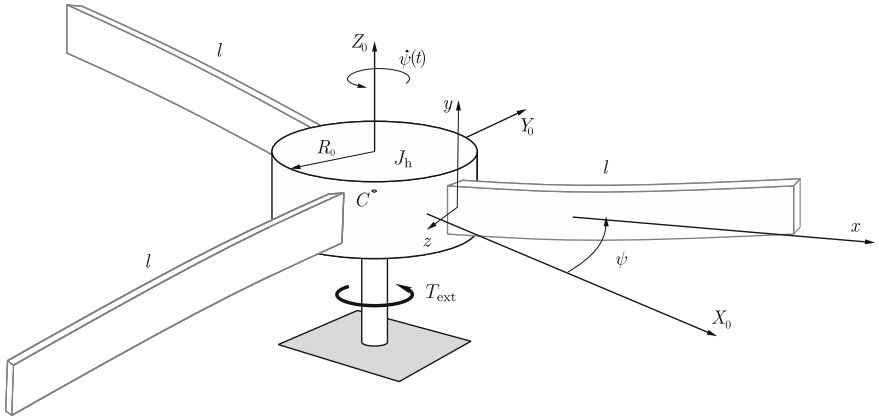

Fig. 1 Model of the rotating hub with three elastic beams

The hub temporary position is represented by an angle $\psi(t)$ with respect to an inertial reference frame (X_0, Y_0, Z_0) and the rotational speed of the system $\dot{\psi}(t)$ is assumed to be arbitrary i.e. not necessarily constant. The system is driven by an external torque T_{ext} applied to the hub. The length of each beam is denoted by l_i, the width and thickness of the cross-section by d_i and h_i $(i = 1, 2, 3)$, respectively. It is assumed the beams are made of 18 laminate layers of graphite-epoxy material with the following stacking sequence $(0°, -60°, 60°, 0°, -60°, 60°, 60°, 60°, -60°, -60°, 0°, 0°, -60°, 0°, 0°, 60°, 60°, -60°)$. This specific configuration exhibits fully isotropic material properties i.e. macroscopic material isotropy and isotropy of the three stiffness tensors **A**, **B** and **D** as well [14].

Furthermore, it is assumed one of these three beams is made of an imperfect laminate due to a slight misalignment of reinforcing fibers in individual layers. Thus, one presumes the actual fiber orientation angle in each kth ply $(k = 1, \ldots, 18)$ may be varied from its nominal value α_k but stays within a range $\langle \alpha_k - \Delta\alpha_k; \alpha_k + \Delta\alpha_k \rangle$ — see Fig. 2. So $\Delta\alpha_k$ represents the assumed maximum allowable deviation of the actual fiber direction in ply k, and therefore it may correspond to the accuracy of laminate layer positioning. Moreover, it is assumed that the magnitude of this misalignment is set 'a priori' and equal for all layers – so it does not depend on the nominal fiber orientations α_k.

This model of the imperfect material/structure, where only the maximal deviations of fiber orientation angles are given, renders their exact values unknown. However, this approach allows to estimate the maximum possible impact of the assumed change in fibres orientations on the mechanical properties of the material by performing a simple sensitivity analysis. This treatment is often encountered in reliability based structural design — see e.g. [10] and represents the so called 'a worst case scenario' analysis. More details are given in Sect. 2.2.

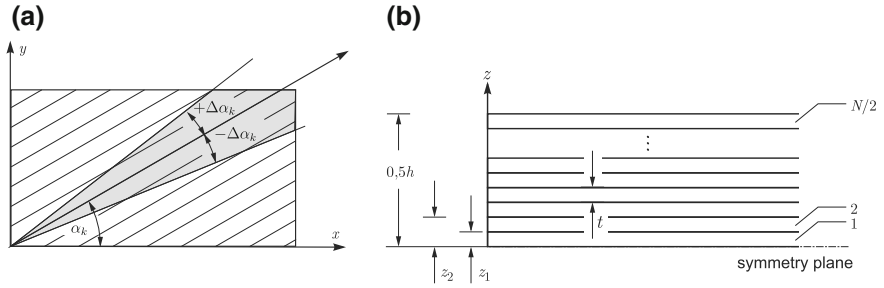

Fig. 2 Model of an inaccurate composite material

2.1 Derivation of Governing Equations

The mechanical equations of motion of the rotor structure are derived according to the extended Hamilton principle of the least action

$$\delta J = \int_{t_1}^{t_2} \left(\delta T - \delta U + \delta W_{\text{ext}}\right) \mathrm{d}t = 0 \tag{1}$$

where J is the action, T is the kinetic energy, U is the potential energy, and the work done by the external loads is given by the W_{ext} term.

Following the detailed derivation procedure given in the former authors paper [5] the system of partial differential equations of motion and the associated boundary conditions can be obtained. Considering the solid cross-section of the beams and their clamping position, as well as multilayered laminate configuration the dynamics of every blade is represented by three equations of motion. These correspond to the individual degrees of freedom, namely bending deflection w_0, transverse shear angle ϑ_y and twist angle φ. The additional differential relation represents the dynamics of the hub given by the rigid body rotation angle ψ. Therefore, the dynamics of the structure is represented by a total of ten partial differential equations of motion.

Since the general form of any individual beam governing equations is identical, for the sake of brevity, only one subset for the representative blade is given below

- δw_0

$$\begin{aligned} b_1\ddot{w}_0 + 2b_1\dot{u}_0\,\dot{\psi}(t) - b_1 w_0\dot{\psi}^2(t) + b_1(R_0 + x + u_0)\ddot{\psi}(t) \\ -\left[a_{55}(\vartheta_y + w_0')\right]' - \left(T_x w_0'\right)' = 0 \end{aligned} \tag{2}$$

BC:
$$w_0\big|_{x=0} = 0, \qquad \left(\vartheta_y + w_0'\right)\big|_{x=l} = 0$$

- $\delta\vartheta_y$

$$B_4\left[\ddot{\vartheta}_y - \vartheta_y\dot{\psi}^2(t) + \ddot{\psi}(t)\right] + a_{55}\vartheta_y + a_{55}w_0' - \left(a_{33}\vartheta_y'\right)' - \left(a_{37}\varphi'\right)' = 0 \tag{3}$$

BC:

$$\vartheta_y\big|_{x=0} = 0, \quad \left(a_{33}\vartheta_y' + a_{37}\varphi'\right)\big|_{x=l} = 0,$$

- $\delta\varphi$

$$(B_4 + B_5)\ddot{\varphi} + (B_4 - B_5)\varphi\dot{\psi}^2(t) - \left(a_{37}\vartheta_y'\right)' - \left(a_{77}\varphi'\right)' + \left[\frac{B_4 + B_5}{m_0 d}T_x\varphi'\right]' = 0, \tag{4}$$

BC:

$$\varphi\big|_{x=0} = 0, \qquad \left(a_{37}\vartheta_y' + a_{77}\varphi'\right)\big|_{x=l} = 0,$$

In the above given relations terms b_1, B_4, B_5 represent specimen cross-section inertias in translation and rotations, respectively. Coefficients a_{33}, a_{55}, a_{77}, a_{37} are the stiffnesses of the beam in bending, shear, twist and bending-twist coupling stiffness. The m_0 factor is a reduced mass term given as $\int_{-h/2}^{h/2}\rho\,\mathrm{d}n$ where ρ is laminate mass density and n is dummy variable measured in specimen thickness direction. Detailed definitions of all these terms can be found in the previous authors paper [5]. Moreover, the term $T_x = b_1(l - x)[R_0 + \frac{1}{2}(l + x)]\dot{\psi}^2$ represents the centrifugal stiffening effect.

The above set of Eqs. (2)–(4) is supplemented by the additional equation governing the hub motion

- $\delta\psi$

$$J_\mathrm{h} + 3\,(B_{22} + B_4 l)\,\ddot{\psi}(t) + \sum_{i=1}^{3}\int_0^l \Big[2b_1(R_0 + x_i)u_{0i}\ddot{\psi}(t) + 2b_1(R_0 + x_i)\dot{u}_{0i}\dot{\psi}(t) + b_1(R_0 + x_i)\ddot{w}_{0i} - B_4\ddot{\vartheta}_{yi}\Big]\,\mathrm{d}x = T_\mathrm{ext} \tag{5}$$

The term B_{22} corresponds to the inertia of the beam in rotation about its tip as a rigid body. When studying this equation please mind the assumed misalignment of reinforcing fibres affects only the blade stiffnesses while all the inertia terms stay unchanged with respect to the nominal beam. Therefore, the beam denotation index i is skipped in the inertia subscripts.

2.2 Impact of Reinforcing Fibers Misalignment

The deviation of composite reinforcing fibers from their nominal orientation results in the change of the material stiffness and, consequently, the blade stiffness coefficients a_{ij}. However, the inertia terms b_i and B_j are not affected since the density of the material is uniform layerwise.

Following the adopted assumptions to the mathematical model of the structure [5], the blade stiffness coefficients a_{ij} are calculated according to the Classical Laminate Theory scheme. Thus, they are expressed in terms of A_{ij}, B_{ij} and D_{ij} members of matrices representing stretching, bending-stretching and bending stiffnesses, respectively. These in turn are given by reduced plane stress state stiffnesses Q_{ij} and finally by individual components $\tilde{C}_{ij}$ of material stiffness tensor in rotated 3D coordinate frame – see appropriate mathematical formulas in [5].

The possible impact of the considered reinforcing fibers misalignment may be reasonably evaluated by performing a simple sensitivity analysis. Therefore, the change of any beam stiffness a_{ij} is given as follows

$$\Delta a_{ij} = \sum_{k=1}^{k=18} \left| \frac{\partial a_{ij}}{\partial \alpha_k} \Delta \alpha_k \right| = f(\tilde{\mathbf{C}}(\alpha_k)) \tag{6}$$

where ij pair is 33, 37, 55 or 77, and k represents the individual laminae order.

The expression $\frac{\partial a_{ij}}{\partial \alpha_k}$ represents the sensitivity of the material stiffness with respect to changes in fibre orientations in k individual laminate layer. Since the sign of the possible deviation $\Delta\alpha_k$ is not arbitrary known, to consider the most unfavourable case, the absolute value operator is used. The proposed general function $f(\cdot)$ represents the dependence of the stiffness change with respect to individual components of material stiffness tensor in rotated coordinate frame.

To calculate the necessary sensitivities a concept of invariants proposed by Tsai and Pagano [12] describing mechanical properties of anisotropic materials has been adopted. This is a convenient approach that allows to represent stiffness transformation equations for any ply rotation in a laminate as a function of general material invariants u_i ($i = 1, 2, \ldots, 11$) and material rotation angle α. Thus the relevant relations may be simplified and the requested components of the material stiffness tensor $\tilde{C}_{ij}$ in rotated coordinate frame are given as

Table 1 The values of individual coefficients in partial differential equations of motion (2–4) for the nominal laminate and for the perturbed one

Nominal values			
$a_{33} = 0.117568\,\mathrm{Nm}^2$	$a_{37} = 0.0\,\mathrm{Nm}^2$	$a_{55} = 67957.50\,\mathrm{N}$	$a_{77} = 0.081397\,\mathrm{Nm}^2$
Perturbed values			
$a_{33} = 0.138754\,\mathrm{Nm}^2$	$a_{37} = -0.000116\,\mathrm{Nm}^2$	$a_{55} = 69537.77\,\mathrm{N}$	$a_{77} = 0.091819\,\mathrm{Nm}^2$

$$
\begin{aligned}
\tilde{C}_{11}(\alpha_k) &= u_1 + u_2\cos(2\alpha_k) + u_3\cos(4\alpha_k) & \tilde{C}_{12}(\alpha_k) &= u_4 - u_3\cos(4\alpha_k)\\
\tilde{C}_{16}(\alpha_k) &= 0.5u_2\sin(2\alpha_k) + u_3\sin(4\alpha_k) & \tilde{C}_{13}(\alpha_k) &= u_8 + u_9\cos(2\alpha_k)\\
\tilde{C}_{22}(\alpha_k) &= u_1 - u_2\cos(2\alpha_k) + u_3\cos(4\alpha_k) & \tilde{C}_{23}(\alpha_k) &= u_8 - u_9\cos(2\alpha_k)\\
\tilde{C}_{26}(\alpha_k) &= 0.5u_2\sin(2\alpha_k) - u_3\sin(4\alpha_k) & \tilde{C}_{33}(\alpha_k) &= C_{33}\\
\tilde{C}_{36}(\alpha_k) &= u_9\sin(2\alpha_k) & \tilde{C}_{44}(\alpha_k) &= u_{10} - u_{11}\cos(2\alpha_k)\\
\tilde{C}_{45}(\alpha_k) &= u_{11}\sin(2\alpha_k) & \tilde{C}_{55}(\alpha_k) &= u_{10} + u_{11}\cos(2\alpha_k)\\
\tilde{C}_{66}(\alpha_k) &= u_5 - u_3\cos(4\alpha_k)
\end{aligned}
\tag{7}
$$

Results of the calculations for the proposed 18 layers stacking sequence and nominal fibre orientations are given in the first row of Table 1. Next, the changes in values of individual coefficients for the misaligned material have been calculated assuming the deviation magnitude $\Delta\alpha_k = 5^\circ$; final results for the mistuned specimen are listed in the second row in Table 1.

The performed numerical simulations confirm the assumed specific stacking sequence to exhibit the fully isotropic properties for the nominal values of fibre orientations – note the bending-twisting stiffness $a_{37} = 0$. However, this stacking sequence configuration is sensitive to possible variations in fibres orientations as confirmed by changes in beam stiffnesses. In particular, it can be observed the possible permitted small misalignment of fibres angle leads to anisotropic material behaviour and induces the mutual coupling of in-plane and out-of-plane specimen deformations ($a_{37} \neq 0$). This can be also observed if comparing the individual components of natural mode shapes of the beam for the nominal material (Fig. 3a) and for the de-tuned one (Fig. 3b), where a minor torsional component $\varphi(\eta)$ is coexistent.

2.3 Ordinary Differential Equations of Motion

In the following stage the individual equations of motion have been rewritten by introducing a dimensionless notation, i.e. a spanwise coordinate $\eta = x/l$ ($\eta \in \langle 0, 1\rangle$) as well as time $\tau = \omega_0 \cdot t$, where t is physical time and $\omega_0 = \sqrt{a_{33}/(b_1 l^4)}$.

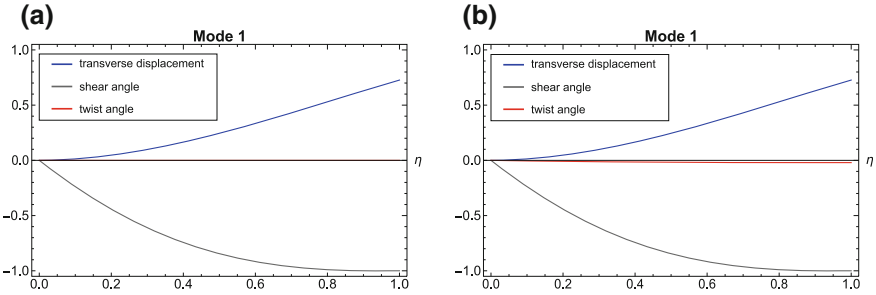

Fig. 3 Mode shape components for nominal (**a**) and de-tuned blade (**b**)

Next, the Galerkin projection method has been applied to reduce the set of PDEs to the system of ordinary differential equations of motion. For this purpose an orthogonality condition for the boundary value problem with the bending-shear-twist vibration components involved has been derived, and is as follows

$$\left(\omega_m^2 - \omega_n^2\right) \int_0^1 \Big[b_1 l^2 W_m(\eta) W_n(\eta) + B_4 Y_m(\eta) Y_n(\eta) + \left(B_4 + B_5\right) \Phi_m(\eta) \Phi_n(\eta) \Big] \mathrm{d}\eta = 0 \tag{8}$$

In the above formula $W(\eta)$, $Y(\eta)$ and $\Phi(\eta)$ correspond to the assumed mode functions representing spatial distribution of transverse displacement, shear and twist angles, respectively. Therefore, for two distinct mode shapes ($m \neq n$) the integral is zero; otherwise it takes a nonzero value depending on the mode normalisation rule. When using the formulated orthogonality condition (8) the three Eqs. (2)–(4) for any individual i ($i = 1, 2, 3$) beam can be added. Thus they are reduced to just one (see any of Eqs. $(9)_{2-4}$) where the generalised coordinate $q_i(\tau)$ $i = 1, 2, 3$ represents the complex deformation of the i blade involving transverse displacement, shear and twist. The final set of governing equations takes the form:

$$\begin{aligned} &(J_\mathrm{h} + J_{\mathrm{b}1} + J_{\mathrm{b}2} + J_{\mathrm{b}3} + \alpha_{\mathrm{h}12} q_1^2 + \alpha_{\mathrm{h}22} q_2^2 + \alpha_{\mathrm{h}32} q_3^2)\dot{\Omega} + \alpha_{\mathrm{h}11} \ddot{q}_1 \\ &+\alpha_{\mathrm{h}21} \ddot{q}_2 + \alpha_{\mathrm{h}31} \ddot{q}_3 + \alpha_{\mathrm{h}13} q_1 \dot{q}_1 \Omega + \alpha_{\mathrm{h}23} q_2 \dot{q}_2 \Omega + \alpha_{\mathrm{h}33} q_3 \dot{q}_3 \Omega + \zeta_\mathrm{h} \Omega = \mu \\ &\ddot{q}_1 + \alpha_{12} \dot{\Omega} + \alpha_{14} q_1 \dot{q}_1 \Omega + (\alpha_{11} + \alpha_{13} \Omega^2) q_1 + \zeta_1 \dot{q}_1 = 0 \\ &\ddot{q}_2 + \alpha_{22} \dot{\Omega} + \alpha_{24} q_2 \dot{q}_2 \Omega + (\alpha_{21} + \alpha_{23} \Omega^2) q_2 + \zeta_2 \dot{q}_2 = 0 \\ &\ddot{q}_3 + \alpha_{32} \dot{\Omega} + \alpha_{34} q_3 \dot{q}_3 \Omega + (\alpha_{31} + \alpha_{33} \Omega^2) q_3 + \zeta_3 \dot{q}_3 = 0 \end{aligned} \tag{9}$$

The first of these equations represents dynamics of the rigid hub. Terms J_h and $J_{\mathrm{b}i}$ are dimensionless mass moment of inertia of the hub and each beam, respectively. All these are expressed as a magnitude of the inertia of the first beam. Since the specimens mass and geometrical dimensions are identical $J_{\mathrm{b}1} = J_{\mathrm{b}2} = J_{\mathrm{b}3} = 1$. Moreover, the term $\Omega = \frac{\mathrm{d}\psi}{\mathrm{d}\tau}$ present in (9) denotes the dimensionless angular velocity of the hub that

is an independent variable of the problem. The parameter μ corresponds to the system excitation (external torque). Within performed numerical simulations this excitation has been considered in two variants: (a) as a driving torque, expressed by a harmonic function $\mu = \mu_0 + \rho \sin \omega\tau$ or (b) as a chaotic Duffing oscillator where $\mu = \rho x$. The variable x was calculated from the Duffing's equation $\ddot{x} + k\dot{x} + x^3 = B_0 + B_1 \cos \omega\tau$ as originally presented by Ueda in [13].

As already reported the last three equations in the set (9) describe dynamics of each beam, where q_1, q_2 and q_3 are the generalised coordinates. Furthermore, ζ_1, ζ_2, ζ_3 and ζ_h are arbitrary introduced viscous damping coefficients, for beams and the hub, respectively. In the performed numerical simulations the beam number 2 is assumed to be a de-tuned one.

3 Numerical Studies

All coefficients α_{ij} (Table 2) representing the dynamic properties of the blades have been calculated based on the specimens stiffnesses a_{mn} as given in Table 1. These correspond to the actual graphite-epoxy laminate material $E_1 = 143.2\,\text{GPa}$, $E_2 = E_3 = 3.1\,\text{GPa}$, $G_{23} = 2.05\,\text{GPa}$, $G_{12} = G_{13} = 3.28\,\text{GPa}$, $\nu_{21} = 0.0075768$, $\nu_{32} = 0.2439$, $\rho = 1350.0\,\text{kg/m}^3$ and blade geometry $l = 0.350\,\text{m}$, $d = 0.034\,\text{m}$, $h = 0.0009\,\text{m}$.

Dynamics of the system is studied by direct numerical simulation of the system represented by Eq. (9). The resonance curves and time series plots are obtained for a system excited by a harmonic torque $\mu(\tau)$. The solutions for the system with harmonic function are sought near the resonance zones for the selected amplitude of excitation ($\rho = 0.01$). The mass moment of inertia of the hub is assumed to be $J_\text{h} = 14.11$.

The obtained resonance curves for amplitude of angular velocity of the hub and displacements of each beam are presented in Fig. 4a, b, respectively. On both graphs two resonances can be observed, the first one close to $\omega \approx 3.52$ and the second one close to $\omega \approx 3.82$. The main resonance is observed for beams No. 1 and No. 3, with very small oscillations of the second beam. In this frequency zone we observe

Table 2 Dimensionless coefficients used in numerical simulations

$\alpha_{11} = \alpha_{31} = 12.3644536$	$\alpha_{21} = 14.5917312$	$\alpha_{h11} = \alpha_{\text{h}31} = 0.010086768$	$\alpha_{\text{h}21} = 0.010085874$
$\alpha_{12} = \alpha_{32} = 1.77991378$	$\alpha_{22} = 1.78007586$	$\alpha_{h12} = \alpha_{\text{h}32} = -0.00765586$	$\alpha_{\text{h}22} = -0.00765438$
$\alpha_{13} = \alpha_{33} = 0.35095587$	$\alpha_{23} = 0.35093716$	$\alpha_{h13} = \alpha_{\text{h}33} = -0.01531173$	$\alpha_{\text{h}23} = -0.01530876$
$\alpha_{14} = \alpha_{34} = -1.55179595$	$\alpha_{24} = -1.5516347$		
$\zeta_1 = \zeta_2 = \zeta_3 = 0.002$		$\zeta_\text{h} = 0.1$	

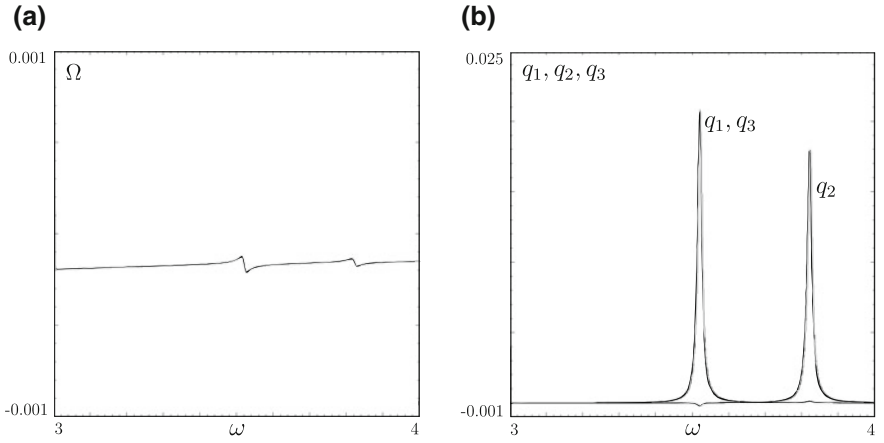

Fig. 4 Resonance curve for amplitude of excitation $\rho = 0.01$ **a** angular velocity of the hub Ω, **b** displacements of each beam q_1, q_2, q_3

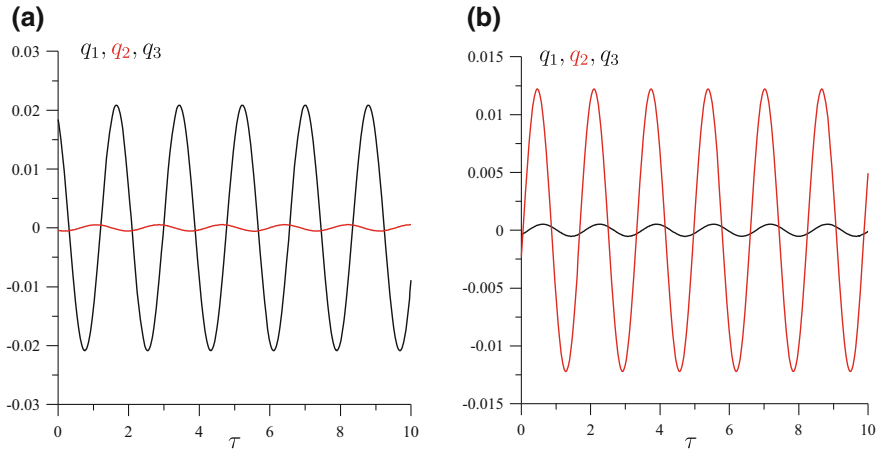

Fig. 5 Time series of each beam **a** close to first resonance zone; **b** close to second resonance zone

synchronisation of motion of beams No. 1 and No. 3 and large reduction in vibrations of the beam No. 2. Around the second resonance zone oscillations are localised in beam No. 2, while motions of beams No. 1 and No. 3 are very small but still synchronised, see time histories in Fig. 5. We may note that the hub motion plays important role in the beams response.

In case of the structure excited by the Duffing oscillator, the Poincaré maps for the individual beams have been obtained. A strange chaotic attractor has been found for each beam, see Figs. 6 and 7a. To study the synchronisation phenomenon the time series plots (Fig. 7b) are studied. It is found the beams No. 1 and No. 3 are completely

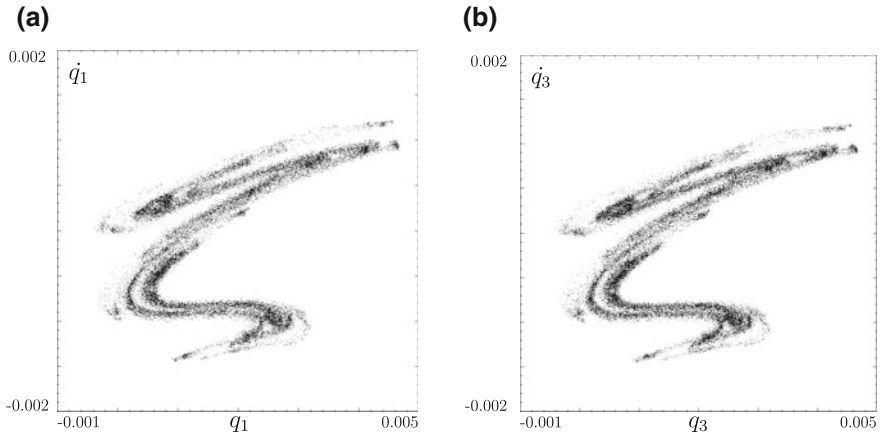

Fig. 6 Portrait of a strange chaotic attractor for **a** beam No. 1; **b** beam No. 3

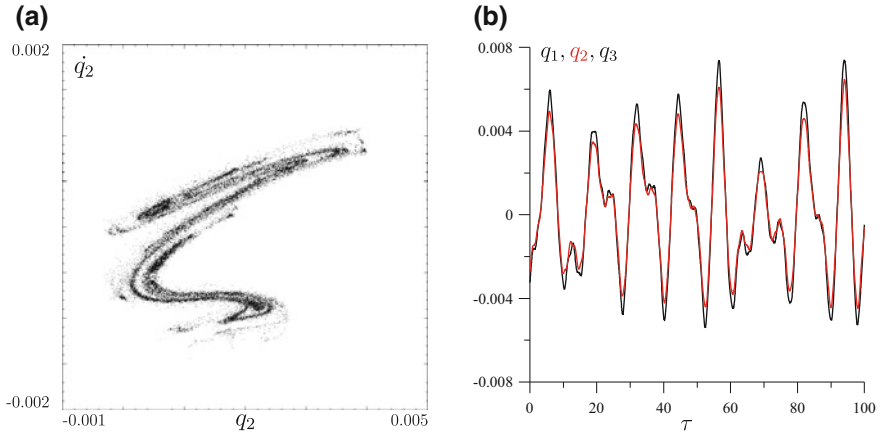

Fig. 7 Portrait of a strange chaotic attractor for a beam No. 2 and time series of each beam

synchronised due to the symmetry. However, the beam No. 2 is synchronised too but its amplitude is smaller than the others ones.

4 Conclusions

For the de-tuned structure excited by harmonic torque two resonances have been observed. The fist resonance occurs close to $\omega \approx 3.52$ and the second one at $\omega \approx 3.82$. The frequency-amplitude curves are exactly the same for the first and the third beam (q_1, q_3). This is due to their full symmetry resulting from analogy in stiffness

and inertia terms. Simultaneously the amplitude of the beam No. 2 is very small. On the other hand, for the second resonance zone vibrations are localised in the beam No. 2 with very small oscillations of beams No. 1 and 3. It should be noted the identical beams No. 1 and 3 exhibit the complete synchronisation of motion, both at the first and the second resonance as well. For the second beam the synchronisation with locked phase is noticed.

In the studied case of the rotor driven by chaotic oscillator the strange chaotic attractor has been observed for each beam. Beams No. 1 and 3 are fully synchronised, beam No. 2 is synchronised too but with a small difference of the amplitude.

Acknowledgements This work was supported by grant UMO-2015/19/N/ST8/03906 from Polish National Science Centre.

References

1. Awrejcewicz, J., Krysko, A.V., Kutepov, I.E., Zagniboroda, N.A., Dobriyan, V., Krysko, A.V.: Chaotic dynamics of flexible Euler-Bernoulli beams. Chaos **23**, 043130–043130-1–25 (2013)
2. Crespo da Silva, M.R.M., Glynn, C.C.: Nonlinear flexural-flexural-torsional dynamics of inextensional beams. I. Equations of motion. J. Struct. Mech. **6**(4), 437–448 (2007)
3. Crespo da Silva, M.R.M., Glynn, C.C.: Nonlinear flexural-flexural-torsional dynamics of inextensional beams. II. Forced motions. J. Struct. Mech. **6**(4), 449–461 (2007)
4. Fukunaga, H.: On isotropic laminate configurations. J. Compos. Mater. **25**(5), 519–535 (1990)
5. Georgiades, F., Latalski, J., Warminski, J.: Equations of motion of rotating composite beam with a nonconstant rotation speed and an arbitrary preset angle. Meccanica **49**(8), 1833–1858 (2014)
6. Kapitaniak, M., Czolczynski, K., Perlikowski, P., Stefanski, A., Kapitaniak, T.: Synchronization of clocks. Phys. Rep. **517**(1–2), 1–69 (2012)
7. Kapitaniak, M., Perlikowski, P., Kapitaniak, T.: Synchronous motion of two vertically excited planar elastic pendula. Commun. Nonlinear Sci. Numer. Simul. **18**(8), 2088–2096 (2013)
8. Koluda, P., Perlikowski, P., Czolczynski, K., Kapitaniak, T.: Synchronization configurations of two coupled double pendula. Commun. Nonlinear Sci. Numer. Simul. **19**(4), 977–990 (2014)
9. Krysko, A.V., Awrejcewicz, J., Kutepov, I.E., Zagniboroda, N.A., Papkova, I.V., Serebryakov, A.V., Krysko, A.V.: Chaotic dynamics of flexible beams with piezoelectric and temperature phenomena. Phys. Lett. A **377**, 2058–2061 (2013)
10. Latalski, J.: Manufacturing tolerances of fiber orientations in optimization of laminated plates. Eng. Optim. **35**(2), 201–213 (2003)
11. Librescu, L., Song, O.: Thin-Walled Composite Beams. Theory and Application. Springer, Dordrecht, The Netherlands (2006)
12. Tsai, S., Pagano, N.: Invariant properties of composite materials. In: Tsai, S., Halpin, J., Pagano, N. (eds.) Composite Materials Workshop, pp. 233–253. Technomic Publishing Company, Lancaster (1968)
13. Ueda, Y.: Explosion of strange attractors exhibited by Duffing's equation. Ann. N. Y. Acad. Sci. **357**(1), 422–434 (1980)
14. Vannucci, P., Verchery, G.: A new method for generating fully isotropic laminates. Compos. Struct. **58**(1), 75–82 (2002)
15. Warminski, J., Balthazar, J.M.: Nonlinear vibrations of a beam with a tip mass attached to a rotating hub, pp. 1619–1624

16. Warminski, J., Szmit, Z., Latalski, J.: Nonlinear dynamics and synchronisation of pendula attached to a rotating hub. Eur. Phys. J. Spec. Top. **223**(4), 827–847 (2014)
17. Yigit, A., Scott, R., Galip Ulsoy, A.: Flexural motion of a radially rotating beam attached to a rigid body. J. Sound Vib. **121**(2), 201–210 (1988)

The Analytical Approach for Identification of Magnetically Induced Vibrations of Working in Faulty State BLDC Motor

Przemysław Szulim and Stanisław Radkowski

Abstract The article discusses the most important stages of modelling the processes taking place in the BLDC motor working in the faulty state. The purpose of the analyses was to determine the relations between magnetically induced vibrations and mechanical damages, which can occur on a real object. Several chapters of this work focus on the successive stages of modelling. Vibrations created as a result of the fluctuation of the rotor magnetic field were analysed, as of the source of the field of the greatest magnitude, dominating inside the motor and playing the key role, from the point of view of the generated vibrations. The obtained results have been discussed and compared with the results obtained from the real object. Usefulness of the conducted analyses in support of diagnostics of this type of motors has been indicated.

Keywords BLDC motor · Analytical modeling · Motor diagnosis

1 Introduction

Precise analysis of an examined object is a primary stage in an assignment of the state diagnostics. It is essential not only because of the more profound knowledge of the object's operation rules but also allows for development of more advanced methods of signal analysis. Diagnostics of the brushless synchronous DC motors is a very interesting scientific task, in which many methods were developed and have since been successfully applied. Still, the most intensively used methods comprise those based on the analysis of the current signal [1, 2], vibration signal [3–5], or methods based on the analysis of the magnetic field around the motor [6–10]. For a better knowledge of the mechanisms of fault influence on the diagnostic symp-

P. Szulim (✉) · S. Radkowski
Warsaw University of Technology, Warsaw, Poland
e-mail: przemyslaw.szulim@pw.edu.pl

S. Radkowski
e-mail: Stanislaw.radkowski@simr.pw.edu.pl

J. Awrejcewicz (ed.), *Dynamical Systems in Theoretical Perspective*,
Springer Proceedings in Mathematics & Statistics 248,
https://doi.org/10.1007/978-3-319-96598-7_28

toms, adequate models are built. In the BLDS motors domain, there have been many modelling strategies developed, among which field methods, circuit methods, and analytical methods are worth mentioning. The latter strategy of BLDC motor modelling has been employed in the last 40 years basically to help designing this kind of motors [11, 12]. Despite available and commonly used MES tools, a large number of publications can be indicated, in which the authors attempted to describe phenomena taking place in the motor by means of analytical description of physical phenomena. Reviewing of the literature shows the development of analytical tools and the models, starting with the simple one-dimensional [13, 14] to relatively advanced two-dimensional motor models [13, 15, 16]. However, a three-dimensional model, precisely describing a rather complex geometric motor structure, still remains quite a challenge. It is worth emphasising that fully analytical models have several serious disadvantages, including: complicatedness and quality of being time-consuming in regard to building the model, the necessity of adopting a series of simplifying assumptions. Their undoubted merit is the mathematical description which can be a starting point for the more sophisticated analyses. In this work, the results of analyses have been shown, conducted based on the electric motor of the BLDC type with particular attention focused on the influence of the selected mechanical damages on the frequency structure of the forces exerted on the motor body.

At the stage of model building, apart from modelling the motor itself, the impairment in the form of demagnetisation, load pulsation and lack of coaxiality were described in an analytical way, the phenomena that will be discussed later on in this work. The model-based description of the component forces exerted on the motor body was compared with results obtained in the course of real tests. They proved several observations made on the basis of the analysis of the analytical motor model, and can constitute the foundation for development of advanced methods of damage detection based on the motor vibroacoustic signal. In this work, a series of simplifying assumptions, discussed in de-tail in subsequent chapters, have been made. In the first step, it should be noticed that only vibrations (forces) arising from the magnetic field of the rotor permanent magnets, will be analyzed in this work. The BLDC motor design has two sources of magnetic field, i.e. permanent magnets located on the rotor, and the stator currents. Focusing attention on one source was dictated by the necessity of limiting the material volume on one hand, and the dominating source of the motor magnetic field was analyzed on the other. In successive publications, the aspect of influence of the stator field will be also analyzed in detail.

2 Analytical Model

In this work, the starting point for acquisition of the desired description of the component forces acting on the motor is an analytical model describing distribution of the magnetic field inside the motor. From the point of view of vibration analysis, only the knowledge of distribution of the magnetic field in the area of the so-called air gap is essential. However, because of different types of use, the most important

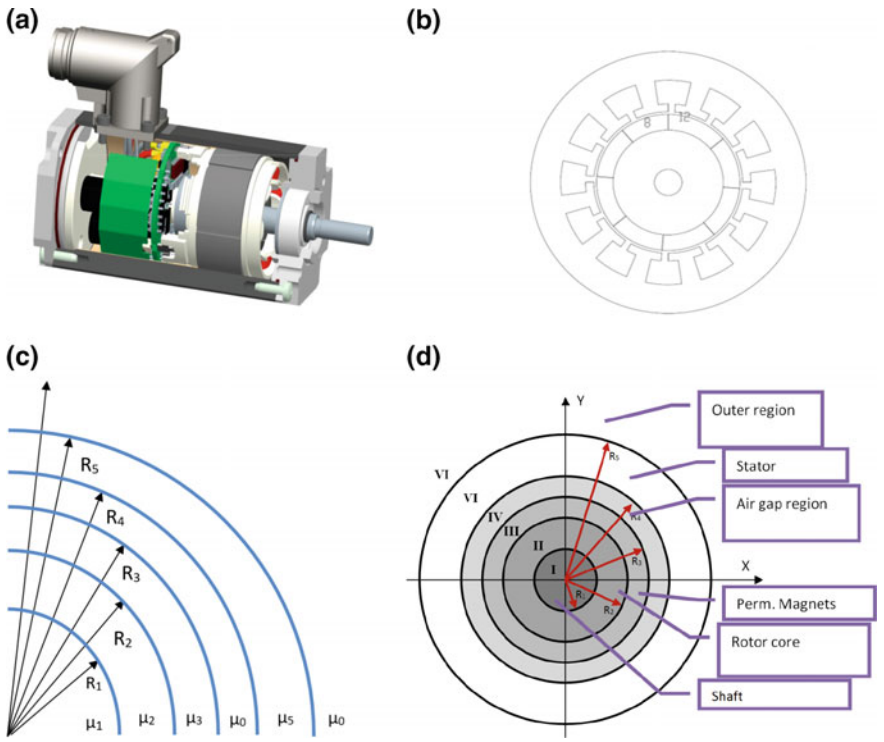

Fig. 1 Two-dimensional motor model: **a** modelled motor, **b** motor cross-section, **c** indication of basic data of characteristic areas, **d** simplified cross-section with characteristic areas indicated

stages of building a complete two-dimensional model describing the field distribution in six characteristic motor regions will be addressed, which is illustrated in Fig. 1. The analysed two-dimensional model assumes the infinitely long body of the motor, which is obviously a great simplification. Another such simplification is substituting the complicated geometry of the cross-section with simple geometric shapes, for which it is relatively easy to generate equations describing the field distribution. Effects connected with the complicated geometry can be introduced into the model through certain functions, which will be discussed in detail later in this article. Each of the six characteristic areas is described by means of certain magnetic permeability and range of changes of the radius r. In the following sub-chapter, the basics of the mathematical apparatus will be discussed and analytical equations derived that constitute the starting point for the subsequent derivations.

2.1 Mathematical Background

Using the Maxwell equation (1) for the magnetostatics case allows for

$$div\boldsymbol{B} = 0 \tag{1}$$

generation of the Eq. (2) of the so-called scalar magnetic potential φ.

$$\Delta\varphi = 0 \tag{2}$$

Using this notion will significantly facilitate calculations. Because of the symmetry, it is worth to analyse the problem in the polar coordinate system $r - \theta$. In such a case, the Laplace equation (2) assumes the following form:

$$\Delta\varphi = \frac{\partial^2\varphi}{\partial r^2} + \frac{1}{r}\frac{\partial\varphi}{\partial r} + \frac{1}{r^2}\frac{\partial^2\varphi}{\partial\theta^2} = 0 \tag{3}$$

Using the separation of variables method makes it possible to obtain the general solution to the Laplace equation (4), where the desired coefficients A, D, C, D, and β are determined by generating an appropriate equation system and using the boundary conditions for individual characteristic areas.

$$\begin{aligned}\varphi(r,\theta) &= (A_0\theta + B_0)(C_0 ln(r) + D_0) \\ &+ \sum_{n=1}^{\infty}(A_n cos(\beta_n x) + B_n sin(\beta_n x))\left(C_n r^n + D_n r^{-n}\right)\end{aligned} \tag{4}$$

$$\begin{aligned}H^r(r,\theta) &= -\frac{\partial\varphi}{\partial r} \\ H^\theta(r,\theta) &= -\frac{1}{r}\frac{\partial\varphi}{\partial\theta}\end{aligned} \tag{5}$$

where H^r is the radial component of the field, and H^θ—the tangential component.

It is worth emphasising that the requested magnetic field is computed from the equation of potential using the relationships (5): Given the general solution of the potential in the form of (4), describing its distribution in one area, and using the equation of the field refraction on the border of two areas in the form (6), the unknown coefficients of the Eq. (4) can be determined.

$$\begin{aligned}\boldsymbol{n}\times\boldsymbol{H}^{IV} &= \boldsymbol{n}\times\boldsymbol{H}^{III} \\ \boldsymbol{n}\cdot\boldsymbol{B}^{IV} &= \boldsymbol{n}\cdot\boldsymbol{B}^{III}\end{aligned} \tag{6}$$

where: $\boldsymbol{B}$—magnetic field induction vector, $\boldsymbol{n}$—vector perpendicular to the boundary surface.

In the case of there being a full symmetry in the geometry of characteristic regions, the Eq. (6) describe the equality of the tangential component of the magnetic field

strength and the radial component of the magnetic induction. A more precise determination of full equations for all characteristic areas exceeds the framework of this article but it can be found in works [7, 17]. The most important results will be mentioned further on in this article.

2.2 Magnetic Field in Magnets Region

From the perspective of further analyses, expansion of Eq. (4) for the region of permanent magnets is worth taking a closer look at. In this case, the region is described by the Poisson partial differential equation (7).

$$\Delta\varphi = div\frac{\boldsymbol{M}}{\mu_r} = \frac{M_r}{r\mu_r} \tag{7}$$

where μ_r—relative magnetic permeability of magnets.

More precise calculations lead to obtaining the full equation of potential (8). Factors M_n^C and M_n^S (9) are the coefficients of the Fourier series of the distribution of the magnetisation vector $\boldsymbol{M}$ for permanent magnets. This vector is shown in Fig. 2 as a function of angle. Even though this is not the only possibility, only the radial magnetisation of the magnets was taken into consideration, which is characterised by the lack of the tangential component of magnetisation and rectangular curve of the vector radial component. At this stage, the effect of demagnetisation of one magnet was taken into account, i.e. the loss of the magnet's magnetic properties. Equation (9) describes the relations of individual coefficients and a certain function $M^C(n)$, whose precise description can be found in work [17], and the rotation angle of the motor shaft β.

$$\begin{aligned} H_r^{III}(r,\theta) = &-\frac{D_0^{III}}{R_2} - \frac{A_0}{\mu_3} - \sum_{n=1}^{\infty}\left[\left(nA_n^{III}r^{n-1} - nB_n^{III}r^{-n-1} - \frac{M_n^C}{\mu_r\left(n^2-1\right)}\right)\right. \\ &\left. cos(n\theta) + n\left(C_n^{III}R_2^{n-1} - D_n^{III}R_2^{-nr^{n-1}-1} - \frac{M_n^S}{\mu_r\left(n^2-1\right)}\right)sin(n\theta)\right] \\ H_\theta^{III}(r,\theta) = &-\sum_{n=1}^{\infty}\left[-n\left(A_n^{III}r^{n-1} + B_n^{III}r^{n-1} - \frac{M_n^C}{\mu_r\left(n^2-1\right)}\right)sin(n\theta)\right. \\ &\left. +n\left(C_n^{III}r^{n-1} + D_n^{III}r^{n-1} - \frac{M_n^S}{\mu_r\left(n^2-1\right)}\right)cos(n\theta)\right] \end{aligned} \tag{8}$$

$$\begin{aligned} M_n^C &= M^C(n)\cos(n\beta) \\ M_n^S &= M^C(n)sin(n\beta) \end{aligned} \tag{9}$$

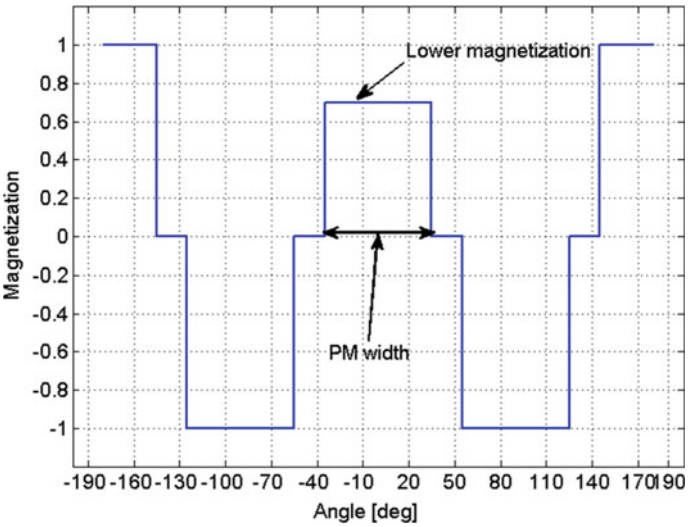

Fig. 2 Radial component of the magnetization vector of permanent magnets with demagnetization effect marked

The system of Eq. (8) is maintained for the remaining five areas. Each of the equations, just like (8), can be expanded into a series of sines and cosines. Using Eq. (6) for two boundaries of the given region, four equations in total are obtained from the equation of potential of a given region. They are compared with the adequate four equations of the neighbouring region using the properties of the Fourier series. Thus, for each of five boundaries of six regions, 20 equations are obtained in total, constituting the system of equations determining the sought coefficients. The system of these equations can be written in the matrix form.

$$\begin{aligned} \boldsymbol{A} \cdot \boldsymbol{X_a} &= -\boldsymbol{I} \cdot M_n^C \\ \boldsymbol{A} \cdot \boldsymbol{X_b} &= -\boldsymbol{I} \cdot M_n^S \end{aligned} \tag{10}$$

where:

$$\boldsymbol{A} = \begin{bmatrix}
\mu_1 R_1^{n-1} & -\mu_2 R_1^{n-1} & \mu_2 R_1^{-n-1} & 0 & 0 & 0 & 0 & 0 & 0 & 0 \\
R_1^{n-1} & -R_1^{n-1} & -R_1^{-n-1} & 0 & 0 & 0 & 0 & 0 & 0 & 0 \\
0 & \mu_2 R_2^{n-1} & -\mu_2 R_2^{-n-1} & -\mu_3 R_2^{n-1} & \mu_3 R_2^{-n-1} & 0 & 0 & 0 & 0 & 0 \\
0 & R_2^{n-1} & R_2^{-n-1} & -R_2^{n-1} & -R_2^{-n-1} & 0 & 0 & 0 & 0 & 0 \\
0 & 0 & 0 & -\mu_3 R_3^{n-1} & \mu_3 R_3^{-n-1} & \mu_0 R_3^{n-1} & -\mu_0 R_3^{-n-1} & 0 & 0 & 0 \\
0 & 0 & 0 & -R_3^{n-1} & -R_3^{-n-1} & R_3^{n-1} & R_3^{-n-1} & 0 & 0 & 0 \\
0 & 0 & 0 & 0 & 0 & -\mu_0 R_4^{n-1} & \mu_0 R_4^{-n-1} & \mu_5 R_4^{n-1} & -\mu_5 R_4^{-n-1} & 0 \\
0 & 0 & 0 & 0 & 0 & -R_4^{n-1} & -R_4^{-n-1} & R_4^{n-1} & R_4^{-n-1} & 0 \\
0 & 0 & 0 & 0 & 0 & 0 & 0 & \mu_5 R_5^{n-1} & -\mu_5 R_5^{-n-1} & \mu_0 R_5^{-n-1} \\
0 & 0 & 0 & 0 & 0 & 0 & 0 & R_5^{n-1} & R_5^{-n-1} & -R_5^{-n-1}
\end{bmatrix}$$

$$\boldsymbol{I} = \begin{bmatrix} 0 \\ 0 \\ \frac{\mu_0}{n\left(n^2-1\right)} \\ \frac{1}{\mu_r\left(n^2-1\right)} \\ \frac{\mu_0}{n\left(n^2-1\right)} \\ \frac{1}{\mu_r\left(n^2-1\right)} \\ 0_{4x1} \end{bmatrix}, \boldsymbol{X_a} = \begin{bmatrix} A_n^I \\ A_n^{II} \\ B_n^{II} \\ A_n^{III} \\ B_n^{III} \\ A_n^{IV} \\ B_n^{IV} \\ A_n^V \\ B_n^V \\ A_n^{VI} \end{bmatrix}, \boldsymbol{X_b} = \begin{bmatrix} B_n^I \\ C_n^{II} \\ D_n^{II} \\ C_n^{III} \\ D_n^{III} \\ C_n^{IV} \\ D_n^{IV} \\ C_n^V \\ D_n^V \\ B_n^{VI} \end{bmatrix}$$

$\boldsymbol{X_a}$ and $\boldsymbol{X_b}$ are vectors of the sought coefficients of equations.

2.3 Modelling of the Eccentricity Fault

The eccentricity fault can result from the presence of failure of, for example, bearings, and is manifested by creation of the heterogenous air gap between the stator and rotor. Mathematically, the description of this process can be started by defining the system of coordinates $r' - \theta'$ related to the rotor, which is illustrated in Fig. 3.

The parameters describing the eccentricity effect are: the shift parameter ε and the revolution angle α. Figure 3 illustrates that part of characteristic regions (rings) remains coaxial relative to the general coordinate system, whereas the other part does not. This results in substantial complicating of calculations because the form of Eq. (6) is getting complicated to a very large degree (the normal vector $\boldsymbol{n}$ for the shifted regions is a function of the ε shift and the revolution angle α). It proves that

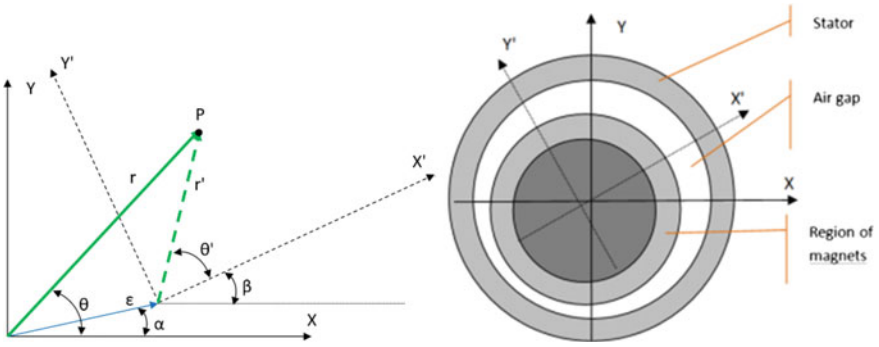

Fig. 3 Geometric description of the eccentricity phenomenon

finding the precise distribution of field for such a case is very difficult or impossible. This is why the perturbation method has been called for, i.e. the method finding the approximate solution. Thanks to the employment of this method, the ultimate equation of potential could be rendered as a sum of the undisturbed solution (without eccentricity) and the successive orders describing the eccentricity effect (11).

$$\varphi^i(r,\theta) = \varphi^i_{(0)}(r,\theta) + \varepsilon\varphi^i_{(1)}(r,\theta) + \varepsilon^2\varphi^i_{(2)}(r,\theta) + \ldots \tag{11}$$

Only the zeroth and the first orders were taken into account in the model. The equation of potential $\varphi^i_{(1)}$ for the ith region requires determining the appropriate coefficients like in the case of Eq. (8), which is practically equal to finding the solution to the potential. The description of the way the sought coefficients were determined was limited to indicating only the ultimate equation allowing for pinpointing the desired coefficients, because of its ample size.

$$\left.\begin{aligned} \boldsymbol{A}\cdot\boldsymbol{X}_{\boldsymbol{a}(1)} &= sin(\alpha-\theta)\left(\boldsymbol{E}\cdot\boldsymbol{X}_{\boldsymbol{b}(0)} + \boldsymbol{J} * M_n^S\right) + cos(\alpha-\theta)\boldsymbol{F}\cdot\boldsymbol{X}_{\boldsymbol{a}(0)} - \boldsymbol{I}\cdot M_n^C \\ \boldsymbol{A}\cdot\boldsymbol{X}_{\boldsymbol{b}(1)} &= -sin(\alpha-\theta)\left(\boldsymbol{E} * \boldsymbol{X}_{\boldsymbol{a}(0)} + \boldsymbol{J} * M_n^C\right) + cos(\alpha-\theta)\boldsymbol{F}\cdot\boldsymbol{X}_{\boldsymbol{b}(0)} - \boldsymbol{I}\cdot M_n^S \end{aligned}\right\} \tag{12}$$

where: $\boldsymbol{X}_{\boldsymbol{a}(1)}$ and $\boldsymbol{X}_{\boldsymbol{b}(1)}$ are vectors of the sought coefficients, the $\boldsymbol{E}, \boldsymbol{F}, \boldsymbol{I}, \boldsymbol{J}$ matrixes, however, were defined in work [7].

3 Mathematical Description of Forces Exerted on the Motor Body

Analysis of forces in motor was based on the Maxwell stress tensor. Two equations below allow to calculate tangential and normal stress acting on a motor mechanical component.

$$\tau = \frac{B_r B_\theta}{\mu_0} \tag{13}$$

$$\sigma = \frac{B_r^2 - B_\theta^2}{2\mu_0} \tag{14}$$

Component of total axial forces in X and in Y direction was presented on Fig. 4. They can be calculated from the Eq. (15). These forces appear due to normal motor work. In case of effect of eccentricity or demagnetization, new frequency components of the force could appear, which will be shown in this paragraph.

$$F_x(\alpha, \varepsilon, \theta') = R_4 l \int_0^{2\pi} \sigma cos(\vartheta) d\vartheta$$

$$F_y(\alpha, \varepsilon, \theta') = R_4 l \int_0^{2\pi} \sigma sin(\vartheta) d\vartheta \tag{15}$$

After expanding Eq. (15) one can observe that the force can be presented as a sum of combination of magnetic field components (radial, tangential, generated by magnets or currents).

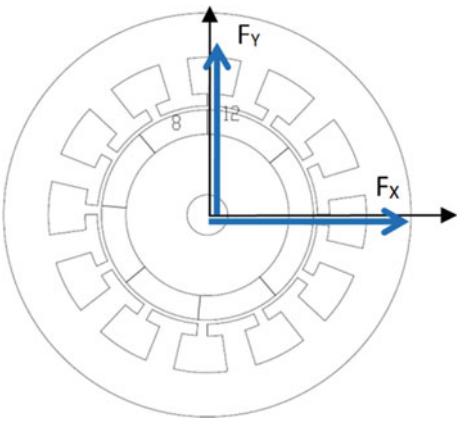

Fig. 4 Forces in BLDC motor

Table 1 Sums and harmonic differences

n_1+n_2		n_1				n_1-n_2		n_1			
		4	12	20	28			4	12	20	28
n_2	4	8	16	24	32	n_2	4	0	8	16	24
	12	16	24	32	40		12	−8	0	8	16
	20	24	32	40	48		20	−16	−8	0	8
	28	32	40	48	56		28	−24	−16	−8	0

$$F_{rx}(\varepsilon,t)=\frac{R_4 l}{2\mu_0}\int_0^{2\pi}\left(B_r^{R^2}+2B_r^R B_r^S+B_r^{S^2}-\left(B_\theta^{R^2}+2B_\theta^R B_\theta^S+B_\theta^{S^2}\right)\right)\cos(\vartheta)d\vartheta \tag{16}$$

where: B^R and B^S magnetic field with indicated source (magnets and phase current respectively), l—axial length of the motor. Due to the assumptions made, described in the introductory part to this work, only the $B_r^{R^2}$ component of the Eq. (16) will be taken into account. Because the integrator in Eq. (16) integrates on dimension it has no influence on the frequency component of the force equation. Square of radial component of the magnets magnetic field is shown in Eq. (17). X_1A, X_2A, AA are the functions of two parameters and are time independent. This equation reveals effect of the amplitude modulation. One can expect many harmonics in frequency spectrum of signal like this. In case of lack of demagnetization, $n_1, n_2 = 4, 12, 20, 28, 36\ldots = (2k-1)p$. The sums of the coefficients lead to appearance of harmonics from the series $2kp$. Due to eccentricity, around each harmonic in spectrum signal appears two additional component with frequency $2kp\omega_\beta \pm \omega_\alpha$. From Eq. (17) one can predict that amplitudes of modulation component can differ left and right. These differences depend on combination of coefficient n_1, n_2. From Eq. (17) one can observe two series of harmonic order: $n_1 - n_2$ and n_1+n_2. Practically both of them create a series of similar values presented in form of the Table 1.

$$\begin{aligned}B_r^{R^2}=\mu_0^2\sum_{n_1=1}^{N}\sum_{n_2=1}^{N}n_1n_2M^C(n_1)M^C(n_2)\{&0.5(1+\varepsilon^2AA(n_1,n_2)[cos\left((n_1-n_2)\omega_\beta t\right)\\&+cos\left((n_1+n_2)\omega_\beta t\right)+0.25\varepsilon(1+\varepsilon)\\&*[(X_1A(n_1,n_2)+X_2A(n_2,n_1))cos\left((n_1-n_2)\omega_\beta t-\omega_\alpha t\right)\\&+(X_1A(n_1,n_2)+X_1A(n_2,n_1))cos\left((n_1+n_2)\omega_\beta t-\omega_\alpha t\right)\\&+(X_2A(n_1,n_2)+X_1A(n_2,n_1))\cos\left((n_1-n_2)\omega_\beta t+\omega_\alpha t\right)\\&+(X_2A(n_1,n_2)+X_2A(n_2,n_1))\cos\left((n_1+n_2)\omega_\beta t+\omega_\alpha t\right)]\}\end{aligned} \tag{17}$$

$$
\begin{aligned}
B_r^{R^2} = \mu_0^2 \sum_{n=1}^{N} \Bigg\{ \sum_{k=1}^{K-n} [& f_1(n,k,\varepsilon)\cos(2np(\theta-\beta)) \\
& + f_2(n,k,\varepsilon)\cos(2np(\theta-\beta)-\theta-\alpha) \\
& + f_3(n,k,\varepsilon)\cos(2np(\theta-\beta)+\theta+\alpha)] \\
& + \sum_{k=1}^{n} [f_4(n,k,\varepsilon)\cos(2np(\theta-\beta)) \\
& + f_5(n,k,\varepsilon)\cos(2np(\theta-\beta)-\theta-\alpha) \\
& + f_6(n,k,\varepsilon)\cos(2np(\theta-\beta)+\theta+\alpha)] \Bigg\}
\end{aligned}
\tag{18}
$$

First conclusion is fact, that to find first N harmonics one need to sum some number of components. This observation allows for rewriting Eq. (17) in the form shown in (18). Equation (18) is a simplified form of Eq. (17). Additional elements $f_1()$–$f_6()$ represent some function independent on time and position. This equation gives a brief look on the mechanism of the frequency component creation. The form of equation allows for an easy analysis from the point of view of the frequency component creation. Also, the effect of the amplitude modulation is clearer. To calculate the amplitude of n-th harmonic one can sum K particular elements (where $K \to \infty$). Equation (18) is valid only in the case of lack of the demagnetization effect. Another interesting property that can be deduced from this equation is different amplitudes of the modulated frequency component due to different $f_1()$–$f_6()$ function values.

4 Test Stand

The view on the test stand was presented in Fig. 5. Analysed was the middle power BLDC motor BG75 × 75 manufactured by Dunkermotren. The most important parameters were presented in the Table 2.

Table 2 Investigated motor parameters

Parameters	Value
Motor nominal power	530 W
Nominal torque	1.5 Nm
Weight	2.8 kg
Size	0.075 × 0.140 m
Number of pole pairs	4
Number of phases	3

On the test stand signals like: vibration, phase currents, magnetic field, torque and speed were measured. Measurement system was composed of dedicated sensors, National Instrument measurement staff and dedicated application.

5 Real Object Investigation

During the experiment, different type of fault (like: eccentricity or unbalance) was applied to the motor. For each type of the fault, measurements were conducted for different load state and different rotational speed. Next, only the selected results from analysis will be presented. In Fig. 6a, one can observe the order analysis of a component of the acceleration signal. The most intensive components belong to the series of $2kp$ (8, 16, 24, 32, 40) which agreed with Eq. (18) and their analysis. Figure 6a shows influence of different degree of eccentricity on spectrum. In this picture, modulation component, especially around the 16-th harmonic, can be clearly observed. This also agrees well with the model. It is worth to note, that modulation components have different amplitude on the left and right sides. The 17-th component shows that its amplitude very strongly depends on the eccentricity level. Another interesting result was presented in Fig. 6b. In this picture, three different levels of load of the motor in presence of eccentricity were presented. From analysis of the Eq. (18) the force theoretically doesn't depend on current so it also doesn't depend on load condition.

Practically, in Fig. 6b one can observe that when load condition changes from no load to the full load state, also amplitudes of frequency component change. But, what is interesting and has practical application, these changes are quite small.

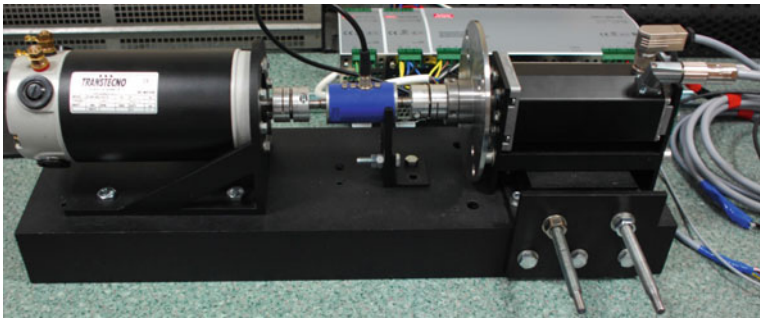

Fig. 5 Test stand

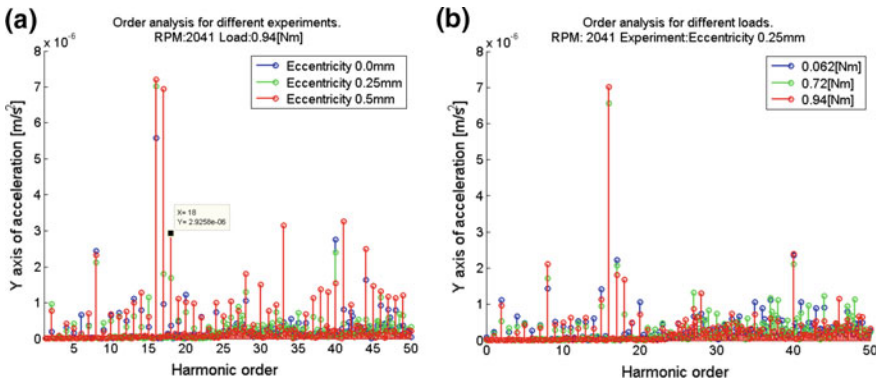

Fig. 6 **a** Frequency spectrum of the radial component of acceleration signal for three degrees of eccentricity. **b** Frequency spectrum of the radial component signal for three load levels

6 Summary

In the paper, comparison analysis of results of the model and real object investigation was presented. At first, the most important steps of building the motor model were briefly presented. The result of this stage was an equation describing distribution of the magnetic field in the air gap region. Next, based on this equation, an analytical formula of force was developed. Analysis of this equation proved that eccentricity or demagnetisation effect should be observed in frequency spectrum of the vibration signal. This prediction was confirmed by the analysis of measurement registered on the real object. This analysis showed that modulation effect is a good measure of dynamic eccentricity defect. Model analysis explained presence of the major component in spectrum. It also explained the effect such as different amplitudes of the modulation frequency component. The prepared analysis proved that model based analysis allows for better prediction of signal changes caused by mechanical faults.

Acknowledgements The works described in the project was funded by the National Research and Development Center under the project: "Technologies for autonomous reconfiguration of materials in vehicles".

References

1. Blödt, M., Granjon, P., Raison, B., Regnier, J.: Mechanical fault detection in induction motor drives through stator current monitoring-theory and application examples. Fault Detect. 451–488 (2010)
2. Benbouzid, M.E.H: A review of induction motors signature analysis as a medium for faults detection. IEEE Trans. Ind. Electron. **47**(5), 984–993 (2000)

3. Chen, Y., Yang, H., Han, Z.Y.: Investigation of electromagnetic vibration of permanent magnet brushless machines. In: International conference on electrical machines and systems, ICEMS 2008, pp. 621–626 (2008)
4. Rezig, A., Mekideche, M.R., Djerdir, A.: Impact of eccentricity and demagnetization faults on magnetic noise generation in brushless permanent magnet DC motors. J. Electr. Eng. Technol. **6**(3), 356–363 (2011)
5. Radkowski, S., Szulim, P.: Analysis of vibration of rotors in unmanned aircraft. In: 19th International conference on methods models automation robotics. MMAR 2014, pp. 748–753 (2014)
6. Lee, S.-T., Kim, K.-T., Hur, J.: Diagnosis technique for stator winding inter-turn fault in BLDC motor using detection coil. In: 2015 9th International conference on power electronics and ECCE Asia (ICPE-ECCE Asia), pp. 2925–2931 (2015)
7. Szulim, P., Gontarz, S.: Using The surrounding magnetic field in diagnosis of the BLDC motor. J. Electr. Eng. **66**(7), 193–198 (2015)
8. Vitek, O., Janda, M., Hajek, V., Bauer, P.: Detection of eccentricity and bearings fault using stray flux monitoring. In: 2011 IEEE International symposium on diagnostics for electric machines, power electronics and drives, SDEMPED, pp. 456–461 (2011)
9. Kohut, P., Holak, K., Uhl, T., Mączak, J., Szulim, P.: Application of vision based damage detection for real civil engineering structure. Key Eng. Mater. **588**, 22–32 (2013)
10. Gontarz, S., Szulim, P., Seńko, J., Dybała, J.: Use of magnetic monitoring of vehicles for proactive strategy development. Transp. Res. Part C Emerg. Technol. **52**, 102–115 (2015)
11. Boules, N.: Two-dimensional field analysis of cylindrical machines with permanent magnet excitation. IEEE Trans. Ind. Appl. **5**, 1267–1277 (1984)
12. Rahideh, A., Korakianitis, T.: Analytical calculation of open-circuit magnetic field distribution of slotless brushless PM machines. Int. J. Electr. Power Energy Syst. **44**(1), 99–114 (2013)
13. Hughes, A., Miller, T.J.E.: Analysis of fields and inductances in air-cored and iron-cored synchronous machines. In: Proceedings of the institution of electrical engineers, vol. 124, pp. 121–126 (1977)
14. Kaźmierczak, M., Kudra, G., Awrejcewicz, J., Wasilewski, G.: Mathematical modelling, numerical simulations and experimental verification of bifurcation dynamics of a pendulum driven by a dc motor. Eur. J. Phys. **36**(5), 055028 (2015)
15. Lubin, T., Mezani, S., Rezzoug, A.: Development of a 2-D analytical model for the electromagnetic computation of axial-field magnetic gears. IEEE Trans. Magn. **49**(11), 5507–5521 (2013)
16. Kępiński, R., Awrejcewicz, J., Lewandowski, D.: Dynamical simulation of a nonlinear stepper motor system. Int. J. Dyn. Control **3**(1), 31–35 (2015)
17. Szulim, P.: Modelowanie silnika BLDC na potrzeby diagnoistyki Część I: Model polowy. PRZEGLĄD ELEKTROTECHNICZNY **1**(2), 149–153 (2017)

Micro-dynamics of Thin Tolerance-Periodic Cylindrical Shells

Barbara Tomczyk and Paweł Szczerba

Abstract Thin linearly elastic Kirchhoff-Love-type open circular cylindrical shells having a functionally (transversally) graded macrostructure and a tolerance-periodic microstructure in circumferential direction are objects of consideration. At the same time, the shells have constant structure in axial direction. On the microscopic level, the geometrical, elastic and inertial properties of these shells are determined by highly oscillating, non-continuous and tolerance-periodic functions in circumferential direction. On the other hand, on the macroscopic level, the averaged (effective) properties of the shells are described by functions being smooth and slowly varying along circumferential direction. The aim of this note is to study some problems of micro-dynamics of these shells, e.g. micro-vibrations depending on a cell size, The micro-dynamic problems will be analysed in the framework of the averaged asymptotic-tolerance model. Contrary to the exact shell equations with highly oscillating, non-continuous and tolerance-periodic coefficients, governing equations of the averaged model mentioned above have continuous and slowly varying coefficients depending also on a cell size. An important advantage of this model is that it makes it possible to investigate micro-dynamics of the tolerance-periodic shells independently of their macro-dynamics.

Keywords Functionally graded shells · Tolerance modelling · Micro-vibrations

1 Introduction

Thin linearly elastic Kirchhoff-Love-type open circular cylindrical shells with a tolerance-periodic microstructure in circumferential direction are analysed. It means that *on the microscopic level*, the shells under consideration consist of many small

B. Tomczyk (✉) · P. Szczerba
Department of Structural Mechanics, Lodz University of Technology, Lodz, Poland
e-mail: barbara.tomczyk@p.lodz.pl

P. Szczerba
e-mail: szczerba.paw@p.lodz.pl

J. Awrejcewicz (ed.), *Dynamical Systems in Theoretical Perspective*,
Springer Proceedings in Mathematics & Statistics 248,
https://doi.org/10.1007/978-3-319-96598-7_29

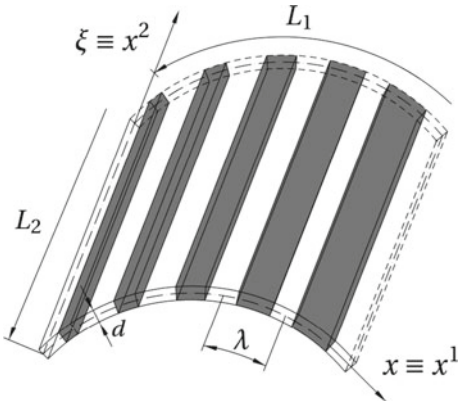

Fig. 1 An example of a shell with a tolerance-periodic microstructure

elements. These elements, called *cells*, are treated as thin shells. It is assumed that *the adjacent cells are nearly identical, but the distant elements can be very different*. An example of such shell is shown in Fig. 1. At the same time, the shells have constant structure in axial direction. On the microscopic level, the geometrical, elastic and inertial properties of such shells are determined by highly oscillating non-continuous *tolerance-periodic functions* in x. By *tolerance periodic functions* we shall mean functions which in every cell can be approximated by periodic functions in x.

On the other hand, *on the macroscopic level*, the averaged (effective) properties of the shells are described by functions being *smooth* and *slowly varying* along circumferential direction. It means that the tolerance-periodic shells under consideration can be treated as made of *functionally graded materials* (FGM), cf. [9], and called *functionally graded shells*. Moreover, since effective properties of the shells are graded in direction normal to interfaces between constituents, this gradation is referred to as *the transversal gradation*.

Dynamic problems of such shells are described by partial differential equations with highly oscillating, tolerance-periodic and non-continuous coefficients. Thus, these equations are too complicated to be applied to the investigations of engineering problems. To obtain averaged equations with continuous and slowly varying coefficients, a lot of different approximate modelling methods have been proposed. Periodic and tolerance-periodic structures are usually described using *homogenized models* derived by means of *asymptotic methods*. The mathematical foundations of the asymptotic modelling technique can be found in Jikov et al. [5]. Unfortunately, in the models of this kind *the effect of a microstructure size* (called *the length-scale effect*) on the overall shell behaviour is neglected in the first approximation which is usually employed, cf. [1].

This effect can be taken into account using *the modified couple stress-based theories of continuous media*, cf. [13]. The mathematical non-classical models of micro/nano-scale structures derived by means of *the modified couple stress theory* contain *an internal material length-scale parameter*. Hence, these models make it possible to investigate the size effect in static and dynamic problems of micro/nano-

structures. We mention here papers by Awrejcewicz et al. [2–4]. In [2, 3], the length-scale effect in chaotic dynamics of size-dependent Timoshenko micro-beams with functionally graded properties along their thickness is studied. In [4], mathematical model for the analysis of static and dynamic problems of functionally graded micro/nano-beams is derived and discussed; the size-dependent model equations are formulated on the basis of the Grigolyuk-Chulkov hypotheses and the modified couple stress theory. We mention also papers by Krysko et al. [7, 8], where the length-scale effect in geometrically and physically nonlinear static and dynamic problems for size-dependent nano-scale beams is investigated; the considerations are carried out within non-classical Bernoulli-Euler, Timoshenko and Sheremetev-Pelekh-Reddy-Levinson mathematical models derived on the basis of the modified couple stress theory.

The length-scale effect can be also taken into account using *the non-asymptotic tolerance averaging technique*, cf. [12]. Governing equations of the tolerance models have constant or slowly varying coefficients depending also on a cell size. Some applications of this method to the modelling of mechanical and thermomechanical problems for various periodic and tolerance-periodic (functionally graded) structures are shown in many works. The extended list of papers and books on this topic can be found in [12].

Recently, the new tolerance and asymptotic models of dynamic problems for thin transversally graded cylindrical shells have been proposed by Tomczyk and Szczerba in [10]. The models introduced in [10] were combined together into *a certain new combined asymptotic-tolerance model*, cf. [11]. An important advantage of the asymptotic-tolerance model is that it makes it possible to study micro-dynamics of tolerance-periodic shells independently of their macro-dynamics.

The aim of the present contribution is to investigate free micro-vibrations of the transversally graded shells under consideration. To this end, the combined asymptotic-tolerance model presented by Tomczyk and Szczerba in [11] will be applied. Governing equations of this model make it possible to analyse the micro-vibrations depending on a microstructure size independently of the shell macro-vibrations (i.e. vibrations independent of a cell size).

2 Formulation of the Problem, Starting Equations

We assume that x^1 and x^2 are coordinates parametrizing the shell midsurface M in circumferential and axial directions, respectively. We denote $x \equiv x^1 \in \Omega \equiv (0, L_1)$ and $\xi \equiv x^2 \in \Xi \equiv (0, L_2)$, where L_1, L_2 are length dimensions of M, cf. Fig. 1. Let $O\,\bar{x}^1\bar{x}^2\bar{x}^3$ stand for a Cartesian orthogonal coordinate system in the physical space R^3 and denote $\bar{\mathbf{x}} \equiv (\bar{x}^1, \bar{x}^2, \bar{x}^3)$. A cylindrical shell midsurface M is given by $M \equiv \left\{\bar{\mathbf{x}} \in R^3 : \bar{\mathbf{x}} = \bar{\mathbf{r}}\left(x^1, x^2\right),\ \left(x^1, x^2\right) \in \Omega \times \Xi\right\}$, where $\bar{\mathbf{r}}(\cdot)$ is the smooth function such that $\partial\,\bar{\mathbf{r}}/\partial x^1 \cdot \partial\,\bar{\mathbf{r}}/\partial x^2 = 0$, $\partial\,\bar{\mathbf{r}}/\partial x^1 \cdot \partial\,\bar{\mathbf{r}}/\partial x^1 = 1$, $\partial\,\bar{\mathbf{r}}/\partial x^2 \cdot \partial\,\bar{\mathbf{r}}/\partial x^2 = 1$. It means that on M we have introduced *the orthonormal parametrization*.

Sub- and superscripts $\alpha, \beta, \ldots$ run over 1, 2 and are related to x^1, x^2, summation convention holds. Partial differentiation related to x^α is represented by ∂_α. Moreover, it is denoted $\partial_{\alpha\ldots\delta} \equiv \partial_\alpha \ldots \partial_\delta$. Let $a^{\alpha\beta}$ stand for the midsurface first metric tensor. Under orthonormal parametrization $a^{\alpha\beta}$ is the unit tensor.

The time coordinate is denoted by $t \in \mathrm{I} \equiv [t_0, t_1]$. Let $d(x)$ and r stand for the shell thickness and the midsurface curvature radius, respectively.

The basic cell Δ is defined by: $\Delta \equiv [-\lambda/2,\ \lambda/2] \in \Omega \equiv (0, L_1)$, where λ is a cell length dimension in $x \equiv x^1$-direction. *The microstructure length parameter* λ satisfies conditions: $\lambda/d_{\max} >> 1$, $\lambda/r << 1$ and $\lambda/L_1 << 1$.

Denote by $u_\alpha = u_\alpha(x, \xi, t)$, $w = w(x, \xi, t)$, $(x, \xi, t) \in \Omega \times \Xi \times \mathrm{I}$, the shell displacements in directions tangent and normal to M, respectively. Elastic properties of the shells are described by shell stiffness tensors $D^{\alpha\beta\gamma\delta}(x)$, $B^{\alpha\beta\gamma\delta}(x)$. Let $\mu(x)$ stand for a shell mass density per midsurface unit area. The external forces will be neglected.

It is assumed that the behaviour of the shell under consideration is described by the action functional determined by Lagrange function L being a highly oscillating function with respect to x and having the well-known form, cf. [6]

$$L = -\frac{1}{2}(D^{\alpha\beta\gamma\delta}\partial_\beta u_\alpha \partial_\delta u_\gamma + \frac{2}{r} D^{\alpha\beta 11} w \partial_\beta u_\alpha + \frac{1}{r^2} D^{1111} w w + B^{\alpha\beta\gamma\delta}\partial_{\alpha\beta} w \partial_{\gamma\delta} w - \mu\, a^{\alpha\beta}\dot{u}_\alpha \dot{u}_\beta - \mu \dot{w}^2). \tag{1}$$

Applying the principle of stationary action we arrive at the system of Euler-Lagrange equations, which can be written in explicit form as

$$\begin{aligned} &\partial_\beta(D^{\alpha\beta\gamma\delta}\partial_\delta u_\gamma) + r^{-1}\partial_\beta(D^{\alpha\beta 11} w) - \mu\, a^{\alpha\beta}\ddot{u}_\beta = 0\,, \\ &r^{-1} D^{\alpha\beta 11}\partial_\beta u_\alpha + \partial_{\alpha\beta}(B^{\alpha\beta\gamma\delta}\partial_{\gamma\delta} w) + r^{-2} D^{1111} w + \mu \ddot{w} = 0. \end{aligned} \tag{2}$$

It can be observed that equations (2) coincide with the well-known governing equations of Kirchhoff-Love theory of thin elastic shells, cf. [6]. For tolerance-periodic shells, coefficients $D^{\alpha\beta\gamma\delta}(x)$, $B^{\alpha\beta\gamma\delta}(x)$, $\mu(x)$ of equations (2) are highly oscillating, non-continuous and tolerance-periodic functions in x. Applying the combined asymptotic-tolerance modelling technique (cf. [12]) to lagrangian (1), the averaged model equations with continuous and slowly varying coefficients depending also on a cell size were derived in [11]. Here, these equations will be used to investigations of free micro-vibration frequencies of an open simply supported cylindrical shell having constant thickness and made of two linearly elastic isotropic materials tolerance-periodically distributed in circumferential direction as shown in Fig. 1. To make the analysis more clear, in the next section the combined asymptotic-tolerance model equations proposed in [11] will be reminded.

3 Modelling Procedure, Equations of Combined Model

The combined modelling technique used to starting lagrangian (1) is realized in two steps. The first step is based on *the consistent asymptotic averaging* of lagrangian (1) under *the consistent asymptotic decomposition* of fields u_α, w, in $\Delta(x) \times \Xi \times \mathrm{I}$

$$u_{\varepsilon\alpha}(x, z, \xi, t) \equiv u_\alpha(x, z/\varepsilon, \xi, t) = u^0_\alpha(z, \xi, t) + \varepsilon \tilde{h}_\varepsilon(x, z) U_\alpha(z, \xi, t) ,$$
$$w_\varepsilon(x, z, \xi, t) \equiv w(x, z/\varepsilon, \xi, t) = w^0(z, \xi, t) + \varepsilon^2 \tilde{g}_\varepsilon(x, z) W(z, \xi, t). \qquad (3)$$

where $\varepsilon = 1/m, \quad m = 1, 2, \ldots, \quad z \in \Delta_\varepsilon(x), \quad \Delta_\varepsilon \equiv (-\varepsilon\lambda/2, \varepsilon\lambda/2), x \in \Omega$, $(\xi, t) \in \Xi \times \mathrm{I}$.

Unknown functions u^0_α, w^0 and U_α, W in (3) are assumed to be continuous and bounded in Ω. Unknowns u^0_α, w^0 and U_α, W are called *macrodisplacements* and *fluctuation amplitudes*, respectively. They are independent of ε. By $\tilde{h}_\varepsilon(x, z) \equiv \tilde{h}(x, z/\varepsilon)$ and $\tilde{g}_\varepsilon(x, z) \equiv \tilde{g}(x, z/\varepsilon)$ in (3) we denote *periodic approximations* of highly oscillating, given a priori *fluctuation shape functions* $h(\cdot)$ and $g(\cdot)$ in $\Delta(x)$. They have to satisfy conditions: $h \in O(\lambda)$, $\lambda\partial_1 h \in O(\lambda)$, $g \in O(\lambda^2)$, $\lambda\partial_1 g \in O(\lambda^2)$, $\lambda^2\partial_{11} g \in O(\lambda^2)$, $< \mu\, h >=< \mu\, g >= 0$, where the *averaging operator* $< \cdot >$ for function $f(x)$ integrable and bounded in every cell is defined by

$$< f > (x) \equiv \frac{1}{\lambda} \int_{x-\lambda/2}^{x+\lambda/2} \tilde{f}(x, z) dz, \quad z \in \Delta(x) , \quad x \in \Omega , \qquad (4)$$

where $\tilde{f}(\cdot)$ is a periodic approximation of $f(\cdot)$ in Δ .

Introducing decomposition (3) into (1), under weak limit passage $\varepsilon \to 0$ we obtain the averaged form of lagrangian (1). Then, applying the principle of stationary action we arrive at *the governing equations of consistent asymptotic model for the tolerance-periodic shells under consideration*. These equations consist of partial differential equations for macrodisplacements u^0_α, w^0 coupled with linear algebraic equations for fluctuation amplitudes U_α, W. After eliminating fluctuation amplitudes from the governing equations by means of

$$U_\gamma = -(G^{-1})_{\gamma\eta} \, [< \partial_1 h D^{1\eta\mu\vartheta} > \partial_\vartheta u^0_\mu + r^{-1} < \partial_1 h D^{1\eta 11} > w^0],$$
$$W = -E^{-1} < \partial_{11} g B^{11\gamma\delta} > \partial_{\gamma\delta} w^0 , \qquad (5)$$

where averages $< \cdot >$ are calculated using (4) and where $G_{\alpha\gamma}(x) =< D^{\alpha 1\gamma 1}(\partial_1 h)^2 > (x)$, $E(x) =< B^{1111}(\partial_{11} g)^2 > (x)$, we arrive finally at *the asymptotic model equations expressed only in macrodisplacements* u^0_α, w^0

$$\partial_\beta(D_h^{\alpha\beta\gamma\delta}\partial_\delta u^0_\gamma + r^{-1} D_h^{\alpha\beta 11} w^0) - < \mu > a^{\alpha\beta}\ddot{u}^0_\beta = 0 ,$$
$$\partial_{\alpha\beta}(B_g^{\alpha\beta\gamma\delta}\partial_{\gamma\delta} w^0) + r^{-1} D_h^{11\gamma\delta}\partial_\delta u^0_\gamma + r^{-2} D_h^{1111} w^0 + < \mu > \ddot{w}^0 = 0 , \qquad (6)$$

where $D_h^{\alpha\beta\gamma\delta}(x) \equiv < D^{\alpha\beta\gamma\delta} > - < D^{\alpha\beta\eta 1}\,\partial_1 h > (G^{-1})_{\eta\zeta} < \partial_1 h D^{1\zeta\gamma\delta} >$,

$$B_g^{\alpha\beta\gamma\delta}(x) \equiv < B^{\alpha\beta\gamma\delta} > - < B^{\alpha\beta 11}\partial_{11} g > E^{-1} < \partial_{11} g B^{11\gamma\delta} > .$$

Coefficients of equations (6) are *slowly varying* in x but they are *independent of the microstructure cell size*. Hence, this model is not able to describe the length-scale effect on the overall shell dynamics and it will be referred to as *the macroscopic model*.

In the first step of combined modelling it is assumed that within the asymptotic model, solutions u_α^0, w^0 to the problem under consideration are known. Hence, there are also known functions $u_{0\alpha} = u_\alpha^0 + hU_\alpha$ and $w_0 = w^0 + gW$, where U_α, W are given by means of (5).

The second step is based on *the tolerance averaging* of lagrangian (1) under so-called *superimposed decomposition*.

The fundamental concepts of the tolerance approach under consideration are those of *two tolerance relations between points and real numbers determined by tolerance parameters, slowly-varying functions, tolerance-periodic functions, fluctuation shape functions and the averaging operation*, cf. [12].

A continuous, bounded and differentiable function $F(\cdot)$ defined in $\bar{\Omega} \equiv [0, L_1]$ is called *slowly-varying of the R-th kind* with respect to cell Δ and tolerance parameters δ, $F \in SV_\delta^R(\Omega, \Delta)$, if it can be treated (together with its derivatives up to the R-th order) as constant on the cell. Nonnegative integer R is assumed to be specified in every problem under consideration.

An integrable and bounded function $f(\cdot)$ defined in $\bar{\Omega} \equiv [0, L_1]$ is called *tolerance-periodic of the R-th kind* with respect to cell Δ and tolerance parameters δ, $f \in TP_\delta^R(\Omega, \Delta)$, if it can be treated (together with its derivatives up to the R-th order) as periodic on the cell.

The *averaging operation* is defined by (4).

The tolerance modelling is based on two assumptions, which strictly related to the concepts of *the tolerance periodic, slowly-varying* and *fluctuation shape functions*. The first of them is called *the tolerance averaging approximation* (tolerance relations which make it possible to neglect terms of an order of tolerance parameters δ), cf. [12]. The second one is termed *the micro-macro decomposition.*

In the problem under consideration, we introduce *the extra micro-macro decomposition* superimposed on the known solutions $u_{0\alpha}$, w_0 obtained within the macroscopic model

$$\begin{aligned} u_{c\alpha}(x, \xi, t) &= u_{0\alpha}(x, \xi, t) + c(x) Q_\alpha(x, \xi, t), \\ w_b(x, \xi, t) &= w_0(x, \xi, t) + b(x) V(x, \xi, t), \end{aligned} \tag{7}$$

where *fluctuation amplitudes* Q_α, V are *the new slowly-varying unknowns*, i.e. $Q_\alpha \in SV_\delta^1(\Omega, \Delta)$, $V \in SV_\delta^2(\Omega, \Delta)$. Functions $c(x)$ and $b(x)$ are *the new* tolerance-periodic, continuous and highly-oscillating *fluctuation shape functions* which are assumed to be known in every problem under consideration. These functions have

to satisfy conditions: $c \in O(\lambda)$, $\lambda\partial_1 c \in O(\lambda)$, $b \in O(\lambda^2)$, $\lambda\partial_1 b \in O(\lambda^2)$, $\lambda^2\partial_{11} b \in O(\lambda^2)$, $< \mu\, c >=< \mu\, b >= 0$.

We substitute the right-hand sides of (7) into (1). The resulting lagrangian is denoted by L_{cb} . Then, we average L_{cb} over cell Δ using averaging formula (4) and applying *the tolerance averaging approximation*. As a result we obtain function $< L_{cb} >$ called *the tolerance averaging of starting lagrangian* (1) *in* Δ *under superimposed decomposition* (7). Then, applying the principle of stationary action and introducing the extra approximation $1 + \lambda/r \approx 1$, we obtain the system of Euler-Lagrange equations for Q_α, V, which can be written in explicit form as

$$\underline{< D^{\alpha 22\delta}(c)^2 >}(x)\partial_{22} Q_\delta - < D^{\alpha 11\delta}(\partial_1 c)^2 > (x) Q_\delta - \underline{< \mu(c)^2 >}(x) a^{\alpha\beta}\ddot{Q}_\beta = r^{-1} < D^{\alpha 111}\partial_1 c\, w_0 > (x) + < D^{\alpha\beta\gamma 1}\partial_1 c\, \partial_\beta u_{0\gamma} > (x), \tag{8}$$

$$\underline{< B^{2222}(b)^2 >}(x)\partial_{2222} V + [\underline{2 < B^{1122} b\partial_{11} b >}(x) - 4\underline{< B^{1212}(\partial_1 b)^2 >}(x)]\partial_{22} V + < B^{1111}(\partial_{11} b)^2 > (x) V + \underline{< \mu(b)^2 >}(x)\ddot{V} = - < B^{\alpha\beta 11}\partial_{11} b\partial_{\alpha\beta} w_0 > (x). \tag{9}$$

Equations (8) and (9) together with *the micro-macro decomposition* (7) constitute *the superimposed microscopic model* (i.e. microscopic model imposed on the macroscopic model obtained in the first step of combined modelling).

Coefficients of the derived model equations are *smooth and slowly-varying* in x and some of them *depend on a cell size* λ (underlined terms). The right-hand sides of (8) and (9) are known under assumption that $u_{0\alpha}$, w_0 were determined in the first step of modelling. The basic unknowns Q_α, V of the model equations must be *the slowly-varying functions in tolerance periodicity direction*. This requirement can be verified only a posteriori *and it determines the range of the physical applicability of the model.* The boundary conditions for Q_α, V should be defined only on boundaries $\xi = 0, \xi = L_2$.

It can be shown, cf. [11], that under assumption that fluctuation shape functions $h(x)$, $g(x)$ of macroscopic model coincide with fluctuation shape functions $c(x)$, $b(x)$ of microscopic model we can obtain microscopic model equations, which are independent of the solutions obtained in the framework of the macroscopic model

$$\underline{< D^{1221}(h)^2 >}(x)\partial_{22} Q_1 - < D^{1111}(\partial_1 h)^2 > (x) Q_1 - \underline{< \mu(h)^2 >}(x)\ddot{Q}_1 = 0\,, \tag{10}$$

$$\underline{< D^{2222}(h)^2 >}(x)\partial_{22} Q_2 - < D^{2112}(\partial_1 h)^2 > (x) Q_2 - \underline{< \mu(h)^2 >}(x)\ddot{Q}_2 = 0\,, \tag{11}$$

$$\underline{< B^{2222}(g)^2 >}(x)\partial_{2222} V + [\underline{2 < B^{1122} g\partial_{11} b >}(x) + - 4\underline{< B^{1212}(\partial_1 g)^2 >}(x)]\partial_{22} V + < B^{1111}(\partial_{11} g)^2 > (x) V + \underline{< \mu(g)^2 >}(x)\ddot{V} = 0. \tag{12}$$

It means, that an important advantage of the combined model is that *it makes it possible to describe selected problems of the shell micro-dynamics* (e.g. the free micro-vibrations, propagation of waves related to the micro-fluctuation amplitudes)

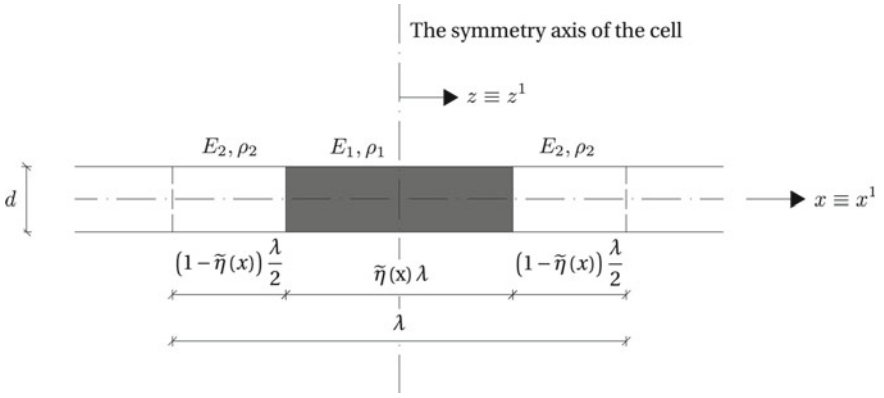

Fig. 2 Basic cell $\Delta \equiv [-\lambda/2,\ \lambda/2] \subset \bar{\Omega} \equiv [0, L_1]$ of the transversally graded shell

independently of the shell macro-dynamics. Moreover, micro-dynamic behaviour of the shells in the axial, circumferential and normal directions can be analysed independently of each other.

4 Applications—Free Micro-vibration Frequencies

4.1 Description of the Problem

In this section we shall investigate micro-vibrations of an open thin simply supported cylindrical shell with L_1, L_2, r, d as its circumferential length, axial length, midsurface curvature radius and constant thickness, respectively. The shell has a functionally graded material structure along circumferential direction and constant structure in the axial direction, cf. Fig. 1. It is assumed that the shell is made of two elastic isotropic materials, which are perfectly bonded on interfaces.

The basic cell Δ is defined by: $\Delta \equiv [-\lambda/2,\ \lambda/2] \subset \Omega \equiv [0, L_1]$, where λ is a cell length dimension in $x \equiv x^1$-direction, cf. Figs. 1 and 2. We recall that *the microstructure length parameter* λ has to satisfy conditions: $\lambda/d >> 1$, $\lambda/r << 1$ and $\lambda/L_1 << 1$. Setting $z \equiv z^1 \in [-\lambda/2,\ \lambda/2]$, we assume that the cell has a symmetry axis for $z = 0$. Inside the cell, the geometrical, elastic and inertial properties of the shell are described by symmetric (i.e. even) functions of argument z.

Properties of the component materials are described by: Young's moduli E_1, E_2, Poisson's ratios ν_1, ν_2 and mass densities ρ_1, ρ_2, cf. Fig. 2. It is assumed that elastic $E(\cdot)$ and inertial $\rho(\cdot)$ properties of the composite shell are tolerance-periodic functions in x, $E(x),\ \rho(x) \in TP^0_\delta(\Omega, \Delta)$, but Poisson's ratio $\nu \equiv \nu_1 = \nu_2$ is

constant. Inside the cell, periodic approximations $\tilde{E}(x,z)$, $\tilde{\rho}(x,z)$ of functions $E(x)$, $\rho(x)$ take the form

$$\tilde{E}(x,z),\ \tilde{\rho}(x,z) = \begin{cases} E_1,\ \rho_1\ for\ z \in (-\tilde{\eta}(x)\lambda/2,\ \tilde{\eta}(x)\,\lambda/2\,), \\ E_2,\ \rho_2\ for\ z \in [-\lambda/2\ ,\ -\tilde{\eta}(x)\lambda/2] \cup [\tilde{\eta}(x)\lambda/2,\ \lambda/2], \end{cases} \tag{13}$$

where $\tilde{\eta}(x)$ is a periodic approximation of distribution function $\eta(x)$ of material properties, cf. Fig. 2. The rigidities $D^{\alpha\beta\gamma\delta}(x)$, $B^{\alpha\beta\gamma\delta}(x)$ of the shell are described by: $D^{\alpha\beta\gamma\delta}(x) = DH^{\alpha\beta\gamma\delta}$, $B^{\alpha\beta\gamma\delta}(x) = BH^{\alpha\beta\gamma\delta}$, where $D = E(x)d/(1-\nu^2)$, $B = E(x)\,d^3/(12(1-\nu^2))$ and the nonzero components of tensor $H^{\alpha\beta\gamma\delta}$ are: $H^{1111} = H^{2222} = 1$, $H^{1122} = H^{2211} = \nu$, $H^{1212} = H^{1221} = H^{2121} = H^{2112} = (1-\nu)/2$. The shell mass density per midsurface unit area is given by $\mu(x) = \rho(x)\,d$.

The periodic approximations of fluctuation shape functions $h(x) \in FS^1_\delta(\Omega, \Delta)$, $g(x) \in FS^2_\delta(\Omega, \Delta)$ can be taken as: $\tilde{h}(x,z) = \lambda \sin(2\pi z/\lambda)$, $\tilde{g}(x,z) = \lambda^2[\cos(2\pi z/\lambda) + c(x)]$, $z \in \Delta(x)$, $x \in \Omega$, where $c(x)$ is a slowly-varying function in x and is determined by condition $< \mu\, g >= 0$:

$$c(x) = -\frac{(\rho_1 - \rho_2)\sin(\pi(\tilde{\eta}(x))}{\pi(\rho_1\tilde{\eta}(x) + \rho_2(1-\tilde{\eta}(x))}.$$

Function $c(x)$ is treated as constant in calculations of derivatives $\partial_1\tilde{g}$, $\partial_{11}\tilde{g}$.

The subsequent analysis will be based on Eqs. (10)–(12). Since coefficients of these equations are functions of x, then the approximate formulae of free vibration frequencies will be derived applying the known Galerkin's method, cf. [6], in the range $0 \le x \le L_1$.

4.2 Free Micro-vibrations in Circumferential Direction

The shell free micro-vibrations along circumferential direction are described by Eq. (10).

Solution to Eq. (10) satisfying the boundary conditions for a shell simply supported on edges $\xi = 0$, $\xi = L_2$ can be assumed in the form

$$Q_1(x,\xi,t) = Q_1^*(x)\sin(\pi\xi/L_2)\cos(\bar{\omega}\,t)\,, \tag{14}$$

where $Q_1^*(x)$ is a slowly-varying function in x satisfying boundary conditions on edges $x = 0$, $x = L_1$ and $\bar{\omega}$ is a frequency of free micro-vibrations along circumferential direction. Substituting (14) into (10), for $\sin(\pi\xi/L_2) \neq 0$, we arrive at equation for $Q_1^*(x)$

$$Q_1^*(x)[-(\pi/L_2)^2 < D^{1221}(h)^2 > (x) > - < D^{1111}(\partial_1 h)^2 > (x) + \bar{\omega}^2 < \mu(h)^2 > (x)] = 0\,, \tag{15}$$

In order to obtain approximate formula of free vibration frequency $\bar{\omega}$, the known Galerkin's method, cf. [6], can be applied to Eq. (15). Solution to Eq. (15) satisfying the boundary conditions for a shell simply supported on edges $x = 0$, $x = L_1$ is assumed as $Q_1^*(x) = A\cos(\pi x/L_1)$. We substitute this solution into (15). For $A \neq 0$, the orthogonality condition of the resulting left-hand side of Eq. (15) and function $\cos(\pi x/L_1)$ has the following form

$$\int_0^{L_1} [-(\pi\ /L_2)^2 < D^{1221}(h)^2 > (x) > - < D^{1111}(\partial_1 h)^2 > (x) + \overline{\omega}^2 < \mu(h)^2 > (x)] \cos^2(\pi x/L_1) dx = 0\,.$$

Setting $\bar{h} = \lambda^{-1} h$, from the above orthogonality condition, we obtain the following formula for $\bar{\omega}$

$$\bar{\omega}^2 = \frac{\int_0^{L_1} [(\pi/L_2)^2 \lambda^2 < D^{1221}(\bar{h})^2 > (x) > + < D^{1111}(\partial_1 h)^2 > (x)] \cos^2(\pi x/L_1) dx}{\lambda^2 \int_0^{L_1} < \mu(\bar{h})^2 > (x) \cos^2(\pi x/L_1) dx}\,. \tag{16}$$

4.3 Free Micro-vibrations in Axial Direction

The shell free micro-vibrations in axial direction are described by Eq. (11).

Solution to Eq. (11) satisfying the boundary conditions for a shell simply supported on edges $\xi = 0$, $\xi = L_2$ can be assumed in the form

$$Q_2(x, \xi, t) = Q_2^*(x) \cos(\pi \xi/L_2) \cos(\breve{\omega}\, t)\,, \tag{17}$$

where $Q_2^*(x)$ is a slowly-varying function in x satisfying boundary conditions on edges $x = 0$, $x = L_1$ and $\breve{\omega}$ is a frequency of free micro-vibrations along axial direction. Substituting (17) into (11), for $\cos(\pi \xi/L_2) \neq 0$, we arrive at equation for $Q_2^*(x)$

$$Q_2^*(x)[-(\pi/L_2)^2 < D^{2222}(h)^2 > (x) > - < D^{1221}(\partial_1 h)^2 > (x) + \breve{\omega}^{\,2} < \mu(h)^2 > (x)] = 0\,, \tag{18}$$

Solution to Eq. (18) satisfying the boundary conditions for a shell simply supported on edges $x = 0, x = L_1$ is assumed as $Q_2^*(x) = B\sin(\pi x/L_1)$. We substitute this solution into (18). By means of Galerkin's method, for $B \neq 0$, the follow-

ing orthogonality condition of the resulting left-hand side of Eq. (18) and function $\sin(\pi x/L_1)$ is obtained

$$\int_0^{L_1} [-(\pi/L_2)^2 < D^{2222}(h)^2 > (x) > - < D^{1221}(\partial_1 h)^2 > (x) + \breve{\omega}^2 < \mu(h)^2 > (x)] \sin^2(\pi x/L_1) dx = 0.$$

Setting $\bar{h} = \lambda^{-1} h$, from the above orthogonality condition, we obtain the following formula for $\breve{\omega}$

$$\breve{\omega}^2 = \frac{\int_0^{L_1} [(\pi/L_2)^2 \lambda^2 < D^{2222}(\bar{h})^2 > (x) > + < D^{1221}(\partial_1 h)^2 > (x)] \sin^2(\pi x/L_1) dx}{\lambda^2 \int_0^{L_1} < \mu(\bar{h})^2 > (x) \sin^2(\pi x/L_1) dx}. \tag{19}$$

4.4 Transversal Free Micro-vibrations

Free transversal micro-vibrations of the shell under consideration are described by Eq. (12).

Solution to Eq. (12) satisfying the boundary conditions for a shell simply supported on edges $\xi = 0$, $\xi = L_2$ can be assumed in the form

$$V(x, \xi, t) = V^*(x) \sin(\pi \xi / L_2) \cos(\omega t), \tag{20}$$

where $V(x)$ is a slowly-varying function in x satisfying boundary conditions on edges $x = 0, x = L_1$ and ω is a frequency of free transversal micro-vibrations. Substituting (20) into (12), for $\sin(\pi \xi / L_2) \neq 0$, we arrive at equation for $V^*(x)$

$$V^*(x)[(\pi/L_2)^4 < B^{2222}(g)^2 > (x) > -2(\pi/L_2)^2(< B^{1122} g \partial_{11} g > (x) + - 2 < B^{1212}(\partial_1 g)^2 > (x)) + < B^{1111}(\partial_{11} g)^2 > (x) - \omega^2 < \mu(g)^2 > (x)] = 0. \tag{21}$$

Solution to Eq. (21) satisfying the boundary conditions for a shell simply supported on edges $x = 0, x = L_1$ is assumed as $V^*(x) = C \sin(\pi x/L_1)$. We substitute this solution into (21). By means of Galerkin's method, for $C \neq 0$, the orthogonality condition of the resulting left-hand side of Eq. (21) and function $\sin(\pi x/L_1)$ is obtained. Setting $\breve{g}(x) = \lambda^{-1} g(x)$, $\bar{g}(x) = \lambda^{-2} g(x)$, from this orthogonality condition, we derive the following formula for ω

$$\omega^2 = [\lambda^4 \int_0^{L_1} < \mu(\bar{g})^2 > (x) \sin^2(\pi x/L_1) dx]^{-1} \int_0^{L_1} [(\pi/L_2)^4 \lambda^4 < B^{2222}(\bar{g})^2 > (x) > +$$
$$- 2(\pi/L_2)^2 \lambda^2 (< B^{1122} \bar{g} \partial_{11} g > (x) > -2 < B^{1212} (\partial_1 \breve{g})^2 > (x))$$
$$+ < B^{1111} (\partial_{11} g)^2 > (x) >] \sin^2(\pi x/L_1) dx. \tag{22}$$

4.5 Numerical Results

Let us introduce two distribution functions of material properties $\eta(x)$:

$$\tilde{\eta}(x) = \sin^2(\pi x/L_1) , \tag{23}$$
$$\tilde{\eta}(x) = (x/L_1)^2. \tag{24}$$

We also define the following dimensionless free micro-vibration frequencies

$$\bar{\Omega}^2 \equiv \frac{(1-\nu^2)\rho_1 (L_1)^2}{E_1} \bar{\omega}^2,$$
$$\breve{\Omega}^2 \equiv \frac{(1-\nu^2)\rho_1 (L_1)^2}{E_1} \breve{\omega}^2,$$
$$\Omega^2 \equiv \frac{12(1-\nu^2)\rho_1 (L_1)^2}{E_1} \omega^2, \tag{25}$$

where frequencies $\bar{\omega}$, $\breve{\omega}$, ω are determined by formulae (16), (19) and (22), respectively.

The subsequent calculations will be made for Poisson's ratio $\nu = 0.3$, for fixed ratios $L_2/L_1 = 2, d/\lambda = 0.1, \lambda/L_1 = 0.1$ and for various ratios $E_2/E_1 \in [0.01,\ 1]$, $\rho_2/\rho_1 \in [0.01,\ 1]$.

In Figs. 3, 4 and 5, there are presented diagrams of dimensionless free micro-vibration frequencies $\bar{\Omega}, \breve{\Omega}, \Omega$ given by $(25)_1, (25)_2, (25)_3$, respectively, versus both ratios $E_2/E_1 - \rho_2/\rho_1$, made for distribution functions of material properties $\eta(x)$ given by (23), cf. Figs. 3a, 4a and 5a, and by (24), cf. Figs. 3b, 4b and 5b.

4.6 Discussion of Results

On the basis of results shown in Figs. 3, 4 and 5, the following conclusions can be formulated:

- Values of dimensionless free micro-vibration frequencies increase with the increasing of ratio E_2/E_1 and decrease with the increasing of ratio ρ_2/ρ_1 .

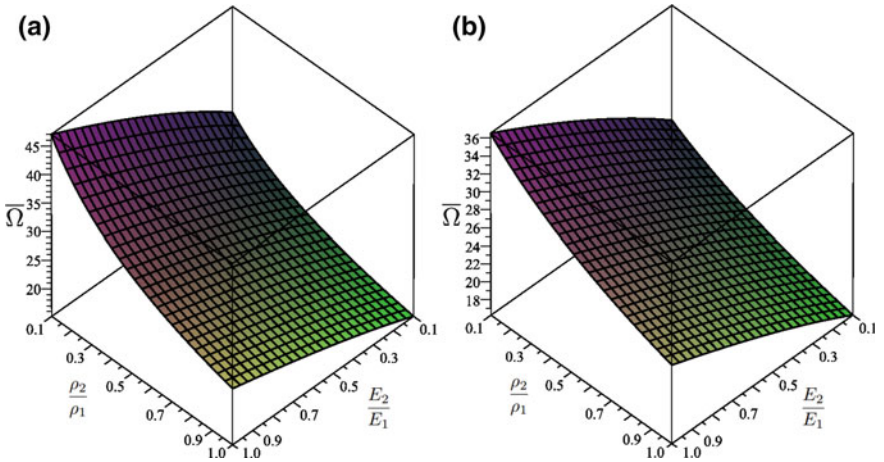

Fig. 3 Diagrams of dimensionless free micro-vibration frequency $\bar{\Omega}$ versus ratios $E_2/E_1 - \rho_2/\rho_1$ made for distribution function $\eta(x)$ given by **a** (23), **b** (24)

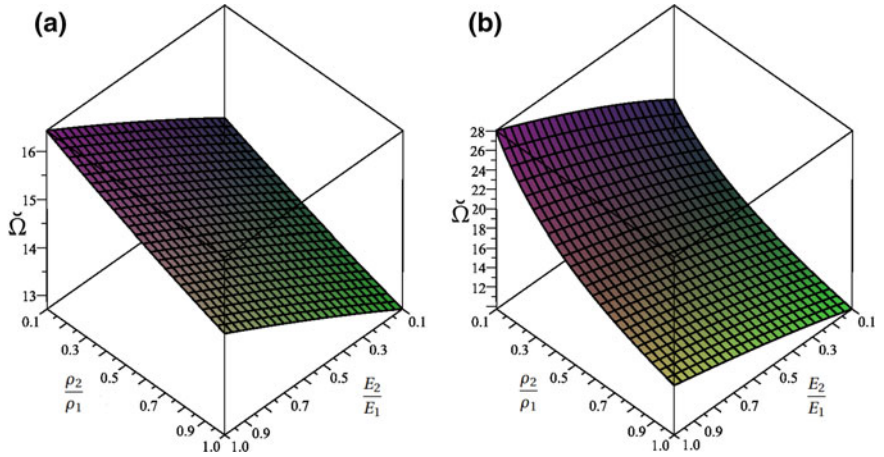

Fig. 4 Diagrams of dimensionless free micro-vibration frequency $\breve{\Omega}$ versus ratios $E_2/E_1 - \rho_2/\rho_1$ made for distribution function $\eta(x)$ given by **a** (23), **b** (24)

- The highest value of frequency $\bar{\Omega}$, cf. Fig. 3, is obtained for $\eta(x)$ given by (23) and for pair of ratios $(E_2/E_1 = 1.0\,,\ \rho_2/\rho_1 = 0.1)$. The smallest value of $\bar{\Omega}$ is obtained for $\eta(x)$ given by (24) and for pair of ratios $(E_2/E_1 = 0.1\,,\ \rho_2/\rho_1 = 1.0)$.
- The highest value of frequency $\breve{\Omega}$, cf. Fig. 4, is obtained for $\eta(x)$ given by (24) and for pair of ratios $(E_2/E_1 = 1.0\,,\ \rho_2/\rho_1 = 0.1)$. The smallest value of $\bar{\Omega}$ is obtained for $\eta(x)$ given by (23) and for pair of ratios $(E_2/E_1 = 0.1\,,\ \rho_2/\rho_1 = 1.0)$.
- The highest value of frequency $\breve{\Omega}$, cf. Fig. 5, is obtained for $\eta(x)$ given by (24) and for pair of ratios $(E_2/E_1 = 1.0\,,\ \rho_2/\rho_1 = 0.1)$. The smallest value of $\bar{\Omega}$ is

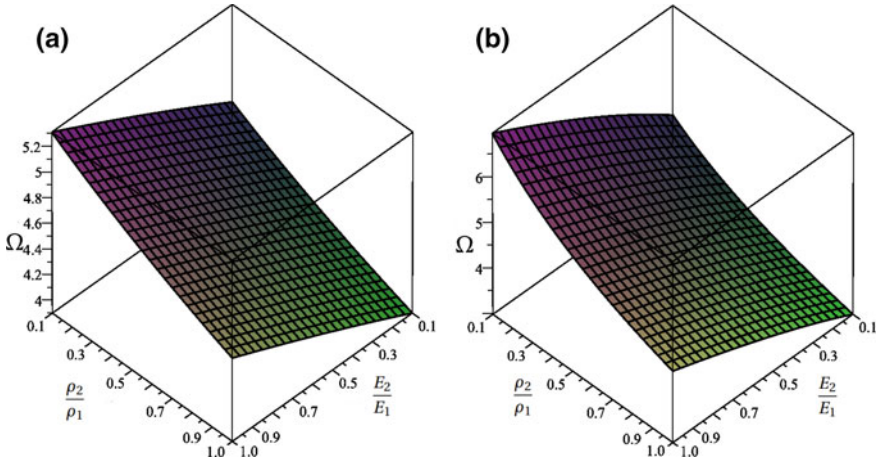

Fig. 5 Diagrams of dimensionless free micro-vibration frequency Ω versus ratios $E_2/E_1 - \rho_2/\rho_1$ made for distribution function $\eta(x)$ given by **a** (23), **b** (24)

obtained for $\eta(x)$ given by (23) and for pairs of ratios ($E_2/E_1 = 0.1\,,\ \rho_2/\rho_1 = 1.0$).

5 Final Remarks

Thin linearly elastic Kirchhoff-Love-type open circular cylindrical shells having a functionally (transversally) graded macrostructure and a tolerance-periodic microstructure in circumferential direction are objects of consideration, cf. Fig. 1. At the same time, the shells have constant structure in axial direction. The averaged combined asymptotic-tolerance model of dynamic problems for such shells was derived in [11]. Contrary to the well-known governing equations of Kirchhoff-Love theory with highly oscillating, non-continuous and tolerance-periodic coefficients, equations of the asymptotic-tolerance model have continuous and slowly varying coefficients depending also on a microstructure size. Hence, this model allows us to describe the effect of a length scale on the dynamic shell behaviour. The main advantage of this model is that it makes it possible to separate the macroscopic description of some special problems from their microscopic description.

In the present paper, applying the asymptotic-tolerance model proposed in [11], the free micro-vibration frequencies of a simply supported tolerance-periodic shell under consideration have been determined, cf. Eqs. (16), (19), (22), and investigated for two different distribution functions of material properties. These frequencies depend on a cell size. The influence of elastic and inertial properties of the considered microstructured shell on the free micro-vibration frequencies has been analysed. From the calculational example it follows that the free micro-vibration frequencies

decrease with the decreasing of differences between *inertial properties* of the component materials, but they increase with the decreasing of differences between *elastic properties* of the shell material components.

References

1. Awrejcewicz, A., Andrianov, I.V., Danishevs'kyy, V.V., Ivankov, A.O.: Asymptotic methods in the theory of plates with mixed boundary conditions. Wiley, Chichester (2014)
2. Awrejcewicz, J., Krysko, A.V., Pavlov, S.P., Zhigalov, M.V., Krysko, V.A.: Chaotic dynamics of size dependent Timoshenko beams with functionally graded properties along their thickness. Mech. Syst. Signal Process. **93**, 415–430 (2017)
3. Awrejcewicz, J., Krysko, A.V., Pavlov, S.P., Zhigalov, M.V.: Nonlinear dynamics size-dependent geometrically nonlinear Timoshenko beams based on a modified moment theory. Appl. Math. Sci. **11**(5), 237–247 (2017)
4. Awrejcewicz, J., Krysko, V.A., Zhigalov, M.V., Krysko, A.V.: Mathematical model of a three-layer micro- and nano-beams on the hypotheses of the Grigolyuk-Chulkov and the modified couple stress theory. Int. J. Solids Struct. **117**, 39–50 (2017)
5. Jikov, V.V., Kozlov, C.M., Olejnik, O.A.: Homogenization of Differential Operators and Functionals. Springer, Berlin-Heidelberg (1994)
6. Kaliski, S. (ed.): Vibrations. PWN-Elsevier, Warsaw-Amsterdam (1992)
7. Krysko, A.V., Awrejcewicz, J., Zhigalov, M.V., Pavlov, S.P., Krysko, V.A.: Nonlinear behaviour of different flexible size-dependent beams models based on the modified couple stress theory. Part 1. Governing equations and static analysis of flexible beams. Int. J. Non-Linear Mech. **93**, 96–105 (2017)
8. Krysko, A.V., Awrejcewicz, J., Zhigalov, M.V., Pavlov, S.P., Krysko, V.A.: Nonlinear behaviour of different flexible size-dependent beams models based on the modified couple stress theory. Part 2. Chaotic dynamics of flexible beams. Int. J. Non-Linear Mech. **93**, 106–121 (2017)
9. Suresh, S., Mortensen, A.: Fundamentals of Functionally Graded Materials. The University Press, Cambridge (1998)
10. Tomczyk, B., Szczerba, P.: Tolerance and asymptotic modelling of dynamic problems for thin microstructured transversally graded shells. Compos. Struct. **162**, 365–373 (2017)
11. Tomczyk, B., Szczerba, P.: Combined asymptotic-tolerance modelling of dynamic problems for functionally graded shells. Compos. Struct. **183**, 176–184 (2018)
12. Woźniak, C., et al. (eds.): Mathematical Modelling and Analysis in Continuum Mechanics of Microstructured Media. Silesian University of Technology Press, Gliwice (2010)
13. Yang, F., Chong, A.C.M., Lam, D.C.C., Tong, P.: Couple stress based strain gradient theory for elasticity. Int. J. Solids Struct. **39**(10), 2731–2743 (2002)

Stokes Flow Through a Tube with Wavy Wall

Włodzimierz Bielski and Ryszard Wojnar

Abstract We propose a study of the flow in a tube with wavy wall adopting Malevich - Mityushev - Adler's method, and find a correction to Hagen-Poiseuille's solution. The problem is to be solved by expanding the velocity and pressure fields in Fourier series involving an infinite set of unknown coefficients. The boundary surface is expanded in Taylor's series. A perturbation expansion in terms of the powers of the small parameter ε of the full set of Stokes' equations yields a cascade of boundary value problems which are solved at each step in closed form. Even in the first order approximation $O(\varepsilon)$, new results are obtained.

Keywords Hagen-Bouillabaisse flow · Hemorheology · Fourier series Perturbation expansion · Rough bottom

1 Introduction

The problem of flow through a tube with a wavy wall appears in different applications. It is important in hemorheology and hemodynamics, both fields of physiology [1, 2]. It is well known that the two leading causes of death, myocardial infarction (heart attack), and stroke, may each directly result from an arterial system that has been slowly and progressively compromised by years of deterioration. An artery wall thickens as a result of invasion and accumulation of white blood cells and proliferation of intimal-smooth-muscle cell creating an atheromatous (fibro-fatty) plaque. This limits dynamic blood flow and in the consequence the oxygen flow within the brain.

W. Bielski (✉)
Institute of Geophysics, Polish Academy of Sciences,
ul. Księcia Janusza 64,01-452 Warsaw, Poland
e-mail: wbielski@igf.edu.pl

R. Wojnar
Institute of Fundamental Technological Research, PAS,
ul. Pawińskiego 5B,02-106 Warsaw, Poland
e-mail: rwojnar@ippt.pan.pl

J. Awrejcewicz (ed.), *Dynamical Systems in Theoretical Perspective*,
Springer Proceedings in Mathematics & Statistics 248,
https://doi.org/10.1007/978-3-319-96598-7_30

The task is related also to problem of stream flow past the rough bottom and walls, in peculiarity in a channel with obstacles on the bottom, studied in geophysics and civil engineering [3, 4] and [5]. And so, M. Lessen and P.-S. Huang investigated Hagen-Poiseuille's flow in a pipe with axially symmetric wavy walls, and studied the effect of small amplitude wall waviness on a steady flow. They assumed that the steady motion is composed of a spatially averaged mean flow and a periodic disturbance due to the wall wave [4].

We adopt the method introduced in Malevich - Mityushev - Adler's papers [6, 7]. The application of an analytical algorithm yields efficient formula for the velocities and discharge. We consider a Stokesian pressure driven flow in pipe with a wavy wall, see Fig. 1. The problem is axially-symmetric, and in cylindrical co-ordinates r, φ, z it does not depend on φ. The radius R of the pipe cross-section is a periodic function of the z-axis. In our example the waviness is described by a cosinus function $R = R_0 + \varepsilon a \cos Kz$, with $K = 2\pi/\lambda$, where λ denotes the length of the wall wave. When the small parameter ε increases, Hagen - Poiseuille's flow ($\varepsilon = 0$) is disturbed and eddies can arise above a critical value.

We apply an overall external gradient pressure $\overline{\nabla p} \equiv -G$ along the z-direction. It can be described by a constant jump along the z-axis of the periodic cell $p(z + \lambda, r) - p(z, r) = -\lambda G$.

Malevich et al. [6, 7], have shown how to apply the asymptotic analysis to reduce the problem of flow in channels with curvilinear walls to the problem of flow with the plane ones.

We consider flow through an axially symmetric pipe with a curvilinear (wavy) wall. Its radius is, however, constant in the mean. In the cylindrical coordinates the z-axis is simply the axis of rotational symmetry of the tube, and the r-axis is perpendicular to the z-axis. In an example, we will accept the wall surface $S(x)$ described by the sinusoid, cf. Fig. 1

$$r = S(z) = R_0 + \varepsilon\, a\, \cos Kz$$

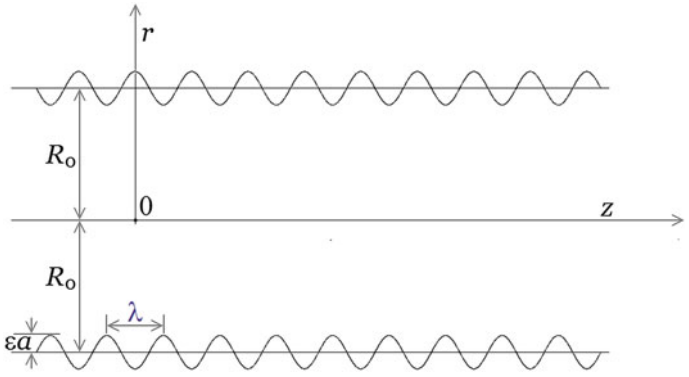

Fig. 1 Cross-section of the considered axially-symmetric tube. Here R_0 is the mean value of the pipe radius, ε is a dimensionless smallness parameter, a is the amplititude of the wall waveness, and λ denotes the length of the wall waveness

where $S(z)$ is a smooth periodic function and ε is a small parameter. The mean value of the $S(z)$ is R_0. The coefficient a renders the amplitude of the wavy shape of the wall, and $K = 2\pi/\lambda$, where λ denotes the length of the wall wave.

For the infinitely differentiable function $S(z)$ a cascade of boundary value problems is deduced. The boundary conditions are substituted by Maclaurin's expansions, and the solution (the velocity and pressure fields) is calculated in the form of both, ε expansions and Fourier's series. The case $\varepsilon = 0$ corresponds to the zero-th approximation problem.

We express the velocity and the pressure as the expansions in powers of ε.

$$p(r, z) = \sum_{m=0}^{\infty} p_m \varepsilon^m \quad \text{and} \quad \boldsymbol{v}(r, z) = \sum_{m=0}^{\infty} \boldsymbol{v}_m \varepsilon^m$$

2 Geometrical Description

Further the steady flow will be considered only. Moreover, the gravity components will be assumed to be zero, and the fluid will be assumed to be incompressible, it is ρ = constant. The axisymmetric flow will be considered with the assumption of no tangential velocity ($v_\varphi = 0$), and the remaining quantities are being independent of the angle φ. The problem becomes two-dimensional. We simplify notation by substitution

$$v_r \equiv u \quad \text{and} \quad v_z \equiv v$$

The continuity equation for the steady flow reads

$$\frac{1}{r}\frac{\partial}{\partial r}(ru) + \frac{\partial v}{\partial z} = 0. \tag{1}$$

Navier-Stokes' equations are

$$\begin{aligned} \rho\left(u\frac{\partial u}{\partial r} + v\frac{\partial u}{\partial z}\right) &= -\frac{\partial p}{\partial r} + \eta\left\{\frac{1}{r}\frac{\partial}{\partial r}\left(r\frac{\partial u}{\partial r}\right) + \frac{\partial^2 u}{\partial z^2} - \frac{u}{r^2}\right\} \\ \rho\left(u\frac{\partial v}{\partial r} + v\frac{\partial v}{\partial z}\right) &= -\frac{\partial p}{\partial z} + \eta\left\{\frac{1}{r}\frac{\partial}{\partial r}\left(r\frac{\partial v}{\partial r}\right) + \frac{\partial^2 v}{\partial z^2}\right\} \end{aligned} \tag{2}$$

In the case of Hagen-Poiseuille's flow in a tube with constant radius equal to R_0, it is $a = 0$. Because the problem is axially-symmetric, we deal with only one velocity component v, directed parallely to the z-axis of the cylindrical co-ordinates. Two equations are identically satisfied and the third equation reads

$$\frac{1}{r}\frac{\partial}{\partial r}\left(r\frac{\partial v}{\partial r}\right) = -\frac{1}{\eta}\frac{\partial p}{\partial z} \tag{3}$$

Integrating Eq. (3) with $\partial p/\partial z =$ constant, and with the boundary condition $v = 0$ at $r = R_0$ results in [8],

$$v = \frac{G}{4\eta}\,(R_0^2 - r^2) \tag{4}$$

Here G denotes the constant pressure gradient $G \equiv -\,\mathrm{d}p/\mathrm{d}z =$ constant. We write also

$$v = G\,\frac{R_0^2}{4\eta}\left(1 - \frac{r^2}{R_0^2}\right) \tag{5}$$

This is Hagen-Poiseuille's law describing the velocity distribution in the steady flow in tube.

3 Axially Symmetric Steady Stokesian Flow

We neglect the inertial terms (at left hand side) in Navier-Stokes equations, and introduce notation $u(r, z) \equiv v_r(r, z)$ and $v(r, z) \equiv v_z(r, z)$.

Let $\boldsymbol{v} = (u, v)$ be an unknown two dimensional velocity field, and p be an unknown field of the pressure. We have $u = u(r, z)$, $v = v(r, z)$ and $p = p(r, z)$. These fields satisfy:
the equation of incompressibility

$$\frac{1}{r}\,\frac{\partial (ru)}{\partial r} + \frac{\partial v}{\partial z} = 0 \tag{6}$$

and Stokes' equations

$$\begin{aligned} -\frac{\partial p}{\partial r} + \eta\left\{\frac{1}{r}\frac{\partial}{\partial r}\left(r\frac{\partial u}{\partial r}\right) + \frac{\partial^2 u}{\partial z^2} - \frac{u}{r^2}\right\} &= 0 \\ -\frac{\partial p}{\partial z} + \eta\left\{\frac{1}{r}\frac{\partial}{\partial r}\left(r\frac{\partial v}{\partial r}\right) + \frac{\partial^2 v}{\partial z^2}\right\} &= 0 \end{aligned} \tag{7}$$

The equations are subject to the boundary conditions

$$u = 0 \quad \text{and} \quad v = 0 \quad \text{at} \quad S(z) \tag{8}$$

3.1 Natural Units

For convenience, new units are introduced, and new variables indicated by primes are given

$$r = R_0\, r' \quad \text{and} \quad z = R_0\, z' \tag{9}$$

Moreover,

$$u = \breve{v}\, u', \quad v = \breve{v}\, v' \quad \text{and} \quad p = \breve{p}\, p' \tag{10}$$

Here R_0 is the mean radius of the pipe cross-section, $\breve{v}$ is equal to four times the maximum velocity in Hagen-Poiseuille's problem, cf. Eq. (5), $\breve{v} = (G/\eta)\, R_0^2$ and $\breve{p} = G\, R_0$. The following equality holds $(R_0/\eta)\, (\breve{p}/\breve{v}) = 1$. In these units our equations are: equation of incompressibility

$$\frac{1}{r'}\, \frac{\partial (r' u')}{\partial r'} + \frac{\partial v'}{\partial z'} = 0$$

and Stokes' equations

$$\begin{aligned} -\frac{\partial p'}{\partial r'} + \frac{1}{r'}\, \frac{\partial}{\partial r'} \left(r' \frac{\partial u'}{\partial r'} \right) + \frac{\partial^2 u'}{\partial (z')^2} - \frac{u'}{(r')^2} &= 0 \\ -\frac{\partial p'}{\partial z'} + \frac{1}{r'}\, \frac{\partial}{\partial r'} \left(r' \frac{\partial v'}{\partial r'} \right) + \frac{\partial^2 v'}{\partial (z')^2} &= 0 \end{aligned}$$

with the boundary conditions $u' = 0$ and $v' = 0$ at $S(z')$. For brevity, the primes for new variables are suppressed in the rest of this paper.

3.2 Zero-th Approximation

We regard Hagen-Poiseuille's solution as the zero-th approximation of a solution we are looking for. We consider the following set of equations treated a zero-th approximation

$$\frac{\partial p_0}{\partial r} = 0 \quad \text{and} \quad \frac{1}{r}\, \frac{\partial}{\partial r} \left(r\, \frac{\partial v_0}{\partial r} \right) = 1 \tag{11}$$

which are subject to the boundary conditions

$$v_0 = 0 \quad \text{at} \quad r = R_0 \tag{12}$$

Moreover, we have

$$u_0 = 0 \quad \text{and} \quad \frac{\partial p_0}{\partial z} = -1 \quad \text{for} \quad 0 \le r \le R_0 \quad \text{and} \quad -\infty < z < \infty \tag{13}$$

In this approximation the velocity vector has only one not vanishing component $v_0 = v_0(r)$, cf. [8]. Hagen-Poiseuille's solution in the natural units reads

$$u_0 = 0, \quad v_0 = \frac{1}{4} \left(1 - r^2 \right) \quad \text{and} \quad \frac{\partial p_0}{\partial z} = -1 \tag{14}$$

4 General Solution

The unknown fields u, v and p satisfy the following set composed of the equation of incompressibility and Stokes' equations

$$\begin{aligned} &\frac{1}{r}\frac{\partial(ru)}{\partial r}+\frac{\partial v}{\partial z}=0\\ &\left\{\frac{1}{r}\frac{\partial}{\partial r}\left(r\frac{\partial u}{\partial r}\right)+\frac{\partial^2 u}{\partial z^2}-\frac{u}{r^2}\right\}-\frac{\partial p}{\partial r}=0\\ &\left\{\frac{1}{r}\frac{\partial}{\partial r}\left(r\frac{\partial v}{\partial r}\right)+\frac{\partial^2 v}{\partial z^2}\right\}-\frac{\partial p}{\partial z}=0 \end{aligned} \tag{15}$$

The equations are subject to the boundary conditions

$$u=0 \quad \text{and} \quad v=0 \quad \text{at } S(z) \tag{16}$$

In the accepted frame of reference, see Fig.1,

$$r=S(x)=1+\varepsilon a\cos Kz \tag{17}$$

4.1 Expansion in ε Series

The unknown velocity components and pressure functions are expanded in the ε series

$$u(r,z)=\sum_{m=0}^{\infty}u_m(r,z)\,\varepsilon^m, \quad v(r,z)=\sum_{m=0}^{\infty}v_m(r,z)\,\varepsilon^m, \quad p(r,z)=\sum_{m=0}^{\infty}p_m(r,z)\,\varepsilon^m \tag{18}$$

At the wall, it is at $r=1+\varepsilon a\cos z$ a Taylor's series of a function, say $g=g(r,z)$, is

$$g(1+\varepsilon a\cos z,z)=\sum_{m=0}^{\infty}\varepsilon^m\frac{(\varepsilon a\cos z)^m}{m!}\cdot\left.\frac{\partial^m g}{\partial r^m}\right|_{r=1}$$

and the wall boundary conditions for the functions (18) are represented by series

$$\begin{aligned} u(1+\varepsilon a\cos z,z)&=\sum_{m=0}^{\infty}\varepsilon^m\sum_{k=0}^{m}\frac{a^k}{k!}\cos^k z\cdot\left.\frac{\partial^k u_{m-k}}{\partial r^k}\right|_{r=1}\\ v(1+\varepsilon a\cos z,z)&=\sum_{m=0}^{\infty}\varepsilon^m\sum_{k=0}^{m}\frac{a^k}{k!}\cos^k z\cdot\left.\frac{\partial^k v_{m-k}}{\partial r^k}\right|_{r=1}\\ p(1+\varepsilon a\cos z,z)&=\sum_{m=0}^{\infty}\varepsilon^m\sum_{k=0}^{m}\frac{a^k}{k!}\cos^k z\cdot\left.\frac{\partial^k p_{m-k}}{\partial r^k}\right|_{r=1} \end{aligned} \tag{19}$$

In this manner the search for solution of the set of Eqs. (15) with the boundary conditions (16) is substituted by solving these equations with the conditions (19).

4.2 Reduced Problem

Solving the problem subject to the boundary conditions given at the waved boundary $r = 1 + \varepsilon a \cos z$ was reduced to the problem with the boundary being a cylindrical surface $r = 1$ without waves, but with modified values of boundary conditions. This means that at each step m the set (15) must be solved with the modified boundary conditions (19).

Substituting expansions (18) into Eq. (15) leads to the equations

$$\begin{aligned} &\frac{1}{r}\frac{\partial (r u_m)}{\partial r} + \frac{\partial v_m}{\partial z} = 0 \\ &\left\{\frac{1}{r}\frac{\partial}{\partial r}\left(r\frac{\partial u_m}{\partial r}\right) + \frac{\partial^2 u_m}{\partial z^2} - \frac{u_m}{r^2}\right\} - \frac{\partial p_m}{\partial r} = 0 \\ &\left\{\frac{1}{r}\frac{\partial}{\partial r}\left(r\frac{\partial v_m}{\partial r}\right) + \frac{\partial^2 v_m}{\partial z^2}\right\} - \frac{\partial p_m}{\partial z} = 0 \end{aligned} \tag{20}$$

The solution u_m, v_m and p_m is looked for in the form of Fourier's series

$$\begin{aligned} u_m(r,z) &= \sum_{s=1}^{\infty} \alpha_s^{(m)}(r)\,(A^{(m)} \sin sz + B^{(m)} \cos sz) \\ v_m(r,z) &= \sum_{s=1}^{\infty} \beta_s^{(m)}(r)\,\frac{\partial}{\partial z}\,(A^{(m)} \sin sz + B^{(m)} \cos sz) \\ p_m(r,z) &= \sum_{s=1}^{\infty} \gamma_s^{(m)}(r)\,(A^{(m)} \sin sz + B^{(m)} \cos sz) \end{aligned} \tag{21}$$

with r-functions $\alpha_s^{(m)}$, $\beta_s^{(m)}$ and $\gamma_s^{(m)}$, as well the constants $A^{(m)}$ and $B^{(m)}$ must be found. Substituting the expansions (21) into Eq. (20) we obtain for the incompressibility equation and for Stokes' equations, respectively,

$$\frac{1}{r}\frac{\mathrm{d}}{\mathrm{d}r}\left(r\alpha_s^{(m)}(r)\right) - \beta_s^{(m)}(r)s^2 = 0 \tag{22}$$

$$\frac{1}{r}\frac{\mathrm{d}}{\mathrm{d}r}\left(r\frac{\mathrm{d}}{\mathrm{d}r}\alpha_s^{(m)}(r)\right) - \left(s^2 + \frac{1}{r^2}\right)\alpha_s^{(m)}(r) - \frac{\mathrm{d}}{\mathrm{d}r}\left(\gamma_s^{(m)}(r)\right) = 0 \tag{23}$$

$$\frac{1}{r}\frac{\mathrm{d}}{\mathrm{d}r}\left(r\frac{\mathrm{d}}{\mathrm{d}r}\beta_s^{(m)}(r)\right) - s^2\beta_s^{(m)}(r) - \gamma_s^{(m)}(r) = 0 \tag{24}$$

4.3 Solution of the System

To solve the system (22)–(24) we differentiate Eq. (24). To eliminate $\gamma_s^{(m)}(r)$ we subtract (23) from the result and get the equation, in which we substitute $\beta_s^{(m)}(r)$ using Eq. (22)

$$\beta_s^{(m)}(r) = \frac{1}{s^2}\frac{1}{r}\frac{\mathrm{d}}{\mathrm{d}r}\left(r\alpha_s^{(m)}(r)\right) \tag{25}$$

After an arrangement we have

$$\begin{aligned}\frac{\mathrm{d}^4\alpha_s^{(m)}}{\mathrm{d}r^4} + \frac{2}{r}\frac{\mathrm{d}^3\alpha_s^{(m)}}{\mathrm{d}r^3} - \left(\frac{3}{r^2} + 2s^2\right)\frac{\mathrm{d}^2\alpha_s^{(m)}}{\mathrm{d}r^2} + \left(\frac{3}{r^3} - \frac{2s^2}{r}\right)\frac{\mathrm{d}\alpha_s^{(m)}}{\mathrm{d}r} + \\ + \left(s^4 + \frac{2s^2}{r^2} - \frac{3}{r^4}\right)\alpha_s^{(m)} = 0\end{aligned} \tag{26}$$

A comment: Equation (26) for large r reads

$$\frac{\mathrm{d}^4\alpha_s^{(m)}}{\mathrm{d}r^4} - 2s^2\frac{\mathrm{d}^2\alpha_s^{(m)}}{\mathrm{d}r^2} + s^4\alpha_s^{(m)} = 0$$

Such an equation is discussed in [6]. Its general solution reads

$$\alpha_s^{(m)}(r) = (C_1^{(sm)}r + C_2^{(sm)})\,\mathrm{e}^{sr} + (C_3^{(sm)}r + C_4^{(sm)})\,\mathrm{e}^{-sr}$$

But this is not our case, as we need the range of $0 \le r \le 1$ (the interior of the tube). □

The solution of the Eq. (26) reads

$$\begin{aligned}\alpha_s^{(m)}(r) = {} & C_1\, r\, I_0(sr) + C_2\, x\, K_0(sr) + \\ & + C_3[2\cdot K_1(sr) + K_0(sr)\, sr]\cdot x\cdot[I_0(sr)\cdot K_1(sr) + K_0(sr)\cdot I_1(sr)] + \\ & + C_4\left(4x^2 I_0^2(sr)\cdot K_1(sr)\cdot s^2 - 8r\cdot I_o(sr)\cdot K_1(sr)\cdot I_1(sr)\cdot s + \right) \\ & + C_4\left(4r^2 I_0(sr)\cdot K_0(sr)\cdot I_1(sr)\cdot s^2 - 8r\cdot I_o^2(sr)\cdot K_0(sr)\cdot s + \right) \\ & + C_4\left(16 I_0(sr)\cdot K_0(sr)\cdot I_1(sr) - s^3 r^3 F(\frac{3}{2}, 3, 3, s^2r^2)\cdot K_0(sr)\right)\end{aligned} \tag{27}$$

where $I_0(sr)$, $I_1(sr)$ and $K_0(sr)$, $K_1(sr)$ are modified Bessel functions of the first and the second kind, respectively, [9]. Unlike the ordinary Bessel functions, which are oscillating as functions of a real argument, I_n and K_n are exponentially growing and decaying functions, respectively. Like the ordinary Bessel function J_n, the function I_n goes to zero at $r = 0$ for $n > 0$ and is finite (equal 1) at $r = 0$ for $n = 0$. Analogously, as Bessel functions of the second kind, the modified function K_n diverges at $x = 0$ with the singularity being of logarithmic type [10].

For small arguments $r \leq n$, both $I_n(r)$ and $K_n(r)$ become, asymptotically, simple powers of their argument

$$I_n(r) \approx \frac{1}{n!}\left(\frac{r}{2}\right)^n \quad n \geq 0, \quad K_0(r) \approx -\ln r, \quad K_n(r) \approx \frac{(n-1)!}{2}\left(\frac{r}{2}\right)^{-n} \quad n > 0 \tag{28}$$

The confluent function is defined as

$$F(a; b; c, r) = \sum_{n=0}^{\infty} \frac{(a)_n\,(b)_n}{(c)_n\,n!}\,r^n \tag{29}$$

where, for example, $(a)_n \equiv a \cdot (a+1) \cdot (a+2) \cdot \cdots \cdot (a+n-1)$.

Finding $\alpha_s^{(m)}$ by Eq. (27), the expressions (25) and (24) give $\beta_s^{(m)}$ and $\gamma_s^{(m)}$, respectively.

5 An Example

In this example we consider the waviness of the tube wall described by the relation

$$R = 1 + \varepsilon \cos z \tag{30}$$

it is we take $a = 1$ and $K = 1$. Moreover, in this example all terms with coefficients ε in powers greater than 2 are omitted. In peculiar, the small parameter expansions (18) read

$$\begin{aligned} u(r,z) &= u_0(r,z) + \varepsilon\,u_1(r,z) + \varepsilon^2\,u_2(r,z) \\ v(r,z) &= v_0(r,z) + \varepsilon\,v_1(r,z) + \varepsilon^2\,v_2(r,z) \\ p(r,z) &= p_0(r,z) + \varepsilon\,p_1(r,z) + \varepsilon^2\,p_2(r,z) \end{aligned} \tag{31}$$

In calculations of the functions $\alpha_s^{(m)}$, $\beta_s^{(m)}$ and $\gamma_s^{(m)}$ we use approximations of the type (28),

$$\begin{aligned} &I_0(r) = 1, \quad I_1(r) = \frac{r}{2} \\ &K_0(r) \approx -\ln r, \quad K_1(r) \approx \frac{1}{r}, \quad F(\frac{3}{2}, 3, 3, s^2r^2) = 1, \quad s = 0, 1, 2 \end{aligned} \tag{32}$$

We get

$$\alpha_s^{(m)}(r) = C_1 \cdot r - C_2 \cdot r \cdot \ln(sr) + C_3\left(\frac{2}{sr} - r \cdot \ln(sr) - \frac{sr}{2}\ln(sr)\right) - C_4 \cdot s^3r^3 \cdot \ln(sr) \tag{33}$$

and consequently, by Eq. (25)

$$\begin{aligned}\beta_s^{(m)}(r) \;=\; \frac{1}{s^2}\,\frac{1}{r}\,\frac{\mathrm{d}}{\mathrm{d}r}\left(r\alpha_s^{(m)}(r)\right) = \frac{1}{s^2}\,\{2C_1 - C_2[1+2\ln(sr)]\} \\ -\,C_3\,\frac{1}{s^2}\left\{\frac{5}{2}+(2+s)\cdot\ln(sr)\right\} -\; C_4\cdot sr^2\cdot[1+4\cdot\ln(sr)]\end{aligned} \tag{34}$$

By Eqs. (24) and (34) we obtain

$$\begin{aligned}\gamma_s^{(m)}(r) \;=\; -\,\{2C_1 - C_2[1+2\ln(sr)]\} +\; C_3\left\{\frac{5}{2}+(2+s)\cdot\ln(sr)\right\} + \\ +C_4\left\{4\cdot s\cdot\left(1+\frac{1}{r}-4\ln(sr)\right)+\; s^3r^2\cdot[1+4\cdot\ln(sr)]\right\}\end{aligned} \tag{35}$$

Above, $u_0(1,z)$ and $v_0(1,z)$ are known and equal to zero, while $p_0(1,z) = -z + C$ is a linear function of z, with C being an arbitrary constant.

5.1 Elaboration of the Example

By Eq. (21) for $m = 1$ we have

$$\begin{aligned}u_1(r,z) &= \alpha_1(r)(A\sin z + B\cos z)\\ v_1(r,z) &= \beta_1(r)(A\cos z - B\sin z)\\ p_1(r,z) &= \gamma_1(r)(A\sin z + B\cos z)\end{aligned} \tag{36}$$

where $\alpha_1(r)$, $\beta_1(r)$ and $\gamma_1(r)$ are given by Eqs. (33), (34) and (35) with $s = 1$, it is We get

$$\begin{aligned}\alpha_1(r) &= C_1\cdot r - C_2\cdot r\cdot\ln r +\; C_3\left(\frac{2}{r} - r\cdot\ln r - \frac{r}{2}\ln r\right) -\; C_4\cdot r^3\cdot\ln r\\ \beta_1(r) \;&=\; 2C_1 - C_2[1+2\ln(sr)] \;-\; C_3\left(\frac{5}{2}+3\cdot\ln r\right) -\; C_4\cdot r^2\cdot(1+4\cdot\ln r)\\ \gamma_1(r) \;&=\; -\,[2C_1 - C_2(1+2\ln r) +\; C_3\left(\frac{5}{2}+3\cdot\ln r\right) + \\ &\qquad +C_4\left\{4\cdot\left(1+\frac{1}{r}-4\ln r\right)+\; r^2\cdot(1+4\cdot\ln r)\right\}\end{aligned} \tag{37}$$

To avoid the singularity at $r = 0$ in expressions for $v_1(r)$ and $p_1(r)$ in the set (36) we put

$$C_2 = 0, \quad C_3 = 0 \quad \text{and} \quad C_4 = 0 \tag{38}$$

Then

$$\alpha_1(r) = C_1\cdot r, \quad \beta_1(r) = 2C_1 \quad \text{and} \quad \gamma_1(r) = -2C_1 \tag{39}$$

and Eq. (36) become

$$\begin{aligned} u_1(r,z) &= C_1 \cdot r \cdot (A\sin z + B\cos z) \\ v_1(r,z) &= 2C_1 \cdot (A\cos z - B\sin z) \\ p_1(r,z) &= -2C_1 \cdot (A\sin z + B\cos z) \end{aligned} \tag{40}$$

If the expansions (18) are limited up to $\mathrm{O}(\varepsilon^2)$, only the terms with $m = 0, 1$ must be left, and the boundary conditions (19) reduce to the following ones

$$\begin{aligned} u(1+\varepsilon a\cos z, z) &\doteq u_0(1,z) + \varepsilon\left(u_1(1,z) + \cos z \cdot \left.\frac{\partial u_0(r,z)}{\partial r}\right|_{r=1}\right) \\ v(1+\varepsilon a\cos z, z) &\doteq v_0(1,z) + \varepsilon\left(v_1(1,z) + \cos z \cdot \left.\frac{\partial v_0(r,z)}{\partial r}\right|_{r=1}\right) \\ p(1+\varepsilon a\cos z, z) &\doteq p_0(1,z) + \varepsilon\left(p_1(1,z) + \cos z \cdot \left.\frac{\partial p_0(r,z)}{\partial r}\right|_{r=1}\right) \end{aligned} \tag{41}$$

where $\doteq$ means the asymptotic equality with the accuracy $O(\varepsilon^2)$. By solution (14)

$$u_0(1,z) = 0, \quad v_0(1,z) = 0$$

and p_0 is a linear function of z only. Moreover

$$\left.\frac{\partial u_0(r,z)}{\partial r}\right|_{r=1} = 0, \quad \left.\frac{\partial v_0(r,z)}{\partial r}\right|_{r=1} = -\frac{1}{2} \quad \text{and} \quad \left.\frac{\partial p_0(r,z)}{\partial r}\right|_{r=1} = 0$$

Hence

$$\begin{aligned} u(1+\varepsilon a\cos z, z) &\doteq u_0(1,z) + \varepsilon\, u_1(1,z) \\ v(1+\varepsilon a\cos z, z) &\doteq v_0(1,z) + \varepsilon\left(v_1(1,z) - \frac{1}{2}\cos z\right) \\ p(1+\varepsilon a\cos z, z) &\doteq p_0(1,z) + \varepsilon\, p_1(1,z) \end{aligned} \tag{42}$$

Next, we submit Fourier's series (21) into Taylor's expansions (19) taken at the wall boundary up to $O(\varepsilon^2)$ approximation, and after exploiting relations (39) we received

$$\begin{aligned} u(1+\varepsilon a\cos z, z) &\doteq u_0(1,z) + \varepsilon \cdot C_1\,(A\sin z + B\cos z) \\ v(1+\varepsilon a\cos z, z) &\doteq v_0(1,z) + \varepsilon \cdot \left(2C_1\,(A\cos z - B\sin z) - \frac{1}{2}\cos z\right) \\ p(1+\varepsilon a\cos z, z) &\doteq p_0(1,z) - \varepsilon \cdot 2C_1\,(A\sin z + B\cos z) \end{aligned} \tag{43}$$

The subscripts and coefficients at z are put $s = 1$. Above, $u_0(1,z)$ and $v_0(1,z)$ are known and equal to zero, cf. Eq. (14).

The boundary conditions should be satisfied separately at each power of ε. Thus we find

$$2C_1 A = \frac{1}{2} \quad \text{and} \quad B = 0 \tag{44}$$

Finally, we get

$$\begin{aligned} u(r,z) &= u_0(r,z) + \varepsilon u_1(r,z) = \frac{1}{2}\,\varepsilon\,\sin z \\ v(r,z) &= v_0(r,z) + \varepsilon v_1(r,z) = \frac{1}{4}\left(1-r^2\right) + \varepsilon\,\cos z \\ p(r,z) &= p_0(r,z) + \varepsilon p_1(r,z) = -z - \frac{1}{2}\,\varepsilon\,\sin z + C \end{aligned} \tag{45}$$

where C is an arbitrary constant (only gradient of pressure are important in the flow).

6 Conclusions

We have presented a study of an axisymmetrical (it is two-dimensional) flow in the tube with wavy wall in the first order approximation of the parameter ε, which denotes the amplitude of the wall waviness. The wall waviness results in appearance of transversal velocity and variations of pressure. These two phenomena are periodic functions of the longitudinal variable z.

Acknowledgements This work was partially supported within statutory activities No 3841/E-41/S/2017 of the Ministry of Science and Higher Education of Poland.

References

1. Ross, R.: The pathogenesis of atherosclerosis: a perspective for the 1990s. Nature **362**(6423), 801–809 (1993)
2. Singh, R.B., Mengi, S.A., Xu, Y.-J., Arneja, A.S., Dhalla, N.S.: Pathogenesis of atherosclerosis: a multifactorial process. Exp. Clin. Cardiology **7**(1), 40–53 (2002)
3. Munson B.R.: Experimental results for oscillating flow in a curved pipe. Phys. Fluids **19**(7) (1975)
4. Lessen, M., Huang, P.-S.: Poiseuille flow in a pipe with axially symmetric wavy walls. Phys. Fluids **19**(7), 945–950 (1976)
5. Wojnar, R., Bielski, W.: Gravity driven flow past the bottom with small waviness, In: Modern Problems in Applied Analysis, eds. Drygaś, P. Rogosin, S. (pp. 181–202). Birkhäuser, Cham (2018)
6. Malevich, A.E., Mityushev, V.V., Adler, P.M.: Stokes flow through a channel with wavy walls. Acta Mechanica **182**(3–4), 151–182 (2006)
7. Malevich, A.E., Mityushev, V.V., Adler, P.M.: Couette flow in channels with wavy walls. Acta Mechanica **197**(3), 247–283 (2008)
8. Landau, L.D., Lifshitz, E.M.: Fluid mechanics, Volume 6 of Course of Theoretical Physics, transl. from the Russian by Sykes, J.B., Reid, W.H. 2nd edn (Pergamon Press, Oxford - New York, 1987)
9. Jahnke, E., Emde, F.: Funktionentafeln mit Formeln und Kurven (Tables of functions with formulae and graphs) 2nd edn. B. G. Teubner, Leipzig and Berlin (1933)
10. Abramowitz, M., Stegun, I.A. (eds.) Handbook of mathematical functions with formulas, graphs, and mathematical tables, Chapter 9, Applied Mathematics Series. 55, National Bureau of Standards, Washington D.C., New York 1972

Implementation of the Adaptive Control Algorithm for the KUKA LWR 4+ Robot

Łukasz Woliński

Abstract Model-based control methods are very attractive in the field of robotics as their tracking performance can exceed the classical controllers (such as the independent joint PID controllers). Using the dynamic model of the manipulator, however, requires detailed knowledge about the manipulator's dynamic parameters such as link masses and inertias or joint friction properties. These parameters are not always easily identifiable and, to some degree, might vary between robots of one kind (e.g. slight differences in masses/inertias) or during the robot operation (e.g. friction changes related to the temperature). Thus, the identified model might not always be suitable for the desired control tasks. A possible method to overcome the aforementioned problems is to use the adaptive control scheme. In that approach, the parameters of the model are constantly updating their values in real-time to assure good tracking performance. This paper deals with the implementation of such an adaptive controller for the KUKA LWR 4+ robot. Using the KUKA's communication protocols, a C++ implementation of the outer-loop adaptive controller (which feeds the KUKA controller with the desired joint torques) was created and its quality evaluated.

Keywords Adaptive control · Redundant robot · Dynamic modeling

1 Introduction

Nowadays, after decades of progress, there are various approaches to the robotic manipulator control. The methods range from the classical independent joint PID control to more advanced model-based methods [14, 17, 23, 25]. Taking into account the dynamic model of the manipulator should, in theory, improve the performance in the position tracking task. In practice, it requires the knowledge of the dynamic

Ł. Woliński (✉)
Institute of Aeronautics and Applied Mechanics,
Warsaw University of Technology, Nowowiejska 24, 00-665 Warsaw, Poland
e-mail: lwolinski@meil.pw.edu.pl

J. Awrejcewicz (ed.), *Dynamical Systems in Theoretical Perspective*,
Springer Proceedings in Mathematics & Statistics 248,
https://doi.org/10.1007/978-3-319-96598-7_31

parameters (masses, locations of the centers of mass, and moments of inertia). As these parameters are seldom available, an identification has to be performed. It is often a demanding task during which a researcher has to solve problems of selecting the set of identifiable parameters and obtaining a sufficiently rich data [26, 27]. There is also a possibility that some dynamic parameters (for example friction coefficients) might vary in robots of one kind, requiring separate identification of each robot [29]. The biggest issue, however, is that if the parameters are not known with the sufficient accuracy, the control quality might not be acceptable.

The aforementioned problems can be overcome with the model not depending on the constant parameters but updating their values over time, based on the position and velocity errors. That is the idea of the adaptive control scheme, first proposed in the 1980s [24]. In that approach, the perfect knowledge of the dynamic parameters is not needed, as the model is constantly updating itself, ensuring small tracking error. Although the adaptive control is not an entirely new concept now, it is still actively researched and extended. In one of the recent papers, the authors propose using multiple adaptive models with a control switching mechanism to select the best model of the manipulator dynamics [9]. Another example is [19] where the adaptive control of manipulators subject to motion constraints is proposed. In yet another example, the adaptive controller based on nonlinear sliding mode control is designed and implemented for the upper-limb medical exoskeleton [5]. Other examples of the adaptive control include: [4, 10, 18].

In this paper, the adaptive control scheme and its implementation for the KUKA lightweight redundant robotic manipulator (LWR 4+) are discussed. Performance of the implemented controller is evaluated on the position tracking task.

The paper is organized as follows: Sect. 2 deals with the controlled object and its model, Sect. 3 describes the theoretical background on the adaptive controller and its implementation, Sect. 4 presents the experimental validation of the controller and the discussion of the results, and Sect. 5 concludes the paper.

2 The KUKA LWR 4+ Model

The studied manipulator is the KUKA LWR 4+ [3], a 7-degree-of-freedom lightweight robot with a redundant anthropomorphic structure. For the purpose of this work, the manipulator is modeled as a multibody system comprised of n rigid links:

$$\mathbf{M}(\mathbf{q})\ddot{\mathbf{q}} + \mathbf{C}(\mathbf{q}, \dot{\mathbf{q}})\dot{\mathbf{q}} + \mathbf{G}(\mathbf{q}) = \boldsymbol{\tau} - \boldsymbol{\tau}_{diss} \tag{1}$$

where $\mathbf{q} \in \mathrm{R}^{n\times 1}$ is the vector of joint coordinates, $\mathbf{M}(\mathbf{q}) \in \mathrm{R}^{n\times n}$ is the manipulator inertia matrix, $\mathbf{C}(\mathbf{q}, \dot{\mathbf{q}})\dot{\mathbf{q}} \in \mathrm{R}^{n\times 1}$ is the Coriolis and centrifugal force vector, $\mathbf{G}(\mathbf{q}) \in \mathrm{R}^{n\times 1}$ is the gravitational force vector, $\boldsymbol{\tau} \in \mathrm{R}^{n\times 1}$ contains driving torques in joints, $\boldsymbol{\tau}_{diss} \in \mathrm{R}^{n\times 1}$ is a vector of dissipative torques (caused by effects like friction), and $n = 7$, as the manipulator has 7 degrees of freedom.

To create the model described by Eq. (1), a recursive algorithm, based on the spatial operator algebra [21], was used [28]. The necessary kinematic data was obtained from the official KUKA documentation [16] and used to derive the modified Denavit-Hartenberg parameters (see Table 1).

The dynamic parameters had to be obtained through the identification procedures described in [26, 27]. Typically, each link can be described by the 10 parameters:

$$\boldsymbol{\theta}_{rbd_j} = \left[m_j \; m_j r_{x_j} \; m_j r_{y_j} \; m_j r_{z_j} \; J_{xx_j} \; J_{yy_j} \; J_{zz_j} \; J_{xy_j} \; J_{xz_j} \; J_{yz_j} \right]^T_{1\times 10}, \; j = 1, \ldots, n \quad (2)$$

where m_j is the j-th link's mass, $m_j r_{x_j}$, $m_j r_{y_j}$ and $m_j r_{z_j}$ are the j-th link's first moments of mass, and J_{xx_j}, J_{yy_j}, J_{zz_j}, J_{xy_j}, J_{xz_j} and J_{yz_j} are the elements of the j-th link's inertia tensor. However, not all of the dynamic parameters could have their values obtained during the identification experiment. Moreover, the values of some theoretically identifiable parameters are close to zero and their contribution to the model is neglible. Therefore, only a set of the most essential parameters was used in the model. That parameters and their values are listed in Table 2. It is worth noting that the dynamic identification of the LWR 4+ was of great importance to many research teams which is documented in [2, 7, 8, 11].

Table 1 Modified DH parameters of the LWR 4+

j	α_j (rad)	a_j (m)	ϕ_j (rad)	d_j (m)
1	0	0	q_1	0
2	$\frac{\pi}{2}$	0	q_2	0
3	$-\frac{\pi}{2}$	0	q_3	0.4
4	$-\frac{\pi}{2}$	0	q_4	0
5	$\frac{\pi}{2}$	0	q_5	0.39
6	$\frac{\pi}{2}$	0	q_6	0
7	$-\frac{\pi}{2}$	0	q_7	0

Table 2 Rigid-body dynamic parameters

Parameter	Value	Unit
$m_2 r_{y_2}$	3.5	kgm
J_{xx_2}	1.23	kgm^2
J_{zz_2}	0.87	kgm^2
$m_4 r_{y_4}$	−1.38	kgm
J_{xx_4}	0.49	kgm^2
J_{zz_4}	0.42	kgm^2
$m_5 r_{y_5}$	0.05	kgm
$m_6 r_{y_6}$	0.02	kgm

The obtained model was used for simulations of the adaptive control before the implementation on the real robot.

3 Adaptive Controller

3.1 Theoretical Background

The idea of the presented adaptive controller [13, 24] is to minimize the position error while estimating online unknown dynamic parameters. The control law is given by the following equation describing the desired driving torques in joints:

$$\boldsymbol{\tau}_{cmd} = \mathbf{Y}(\mathbf{q}, \dot{\mathbf{q}}, \dot{\mathbf{q}}_r, \ddot{\mathbf{q}}_r)\hat{\boldsymbol{\theta}} - \mathbf{K}\mathbf{s} \tag{3}$$

where:

$$\mathbf{s} = \dot{\mathbf{q}} - \dot{\mathbf{q}}_r, \tag{4}$$

$$\dot{\mathbf{q}}_r = \dot{\mathbf{q}}_d + \Lambda\mathbf{e}, \tag{5}$$

$$\mathbf{e} = \mathbf{q}_d - \mathbf{q} \tag{6}$$

while $\mathbf{q}_d \in \mathrm{R}^{n\times 1}$ is the desired joint trajectory, and $\mathbf{K} \in \mathrm{R}^{n\times n}$ and $\Lambda \in \mathrm{R}^{n\times n}$ are diagonal positive definite matrices. The vector $\hat{\boldsymbol{\theta}} \in \mathrm{R}^{p\times 1}$ is a current estimate of the dynamic parameters $\boldsymbol{\theta} \in \mathrm{R}^{p\times 1}$ (where p is the number of the parameters), and is defined as:

$$\hat{\boldsymbol{\theta}} = \left[\hat{\boldsymbol{\theta}}_{rbd}^T \; \hat{\boldsymbol{\theta}}_f^T\right]_{1\times p}^T \tag{7}$$

with $\hat{\boldsymbol{\theta}}_{rbd}$ containing the estimates of mass and inertia parameters of the links (see Eq. (2)) and $\hat{\boldsymbol{\theta}}_f$ containing friction parameters.

The manipulator regressor matrix $\mathbf{Y}(\mathbf{q}, \dot{\mathbf{q}}, \dot{\mathbf{q}}_r, \ddot{\mathbf{q}}_r) \in \mathrm{R}^{n\times p}$ satisfies the equation:

$$\mathbf{Y}(\mathbf{q}, \dot{\mathbf{q}}, \dot{\mathbf{q}}_r, \ddot{\mathbf{q}}_r)\hat{\boldsymbol{\theta}} = \mathbf{M}(\mathbf{q})\ddot{\mathbf{q}}_r + \mathbf{C}(\mathbf{q}, \dot{\mathbf{q}})\dot{\mathbf{q}}_r + \mathbf{G}(\mathbf{q}) + \boldsymbol{\tau}_f(\dot{\mathbf{q}}_r) \tag{8}$$

which is based on the linearity-in-parameters property of the manipulator dynamic model. The term $\boldsymbol{\tau}_f(\dot{\mathbf{q}}_r)$ in Eq. (8) represents the dissipation torques caused by the viscous and Coulomb friction:

$$\tau_{f_j} = F_{v_j}\dot{q}_{r_j} + F_{C_j}sgn(\dot{q}_{r_j}),\ j = 1, \ldots, n \tag{9}$$

where F_{v_j} and F_{C_j} are j-th joint viscous and Coulomb friction parameters, respectively.

Basically, Eq. (3) describes the model-based controller with a PD compensation. The parameters of the manipulator dynamic model are updated according to the following adaptation law:

$$\dot{\hat{\boldsymbol{\theta}}} = -\Gamma \mathbf{Y}^T(\mathbf{q}, \dot{\mathbf{q}}, \dot{\mathbf{q}}_r, \ddot{\mathbf{q}}_r)\mathbf{s} \tag{10}$$

where $\Gamma \in \mathrm{R}^{p \times p}$ is a diagonal positive definite matrix describing the speed of parameters' adaptation.

To implement the controller based on Eqs. (3) and (10), the formula to derive the regressor matrix $\mathbf{Y}$ is needed. In general, this is a demanding task [25]. However, an efficient algorithm, based on the recursive Newton-Euler formulation, for computing the regressor $\mathbf{Y}_{rbd}$ corresponding to the rigid-body dynamics of the manipulator is presented in [13]. It requires only the knowledge of the kinematic parameters such as link lenghts and locations of joints. In this work, to account for the viscous and Coulomb friction (modeled as Eq. (9)) the algorithm from [13] was extended to compute the regressor in the following form:

$$\mathbf{Y} = \begin{bmatrix} \mathbf{Y}_{rbd} & \mathbf{Y}_f \end{bmatrix}_{n \times p} \tag{11}$$

where:

$$\mathbf{Y}_f = \begin{bmatrix} \dot{q}_{r_1} & 0 & \dots & 0 & sgn(\dot{q}_{r_1}) & 0 & \dots & 0 \\ 0 & \dot{q}_{r_2} & \dots & 0 & 0 & sgn(\dot{q}_{r_2}) & \dots & 0 \\ \vdots & \vdots & \ddots & 0 & \vdots & \vdots & \ddots & 0 \\ 0 & \dots & 0 & \dot{q}_{r_n} & 0 & \dots & 0 & sgn(\dot{q}_{r_n}) \end{bmatrix}_{n \times 2n}. \tag{12}$$

The stability issues of the adaptive control method are discussed in [13, 24].

It should also be mentioned that the elements of $\hat{\boldsymbol{\theta}}$ do not necessarily converge to the real values of the dynamic parameters given in $\boldsymbol{\theta}$. Similarly as in the case of the offline identification, a sufficiently exciting trajectory has to be used as the desired trajectory $\mathbf{q}_d$ to obtain the real $\boldsymbol{\theta}$ [24].

3.2 Implementation

The implementation of the controller described in Sect. 3.1 was possible thanks to the KUKA's *Fast Research Interface* (FRI), which allows for a communication between the KUKA Robot Controller (KRC) and a remote PC over the Ethernet [22]. The data includes measured and commanded joint positions and torques, and it can be exchanged with a frequency between 10 and 1000 Hz. On the side of the user PC, the FRI consists of C++ libraries which allow implementation of the various control algorithms. In this work, software libraries developed at Stanford [15] were used, as they extend the KUKA FRI libraries and facilitate saving the measured data in real-time.

The FRI allows two control modes: position control and impedance control. For the purpose of this work, a joint impedance controller was used as it allows to command the desired driving torques in joints. It is described by the following equation [22]:

$$\tau_j = k_j(q_{d_j} - q_j) + D(d_j) + G(q_j) + \tau_{cmd_j},\ j = 1, \ldots, 7 \tag{13}$$

where k_j is the stiffnes of the virtual spring, q_{d_j} is the desired postion of the j-th joint, q_j is the measured postion of the j-th joint, $D(d_j)$ is the damping term dependent on the standardized damping value $d_j \in < 0, 1 >$, $G(q_j)$ is the gravity compensation term, and τ_{cmd_j} is the joint torque commanded by the user.

For the experiment, the parameters from Eq. (13) were set to: $k_j = 0\frac{Nm}{rad}$ and $d_j = 0.7$, the same for each joint, and τ_{cmd_j} was used to set the desired joint torques.

Since the KRC already compensates the gravity, as shown in Eq. (13), the algorithm for the computation of the manipulator regressor matrix $\mathbf{Y}$ was used with the gravity acceleration set to zero. As a result, Eq. (8) was transformed to:

$$\mathbf{Y}(\mathbf{q}, \dot{\mathbf{q}}, \dot{\mathbf{q}}_r, \ddot{\mathbf{q}}_r)\hat{\boldsymbol{\theta}} = \mathbf{M}(\mathbf{q})\ddot{\mathbf{q}}_r + \mathbf{C}(\mathbf{q}, \dot{\mathbf{q}})\dot{\mathbf{q}}_r + \boldsymbol{\tau}_f(\dot{\mathbf{q}}_r) \tag{14}$$

while the user-commanded torques $\boldsymbol{\tau}_{cmd}$ remained in the same form as in Eq. (3).

The mass and inertia part of the vector $\hat{\boldsymbol{\theta}} \in \mathrm{R}^{21\times 1}$ (Eq. (7)) consisted of the following 7 dynamic parameters ($m_2 r_{y_2}$ was omitted as it does not generate any torque in Eq. (3) because of the gravity acceleration being set to zero):

$$\hat{\boldsymbol{\theta}}_{rbd} = \left[J_{xx_2}\ J_{zz_2}\ m_4 r_{y_4}\ J_{xx_4}\ J_{zz_4}\ m_5 r_{y_5}\ m_6 r_{y_6}\right]^T_{1\times 7}, \tag{15}$$

while the viscous and Coulomb friction coefficients were grouped in the following order:

$$\hat{\boldsymbol{\theta}}_f = \left[F_{v_1}\ \ldots\ F_{v_7}\ F_{C_1} \ldots\ F_{C_7}\right]^T_{1\times 14}. \tag{16}$$

The dynamic parameters $\hat{\boldsymbol{\theta}}_{rbd}$ (Eq. (15)) were initialized with the values from Table 2 while the friction parameters $\hat{\boldsymbol{\theta}}_f$ (Eq. (16)) were initialized with zeroes. The parameters were updated according to the discrete version of Eq. (10):

$$\hat{\boldsymbol{\theta}} = \hat{\boldsymbol{\theta}}_{prev} - \Gamma\mathbf{Y}^T(\mathbf{q}, \dot{\mathbf{q}}, \dot{\mathbf{q}}_r, \ddot{\mathbf{q}}_r)\mathbf{s}\Delta t \tag{17}$$

where $\hat{\boldsymbol{\theta}}_{prev}$ is the estimate of the dynamic parameters from the previous step and Δt is a length of the time step.

As the FRI allows to read the measured joint positions but not the velocities, the Kalman filter [12] had to be implemented in C++ to estimate the joint velocities. Because the computation time of Eqs. (3) and (17) in each time step never exceeded 0.3 ms (using the Dell Vostro 3900 PC with 8 GB RAM and Intel® Core™ i5-4460 CPU @ 3.20 GHz × 4), the FRI was exchanging measured and commanded data each 1 ms (i.e., in the fastest possible way).

4 Experimental Validation

The end effector trajectory for the experiment was designed to contain the linear and circular segments. The desired joint positions $\mathbf{q}_d$, velocities $\dot{\mathbf{q}}_d$ and accelerations $\ddot{\mathbf{q}}_d$ were precomputed, for use in the controller, by solving offline the inverse kinematics task. As LWR 4+ is a redundant robot, damping on the null-space motion was introduced in the inverse kinematics solution to ensure all the joints coming to rest when the end effector stops [6].

The result of the experiment is shown in Fig. 1 with the actual trajectory of the end effector in solid line and desired in dashed line. It is clearly visible that the end effector does not perfectly track the reference path. However, the shape of the actual trajectory is similar to the desired one. Furthermore, Fig. 2 shows good position tracking of the first joint (again – actual positions in solid line and desired in dashed). On the other hand, position errors are bigger on the seventh joint (see Fig. 3). Overall, the position tracking of joints 1 to 4 is much better than of joints 5 to 7.

The last three links are much lighter than the first four and therefore effects like friction (rather than inertia) dominate their dynamics. Various attempts were made to improve the behavior of that lighter joints. Increasing the gains $\mathbf{K}$ and Λ did not result with noticeably better outcome. Similarly, modifying the elements of Γ responsible for the speed of adaptation of the friction parameters of the last three joints did not improve the situation, as it led to inducing vibrations of that joints.

The biggest position errors are visible during joints' braking and accelerating from rest, suggesting the insufficient stiction compensation. Therefore, the attempt to smooth the Coulomb friction model was made. Based on [1], the sign function

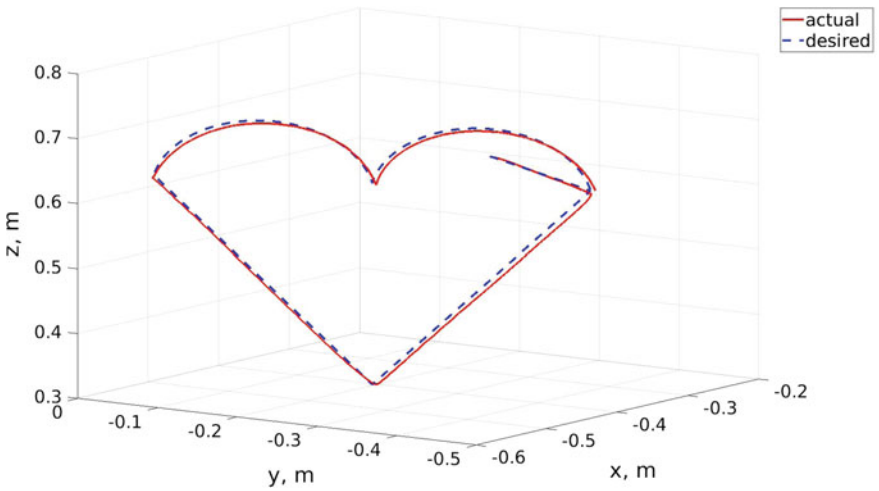

Fig. 1 Comparison of actual and desired positions of the robot end effector

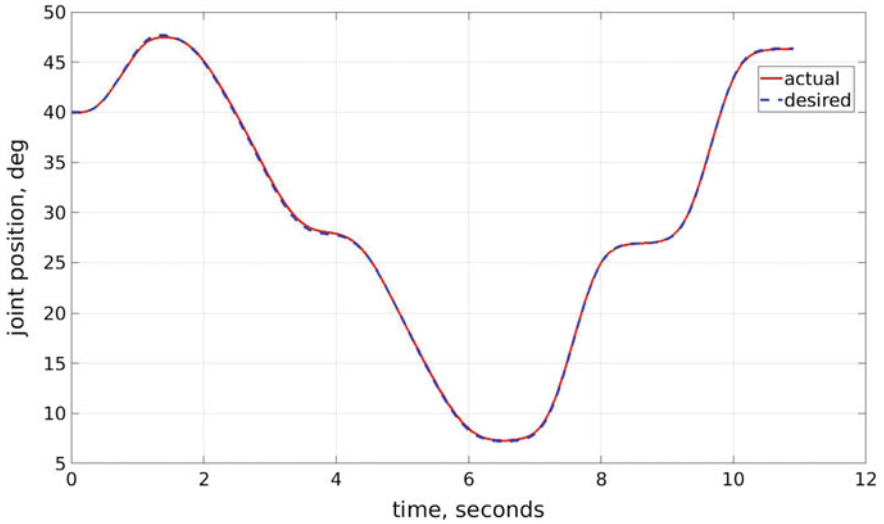

Fig. 2 Comparison of actual and desired positions of joint 1

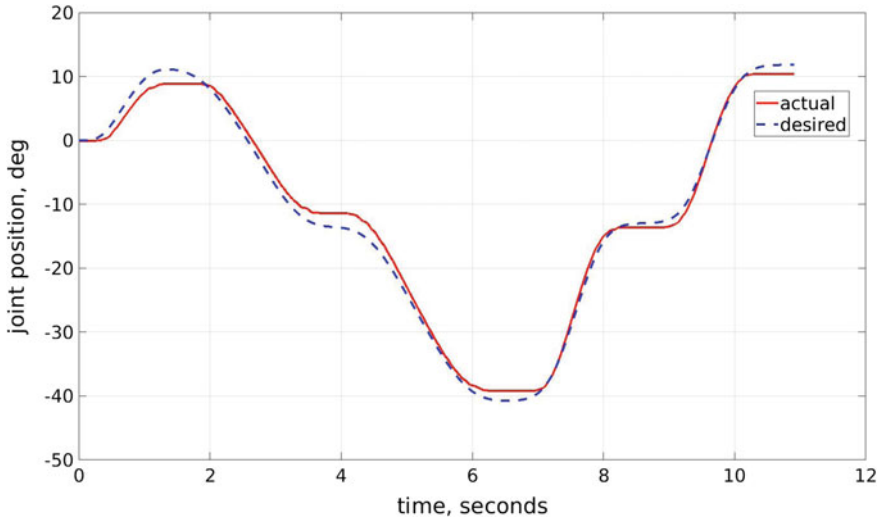

Fig. 3 Comparison of actual and desired positions of joint 7

was changed to the arctangent to avoid sudden changes of the control torque (and, in turn, vibration of the joints):

$$\tau_{C_j} = \tfrac{2}{\pi} F_{C_j} atan(A\dot{q}_{r_j}),\ j = 1, \ldots, 7 \tag{18}$$

with different values of the scaling parameter A (ranging from 5 to 1000). Again, it did not increase the control quality nor eliminated the oscillations problem.

The cause of the control problems with the last three joints probably lies in unmodeled effects. Perhaps the Coulomb friction model should be more advanced and include more sophisticated terms than the simple sign function or arctangent from Eq. (18). As this phenomenon involves discontinuities (caused by the appearance of the zero relative velocity between two neighboring links connected by a revolute joint), a model of the stick-slip dynamics should be considered [20].

It is worth noting that the authors of [2] received similar results, that is, the good position tracking for the first four joints but worse for the last three. As their model-based controller (with constant, time-invariant parameters) worked with the sampling time of 10 ms, they suggested that lower sampling period would improve the tracking performance. However, as described earlier, the adaptive controller of the author of this project works with the smallest possible sampling time in FRI, which is 1 ms. It is conceivable that there is not much room to drastically improve the quality of one's own position controller as FRI allows only the high-level access, and the low-level internal KUKA servocontrollers work with a cycle rate of 3 kHz [3], i.e. much faster than the FRI is communicating with the user's computer.

5 Conclusions

In this paper, an implementation of the adaptive controller for the KUKA LWR 4+ robot was presented. The dynamic model of the manipulator was discussed and the controller was described. The experimental validation of the implemented controller (position tracking task) is shown and the results are discussed. Although the control quality is not perfect, the results are promising. Future works will include testing more stiction models to improve the position tracking. Furthermore, including the measurements from the LWR's joint torque sensors in the control algorithm is planned to enable interaction with the environment.

Acknowledgements This work was supported by the Faculty of Power and Aeronautical Engineering Dean's Grant for year 2017.

References

1. Awrejcewicz, J., Olejnik, P.: Stick-slip dynamics of a two-degree-of-freedom system. Int. J. Bifurcation Chaos **13**(04), 843–861 (2003). URL https://www.worldscientific.com/doi/abs/10.1142/S0218127403006960
2. Bargsten, V., Zometa, P., Findeisen, R.: Modeling, parameter identification and model-based control of a lightweight robotic manipulator. In: 2013 IEEE International Conference on Control Applications (CCA), pp. 134–139 (2013). https://doi.org/10.1109/CCA.2013.6662756

3. Bischoff, R., Kurth, J., Schreiber, G., Koeppe, R., Albu-Schaeffer, A., Beyer, A., Eiberger, O., Haddadin, S., Stemmer, A., Grunwald, G., Hirzinger, G.: The KUKA-DLR lightweight robot arm – a new reference platform for robotics research and manufacturing. In: ISR 2010 (41st International Symposium on Robotics) and ROBOTIK 2010 (6th German Conference on Robotics), pp. 1–8 (2010)
4. Bottero, A., Gerio, G., Perna, V., Gagliano, A.: Adaptive control techniques and feed forward compensation of periodic disturbances in industrial manipulators. In: 2014 IEEE/ASME 10th International Conference on Mechatronic and Embedded Systems and Applications (MESA), pp. 1–7 (2014). https://doi.org/10.1109/MESA.2014.6935612
5. Brahmi, B., Saad, M., Ochoa-Luna, C., Rahman, M.H.: Adaptive control of an exoskeleton robot with uncertainties on kinematics and dynamics. In: 2017 International Conference on Rehabilitation Robotics (ICORR), pp. 1369–1374, (2017). https://doi.org/10.1109/ICORR.2017.8009439
6. Flacco, F., De Luca, A.: Discrete-time redundancy resolution at the velocity level with acceleration/torque optimization properties. Rob. Autonomous Syst. **70**, 191–201 (2015). https://doi.org/10.1016/j.robot.2015.02.008, URL http://www.sciencedirect.com/science/article/pii/S0921889015000329
7. Gaz, C., Flacco, F., Luca, A.D.: Identifying the dynamic model used by the KUKA LWR: a reverse engineering approach. In: 2014 IEEE International Conference on Robotics and Automation (ICRA), pp. 1386–1392 (2014). https://doi.org/10.1109/ICRA.2014.6907033
8. Gaz, C., Flacco, F., Luca, A.D.: Extracting feasible robot parameters from dynamic coefficients using nonlinear optimization methods. In: 2016 IEEE International Conference on Robotics and Automation (ICRA), pp. 2075–2081, (2016) https://doi.org/10.1109/ICRA.2016.7487356
9. Hao, J., Tao, G., Rugthum, T.: A dynamic prediction error based adaptive multiple-model control scheme for robotic manipulators. In: 2017 American Control Conference (ACC), pp. 1791–1796 (2017). https://doi.org/10.23919/ACC.2017.7963212
10. Hayat, R., Buss, M.: Model identification for robot manipulators using regressor-free adaptive control. In: 2016 UKACC 11th International Conference on Control (CONTROL), pp. 1–7 (2016). https://doi.org/10.1109/CONTROL.2016.7737544
11. Jubien, A., Gautier, M., Janot, A.: Dynamic identification of the Kuka LightWeight robot: comparison between actual and confidential KUKA's parameters. In: Proceedings of the IEEE/ASME International Conference on Advanced Intelligent Mechatronics 2014, Besancon, France, pp. 483–488 (2014)
12. Kalman, R.E.: A new approach to linear filtering and prediction problems. J. Basic Eng. **82**(1), 35–45 (1960)
13. Kawasaki, H., Bito, T., Kanzaki, K.: An efficient algorithm for the model-based adaptive control of robotic manipulators. IEEE Trans. Rob. Autom. **12**(3), 496–501 (1996)
14. Kelly, J., Davila, V.S., Loría, A.: Control of Robot Manipulators in Joint Space. Springer, London (2005)
15. Kröger, T.: Fast Research Interface Library. http://cs.stanford.edu/people/tkr/fri/html/annotated.html (2014). online; Accessed: 25 Apr (2017)
16. KUKA (06.07.2010) Lightweight Robot 4+ Specification, Version: Spez LBR 4+ V2en
17. Lewis, F.W., Dawson, D.M., Abdallah, C.T.: Robot Manipulator Control: Theory and Practice. CRC Press (2003)
18. Li, J., Ma, H., Yang, C., Fu, M.: Discrete-time adaptive control of robot manipulator with payload uncertainties. In: 2015 IEEE International Conference on Cyber Technology in Automation, Control, and Intelligent Systems (CYBER), pp. 1971–1976 (2015) https://doi.org/10.1109/CYBER.2015.7288249
19. Li, M., Li, Y., Ge, S.S., Lee, T.H.: Adaptive control of robotic manipulators with unified motion constraints. IEEE Trans. Syst.ems, Man, and Cyber.: Syst. **47**(1), 184–194 (2017). https://doi.org/10.1109/TSMC.2016.2608969
20. Olejnik, P., Awrejcewicz, J., Fečkan, M.: Modeling. With Friction and Impacts. World Scientific Publishing Company, Analysis and Control of. Dynamical Systems (2017). https://doi.org/10.1142/10577

21. Rodriguez, G., Jain, A., Kreutz-Delgado, K.: Spatial operator algebra for manipulator modelling and control. Int. J. Rob. Res. **10**(4), 371–381 (1991)
22. Schreiber, G., Stemmer, A., Bischoff, R.: The fast research interface for the KUKA lightweight robot. In: Proceedings of the IEEE ICRA 2010 Workshop on ICRA 2010 Workshop on Innovative Robot Control Architectures for Demanding (Research) Applications – How to Modify and Enhance Commercial Controllers, pp. 15–21 (2010)
23. Siciliano, B., Khatib, O. (eds.): Springer Handbook of Robotics. Springer International Publishing (2016). https://doi.org/10.1007/978-3-319-32552-1
24. Slotine, J.J.E., Bito, T., Li, W.: On the adaptive control of robot manipulators. Int. J. Rob. Res. **6**(3), 49–59 (1987)
25. Spong, M.W., Hutchinson, S., Vidyasagar, M.: Robot Modeling and Control. Wiley (2006)
26. Swevers, J., Ganseman, C., Tukel, D.B., De Schutter, J., Van Brussel, H.: Optimal robot excitation and identification. IEEE Trans. Rob. Autom. **13**(5), 730–740 (1997)
27. Swevers, J., Verdonck, W., De Schutter, J.: Dynamic model identification for industrial robots. IEEE Control Syst. **27**(5), 58–71 (2007)
28. Woliński, L., Malczyk, P.: Dynamic modeling and analysis of a lightweight robotic manipulator in joint space. Arch. Mechanical Eng. **62**(2), 279–302 (2015). http://dx.doi.org/10.1515/meceng-2015-0016, https://doi.org/10.1023/A:1021909032551
29. Woliński, L., Wojtyra, M.: Comparison of dynamic properties of two LWR 4+ robots. In: ROMANSY 21 - Robot Design, Dynamics and Control. Proceedings of the 21st CISM-IFToMM Symposium, vol. 569, pp. 413–420 (2016) https://doi.org/10.1007/978-3-319-33714-2

Vibrations of a Multi-span Beam Subjected to a Moving Stochastic Load

Filip Zakęś and Paweł Śniady

Abstract The dynamic behavior of multi-span uniform continuous beam excited by moving stochastic load is studied. In this paper we consider two models of moving load, namely: load described by space-time stochastic process and random train of concentrated forces moving with constant velocity. It is assumed that forces have random amplitudes and their appearance on the beam is described by point stochastic process (Poisson process). Solution of the problem in terms of expected values, variances and cumulants of the higher order (for the second case of load) was obtained by introducing dynamic influence function. In determination of the dynamic influence function Volterra integral equations was applied. Solution is illustrated with two numerical examples of 2- and 3-span beam.

Keywords Multi-span beam · Moving load · Stochastic vibrations

1 Introduction

The problem of a dynamic response of a structure subjected to a moving load is both interesting from the theoretical point of view and significant in structural designing. This problem occurs in dynamics of various types of structures such as bridges, roadways, railways and runways. Different types of structures and girders like beams, plates, shells, frames as well as different models of moving loads have been considered [1]. Most studies were focused on single-span girders like a string, a beam, a plate or a shell. An important and interesting problem are the vibrations of a multi-span beam caused by the moving load. There are many structures, for example bridges, which are multi-span. There are not so many papers focused on the dynamic

F. Zakęś (✉) · P. Śniady
Faculty of Environmental Engineering and Geodesy, Wroclaw University of Environmental and Life Sciences, Grunwaldzka, 55 50-357 Wroclaw, Poland
e-mail: filip.zakes@upwr.edu.pl

P. Śniady
e-mail: pawel.sniady@upwr.edu.pl

J. Awrejcewicz (ed.), *Dynamical Systems in Theoretical Perspective*,
Springer Proceedings in Mathematics & Statistics 248,
https://doi.org/10.1007/978-3-319-96598-7_32

response problem of the multi-span beam due to the moving load. Vibrations of a multi-span Bernoulli-Euler beam with an arbitrary geometry in each span subjected to moving forces [2–5], or moving masses [6, 7] or moving oscillators [8–10] have been considered. Also the vibration of a multi-span Timoshenko beam due to moving load have been considered [11, 12]. In terms of stochastic vibrations the analytical methods have been developed to determine probabilistic characteristics of dynamic response of a single-span beam [13], a suspension bridge [14] and a composite sandwich beam [15]. The impulse response function is frequently applied to cases of non-moving "white noise" type of stochastic loads. Recently published papers [16] and [17] including this type of random excitation are worth mentioning.

Main goal of this work is to propose a numerical method to determine probabilistic characteristics of a multi span Euler-Bernoulli uniform continuous beam subjected to two types of moving random load, namely load described by space-time stochastic process and random train of point forces moving with constant velocity. Solution of the problem in terms of expected values, variances and cumulants of the higher order was obtained by applying dynamic influence function instead of impulse response function.

2 Vibrations of Multi-span Beam Due to a Moving Force

Let us consider a uniform multi-span Euler-Bernoulli beam subjected to a force P moving with constant velocity v. The beam rests on $k+2$ supports (see Fig. 1), where intermediate supports are arbitrarily located. Number k corresponds with degree of static indeterminacy of the beam. In further analysis we will replace the multi-span beam with a simply supported one loaded with given moving force and k redundant forces $X_i(t)$ $(i = 1, 2, \ldots, k)$ situated in the positions of the intermediate supports (see Fig. 2).

Let us introduce dimensionless variables $\xi = \frac{x}{L}$ and $T = \frac{vt}{L}$. Equation of motion describing vibrations of the beam resulting from the moving force P has the form:

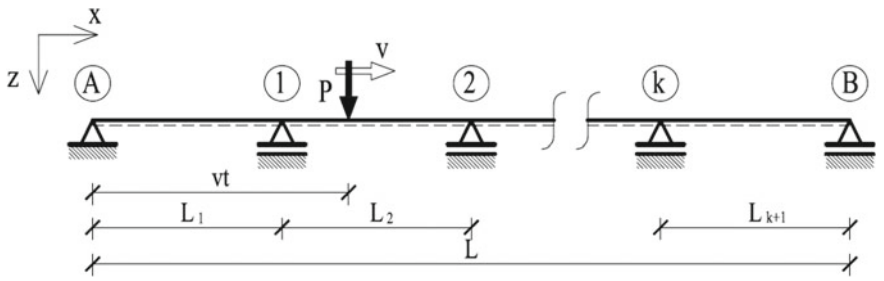

Fig. 1 A multi-span beam subjected to a moving force

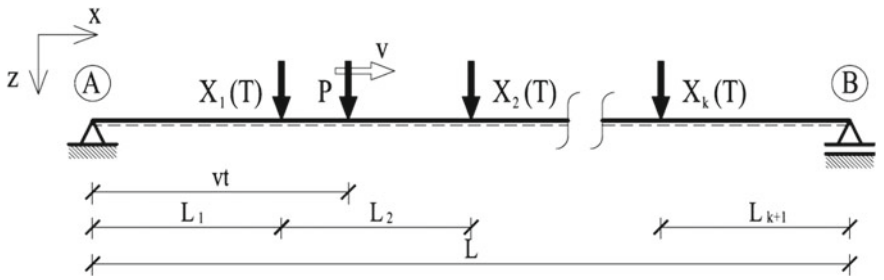

Fig. 2 A single-span beam subjected to a moving force and "k" redundant forces

$$\left[w^P(\xi,T)\right]^{IV} + c_o\dot{w}^P(\xi,T) + \sigma^2\ddot{w}^P(\xi,T) = P_0\delta(\xi - T), \tag{1}$$

while vibrations due to a concentrated time-varying force $X_i(T)$ can be described as:

$$\left[w^{X_i}(\xi,T)\right]^{IV} + c_o\dot{w}^{X_i}(\xi,T) + \sigma^2\ddot{w}^{X_i}(\xi,T) = X_{0i}(T)\delta(\xi - \xi_i), \tag{2}$$

where: $c_0 = c\frac{vL^3}{EI}$, $\sigma^2 = \frac{mv^2L^2}{EI}$, $P_0 = \frac{PL^3}{EI}$, $X_{0i} = \frac{X_i(T)L^3}{EI}$. EI, L, m and c denote flexural rigidity, length of the beam, mass per unit length and damping coefficient respectively. Roman numerals in Eqs. (1) and (2) denote differentiation with respect to spatial coordinate ξ while dots $(\cdot)$ denote differentiation with respect to dimensionless time T. Vibrations of the simply supported beam resulting from the moving force have the form:

$$\begin{aligned}
w^P(\xi,T) = {} & 2P_0\sum_{n=1}^{\infty}\frac{\left[(n\pi)^2-\sigma^2\right]\sin n\pi T\sin n\pi\xi}{(n\pi)^2\left[(n\pi)^2-\sigma^2\right]^2+4\alpha^2\sigma^4} \\
& - 4P_0\alpha\sigma^2\sum_{n=1}^{\infty}\frac{\cos n\pi T\sin n\pi\xi}{(n\pi)\left\{\left[(n\pi)^2-\sigma^2\right]^2+4\alpha^2\sigma^4\right\}} \\
& + 4P_0\alpha^2\sigma^2e^{-\alpha T}\sum_{n=1}^{\infty}\frac{\sin\Omega_n T\sin n\pi\xi}{\Omega_n(n\pi)\left\{(n\pi)^2\left[(n\pi)^2-\sigma^2\right]^2+4\alpha^2\sigma^4\right\}} \\
& - 2P_0e^{-\alpha T}\sum_{n=1}^{\infty}\frac{(n\pi)\left[(n\pi)^2-\sigma^2\right]\sin\Omega_n T\sin n\pi\xi}{\Omega_n\left\{(n\pi)^2\left[(n\pi)^2-\sigma^2\right]^2+4\alpha^2\sigma^4\right\}} \\
& + 4P_0\alpha\sigma^2e^{-\alpha T}\sum_{n=1}^{\infty}\frac{\cos\Omega_n T\sin n\pi\xi}{(n\pi)\left\{(n\pi)^2\left[(n\pi)^2-\sigma^2\right]^2+4\alpha^2\sigma^4\right\}},
\end{aligned} \tag{3}$$

while solution for the case of concentrated time-varying force can be presented in the convolution form:

$$\left[w^P(\xi,T)\right]^{IV} + c_o\dot{w}^P(\xi,T) + \sigma^2\ddot{w}^P(\xi,T) = P_0\delta(\xi - T), \tag{4}$$

where $h_i(\xi, T)$ is the impulse response function described as:

$$h_i(\xi,T) = \frac{2vL^2}{\sigma^2 EI}e^{-\alpha T}\sum_{n=1}^{\infty}\frac{\sin\Omega_n T \sin n\pi\xi_i \sin n\pi\xi}{\Omega_n}, \tag{5}$$

where $\alpha = \frac{cL}{2mv}$ and $\Omega_n = \sqrt{\frac{(n\pi)^4}{\sigma^2} - \alpha^2}$.

By combining solutions presented above we can present vibrations of the multi-span beam as:

$$w(\xi,T) = \frac{L}{v}\sum_{i=1}^{k}\int_0^T h_i(\xi, T-\tau)X_i(\tau)d\tau + w^P(\xi,T). \tag{6}$$

Functions $X_i(T)$ describing reactions in the intermediate supports are obtained from Volterra integral equations of the first order:

$$\frac{L}{v}\sum_{i=1}^{k}\int_0^T h_i\left(\xi_j, T-\tau\right)X_i(\tau)d\tau + w^P(\xi_i,T) = 0 \quad kj = 1,2,\ldots,k. \tag{7}$$

Zero value on the right side of the Eq. (7) corresponds with zero deflection at the position ξ_i of the "i" intermediate support. Numerical procedure of solving Volterra integral equations as well as more detailed description of the method presented above was given in the authors previous works [18, 19].

3 Stochastic Moving Load

There are many cases when moving load has to be described as a stochastic process, particularly the motions of vehicles on a bridge. Solution for a multi-span beam excited by a moving point force can be used to determine probabilistic characteristics of a dynamic response resulting from the moving random load. For this purpose let us introduce the dynamic influence function $H(\xi, T)$ which describes vibrations of the multi span beam due to a unitary concentrated force $P = 1$. In further calculations it will be used instead of impulse response function in analysis of two types of moving random loads. In the first case we assume the random moving load as a weak space-time stationary stochastic process (see Fig. 3) and in the second one the beam is subjected to a random train of moving forces (see Fig. 4). Finding solution by using the direct eigen function transformation, as can be done in other types of stochastic excitations is difficult even for a single span beam. Therefore method based on the

dynamic influence function and the numerical procedures for the multi-span beam will be applied.

3.1 Space-Time Stationary Stochastic Process

Let us consider a beam subjected to a moving load process $p(x - vt) = p[L(\xi - T)]$ which can be considered as a weak space-time stationary stochastic process (see Fig. 3). Load is presented as a sum of deterministic and stochastic part:

$$p(x - vt) = \bar{p} + \tilde{p}(x - vt) = \bar{p} + \tilde{p}[L(\xi - T)] = \bar{p} + \tilde{p}(L\tau), \tag{8}$$

where $\bar{p} = const.$ and $E\left[\tilde{p}(x - vt)\right] = 0$. Symbol $E[]$ denotes expected value.

Solution for the deterministic part $\bar{p} = const.$ is presented above. Therefore we shall focus only on the vibration of the beam resulting from the stochastic load. Let as assume that the covariance function of the load process is known and has the form:

$$C_{PP}(\tau_1, \tau_2) = E\left[\tilde{p}(L\tau_1)\tilde{p}(L\tau_2)\right] = C_{PP}[L(\tau_1 - \tau_2)]. \tag{9}$$

If we take into account only the load which at given time T is on the beam, the dynamic response will be presented as:

$$w(\xi, T) = \frac{L}{v} \int_{T-1}^{T} H(\xi, T - \tau)\tilde{p}(L\tau)d\tau. \tag{10}$$

and therefore the variance of the beam deflection has the form:

$$\sigma_w^2(\xi, T) = \left(\frac{L}{v}\right)^2 \int_0^1 \int_0^1 H(\xi, \tau_1)H(\xi, \tau_2)C_{PP}[L(\tau_1 - \tau_2)]d\tau_1 d\tau_2. \tag{11}$$

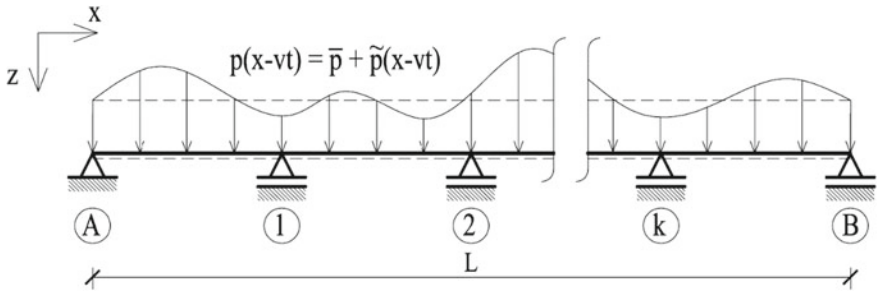

Fig. 3 Multi-span beam subjected to a space-time stochastic process

Let us assume the moving excitation as a stationary "white noise" where covariance function of the load is described as:

$$C_{PP}[L(\tau_1 - \tau_2)] = \sigma_P^2 \delta[L(\tau_1 - \tau_2)], \tag{12}$$

where σ_P^2 is the variance of the load and δ denotes the Dirac delta. Substituting expression (12) into Eq. (11) we obtain integral formulae for the variance of the deflection of the multi-span beam:

$$\sigma_w^2(\xi, T) = \frac{\sigma_P^2 L}{v^2} \int_0^1 H^2(\xi, T - \tau) d\tau. \tag{13}$$

3.2 Random Train of Moving Forces

Let us consider a multi-span beam loaded by a train of moving forces (see Fig. 4). All of the forces A_r move in the same direction with equal velocity v. Times t_r of the forces arrival at the beam are random and described by a Poisson process $N(t)$ with parameter λ:

$$E[dN(t)] = \lambda dt; \quad E\left[d^2N(t)\right] = \lambda dt,$$

$$E[dN(t_1)dN(t_2)] = \lambda^2 dt_1 dt_2 \quad \text{for } t_1 \neq t_2. \tag{14}$$

The dynamic response of the multi-span beam can be presented in the form of a Stieltjes stochastic integral with respect to the Poisson process in terms of dimensionless variables ξ and T:

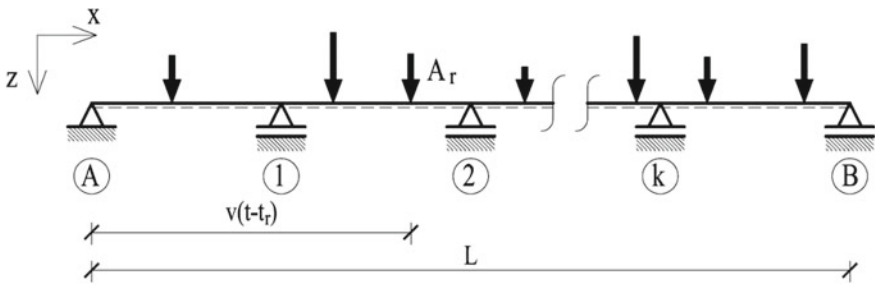

Fig. 4 Multi-span beam subjected to a random train of moving forces

$$w(\xi, T) = \frac{L}{v} \int_0^T A(\tau) H(\xi, T - \tau) dN(\tau). \tag{15}$$

where amplitudes $A(\tau)$ are random variables that are mutually independent and independent of the instant τ. We assume that expected values $E[A^s(\tau)] = E[A^s] = const.$ for $s = 1, 2, 3 \ldots$ are known. Taking into account the Poisson process properties we obtain formulas for the expected value $E[w(\xi, T)]$, variance $\sigma_w^2(\xi, T)$ and cumulants of the s-order $\kappa_w^s(\xi, T)$ of the multi-span beam deflection:

$$E[w(\xi, T)] = E[A]\lambda \frac{L}{v} \int_0^T H(\xi, T - \tau) d\tau, \tag{16}$$

$$\sigma_w^2(\xi, T) = E\left[A^2\right]\lambda \frac{L}{v} \int_0^T H^2(\xi, T - \tau) d\tau, \tag{17}$$

$$\kappa_w^s(\xi, T) = E\left[A^s\right]\lambda \frac{L}{v} \int_0^T H^s(\xi, T - \tau) d\tau. \tag{18}$$

4 Numerical Examples

4.1 Two-Span Beam

First example is of a two-span beam subjected to space-time stationary stochastic load (see Fig. 5). Total length of the beam is equal to $L = 40$ m, its flexural rigidity is equal to $EI = 2 \times 10^9$ Nm^2 and mass per unit length $m = 1000$ kg/m. Figure 6

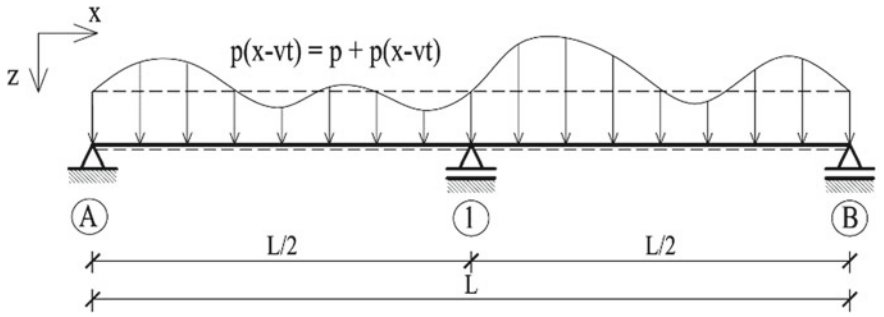

Fig. 5 Two-span beam subjected to a space-time stochastic process

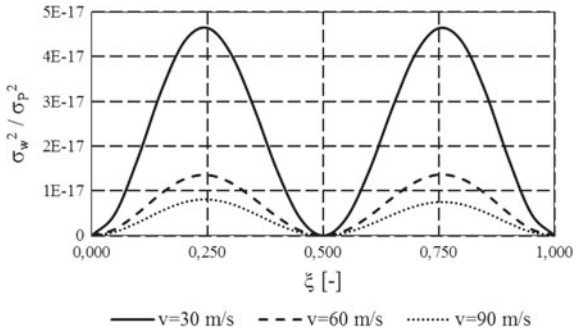

Fig. 6 Variance of the beam deflection at time $T = 1$

presents variance of the beam deflection due to a stochastic load moving with various velocities v equal to 30, 60 and 90 m/s.

4.2 Three-Span Beam

In the second example we shall consider three-span beam subjected to a random train of moving forces (see Fig. 7). Total length of the beam is equal to $L = 60$ m while the other beam properties EI and m are the same as in the previous example. Three various velocities v equal to 30, 60 and 90 m/s have been analyzed. Figure 8 presents the expected value of beam deflection in the middle of left, central and right span as well as expected value of the beam deflection at time $T = 1$. Figure 9 presents variances of the beam deflection. It can be observed that both expected values and variances of the dynamic response decrease while load velocity increases.

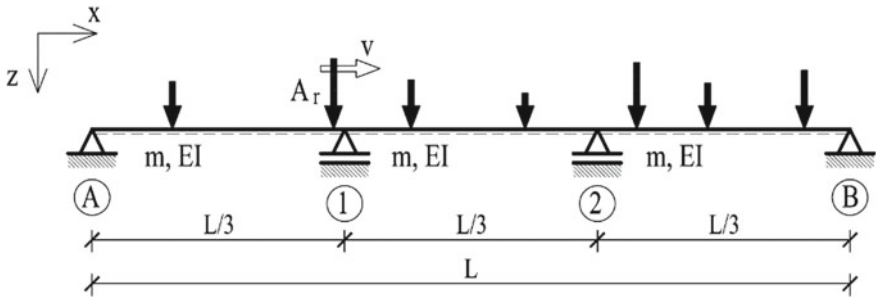

Fig. 7 Three-span beam subjected to a random stream of moving forces

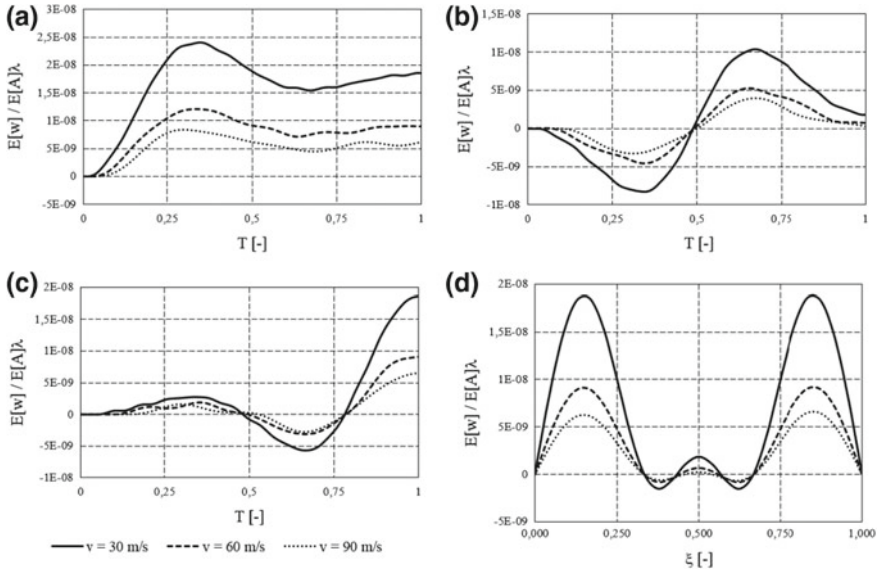

Fig. 8 Variance Expected value of the beam deflection **a** in the middle of left span, **b** in the middle of the central span, **c** in the middle of the right span, **d** expected value of beam deflection at time $T = 1$

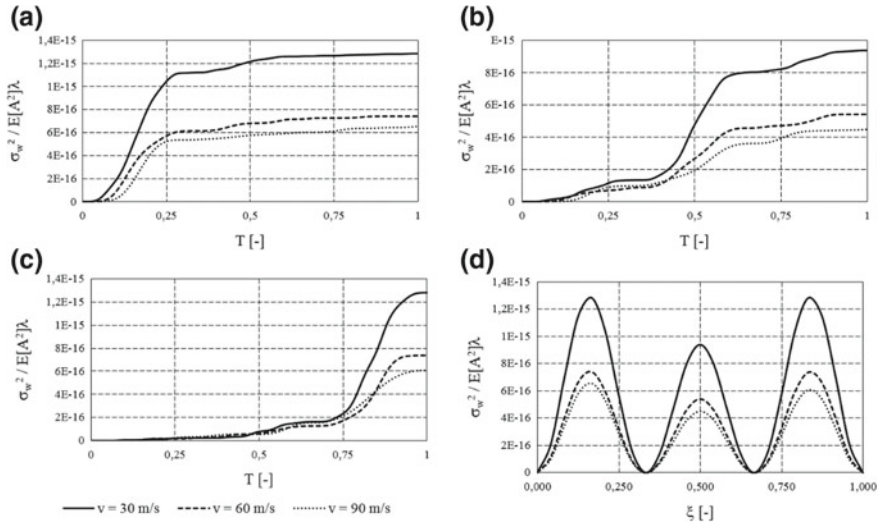

Fig. 9 Variance of the beam deflection **a** in the middle of left span, **b** in the middle of the central span, **c** in the middle of the right span, **d** variance of beam deflection at time $T = 1$

5 Conclusions

In this paper an analytical-numerical method of determining vibrations of a multi-span uniform continuous Euler-Bernoulli beam resulting from the moving random load was presented. Main idea of the method is to introduce dynamic influence function instead of impulse response function which leads to simple integral formulas that are convenient in numerical calculations. By applying Volterra integral equations of the first order, known analytical solutions for the simply supported beam loaded with moving force and concentrated time-varying force can be used in analysis of more complex system that is a multi-span beam.

In the paper two models of moving stochastic load was considered. The first one is space-time stationary stochastic "white noise" process and the second one is random stream of moving point forces arriving at the beam according to Poisson process with parameter λ which can simulate traffic flow on the bridge. Two numerical examples was presented in order to show the effectiveness of proposed method. Results show that with the increase of load speed the probabilistic characteristics of dynamic response (expected value and variance) decrease.

After introduction of proper modifications presented method can be expanded for beams with different boundary conditions or beams with elastic intermediate supports [18]. It is also possible to apply the method in analysis of more complex structures such as plates subjected to moving stochastic load.

References

1. Fryba, L.: Vibration of solids and structures under moving loads. Telford, London (1999)
2. Johansson, C., Pacoste, C., Karoumi, R.: Closed-form solution for the mode superposition analysis of the vibration in multi-span beam bridges caused by concentrated moving loads. Comput. Struct. **119**, 85–94 (2013). Elsevier
3. Dugush, Y.A., Eisenberger, M.: Vibrations of non-uniform continuous beams under moving loads. J. Sound Vib. **245**, 911–926 (2002). Elsevier
4. Martinez-Castro, A.E., Museros, P., Castello-Linares, A.: Semi-analytic solution in the time domain for non-uniform multi-span Bernoulli-Euler beams traversed by moving loads. J. Sound Vib. **294**, 278–297 (2006). Elsevier
5. Salvo, V.D., Muscolino, G., Palmeri, A.: A substructure approach tailored to the dynamic analysis of multi-span continuous beams under moving loads. J. Sound Vib. **329**, 3101–3120 (2010). Elsevier
6. Ichikawa, M., Miyakawa, Y., Matsuda, A.: Vibration analysis of the continuous beam subjected to a moving mass. J. Sound and Vib. **230**, 493–506 (2000). Elsevier
7. Lee, H.P.: Dynamic response of a beam on multiple supports with a moving mass. Struct. Eng. Mech. **4**, 303–312 (1996). Techno-press
8. Yang, Y.B., Liao, S.S., Lin, B.: Impact formulas for vehicle moving over simple and continuous beams. J. Struct. Eng. **121**, 1644–1650 (1995). ASCE
9. Cheung, Y.K., Au, F.T.K., Zheng, D.Y., Cheng, Y.S.: Vibration of multi-span non-uniform bridges under moving vehicles and trains by using modified beam vibration functions. J. Sound Vib. **228**, 611–628 (1999). Elsevier
10. Chatterjee, P.K., Datta, T.K., Surana, C.S.: Vibration of continuous bridges under moving vehicle. J. Sound Vib. **169**, 619–632 (1994). Elsevier

11. Ariaei, A., Ziaei-Rad, S., Malekzadeh, M.: Dynamic response of a multi-span Timoshenko beam with internal and external flexible constraints subject to a moving mass. Arch. Appl. Mech. **83**, 1257–1272 (2013). Springer
12. Wang, R.-T., Lin, T.-Y.: Random vibration of multi-span Timoshenko beam due to a moving load. J. Sound Vib. **213**, 127–138 (1998). Elsevier
13. Iwankiewicz, T.: Śniady P: Vibration of a beam under a random stream of moving forces. J. Struct. Mech. **12**, 13–26 (1984)
14. Bryja, D., Śniady, P.: Random vibration of a suspension bridge due to highway traffic. J. Sound Vib. **125**, 379–387 (1988). Elsevier
15. Misiurek, K., Śniady, P.: Stochastic vibrations of sandwich beam traversed by random moving load. J. Civil Eng. Env. Architec. **61**, 119–130 (2013). Publishing House Rzeszow University of Technology
16. Awrejcewicz, J., Krysko, A.V., Papkova, I.V., Zakharov, V.M., Eurofeev, N.P., Krylova, EYu., Mrozowski, J., Krysko, V.A.: Chaotic dynamics of flexible beams driven by external white noise. Mechanical Syst. Signal Process. **79**, 225–254 (2016). Elsevier
17. Krysko A.V., Awrejcewicz J., Papkova I.V., Szymanowska O., Krypko V.A.: Principal component analysis in the nonlinear dynamics of beams: Purification of the signal from noise induced by the nonlinearity of beam vibrations. Adv. Math. Phys. 1–9 (2017). Hindawi
18. Zakęś, F. Śniady, P.: Application of Volterra integral equations in dynamics of multispan uniform continuous beams subject to a moving load. Shock Vib. 1–12 (2016). Hindawi
19. Śniady, P., Zakęś, F.: Vibrations of multi-span continuous beams under moving force. J. Civil Eng. Env. Architec. **61**, 185–195 (2014). Publishing House Rzeszow University of Technology